

## 1

**Inorganic Semiconductors for Light-emitting Diodes**

*E. Fred Schubert, Thomas Gessmann, and Jong Kyu Kim*

## 1.1

**Introduction**

During the past 40 years, light-emitting diodes (LEDs) have undergone a significant development. The first LEDs emitting in the visible wavelength region were based on GaAsP compound semiconductors with external efficiencies of only 0.2%. Today, the external efficiencies of red LEDs based on AlGaInP exceed 50%. AlGaInP semiconductors are also capable of emitting at orange, amber, and yellow wavelengths, albeit with lower efficiency. Semiconductors based on AlGaInN compounds can emit efficiently in the UV, violet, blue, cyan, and green wavelength range. Thus, all colors of the visible spectrum are now covered by materials with reasonably high efficiencies. This opens the possibility to use LEDs in areas beyond conventional signage and indicator applications. In particular, LEDs can now be used in high-power applications thereby enabling the replacement of incandescent and fluorescent sources. LED lifetimes exceeding  $> 10^5$  h compare favorably with incandescent sources ( $\sim 500$  h) and fluorescent sources ( $\sim 5000$  h), thereby contributing to the attractiveness of LEDs.

Inorganic LEDs are generally based on p-n junctions. However, in order to achieve high internal quantum efficiencies, free carriers need to be spatially confined. This requirement has led to the development of heterojunction LEDs consisting of different semiconductor alloys and multiple quantum wells embedded in the light-emitting active region. The light-extraction efficiency, which measures the fraction of photons leaving the semiconductor chip, is strongly affected by the device shape and surface structure. For high internal-efficiency active regions, the maximization of the light-extraction efficiency has proven to be the key to high-power LEDs.

This chapter reviews important aspects of inorganic LED structures. Section 1.2 introduces the basic concepts of optical emission. Band diagrams of direct and indirect semiconductors and the spectral shape of spontaneous emission will be discussed along with radiative and nonradiative recombination processes. Spontaneous emission can be controlled by placing the active region in an optical

cavity resulting in a substantial modification of the LED emission characteristics. Theory and experimental results of such resonant-cavity LEDs (RCLEDs) are discussed in Section 1.3. The electrical characteristics of LEDs, to be discussed in Section 1.4, include parasitic voltage drops and current crowding phenomena that result in nonuniform light emission and shortened device lifetimes. Due to total internal reflection at the surfaces of an LED chip, the light-extraction efficiency in standard devices is well below 100 %. Section 1.5 discusses techniques such as chip shaping utilized to increase the extraction efficiency. A particular challenge in achieving efficient LEDs is the minimization of optical absorption processes inside the semiconductor. This can be achieved by covering absorbing regions, such as lower-bandgap substrates, with highly reflective mirrors. Such mirrors should have omnidirectional reflection characteristics and a high angle-integrated, TE-TM averaged reflectivity. A novel electrically conductive omnidirectional reflector is discussed in Section 1.6. Section 1.7 reviews the current state of the art in LED packaging including packages with low thermal resistance.

## 1.2 Optical Emission Spectra

The physical mechanism by which semiconductor light-emitting diodes (LEDs) emit light is spontaneous recombination of electron-hole pairs and simultaneous emission of photons. The spontaneous emission process is fundamentally different from the stimulated emission process occurring in semiconductor lasers and superluminescent LEDs. The characteristics of spontaneous emission that determine the optical properties of LEDs will be discussed in this section.

The probability that electrons and holes recombine *radiatively* is proportional to the electron and hole concentrations, that is,  $R \propto n p$ . The recombination rate per unit time per unit volume can be written as

$$R = -\frac{dn}{dt} = -\frac{dp}{dt} = B n p \quad (1.1)$$

where  $B$  is the *bimolecular recombination coefficient*, with a typical value of  $10^{-10} \text{ cm}^3/\text{s}$  for direct-gap III-V semiconductors.

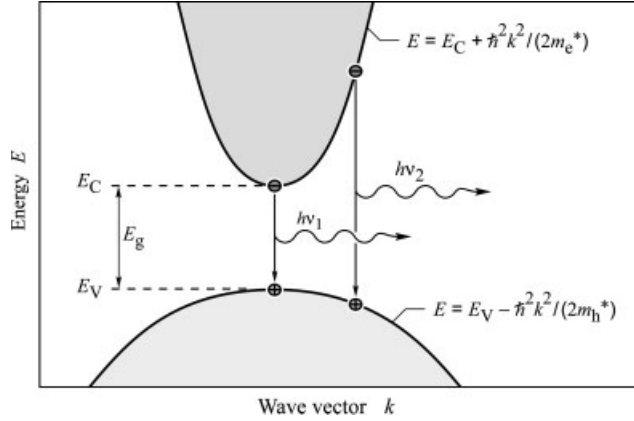
Electron-hole recombination is illustrated in Fig. 1.1. Electrons in the conduction band and holes in the valence band are assumed to have the parabolic dispersion relations

$$E = E_C + \frac{\hbar^2 k^2}{2 m_e^*} \quad (\text{for electrons}) \quad (1.2)$$

and

$$E = E_V - \frac{\hbar^2 k^2}{2 m_h^*} \quad (\text{for holes}) \quad (1.3)$$

**Fig. 1.1** Parabolic electron and hole dispersion relations showing “vertical” electron–hole recombination and photon emission.



where  $m_e^*$  and  $m_h^*$  are the electron and hole effective masses,  $\hbar$  is Planck's constant divided by  $2\pi$ ,  $k$  is the carrier wave number, and  $E_V$  and  $E_C$  are the valence and conduction band-edge energies, respectively.

The requirement of energy and momentum conservation leads to further insight into the radiative recombination mechanism. It follows from the Boltzmann distribution that electrons and holes have an average kinetic energy of  $kT$ . Energy conservation requires that the photon energy is given by the difference between the electron energy,  $E_e$ , and the hole energy,  $E_h$ , i. e.

$$\hbar \nu = E_e - E_h \approx E_g \quad (1.4)$$

The photon energy is approximately equal to the bandgap energy,  $E_g$ , if the thermal energy is small compared with the bandgap energy, that is,  $kT \ll E_g$ . Thus the desired emission wavelength of an LED can be attained by choosing a semiconductor material with appropriate bandgap energy. For example, GaAs has a bandgap energy of 1.42 eV at room temperature resulting in infrared emission of 870 nm.

It is helpful to compare the average carrier momentum with the photon momentum. A carrier with kinetic energy  $kT$  and effective mass  $m^*$  has the momentum

$$p = m^* v = \sqrt{2 m^* \frac{1}{2} m^* v^2} = \sqrt{2 m^* kT} \quad (1.5)$$

The momentum of a photon with energy  $E_g$  can be obtained from the de Broglie relation

$$p = \hbar k = \hbar \nu / c = E_g / c \quad (1.6)$$

Calculation of the carrier momentum (using Eq. (1.5)) and the photon momentum (using Eq. (1.6)) yields that the carrier momentum is *orders of magnitude lar-*

ger than the photon momentum. Therefore the electron momentum must not change significantly during the transition. The transitions are therefore “vertical” as shown in Fig. 1.1, i. e. electrons recombine with only those holes that have the same momentum or  $k$  value.

Using the requirement that electron and hole momenta are the same, the photon energy can be written as the *joint dispersion relation*

$$\hbar \nu = E_C + \frac{\hbar^2 k^2}{2 m_e^*} - E_V + \frac{\hbar^2 k^2}{2 m_h^*} = E_g + \frac{\hbar^2 k^2}{2 m_r^*} \quad (1.7)$$

where  $m_r^*$  is the reduced mass given by

$$\frac{1}{m_r^*} = \frac{1}{m_e^*} + \frac{1}{m_h^*} \quad (1.8)$$

Using the joint dispersion relation, the joint density of states can be calculated and one obtains

$$\rho(E) = \frac{1}{2\pi^2} \left( \frac{2 m_r^*}{\hbar^2} \right)^{3/2} \sqrt{E - E_g} \quad (1.9)$$

The distribution of carriers in the allowed bands is given by the Boltzmann distribution, i. e.

$$f_B(E) = e^{-E/(kT)} \quad (1.10)$$

The *emission intensity* as a function of energy is proportional to the product of Eqs. (1.9) and (1.10),

$$I(E) \propto \sqrt{E - E_g} e^{-E/(kT)} \quad (1.11)$$

The emission lineshape of an LED, as given by Eq. (1.11), is shown in Fig. 1.2. The maximum emission intensity occurs at

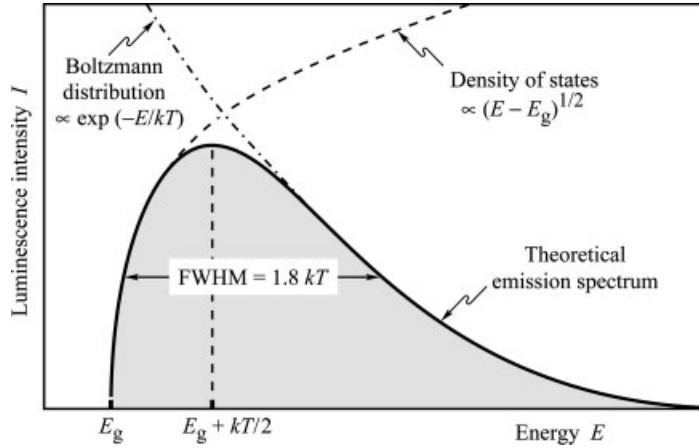
$$E = E_g + \frac{1}{2} kT \quad (1.12)$$

The full width at half maximum of the emission is given by

$$\Delta E = 1.8 kT \quad (1.13)$$

For example, the theoretical room-temperature linewidth of a GaAs LED emitting at 870 nm is  $\Delta E = 46$  meV or  $\Delta\lambda = 28$  nm.

The spectral linewidth of LED emission is important in several respects. *First*, the linewidth of an LED emitting in the visible range is relatively narrow compared with the range of the entire visible spectrum. The LED emission is even narrower than the spectral width of a single color as perceived by the human eye. For example, *red* colors range from 625 to 730 nm, which is much wider



**Fig. 1.2** Theoretical emission spectrum of an LED. The full width at half maximum (FWHM) of the emission line is  $1.8 kT$ .

than the typical emission spectrum of an LED. Therefore, LED emission is perceived by the human eye as *monochromatic*.

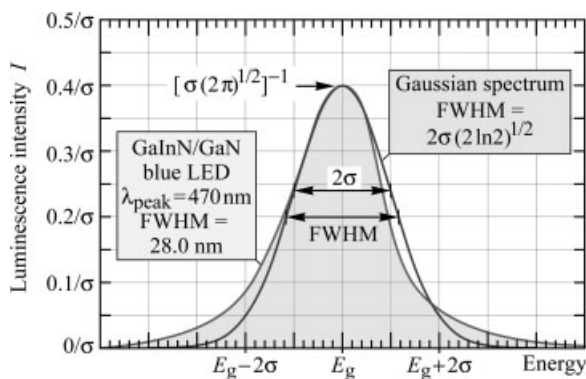
Secondly, optical fibers are dispersive, which leads to a range of propagation velocities for a light pulse comprising a range of wavelengths. The material dispersion in optical fibers limits the “*bit rate  $\times$  distance product*” achievable with LEDs. The spontaneous lifetime of carriers in LEDs in direct-gap semiconductors typically is of the order of 1–100 ns depending on the active region doping concentration (or carrier concentrations) and the material quality. Thus, modulation speeds up to 1 Gbit/s are attainable with LEDs.

A spectral width of  $1.8kT$  is expected for the thermally broadened emission. However, due to other broadening mechanisms, such as *alloy broadening* (i.e. the statistical fluctuation of the active region alloy composition), the spectral width at room temperature in III-V nitride LEDs can be broader, typically (3 to 8) $kT$ . Experimental evidence shown in Fig. 1.3 supports the use of a Gaussian function to describe the spectral power density function of an LED. Therefore,

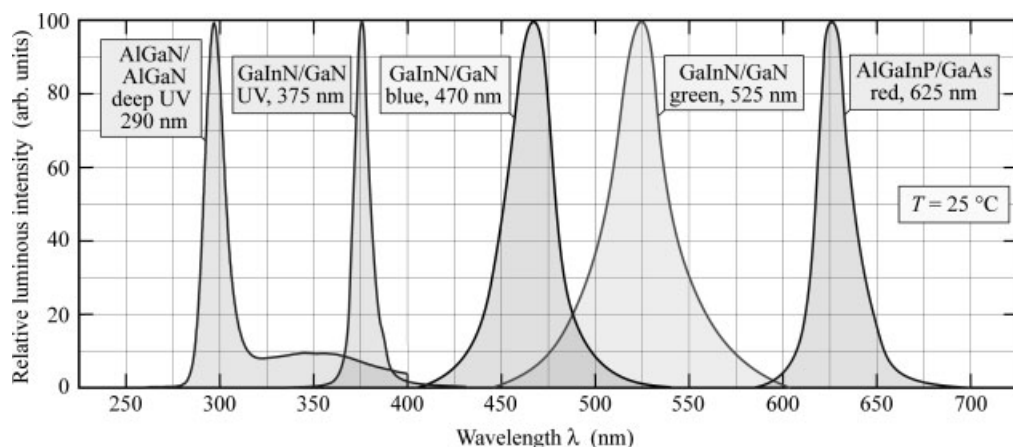
$$P(\lambda) = P \frac{1}{\sigma\sqrt{2\pi}} \exp \left[ -\frac{1}{2} \left( \frac{\lambda - \lambda_{\text{peak}}}{\sigma} \right)^2 \right] \quad (1.14)$$

where  $P$  is the total optical power emitted by the LED. Inspection of Fig. 1.3 indeed reveals that the Gaussian curve is a very good match for the experimental emission spectrum. Giving the line widths in terms of units of  $kT$  is very useful as it allows for convenient comparison with the theoretical line width of  $1.8kT$ .

The emission spectra of an AlGaInP red, a GaInN green, and a GaInN blue LED are shown in Fig. 1.4. The LEDs shown in Fig. 1.4 have an active region comprised of a ternary or quaternary alloy, e.g.  $\text{Ga}_{1-x}\text{In}_x\text{N}$ . In this case, alloy broadening leads to spectral broadening that goes beyond  $1.8kT$ . Alloy broadening due to inhomogeneous distribution of In in the active region of green  $\text{Ga}_{1-x}\text{In}_x\text{N}$  LEDs



**Fig. 1.3** Theoretical emission spectrum of a semiconductor exhibiting substantial alloy broadening. The full width at half maximum (FWHM) is related to the standard deviation ( $\sigma$ ) by the equation shown in the figure.



**Fig. 1.4** Emission spectrum of AlGaInP/GaAs red, GaInN/GaN green, GaInN/GaN blue, GaInN/GaN UV, and AlGaInP/GaAs deep UV LEDs at room temperature (adopted from refs. [3–5]).

can cause linewidths as wide as  $10kT$  at room temperature [1]. It should be noted, however, that a recent study found inhomogeneous strain distribution in GaInN quantum wells as a result of electron damage during TEM experiments [2]. It was concluded that the damage might lead to a “false” detection of In-rich clusters in a homogeneous quantum-well structure.

Efficient recombination occurs in direct-gap semiconductors. The recombination probability is much lower in indirect-gap semiconductors because a phonon is required to satisfy momentum conservation. The radiative efficiency of indirect-gap semiconductors can be increased by isoelectronic impurities, e.g. N in GaP. Isoelectronic impurities can form an optically active deep level that is localized in real space (small  $\Delta x$ ) but, as a result of the uncertainty relation, delocalized in  $k$  space (large  $\Delta k$ ), so that recombination via the impurity satisfies momentum conservation.

During *nonradiative* recombination, the electron energy is converted to vibrational energy of lattice atoms, i.e. phonons. There are several physical mechan-

isms by which nonradiative recombination can occur with the most common ones being recombination at point defects (impurities, vacancies, interstitials, antisite defects, and impurity complexes) and at spatially extended defects (screw and edge dislocations, cluster defects). The defects act as efficient recombination centers (Shockley–Read recombination centers) in particular, if the energy level is close to the middle of the gap.

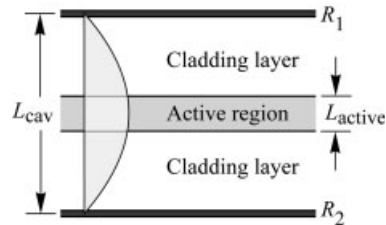
### 1.3

#### Resonant-cavity-enhanced Structures

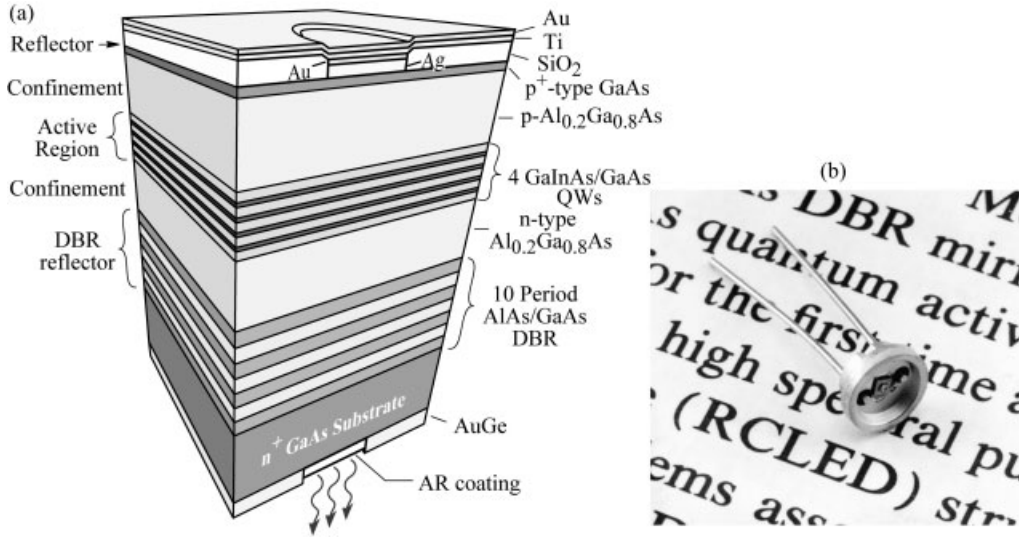
Spontaneous emission implies the notion that the recombination process occurs *spontaneously*, that is without a means to influence this process. In fact, spontaneous emission has long been believed to be uncontrollable. However, research in microscopic optical resonators, where spatial dimensions are of the order of the wavelength of light, showed the possibility of controlling the spontaneous emission properties of a light-emitting medium. The changes of the emission properties include the spontaneous emission rate, spectral purity, and emission pattern. These changes can be employed to make more efficient, faster, and brighter semiconductor devices. The changes in spontaneous emission characteristics in resonant-cavity (RC) and photonic-crystal (PC) structures were reviewed by Joannopoulos et al. [6].

Resonant-microcavity structures have been demonstrated with different active media and different microcavity structures. The first resonant-cavity structure was proposed by Purcell (1946) for emission frequencies in the radio frequency (rf) regime [7]. Small metallic spheres were proposed as the resonator medium. However, no experimental reports followed Purcell's theoretical publication. In the 1980s and 1990s, several resonant cavity structures have been realized with different types of optically active media. The active media included organic dyes [8, 9], semiconductors [10, 11], rare-earth atoms [12, 13], and organic polymers [14, 15]. In these publications, clear changes in spontaneous emission were demonstrated including changes in spectral, spatial, and temporal emission characteristics.

The simplest form of an optical cavity consists of two coplanar mirrors separated by a distance  $L_{\text{cav}}$  as shown in Fig. 1.5. About one century ago, Fabry and Perot were the first to build and analyze optical cavities with coplanar reflectors



**Fig. 1.5** Schematic illustration of a resonant cavity consisting of two metal mirrors with reflectivity  $R_1$  and  $R_2$ . The active region has a thickness  $L_{\text{active}}$  and an absorption coefficient  $a$ . Also shown is the standing optical wave. The cavity length is  $L_{\text{cav}}$  is equal to  $\lambda / 2$ .



**Fig. 1.6** (a) Schematic structure of a substrate-emitting GaInAs/GaAs RCLED consisting of a metal top reflector and a bottom distributed Bragg reflector (DBR). The RCLED emits at 930 nm. The reflectors are an AlAs/GaAs DBR and a Ag top reflector. (b) Picture of the first RCLED (after ref. [20]).

[16]. These cavities had a large separation between the two reflectors, i. e.  $L_{\text{cav}} \gg \lambda$ . However, if the distance between the two reflectors is of the order of the wavelength,  $L_{\text{cav}} \approx \lambda$ , new physical phenomena occur, including the enhancement of the optical emission from an active material inside the cavity.

At the beginning of the 1990s, the *resonant-cavity light-emitting diode* (RCLED) was demonstrated, initially in the GaAs material system [17], shown in Fig. 1.6, and subsequently in organic light-emitting materials [14]. Both publications reported an emission line narrowing due to the resonant cavities. RCLEDs have many advantageous properties when compared with conventional LEDs, including higher brightness, increased spectral purity, and higher efficiency. For example, the RCLED spectral power density at the resonance wavelength was shown to be enhanced by more than one order of magnitude [18, 19].

The enhancement of spontaneous emission can be calculated based on the changes of the *optical mode density* in a one-dimensional (1D) resonator, i. e. a coplanar Fabry–Perot cavity. We first discuss the basic physics causing the changes of the spontaneous emission from an optically active medium located inside a microcavity and give analytical formulas for the spectral and integrated emission enhancement. The spontaneous radiative transition rate in an optically active, homogeneous medium is given by (see, for example, ref. [21])

$$W_{\text{spont}} = \tau_{\text{spont}}^{-1} = \int_0^\infty W_{\text{spont}}^{(\ell)} \rho(\nu_\ell) d\nu_\ell \quad (1.15)$$



where  $W_{\text{spont}}^{(\ell)}$  is the spontaneous transition rate into the optical mode  $\ell$  and  $\varrho(\nu_\ell)$  is the optical mode density. Assuming that the optical medium is homogeneous, the spontaneous emission lifetime,  $\tau_{\text{spont}}$ , is the inverse of the spontaneous emission rate. However, if the optical mode density in the device depends on the spatial direction, as in the case of a cavity structure, then the emission rate given in Eq. (1.15) depends on the direction. Equation (1.15) can be applied to some small range of solid angle along a certain direction, for example the direction perpendicular to the reflectors of a Fabry–Perot cavity. Thus, Eq. (1.15) can be used to calculate the emission rate along a specific direction, in particular the optical axis of a cavity.

The spontaneous emission rate into the optical mode  $\ell$ ,  $W_{\text{spont}}^{(\ell)}$ , contains the dipole matrix element of the two electronic states involved in the transition [21]. Thus  $W_{\text{spont}}^{(\ell)}$  will *not* be changed by placing the optically active medium inside an optical cavity. However, the optical mode density,  $\varrho(\nu_\ell)$ , is strongly modified by the cavity. Next, the changes in optical mode density will be used to calculate the changes in spontaneous emission rate.

We first compare the optical mode density in free space with the optical mode density in a cavity. For simplicity, we restrict our considerations to the one-dimensional case, i.e. to the case of a coplanar Fabry–Perot cavity. Furthermore, we restrict our considerations to the emission along the optical axis of the cavity.

In a one-dimensional homogeneous medium, the density of optical modes per unit length per unit frequency is given by

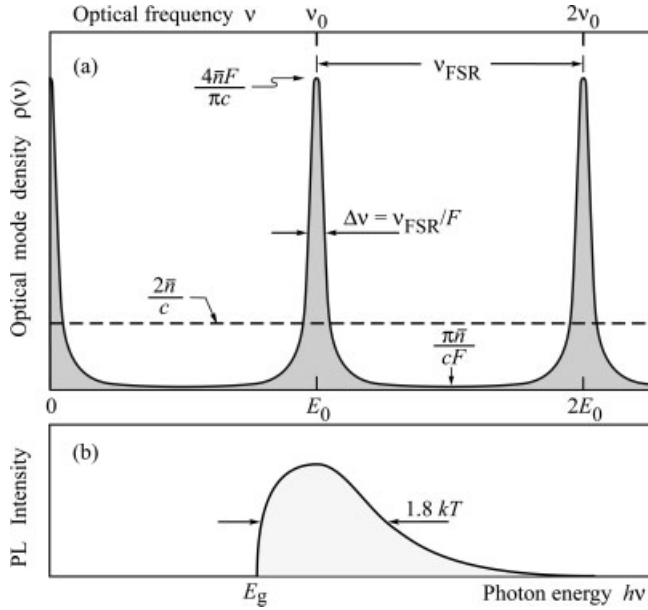
$$\rho^{1D}(\nu) = \frac{2n}{c} \quad (1.16)$$

where  $n$  is the refractive index of the medium. Equation (1.16) can be derived using a similar formalism commonly used for the derivation of the mode density in free space. The constant optical mode density given by Eq. (1.16) is shown in Fig. 1.7.

In planar cavities, the optical modes are discrete and the frequencies of these modes are integer multiples of the fundamental mode frequency, as shown schematically in Fig. 1.7. The fundamental and first excited mode occur at frequencies of  $\nu_0$  and  $2\nu_0$ , respectively. For a cavity with two metallic reflectors (no distributed Bragg reflectors) and a  $\pi$  phase shift of the optical wave upon reflection, the fundamental frequency is given by  $\nu_0 = c / 2nL_{\text{cav}}$ , where  $c$  is the velocity of light in vacuum and  $L_{\text{cav}}$  is the length of the cavity. In a *resonant cavity*, the emission frequency of an optically active medium located inside the cavity equals the frequency of one of the cavity modes.

The optical mode density along the cavity axis can be derived using the relation between the mode density in the cavity and the optical transmittance through the cavity,  $T(\nu)$ ,

$$\rho(\nu) = K T(\nu) \quad (1.17)$$



**Fig. 1.7**  
(a) Optical mode density of a one-dimensional planar microcavity (solid line) and of homogeneous one-dimensional space. (b) Theoretical shape of the luminescence spectrum of bulk semiconductors.

where  $K$  is a constant. The value of  $K$  can be determined by a normalization condition, i.e. by considering a single optical mode. The transmittance through a Fabry–Perot cavity can be written as

$$T(\nu) = \frac{T_1 T_2}{1 + R_1 R_2 - 2\sqrt{R_1 R_2} \cos(4\pi n L_{\text{cav}} \nu/c)} \quad (1.18)$$

The transmittance has maxima at  $\nu = 0, \nu_0, 2\nu_0, \dots$ , and minima at  $\nu = \nu_0/2, 3\nu_0/2, 5\nu_0/2, \dots$ .

The optical mode density of a one-dimensional cavity for emission along the cavity axis is given by

$$\rho(\nu) = \frac{(R_1 R_2)^{3/4}}{T_1 T_2} \frac{4n}{c} (1 - \sqrt{R_1 R_2}) T(\nu) \quad (1.19)$$

This equation allows one to calculate the density of optical modes at the maxima and minima. At the *maxima*, the mode density is given by

$$\rho_{\text{max}} = \frac{(R_1 R_2)^{3/4}}{1 - \sqrt{R_1 R_2}} \frac{4n}{c} \quad (1.20)$$

Because the emission rate at a given wavelength is directly proportional to the optical mode density, the emission rate *enhancement spectrum* is given by the ratio of the 1D cavity mode density to the 1D free-space mode density. The enhancement factor at the resonance wavelength is thus given by the ratio of the optical mode densities with and without a cavity, i.e.

$$G_e = \frac{\rho_{\max}}{\rho^{1D}} \approx \frac{2}{\pi} F \approx \frac{2}{\pi} \frac{\pi(R_1 R_2)^{1/4}}{1 - \sqrt{R_1 R_2}} \quad (1.21)$$

This equation shows that a strong enhancement of the spontaneous emission rate along the cavity axis can be achieved with microcavities.

Equation (1.21) represents the *average* emission rate enhancement out of *both* reflectors of the cavity. To find the enhancement out a *single* direction, we multiply the enhancement given by Eq. (1.21) by the fraction of the light exiting the mirror with reflectivity  $R_1$  (i. e.  $1 - R_1$ ) divided by the average loss of the two mirrors for one round trip in the cavity {i. e.  $(1/2) [(1 - R_1) + (1 - R_2)]$ }. For large  $R_1$  and  $R_2$ , this consideration gives for the enhancement of the emission exiting  $R_1$

$$G_e \approx \frac{2(1 - R_1)}{2 - R_1 - R_2} \frac{2F}{\pi} \approx \frac{1 - R_1}{1 - \sqrt{R_1 R_2}} \frac{2F}{\pi} \approx \frac{2}{\pi} \frac{\pi(R_1 R_2)^{1/4} (1 - R_1)}{(1 - \sqrt{R_1 R_2})^2} \quad (1.22)$$

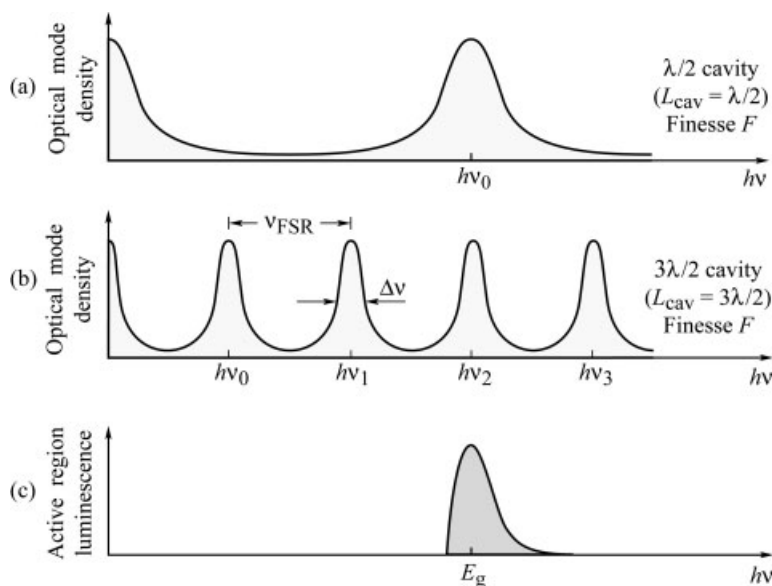
where we used the approximation  $1 - (R_1 R_2)^{1/2} \approx (1/2) (1 - R_1 R_2) \approx (1/2) (2 - R_1 - R_2)$ . Equation (1.22) represents the emission rate enhancement from a *single* reflector with reflectivity  $R_1$ .

The total enhancement *integrated over wavelength*, rather than the enhancement at the resonance wavelength, is relevant for many practical devices. *On resonance*, the emission is enhanced along the axis of the cavity. However, sufficiently far *off resonance*, the emission is suppressed. Because the natural emission spectrum of the active medium (without a cavity) can be much broader than the cavity resonance, it is, *a priori*, not clear whether the integrated emission is enhanced. To calculate the wavelength-integrated enhancement, the spectral width of the cavity resonance and the spectral width of the natural emission spectrum must be determined. The resonance spectral width can be calculated from the finesse of the cavity or the cavity quality factor.

The theoretical width of the emission spectrum of bulk semiconductors is  $1.8kT$  (see, for example, ref. [22]), where  $k$  is Boltzmann's constant and  $T$  is the absolute temperature. At room temperature,  $1.8kT$  corresponds to an emission linewidth of  $\Delta\lambda_n = 31$  nm for an emission wavelength of 900 nm. For a cavity resonance width of 5–10 nm, one part of the spectrum is strongly enhanced, whereas the rest of the spectrum is suppressed. The integrated enhancement ratio (or suppression ratio) can be calculated analytically by assuming a Gaussian natural emission spectrum. For semiconductors at 300 K, the linewidth of the natural emission is, in the case of high-finesse cavities, *larger* than the width of the cavity resonance. The Gaussian emission spectrum has a width of  $\Delta\lambda_n = 2\sigma (2 \ln 2)^{1/2}$  and a peak value of  $(\sigma (2\pi)^{1/2})^{-1}$ , where  $\sigma$  is the standard deviation of the Gaussian function. The integrated enhancement ratio (or suppression ratio) is then given by [23]

$$G_{\text{int}} = \frac{\pi}{2} G_e \Delta\lambda \frac{1}{\sigma\sqrt{2\pi}} = G_e \sqrt{\pi \ln 2} \frac{\Delta\lambda}{\Delta\lambda_n} \quad (1.23)$$

where the factor of  $\pi/2$  is due to the Lorentzian lineshape of the enhancement spectrum. Hence, the integrated emission enhancement depends on the natural



**Fig. 1.8** Optical mode density for (a) a short and (b) a long cavity with the same finesse  $F$ . (c) Spontaneous free-space emission spectrum of an LED active region. The spontaneous emission spectrum has a better overlap with the short-cavity mode spectrum compared with the long-cavity mode spectrum.

emission linewidth of the active material. The value of  $G_{\text{int}}$  can be quite different for different types of optically active materials. Narrow atomic emission spectra can be enhanced by several orders of magnitude [12]. On the other hand, materials having broad emission spectra such as dyes or polymers may not exhibit any integrated enhancement at all. Equation 1.23 also shows that the width of the resonance has a profound influence on the integrated enhancement. [8, 9] Narrow resonance spectral widths, i. e. high finesse values or long cavities, reduce the integrated enhancement [18].

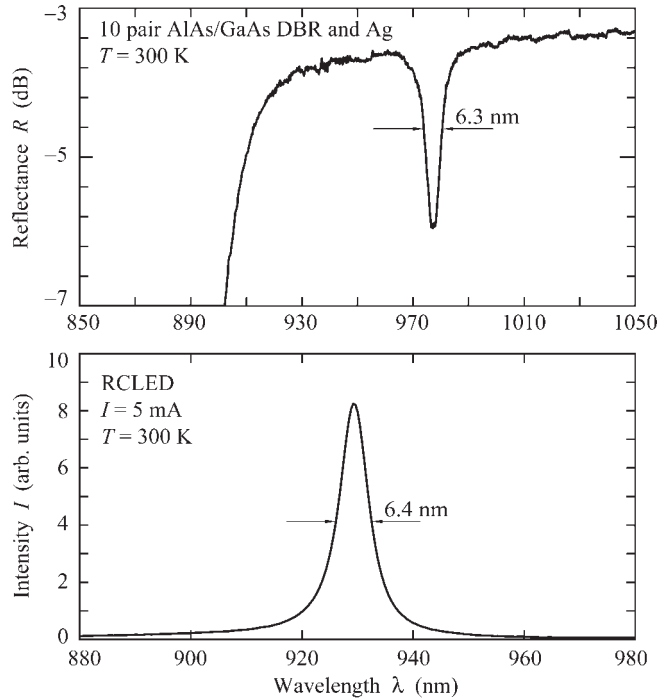
The relation between the overlap of the spontaneous emission spectrum and the cavity length is illustrated in Fig. 1.8, which shows the optical mode density of a short and a long cavity. Both cavities have the same mirror reflectivities and finesse. The natural emission spectrum of the active region is shown in Fig. 1.8(c). The best overlap between the resonant optical mode and the active region emission spectrum is obtained for the *shortest* cavity. Thus a cavity length of  $\lambda/2$  provides the largest enhancement.

The largest enhancements are achieved with the shortest cavities, which in turn are obtained if the *fundamental* cavity mode is in resonance with the emission from the active medium. The cavity length is shortest for metallic reflectors. DBRs with a short penetration depth, i.e. DBRs consisting of two materials with a large difference in refractive index, also reduce the cavity length.

The reflection and emission properties of the RCLED are shown in Fig. 1.9(a) and (b). The reflection spectrum of the RCLED exhibits a highly reflective band for wavelengths  $> 900$  nm and a dip in the reflectivity at the cavity resonance. The spectral width of the cavity resonance is 6.3 nm. The emission spectrum of an electrically pumped device, shown in Fig. 1.9(b), has nearly the same shape and width as the cavity resonance.

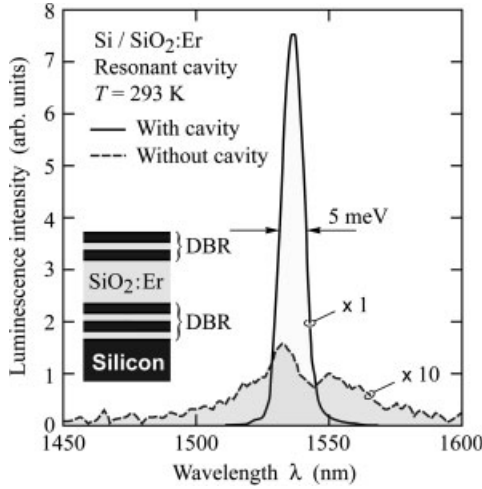
In conventional LEDs, the spectral characteristics of the devices reflect the thermal distribution of electrons and holes in the conduction and valence band. The spectral characteristics of light emission from microcavities are as intriguing as they are complex. However, restricting our considerations to the optical axis of the cavity simplifies the cavity physics considerably. If we assume that the cavity resonance is much narrower than the natural emission spectrum of the semiconductor, then the on-resonance luminescence is enhanced whereas the off-resonance luminescence is suppressed. The on-axis emission spectrum should therefore reflect the enhancement, that is, the resonance spectrum of the cavity. The experimental results shown in Fig. 1.9 confirm this conjecture.

Particularly high spontaneous emission enhancements can be attained with emitters that have very narrow emission lines. Atomic transitions, e.g. in rare-earth elements have such narrow emission lines. For this reason, rare-earth doped cavities are a prime example of the emission enhancement provided by resonant cavities. The emission spectrum of an erbium-doped Si/SiO<sub>2</sub> resonant cav-



**Fig. 1.9**

(a) Reflectance of a resonant cavity consisting of a 10-pair AlAs/GaAs distributed Bragg reflector and an Ag reflector. (b) Emission spectrum of a RCLED consisting of a 10-pair AlAs/GaAs distributed Bragg reflector and an Ag reflector (after ref. [20]).



**Fig. 1.10** Photoluminescence spectra of Er-doped  $\text{SiO}_2$ . One of the spectra is for the Er-doped  $\text{SiO}_2$  located in a cavity resonant at 1540 nm. The other spectrum is without a cavity. The emission enhancement factor is 50 (after ref. [12]).

ity is shown in Fig. 1.10 [12]. A distinct narrowing of the Er emission spectrum is found for emission along the optical axis. A huge emission enhancement with cavity is found, a factor greater than 50, when compared to a noncavity structure.

The peak emission wavelength depends on the emission angle with respect to the surface normal (polar angle). Denoting the polar emission angle in air as  $\Theta_0$ , the emission wavelength is given by

$$\lambda_e = \lambda_{\text{res}} \cos \left[ \arcsin \left( \frac{1}{n} \sin \Theta_0 \right) \right] \quad (1.24)$$

where  $\lambda_{\text{res}}$  is the resonance wavelength of the cavity. For small angles, the equation can be approximated by

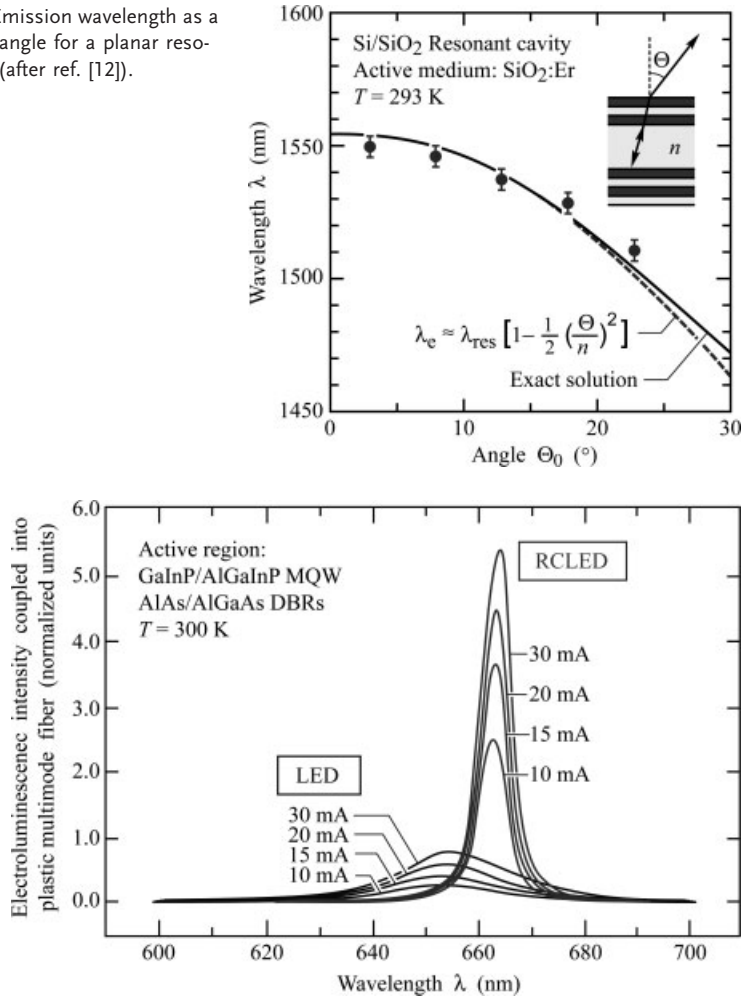
$$\lambda_e = \lambda_{\text{res}} \left( 1 - \frac{\Theta_0^2}{2n^2} \right) \quad (1.25)$$

where the refractive index  $n$  is the effective refractive index of the medium. The angular dependence of the peak emission wavelength is shown in Fig. 1.11. The dashed line is the approximate solution of Eq. (1.25). A refractive index of 1.5 has been used in this calculation.

RCLEDs are now commercial products that are manufactured by the millions per year. Primary applications are in signage and communication. The devices are particularly well suited for plastic optical fiber systems. The directed emission pattern improves LED-fiber coupling efficiency. The narrow emission line reduces material and chromatic dispersion effects. As a result, RCLEDs enable longer transmission distances and simultaneously higher data rates.

The enhanced coupling and narrow emission line of the fiber-coupled intensity is shown in Fig. 1.12. Inspection of the figure reveals the much higher power coupled to a fiber and the narrower emission spectrum of the RCLED.

**Fig. 1.11** Emission wavelength as a function of angle for a planar resonant cavity (after ref. [12]).

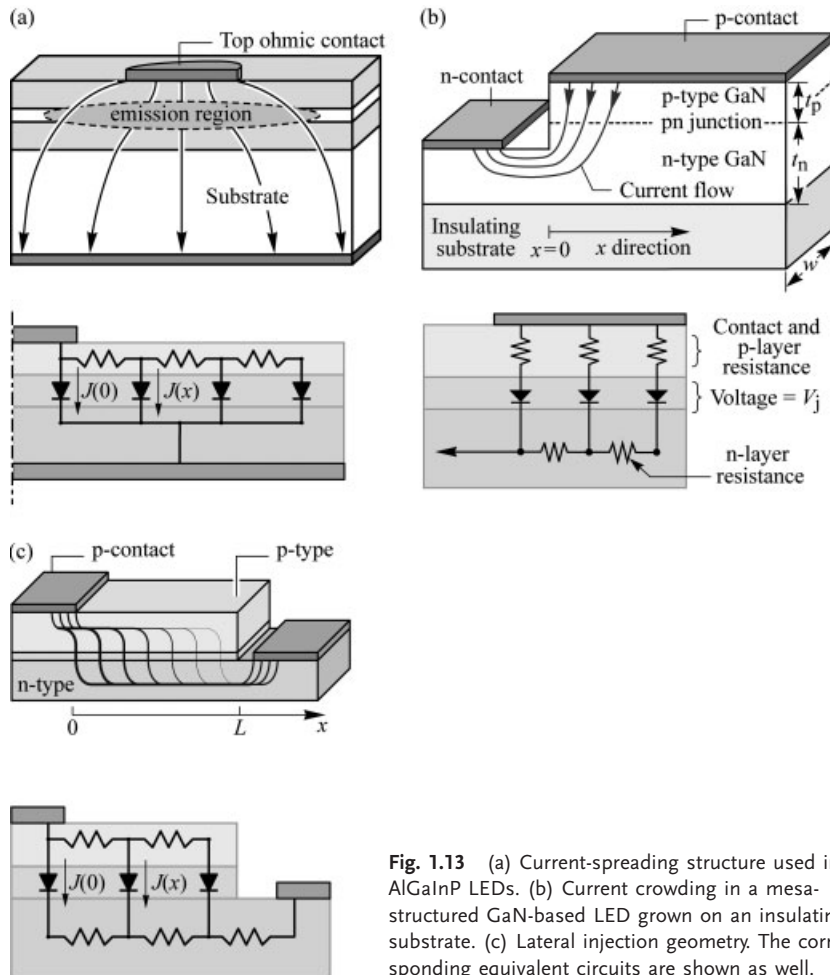


**Fig. 1.12** Spectra of light coupled into a plastic optical fiber from an GaInP/AlGaInP MQW RCLED and a conventional GaInP/AlGaInP LED at different drive currents. Note the narrower spectrum and higher coupled power of the RCLED (after ref. [24]).

## 1.4

### Current Transport in LED Structures

LEDs can be grown on conductive as well as insulating substrates. Whereas the current flow is mostly vertical (normal to the substrate plane) in structures grown on conductive substrates, it is mostly lateral (horizontal) in devices grown on insulating substrates. The location and size of ohmic contacts are relevant to light extraction, as metal contacts generally are opaque. This section discusses the current flow patterns of different device structures aimed at high extraction efficiency.



**Fig. 1.13** (a) Current-spreading structure used in AlGaInP LEDs. (b) Current crowding in a mesa-structured GaN-based LED grown on an insulating substrate. (c) Lateral injection geometry. The corresponding equivalent circuits are shown as well.

In LEDs with thin top confinement layers, the current is injected into the active region mostly under the top electrode. Thus, light is generated under an opaque metal electrode, which results in a low extraction efficiency. The problem can be avoided with a *current-spreading layer* or *window layer* that spreads the current under the top electrode to regions not covered by the opaque top electrode.

The usefulness of current-spreading layers was shown by Nuese et al. [25] who demonstrated a substantial improvement of the optical output power in GaAsP LEDs. The effect of the current-spreading layer is illustrated schematically in Fig. 1.13(a). Current-spreading layers are employed in top-emitting LEDs. A GaP current-spreading layer in an AlGaInP LED was reported by Kuo et al. [26] and Fletcher et al. [27, 28]. AlGaAs current-spreading layers in AlGaInP LEDs were reported by Sugawara et al. [29–31].



For circular contact geometry, the thickness of the current spreading layer,  $t$ , results a current-spreading length  $L_s$  given by [32]

$$t = \rho L_s \left( r_c + \frac{L_s}{2} \right) \ln \left( 1 + \frac{L_s}{r_c} \right) \left( J_0 \frac{e}{n_{\text{ideal}} kT} \right) \quad (1.26)$$

where  $J_0$  is the current density at the edge of the contact,  $r_c$  is the contact radius. The equation allows one to calculate the required current-spreading layer thickness  $t$  for a given resistivity of this layer and the desired current-spreading length  $L_s$ .

*Current crowding* also occurs in mesa-structured LEDs grown on *insulating* substrates, e. g. GaInN/GaN LEDs grown on sapphire substrates. In common GaInN devices, the p-type contact is located on the top of the mesa, and the n-type contact is located on an n-type buffer layer at the bottom of the mesa. As a result, the current crowds at the edge of the mesa contact adjoining the n-type contact.

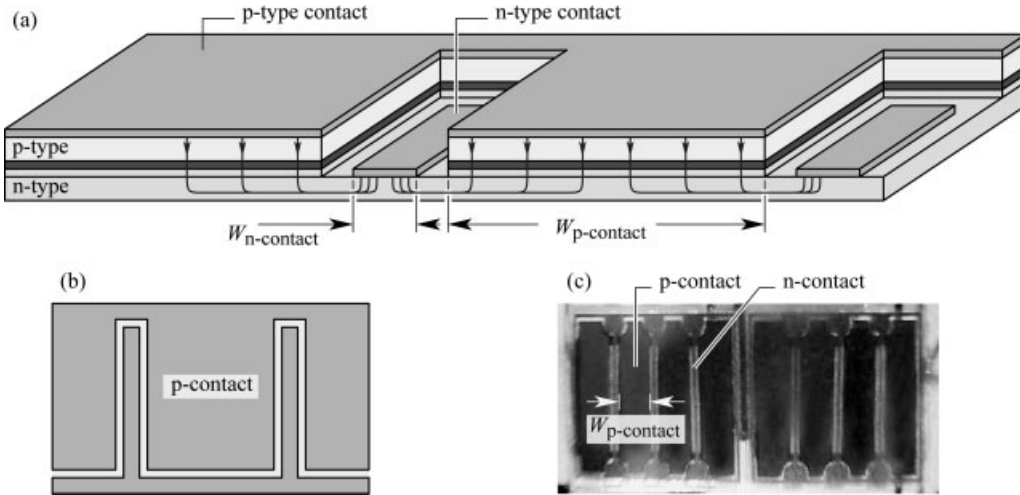
A lateral p-side-up mesa LED grown on an insulating substrate is shown in Fig. 1.13(b). It is intuitively clear that the p-n junction current crowds near the edge of the mesa as indicated in the figure. An equivalent circuit model is shown in Fig. 1.13(b) and includes the p-type contact resistance and the resistances of the n-type and p-type cladding layers. The p-n junction is approximated by an ideal diode. The circuit model also shows several nodes separated by a distance  $dx$ . The current distribution decreases exponentially with distance from the contact edge. The current-spreading length is given by [33]

$$L_s = \sqrt{(\rho_c + \rho_p t_p) t_n / \rho_n} \quad (1.27)$$

where  $\rho_{n,p}$  and  $t_{n,p}$  are the resistivities and thickness of the n-type and p-type layers, respectively, and  $\rho_c$  is the specific contact resistance. This equation shows that the current distribution depends on epitaxial layer thicknesses and material resistivities. A thick low-resistivity n-type buffer layer is needed to ensure that current crowding is minimized. For *low* p-type contact and confinement resistances, strong current crowding results, unless the n-type buffer layer is very conductive so that  $t_n / \rho_n$  is very large. In GaN/GaInN devices, the sum of p-type contact and p-type layer resistances can be larger than the n-type cladding resistance, especially if  $t_n$  is small.

A device structure with a lateral current-injection scheme is shown in Fig. 1.13(c). The current is transported laterally in both the n-type and p-type cladding layers. Light is generated in the region between the contacts where the extraction is not hindered by contacts. If the n-type sheet resistance  $\rho_n / t_n$  is much lower than the p-type sheet resistance  $\rho_p / t_p$ , the current prefers to flow laterally in the low-resistance n-layer rather than the p-layer. As a result, the junction current crowds near the p-type contact.

A schematic equivalent circuit suitable for the quantitative analysis is shown in Fig. 1.13(c) where a pn-junction current density of  $J(0)$  is assumed at the edge of the p-type contact. The analytic solution of the equivalent circuit shown in Fig. 1.13(c) is an exponential function [34, 35].



**Fig. 1.14** (a) Interdigitated stripe-contact structure for uniform current injection. (b) Top view. (c) Photograph of flip-chip GaInN LED (after LED Museum, see ref. [38]).

For uniform light generation across the gap between the contacts, it is desirable to have a long exponential decay length  $L_s$ . This can be achieved by high doping or thick confinement layers. To attain high powers, one may be tempted to scale the device structure in size. However, for large contact separations  $L$ , the device becomes generally more resistive unless very thick confinement layers are being used (which may be impractical). Scaling such device structures can be accomplished by employing arrays of many small devices rather than scaling up a single device.

Note that current crowding becomes increasingly severe with larger device sizes, unless novel contact geometries are introduced to alleviate the problem. Such novel contact geometries include interdigitated structures with p-type finger widths of less than  $L_s$  [36, 37]. For device dimensions much smaller than  $L_s$ , the current crowding effect can be neglected.

The schematic structure and a photograph of an interdigitated stripe-contact geometry are shown in Fig. 1.14. Uniform current injection into the active region is achieved by the p-type contact width ( $W_{p\text{-contact}}$ ) being smaller than the current-spreading length. The width of the n-type contact ( $W_{n\text{-contact}}$ ) must be at least equal to the contact transfer length to ensure low contact resistance. The contact transfer length follows from the transmission line model (TLM) used for characterization of ohmic contacts (see, for example, ref. [39]).

## 1.5

### Extraction Efficiency

The active region of an idealized LED emits *one photon for every electron* injected. Each charge quantum-particle (electron) produces one light quantum-particle (photon). Thus the active region of an idealized LED has a *quantum efficiency* of one. The *internal quantum efficiency* is defined as

$$\eta_{\text{int}} = \frac{\text{\# of photons emitted from active region per second}}{\text{\# of electrons injected into LED per second}} = \frac{P_{\text{int}} / (h \nu)}{I / e} \quad (1.28)$$

where  $P_{\text{int}}$  is the optical power emitted from the active region and  $I$  is the injection current.

Photons emitted by the active region should escape from the LED chip. In an idealized LED, all photons emitted by the active region are also emitted into free space. Such an LED would have 100 % *extraction efficiency*. However, in a real LED, not all the power emitted from the active region is emitted into free space. Some photons may never leave the semiconductor chip. This is due to a number of possible loss mechanisms. For example, light emitted by the active region can be re-absorbed in the substrate of the LED, assuming that the substrate is absorbing at the emission wavelength. Light may be incident on a metallic contact surface and be absorbed by the metal. In addition, the phenomenon of *total internal reflection*, also referred to as the *trapped light phenomenon*, reduces the ability of the light to escape from the semiconductor. The *light extraction efficiency* is defined as

$$\eta_{\text{extraction}} = \frac{\text{\# of photons emitted into free space per second}}{\text{\# of photons emitted from active region per second}} = \frac{P / (h \nu)}{P_{\text{int}} / (h \nu)} \quad (1.29)$$

where  $P$  is the optical power emitted into free space.

The extraction efficiency can be a severe limitation for high-performance LEDs. It is quite difficult to increase the extraction efficiency beyond 50 % without resorting to highly sophisticated and costly device processes.

The *external quantum efficiency* is defined as

$$\eta_{\text{ext}} = \frac{\text{\# of photons emitted into free space per second}}{\text{\# of electrons injected into LED per second}} = \frac{P / (h \nu)}{I / e} = \eta_{\text{int}} \eta_{\text{extraction}} \quad (1.30)$$

The external quantum efficiency gives the ratio of the number of usable light particles to the number of injected charge particles.

One of the most important problems facing high-efficiency LEDs is the occurrence of trapped light within the semiconductor. Owing to the high refractive index of semiconductors, light incident on a planar semiconductor/air interface is totally internally reflected, if the angle of incidence is sufficiently large. Snell's law gives the critical angle of total internal reflection. This angle defines the escape cone. Light rays with a propagation direction that lies within the escape

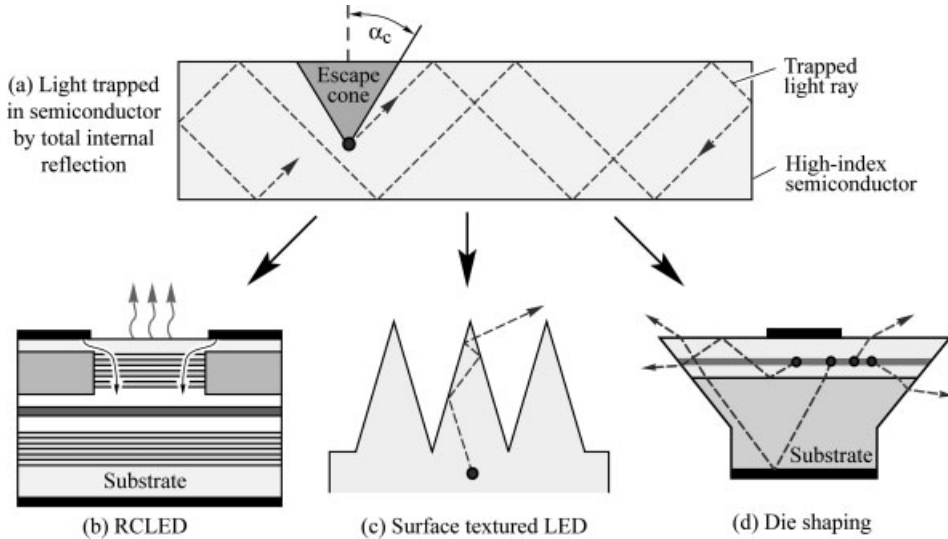
cone are able to leave the LED chip. Light trapped in the semiconductor will eventually be reabsorbed by a defect, the substrate, active region, or another absorbing layer.

If the light is absorbed by the substrate, the electron–hole pair will most likely recombine nonradiatively due to the inherently low efficiency of substrates. If the light is absorbed by the active region, the electron–hole pair may re-emit a photon (“recycling” of a photon) or recombine nonradiatively. If re-emitted as a photon, the photon propagation direction may fall into the escape cone. Thus the exact magnitude of the active region internal quantum efficiency and the probability of a photon to be emitted into the escape cone will determine the overall quantum efficiency of a device and the strategy (direct light extraction or light extraction by photon recycling) to attain higher efficiency. In the limit of low and high internal efficiency, photon recycling is an ineffective and effective strategy to maximize power efficiency, respectively.

The occurrence of trapped light is illustrated in Fig. 1.15. A light ray emitted by the active region will be subject to total internal reflection, as predicted by Snell’s law. In the high-index approximation, the angle of total internal reflection is given by

$$\alpha_c = \bar{n}_s^{-1} \quad (1.31)$$

where  $\bar{n}_s$  is the semiconductor refractive index and the critical angle  $\alpha_c$  is given in radians. For high-index semiconductors, the critical angle is quite small. For example, for the GaAs refractive index of 3.3, the critical angle for total internal



**Fig. 1.15** (a) Light rays emanating from a point-like emitter are trapped inside the semiconductor due to total internal reflection. Only light rays with propagation directions falling within the escape cone can leave the semiconductor. Strategies increasing the extraction efficiency include (b) resonant-cavity (c) textured (d) chip-shaped LEDs.

reflection is only  $17^\circ$ . Thus, most of the light emitted by the active region is trapped inside the semiconductor.

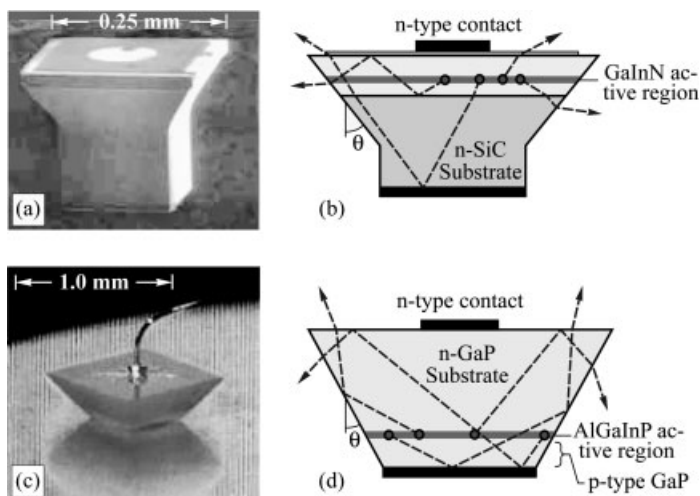
The light-escape problem has been known since the 1960s. It has also been known that the geometrical shape of the LED die plays a critical role. The optimum LED would be spherical in shape with a point-like light-emitting region in the center of the LED. Light emanating from the point-like active region is incident at a normal angle at the semiconductor/air interface. As a result, total internal reflection would not occur. Note, however, that the light is still subject to Fresnel reflection at the interface unless the sphere is coated with an antireflection coating.

The most common LED structure has the shape of a rectangular parallelepiped. Such LED dies are fabricated by cleaving the wafer along its natural cleaving planes. The LEDs have a total of six escape cones, two of them perpendicular to the wafer surface, and four of them parallel to the wafer surface [40]. The bottom escape cone will be absorbed by the substrate if the substrate has a lower bandgap than the active region. The four in-plane escape cones will be at least partially absorbed by the substrate. Light in the top escape cone will be obstructed by the top contact, unless a thick current-spreading layer is employed. Thus the simple rectangular parallelepiped LED has low extraction efficiency. However, low manufacturing cost is an advantage.

There are different strategies to increase light extraction from LEDs including the resonant-cavity, surface-roughened, and chip-shaped LED shown in Fig. 1.15(b), (c), and (d), respectively. The resonant-cavity light-emitting diode (RCLED) has a light-emitting region inside an optical cavity [41, 42]. The optical cavity has a thickness of typically one-half or one times the wavelength of light, i. e. a fraction of a micrometer for devices emitting in the visible or in the infrared. The resonance wavelength of the cavity coincides with the emission wavelength of the active region. The spontaneous emission properties from a light-emitting region located inside the resonant cavity are enhanced by the change in optical mode density that has a maximum at or near the emission wavelength. The RCLED was the first practical device making use of spontaneous emission enhancement occurring in resonant cavities.

Other efficient ways to increase the light extraction efficiency include the use of *textured semiconductor surfaces* (see, for example, refs. [43–47]) and the use of tapered output couplers [48–50]. A cone-shaped surface roughening is shown in Fig. 1.15(b). Light rays emanating from the active region below the base of the cone undergo multiple reflections until they eventually have near-normal incidence at the semiconductor/air interface and escape from the chip. For infrared GaAs-based devices, external quantum efficiencies of 40% have been demonstrated with surface-textured LEDs and devices having tapered output couplers. A detailed discussion of properties and fabrication of microstructured surfaces was given by Sinzinger and Jahns [51].

Several chip-shaped LEDs have been commercialized including the *pedestal-shaped chip* shown in Figs. 1.16(a) and (b) and the *truncated inverted pyramid (TIP) chip* shown in Figs. 1.16(c) and (d) [52]. The ray traces indicated in the fig-



**Fig. 1.16** Die-shaped devices: (a) Blue GaInN emitter on SiC substrate with trade name “Aton”. (b) Schematic ray traces illustrating enhanced light extraction. (c) Micrograph of truncated inverted pyramid (TIP) AlGaInP/GaP LED. (d) Schematic diagram illustrating enhanced extraction (after Osram, 2001; ref. [52]).

ures show that light rays at the base of the pyramid can escape from the semiconductor after undergoing one or multiple internal reflections. The TIP geometry reduces the mean photon pathlength within the crystal, and thus reduces internal losses. Ray-tracing computer models are employed to optimize the sidewall angle  $\theta$  to maximize light extraction.

The TIP LED is a high-power LED with a large p-n junction area of  $500\ \mu\text{m} \times 500\ \mu\text{m}$ . The luminous efficiency of TIP LEDs exceeds  $100\ \text{lm/W}$  and is one of the highest ever achieved with LEDs [52]. A peak luminous efficiency of  $102\ \text{lm/W}$  was measured for orange-spectrum ( $\lambda \approx 610\ \text{nm}$ ) devices at an injection current of  $100\ \text{mA}$ . This luminous efficiency exceeds that of most fluorescent ( $50\text{--}104\ \text{lm/W}$ ) and all metal-halide ( $68\text{--}95\ \text{lm/W}$ ) lamps. In the amber color regime, the TIP LED provides a photometric efficiency of  $68\ \text{lm/W}$  ( $\lambda \approx 598\ \text{nm}$ ). This efficiency is comparable to the efficiency of high-pressure sodium discharge lamps. A peak external quantum efficiency of  $55\%$  was measured for red-emitting ( $\lambda \approx 650\ \text{nm}$ ) TIP LEDs. Under pulsed operation ( $1\%$  duty cycle), an efficiency of  $60.9\%$  was achieved, which sets a lower bound on the extraction efficiency of these devices [52].

## 1.6

### Omnidirectional Reflectors

There are several different ways to obtain highly reflective coatings in the visible wavelength region. Metallic layers provide robust reflectors capable of reflecting visible light over a wide range of wavelengths and incident angles. Metals reflect visible light since this frequency range is well below typical plasma frequencies of the free-electron gas. However, electron oscillations induced by incident light waves not only result in reflection but also in substantial absorption caused by electron–phonon scattering.

Distributed-Bragg reflectors (DBRs) are periodic structures with a unit cell of two dielectric layers having different refractive indices  $n_i$  and thicknesses  $d_i$  ( $i = 1, 2$ ). DBRs can be regarded as one-dimensional photonic-crystals with a high-reflectivity stop band (“photonic-crystal gap”) comprising the nonpropagating light states in the crystal. DBRs are usually designed to have a certain center wavelength  $\lambda_{\text{center}}$  at *perpendicular* incidence. However, the DBR reflectivity depends on the incidence angle  $\theta$  such that the stop band shifts towards shorter wavelengths for increasing  $\theta$  without changing its spectral width [53]. As a result, DBRs become transparent for oblique angles of incidence.

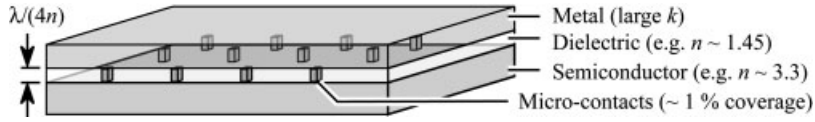
The reflection properties of metals and DBRs depend on the polarization of the incident lightwave. According to Brewster’s law, the reflection of light polarized parallel to the plane of incidence (TM-mode) has a minimum at the incidence angle

$$\tan \theta_B = \frac{n_1}{n_2} \quad (1.32)$$

where  $n_1$  and  $n_2$  are the refractive indices of the adjacent materials. This is particularly important for DBRs that exhibit a drastic reflectivity decrease at  $\theta_B$ . DBRs with improved wide-angle reflectivity can be achieved, e. g., by using *aperiodically* stacked layers with thickness gradients or random thickness distributions [54, 55].

Much research was devoted to DBRs with a *complete* photonic-crystal bandgap represented by a certain frequency range where all incoming photons regardless of their momentum vector  $\hbar \vec{k}$  are reflected. These omnidirectional reflectors (ODRs) have a wide range of interesting applications such as all-dielectric coaxial waveguides [56], omnidirectional mirror fibers [57], and light transport tubes [58].

Omnidirectional reflection characteristics can also be obtained with distributed Bragg reflectors that have a very high index contrast such as Si/SiO<sub>2</sub>. Another approach used polystyrene and tellurium layers in a DBR [59]. Due to the large difference of the refractive indices,  $n_{\text{SiO}_2} = 1.45$ ;  $n_{\text{polystyrene}} = 1.8$ ;  $n_{\text{Si}} = 3.5$ ;  $n_{\text{tellurium}} = 5$ , the Brewster angle  $\theta_B$  is much larger than the critical angle  $\theta_c$  for total reflection resulting in a nearly complete photonic-crystal bandgap in the wavelength range from 10 to 15  $\mu\text{m}$ . Still another approach consists of the use of birefringent polymers in DBRs with two different refractive indices parallel and vertical to the DBR layer planes [58]. By adjusting the differences between the vertical and in-plane indices the value of the Brewster angle can be controlled.



**Fig. 1.17** Perspective view of an omnidirectional reflector (ODR). The ODR also serves as ohmic contact.

Brewster angles up to  $90^\circ$  (grazing incidence) and even imaginary values are possible resulting in high reflectivity for TM-polarized light at virtually all incident angles.

Unfortunately, the applicability of the above-mentioned omnidirectional DBRs in LEDs is limited since they are electrically insulating. In addition, these omnidirectional DBR structures present a considerable thermal barrier preventing efficient heat sinking due to their large thermal resistance and thickness. DBRs have been used as a substrate coating to enhance the light extraction [60, 61]. However, the active region of a LED emits light isotropically and therefore the poor reflectivity of the regular DBRs at oblique incidence angles results in undesired losses particularly for wave-guided modes as discussed above.

A very promising electrically conductive omnidirectional reflector suitable for use in LEDs is shown in Fig. 1.17 [62, 63]. The reflector comprises the LED semiconductor material with a refractive index  $n_s$ , a low-refractive index layer ( $n_{li}$ ), and a metal with a complex refractive index  $N_m = n_m + i k_m$ , where  $k_m$  is the extinction coefficient.

The low-index layer is perforated by many small ohmic contacts that cover only a small fraction of the entire area. The array of microcontacts allows the electrical current to pass through the dielectric layer. Assuming that the ohmic contacts have an area of 1 % of the reflector, and that the alloyed ohmic contact metal is 50 % reflective, the reflectivity of the ODR is reduced by only 0.5 %. The ODR described here can be used with low-cost Si substrates or metal substrates using conductive epoxy or a metal-to-metal bonding process. These bonding processes have much less stringent requirements than direct semiconductor-to-semiconductor wafer bonding processes.

The reflectance of the semiconductor/metal reflector as a function of the incident angle  $\theta$  is given by [64]

$$R_{TE} = \left| \frac{n_s \cos\theta_1 - N_m \cos\theta_2}{n_s \cos\theta_1 + N_m \cos\theta_2} \right|^2 \quad (1.33a)$$

$$R_{TM} = \left| \frac{\frac{n_s}{\cos\theta_1} - \frac{N_m}{\cos\theta_2}}{\frac{n_s}{\cos\theta_1} + \frac{N_m}{\cos\theta_2}} \right|^2 \quad (1.33b)$$

The reflectance of the triple-layer ODR as a function of the incident angle  $\theta$  (see Fig. 1.18) is given by [64]



$$R = \left| \frac{r_{01} + r_{12} \exp(2i\phi)}{1 + r_{01} \cdot r_{12} \exp(2i\phi)} \right|^2 \quad (1.34a)$$

where,

$$r_{01\text{TE}} = \frac{n_s \cos \theta_1 - n_i \cos \theta_2}{n_s \cos \theta_1 + n_i \cos \theta_2} \quad (1.34b)$$

$$r_{01\text{TM}} = \frac{n_i \cos \theta_1 - n_s \cos \theta_2}{n_i \cos \theta_1 + n_s \cos \theta_2} \quad (1.34c)$$

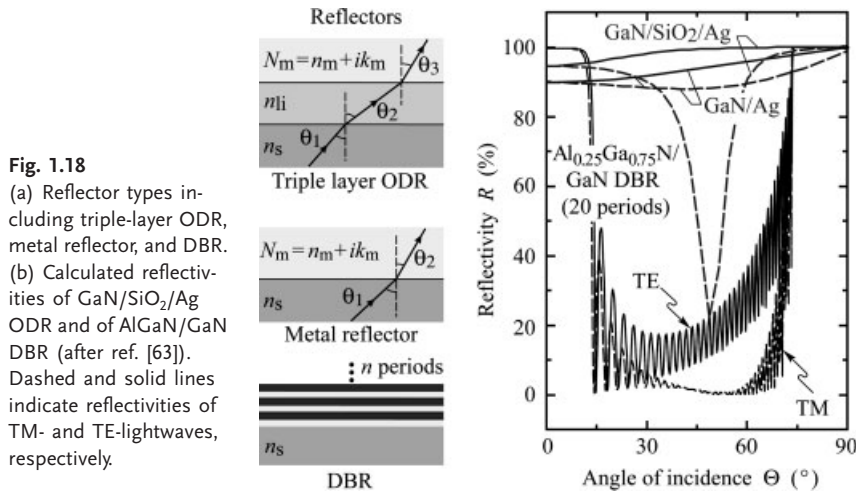
$$r_{12\text{TE}} = \frac{n_i \cos \theta_2 - N_m \cos \theta_3}{n_i \cos \theta_2 + N_m \cos \theta_3} \quad (1.34d)$$

$$r_{12\text{TM}} = \frac{N_m \cos \theta_2 - n_i \cos \theta_3}{N_m \cos \theta_2 + n_i \cos \theta_3} \quad (1.34e)$$

and

$$\phi = \frac{2\pi}{\lambda} n_i h \cos \theta_2 \quad (1.34f)$$

Equations (1.34) apply to a low-index dielectric layer thickness of  $\lambda_0/(4n_i)$ , i. e., to a quarter wavelength layer. Fig. 1.18(b) shows the reflectivity  $R(\theta)$  at  $\lambda = 470$  nm of a triple-layer ODR (GaN/SiO<sub>2</sub>/Ag), metal reflectors (GaN/Ag and GaN/Ni/Au), and 20 periods of Al<sub>0.25</sub>Ga<sub>0.75</sub>N/GaN DBR. The reflectivity curves were calculated using the optical transfer matrix method [53, 64] and using parameters,  $n_{\text{Ag}} = 0.132$ ,  $k_{\text{Ag}} = 2.72$ ,  $n_{\text{SiO}_2} = 1.46$ ,  $n_{\text{GaN}} = 2.45$  at 470 nm [65]. As opposed to the ODR and metal reflectors,  $R(\theta)$  of the DBR sharply drops above 14° and recovers only at angles close to grazing incidence. Note that the reflectivity for TE-polarized light of the GaN/SiO<sub>2</sub>/Ag ODR is higher than that of the GaN/Ag reflector for all angles of incidence.



Because the LED active region emits light isotropically, the total substrate reflectivity averaged over the solid angle would be a suitable figure-of-merit. The average reflectivity is given by

$$\bar{R}(\lambda) = \frac{1}{2\pi} \int_0^{\pi/2} R(\lambda, \theta) 2\pi \sin\theta d\theta \quad (1.35)$$

where  $\lambda$  denotes the emission wavelength and  $\theta$  the angle of incidence in the semiconductor. As a result, the angle averaged reflectivity  $\bar{R}$  is much larger for a GaN/SiO<sub>2</sub>/Ag ODR ( $\bar{R} = 0.93$  at  $\lambda = 470$  nm) and Ag reflector ( $\bar{R} = 0.92$  at  $\lambda = 470$  nm) than for the DBR ( $\bar{R} = 0.49$  for TE-polarized,  $\bar{R} = 0.38$  for TM-polarized at  $\lambda = 470$  nm). The averaged reflectivity of triple-layer ODRs exceeds the value of  $\bar{R}$  for the transparent DBR by about a factor of two.

Note that the reflectivity increase is significant. The power of a wave-guided mode,  $P$ , attenuated by multiple reflection events (with reflectivity  $R$ ) depends on the number of reflection events,  $N$ , according to

$$P = P_0 R^N \quad (1.36)$$

where  $P_0$  is the initial power of the mode.

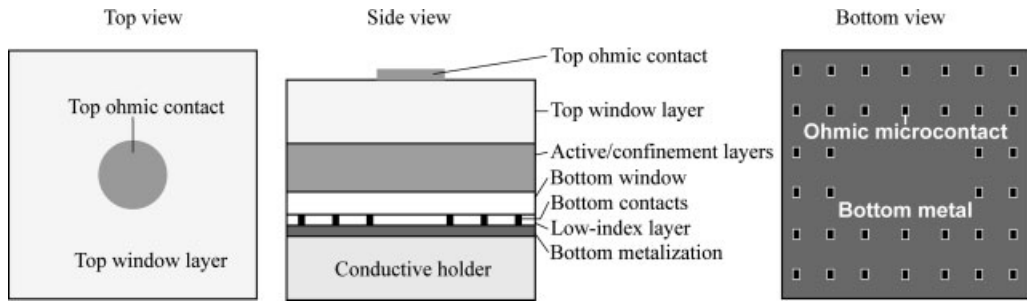
At perpendicular incidence, the reflectance of the triple-layer ODR is given by [62, 63]

$$R_{\text{ODR}}(\theta_1 = 0) = \frac{\{(n_S - n_{li})(n_{li} + n_m) + (n_S + n_{li})k_m\}^2 + \{(n_S - n_{li})k_m + (n_S + n_{li})(n_{li} - n_m)\}^2}{\{(n_S + n_{li})(n_{li} + n_m) + (n_S - n_{li})k_m\}^2 + \{(n_S + n_{li})k_m + (n_S - n_{li})(n_{li} - n_m)\}^2} \quad (1.37)$$

For an AlGaInP/SiO<sub>2</sub>/Ag structure emitting at  $\lambda = 630$  nm, Eq. (1.37) yields a normal-incidence reflectance  $R_{\text{ODR}}(\theta = 0) > 98\%$ . This value exceeds the corresponding value for a structure *without* a low-index layer by about 3 %, thereby reducing optical losses by a substantial amount. Due to the power-law dependence this improvement of  $R$  is of great importance and shows the huge potential of ODRs. The triple-layer ODR can be improved significantly by using novel low- $n$  materials such as nanoporous SiO<sub>2</sub> that has a refractive index as low as 1.10 [66]. It is transparent in the visible and near UV spectrum. In contrast, SiO<sub>2</sub> has a refractive index of about 1.46 and very good transparency in the visible and near UV spectrum.

The schematic structure of an ODR-based LED is shown in Fig. 1.19. It consists of a top current-spreading (or window) layer, the active and confinement layers, a bottom window layer, the ODR, and a submount such as a Si or metal wafer. The active layers include the lower and upper confinement layers and the bulk or multiple-quantum-well (MQW) active region. The wafer is grown in the standard “p-side up” mode that is employed in nearly all LEDs at the present time.

The wide-angle reflectivity of the ODR allows wave guiding of light rays with much smaller attenuation than a DBR. As a result, light extraction at the edges of the LED chip is strongly increased.

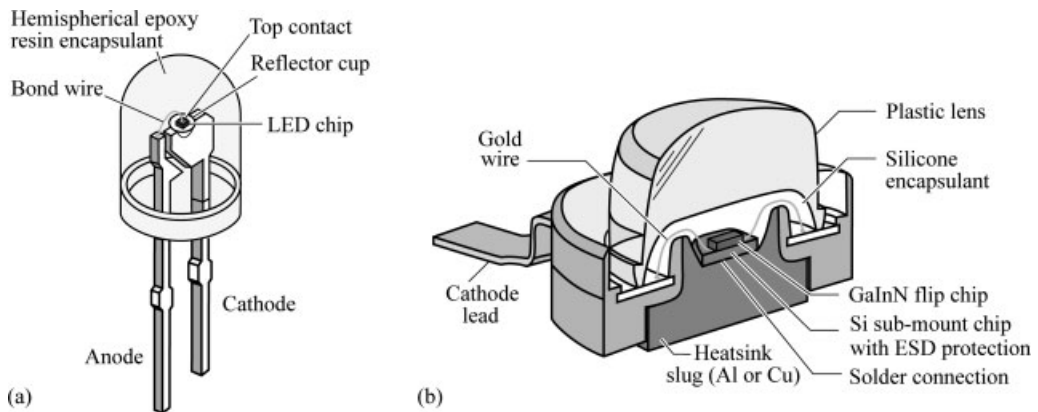


**Fig. 1.19** Schematic of the omnidirectional reflector (ODR) LED. An array of microcontacts perforating the ODR serves as p-type ohmic contact to the epitaxial AlGaInP layers.

## 1.7 Packaging

Virtually all LEDs are encapsulated with an optically transparent polymer. Encapsulants have several requirements including high transparency, high refractive index, chemical stability, high-temperature stability, and hermeticity. The refractive index contrast between the semiconductor and air is reduced by the encapsulant. A reduced index contrast at the semiconductor surface increases the angle of total internal reflection thereby enlarging the LED escape cone and extraction efficiency. Furthermore, encapsulants provide protection against unwanted mechanical shock, humidity, and chemicals. The encapsulant also stabilizes the LED chip and bonding wires. Finally the epoxy resin provides mechanical stability to the two metal leads of the LED and holds them in place.

A *low-power package* is shown in Fig. 1.20(a). The device is attached to the bottom of a cup-like depression (“reflector cup”) formed in one of the lead wires



**Fig. 1.20** (a) LED with hemispherical encapsulant. (b) Cross section through high-power package. The heatsink slug can be soldered to a printed circuit board for efficient heat removal (adopted from ref. [68]).

(usually the cathode lead). A bond wire connects the LED top contact to the other lead wire (usually the anode lead). The LED package shown in the figure is frequently referred to as a “5 mm” or “T1-3/4” package.

In low-power LEDs, the encapsulant has the shape of a hemisphere, so that the angle of incidence at the encapsulant/air interface is always normal. As a result, total internal reflection does not occur at the encapsulant/air interface.

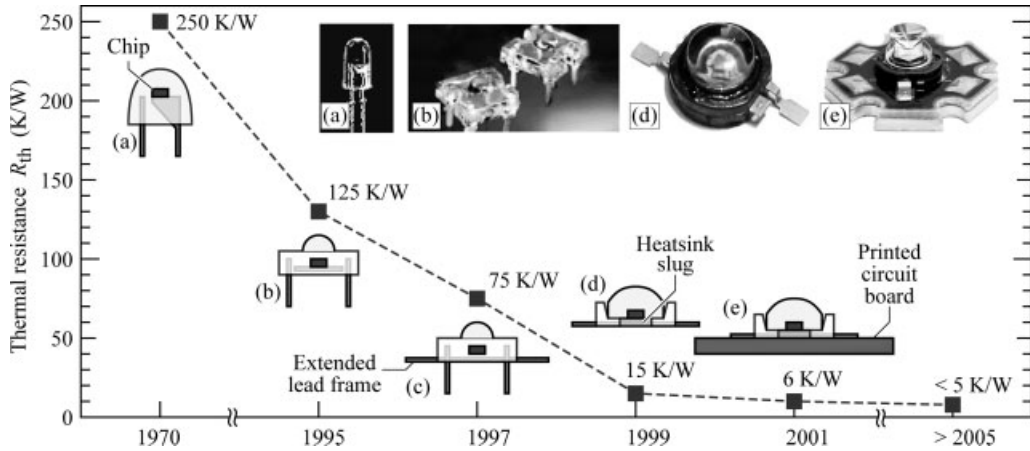
A *power package* is shown in Fig. 1.20 (b). Power packages have a *thermally conductive path* from the LED chip, through the package, to a heat sink, e. g. a printed circuit board. The power package shown in the figure has several advanced features. First, the package contains an Al or Cu heatsink slug with low thermal resistivity. Second, the chip is encapsulated with silicone. Because standard silicone retains mechanical softness in its cured state, the silicone encapsulant is covered with a plastic cover that also serves as a lens. Third, the chip is directly mounted on a Si submount that includes electrostatic discharge (ESD) protection [67]. Electrostatic discharge-protection circuits typically consist of a series of Si diodes or of a Si Zener diode. The current caused by an electrostatic discharge, which can be understood as a short high-voltage pulse applied to the electrodes of the device, will bypass the LED and flow mostly through the series of low-resistance Si diodes thereby protecting the LED.

The thermal resistance of LED packages together with the maximum temperature of operation determines the maximum thermal power that can be dissipated in the package. The maximum temperature of operation may be determined by reliability considerations, by the degradation of the encapsulant, and by internal quantum-efficiency considerations. Several types of LED packages and their thermal resistance are shown in Fig. 1.21 [69]. Early LED packages introduced in the late 1960s and still used for low-power packages, have a high thermal resistance of about 240 K/W. Packages using *heatsink slugs* made of Al or Cu that transfer heat from the chip directly to a printed circuit board (PCB) that in turn spreads the heat, have thermal resistances of 6–12 K/W. It is expected that thermal resistances of  $< 5$  K/W will be achieved for advanced passively cooled power packages.

Note that the packages shown in Fig. 1.21 do not use *active cooling* (fan cooling). Heatsinks with cooling fins and fan are commonly used to cool electronic microchips including Si CMOS microprocessors. They have thermal resistances  $< 0.5$  K/W. The use of active cooling devices would reduce the power efficiency of LED-based systems and are therefore not used.

A common encapsulant is *epoxy resin* (also called epoxy) that remains transparent and does not show degradation over many years for long-wavelength visible-spectrum and IR LEDs. However, it has been reported that epoxy resins lose transparency in LEDs emitting at shorter wavelengths, i. e. in the blue, violet, and UV [70]. Epoxy resins are chemically stable up to temperatures of about 120 °C. However, prolonged exposure to temperatures  $> 120$  °C leads to yellowing (loss of transparency).

To overcome the limited thermal stability of epoxies, *silicone encapsulants* have been used starting in the early 2000s. Silicone is a polymer that contains Si and O thereby resembling  $\text{SiO}_2$  more so than epoxy resins. This resemblance sug-



**Fig. 1.21** Thermal resistance of LED packages: (a) 5 mm (b) low-profile (c) low-profile with extended lead frame (d) heatsink slug (e) heatsink slug mounted on printed circuit board (PCB). Trade names for these packages are “Piranha” ((b) and (c), Hewlett Packard Corp.), “Barracuda” ((d) and (e), Lumileds Corp.), and “Dragon” ((d) and (e), Osram Opto Semiconductors Corp.) (adopted from ref. [69]).

gests that silicone encapsulants are chemically and thermally stable and do not lose transparency as easily as epoxy resins. Indeed, standard silicones are stable up to temperatures of about 160 °C, i. e. significantly higher than epoxy. It is desirable to develop encapsulants that are SiO<sub>2</sub>-like because silica has excellent thermal and chemical stability [71].

*Poly (methyl methacrylate)* or briefly *PMMA* is a less common encapsulant used for LEDs. PMMA is also known under the name of acrylic glass and under the product name Plexiglas. The relatively low refractive index of PMMA ( $\bar{n} = 1.49$  in the wavelength range 500 – 650 nm) results in a limited extraction efficiency when used with high-index semiconductors.

## 1.8

### Conclusion

In this chapter, properties of inorganic LEDs have been reviewed, including optical emission spectra, direct and indirect semiconductors, radiative and nonradiative recombination processes, and double-heterostructure active regions, and quantum-well active regions. We also reviewed advanced device physics including resonant-cavity designs that result in enhanced LED emission characteristics and current transport in a variety of LED structures. Advanced LED fabrication techniques for achieving high extraction efficiency, such as chip shaping, highly efficient omnidirectional reflectors, and packaging issues, were also discussed.

Inorganic semiconductor LEDs are environmentally benign and very promising candidates for high-power, high-efficiency, and low-cost lighting and illumination applications. AlGaInP-based compound semiconductors are capable of emitting in the red, orange, amber, and yellow wavelength regions with high external efficiency. AlGaInN-based semiconductors are efficient sources in the UV, violet, blue, cyan, and green wavelength regions. This enables high-brightness inorganic LEDs to be used for high-efficiency white-light sources with excellent color-rendering capabilities in solid-state lighting applications.

## References

- 1 Lin Y.-Sh., Ma K.-J., Hsu C., Feng S.-W., Cheng Y.-C., Liao C.-C., Yang C.-C., Chou C.-C., Lee C.-M., Chyi J.-I. "Dependence of composition fluctuation on indium content in InGaInN multiple quantum wells" *Appl. Phys. Lett.* **77**, 2988 (2000).
- 2 Smeeton T. M., Kappers M. J., Barnard J. S., Vickers M. E., Humphreys C. J. "Electron-beam-induced strain within InGaIn quantum wells: False indium 'cluster' detection in the transmission electron microscope" *Appl. Phys. Lett.* **83**, 5419 (2003).
- 3 Toyoda Gosei Corporation, Japan, General LED catalogue (2000).
- 4 Xi Y., Schubert E. F. "Junction-temperature measurements in GaN ultraviolet light-emitting diodes using diode forward voltage method" *Appl. Phys. Lett.* **85**, 2163 (2004).
- 5 Xi Y., Xi J.-Q., Gessmann Th., Shah J. M., Kim J. K., Schubert E. F., Fisher A. J., Crawford M. H., Bogart K. H. A., Allerman A. A. "Junction and carrier temperature measurements in deep ultraviolet light-emitting diodes using three different methods" *Appl. Phys. Lett.* **86**, 031907 (2005).
- 6 Joannopoulos J. D., Meade R. D., Winn J. N. "Photonic crystals" (Princeton University Press, Princeton, 1995).
- 7 Purcell E. M. "Spontaneous emission probabilities at radio frequencies" *Phys. Rev.* **69**, 681 (1946).
- 8 De Martini F., Innocenti G., Jacobovitz G. R., Mataloni P. "Anomalous spontaneous emission time in a microscopic optical cavity" *Phys. Rev. Lett.* **59**, 2955 (1987).
- 9 Suzuki M., Yokoyama H., Brorson S. D., Ippen E. P. "Observation of spontaneous emission lifetime change of dye-containing Langmuir-Blodgett films in optical microcavities" *Appl. Phys. Lett.* **58**, 998 (1991).
- 10 Yablonoitch E., Gmitter T. J., Bhat R. "Inhibited and enhanced spontaneous emission from optically thin AlGaAs/GaAs double heterostructures" *Phys. Rev. Lett.* **61**, 2546 (1988).
- 11 Yokoyama H., Nishi K., Anan T., Yamada H., Boorson S. D., Ippen E. P. "Enhanced spontaneous emission from GaAs quantum wells in monolithic microcavities" *Appl. Phys. Lett.* **57**, 2814 (1990).
- 12 Schubert E. F., Vredenberg A. M., Hunt N. E. J., Wong Y. H., Becker P. C., Poate J. M., Jacobson D. C., Feldman L. C., Zydzik G. J. "Giant enhancement in luminescence intensity in Er-doped Si/SiO<sub>2</sub> resonant cavities" *Appl. Phys. Lett.* **61**, 1381 (1992).
- 13 Hunt N. E. J., Vredenberg A. M., Schubert E. F., Becker P. C., Jacobson D. C., Poate J. M., Zydzik G. J. "Spontaneous emission control of Er<sup>3+</sup> in Si/SiO<sub>2</sub> microcavities" in "Confined electrons and photons" edited by E. Burstein, C. Weisbuch (Plenum Press, New York, 1995).
- 14 Nakayama T., Itoh Y., Kakuta A. "Organic photo- and electroluminescent devices with double mirrors" *Appl. Phys. Lett.* **63**, 594 (1993).
- 15 Dodabalapur A., Rothberg L. J., Miller T. M. "Color variation with electroluminescent organic semiconductors in multimode resonant cavities" *Appl. Phys. Lett.* **65**, 2308 (1994).

- 16 Fabry G., Perot A. "Theory and applications of a new interference method for spectroscopy" (translated from French) *Ann. Chim. Phys.* **16**, 115 (1899).
- 17 Schubert E. F., Wang Y. H., Cho A. Y., Tu L. W., Zydzik G. J. "Resonant cavity light-emitting diode" *Appl. Phys. Lett.* **60**, 921 (1992).
- 18 Hunt N. E. J., Schubert E. F., Logan R. A., Zydzik G. J. "Enhanced spectral power density and reduced linewidth at 1.3  $\mu\text{m}$  in an InGaAsP quantum well resonant cavity light-emitting diode" *Appl. Phys. Lett.* **61**, 2287 (1992).
- 19 Hunt N. E. J., Schubert E. F., Sivco D. L., Cho A. Y., Kopf R. F., Logan R. A., Zydzik G. J. "High efficiency, narrow spectrum resonant cavity light-emitting diodes" in "Confined electrons and photons" edited by E. Burstein, C. Weisbuch (Plenum Press, New York, 1995).
- 20 Schubert E. F., Hunt N. E. J., Micovic M., Malik R. J., Sivco D. L., Cho A. Y., Zydzik G. J. *Science* **265**, 943 (1994).
- 21 Yariv A. "Theory and applications of quantum mechanics" (John Wiley and Sons, New York, 1982) p. 143.
- 22 Schubert E. F. "Doping in III-V semiconductors" page 512 (Cambridge University Press, Cambridge U.K., 1993).
- 23 Hunt N. E. J., Schubert E. F., Kopf R. F., Sivco D. L., Cho A. Y., Zydzik G. J. "Increased fiber communications bandwidth from a resonant cavity light-emitting diode emitting at  $\lambda = 940 \text{ nm}$ " *Appl. Phys. Lett.* **63**, 2600 (1993).
- 24 Streubel K., Helin U., Oskarsson V., Backlin E., Johanson A. "High-brightness visible (660 nm) resonant-cavity light-emitting diode" *IEEE Photon. Technol. Lett.* **10**, 1685 (1998).
- 25 Nuese C. J., Tietjen J. J., Gannon J. J., Gossenberger H. F. "Optimization of electroluminescent efficiencies for vapor-grown GaAsP diodes" *J. Electrochem Soc.: Solid State Science* **116**, 248 (1969).
- 26 Kuo C. P., Fletcher R. M., Osentowski T. D., Lardizabal M. C., Craford M. G., Robbins V. M. "High performance AlGaInP visible light-emitting diodes" *Appl. Phys. Lett.* **57**, 2937 (1990).
- 27 Fletcher R. M., Kuo C. P., Osentowski T. D., Huang K. H., Craford M. G. "The growth and properties of high performance AlInGaP emitters using lattice mismatched GaP window layers" *J. Electronic Materials* **20**, 1125 (1991).
- 28 Fletcher R. M., Kuo C. P., Osentowski T. D., Robbins V. M. "Light-emitting diode with an electrically conductive window" US Patent 5,008,718 (1991).
- 29 Sugawara H., Ishakawa M., Hatakoshi G. "High-efficiency InGaAlP/GaAs visible light-emitting diodes" *Appl. Phys. Lett.* **58**, 1010 (1991).
- 30 Sugawara H., Ishakawa M., Kokubun Y., Nishikawa Y., Naritsuka S., Itaya K., Hatakoshi G., Suzuki M. "Semiconductor light-emitting device" United States Patent 5,153,889, issued Oct. 6 (1992).
- 31 Sugawara H., Itaya K., Nozaki H., Hatakoshi G. "High-brightness InGaAlP green light-emitting diodes" *Appl. Phys. Lett.* **61**, 1775 (1992).
- 32 Schubert E. F. "Light-Emitting Diodes" (Cambridge University Press, 2003).
- 33 Guo X., Schubert E. F. "Current crowding and optical saturation effects in GaInN/GaN light-emitting diodes grown on insulating substrates" *Appl. Phys. Lett.* **78**, 3337 (2001).
- 34 Joyce W. B., Wemple S. H. "Steady-state junction-current distributions in thin resistive films on semiconductor junctions (solutions of  $\nabla^2 v = \pm e$ )" *J. Appl. Phys.* **41**, 3818 (1970).
- 35 Rattier M., Bensity H., Stanley R. P., Carlin J.-F., Houdre R., Oesterle U., Smith C. J. M., Weisbuch C., Krauss T. F. "Toward ultra-efficient aluminum oxide microcavity light-emitting diodes: Guided mode extraction by photonic crystals" *IEEE J. Selected Topics in Quant. Electron.* **8**, 238 (2002).
- 36 Guo X., Li Y.-L., Schubert E. F. "Efficiency of GaN/GaInN light-emitting diodes with interdigitated mesa geometry" *Appl. Phys. Lett.* **79**, 1936 (2001).
- 37 Steigerwald D. A., Rudaz S. L., Thomas K. J., Lester S. D., Martin P. S., Imler W. R., Fletcher R. M., Kish Jr. F. A., Maranowski S. A. "Electrode structures for light-emitting devices" US patent 6,307, 218 (2001).



- 38 LED Museum on the Internet < <http://ledmuseum.home.att.net/agilent.htm> > (2004).
- 39 Schroder D. K. "Semiconductor material and device characterization" (John Wiley and Sons, New York, 1998).
- 40 Huang K.-H., Yu J. G., Kuo C. P., Flethcer R. M., Osentowski T. D., Stinson L. J., Craford M. G., Liao A. S. H. "Twofold efficiency improvement in high-performance AlGaInP light-emitting diodes in the 555-620 nm spectral region using thick GaP window layer" *Appl. Phys. Lett.* **61**, 1045 (1992).
- 41 Schubert E. F., Hunt N. E. J., Micovic M., Malik R. J., Sivco D. L., Cho A. Y., Zyzdik G. J. *Science* **265**, 943 (1994).
- 42 Streubel K., Helin U., Oskarsson V., Backlin E., Johanson A. "High-brightness visible (660 nm) resonant-cavity light-emitting diode" *IEEE Photon. Technol. Lett.* **10**, 1685 (1998).
- 43 Schnitzer I., Yablonovitch E., Caneau C., Gmitter T. J., Scherer A. "30 % external quantum efficiency from surface-textured, thin-film light-emitting diodes" *Appl. Phys. Lett.* **63**, 2174 (1993).
- 44 Windisch R., Schoberth S., Meinlschmidt S., Kiesel P., Knobloch A., Heremans P., Dutta B., Borghs G., Doehler G. H. "Light propagation through textured surfaces" *J. Opt. A: Pure Appl. Opt.* **1**, 512 (1999).
- 45 Windisch R., Dutta B., Kuijk M., Knobloch A., Meinlschmidt S., Schoberth S., Kiesel P., Borghs G., Doehler G. H., Heremans P. "40 % efficient thin-film surface textured light-emitting diodes by optimization of natural lithography" *IEEE Trans. Electron Dev.* **47**, 1492 (2000).
- 46 Windisch R., Rooman C., Kuijk M., Borghs G., Heremans P. "Impact of texture-enhanced transmission on high-efficiency surface-textured light-emitting diodes" *Appl. Phys. Lett.* **79**, 2315 (2001).
- 47 Windisch R., Rooman C., Dutta B., Knobloch A., Borghs G., Doehler G. H., Heremans P. "Light-extraction mechanisms in high-efficiency surface-textured light-emitting diodes" *IEEE J. Selected Topics Quant. Electronics* **8**, 248 (2002).
- 48 Schmid W., Eberhard F., Jager R., King R., Joos J., Ebeling K. "45 % quantum-efficiency light-emitting diodes with radial outcoupling taper" *Proceedings SPIE* **3938**, 90 (2000).
- 49 Schmid W., Scherer M., Jager R., Strauss P., Streubel K., Ebeling K. "Efficient light-emitting diodes with radial outcoupling taper at 980 and 630 nm emission wavelength" *Proc. SPIE* **4278**, 109 (2001).
- 50 Schmid W., Scherer M., Karnutsch C., Pobl A., Wegleiter W., Schad S., Neubert B., Streubel K. "High-efficiency red and infrared light-emitting diodes using radial outcoupling taper" *IEEE J. Select. Topics Quant. Electronics* **8**, 256 (2002).
- 51 Sinzinger S., Jahns J. "Microoptics" (Wiley-VCH, New York, 1999).
- 52 Krames M. R., Ochiai-Holcomb M., Höfler G. E., Carter-Coman C., Chen E. I., Tan I.-H., Grillot P., Gardner N. F., Chui H. C., Huang J.-W., Stockman S. A., Kish F. A., Craford M. G., Tan T. S., Kocot C. P., Hueschen M., Posselt J., Loh B., Sasser G., Collins D. "High-power truncated-inverted-pyramid (Al<sub>0.5</sub>Ga<sub>0.5</sub>)In<sub>0.5</sub>P/GaP light-emitting diodes exhibiting > 50 % external quantum efficiency" *Appl. Phys. Lett.* **75**, 2365 (1999).
- 53 McLeod H. A., "Thin-Film Optical Filters", (New York: McGraw-Hill, 1989), p. 32–43.
- 54 Popov K. V., Dobrowolski J. A., Tikhonravov A. V., Sullivan B. T. "Broadband high-reflection multilayer coatings at oblique angles of incidence" *Applied Optics* **36**, 2139 (1997).
- 55 Xu J., Fang H., Lin Zh. "Expanding high-reflection range in a dielectric multilayer reflector by disorder and inhomogeneity" *J. Phys D: Appl. Phys.* **34**, 445 (2001).
- 56 Ibanescu M., Fink Y., Fan S., Thomas E. L., Joannopoulos J. D. "An all-dielectric coaxial waveguide" *Science* **289**, 415 (2000).
- 57 Hart S. D., Maskaly G. R., Temelkuran B., Prideaux P. H., Joannopoulos J. D., Fink Y. "External reflection from omnidirectional dielectric mirror fibers" *Science* **296**, 510 (2002).
- 58 Weber M. F., Stover C. A., Gilbert L. R., Nevitt T. J., Ouderkirk A. J. "Giant birefringent optics in multilayer polymer mirrors" *Science* **287**, 2451 (2000).



- 59 Fink Y., Winn J. N., Fan S., Chen Ch., Michel J., Joannopoulos J. D., Thomas E. L. "A dielectric omnidirectional reflector" *Science* **282**, 1679 (1998).
- 60 Kato T., Susawa H., Hirotsu M., Saka T., Ohashi Y., Shichi E., Shibata S. "GaAs/AlGaAs surface emitting IR LED with Bragg reflector grown by MOCVD" *J. Cryst. Growth* **107**, 832 (1991).
- 61 Chiou S. W., Lee C. P., Huang C. K., Chen C. W. "Wide-angle distributed Bragg reflectors for 590 nm amber AlGaInP light-emitting diodes" *J. Appl. Phys.* **87**, 2052 (2000).
- 62 Gessmann Th., Li Y.-L., Schubert E. F., Graff J. W., Sheu J. K. "GaInN light-emitting diodes with omnidirectional reflectors" *SPIE Proceedings Series 4996: Light-emitting diodes: Research Manufacturing, and Applications* (2003).
- 63 Kim J. K., Gessmann Th., Luo H., Schubert, E. F. "GaInN light-emitting diodes with RuO<sub>2</sub>/SiO<sub>2</sub>/Ag omnidirectional reflector" *Appl. Phys. Lett.* **84**, 4508 (2004).
- 64 Born M., Wolf E., "Principle of Optics 6th edition", (Pergamon Press, 1987), p. 62.
- 65 Palik E. D., "Handbook of Optical Constants of Solids" (Academic Press, Orlando, 1985) p. 357.
- 66 Xi J. Q., Ojha M., Cho W., Gessmann Th., Schubert E. F., Plawsky J. L., Gill W. N. "OmniDirectional Reflector Using a Low Refractive Index Material" *Opt. Lett.* **30**, 1518 (2005).
- 67 Krames M. R., Steigerwald D. A., Kish Jr. F. A., Rajkomar P., Wierer Jr. J. J., Tan T. S. "III-nitride light-emitting device with increased light generating capability" US patent 6,486,499 B1 (2002).
- 68 Krames M. R. "Overview of current status and recent progress of LED technology" *US Department of Energy Workshop "Solid State Lighting – Illuminating the Challenges"* Crystal City, VA, Nov. 13–14, 2003.
- 69 Arik M., Petroski J., Weaver S. "Thermal challenges in the future generation solid state lighting applications: light-emitting diodes" *Eighth Intersociety Conference on Thermal and Thermomechanical Phenomena in Electronic Systems* (Cat. No.02CH37258) May 30–June 1 2002, p. 113, (IEEE, Piscataway NJ, 2002).
- 70 Barton D. L., Osinski M., Perlin P., Helms C. J., Berg N. H. "Life tests and failure mechanisms of GaN/AlGaIn/InGaIn light-emitting diodes" *Proc. SPIE* **3279**, 17 (1998).
- 71 Crivello, James V., personal communication (2004).

## 2

# Electronic Processes at Semiconductor Polymer Heterojunctions

Arne C. Morteani, Richard H. Friend, and Carlos Silva

## 2.1

### Introduction

Until the 1970s, organic polymeric materials – “plastics” – were considered to be insulators and were employed in numerous applications such as electrical wire insulation or the insulating interlayer in capacitors. It was then discovered that doped polyacetylene exhibits metallic conductivity [1, 2]. Later it was found that undoped conjugated polymers can exhibit semiconductor properties and in particular the discovery of electroluminescence in poly-*p*-phenylenevinylene (PPV) triggered the fast expansion of this field of research [3]. Like other plastics, conjugated polymers can be solution processed. This makes possible easy and cheap fabrication of polymer-based field-effect transistors ([4–7], see also ref. [8] for a review), light-emitting diodes (LEDs) [9, 10], and photovoltaic cells [10–12] that also exhibit new and useful mechanical properties such as flexibility.

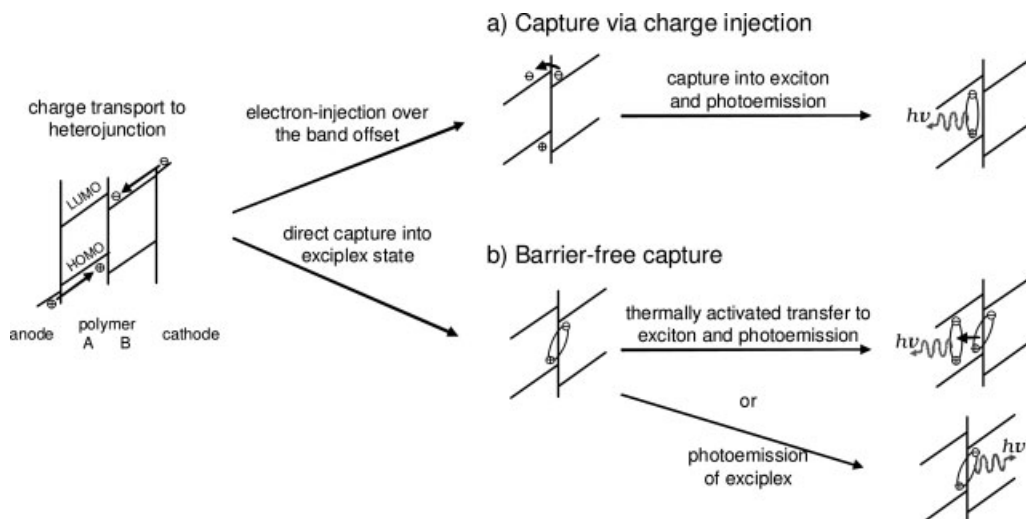
The photophysics of  $\pi$ -conjugated polymers are reviewed in detail in other chapters of this book. (See, for example, Chapter 3.) Here, we focus on the electronic and photophysical phenomena that occur at the heterojunction between two different semiconductor polymers. The heterojunctions are formed by combining four different polyfluorene copolymers in blend or bilayer thin films and are investigated using time-resolved and steady-state, temperature- and electric-field-dependent photoluminescence measurements as well as electroluminescence and time-resolved spectroscopy. We review a body of work carried out in our laboratories over the last few years, and published in numerous journal articles (see refs. [13–17]).

The heterojunction formed between dissimilar organic semiconductors is generally found to be remarkably free of gap states and other defects that would otherwise compromise semiconductor device operation. Heterojunction light-emitting diodes (LEDs) are designed so that the offsets between conduction and valence band edges are of type II (see Section 2.1.4.1) and electrons and holes accumulate on opposite sides of the heterojunction (see Fig. 2.1). In a non-interacting electron picture, type-II heterojunctions would destabilize an exciton

present in either semiconductor, since the exciton state would be higher in energy than the charge-separated state. However, organic semiconductors are low dielectric constant materials (typically less than 4) so that Coulomb interaction between electron and hole gives a substantial exciton binding energy (of order 0.5 eV). To a first approximation, when this binding energy is larger than the band-edge offsets, excitons are stable at the interface [18]. By selecting semiconductors with larger band-edge offsets, charge separation at the heterojunction can be readily achieved, giving efficient photovoltaic behavior.

LEDs made using molecular semiconductors are generally fabricated as multiple-layer heterojunction structures by successive vacuum sublimation steps [19]. However, with solution-processed polymers it is possible to make 'distributed heterojunction' diodes by demixing of two polymers codeposited from common solution [20]. This is an obviously desirable structure for photovoltaic diodes, because it can allow excitons photogenerated throughout the bulk of the layer to be sufficiently close to the heterojunction so that they can be ionized. This has been exploited to produce promising photovoltaic performance [21–23]. More surprisingly, we have found that similar demixed polymer blends forming type-II heterostructures can be used to fabricate high-performance LEDs.

We find that localized excited-state complexes, so-called exciplexes, form at heterojunctions with charge-transfer character. This gives rise to a number of



**Fig. 2.1** Illustration of the two mechanisms for electron–hole capture discussed in the text. Electrons and holes are transported through their respective transport materials and accumulate at the heterojunction. a) Injection of one of the charges into the opposite polymer makes possible charge capture within the polymer bulk and formation of intramolecular excitons. b) Barrier-free electron–hole capture

directly produces a neutral excited-state, the exciplex, without prior injection of a charge carrier into the opposite polymer. The exciplex can be thermally activated and transfer to the bulk exciton, leading to exciton electroluminescence. With small oscillator strength, it can also decay radiatively and emit red-shifted exciplex electroluminescence.

novel electronic and photophysical processes at the interface. We investigate the crucial role of the exciplex during charge capture and exciton dissociation. Specifically, we find that electron–hole capture produces the interfacial exciplex state directly, which can be subsequently excited thermally to the bulk exciton state. This fast, barrier-free capture process suggests a reason for the high efficiencies seen from some polymer blend light-emitting diodes. We find that exciton dissociation does not yield free charges directly but rather produces a geminate electron–hole pair, which subsequently dissociates fully to form uncorrelated charges or collapses into the exciplex state. We develop a comprehensive model of the electronic processes at the heterojunction that not only describes exciton dissociation, but also includes barrier-free capture. We show that excitons can be recovered even after they have undergone charge transfer at the heterojunction [14]. We describe the influence of the film morphology on the above mechanisms and in particular the morphology-dependent trapping of excitons at the heterojunction.

### 2.1.1

#### Molecular Complexes and Exciplexes

The aim of this chapter is to elucidate the various electronic and optical processes that occur at heterojunctions between two semiconductor polymers. Most of the results presented are related to the presence of localized electronic states at heterojunctions between different polyfluorenes. These have an analog in solution systems of small molecules where they are called exciplex states. Here, we give an overview of the theories that have been developed for small-molecule solution systems (for more details see also [24] and [25]). In Section 2.1.3, we then discuss if and how these are applicable to solid-state films of blended conjugated polymers.

When two or more molecules come in close contact this can lead to a stabilization of the overall system via the delocalization of the electronic wavefunctions across the molecule boundaries. The resulting *molecular complex* can no longer be treated as two isolated molecules but has to be considered as a single quantum-mechanical system. As a consequence the molecules absorb and/or emit in a cooperative manner. If the complexation occurs in the ground-state we speak of a *ground-state* or *absorption complex* or an *aggregate*. (The latter term is widely used in the conjugated polymer community although it should be used with care to distinguish between true H- or J-type molecular aggregates.) When complexation occurs only while one of the molecules is in the excited-state we talk of an *excited-state complex* or simply an *exciplex*. The molecules in ground-state complexes absorb cooperatively, while those bound to form an exciplex emit cooperatively. The resulting absorption and emission spectra differ from those of the isolated molecules. Ground-state complexes need not form exciplexes upon excitation and exciplexes need not produce ground-state complexes when emitting. A special case of the exciplex is the *excimer* that is an exciplex composed of two identical molecules,

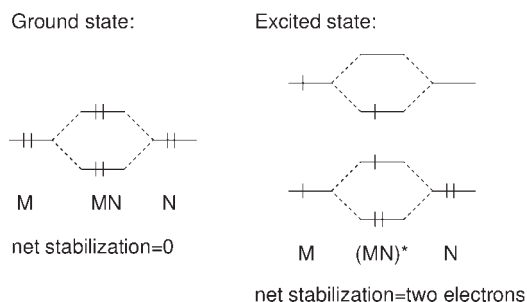


What are the characteristic properties of exciplexes? Perhaps the most general distinguishing characteristic of an electronically excited-state is its emission spectrum. In the bulk material, it is often difficult to distinguish spectroscopically (at least at steady state) between  $M^*$  and  $(MM)^*$ . However,  $(NM)^*$  spectral signatures are specific to intermolecular interactions. Thus, if exciplexes exist, they should, in principle, exhibit fluorescence (singlet exciplexes) or phosphorescence (triplet exciplexes) that is distinct from that of both  $M^*$  and  $N^*$ . Furthermore, since the ground-state complex  $MN$  is generally less bound than  $(MN)^*$ , emission from the exciplex will usually occur to a weakly bound or dissociative ground-state.

In the following, we will summarize the quantum mechanics and photophysics of exciplexes. Ground-state complexes will not be treated further since they are not the subject of this chapter.

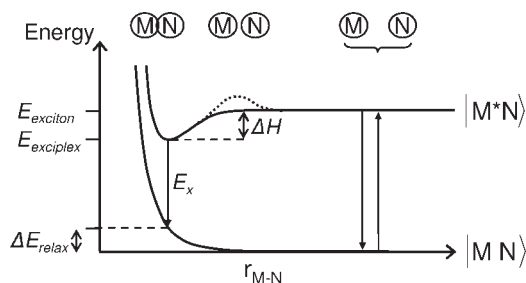
The enhanced stabilization of the excited-state complex  $(MN)^*$  as compared to the ground-state complex  $MN$  can be understood from a simple model of molecular orbital interactions (Fig. 2.2). When  $M$  and  $N$  are brought into contact, then the major electronic interactions will be among their highest filled or partially filled orbitals. (Note that this sketch is for the special case when  $N = M$  so there is no energy offset in the molecular orbitals.) According to the rules of perturbation theory, the HOMO of  $M$  will interact with the HOMO of  $N$  to form two new orbitals. Similarly, the LUMOs of both molecules will interact to produce two new LUMOs of the complex. The two new orbitals split in energy relative to the original HOMOs (or LUMOs). This means that in the complex one of the new HOMOs (LUMOs) is lower in energy and one higher in energy than the original HOMOs (LUMOs). The stabilized orbital is called *bonding* while the destabilized one is the *antibonding* orbital.

In the ground-state complex of  $M$  and  $N$ , the four electrons that occupied the HOMOs of  $M$  and  $N$  occupy the new set of HOMOs. Two electrons are stabilized and two electrons are destabilized. Thus, no gain in energy is achieved by inter-



**Fig. 2.2** Visualization of the molecular orbital interactions in ground-state and excited-state complexes of molecules  $M$  and  $N$ . The sketch is drawn for two identical molecules ( $M = N$ ). For dissimilar molecules, charge-transfer interactions stabilize the complex further.

**Fig. 2.3** Potential energy surface description of exciplex formation between two molecules M and N.  $|MN\rangle$  and  $|M^*N\rangle$  are the ground- and excited-state curves.  $r_{M-N}$  stands for the intermolecular distance.  $E_{\text{exciton}}$  and  $E_{\text{exciplex}}$  are the exciton and exciplex energy levels, while  $E_x$  is the energy of exciplex photoemission.  $\Delta E_{\text{relax}}$  is the energy of geometrical relaxation and  $\Delta H$  is the enthalpy associated with exciplex formation. The dotted line illustrates a possible activation barrier for exciplex formation.



action of M and N during their collisions. In the exciplex, however, since one of the partners is electronically excited, *three* electrons are stabilized, while only one electron is destabilized as the electrons redistribute themselves from their original non-interacting orbitals to the new orbitals of the exciplex. Exciplex effects are often stronger than excimer effects because of their partial ionic character.

Let us now consider a potential energy surface description of exciplex formation (Fig. 2.3). At large separations of the (ground-state) molecules M and N, the absorption spectrum of either component would be identical to that of each monomer, i.e. neither component would influence the other. As M and N approach, the absorption spectrum remains constant. Eventually, M and N undergo collisions. Since there are no substantial attractions between M and N in their ground-states, steric hindrance will repel the molecules and very few (dissociative) complexes will exist at any given time. As a result, no new absorptions will be observed.<sup>1)</sup>

Now consider the situation for the approach and collision of  $M^*$  and N on the excited-state surface (upper surface in Fig. 2.3). At a large separation of  $M^*$  and N, the emission spectrum is that of the isolated molecule,  $M^*$ . As the two molecules approach, the bonding between them may increase due to charge transfer and excitation exchange interactions. This will cause a minimum to occur in the potential-energy curve. This enthalpy decrease is usually accompanied by an entropy decrease, since the complexation reduces the degrees of freedom of the system (e.g. translations or rotations of one molecule with respect to the other). If the overall free-energy change  $\Delta G = \Delta H - T\Delta S$  is negative an excited-state complex – an exciplex – will form. The exciplex minimum of the potential energy curve can sometimes only be reached by overcoming a potential energy maximum and this is illustrated by the dotted line in Fig. 2.3. In these cases, the formation of an exciplex via the approach of two molecules is a thermally activated process.

Emission from the exciplex will occur according to the Franck–Condon principle i.e., vertically from the excited-state minimum (no change of the nuclear configuration during the emission process). The separation of M and N in the ex-

1) This instability of the ground-state complex is a somewhat arbitrary feature of the exciplex definition.

cited-state minimum corresponds to a point on the repulsive part of the ground-state potential curve. That is, the exciplex is stabilized via configurational (or “geometrical”) relaxation of the molecules with respect to their ground-state configurations. Franck–Condon emission will therefore lead exclusively to repulsive states on the ground surface. Within a few collisions, D and A will fly apart rapidly. This process is the emission analog of directly dissociative absorption. The absence of any quantization of the vibronic “levels” results in the total absence of vibrational structure in the emission spectra of excimers and exciplexes.

We are now in a position to appreciate the single most definitive kind of direct spectroscopic evidence for the formation of an excimer or exciplex: the observation of a concentration-dependent, vibrationally unstructured emission that occurs to the red of the emission spectra of either one of the constituent molecules of the complex. The fact that the exciplex does not decay to the configurationally relaxed ground-state also means that the exciplex emission energy  $E_x$  is lower than the energy of the exciplex state  $E_{\text{exciplex}}$  with respect to the (relaxed) system ground-state. They differ exactly by the relaxation energy  $\Delta E_{\text{relax}}$ .

### 2.1.2

#### Review of Molecular Exciplexes in Solution

In most heterocomplexes the two constituents differ in their ionization potentials and electron affinities. This can promote a partial charge transfer upon contact of the two molecules causing a considerable electric dipole to form across the interface. The importance of the charge-transfer interactions can therefore become dominant over the excitation exchange interactions. Indeed, most exciplexes appear to be stabilized mainly by charge-transfer interactions [24].

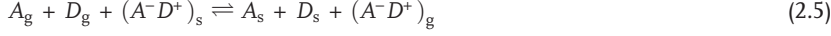
In Fig. 2.2, we discussed exciplex formation using a picture of two neutral molecules approaching each other. We now consider their high charge-transfer character and treat them as the product of two ions brought together. At small distances the coulomb attraction of the positive charge on the donor, D, and the negative charge on the acceptor, A, will lead to a stabilization of the overall system. This stabilization energy, C, can be seen as a (Coulombic) *exciplex binding energy* in analogy to the exciton binding energy in organic and inorganic semiconductors.

The emissive properties of solution-phase exciplexes has been reviewed by Weller [25], and we summarize the basic concepts that determine the emission energy of these in the following. Neglecting any orbital overlaps, we derive the energy  $E_x^0$  of the “quasiclassical” exciplex state in the gas phase above the separated ground-state molecules to be:

$$E_x^0 = IP_D - EA_A - C \quad (2.4)$$

where  $IP_D$  is the ionisation potential of the donor and  $EA_A$  represents the electron affinity of the acceptor. Equation (2.4) is only an approximation and needs to be altered in order to achieve an accurate description. Firstly, the orbital overlap be-

tween the constituent molecules is expected to either stabilize or destabilize the exciplex by an amount  $\Delta E_{(\text{de})\text{stab}}$ . Secondly, there will be an enthalpy of solvation,  $\Delta H_X^{\text{sol}}$  associated with the exciplex formation, i.e. with



where the subscripts g and s refer to gas phase or solution phase, respectively. With these modifications the energy of the “nonclassical” and solvated exciplex,  $E_X$ , becomes

$$E_X = E_X^0 + \Delta E_{(\text{de})\text{stab}} - \Delta H_X^{\text{sol}} = IP_D - EA_A + \Delta E_{(\text{de})\text{stab}} - \Delta H_X^{\text{sol}} - C \quad (2.6)$$

For the experimental verification of this expression it is useful to replace  $IP_D$  and  $EA_A$  with their solvent-dependent equivalents, i.e. with the oxidation potential  $E_D^{\text{ox}}$  and the reduction potential  $E_A^{\text{red}}$ . These are related to the ionization potential and electron affinity by:

$$E_D^{\text{ox}} = IP_D + \Delta G_{D^+}^{\text{sol}} \quad (2.7)$$

$$E_A^{\text{red}} = EA_A + \Delta G_{A^-}^{\text{sol}} \quad (2.8)$$

where  $\Delta G_{D^+}^{\text{sol}}$  and  $\Delta G_{A^-}^{\text{sol}}$  are the solvation free energies associated with the processes.



and



The subscript g refers to gas phase and s to the solution in which the oxidation and reduction potentials have been determined. The complete expression for the exciplex energy  $E_X$  becomes

$$E_X = E_D^{\text{ox}} - E_A^{\text{red}} + E_{(\text{de})\text{stab}} - (\Delta H_X^{\text{sol}} + \Delta G_{D^+}^{\text{sol}} - \Delta G_{A^-}^{\text{sol}} + C) \quad (2.11)$$

Exciplexes (in the general definition given at the beginning of this section) are classified according to the sign and magnitude of the (de)stabilization energy  $E_{(\text{de})\text{stab}}$  [25]. Generally, for the materials systems studied here,  $E_{(\text{de})\text{stab}} \approx -0.15$  eV.

For exciplexes with  $E_{(\text{de})\text{stab}}$  of this order, the following empirical equality is found for the maximum  $h\nu_X^{\text{max}} = E_X$  of the exciplex emission [25].

$$E_X = E_D^{\text{ox}} - E_A^{\text{red}} - 0.15 \pm 0.10 \text{ eV} \quad (2.12)$$



There is generally excellent agreement of this empirical equation with the experimental data. The unit slope of the dependence of  $E_X$  on  $E_D^{\text{ox}} - E_A^{\text{red}}$  is remarkable and was suggested to be due to the fact that the solvation free energies in Eq. (2.13) are of similar magnitude as the Coulomb attraction term and also have a similar dependence on the size of the ions [25]. We will show in a later section that the exciplexes investigated in this chapter also follow the unit-slope behavior and can therefore be classified as molecular systems. The offset of 0.15 eV gives an estimate to the *exciplex binding energy*. Using Eq. (2.11) and Eq. (2.12) and setting  $E_{(\text{de})\text{stab}} = 0$  we find

$$C + (\Delta H_X^{\text{sol}} + \Delta C_{D^+}^{\text{sol}} - \Delta G_A^{\text{sol}}) = 0.15 \pm 0.10 \text{ eV} \quad (2.13)$$

### 2.1.3

#### Exciplexes at the Polymer Heterojunction

In the previous section we discussed the standard knowledge on exciplex states that form between small molecules in solution. In this section exciplex states at the heterojunction between two polymer semiconductors in a solid-state (blend) film are investigated. The question arises as to how the theoretical frameworks described above are applicable. The meaning of terms like “collision”, “concentration”, and “solvation” in the context of solid-state polymer systems needs to be clarified as well as the applicability of Eq. (2.12).

In solution systems two molecules come in close contact only during collisions, while in a solid-state film they are permanently in contact. Therefore, intermolecular processes should be strongly enhanced in solid-state systems, which indeed is the case for ground-state complexation. However, many intermolecular processes, e.g. exciplex formation, require one of the molecules to be in the excited-state. Here, excited-state or “exciton” diffusion towards the interface between two dissimilar polymer phases plays a similar role as molecular diffusion and collision in solutions. Hence, “intermolecular distance” can be replaced by “distance of the exciton from the interface” and models like the one depicted in Fig. 2.3 can be (carefully) applied. During subsequent collisions two molecules explore different relative orientations in order to find one that facilitates exciplex formation. This is not possible in the solid state where the molecules are immobile. The analog would be that the exciton visits different heterojunction sites until it finds a suitable one where a reaction is possible. This is an interesting question because most of the models developed in this chapter describe only a single “kind” of heterojunction. However, different processes occur at different sites along the heterojunction.

It is now also clear what the polymer film equivalent of the concentration of a solution has to be. A highly concentrated solution results in a high frequency of collisions. In a polymer blend film excitons encounter heterojunctions more frequently when the heterojunction density is high. Hence, a high concentration of a solution corresponds to a well-mixed polymer blend with small-scale phase separation. The degree of mixing of the components in a polymer blend (i.e. the

**Table 2.1** Abbreviations and full names for the four polyfluorene polymers used in this chapter.

short name	full name
<b>F8</b>	poly(9,9'-dioctylfluorene)
<b>F8BT</b>	poly(9,9'-dioctylfluorene-co-benzothiadiazole)
<b>PFB</b>	poly(9,9'-dioctylfluorene-co-bis-N,N'-(4-butylphenyl)-bis-N,N'-phenyl-1,4-phenylenediamine)
<b>TFB</b>	9,9'-dioctylfluorene-co-N-(4-butylphenyl)diphenylamine)

“blend morphology”) is therefore a useful experimental parameter for the investigation of polymer systems – just as the solute concentration is for research on solution systems.

Another term used in the descriptions above is “solvation”. In solid-state films there is a dielectric response of the surrounding molecules that also leads to a stabilization of the system in analogy to polar solvation. In Section 2.1.4.6 (Fig. 2.20) we show that Eq. (2.12) holds for polymeric exciplex systems. This means that the correlation between the solvation free energies and the exciplex binding energy that was described earlier also holds for the polymer system.

Finally, we discussed that exciplex formation is accompanied by an entropy decrease. In a solid-state film this change in entropy is small, which in theory should facilitate exciplex formation.

#### 2.1.4

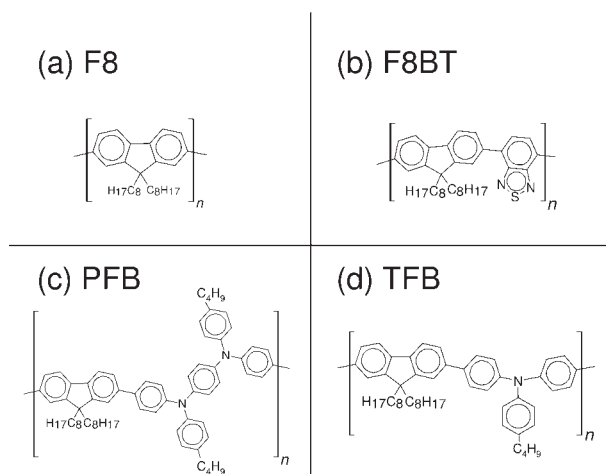
#### The Polymers used in this Chapter

The polymers used in this chapter are all polyfluorene derivatives. They are ABAB copolymers with A being the fluorene group shown in Fig. 2.4(a). Due to their high chemical stability, flexible chemistry and good charge transport and luminescence properties, polyfluorenes are very common materials for polymer optoelectronics and have been used to make highly efficient LEDs [26, 13] as well as good photovoltaic diodes [27, 28] and transistors [29]. Table 2.1 lists the abbreviated and full names of all the polymers that appear in this chapter. The chemical structures of each of the polymers are displayed in Fig. 2.4.

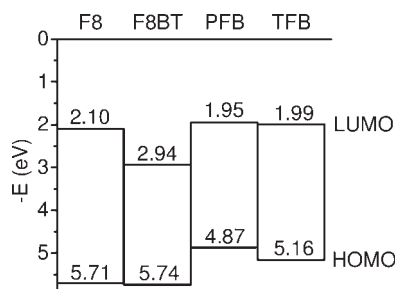
The HOMO and LUMO energies for all polymers are given in Fig. 2.5. These values have been determined via cyclic voltametry [30].

##### 2.1.4.1 Type-II Heterojunctions

The four different polyfluorene materials listed in Table 2.1 can be paired in six different ways. Some of these combinations have been employed successfully for various optoelectronic devices. For example, blend films of TFB and F8BT (written as TFB:F8BT) have been employed for efficient light-emitting diodes (see, e.g.

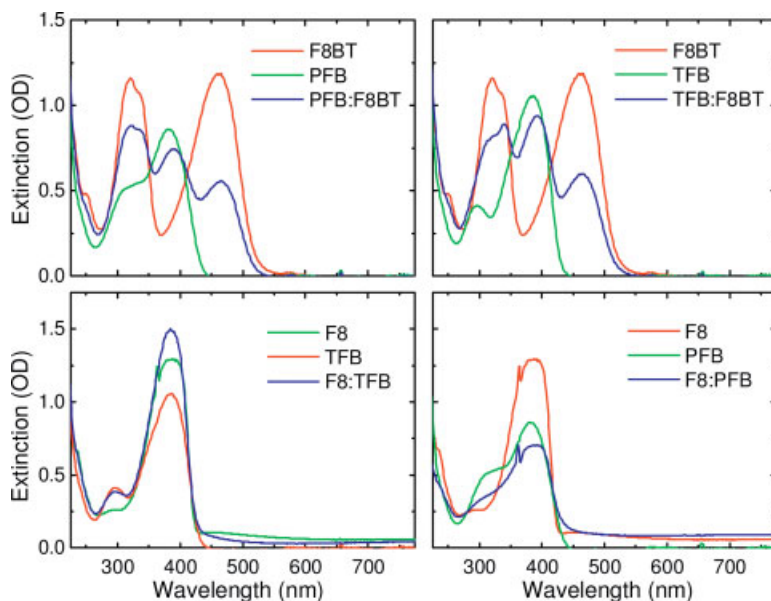


**Fig. 2.4** Chemical structures of F8, F8BT, PFB, and TFB.



**Fig. 2.5** Visualization of the HOMO and LUMO energies of F8, F8BT, PFB, and TFB. These values have been determined via cyclic voltametry [30].

refs. [10, 13] but produce bad photovoltaic diodes [14]. PFB:F8BT, on the other hand, shows promise for photovoltaic diodes (see e.g. refs. [14, 28, 31, 32]) while making poor LEDs [13]. The two systems form *type-II heterojunctions*, i.e. both HOMO and LUMO energies are higher in one polymer than in the other leading to an interface with charge-transfer character. Type-II heterojunctions have generally been found to be useful for device optimization. In LEDs they cause charges to accumulate at opposite sides of the junction leading to a well-defined recombination zone whose position in the device can be controlled, as well as producing less leakage current. In photovoltaic diodes, the heterojunction facilitates exciton dissociation and charge generation, because the loss of the exciton binding energy is offset by the transfer of the electron (hole) into the energetically favorable LUMO (HOMO) orbital. Moreover, for both LEDs and photovoltaic diodes, bipolar currents are necessary and therefore a combination of electron- and hole-transporting polymers (n- and p-type polymers) is needed. This requirement usually leads to a donor-acceptor or type-II heterojunction. On the contrary, type-I systems (i.e. the LUMO and HOMO energies of one polymer are equal or lie between those of the other) do not have any of the above advantages. The only process of interest happening at these interfaces is that excitons undergo resonance energy transfer from the higher-bandgap to the lower-bandgap material.



**Fig. 2.6** Extinction spectra of binary blend and pure polymer films. All films were spun from chloroform and are  $\sim 170$  nm thick. At the time this measurement was done, the films containing F8 were significantly scratched, which explains the large scattering background seen in the spectra.

This is sometimes used to alter the color of LEDs or to improve light harvesting in photovoltaic diodes.

Of the binary systems that can be formed from the polymers in Fig. 2.5, two are of type I and the remaining four are type II. (The heterojunctions between PFB and TFB as well as between F8 and F8BT are effectively type I because of the near-degeneracy of the LUMOs of PFB and TFB and the HOMOs of F8 and F8BT.) This leaves four type-II heterojunctions: PFB:F8BT, TFB:F8BT, F8:PFB, and F8:TFB.

In the following sections, we investigate blend films spun from chloroform solution at a weight ratio of 50:50 (if not indicated differently). In films prepared in this way, the two polymers are well intermixed and hence the film contains a high density of interface sites. This makes it easier to detect signals due to the heterojunction. The thickness of the polymer films was  $\sim 170$  nm.

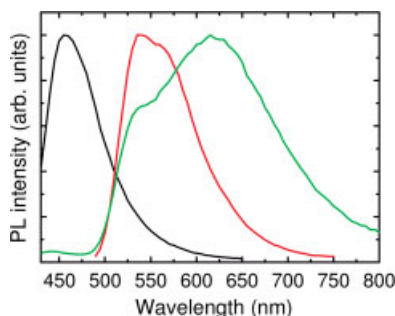
Figure 2.6 shows the extinction spectra of all possible binary polymer blends together with those of the individual polymers. The lack of additional features in any of the blends points to the absence of ground-state interactions between the different polymers.

### 2.1.4.2 The PFB:F8BT Exciplex

In Fig. 2.7, the PL spectra of a PFB:F8BT blend and its pure components are plotted. The blend exhibits a strong emission, peaked around  $\sim 625$  nm, that is not observed in the pure polymers. We show that this red emission is due to exciplex states at the PFB:F8BT heterojunction.

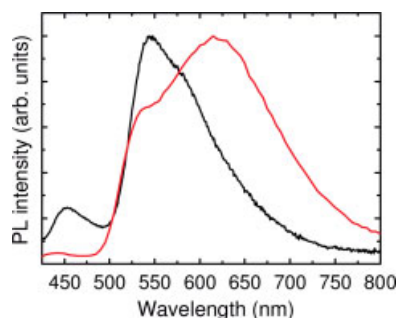
Exciplex states only exist at the interface between the two dissimilar polymers in the blend. Reducing the density of these interfaces in the polymer blend is expected to reduce the amount of exciplex observed. For example, annealing mobilizes the polymers and causes the film to move closer to thermodynamic equilibrium, i.e. the two polymers phase separate and the density of heterojunction sites decreases. Indeed, we observe that the amount of exciplex emission is reduced by the annealing treatment [30].

A second way to vary the density of heterojunctions in the film is to compare films spun from different solvents. The process of demixing during spin coating of PFB and F8BT has been reported in detail elsewhere [27]. The morphology is dependent on the solvent used and its evaporation rate during spin coating. In films prepared under ambient conditions using xylene as solvent,  $\mu\text{m}$ -size features can be observed by tapping-mode AFM. The lengthscale of these is set by the film thickness at the point where F8BT becomes insoluble, and fluorescence microscopy shows that two phases, each rich in one of the polymers, are present. For 50:50 PFB:F8BT blends, the average compositions of the two phases are estimated from Raman spectroscopy to be 80% F8BT and  $<50\%$  F8BT [33]. For blend films of TFB and F8BT, prepared under similar conditions, we find a very similar morphology, which can be seen in the fluorescence image shown in Fig. 2.21 in Section 2.2. These  $\mu\text{m}$ -size features are generated from luminescence throughout the thickness of the film and indicate the bulk nature of this phase separation. Spin coating from chloroform solutions by contrast results in nm-size features that cannot be observed using AFM [27]. This is due to the high evaporation rate of the chloroform, which doesn't allow large-scale phase separation to occur. Films spun from xylene have therefore a much smaller density of heterojunction sites than those spun from chloroform. Figure 2.8 shows the PL emissions from two PFB:F8BT blends that contain the same weight ratio of PFB and F8BT (50:50) but were spin coated from either a chloroform or a xylene solution. Exciplex formation in the film spun from chloroform is much stronger.

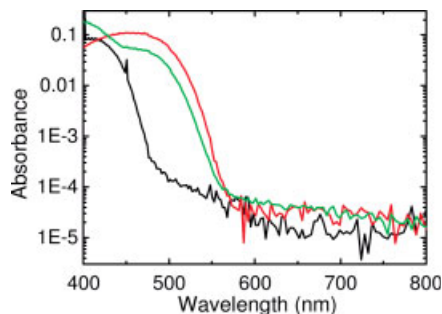


**Fig. 2.7** Photoluminescence spectra of PFB (black), F8BT (red), and a PFB:F8BT blend.

**Fig. 2.8** Photoluminescence spectra of 50:50 PFB:F8BT blends spun from xylene (black) and chloroform solution (red). The red exciplex emission is strongly enhanced in the chloroform blend.



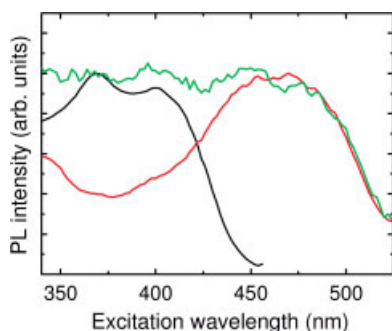
**Fig. 2.9** Photothermal deflection spectra of PFB (black), F8BT (red), and a PFB:F8BT blend film (green). The weight ratio of the blend was 90:10, and it was spun from chloroform.



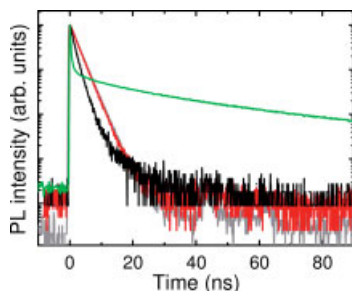
Both the annealing and the solvent-dependent experiments make clear that the red emission in PFB:F8BT scales with the density of heterojunction sites in the film. Hence, it must be due to an intermolecular interaction between two different molecules, i.e. between the F8BT and the PFB.

The observed phenomena would also agree with a model that involves ground-state interactions between the two polymers. We already investigated the UV-Vis spectra of the PFB:F8BT blend. However, UV-Vis spectroscopy provides only a rough means to investigate small absorbance features. Possible ground-state interactions, on the other hand, are expected to show only weak signatures because of the relatively low density of interface sites in the phase-separated polymer blend and the possibly low oscillator strength of ground-state complexes. We therefore employ *photothermal deflection spectroscopy* (PDS) to investigate the absorption edge with higher sensitivity. In Fig. 2.9, the PDS spectra for F8BT, PFB, and a 10:90 F8BT:PFB blend are plotted. No subbandgap absorption features can be observed. We therefore conclude that there are no ground-state interactions and the observed red emission is solely due to an excited-state complex.

The absence of an absorption cross section for the exciplex means that it cannot be excited optically. Instead, an exciplex is formed by complexation of a ground-state molecule with an excited-state molecule, i.e. by Dexter-type energy transfer from a bulk exciton. Figure 2.10 plots the photoluminescence excitation spectra of the PFB, the F8BT, and the exciplex emission, all measured from the same 50:50 PFB:F8BT blend. The PLE signature of the exciplex is a superposition of those of the two excitons. Hence, the exciplex is excited via energy transfer from the two bulk excitons.



**Fig. 2.10** Photoluminescence excitation spectra of a PFB:F8BT blend. The detection wavelengths are 465 nm (black), 540 nm (red), and 600 nm (green), corresponding to the PFB and F8BT exciton emissions and the exciplex emission, respectively. The exciplex spectrum resembles a superposition of the two exciton spectra, pointing towards indirect excitation of the exciplex via transfer from the excitons. The spectra were taken using a *SpexNova* spectrofluorimeter and are not corrected for the spectral response.



**Fig. 2.11** Photoluminescence decays of PFB (black curve, detection wavelength 450 nm), F8BT (red and gray curves, detection at 540 nm and 620 nm, respectively), and a PFB:F8BT blend (green curve, detection at 620 nm).

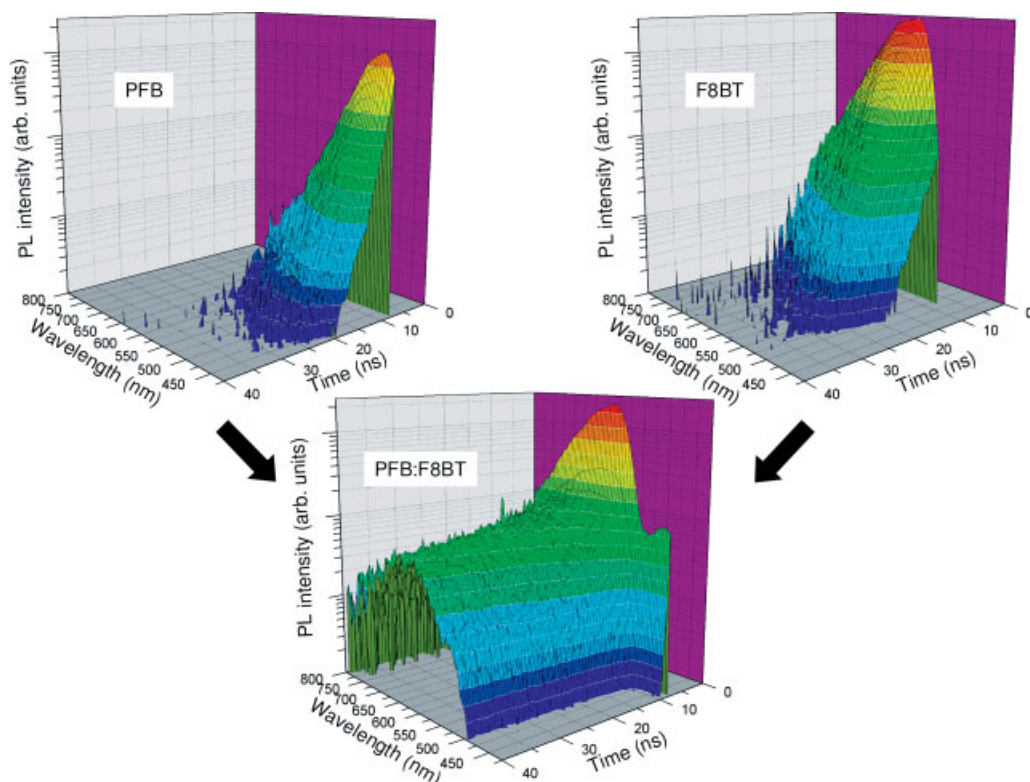
Exciplexes have charge-transfer character and hence a small electron–hole overlap. This reduces the oscillator strength of the exciplex and, if nonradiative processes are not dominant, lengthens its photoluminescence time constant. Figure 2.11 shows the PL decay measured from a PFB:F8BT blend together with those of the pure polymers. In the blend a delayed emission is visible that is absent in the pure polymers and has a time constant of 45 ns (when fitted between 30 and 90 ns). This is the long-lived exciplex state.

At short times the decay from the blend is faster than that from the pure polymers. This is due to the energy transfer from the excitons to the exciplex, as well as the charge separation that excitons undergo at the heterojunction. In Section 2.3.1 we investigate these phenomena and develop a model for charge generation and exciplex formation at the heterojunction.

The appearance of the new, red, long-lived exciplex emission becomes even more obvious when plotting three-dimensional, time-resolved emission spectra (TRES). Figure 2.12 shows that the PL emission of the pure polymers decays monoexponentially with no spectral changes throughout their lifetime, whereas the blend PL evolves into the red exciplex peak.

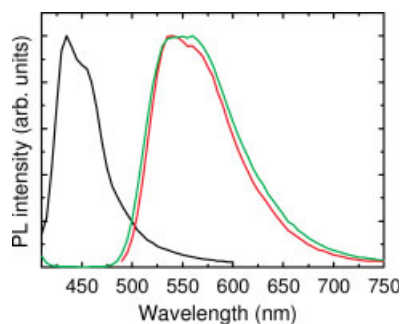
We have shown via absorption, PL, morphology-dependent PL, PDS, photoluminescence excitation, and time-resolved photoluminescence spectroscopy that exciplexes form at the PFB:F8BT heterojunction. We note that exciplexes of polyfluorenes with triphenylamine monomers have been observed recently [34].





**Fig. 2.12** Time-resolved emission spectra of PFB, F8BT and a PFB:F8BT blend. The long-lived exciplex appears upon blending of the two polymers.

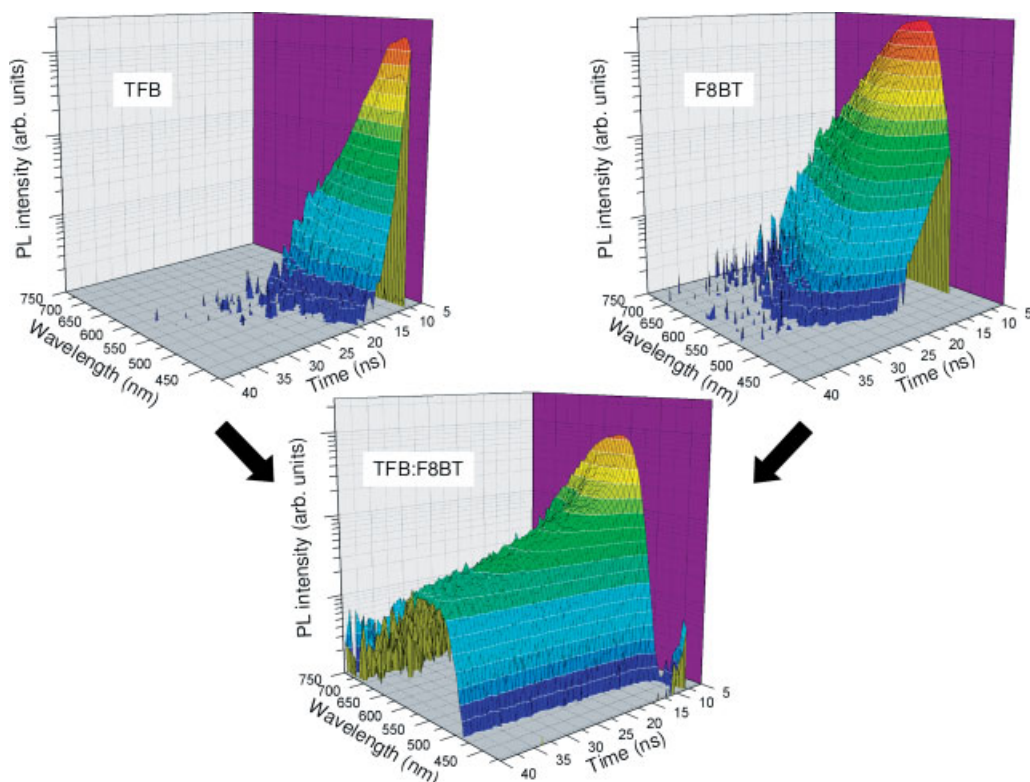
**Fig. 2.13** Photoluminescence spectra of TFB, F8BT, and a TFB:F8BT blend.



#### 2.1.4.3 The TFB:F8BT Exciplex

Fig. 2.13 shows the PL emission of a TFB:F8BT blend together with those of the single components. In the blend, the TFB emission is quenched completely due to even more efficient energy transfer than in the PFB:F8BT case. The blend PL closely resembles the F8BT exciton, with a slight enhancement of the red part of the spectrum. We show that this is due to an underlying exciplex state.



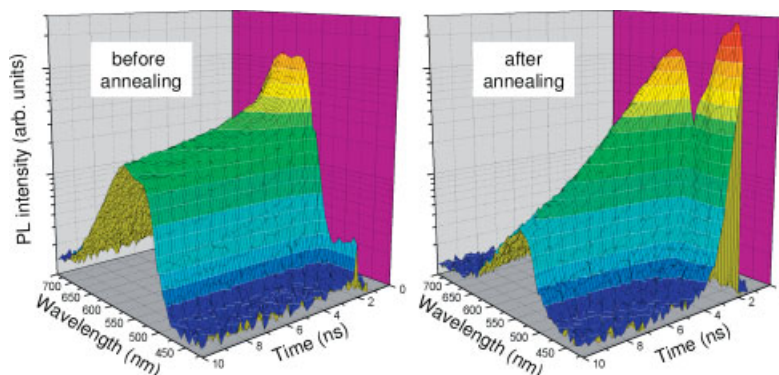


**Fig. 2.14** Time-resolved emission spectra of similar samples as in Fig. 2.13. The long-lived exciplex appears upon blending.

When investigating the PFB:F8BT exciplex, we have seen that time-resolved spectroscopy provides a sensitive tool to detect long-lived exciplex states. In Fig. 2.14, we now consider time-resolved spectra of the TFB:F8BT system and this blend also exhibits a new delayed emission not seen in the pure components. This emission is spectrally very similar to the F8BT exciton (which explains why it is difficult to see in CW spectroscopy) but has a much longer lifetime ( $\sim 27$  ns when fitting the decay at 575 nm between 30 and 90 ns). Therefore, a new electronic state has to be responsible for it. In analogy to the PFB:F8BT system, we postulate that this new state is an exciplex that forms at the TFB:F8BT heterojunction.

From Fig. 2.14 we also see that at early times both the TFB and the F8BT excitons decay faster in the blend than in the pure polymers. As pointed out for the PFB:F8BT case above, this is because of efficient energy transfer from the excitons to the exciplex state. The exact process is investigated in Section 2.3.1.

The hypothesis of a TFB:F8BT exciplex is also supported by the annealing experiments shown in Fig. 2.15. The exciplex disappears when annealing causes the polymers to phase separate. We also see that the exciton decays slow down, as would be expected for a decreased transfer to the exciplex.



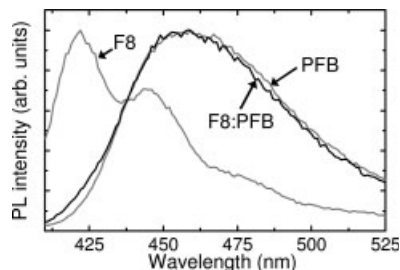
**Fig. 2.15** Time-resolved emission spectra of a TFB:F8BT blend before and after annealing for 2.5 h at 314 °C. When annealing the film, the delayed exciplex emission disappears. The data are not corrected for the spectral response of the TCSPC apparatus.

When investigating the PFB:F8BT system above we also used photoluminescence excitation spectroscopy to directly show the energy transfer to the exciplex. This is not possible here because of the very similar emission spectra of the F8BT exciton and the long-lived exciplex emission. The reasons for this similarity will be discussed in Section 2.2. We therefore conclude that the heterojunction between TFB and F8BT also supports exciplex formation.

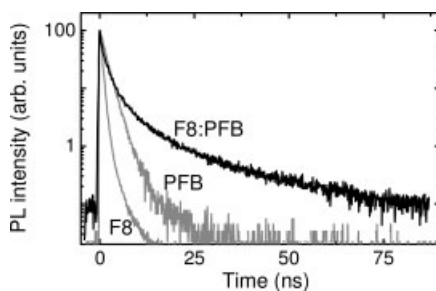
#### 2.1.4.4 The F8:PFB Exciplex

In Fig. 2.16, the PL emission spectra of the pure polymers F8 and PFB are compared with a F8:PFB blend. In the blend, efficient PFB emission obscures the weak F8 emission but no additional emission peaks are visible in these CW spectra. Figure 2.17 compares the time-resolved PL decays of the pure polymers with that of the blend. The pure polymers show almost monoexponential decays over three orders of magnitude with 590 ps (F8) and 1.7 ns (PFB) lifetimes. In the blend, the fast excitonic decay is observed as well, but in addition a long-lived emission with a lifetime of roughly 26 ns (when fitted in the 30 to 90 ns window) is detected.

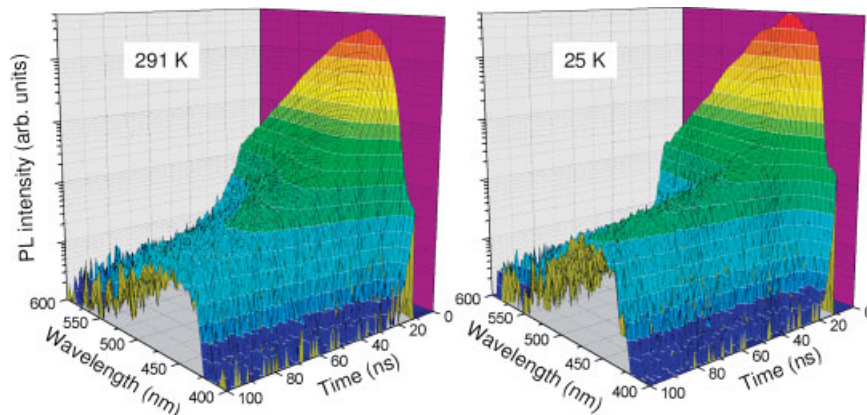
In Fig. 2.18, the full time-resolved spectrum of the blend is drawn. Clearly, a distinct, long-lived excited-state exists in the blend, which is particularly obvious



**Fig. 2.16** Photoluminescence spectra of F8, PFB and a F8:PFB blend.



**Fig. 2.17** Photoluminescence decays of F8, PFB and a F8:PFB blend (weight ratio 90:10, spun from Chloroform) detected at 475 nm.

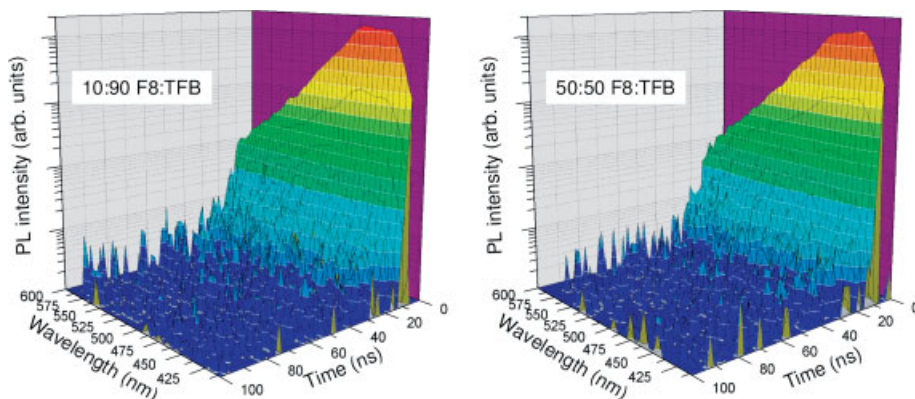


**Fig. 2.18** Time-resolved emission spectra a 90:10 F8:PFB blend at room temperature and at 25 K.

from the low-temperature measurement. Again, we postulate that this emission is due to an exciplex at the F8:PFB interface. The effect is  $\sim 1$  order of magnitude weaker here than in the TFB:F8BT blend in Fig. 2.15. The simplest explanation for this would be to assume a smaller density of heterojunctions in the F8:PFB blend. This could, for example, be caused by a lower miscibility of the two components.

#### 2.1.4.5 No F8:TFB Exciplex?

The last type-II heterojunction system that we consider is the blend of F8 and TFB. Time-resolved spectroscopy has proved to be the most sensitive tool to detect exciplex states in polymer blends and we show corresponding spectra for two different blend ratios in Fig. 2.19. No long-lived, red-shifted emission is visible at all. This is surprising because we have seen that both TFB and F8 are exciplex-forming molecules, i.e. significant orbital overlap between the two molecules should be possible. In the following section, we derive that the energetic conditions for exciplex formation are not met in the F8:TFB system – despite its type-II character.



**Fig. 2.19** Time-resolved emission spectra of F8:TFB blends of different weight ratios as given in the figure. No exciplex emission is detected.

#### 2.1.4.6 Comparison with Model: a Reason that there is no Exciplex in F8:TFB

We now compare the experimental results from the previous section with the standard exciplex theory developed previously. We note again that these models have been developed for molecular systems in solution.

We remind the reader of Eq. (2.12), which describes the dependence of the exciplex emission energy  $E_X$  on the difference of the oxidation potential of the donor,  $E_D^{\text{ox}}$ , and the reduction potential of the acceptor,  $E_A^{\text{red}}$ :

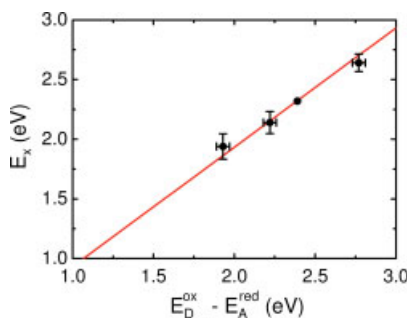
$$E_X = E_D^{\text{ox}} - E_A^{\text{red}} - B \quad (2.14)$$

where  $B$  stands for the exciplex binding energy  $C$  corrected for the solvation free energy associated with exciplex formation and was found empirically (for solution systems) to be

$$B = 0.15 \pm 0.10 \text{ eV} \quad (2.15)$$

In order to compare with experiment, we derive  $E_X$  from the exciplex peaks of the delayed PL in Figs. 2.12, 2.14, and 2.18 (see also Figs. 2.23, and 2.27 in the following section).  $E_D^{\text{ox}}$  and  $E_A^{\text{red}}$  are nothing else than the HOMO and LUMO levels that were given in Fig. 2.5. In Fig. 2.20, the experimental data are plotted together with a fit according to Eq. (2.14) using  $B$  as the only fit parameter. The data agrees well with the theory (we note that the slope of 1 as required by Eq. (2.14) is well reproduced) and the fit yields  $B = 0.067 \text{ eV}$ , which is within the boundaries given by Eq. (2.15). Neglecting “solvation” effects, this gives a rough estimate for the exciplex binding energy  $C$

$$C \approx B = 0.067 \text{ eV} \quad (2.16)$$



**Fig. 2.20** Exciplex photoemission energy  $E_X$  plotted versus the difference between the oxidation potential of the donor  $E_D^{\text{ox}}$  and the reduction potential of the acceptor  $E_A^{\text{red}}$  (i.e. the difference between HOMO and LUMO). Shown are results for PFB:F8BT, TFB:F8BT, F8:PFB, and PFB:F8T2. The straight line is a fit to the data according to Eq. (2.14) and yields  $B=0.067$  eV. To reflect the inhomogeneous broadening of  $E_X$ , error bars representing 1/4 of the estimated FWHM of the exciplex peak were introduced. The HOMO and LUMO levels were measured with an error of  $\pm 0.03$  eV (see Section 2.1.4), which gives an error of 0.04 eV for  $E_D^{\text{ox}} - E_A^{\text{red}}$ , and corresponding x-error bars are drawn.

We have shown that all of the polyfluorene exciplex systems found in the previous section follow Eq. (2.14) and Eq. (2.15) and hence that these equations are also valid for exciplexes in solid-state polymer systems. This enables us to predict the emission energy a possible F8:TFB exciplex would have. From Fig. 2.5 we derive:  $E_{\text{TFB}}^{\text{ox}} - E_{\text{F8}}^{\text{red}} = 3.06$  eV. Hence, the emission energy of the F8:TFB exciplex would be  $E_X = E_{\text{TFB}}^{\text{ox}} - E_{\text{F8}}^{\text{red}} - B = 3.06 - 0.067$  eV = 2.99 eV, which corresponds to an emission wavelength  $\lambda_X$  of 415 nm. From Fig. 2.13 we see that this is below the emission maximum of the TFB exciton emission. We described (Fig. 2.3) that the exciplex energy level  $E_{\text{exciplex}}$  with respect to the system ground-state differs from  $E_X$  by the energy of geometrical relaxation  $\Delta E_{\text{relax}}$ . Hence, here we surely expect  $E_{\text{exciplex}} \geq E_{\text{exciton}}$ . The band offsets at the F8:TFB heterojunction are not large enough to offset the  $\sim 0.4$  eV loss of Coulombic binding energy. That is, exciplex formation in blends of F8 and TFB is inhibited due to energetic reasons – though the two constituent molecules are known to be exciplex forming in principle.

In summary, we find exciplex states at *all* polyfluorene heterojunctions where the energetic conditions are met. We therefore consider it a *universal* property of polyfluorene semiconductor polymers. Given that excimer and aggregate formation are very commonly seen in polymeric semiconductors (see [35] for a review), we consider exciplex formation to also be common, not only in polyfluorenes. As shown in Figs. 2.14 and 2.18 and elaborated in the following section, exciplex formation is not always evident from steady-state PL measurements. Hence it might occur more often than usually assumed. The following sections are concerned with the effects of exciplex formation on the two fundamental processes occurring in optoelectronic devices, charge capture and exciton dissociation.

## 2.2

### Charge Capture at Polymer Heterojunctions

This section focuses on the mechanism of electron–hole capture at the heterojunction between two semiconductor polymers. In particular, the implications of exciplex formation at the interface are discussed. We show that the exciplex state makes possible a new pathway of electron–hole capture, which we termed “barrier-free capture”. In Section 2.2.1, this is investigated in detail for the PFB:F8BT and TFB:F8BT heterojunctions and in Section 2.2.2 we show that the F8:PFB interface also exhibits similar phenomena. These investigations are mainly carried out by considering the photoluminescence spectra of simple polymer blend films. In Section 2.2.3, we compare the electroluminescence spectra seen from polymer bilayers and blends at various temperatures and thereby give more direct evidence for the barrier-free capture mechanism. Finally, in Section 2.2.4, we establish the voltage and temperature regime in which barrier-free capture occurs.

#### 2.2.1

##### Barrier-free Electron–Hole Capture in Polymer Blend LEDs

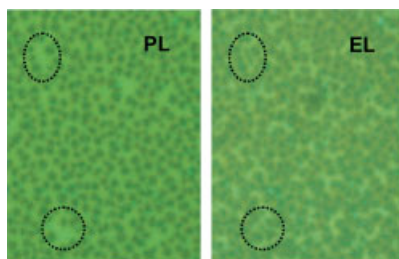
We show that polymer blend light-emitting diodes can be optimized to achieve high efficiencies (above  $19 \text{ lm W}^{-1}$ ) and very low turn-on voltages ( $100 \text{ cd m}^{-2}$  at 2.1 V). This very low voltage operation is achieved because electron–hole capture across the heterojunction is arranged to be a barrier-free process where capture occurs directly into the interfacial exciplex state. This is possible because the exciplex has charge-transfer character but is lower in energy than the charge-separated state. We show that the exciplex can be thermally excited and transfer towards the bulk exciton state. The barrier for thermal excitation is small (100–250 meV) and this process can give efficient bulk exciton emission at room temperature.

We investigate the properties of two different type-II heterojunction systems that sit on either side of the exciton destabilization threshold: blends of the hole-accepting TFB with the electron-accepting F8BT that show excellent LED performance (see below) and blends of the hole-accepting PFB with F8BT that make poor LEDs but show promise for use as photovoltaic diodes [27]. These and related polymers have been used extensively for LEDs [10, 26, 36].

Time-resolved PL measurements were carried out using time-correlated single-photon counting (TCSPC). Time-integrated PL and EL measurements were performed using the TCSPC apparatus in time-integrated mode. The temperature was controlled using an Oxford Instruments OptistatCF Helium cryostat.

In Fig. 2.21, micrographs of the PL and EL emission from the same region of a TFB:F8BT blend device are shown. The polymer film was spun from xylene solution, so that distinct phases rich in either of the polymers of several  $\mu\text{m}$  in size are seen. Comparison of the PL and the EL images reveals that EL emission is predominantly produced at the interfaces between the TFB-rich and F8BT-rich phases. This is consistent with electron–hole capture occurring at the interface.





**Fig. 2.21** Optical microscopy images of photoluminescence, PL, and electroluminescence, EL, from the same region of a TFB:F8BT light-emitting diode (80-nm polymer layer spun from xylene solution at a weight ratio of 50:50). The EL image was measured at a forward voltage of 2.9 V, and the PL image was obtained by exciting in the blue spectral region using a color-filtered Hg lamp. Note that the

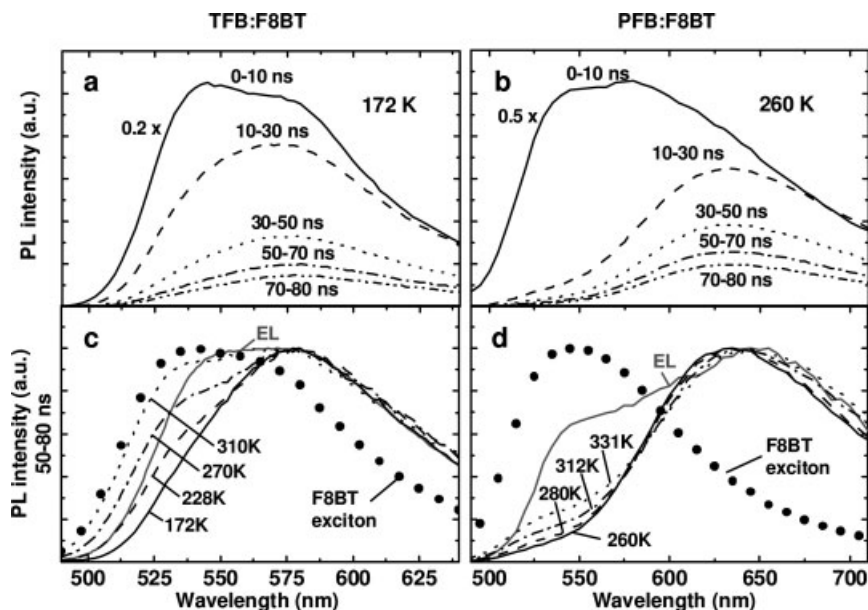
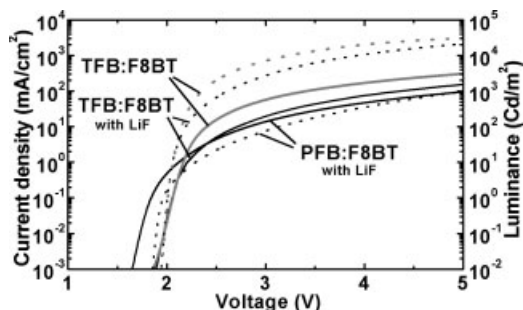
bright regions in the PL image are therefore from the green-emitting F8BT-rich phase, and the dark regions from the TFB-rich phase. In the EL image, strong emission is observed at the interfaces between these two phases, and weaker emission is observed from regions of the pure phases. The dotted circles pick out two regions where this is readily observed. The phases visible in the film are a few  $\mu\text{m}$  in size.

The current–voltage–luminance characteristics of LEDs made with these blends are shown in Fig. 2.22. TFB:F8BT devices show yellow-green emission with very low threshold voltages for light emission (below 2 V), standard display brightnesses of  $100 \text{ cd/m}^2$  at 2.1 V, with efficiencies above  $19 \text{ lm/W}$ , and very bright operation at higher voltages. These devices show excellent stability under operation (many thousands of hours at room temperature). Diodes made with PFB in place of TFB show much lower light outputs, though similar current densities in the forward direction.

The very low threshold voltage is surprising given the type-II nature of the heterojunction. An important reason for this is that in these systems electron–hole capture at the heterojunction does *not* require prior injection of one of the charges into the opposite polymer (via thermionic injection or tunnelling) – a process that is depicted in Fig. 2.1(a). Instead, charge capture occurs directly across the interface to produce the neutral state (Fig. 2.1(b)). This state is directly accessible from the charge-separated state because it is localized at the heterojunction and has significant charge-transfer character and therefore direct overlap with the charge-separated state. Furthermore, it is stabilized with respect to the charge-separated state through conformational relaxation. As described previously in this chapter, such interface states are often termed exciplexes [34, 37–47].

We have introduced exciplex states in Section 2.1 and shown that they form in both polymer blend systems discussed here. Time-resolved spectroscopy has proven to be a useful tool to investigate exciplex states and in Figs. 2.23 (a) and 2.23 (b) we again display time-resolved emission spectra of blends of TFB:F8BT and PFB:F8BT, respectively. For better illustration of the spectral time evolution, we plot 2-D spectra representing subsequent time intervals instead of full 3-D graphs as were shown previously. At short times (0–10 ns after excitation) F8BT exciton emission is predominantly observed (peaked at 540 nm), whereas at longer times the long-lived, red-shifted exciplex emission becomes visible. This de-

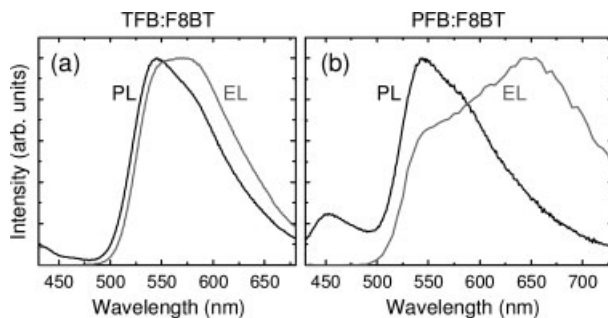
**Fig. 2.22** Current–voltage–luminance characteristics for TFB:F8BT and PFB:F8BT light-emitting-diodes (current: solid lines, luminance: dotted lines) with 40:60 (gray lines) and 20:80 (black lines) blend composition (by weight) respectively. As indicated, some of the devices had a thin (4 nm) LiF interlayer between the polymer film and the Ca cathode. Optimization and I-V-L-measurements courtesy of Cambridge Display Technology Ltd., see also [13]. The devices were constructed with a polymer film (70 nm) that was spun from xylenes solution with weight ratios as given in the figure and the cathodes were either Ca (70 nm) or LiF (4 nm) / Ca (20 nm).



**Fig. 2.23** a and b, Time-resolved photoluminescence (PL) spectra of blends of TFB and F8BT at 172 K (a) and PFB and F8BT at 260 K (b) (170 nm films spun from chloroform solution, weight ratio 50:50). The time intervals over which the photoluminescence was integrated are shown in the figures (spectra are normalized to 1 ns). For long delays (greater than 30 ns) the emission spectra do not evolve further and the decay becomes monoexponential with 51 ns (a) and 57 ns (b) time con-

stant. c and d, Temperature-dependent, time-resolved photoluminescence spectra of the same blends as (a) and (b) integrated over 50–80 ns. The temperatures at which the spectra were taken are indicated in the figure. The F8BT exciton emission was measured by integrating the photoluminescence for delays of 0–1 ns (at 310 K (c) and 331 K (d)). At these times the exciton emission is still dominant over the exciplex emission. For comparison, also the EL spectra from Fig. 2.24 are shown.





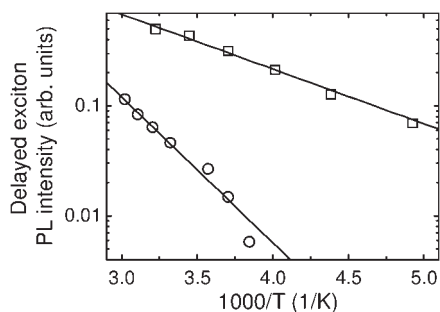
**Fig. 2.24** Comparison of time-integrated PL and EL from TFB:F8BT (a) and PFB:F8BT blends (b) spun from Xylene solution (weight ratio 50:50, thickness 80 nm). The electroluminescence was measured at 2.3 V (a) and 1.9 V (b) forward bias.

layered emission is not observed in pure films of either polymer, which show mono-exponential decays with lifetimes  $< 3$  ns. The blue emissions of the TFB (PFB) bulk excitons, peaked at 435 nm (455 nm), are not shown in the figure since they decay completely within the first few nanoseconds.

Whereas under photoexcitation the exciplex is excited indirectly via energy transfer from the excitons, it is the primary neutral excitation in electroluminescence. This is shown in Fig. 2.24, parts (a) and (b), where the EL emission for both TFB and PFB blends is dominated by the exciplexes. This becomes particularly clear when comparing the EL spectra with the delayed emission spectra in Fig. 2.23, parts (c) and (d). In contrast, the time-integrated PL from similarly prepared blend films (also plotted in Fig. 2.24) is primarily due to bulk excitons. We note that exciplex EL emission has been observed previously, which suggests that these exciplexes may also be formed by the mechanism of direct electron-hole capture at the interface [37, 41, 42].

Figures 2.23(c) and (d) show the spectral dependence of the photoluminescence integrated over 50–80 ns after excitation as a function of temperature. At these times the initial bulk exciton population has completely decayed and all the remaining emission originates from the long-lived exciplex states. We see at low temperature emissions red-shifted by about  $140 \pm 20$  meV (TFB:F8BT) and  $360 \pm 30$  meV (PFB:F8BT), and these are characteristic of the exciplex. At higher temperatures the long-lived exciplex can be thermally excited to form an F8BT exciton that then can diffuse away from the heterojunction and the emission of F8BT rises at the blue edge of the exciplex. Similar ‘endothermic transfer’ has been shown for intramolecular exciplexes [48], for excimers [49] and for phosphorescent LEDs [50]. We emphasize again that the delayed F8BT exciton emission observed here is not seen in the pure polymers. The ratio of delayed F8BT exciton emission to exciplex emission is a thermally activated process with activation energy  $100 \pm 20$  meV (TFB:F8BT) and  $250 \pm 50$  meV (PFB:F8BT), respectively (see Arrhenius plot in Fig. 2.25). These activation energies are lower than the spectral shifts of the exciplexes, which is due to the configurational relaxation of the exciplexes as is explained in detail on Section 2.1. Later in this section, we will show that temperature-dependent EL spectra are similar to the time-delayed PL spectra shown in Fig. 2.23, with similar thermal activation from exciplex to bulk exciton (see Section 2.2.3). A major contribution to the EL emission from the TFB-blend

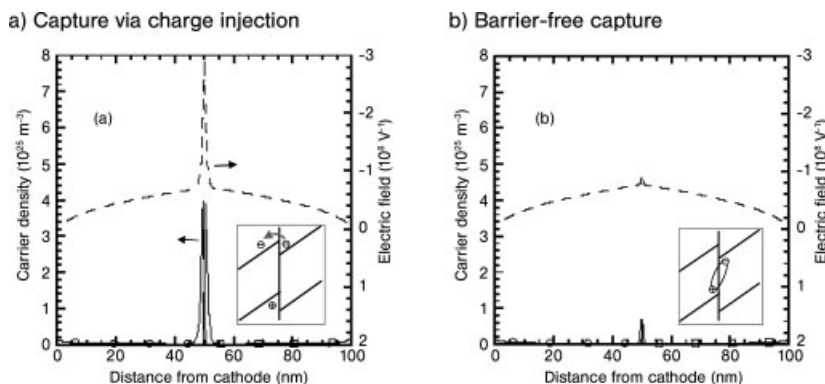
**Fig. 2.25** Delayed F8BT exciton fluorescence from the TFB:F8BT (squares) and PFB:F8BT (circles) blends from Fig. 2.23(c) and (d) versus inverse temperature (detection wavelength 520 nm). The data was calculated from the spectra of Fig. 2.23 by assuming negligible back-transfer at the lowest temperatures. Subtracting the 172 K (TFB:F8BT) and 250 K (PFB:F8BT) spectra from the higher-temperature spectra then yields an estimate for the delayed exciton emission. The straight lines are Boltzmann fits with activation energies of 99 meV (TFB:F8BT) and 263 meV (PFB:F8BT). Evaluation at all wavelengths between 500 and 540 nm gives estimates for the back-transfer activation energies of  $100 \pm 20$  meV and  $250 \pm 50$  meV.



LEDs is from excitons in bulk F8BT that had been thermally excited from interfacially trapped exciplexes. We note that endothermic excitation rates of  $10^8$  Hz are readily achieved at room temperature considering that  $\exp[-0.25 \text{ eV}/(k_B 300 \text{ K})] \approx 10^{-4}$  and vibronic attempt frequencies are typically of order  $10^{12}$  Hz and higher. Also, similar activation energies have been found for comparable processes [48, 49].

We have introduced a mechanism for barrier-free electron–hole capture that can be described as ‘reverse photoinduced charge transfer’. In contrast to photoinduced charge transfer, the neutral excited-state (the exciplex) here is lower in energy than the charge-separated state. We note that photoinduced charge transfer can be a very rapid and efficient process, resulting from overlap of wavefunctions of neutral and charge-separated states [51], and we consider that exciplex formation from electron and hole either side of the heterojunction should be similarly rapid. For EL operation, however, in addition to the correct selection of the heterojunction energetics, we need coincidence of electron and hole opposite one another across the heterojunction. Without lateral motion of electrons and/or holes in the plane of the heterojunction this would be an infrequent occurrence [52]. Therefore this lateral motion of the charges within their mutual electric fields will indeed be the rate-limiting step for capture. Greenham and Bobbert [53] have performed numerical simulations of charge densities in working LEDs, using this model (see Fig. 2.26). They find that high current densities can be supported, and that local charge densities can be considerably lower than those modeled to be present when carriers are required to surmount the heterojunction barrier prior to capture [54, 55]. Lower charge densities are expected to lead to reduced polaron quenching and hence higher LED efficiencies.

Our measurements of thermal activation to allow energy transfer from the exciplexes into the F8BT bulk provide an estimate of their energy relative to the transition state and to a first approximation relative to the exciton state. Furthermore, TFB:F8BT gives very high EL efficiency (and poor photovoltaic perfor-



**Fig. 2.26** Modelled carrier densities and electric fields in a cathode/F8BT(50 nm)/TFB(50 nm)/anode device assuming charge capture via charge injection (a) and barrier-free capture into an exciplex (b). When assuming barrier-free capture, much lower electric fields and charge densities are required at the heterojunction. Graph copied directly from [53].

mance), whereas PFB:F8BT gives poor EL efficiency (Fig. 2.22), but efficient photovoltaic performance. We consider therefore that the fully charge-separated state lies above or close to the energy of the F8BT exciton for TFB:F8BT, but below for PFB:F8BT. The interplay of charge-separated, exciplex and exciton states is further elaborated in Section 2.3.

In Section 2.1.1, we considered the nature of triplet exciplexes to range from delocalized excitations with small exchange energy, to highly localized triplet excitations residing primarily on one or other side of the heterojunction [25, 56, 57]. The formation of the exciplex should control spin-singlet (versus triplet) formation probability in these blend LEDs, and this will have considerable impact on the overall device efficiency (since triplet excitons do not result in radiative emission in these materials) [58]. We note that the singlet yield in TFB:F8BT has been found to be unexpectedly high [59] and this requires further understanding.

In summary, we show that a new mechanism in heterojunction LEDs, ‘reverse photoinduced charge transfer’, allows barrier-free electron–hole capture and hence low-voltage, high-efficiency operation of polymer blend diodes. The trapping of the exciton at the heterojunction to form a spectroscopically distinct state (the exciplex) here provides direct evidence for this process. We note that electrons and holes are confined to the electron- and hole-transporting semiconductors, respectively, and that this is desirable for long-lived device operation [60]. These device structures and device-operation mechanisms allow very efficient LEDs to be processed conveniently, by simple solution-processing techniques such as ink-jet printing. Though we have addressed just two materials systems here (suitable for green to red emission), we can extend to other materials systems, in particular to the blue-emitting F8:PFB exciplex system discussed in the next section.

## 2.2.2

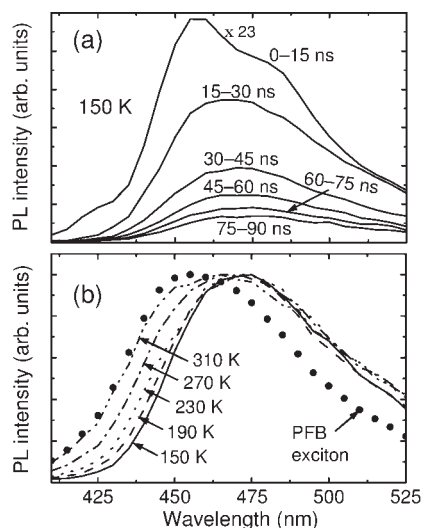
**Endothermic Exciplex-to-Exciton Energy Transfer at the F8:PFB Heterojunction**

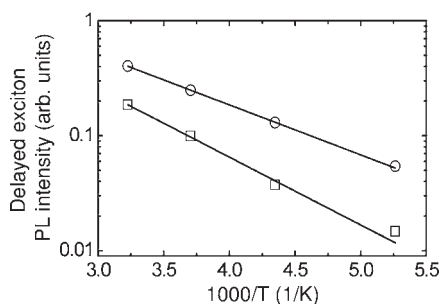
We show that the exciplex states that form at the interface between F8 and PFB can be thermally excited to form bulk excitons. This is observed as delayed PFB exciton emission in time-resolved photoluminescence measurements. These findings are analogous to those presented for PFB:F8BT and TFB:F8BT interfaces in the previous section and therefore support the generality of the phenomenon of endothermic exciplex-to-exciton energy transfer in polyfluorene blends.

In Section 2.1.4.4 we have shown that exciplex formation also occurs in blends of PFB with F8. We further characterize this system by considering time-resolved emission spectra for different film temperatures, as we have done for the PFB:F8BT and TFB:F8BT systems in Fig. 2.23. An example, taken at 150 K, is shown in Fig. 2.27(a). At short times (0–15 ns after excitation) PFB exciton emission, peaked at 455 nm, is predominantly observed together with some weak F8 exciton emission at 425 nm. At longer times the spectrum evolves into a red-shifted, broad peak at 475 nm that does not show any vibronic structure. For times  $> 30$  ns there is no further spectral evolution and the decay is found to be roughly monoexponential with 41 ns decay constant. As already shown in Fig. 2.17, this long-lived, red-shifted emission is not observed in the pure polymers and is due to exciplex states that form at the F8:PFB heterojunction.

Figures 2.27(b) shows the spectral dependence of the long-time photoluminescence integrated over 30–90 ns after excitation as a function of temperature. At these times the initial exciton population has completely decayed and all the remaining emission originates from the long-lived exciplex states. At low temperatures, we see the red-shifted emission characteristic of the exciplex. For higher temperatures, however, the emission spectrum increasingly acquires excitonic

**Fig. 2.27** (a) Time-resolved photoluminescence spectra of an F8:PFB blend (weight ratio 50:50, spun from chloroform) at 150 K. The time intervals over which the PL was integrated are shown in the figures. For long delays (greater than 30 ns) the spectra do not evolve further and the decay becomes monoexponential with 41-ns time constant. (b) Temperature-dependent time-resolved PL spectra of the same blend as in (a) integrated over 30–90 ns. The temperatures at which the spectra were taken are indicated in the figure. The PFB exciton emission was measured by integrating the blend's PL for delays of 0–1 ns (at 310 K).





**Fig. 2.28** Delayed PFB exciton fluorescence from the F8:PFB blend from Fig. 2.27 versus inverse temperature for the detection wavelengths 420 nm (squares) and 435 nm (circles). The data was calculated from the spectra of Fig. 2.27(b) by assuming negligible back-transfer at 150 K, i.e. the 150 K spectrum to represent only exciplex emission. Subtracting this from the higher temperature spectra then yields an estimate for the delayed exciton

emission. The straight lines are Boltzman fits with activation energies of 117 meV (420 nm) and 86 meV (435 nm) (This variation with detection wavelength is considered to arise from unknown changes of the exciplex spectrum with temperature, see also Section 2.4.). Evaluation at all wavelengths between 410 and 450 nm gives an estimate for the back-transfer activation energy of  $100 \pm 20$  meV.

character. This is because the long-lived exciplex can be thermally excited and transfer towards the bulk PFB exciton that then diffuses away from the heterojunction and emits. Thereby a population of ‘secondary’ PFB excitons that are generated from the exciplex population is produced (see Section 2.3.1 for more on secondary excitons) and the emission of PFB rises at the blue edge of the exciplex. The PFB exciton emission as a fraction of the total emission is a simple thermally activated process with activation energy  $100 \pm 20$  meV (see Arrhenius plot in Fig. 2.28). As was the case for the two other exciplex systems investigated above, the activation energy is again slightly lower than the exciplex’s spectral red-shift of  $120 \pm 20$  meV, which is due to the configurational relaxation of the exciplex.

We have shown that endothermic transfer from the exciplex to the bulk exciton occurs in the F8:PFB blends. This is consistent with the findings presented in the previous section. We conclude that not only exciplex formation, but endothermic transfer to the exciton is also a universal property of polyfluorene heterojunctions.

### 2.2.3

#### Barrier-free Capture in Polymer Bilayer LEDs at Low Temperatures

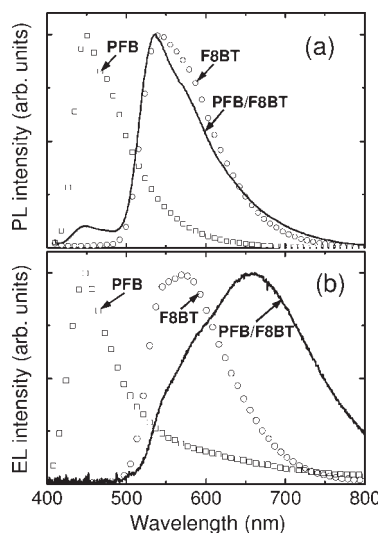
The analysis in Section 2.2.1 was based on the investigation of polymer blend films and LEDs. These are, while being convenient to manufacture, rather badly defined structures and hence not ideal to investigate new physical phenomena. In strongly phase-separated blends, high leakage currents (e.g.  $\sim 400$  mA/cm<sup>2</sup> at 3 V for 50:50 PFB:F8BT blends spun from xylene) disturb the electric fields in the device and cause significant device heating that in turn makes the emission spectra voltage dependent (this is discussed in detail in

Section 2.2.4). These difficulties are not encountered for well-mixed polymer blends. However, we find that in well-mixed blends even the photoluminescence spectra are dominated by exciplex emission (see e.g. Fig. 2.7) and hence the characteristic exciplex enhancement in EL (as was shown in Fig. 2.24) is hardly seen. This means that in these blends the spectral shape of the electroluminescence would be independent of whether process (a) or (b) in Fig. 2.1 occurs because excitons could quickly transfer towards a nearby interface site. In well-mixed blends it is therefore impossible to show that the exciplex is the primary product of charge capture and hence to prove that barrier-free capture occurs. We address these concerns here by presenting electroluminescence measurements from bilayer light-emitting diodes, where leakage currents are prevented, while a low density of interface sites (in fact the lowest possible) is maintained.

In Section 2.2.1, we have shown the endothermic transfer from the exciplex to the exciton using temperature-dependent *photoluminescence* spectroscopy. However, this process is crucial for the argument that high *electroluminescence* efficiencies can be achieved via the barrier-free process. Here, we present temperature-dependent electroluminescence data and thereby provide more direct evidence of the ideas proposed in Section 2.2.1. We note that these experiments are not trivial because the lower charge carrier mobility at lower temperatures strongly decreases the light output if the driving voltage is not altered. A constant, low voltage on the other hand is desirable since at high voltages the device is simply “flooded” with charge carriers and the heterojunction barriers play only a minor role (see Section 2.2.4).

By investigating bilayer and blend light-emitting diodes at different temperatures we give conclusive evidence that barrier-free capture is the *only* capture mechanism occurring at the heterojunction between PFB and F8BT (at moderate voltages).

The bilayer devices were prepared using ethylene bis(4-azido-2,3,5,6-tetrafluorobenzenesulfonamide) as a deep-UV crosslinker as described elsewhere [61]. The crosslinking occurs via a nonspecific nitrene insertion into alkyl C–H (and aromatic C–H) bonds and therefore does not affect the primary conjugation. The first layer (40 nm) was prepared by spin coating from a xylene solution containing both PFB and the crosslinking reagent in a weight ratio of 98:2 onto an oxygen-plasma-treated indium tin-oxide (ITO) substrate coated with a 30–60 nm hole-injection layer (poly(4-styrenesulfonate)-doped poly(3,4-ethylenedioxythiophene), PEDOT:PSS 1:16 in H<sub>2</sub>O). The PFB was then crosslinked by UV-exposure and the second layer (80 nm) spun on top of the first from a xylene solution of F8BT. For comparison, an F8BT-only device was spun from a similar solution. The crosslinking technique forms a PFB/F8BT bilayer with a well-defined interface, and was shown to have a negligible effect on the transport properties as well as the PL and EL emission spectra of the PFB [61]. Single-layer, PFB-only and polymer blend LEDs were produced by spin coating 170-nm films from common chloroform solution onto a PEDOT:PSS / ITO substrate. For all devices, cathodes were formed by thermal evaporation of Ca (60 nm) and encapsulated with a thick Al overlayer.



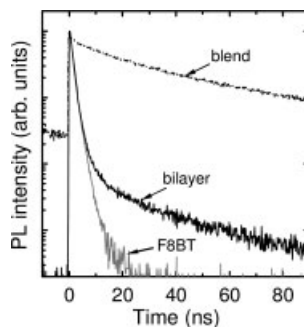
**Fig. 2.29** (a) PL spectra taken from PFB and F8BT single layer LEDs and from a PFB/F8BT bilayer LED by optically exciting through the ITO anode. (b) EL spectra from the same devices (Biases applied were 6 V for PFB, 5 V for F8BT and 3.2 V for the PFB/F8BT bilayer). All measurements were done at room temperature.

For EL, the devices were driven under constant forward bias (Ca negative with respect to PEDOT:PSS / ITO) and their emission was recorded using an Oriel InstaSpec IV spectrograph. The temperature was varied using a continuous-flow He cryostat (Oxford Instruments OptistatCF). For PL, the devices were optically excited through the ITO anode using a 407-nm pulsed diode laser (Pico-Quant LDH400).

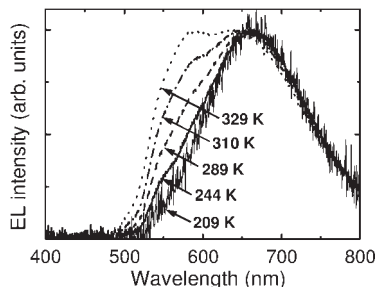
Figure 2.29(a) compares the PL emission from a PFB/F8BT bilayer with that from the pure polymers. The bilayer spectrum is a simple superposition of the PFB and F8BT exciton features. Figure 2.29(b) shows EL spectra taken from the same devices. Unlike the PL case, electrical excitation of the bilayer yields mainly the red-shifted exciplex emission (centered around 650 nm [13, 14]), while the F8BT exciton emission is strongly suppressed, and the PFB exciton is completely absent. This agrees with the concept of barrier-free charge capture as depicted in Fig. 2.1(b). The neutral states generated through electrical excitation are the interfacial exciplex states, *not* the bulk excitons that are generated in optical excitation. This leads to a strong enhancement of the exciplex emission in EL with respect to PL.

However, as we have shown previously (refs. [13, 14]), significant exciplex PL *can* be observed in *blends* of PFB and F8BT, and, in these structures, the exciplex emission is only modestly enhanced in EL. Generally, PL emission from exciplexes is possible because they can be excited via energy transfer from photoexcited bulk excitons that migrate towards interface sites. This effect is stronger in a well-mixed blend that has a much higher density of interface sites than a bilayer. In the time-integrated PL spectra in Fig. 2.29(a), no exciplex PL can be identified. However, even in the bilayer, a small density of exciplexes is still excited via transfer from the photogenerated excitons and this can be seen in time-resolved PL measurements. Fig. 2.30 shows the PL decay measured at 650 nm from the same bilayer device as in Fig. 2.29. For comparison, similar decay curves are

**Fig. 2.30** Photoluminescence decays at 650 nm of the PFB/F8BT bilayer LED and the F8BT-only LED from Fig. 2.29 as well as the PFB:F8BT blend LED from Fig. 2.31. The long-lived exciplex emission is clearly visible in both the blend and the bilayer data but its relative intensity is much lower in the bilayer device. An exponential fit of the delayed emission between 30–90 ns yields 51.5 and 38.7 ns for the blend and the bilayer device, respectively.



**Fig. 2.31** EL spectra of the same PFB/F8BT bilayer LED as in Fig. 2.29 at 3.2 V applied bias measured at different temperatures. Because of the high noise level, the 209 K graph was truncated for wavelengths below 480 nm.

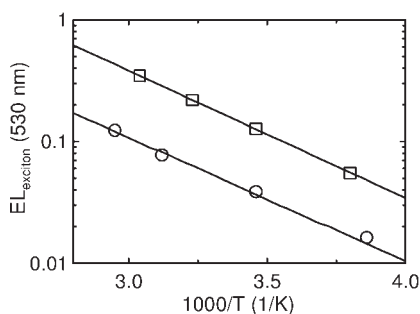


shown for the F8BT-only device as well as for a polymer blend device exhibiting strong exciplex formation (see below). For short times (0–10 ns), the decay of the bilayer PL is dominated by the F8BT exciton emission. For longer times ( $> 20$  ns), the bilayer PL shows a slowly decaying emission very similar to that observed from the blend. This is the long-lived exciplex emission as was shown previously. The exciplex decay in the bilayer is faster than that observed from the blend sample. This is due to exciton retrapping, as will be explained in Section 2.4.

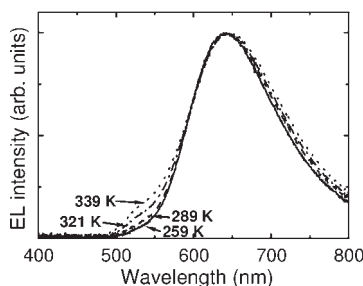
Apart from the dominant exciplex PL, the bilayer EL spectrum in Fig. 2.29(b) still contains some F8BT exciton emission that is visible as a yellow-green shoulder of the red exciplex peak. We show that this is due to endothermic transfer from the exciplex to the exciton, by considering the dependence of the bilayer EL on device temperature at constant applied bias. From Fig. 2.31, one can see that the excitonic contribution to the emission spectrum is thermally activated and frozen out completely below 209 K. The activation energy of this process is found to be  $200 \pm 50$  meV (see Arrhenius plot in Fig. 2.32). This is consistent with the values extracted with our time-resolved PL [13] and electric-field-dependent PL [14] measurements, and confirms the origin of the exciton EL to be endothermic transfer from the exciplex as depicted in Fig. 2.1(b).

For completeness, we show an example for the temperature dependence of the EL spectra from polymer blend LEDs in Fig. 2.33. Only a very small F8BT exciton contribution to the EL spectrum is visible at any temperature. This is due to exciton retrapping and will be discussed in detail in Section 2.4. Despite this, the





**Fig. 2.32** Relative F8BT EL at 530 nm for the bilayer LED from Fig. 2.31 (squares) and the blend LED from Fig. 2.33 (circles) as a function of inverse temperature. The data was determined from the spectra of Figs. 2.31 and 2.33 by assuming negligible back-transfer at the lowest temperatures and subtracting these spectra from the higher-temperature ones (same analysis as in Section 2.2, Figs. 2.25 and 2.28). Straight lines are Arrhenius fits with activation energies of 208 meV for the bilayer and 202 meV for the blend device. Performing Arrhenius fits for different wavelengths within 510–590 nm gives an overall estimate of  $200 \pm 50$  meV for both devices.



**Fig. 2.33** EL spectra of a PFB:F8BT blend (95:5 weight ratio, spun from chloroform) LED at 4.3 V applied bias measured at different temperatures.

exciton contribution is clearly thermally activated and we find an activation energy of  $200 \pm 50$  meV (see Fig. 2.32). This is similar to the bilayer case that confirms that the energetics at the interface are unaltered.

We have shown an extreme enhancement of the exciplex emission in bilayer EL as compared to PL and the appearance of weak exciton EL only through thermal activation from the exciplex at higher temperatures. At low temperatures, the exciton contribution is frozen out completely and only exciplex electroluminescence is seen. This demonstrates unambiguously that the *only* source of bulk excitons during electrical excitation is endothermic energy transfer from exciplex states that are generated via barrier-free electron–hole capture and confirms the work presented in Section 2.2.1 that was based on room-temperature emission from polymer blend LEDs and time-resolved PL.

#### 2.2.4

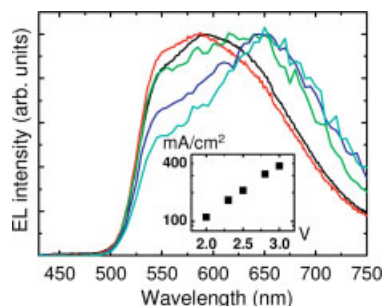
##### The High-voltage Limit of the Barrier-free Capture Regime

As explained in Section 2.2.1, the barrier-free electron–hole capture mechanism (depicted in Fig. 2.1(b)) relies on the fact that charge transport is blocked by the barriers that result from the offsets of the HOMO and LUMO levels of the two polymers. Since the carriers cannot progress across the heterojunction,

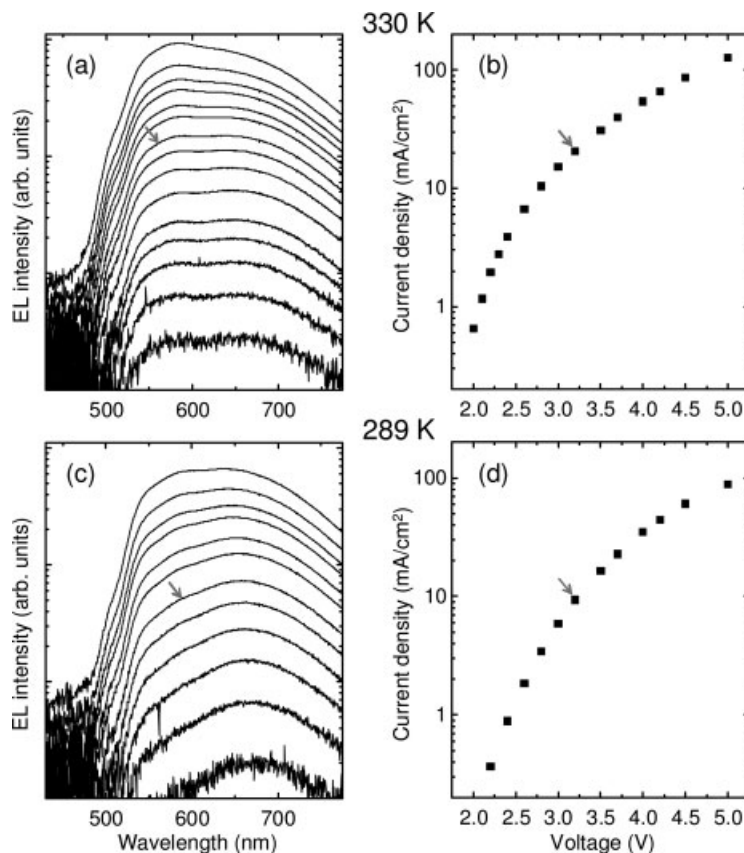
they diffuse two-dimensionally along the interface until they encounter an oppositely charged carrier on the opposite site of the interface and these form an exciplex. If, however, a high electric field exists across the heterojunction, the charges might tunnel through the barrier and into the opposite polymer. These minority carriers would then quickly recombine with the oppositely charged majority carriers in the bulk phase. Hence, at high driving voltages, a crossing-over from the barrier-free capture regime (Fig. 2.1(b)) to capture via the charge-injection regime (Fig. 2.1(a)) should occur. Because in the latter, capture occurs in the polymer bulk, this should result in a higher relative exciton emission (as compared to exciplexes). Here, we investigate the high-voltage behavior of blend and bilayer devices of PFB and F8BT and show that at low temperatures this crossing-over can indeed be seen. We also demonstrate that at the driving voltages used in Fig. 2.31 and Fig. 2.33 of the previous section no high-voltage effects occur and that therefore the analysis done in that section is valid.

The bilayer electroluminescence was measured from the same device as in the previous section (Fig. 2.31). Two different blend devices were investigated, one containing a 50:50 (by weight) PFB:F8BT blend film spun from xylene solution and one containing a 95:5 PFB:F8BT blend film spun from chloroform solution. The former shows strong phase separation with  $\mu\text{m}$ -sized phases (see micrographs in Fig. 2.21) while in the latter the F8BT is well mixed into the PFB. The chloroform device was the same as the one from Fig. 2.33 in the previous section.

In Fig. 2.34, we show voltage-dependent EL measurements from a 50:50 PFB:F8BT blend spun from xylene together with some values for the current density at different voltages (measured from a different but similar device). An extremely strong voltage dependence is seen in the EL spectra. The lowest applied voltages, 1.87 V, 1.90 V, and 1.95 V, are barely above the turn-on of the device (compare also Fig. 2.22 in Section 2.2.1) but nevertheless large differences in the emission spectra are seen. The fields at these voltages are very low so that field-induced charge injection across the heterojunction is very unlikely. On the other hand, the high leakage currents cause a power consumption of order  $100 \text{ mW}/\text{cm}^2$  most of which can be assumed to be dissipated as heat in the polymer film. This can readily lead to an increase in the device temperature of many tens of  $^{\circ}\text{C}$  [62]. We therefore postulate that the observed increase in the relative



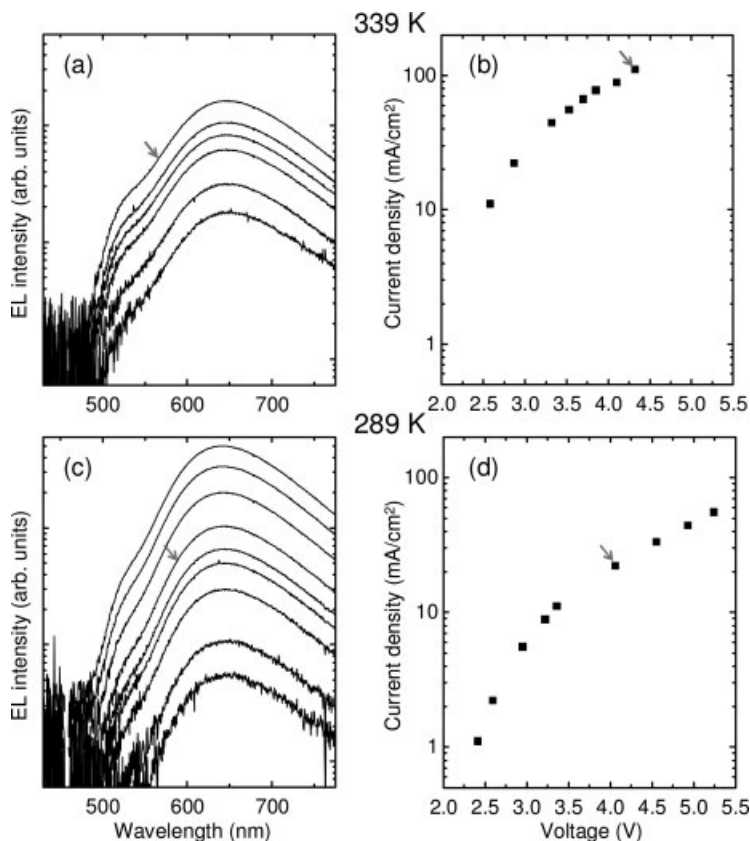
**Fig. 2.34** Electroluminescence from a 50:50 by weight PFB:F8BT blend spun from xylene solution. Applied voltages were 1.87, 1.9, 1.95, 2.5, and 3.0 V for the cyan, blue, green, red, and black graph, respectively. Typical I-V-values, measured from a different but similar device, are plotted in the inset.



**Fig. 2.35** Electroluminescence spectra from the same PFB/F8BT bilayer device as in Fig. 2.31 measured at 330 K (a) and 289 K (c) at different voltages. The spectra are not normalized and higher intensity corresponds to higher voltage. The corresponding voltages and current densities are plotted in panels (b) and (d), respectively. The data corresponding to 3.2 V applied bias are marked with an arrow.

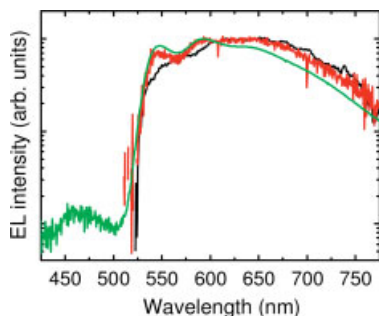
F8BT exciton emission (as opposed to exciplex emission) is simply due to device heating. At higher voltages, higher currents result in a higher temperature of the polymer film that facilitates the endothermic transfer from the exciplex to the exciton and increases exciton EL.

We now consider the bilayer and blend devices that we have measured previously in Section 2.2.3 (Figs. 2.31 and 2.33). In Fig. 2.35, EL spectra from the bilayer device are plotted for different voltages at two different (heat bath) temperatures (Fig. 2.35(a) and (c)). While at low driving voltages the spectra do not vary, an increase in the green F8BT exciton part of the spectrum is seen for high voltages. From Fig. 2.35(b) and (d), we see that, at higher voltages, the measured currents approach those seen in the strongly phase-separated blend device from Fig. 2.34 and we therefore assign the spectral changes to current heating of the

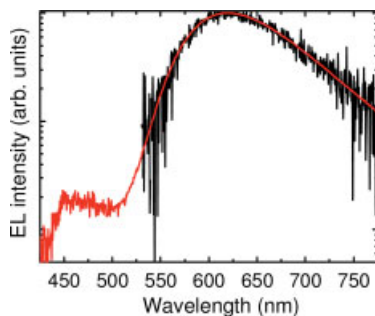


**Fig. 2.36** Electroluminescence spectra from the same PFB:F8BT blend device as in Fig. 2.33 measured at 339 K (a) and 289 K (c) at different voltages. The spectra are not normalized and higher intensity corresponds to higher voltage. The corresponding voltages and current densities are plotted in panels (b) and (d), respectively. The data corresponding to  $\sim 4.3$  V applied bias are marked with an arrow.

device. Of course, this assignment is somewhat arbitrary since the changes could also be due to injection across the heterojunction. However, later in this section we show that at low temperatures the injection regime is only reached at a driving voltage of  $\sim 10$  V. In any case, we state that for low voltages ( $< 4$  V) no spectral changes are seen and current heating can be excluded. In the previous section we have shown that at a driving voltage of 3.2 V barrier-free capture occurs (Fig. 2.31), which we therefore conclude to be the case for the whole voltage range up to 4 V. We only showed data for two temperatures in Fig. 2.35 because the spectral changes become insignificant for lower temperatures. Figure 2.36 shows a similar analysis for the 95:5 PFB:F8BT blend device (the same device that was used in Fig. 2.33). Only very small spectral changes are observed up to 4.3 V (the voltage used in Fig. 2.33) indicating that here also EL operation occurs in the barrier-free regime.



**Fig. 2.37** Electroluminescence from the same PFB/F8BT bilayer device as in Fig. 2.31 measured at 43 K and 9 V (black curve), 10 V (red), and 13 V (green) bias. Current densities were 0.02, 0.14, and 11 mA/cm<sup>2</sup>. At higher fields, injection over the heterojunction becomes feasible and capture occurs in the bulk resulting in *both* yellow-green F8BT and blue PFB exciton luminescence. Because of the high noise level, the 9-V curve has been smoothed using an adjacent averaging algorithm and both the 9- and 10-V curves have been truncated below 510 nm.



**Fig. 2.38** Electroluminescence from the same PFB:F8BT blend device as in Fig. 2.33 measured at 10 K and 10.7 V (black curve) and 14.9 V (red) bias. Current densities were 0.11, and 8.9 mA/cm<sup>2</sup>. As was the case in Fig. 2.37, PFB exciton electroluminescence is seen at high fields. Because of the high noise level, the 10.7-V curve has been truncated below 530 nm.

We have seen that current heating can strongly alter the EL spectra at higher voltages. To avoid this effect and detect the high-voltage limit of the barrier-free capture regime (or the low-voltage limit of the “capture via the field-assisted charge-injection” regime) we have performed EL measurements at very low temperatures where endothermic transfer is reliably frozen out. In Fig. 2.37, EL spectra from the PFB/F8BT bilayer device measured at 43 K are shown. At 9 V, almost pure exciplex emission is seen. Above 10 V, however, not only does the F8BT exciton emission rise but also EL emission from the blue PFB exciton is visible. This can not simply be due to device heating because thermal activation of the exciplex to produce PFB excitons is not possible at any reasonable temperature. Therefore, charge injection across the heterojunction occurs and excitons form by capture in the bulk material. In Fig. 2.38, we show similar EL spectra for the blend device. Also here, PFB exciton EL is seen at higher voltages, but absolutely no F8BT exciton emission occurs. This is because the low F8BT fraction in this blend results in F8BT phases much smaller than the exciton diffusion length. Any F8BT excitons are therefore immediately captured at the heterojunction.

For the model system of the PFB:F8BT heterojunction, we have identified a voltage and temperature range in which charge capture occurs via the barrier-free mechanism (as depicted in Fig. 2.1(b)). Generally, barrier-free capture is dominant at low driving voltages but for increasing bias field-induced charge injection across the heterojunction becomes important. At low temperatures, the threshold voltage was found to be  $\sim 10$  V. At room temperature, only a lower limit of  $\sim 4$  V could be found because of the effects of Joule heating that occurs at higher voltages.

## 2.3

### Exciton Dissociation at Polymer Heterojunctions

#### 2.3.1

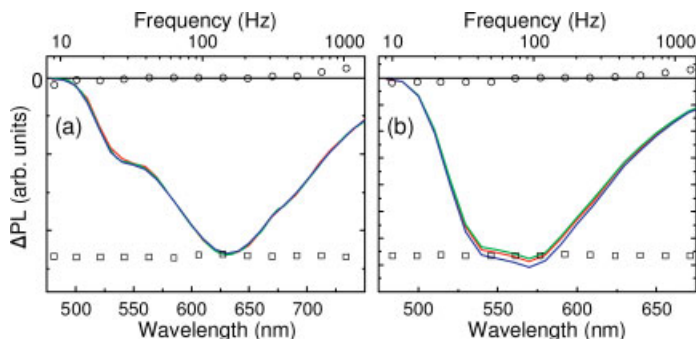
##### Exciton Dissociation and Exciton Regeneration

As mentioned previously in this chapter, type-II heterojunction systems are typically employed in photovoltaic diodes to achieve charge generation at the interface [21, 27, 63]. Device architectures are similar to those of light-emitting diodes and involve a thin film of a blend of hole-accepting and electron-accepting polymers sandwiched between two electrodes. However, some type-II polymer blends show low photocurrents and high luminescence quantum yields, leading to very efficient light-emitting diodes [13, 18, 26, 64].

The high luminescence quantum yield is commonly rationalized by the proposition that excitons can be stable at the heterojunction if their Coulombic binding energy is higher than the band-edge offsets [18]. In this case, the only process that might occur when an exciton encounters the heterojunction is energy transfer from the material with the larger band-gap to the other component. This picture classifies type-II heterojunctions into those above and those below a charge-separation threshold, producing high photocurrents or luminescence quantum yields, respectively. This simple classification is incomplete because even systems that show high luminescence efficiencies often also show significant charge generation (see below). By considering the dependence of photoluminescence (PL) spectra and dynamics on applied electric field, we develop here an alternative, unified description of the excitation dynamics at the polymer heterojunction. We show that in *all* blends the exciton first dissociates at the heterojunction and forms an interfacial geminate charge pair. However, geminate-pair recombination via an intermediate exciplex state can regenerate the bulk exciton. These circular transitions between the different excited-states at the heterojunction are driven by thermal energy, and a fine balance of the kinetics determines the net charge separation and photoluminescence yields.

We have shown that exciplex states form in blends of F8BT with PFB, and F8BT with TFB, and that these exciplex states can undergo endothermic energy transfer to form bulk F8BT excitons [13]. We again investigate films of PFB:F8BT and TFB:F8BT spin coated from common chloroform solution, i.e. films exhibiting very limited demixing (of the order of 10 nm [27]) resulting in a large interfacial area of contact between the two polymers. Note that PFB:F8BT blends can display high charge-separation yields (4% photocurrent external quantum efficiency) and low EL efficiencies ( $< 0.64 \text{ lm/W}$ ) whereas the TFB:F8BT system displays low photocurrents (we find 82% lower short-circuit current than in PFB:F8BT at 457 nm excitation), but very high electroluminescence efficiencies (up to  $19.4 \text{ lm/W}$ ) [13, 28]. Hence, these blends are good examples of the contrasting properties of type-II polymer heterojunctions as described above.

For all measurements, polymer blends (weight ratio 50:50) were spin coated from common chloroform solution onto oxygen-plasma-treated ITO substrates



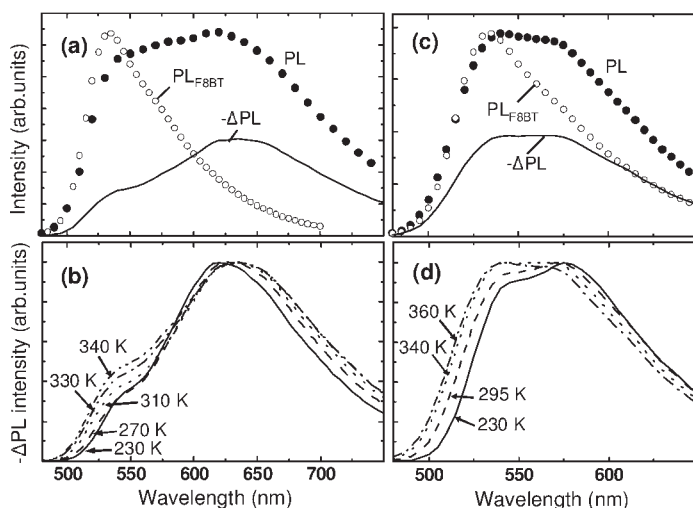
**Fig. 2.39** Photoluminescence quenching spectra for 5 (red continuous curve), 10 (green curve), and 20 mW (blue curve) excitation power normalized to the corresponding excitation power as well as photoluminescence quenching versus modulation frequency (squares: X channel, circles: Y channel) measured at 560 (a) and 640 nm (b). Data is shown for PFB:F8BT (a) and TFB:F8BT (b) blend devices at 6 (a) and 15 V (b) reverse bias. All measurements were done at room temperature.

to form 170-nm thin films. Ca electrodes (60 nm) were then deposited by thermal evaporation and encapsulated by a 300-nm Al layer. All devices were fabricated under  $N_2$  atmosphere. An electric field was applied by reverse-biasing the device to prevent charge injection (ITO negative with respect to Ca). Quasi-steady-state photoluminescence quenching data,  $\Delta PL$ , were measured as described elsewhere [14]. As demonstrated in Fig. 2.39, the data was found to be independent of modulation frequency and excitation power.

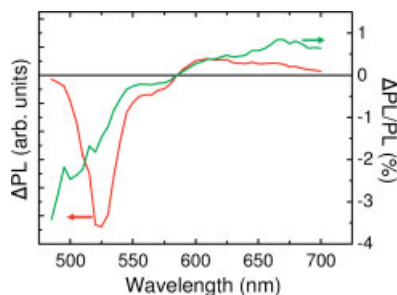
Time-resolved PL measurements were also performed using time-correlated single-photon counting (TCSPC) and photoluminescence upconversion (PLUC) spectroscopies. Descriptions of the setups can be found in refs. [14, 65], respectively. All measurements were taken in continuous-flow He cryostats (Oxford Instruments OptistatCF) under inert conditions. Finally, PL efficiency measurements were performed on simple polymer thin films spin coated on Spectrosil substrates using an integrating sphere coupled to an Oriel InstaSpec IV spectrograph and excitation with the same  $Ar^+$  laser as above.

Figure 2.40(a) compares the PL spectrum of a diode made with blended PFB:F8BT with that of pure F8BT. Red-shifted exciplex emission, in addition to bulk F8BT contribution (i.e. the F8BT-only spectrum), is evident in the blend film. (Neither PFB nor TFB are excited at 457 nm. See Fig. 2.6.) Also shown in the same figure is the electromodulation spectrum,  $-\Delta PL$ , taken by applying 10 V bias across the device. The electric field preferentially quenches the exciplex contribution in the red part of the spectrum ( $> 50\%$  quenching for wavelengths  $> 650$  nm). Quenching of the F8BT exciton emission is also observed, but this decreases with decreasing temperature, as demonstrated in Fig. 2.40(b). Similar phenomena are observed in the TFB:F8BT diode (Figs. 2.40(c) and 2.40(d)), although the relative contribution of F8BT bulk emission is higher in the same temperature range. In contrast to the blends, pure F8BT shows net PL quenching of  $< 1\%$  and only Stark shifts by  $< 1$  nm at these fields (Fig. 2.41).





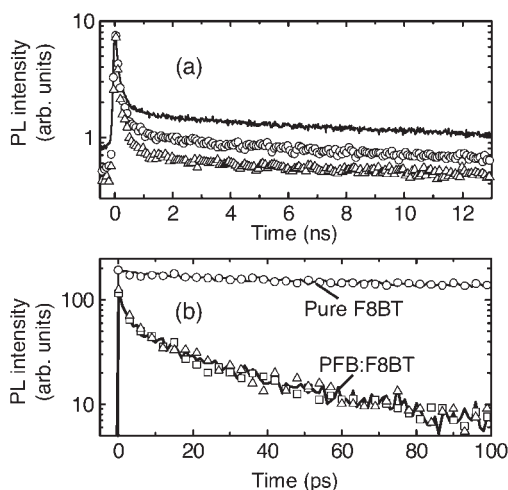
**Fig. 2.40** (a) Photoluminescence intensity (PL, solid circles) and reduction of photoluminescence intensity due to an applied reverse bias of 10 V ( $\Delta$ PL, continuous line) for a PFB:F8BT blend device at 340 K. PL and  $-\Delta$ PL are plotted on the same scale and reflect their relative intensities. (b)  $\Delta$ PL spectra (at 10 V) from the same device as in (a) at different temperatures. (c) PL (solid circles) and  $\Delta$ PL at a reverse bias of 15 V (continuous line) for a TFB:F8BT blend device at 340 K. (d)  $\Delta$ PL spectra from the same device as in (c) at different temperatures. For comparison the PL spectrum from an F8BT-only device (open circles) is plotted in both parts (a) and (c).



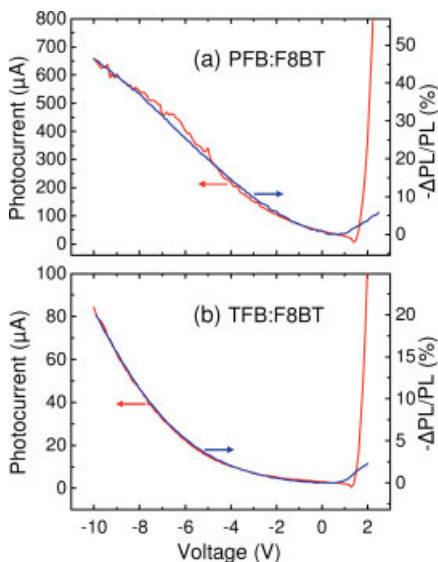
**Fig. 2.41** Change  $\Delta$ PL (red curve) and relative change  $\Delta$ PL/PL (green curve) of the photoluminescence from an F8BT-only device due to an applied reverse bias of 15 V (temperature 295 K). The pattern corresponds to a Stark shift of  $< 1$  nm. Net quenching is less than 1%.

If the PL quenching arises from field assisted dissociation of an emissive state, its luminescence decay rate should be field-dependent. Figure 2.42(a) shows TCSPC measurements at 640 nm in a PFB:F8BT diode with different applied voltages. All curves consist of an instrument-limited decay, and a slow, roughly monoexponential decay with  $40 \pm 5$  ns decay constant. The two components are assigned to the bulk exciton and the exciplex state, respectively (see above). Exciplex generation occurs within  $\sim 1$  ns and its generation efficiency is strongly field dependent, while its decay constant shows no significant variation with applied field. Therefore, an exciplex precursor must be quenched by the field. To investigate the field dependence on the bulk exciton decay rate, we have performed field-





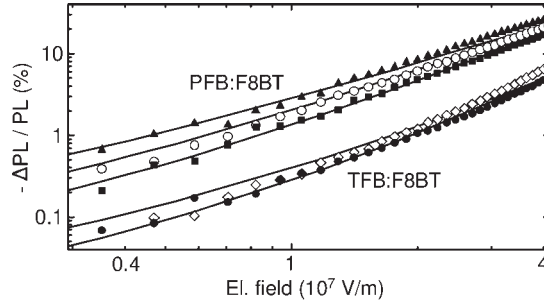
**Fig. 2.42** (a) Photoluminescence decay measured using TCSPC (excitation: 407 nm,  $< 4 \text{ nJ/cm}^2$ , detection: 640 nm) from a PFB:F8BT device at room temperature under 0 V (continuous line), 13 V (circles) and 30 V (triangles) applied reverse biases. (b) PLUC measurements (excitation: 405 nm,  $42 \text{ nJ/cm}^2$ , detection: 550 nm) from a similar device at 0 V (continuous line), 5 V (squares) and 12.5 V (triangles) reverse bias. For comparison, data for a device with pure F8BT at 0 V (continuous line) and 12 V (circles) are also plotted. PLUC experiments were performed by Paiboon Sreearunothai and Laura Herz.



**Fig. 2.43** (Photo-)Current and relative electric-field quenching versus applied voltage measured from the same PFB:F8BT and TFB:F8BT blend devices as in Fig. 2.40. The detection wavelength was 700 nm (PFB:F8BT) and 580 nm (TFB:F8BT), respectively. The current was not corrected for the dark current and hence is not the pure photocurrent.

dependent PLUC measurements. The results are displayed in Fig. 2.42(b). The exciton decay dynamics are not field dependent [66]. Therefore, a dark intermediate state must be dissociated by the field. We postulate that this state is an interfacial geminate polaron pair that follows charge transfer from the bulk exciton [67–70]. Branching from this geminate pair then produces either exciplex states or free charges and the branching ratio is field-dependent. Furthermore, in Fig. 2.43, we find the field-induced reduction of exciplex PL to closely correlate with increased (photo)current.

**Fig. 2.44** Relative electric field quenching of the PFB:F8BT and TFB:F8BT exciplex photoluminescence intensities (measured at 700 nm and 580 nm, respectively), in the same devices as in Fig. 2.40, versus electric field at 230 K (solid squares), 250 K (open and solid circles), 290 K (solid triangles) and 295 K (open diamonds). The solid lines through the data are



Onsager simulations (parameters for PFB:F8BT:  $\epsilon = 3.5$ ,  $r_{gp} = 3.0$  nm at  $T = 230$  K and 3.1 nm at 250 K and 290 K; for TFB:F8BT:  $\epsilon = 3.5$ ,  $r_{gp} = 2.3$  nm at  $T = 250$  K and 2.2 nm at 295 K).

To estimate the electron–hole separation within the geminate pair,  $r_{gp}$ , we consider the field-dependent changes in PL intensity plotted in Fig. 2.44. Neglecting the effects of energetic disorder [71] and of a possible interfacial dipole layer [70], geminate-pair dissociation in electric fields is most easily described within the Onsager model (see references [72, 73, p. 484]), which yields the dissociation probability  $f_\epsilon(r_{gp}, T, F) = f(F)$  of bulk geminate pairs in a medium with dielectric constant  $\epsilon$ , under an applied field  $F$  and at temperature  $T$ :

$$f_\epsilon(r_{gp}, T, F) = \frac{1}{2} \int_0^\pi d\theta \sin \theta e^{-(A+B)} \sum_{m,n=0}^{\infty} \frac{A^m}{m!} \frac{B^{m+n}}{(m+n)!} \quad (2.17)$$

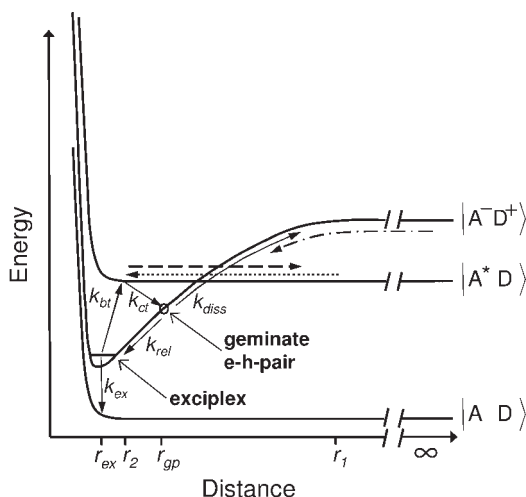
where  $A = 2q/r_{gp}$ ,  $B = \beta r_{gp}(1 + \cos \theta)$ ,  $q = e^2/8\pi\epsilon\epsilon_0 kT$ , and  $\beta = eF/2kT$ . The averaging over  $\theta$  was done to represent an isotropic blend morphology. Since the only material parameter is the dielectric constant  $\epsilon$ , which we approximate to be 3.5 for all polymers<sup>1)</sup>, Onsager theory should be applicable also to geminate pairs at the interface. The field-dependent relative reduction of the geminate-pair population  $n_{gp}$  is given by

$$-\frac{\Delta n_{gp}}{n_{gp}} = \frac{f(F) - f(0)}{1 - f(0)} \quad (2.18)$$

Because the PL intensity is proportional to the excited-state population, we can assume  $\frac{\Delta n_{gp}}{n_{gp}} = \frac{\Delta PL}{PL}$  and compare with experiment. Fig. 2.44 plots  $-\frac{\Delta PL}{PL}$  versus electric field<sup>2)</sup> at various temperatures for PFB:F8BT and TFB:F8BT devices (measured in the red part of the spectrum where exciton emission is insignificant). Plotted in the same graph are simulations of  $-\frac{\Delta n_{gp}}{n_{gp}}$  using a  $\delta$ -function distribution for  $r_{gp}$ . The simple model fits the data satisfactorily, which supports the assump-

- 1) Dielectric constants of conjugated polymers typically lie between 3 and 4 [74, 75].
- 2) The internal field was calculated as  $F = (\text{applied voltage} + \chi)/170$  nm;  $\chi$  is the voltage

corresponding to minimum  $-\Delta PL/PL$ , found to be 0.7 V (PFB:F8BT) and 0.3 V (TFB:F8BT) forward bias.



**Fig. 2.45** Potential energy diagram describing the energetics and kinetics at type-II polymer heterojunctions. The energetic order of  $|A^- D^+\rangle_{r=\infty}$  and  $|A^* D\rangle_{r=\infty}$  may be reversed for PFB:F8BT vs. TFB:F8BT.

tion of a geminate pair intermediate prior to exciplex formation and yields  $r_{gp} \approx 3.1$  nm (PFB:F8BT) and  $r_{gp} \approx 2.2$  nm (TFB:F8BT). The large separation is probably caused by polaron-pair thermalization following the initial charge-transfer step [67, 73].

We now return to the  $\Delta$ PL spectra in Fig. 2.40, which contain bulk F8BT components that are not due to electric-field-promoted dissociation of those states, as was shown above. The zero-field steady-state photoluminescence is due to three different excited-state populations: (i) “primary” excitons, generated in the bulk by the laser excitation; (ii) exciplexes, generated via energy transfer from bulk excitons; and (iii) “secondary” excitons, generated via endothermic back-transfer from the exciplexes (see Section 2.2 and ref. [13]). Since the exciplex density is reduced by application of an electric field, there is less secondary-exciton generation, and hence the observed  $\Delta$ PL contains an excitonic contribution. Further evidence for this hypothesis is provided by the temperature dependence of the  $\Delta$ PL spectra shown in Figs. 2.40(b) and 2.40(d).<sup>1</sup> The ratio of secondary excitons to exciplexes is found to follow an Arrhenius function with activation energy  $200 \pm 50$  meV (PFB:F8BT) and  $100 \pm 30$  meV (TFB:F8BT).<sup>2</sup> These activation energies are consistent with those values extracted with our previous TCSPC and electroluminescence measurements (see Section 2.2 and Section 2.2.3).

Figure 2.45 summarizes the above findings. The potential energy curves represent the ground-state ( $|AD\rangle$ ), the exciton residing on F8BT ( $|A^*D\rangle$ ), and the electron and the hole residing in the respective component across the heterojunction ( $|A^-D^+\rangle$ ), where A and D symbolize the acceptor (F8BT) and the donor (PFB or

<sup>1</sup> At temperatures below 230 K the  $\Delta$ PL arising from the excitons’ Stark shift obscures the weak quenching signal.

<sup>2</sup> The activation energies were evaluated using the same Arrhenius analysis that was employed in the previous sections (see Figs. 2.25, 2.28, 2.32).

TFB), respectively. The diagram is drawn to project three different coordinates at the same time, i.e. the abscissa represents *either* the distance of the two dissimilar ground-state molecules ( $|AD\rangle$ ) *or* the distance of the exciton from the interface ( $|A^*D\rangle$ ) *or* the separation of the geminate polarons ( $|A^-D^+\rangle$ ). The exciplex state is then located in the minimum of the  $|A^-D^+\rangle$  potential. When the system is photoexcited, an exciton is generated at a certain distance  $r_1$  from the heterojunction. It then diffuses to a separation  $r_2$  (dotted arrow), where it dissociates and an interfacial geminate electron–hole pair is formed with rate constant  $k_{ct}$ . This geminate-pair can either dissociate ( $k_{diss}$ ) or relax into the luminescent exciplex state ( $k_{rel}$ ). The ratio  $k_{diss}/k_{rel}$  is strongly field dependent and determines the degree of luminescence quenching. The exciplex state can then either decay ( $k_{ex}$ ), or back-transfer to a bulk exciton in F8BT ( $k_{bt}$ ), but is itself too strongly bound to dissociate under the field. We note that the transition from geminate pairs to excitons via  $k_{rel} \rightarrow k_{bt}$  represents a novel mechanism for geminate pair recombination at polymeric heterojunctions. The secondary excitons produced might enter the cycle again, or diffuse away from the heterojunction (dashed arrow) and decay. The model is also applicable to electrical excitation, where the excited-state is produced via charge injection (dash-dotted arrow).<sup>1)</sup> The regeneration of the exciton via the thermally-driven circular process  $k_{ct} \rightarrow k_{rel} \rightarrow k_{bt}$  means that even though charge transfer occurs, the excitation energy might eventually still be emitted in the form of bulk exciton luminescence.

An estimate of the contribution of the regeneration process to the PL of the blend can be derived by normalizing the  $\Delta$ PL spectrum to the PL spectrum at higher wavelengths where the emission is solely due to exciplexes. We assume that this renormalized  $\Delta$ PL then represents the contribution of exciplex and secondary exciton emission to the total PL. We infer thereby that at room temperature in the PFB:F8BT blend  $\sim 20\%$  of the visible emission comes from primary excitons. In TFB:F8BT we find a primary exciton contribution of  $< 2\%$ , which implies that  $> 98\%$  of the excitons undergo charge transfer at a heterojunction. Despite this, the relative PL quenching with respect to pure F8BT is only  $< 57\%$  (PL yield of F8BT 80%, of TFB:F8BT 35%) indicating the great importance of the exciton-regeneration mechanism. Secondary exciton and exciplex emission maintain a high PL yield in spite of most excitons encountering a heterojunction. On the other hand, the PFB:F8BT PL yield is only 4%, consistent with large geminate-pair dissociation and low back-transfer efficiency, i.e. with low “regeneration efficiency”.

In Section 2.2.1, we mentioned the importance of spin multiplicity for light-emitting diode operation and suggested the exciplex state play an important role. We now extend these considerations to the geminate pair. Employing a similar argument as for the exciplex, we expect spin randomization to occur while the system is in the geminate-pair state. Hence, during the regeneration cycle, the system visits two states (the exciplex and the geminate pair) in which intersystem

1) We note that the model presented here incorporates and is in complete agreement with the concepts of barrier-free charge capture

and reverse photoinduced charge-transfer as described in Section 2.2.

crossing is facilitated. Indeed, recent work from our group indicates a strongly enhanced triplet yield under photoexcitation in the polymer blends with respect to the pure polymers [76]. Direct evidence for spin randomization has recently been found in an intramolecular donor-acceptor system by simultaneous application of electric and magnetic fields [77]. There, a small magnetic field of 0.09 Tesla inhibits the intersystem crossing within the radical-ion pair. This is seen via reduced electric-field quenching of the locally excited state, because back-electron transfer to the locally excited state is more efficient in the singlet state. Spin-dependent recombination and dissociation of solvent-separated radicalion pairs has been modeled extensively by Burshtein and coworkers [78–85] and we suggest that similar theories might apply here.

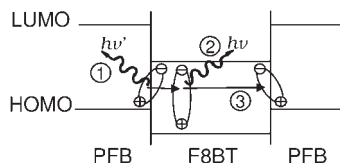
In summary, we have developed a comprehensive description of the excitonic and electronic processes at type-II polymer heterojunctions that support exciplex formation. The two blends studied here represent important examples for efficient charge generation on the one hand and high luminescence yields on the other, and in this sense represent the two extremes of type-II heterojunctions found in common semiconductor polymer blends. The very different behavior was shown to arise from different geminate-pair separations (3.1 nm vs. 2.2 nm) and back-transfer activation energies (200 meV vs. 100 meV) that affect strongly the kinetics between the states involved. We note that both thermalization distance as well as activation energy are generally expected to be larger for larger band-edge offsets between the two polymers and that this provides the link to the classification scheme described in the introduction [18].

In photovoltaic operation the collapse of the geminate pair into the exciplex provides an unwanted loss channel. We suggest that optimized interfaces require not only large band-edge offsets to enable large thermalization distances ( $r_{gp}$ ), but also inhibited exciplex stabilization. This can be achieved by increasing intermolecular distances and decreasing configurational relaxation [25].

## 2.4

### Morphology-dependent Exciton Retrapping at Polymer Heterojunctions

In the previous sections, we have shown that bulk excitons can be generated via transfer from electrically excited exciplexes (Section 2.2), but also that photoexcited excitons can be trapped at the interface to form exciplexes (Section 2.1.4.2 and Section 2.3.1). Hence, also excitons that have been generated by transfer from an exciplex might get “retrapped” at the interface and again form exciplexes (process (3) in Fig. 2.46). This is expected to influence the electroluminescence spectral shape and efficiency and should be more likely in a blend with phase dimensions comparable to the exciton diffusion length than in a bilayer, for example. We investigate the photoluminescence of simple films (170 nm) of blends of PFB and F8BT spun onto Spectrosil substrates from common chloroform solution. Limited demixing results in phases of the order of 10 nm or less [14, 27]. In order to achieve different morphologies, the weight ratio was varied between



**Fig. 2.46** Illustration of exciton retrapping at PFB:F8BT heterojunctions. An exciplex state that was formed at the heterojunction via barrier-free charge capture (Section 2.2) or relaxation of an interfacial geminate pair (Section 2.3) can either decay radiatively and emit (1) or transfer endothermally to the bulk

exciton state. In large bulk phases, this exciton is likely to emit (2), but in nm-scale phases it diffuses to another interface site and is re-trapped to again form an exciplex (3). Exciton retrapping therefore lowers the ratio of delayed exciton to exciplex emission.

5:95 and 97.5:2.5. All samples were prepared and measured under inert atmosphere. Time-resolved PL measurements were done by TCSPC.

Figures 2.31 and Fig. 2.33 show EL spectra of a bilayer and a blend LED. The high evaporation rate of the chloroform solution together with the low fraction of F8BT molecules results in very limited demixing in the blend with F8BT phase measures of the order of the 10 nm or less [27, 14]. Strong retrapping is expected for this type of morphology and indeed the F8BT exciton contribution to the EL spectrum is much smaller for the blend device than for the bilayer at any temperature. From Fig. 2.32, we infer this contribution to be reduced to  $< 30\%$  of its value for the bilayer LED and hence  $> 70\%$  of the generated excitons are re-trapped at an interface. Despite this, the activation energy of the exciton contribution is evaluated to be similar to the bilayer case ( $200 \pm 50$  meV, see Fig. 2.32), which confirms that the energetics at the interface are unaltered. Hence, the retrapping of excitons at the polymer/polymer interface is an important process that only depends on the morphology of the system but strongly influences the efficiency of exciton electroluminescence. The high evaporation rate of the chloroform solution together with the low fraction of F8BT molecules results in very limited demixing in the blend with F8BT phase measures of the order of 10 nm or less [14, 27]. Much stronger exciton retrapping is expected for this type of morphology than for a bilayer with only two macroscopic phases and hence the F8BT exciton contribution to the EL spectrum is much smaller for the blend device than for the bilayer at any temperature. A lower limit for the trapping efficiency in the blend film can be estimated by considering that the ratio of the exciton population  $m$  to the exciplex population  $x$  is  $\sim 70\%$  lower in the blend than in the bilayer device

$$\frac{m_{\text{blend}}}{x_{\text{blend}}} = (1 - 0.7) \frac{m_{\text{bilayer}}}{x_{\text{bilayer}}} \quad (2.19)$$

Let now  $q$  be the difference of the trapping efficiencies in the blend and the bilayer film, and  $p \leq 1$  be the fraction of trapped excitons that again become exciplexes and do not decay nonradiatively at the interface. We can then write

$$\frac{m_{\text{blend}}}{x_{\text{blend}}} = \frac{m_{\text{bilayer}} - q m_{\text{bilayer}}}{x_{\text{bilayer}} + p q m_{\text{bilayer}}} \quad (2.20)$$

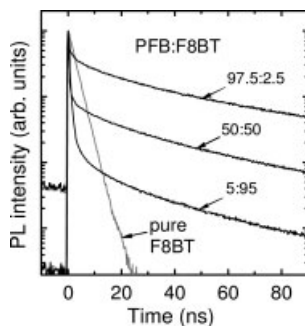
From Eq. 2.19 and Eq. 2.20, we infer

$$q = \frac{0.7}{1 + 0.3 p \frac{m_{\text{blend}}}{x_{\text{blend}}}} \quad (2.21)$$

With  $m_{\text{blend}}/x_{\text{blend}} < 1$  we find that at least  $0.7/(1 + 0.3) = 54\%$  of the excitons in the blend device are retrapped at the interface. We note that this value only reflects the additional trapping in the blend as compared to the bilayer. The total trapping efficiency might be significantly higher. We conclude that the retrapping of excitons at the polymer/polymer interface is an important process that only depends on the morphology of the system but strongly influences the efficiency of exciton electroluminescence.

A more detailed evaluation of the retrapping phenomenon requires the comparison of different blend morphologies. This is not possible via EL investigations because altering the morphology of the polymer blend in the device also alters the field distribution, efficiency, and I-V characteristics. In particular, current heating can unintentionally alter the emission spectrum [16, 62]. We show that these problems can be circumvented by considering time-resolved PL measurements instead. We consider polymer blend films spun from chloroform solution with different weight ratios of the two components. This gives a range of different morphologies because for smaller fractions of F8BT, the size of the F8BT phases is reduced. We hence expect different exciton retrapping efficiencies.

Figure 2.47 shows PL decay curves measured at 620 nm for several different blend ratios as well as for pure F8BT. The emission from the blends decays roughly biexponentially. We assign the fast decay to the photoexcited exciton and the slowly decaying component to the long-lived exciplex state [13]. Generally, exciplex states are generated via energy transfer from photoexcited excitons and this explains the faster exciton decay in the blend films than in the pure F8BT. Fitting the delayed exciplex emission with a simple exponential decay yields different time constants  $\tau_{\text{delayed}}$  for different blends. From Table 2.2 we see that



**Fig. 2.47** Photoluminescence decays (measured at 620 nm) of pure F8BT and of PFB:F8BT blends for different weight ratios as indicated in the figure. Fitting the delayed emission from the blends between 30–90 ns yields the time constants  $\tau_{\text{delayed}}$  given in Table 2.2. The decays have been normalized to their peak intensity.

**Table 2.2** Time constants  $\tau_{\text{delayed}}$  and exciton-to-exciplex ratios  $r$  of the delayed PL emission from polymer blend samples with different PFB:F8BT blend ratios. The time constants were determined from single exponential fits of the PL decays in Fig. 2.47 between 30 and 90 ns. The fitting errors were  $< 0.3$  ns for all decays.

blend ratio	$\tau_{\text{delayed}}$ (ns)	$r$	blend ratio	$\tau_{\text{delayed}}$ (ns)	$r$
5:95	38.6	0.64	75:25	47.8	0.12
10:90	40.8	0.42	90:10	50.4	–
25:75	42.3	0.25	95:5	53.0	–
50:50	44.5	0.16	97.5:2.5	54.0	–
60:40	45.9	0.15			

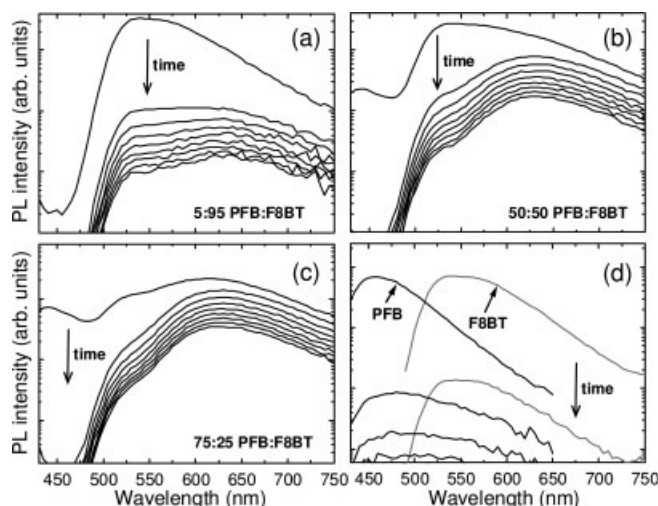
the exciplex decays more slowly for blends containing lower fractions of F8BT. This is at first sight surprising since the localized exciplex should not depend on the morphology of the blend. However, it can be rationalized by the fact that the higher retrapping efficiency in blends with smaller F8BT fractions (i.e. smaller F8BT phases) results in a less-efficient depopulation of the exciplex through back-transfer to the short-lived exciton and hence a slower decay of the exciplex population. In this picture, the decay constant should approach a maximum value for blends where retrapping is  $\sim 100\%$  efficient and back-transfer to the exciton can be neglected completely. From Table 2.2, we find a lower limit of 54 ns for this “pure” exciplex decay constant.

Fig. 2.48 shows time-dependent PL spectra for several blends as well as for the pure polymers. At short times (0–10 ns), the spectra are mostly dominated by the exciton emission but at longer times the PL from the blends evolves into the red exciplex peak. After  $\sim 30$  ns the spectra do not evolve any further and decay with the time constants  $\tau_{\text{delayed}}$  given in Table 2.2. The delayed emission still contains an F8BT exciton contribution (visible as a green shoulder at  $\sim 535$  nm). Since pure F8BT shows no delayed emission at all this has to be due to the endothermic transfer from the exciplex. Hence, the delayed PL emission has the same origin as the EL emission (i.e. the exciplex) and the two phenomena are very comparable.

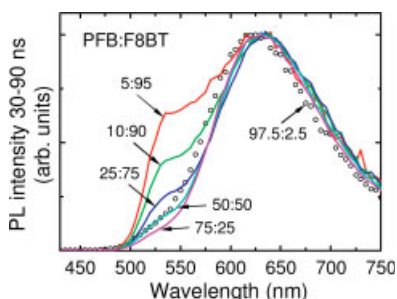
In Fig. 2.49, the delayed emission spectra for different blend ratios are compared. The F8BT exciton contribution decreases monotonically for higher PFB:F8BT ratios and is almost 100% suppressed in the 97.5:2.5 blend. This agrees well with an increased exciton retrapping probability as would be expected for smaller F8BT phases. Since no delayed emission is observed from pure F8BT, the effect has to be due to the interface with the PFB. We consider this strong evidence for the retrapping model.

The exciplex emission in Fig. 2.49 blue-shifts for blends with low fractions of F8BT. Since the energetics at the interface are not affected by the blend ratio,





**Fig. 2.48** Time-resolved photoluminescence spectra of PFB:F8BT blends of different weight ratios, (a), (b) and (c), and of films of pure PFB and F8BT (d). The spectrum with the highest intensity represents the PL emission integrated over the first 10 ns. The less-intense spectra are the delayed PL integrated over subsequent 10-ns time windows, i.e. over 10–20 ns, 20–30 ns, ..., 80–90 ns.

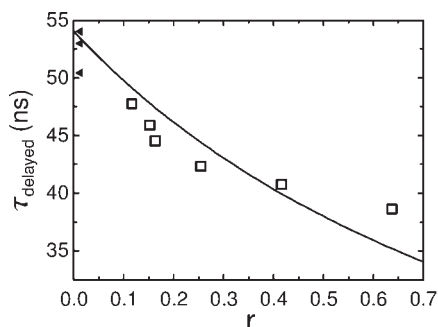


**Fig. 2.49** Delayed emission spectra, integrated over 30–90 ns after excitation, for blends of different weight ratios. For low fractions of F8BT, the exciplex shifts to the blue, as is shown for the case of a 97.5:2.5 blend. The spectra have been normalized.

we suggest that the blue-shift is a consequence of the retrapping phenomenon. Generally, the back-transfer from the exciplex to the exciton is more efficient for higher-energy exciplexes than for lower-energy ones due to the lower activation energy. Hence, if back-transfer is suppressed by strong retrapping, the average energy of the exciplex population increases. We note that similar blue-shifts can also be seen in temperature-dependent EL, and temperature- and time-dependent PL [13], and temperature- and electric-field-dependent PL [14] measurements. We suggest the blue-shift in these cases to be due also to reduced back-transfer, although here this reduction is caused by the lower sample temperature and not by increased retrapping.

In order to quantify the retrapping phenomenon, we determine the ratio  $r$  of the exciton and the exciplex contributions to the delayed emission spectra in Fig. 2.49. We assume the peak intensities of the spectra (at  $\sim 630$  nm) to be a mea-

**Fig. 2.50** Time constant  $\tau_{\text{delayed}}$  as a function of the exciton-to-exciplex ratio  $r$  of the delayed PL emission from PFB:F8BT polymer blends. The data is the same as in Table 2.2. As explained in the text,  $r$  was not determined for very small values. Instead only the values of  $\tau_{\text{delayed}}$  are indicated by triangular markers on the y-axis. The line represents fits to the data using either Eq. (2.31) or Eq. (2.33) (see text for details).



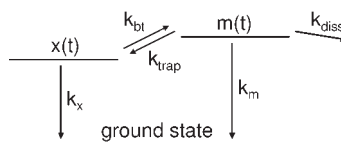
sure of the exciplex contribution and the intensities at 535 nm (i.e. the peak of the F8BT exciton emission, see Fig. 2.48(d)) to correspond to the exciton contribution. The values of  $r$  derived thereby are listed in Table 2.2. The approximation fails when the overlap of the two spectra is large or their spectral shapes change that is the case for very weak F8BT emission and strongly blue-shifted exciplex emission. We therefore do not determine  $r$  for blends of 10% F8BT or less.

Figure 2.50 plots the exciplex decay constant  $\tau_{\text{delayed}}$  versus  $r$ . Clearly, there is a strong correlation, and the decay constant of the exciplex population decreases as this decay is facilitated via more efficient transfer to the excitons.

#### 2.4.1

##### Predicted Similarity of EL and Delayed PL Spectra

This correlation  $\tau_{\text{delayed}}(r)$  can also be derived from a simple kinetic model shown in Fig. 2.51. The figure depicts the F8BT exciton (with population  $m(t)$ ), the exciplex (population  $x(t)$ ), and the system ground-state. We only consider F8BT excitons for this model because there is no back-transfer from the exciplex to the high-energy PFB exciton level. The transitions between the states are also indicated in the figure, where  $k_m$  is the decay rate constant of excitons in pure F8BT,  $k_{\text{trap}}$  is the retrapping rate constant,  $k_{\text{bt}}$  is the back-transfer rate constant from the exciplex to the exciton,  $k_{\text{diss}}$  is the rate constant of charge generation at the heterojunction, and  $k_x$  is the “pure” exciplex decay rate constant (i.e. the time constant of only those decay channels that lead to the ground-state). In previous work we have shown that charge transfer at the heterojunction initially produces an interfacial geminate polaron pair that subsequently fully dissociates or relaxes into the exciplex [14]. Since here we are not interested in this geminate-pair intermediate we can describe the process as a branching directly from the



**Fig. 2.51** A kinetic model of the electronic transitions at the polymer/polymer interface. See text for further details.

exciton to either free charges,  $k_{\text{diss}}$ , or exciplex states,  $k_{\text{trap}}$ . We neglect a possible morphology dependence of the branching ratio  $c_{\text{diss}} = k_{\text{diss}}/k_{\text{trap}}$  [70–89] and assume  $c_{\text{diss}}$  to be constant for all samples and all heterojunction sites, and this allows us to substitute  $k_{\text{diss}} \mapsto c_{\text{diss}} k_{\text{trap}}$ . Figure 2.51 is then described by the set of differential equations

$$\frac{dx(t)}{dt} = -k_x x(t) - k_{\text{bt}} x(t) + k_{\text{trap}} m(t) \quad (2.22)$$

$$\frac{dm(t)}{dt} = -k_m m(t) - k_{\text{trap}} m(t) - c_{\text{diss}} k_{\text{trap}} m(t) + k_{\text{bt}} x(t) \quad (2.23)$$

With the initial conditions  $m(0) = m_0$  and  $x(0) = 0$  (i.e. no direct photoexcitation of the exciplex) these equations are readily solved and yield biexponential functions of the form

$$m(t) = C_{m,1} e^{-k_1 t} + C_{m,2} e^{-k_2 t} \quad (2.24)$$

$$x(t) = C_{x,1} e^{-k_1 t} + C_{x,2} e^{-k_2 t} \quad (2.25)$$

where

$$k_{1,2} = \frac{1}{2} (k_{\text{bt}} + k_m + k_{\text{trap}} + c_{\text{diss}} k_{\text{trap}} + k_x \pm \rho), \quad (2.26)$$

and

$$C_{m,1,2} = \frac{m_0}{2\rho} (\rho \pm \sigma), \quad C_{x,1,2} = \mp k_{\text{trap}} m_0 \rho \quad (2.27)$$

with

$$\rho = \sqrt{(k_{\text{bt}} + k_m + (1 + c_{\text{diss}}) k_{\text{trap}} + k_x)^2 - 4 (k_{\text{bt}} (c_{\text{diss}} k_{\text{trap}} + k_m) + ((1 + c_{\text{diss}}) k_{\text{trap}} + k_m) k_x)} \quad (2.28)$$

and

$$\sigma = -k_{\text{bt}} + c_{\text{diss}} k_{\text{trap}} + k_m + k_{\text{trap}} - k_x \quad (2.29)$$

At long times after the excitation pulse,  $t \gg k_1^{-1}$ , both the exciton and exciplex populations decay with rate  $k_2$  and the ratio of their emission intensities becomes independent of time to be

$$r = \left. \frac{PL_{\text{exciton}}}{PL_{\text{exciplex}}} \right|_{t \gg 1/k_1} = \frac{\eta_m k_m C_{m,2}}{\eta_x k_x C_{x,2}} \quad (2.30)$$

where  $\eta_m$  and  $\eta_x$  are the quantum yields of the exciton and exciplex emissions, respectively. From Eqs. (2.26), (2.27), and (2.30), we derive the time constant of the delayed emission to be

$$\tau_{\text{delayed}}(r) = k_2^{-1}(r) = \frac{k_m (1 + c_{\text{diss}}) + k_x \eta_{x/m} r}{k_m \left( (1 + c_{\text{diss}}) k_x + c_{\text{diss}} k_{\text{bt}} + k_x \eta_{x/m} r \right)} \quad (2.31)$$

where  $\eta_{x/m} = \eta_x/\eta_m$ . This is the expected functional form of the data in Fig. 2.50. We consider that, with  $k_m^{-1}=2.45$  ns (as determined from the decay of pure F8BT measured at 535 nm),  $c_{\text{diss}} > 0$ ,  $k_x^{-1} \geq 54$  ns,  $r \leq 0.64$  (see Table 2.2) and an upper limit  $\eta_{x/m} < 1$ ,

$$k_x \eta_{x/m} r < 3\% (k_m (1 + c_{\text{diss}}) + k_x \eta_{x/m} r) \quad (2.32)$$

and simplify Eq. (2.31) as a simple inverse proportionality

$$\tau_{\text{delayed}}(r) \approx \frac{A}{B + r} \quad (2.33)$$

with

$$A = \frac{1 + c_{\text{diss}}}{k_x \eta_{x/m}}, \quad B = \frac{k_x + c_{\text{diss}} (k_{\text{bt}} + k_x)}{k_x \eta_{x/m}} \quad (2.34)$$

As mentioned above, very low values of  $r$  could not be determined accurately. When fitting the data, however, we would like to also account for the longest lifetimes measured (see Table 2.2). We therefore assume  $r \approx 0$  for  $\tau_{\text{delayed}}=54.0$  ns and include (0,54 ns) as a data point. This approximation is justified because choosing a value for  $r$  between 0 and 0.12 alters the fit curve and its parameters by less than 2%. Figure 2.50 shows a corresponding fit using Eq. (2.33), and we see that the experimental correlation between  $\tau_{\text{delayed}}$  and  $r$  is well reproduced by the function derived from the model.

The fit in Fig. 2.50 yields the parameter values  $A=80.2$  ns and  $B=1.56$ . We consider that this agrees well with realistic assumptions for the physical parameters  $c_{\text{diss}}$ ,  $k_x$ ,  $k_{\text{bt}}$ , and  $\eta_{x/m}$ . Previous work [90] has shown that optimized photovoltaic devices made from PFB and F8BT can reach external quantum efficiencies of  $\sim 10\%$ , and we hence assume  $c_{\text{diss}} \approx 0.1$ . Inserting this and an estimate  $k_x^{-1} \approx 54$  ns (see above) in Eqs. (2.34) yields  $k_{\text{bt}}^{-1} = 96$  ns,  $\eta_{x/m} = 0.74$ . The value  $k_{\text{bt}}^{-1} \approx 100$  ns is consistent with endothermic excitation rates calculated from the product of the Boltzman factor  $\exp[-0.2 \text{ eV}/(k_B 300 \text{ K})] \approx 10^{-4}$  and typical intermolecular vibronic attempt frequencies of order  $10^{11}$  Hz [91]. The value  $\eta_{x/m} = 0.74$  means that  $\eta_x = \eta_{x/m} \eta_m = 41\%$  (using  $\eta_m = 55\%$  as measured previously [28]). With  $k_x^{-1} = 54$  ns we then derive the radiative time constant of the exciplex to be  $k_{x,\text{rad}}^{-1} = 133$  ns. This is consistent with the value of 118 ns found by fitting the exciplex PL decay at very low temperatures where most nonradiative channels are frozen out [13].

We conclude that the experimental data agrees well with a simple kinetic model of exciton retrapping. This confirms that retrapping is responsible for reduced exciton emission in polymer blends.

By considering the EL spectra from Section 2.2.3, we have shown that the amount of EL observed from the endothermically generated bulk excitons is dependent on the film morphology, and we introduced the concept of retrapping of excitons. For nm-scale morphologies, excitons are likely to encounter again an interface during their lifetime and get retrapped into an exciplex, which can reduce exciton EL by more than 70%.

We investigated exciton retrapping in detail using time-resolved photoluminescence measurements. The delayed emission seen from polymer blends is due to the long-lived exciplex emission as well as the emission from excitons that are generated from the exciplex throughout its lifetime. The delayed emission spectra are hence similar to the EL emission. We have shown that the delayed emission lifetime  $\tau_{\text{delayed}}$  as well as the relative amount of delayed *exciton* emission  $r$  strongly vary for different morphologies and hence different retrapping efficiencies and that they are negatively correlated. For very low fractions of F8BT we find that the retrapping efficiency is  $\sim 100\%$ . The correlation  $\tau_{\text{delayed}}(r)$  was well reproduced by a kinetic model of retrapping at the polymer interface.

The retrapping efficiency directly and only relates to the exciton diffusion length and the nanoscale morphology of the film, and we suggest this as a probe of these fundamental qualities.

Highly efficient LED operation is only achieved through efficient exciton EL (Section 2.2), and exciton retrapping has hence to be reduced. In blend LEDs, this could be achieved via large phases and sharp phase interfaces to provide uninterrupted escape paths for the excitons. On the other hand, this morphology potentially promotes large leakage currents, which is detrimental to efficient operation. Bilayer or vertically phase-separated blends could provide a solution to circumvent this trade-off.

## 2.5

### Summary

#### 2.5.1

#### Exciplex Formation is General in Polyfluorenes

In Section 2.1.4, the electronic and photophysical properties of donor–acceptor or “type-II” heterojunctions between two semiconductor polymers were investigated. Exciplex formation was found to be a general phenomenon for type-II heterojunctions between polyfluorene copolymers. These are among the most widely used materials in polymer optoelectronics, but the presence of exciplexes had not yet been fully appreciated. This is because the exciplex population is often depopulated via efficient endothermic transfer towards the exciton, which leads to bulk exciton instead of exciplex emission. However, via time- and temperature-dependent photoluminescence (PL) spectroscopy the exciplex states can be identified. Employing a relationship known from small-molecule solution systems that relates the relative HOMO and LUMO levels of the molecules to the exciplex emis-

sion energy, it is possible to show that exciplex formation occurs at *every* heterojunction where the basic energetic conditions (when the predicted exciplex energy level being below the exciton) are met. This generality of exciplex formation in the important class of polyfluorene copolymers was motivation to investigate their role during the two basic processes occurring in optoelectronic diodes, charge capture and exciton dissociation.

### 2.5.2

#### **Electron–Hole Capture can Occur Barrier-free via an Exciplex Intermediate**

We discussed in Section 2.2 that the exciplex state mediates a new pathway for the formation of an exciton from two uncorrelated charges. This process was termed “barrier-free” electron–hole capture, because the neutral state formed can be reached without overcoming the band offsets at the heterojunction. The neutral state is the exciplex and it is readily accessible because of its charge-transfer character and its energetic position below the charge-separated state. The transition from the separated charges to the exciplex can be seen as a “reverse photoinduced charge transfer”, and, in analogy to forward charge transfer, it can be expected to be fast and efficient. If the actual capture is fast, the rate-limiting process is the diffusion of electron and hole along the heterojunction in order to encounter each other at opposite sides of the junction. Contrary to the case of field-assisted charge injection across the interface, barrier-free capture does not require high electric fields and strong charge accumulation at the heterojunction. This leads to low turn-on voltages and low charge-induced luminescence quenching. Following the reverse charge transfer, the exciplex state can emit (with low oscillator strength) or endothermically transfer to the bulk exciton. If the latter process is efficient, this can lead to extremely efficient light-emitting diodes, as was shown in Section 2.2.1. The presented barrier-free capture mechanism facilitates EL operation, when charge injection across the heterojunction is impossible or very inefficient. For high voltages, this condition breaks down and “conventional” capture via charge injection and recombination in the polymer bulk occurs and this was shown in Section 2.2.4.

To optimize the heterojunction for light-emitting diodes, one should generally aim to (a) facilitate exciplex formation from uncorrelated charges, (b) prevent charge injection across the heterojunction, and (c) facilitate the endothermic transfer from the exciplex to the exciton. As is common with optimization problems, these requirements are conflicting. This is illustrated by the following trade-offs: exciplex formation yields can be improved by increasing the charge-transfer character of the exciplex. However, this lowers the exciplex energy and hence increases the activation energy for the transfer to the exciton. As another example, the activation energy can be reduced by lowering the band offsets, but this will facilitate injection of unpaired charges across the heterojunction. The very high efficiency found for the TFB:F8BT device motivates further research.

## 2.5.3

**Dissociated Excitons can be Regenerated via Geminate-Pair and Exciplex Intermediates**

In Section 2.3, we investigated exciton dissociation at the heterojunction. We showed that dissociation at the interface does not produce uncorrelated charges directly but rather an interfacial geminate pair that is bound by Coulomb interactions. This electron–hole pair either collapses or fully dissociates via thermal activation and the branching between these two possibilities was shown to follow Onsager theory of geminate recombination. The collapse of the geminate pair can result in an exciplex state as shown in Section 2.3.1. Alternatively, back-electron transfer might also yield the ground-state. As mentioned above, the exciplex can be activated thermally and transfer to the bulk exciton state. Therefore, the excitation can undergo thermally driven circular transitions from the exciton to the geminate pair to the exciplex and back to the exciton. This process was termed “exciton regeneration” and was suggested to be highly efficient in TFB:F8BT blends. Efficient regeneration can yield large quantities of “secondary excitons” (i.e. excitons that have undergone one or more regeneration cycles at the heterojunction) which maintains a high PL yield despite exciton dissociation at the heterojunction. The collapse of the geminate pair lowers the efficiency of charge generation and this reduces the quantum yield of photovoltaic devices.

To optimize the heterojunction for photovoltaic diodes one should generally aim to inhibit geminate-pair recombination. One way to achieve this might be to increase the band offsets. (In fact, it is not clear whether this would actually help, see below.) More subtle ways are to reduce exciplex stabilization via increasing intermolecular distances or decreasing configurational relaxation. Interfacial geminate pairs might also form (and lower photovoltaic efficiencies) at interfaces that do not support exciplex formation. However, the exciplex is a marker for their existence and a useful probe for their investigation.

## 2.5.4

**High Interface Densities Lower the Barrier-free Capture and Exciton-Regeneration Efficiencies**

In Section 2.4, we discussed the influence of the film morphology on the above mechanisms. No qualitative differences were found between bilayers and blends of different degrees of phase separation, which demonstrates that both barrier-free capture as well as exciton regeneration are properties only of the energetics and molecular structure of the heterojunction. However, the film morphology plays a crucial role in determining the fate of excitons that have been generated at the heterojunction, be it via barrier-free capture or via exciton regeneration. In morphologies with high interface densities (e.g. in well-mixed blends), these excitons are likely to diffuse and again encounter a heterojunction site during their lifetime and dissociate. This process was termed “exciton retrapping”. It lowers the effective efficiency of both barrier-free capture and exciton regeneration,

and was shown to reduce the secondary exciton population below the detection limit in strongly mixed blends. While this might be an advantage in photovoltaic devices, it is surely detrimental to efficient LED operation via barrier-free capture. However, it might be possible to circumvent this problem by employing strongly phase-separated blends or bilayer systems. For the former, it is crucial to balance the trade-off between decreasing exciton retrapping and increasing leakage currents with higher phase separation.

### 2.5.5

#### **Conclusion**

In conclusion, the presence of exciplexes at the polymer heterojunction requires a revision of the models that are usually applied to charge capture and exciton dissociation at the interface. Alternative models have been presented here. A better understanding of the heterojunction will benefit the optimization of any optoelectronic device, but in particular for light-emitting diodes the new mechanism promises great improvements of device efficiency. Generally, the exciplex is an ideal probe for the investigation of electronic and photophysical phenomena that occur at the polymer heterojunction. The findings presented are important because it was shown here that exciplex formation is a ubiquitous phenomenon at polyfluorene heterojunctions.

#### **Acknowledgments**

We gratefully acknowledge our colleagues who contributed to this work as co-authors in the publications that were reviewed here. They are Neil Greenham, Anoop Dhoot, Ji-Seon Kim, Craig Murphy, Ellen Moons, Salvatore Ciná, Jeremy Burroughes, Paiboon Sreearunothai, Laura Herz, and Peter Ho. This work was supported by the UK Engineering and Physical Sciences Research Council (EPSRC). ACM acknowledges the Cambridge Gates Trust for a graduate scholarship. CS acknowledges the EPSRC for an Advanced Research Fellowship.



## References

- 1 T. Ito, H. Shirakawa, and S. Ikeda. Simultaneous polymerization and formation of polyacetylene film on the surface of concentrated soluble ziegler-type catalyst solution. *J. Polym. Sci.: Polym. Chem. Edition*, 12(1):11, 1974.
- 2 H. Shirakawa, T. Ito, and S. Ikeda. Electrical properties of polyacetylene with various cis-trans compositions. *Die Makromolekulare Chemie*, 179(6):1565, 1978.
- 3 J. H. Burroughes, D. D. C. Bradley, A. R. Brown, R. N. Marks, K. Mackay, R. H. Friend, P. L. Burns, and A. B. Holmes. Light-emitting-diodes based on conjugated polymers. *Nature*, 347(6293):539–541, 1990.
- 4 H. Sirringhaus, N. Tessler, and R.H. Friend. Integrated, high-mobility polymer field-effect transistors driving polymer light-emitting diodes. *Synth. Met.*, 102(1-3):857–860, 1999.
- 5 H. Sirringhaus, P.J. Brown, R.H. Friend, M.M. Nielsen, K. Bechgaard, B.M.W. Langeveldvoss, A.J.H. Spiering, R.A.J. Janssen, E.W. Meijer, P. Herwig, and D.M. Deleeuw. Two-dimensional charge transport in self-organized, high-mobility conjugated polymers. *Nature*, 401(6754):685–688, 1999.
- 6 H. Sirringhaus, T. Kawase, R.H. Friend, T. Shimoda, M. Inbasekaran, W. Wu, and E. P. Woo. High-resolution inkjet printing of all-polymer transistor circuits. *Science*, 290:2123–2126, 2000.
- 7 N. Stutzmann, R. H. Friend, and H. Sirringhaus. Self-aligned, vertical-channel, polymer field-effect transistors. *Science*, 299(5614):1881–1884, 2003.
- 8 G. Horowitz. Organic thin film transistors: From theory to real devices. *J. Mater. Res.*, 19(7):1946–1962, 2004.
- 9 R. H. Friend, R. W. Gymer, A. B. Holmes, J. H. Burroughes, R. N. Marks, C. Taliani, D. D. C. Bradley, D. A. Dos Santos, J. L. Bredas, M. Logdlund, and W. R. Salaneck. Electroluminescence in conjugated polymers. *Nature*, 397(6715):121–128, 1999.
- 10 E. Moons. Conjugated polymer blends: linking film morphology to performance of light emitting diodes and photodiodes. *J. Phys.-Condes. Matter*, 14(47):12235–12260, 2002.
- 11 H. Spanggaard and F. C. Krebs. A brief history of the development of organic and polymeric photovoltaics. *Sol. Energy Mater. Sol. Cells*, 83(2–3):125–146, 2004.
- 12 H. Hoppe and N. S. Sariciftci. Organic solar cells: An overview. *J. Mater. Res.*, 19(7):1924–1945, 2004.
- 13 A. C. Morteani, A. S. Dhoot, J. S. Kim, C. Silva, N. C. Greenham, C. Murphy, E. Moons, S. Cina, J. H. Burroughes, and R. H. Friend. Barrier-free electron-hole capture in polymer blend heterojunction light-emitting diodes. *Adv. Mater.*, 15(20):1708–1712, 2003.
- 14 A. C. Morteani, P. Sreearunothai, L. M. Herz, R. H. Friend, and C. Silva. Exciton regeneration at polymeric semiconductor heterojunctions. *Phys. Rev. Lett.*, 92(24):247402, 2004.
- 15 A. C. Morteani, R. H. Friend, and C. Silva. Endothermic exciplex-exciton energy-transfer in a blue-emitting polymeric heterojunction system. *Chem. Phys. Lett.*, 391(1-3):81–84, 2004.
- 16 A. C. Morteani, P. K. H. Ho, R. H. Friend, and C. Silva. Electric field-induced transition from heterojunction to bulk charge recombination in bilayer polymer light-emitting diodes. *Appl. Phys. Lett.*, 86:163501, 2005.
- 17 A. C. Morteani, R. H. Friend, and C. Silva. Exciton trapping at heterojunctions in polymer blends. *J. Chem. Phys.*, Vol 122, art. no 244906 (2005).
- 18 J. J. M. Halls, J. Cornil, D. A. dos Santos, R. Silbey, D. H. Hwang, A. B. Holmes, J. L. Bredas, and R. H. Friend. Charge- and energy-transfer processes at polymer/polymer interfaces: A joint experimental and theoretical study. *Phys. Rev. B*, 60(8):5721–5727, 1999.
- 19 C. W. Tang and S. A. Vanslyke. Organic electroluminescent diodes. *Appl. Phys. Lett.*, 51(12):913–915, 1987.
- 20 M. Berggren, O. Inganäs, G. Gustafsson, J. Rasmussen, M. R. Andersson, T. Hjertberg, and O. Wennerström. Light-emitting-diodes with variable colors from polymer blends. *Nature*, 372(6505):444–446, 1994.

- 21 J. J. M. Halls, C. A. Walsh, N. C. Greenham, E. A. Marseglia, R. H. Friend, S. C. Moratti, and A. B. Holmes. Efficient photodiodes from interpenetrating polymer networks. *Nature*, 376(6540):498–500, 1995.
- 22 G. Yu, J. Gao, J. C. Hummelen, F. Wudl, and A. J. Heeger. Polymer photovoltaic cells - enhanced efficiencies via a network of internal donor-acceptor heterojunctions. *Science*, 270(5243):1789–1791, 1995.
- 23 J. J. M. Halls, A. C. Arias, J. D. MacKenzie, W. S. Wu, M. Inbasekaran, E. P. Woo, and R. H. Friend. Photodiodes based on polyfluorene composites: Influence of morphology. *Adv. Mater.*, 12(7):498, 2000.
- 24 N.J. Turro. *Modern Molecular Photochemistry*. University Science Books, Sausalito, 1991.
- 25 A. Weller. Singlet- and triplet-state exciplexes. In M. Gordon and W.R. Ware, editors, *The Exciplex*, pages 23–38. Academic Press Inc., New York, 1975.
- 26 L. C. Palilis, D. G. Lidzey, M. Redecker, D. D. C. Bradley, M. Inbasekaran, E. P. Woo, and W. W. Wu. High performance blue light-emitting diodes based on conjugated polymer blends. *Synth. Met.*, 121(1-3):1729–1730, 2001.
- 27 A. C. Arias, J. D. MacKenzie, R. Stevenson, J. J. M. Halls, M. Inbasekaran, E. P. Woo, D. Richards, and R. H. Friend. Photovoltaic performance and morphology of polyfluorene blends: A combined microscopic and photovoltaic investigation. *Macromolecules*, 34(17):6005–6013, 2001.
- 28 H. J. Snaith, A. C. Arias, A. C. Morteani, C. Silva, and R. H. Friend. Charge generation kinetics and transport mechanisms in blended polyfluorene photovoltaic devices. *Nano Lett.*, 2(12):1353–1357, 2002.
- 29 L.L. Chua, P.K.H. Ho, H. Sirringhaus, and R.H. Friend. Self-organised bilayer polymer field-effect transistors. *Adv. Mater.*, in press.
- 30 A.Č. Morteani. The electronics and photophysics of polymer heterojunctions, PhD Thesis, University of Cambridge (2004).
- 31 H. Snaith, N. C. Greenham, and R. H. Friend. The origin of collected charge and open-circuit voltage in blended polyfluorene photovoltaic devices. *Adv. Mater.*, submitted.
- 32 H. J. Snaith and R. H. Friend. Morphological dependence of charge generation and transport in blended polyfluorene photovoltaic devices. *Thin Solid Films*, 451-52:567–571, 2004.
- 33 R. Stevenson, A. C. Arias, C. Ramsdale, J. D. MacKenzie, and D. Richards. Raman microscopy determination of phase composition in polyfluorene composites. *Appl. Phys. Lett.*, 79(14):2178–2180, 2001.
- 34 X. Z. Jiang, M. S. Liu, and A. K. Y. Jen. Bright and efficient exciplex emission from light-emitting diodes based on hole-transporting amine derivatives and electron-transporting polyfluorenes. *J. Appl. Phys.*, 91(12):10147–10152, 2002.
- 35 B. J. Schwartz. Conjugated polymers as molecular materials: How chain conformation and film morphology influence energy transfer and interchain interactions. *Annu. Rev. Phys. Chem.*, 54:141–172, 2003.
- 36 T. M. Brown, R. H. Friend, I. S. Millard, D. J. Lacey, T. Butler, J. H. Burroughes, and F. Cacialli. Electronic line-up in light-emitting diodes with alkali-halide/metal cathodes. *J. Appl. Phys.*, 93(10):6159–6172, 2003.
- 37 T. Granlund, L. A. A. Pettersson, M. R. Anderson, and O. Inganäs. Interference phenomenon determines the color in an organic light emitting diode. *J. Appl. Phys.*, 81(12):8097–8104, 1997.
- 38 M. M. Alam and S. A. Jenekhe. Nano-layered heterojunctions of donor and acceptor conjugated polymers of interest in light emitting and photovoltaic devices: Photoinduced electron transfer at polythiophene/polyquinoline interfaces. *J. Phys. Chem. B*, 105(13):2479–2482, 2001.
- 39 X. J. Zhang, D. M. Kale, and S. A. Jenekhe. Electroluminescence of multi-component conjugated polymers. 2. photophysics and enhancement of electroluminescence from blends of polyquinolines. *Macromolecules*, 35(2):382–393, 2002.

- 40 J. F. Wang, Y. Kawabe, S. E. Shaheen, M. M. Morrell, G. E. Jabbour, P. A. Lee, J. Anderson, N. R. Armstrong, B. Kippelen, E. A. Mash, and N. Peyghambarian. Exciplex electroluminescence from organic bilayer devices composed of triphenyldiamine and quinoxaline derivatives. *Adv. Mater.*, 10(3):230, 1998.
- 41 M. Berggren, G. Gustafsson, O. Inganäs, M. R. Andersson, T. Hjertberg, and O. Wennerström. White-light from an electroluminescent diode made from poly[3(4-octylphenyl)-2,2'-bithiophene] and an oxadiazole derivative. *J. Appl. Phys.*, 76(11):7530–7534, 1994.
- 42 D. D. Gebler, Y. Z. Wang, D. K. Fu, M. Swager, and A. J. Epstein. Exciplex emission from bilayers of poly(vinyl carbazole) and pyridine based conjugated copolymers. *J. Chem. Phys.*, 108(18):7842–7848, 1998.
- 43 D. D. Gebler, Y. Z. Wang, D. K. Fu, M. Swager, and A. J. Epstein. Exciplex emission from bilayers of poly(vinyl carbazole) and pyridine based conjugated copolymers. *J. Chem. Phys.*, 108(18):7842–7848, 1998.
- 44 D. D. Gebler, Y. Z. Wang, J. W. Blatchford, S. W. Jessen, D. K. Fu, T. M. Swager, A. G. MacDiarmid, and A. J. Epstein. Exciplex emission in bilayer polymer light-emitting devices. *Appl. Phys. Lett.*, 70(13):1644–1646, 1997.
- 45 J. Kalinowski, M. Cocchi, P. Di Marco, W. Stampor, G. Giro, and V. Fattori. Impact of high electric fields on the charge recombination process in organic light-emitting diodes. *J. Phys. D-Appl. Phys.*, 33(19):2379–2387, 2000.
- 46 N. Ohta, S. Umeuchi, Y. Nishimura, and I. Yamazaki. Electric-field-induced quenching of exciplex fluorescence and photocurrent generation in a mixture of ethylcarbazole and dimethyl terephthalate doped in a pmma polymer film. *J. Phys. Chem. B*, 102(19):3784–3790, 1998.
- 47 G. H. Zhang and J. K. Thomas. Spectroscopic investigation of photoinduced charge separation and recombination in solid polymers. *J. Phys. Chem. A*, 102(28):5465–5475, 1998.
- 48 M. Lor, J. Thielemans, L. Viaene, M. Cotlet, J. Hofkens, T. Weil, C. Hampel, K. Mullen, J. W. Verhoeven, M. Van der Auweraer, and F. C. De Schryver. Photo-induced electron transfer in a rigid first generation triphenylamine core dendrimer substituted with a peryleneimide acceptor. *J. Am. Chem. Soc.*, 124(33):9918–9925, 2002.
- 49 R. Jakubiak, C. J. Collison, W. C. Wan, L. J. Rothberg, and B. R. Hsieh. Aggregation quenching of luminescence in electroluminescent conjugated polymers. *J. Phys. Chem. A*, 103(14):2394–2398, 1999.
- 50 C. Adachi, R. C. Kwong, P. Djurovich, V. Adamovich, M. A. Baldo, M. E. Thompson, and S. R. Forrest. Endothermic energy transfer: A mechanism for generating very efficient high-energy phosphorescent emission in organic materials. *Appl. Phys. Lett.*, 79(13):2082–2084, 2001.
- 51 M. J. Rice and Y. N. Gartstein. Theory of photoinduced charge transfer in a molecularly doped conjugated polymer. *Phys. Rev. B*, 53(16):10764–10770, 1996.
- 52 N. R. Armstrong, R. M. Wightman, and E. M. Gross. Light-emitting electrochemical processes. *Annu. Rev. Phys. Chem.*, 52:391–422, 2001.
- 53 N. C. Greenham and P. A. Bobbert. Two-dimensional electron-hole capture in a disordered hopping system. *Phys. Rev. B*, 68(24):art. no.–245301, 2003.
- 54 B. K. Crone, P. S. Davids, I. H. Campbell, and D. L. Smith. Device model investigation of bilayer organic light emitting diodes. *J. Appl. Phys.*, 87(4):1974–1982, 2000.
- 55 V. I. Arkhipov, E. V. Emelianova, and H. Bassler. Charge carrier transport and recombination at the interface between disordered organic dielectrics. *J. Appl. Phys.*, 90(5):2352–2357, 2001.
- 56 L. J. Johnston, J. C. Scaiano, and T. Wilson. A long-lived triplet exciplex of acetone and durene - absorption-spectrum, energy-transfer, and kinetics. *J. Am. Chem. Soc.*, 109(5):1291–1297, 1987.
- 57 E. C. Lim. Photoassociation in the lowest triplet-state of aromatic molecules - triplet excimers and exciplexes. *Pure Appl. Chem.*, 65(8):1659–1664, 1993.

- 58 J. S. Wilson, A. S. Dhoot, Ajab Seeley, M. S. Khan, A. Kohler, and R. H. Friend. Spin-dependent exciton formation in pi-conjugated compounds. *Nature*, 413(6858):828–831, 2001.
- 59 A. S. Dhoot and N. C. Greenham. Triplet formation in polyfluorene devices. *Adv. Mater.*, 14(24):1834–1837, 2002.
- 60 H. Aziz, Z. D. Popovic, N. X. Hu, A. M. Hor, and G. Xu. Degradation mechanism of small molecule-based organic light-emitting devices. *Science*, 283(5409):1900–1902, 1999.
- 61 P. K. H. Ho. in preparation.
- 62 N. Tessler, N. T. Harrison, D. S. Thomas, and R. H. Friend. Current heating in polymer light emitting diodes. *Appl. Phys. Lett.*, 73(6):732–734, 1998.
- 63 C. J. Brabec, N. S. Sariciftci, and J. C. Hummelen. Plastic solar cells. *Adv. Func. Mater.*, 11(1):15–26, 2001.
- 64 Y. Cao, I. D. Parker, G. Yu, C. Zhang, and A. J. Heeger. Improved quantum efficiency for electroluminescence in semiconducting polymers. *Nature*, 397(6718):414–417, 1999.
- 65 G. R. Hayes, I. D. W. Samuel, and R. T. Phillips. Exciton dynamics in electroluminescent polymers studied by femtosecond time-resolved photoluminescence spectroscopy. *Phys. Rev. B*, 52(16):11569–11572, 1995.
- 66 T. Virgili, G. Cerullo, L. Luer, G. Lanzani, C. Gadermaier, and D. D. C. Bradley. Understanding fundamental processes in poly(9,9-dioctylfluorene) light-emitting diodes via ultrafast electric-field-assisted pump-probe spectroscopy. *Phys. Rev. Lett.*, 90(24):art. no.–247402, 2003.
- 67 M. Yokoyama, Y. Endo, A. Matsubara, and H. Mikawa. Mechanism of extrinsic carrier photogeneration in poly-n-vinylcarbazole. ii. quenching of exciplex fluorescence by electric field. *J. Chem. Phys.*, 75(6):3006–11, 1981.
- 68 M. W. Wu and E. M. Conwell. Theory of photoinduced charge transfer in weakly coupled donor-acceptor conjugated polymers: application to an meh-ppv : Cn-ppv pair. *Chem. Phys.*, 227(1-2):11–17, 1998.
- 69 N. Ohta. Electric field effects on photochemical dynamics in solid films. *Bull. Chem. Soc. Jpn.*, 75(8):1637–1655, 2002.
- 70 V. I. Arkhipov, P. Heremans, and H. Bassler. Why is exciton dissociation so efficient at the interface between a conjugated polymer and an electron acceptor? *Appl. Phys. Lett.*, 82(25):4605–4607, 2003.
- 71 V. R. Nikitenko, D. Hertel, and H. Bassler. Dispersive geminate recombination in a conjugated polymer. *Chem. Phys. Lett.*, 348(1-2):89–94, 2001.
- 72 L. Onsager. Initial recombination of ions. *Phys. Rev.*, 54:554, 1938.
- 73 M. Pope and C. E. Swenberg. *Electronic Processes in Organic Crystals and Polymers*. Oxford University Press, 2nd edition, 1999.
- 74 C. M. Ramsdale and N. C. Greenham. Ellipsometric determination of anisotropic optical constants in electroluminescent conjugated polymers. *Adv. Mater.*, 14(3):212, 2002.
- 75 C.M. Ramsdale and N.C. Greenham. The optical constants of emitter and electrode materials in polymer light-emitting diodes. *J. Phys. D., Appl. Phys.*, 36(4):L29–L34, 2002.
- 76 T. Ford. personal communication.
- 77 M. Mizoguchi and N. Ohta. Fluorescence of an electron donor-acceptor system in a polymer film under the simultaneous application of electric field and magnetic field. *Chem. Phys. Lett.*, 372(1–2):66–72, 2003.
- 78 V. S. Gladkikh, A. I. Burshtein, G. Angulo, and G. Grampp. Quantum yields of singlet and triplet recombination products of singlet radical ion pairs. *Phys. Chem. Chem. Phys.*, 5(12):2581–2588, 2003.
- 79 A. I. Burshtein and A. Y. Sivachenko. Photochemical accumulation and recombination of ion pairs undergoing the singlet-triplet conversion. *Chem. Phys.*, 235(1–3):257–266, 1998.
- 80 A. I. Burshtein and E. Krissinel. Photochemical charge separation suppressed by spin conversion. *J. Phys. Chem. A*, 102(5):816–824, 1998.
- 81 A. I. Burshtein and E. Krissinel. Photo-separation of ion radicals following exciplex formation and spin conversion. *J. Phys. Chem. A*, 102(39):7541–7548, 1998.
- 82 A. I. Burshtein and K. L. Ivanov. The crucial role of triplets in photoinduced charge transfer and separation. *Phys. Chem. Chem. Phys.*, 4(17):4115–4125, 2002.

- 83 A. I. Burshtein. Diffusional and spin-dependent theory of chemiluminescence resulting from backward electron transfer. *Chem. Phys.*, 289(2-3):251–261, 2003.
- 84 A. I. Burshtein. Reversible charge separation through exciplex formation. *J. Chem. Phys.*, 117(16):7640–7648, 2002.
- 85 A. I. Burshtein. Unified theory of photochemical charge separation. volume 114 of *Advances in Chemical Physics*, pages 419–587. John Wiley Sons Inc, New York, 2000.
- 86 C. Im, W. Tian, H. Bassler, A. Fechtenkotter, M. D. Watson, and K. Mullen. Photoconduction in organic donor-acceptor systems. *Journal of Chemical Physics*, 119(7):3952–7, 2003.
- 87 P. Peumans and S. R. Forrest. Separation of geminate charge pairs at donor-acceptor interfaces in disordered solids. *Chemical Physics Letters*, 398:27–31, 2004.
- 88 T. Offermans, S.C.J. Meskers, and R. A. J. Janssen. Monte-Carlo simulations of geminate electronhole pair dissociation in a molecular heterojunction: a two-step dissociation mechanism. *Chemical Physics*, in press.
- 89 V. D. Mihailetschi, L. J. A. Koster, J. C. Hummelen, and P. W. M. Blom. Photocurrent generation in polymer-fullerene bulk heterojunctions. *Physical Review Letters*, 93(21):216601, 2004.
- 90 A. C. Arias, N. Corcoran, M. Banach, R. H. Friend, J. D. MacKenzie, and W. T. S. Huck. Vertically segregated polymer-blend photovoltaic thin-film structures through surface-mediated solution processing. *Applied Physics Letters*, 80(10):1695–1697, 2002.
- 91 R. G. Della Valle, E. Venuti, L. Farina, A. Brillante, M. Masino, and A. Girlando. Intramolecular and low-frequency intermolecular vibrations of pentacene polymorphs as a function of temperature. *Journal of Physical Chemistry B*, 108(6):1822–1826, 2004.

## 3

**Photophysics of Luminescent Conjugated Polymers***D. Hertel and H. Bässler*

## 3.1

**Introduction**

There is currently an intense endeavor to exploit the unique properties of conjugated polymers for the development of optoelectronic devices like light-emitting diodes, photovoltaic cells and field effect transistors. This requires detailed knowledge of their photophysical properties. In the beginning it had been proposed that the properties of conjugated polymers resemble those of a one-dimensional semiconductor implying that electron–electron interaction is negligible relative to electron–lattice interaction and, concomitantly, the elementary optical excitations are electronically decoupled polarons [1]. This would have had a serious negative impact on their electroluminescent properties because an efficiently screened coulombic potential would have reduced the cross section for electron–hole recombination greatly. Recall that in inorganic light-emitting diodes (LEDs) the lower cross section as compared with organic LEDs is overcompensated by the higher charge carrier concentration and by their higher mobility. The observation that electroluminescence from organic materials is, on the contrary, efficient and controlled by Langevin-type electron–hole recombination [2] like in classic molecular solids has been a strong argument against the above notion [3, 4]. This implies that a free electron–hole pair recombines whenever its mutual distance is comparable to the coulombic capture radius,  $r_c = e^2/4\pi\epsilon\epsilon_0kT$ , where  $\epsilon_0$  is the dielectric permittivity and  $\epsilon$  is the relative dielectric constant. There is independent and compelling evidence that conjugated polymers do not behave fundamentally different from other organic materials. This includes (i) the recognition of strong electron–electron correlation in polyenes and polyacetylene [5, 6], (ii) the large energy gap between the first singlet and triplet states [7, 8, 9], (iii) the large exciton binding energy inferred by fluorescence quenching studies [10, 11], electoreflexion [12] as well as analytic molecular theory [13, 14], (iv) the absorption spectra of optically and chemically generated charge carriers being those of radical ions [15] rather than reflecting transitions among polaron and band states [16] and (v) both stationary [17] and time-resolved fluorescence [18, 19] and, importantly, phosphorescence spectroscopy [20].

*Organic Light Emitting Devices. Synthesis, Properties and Applications.*

Edited by Klaus Müllen and Ullrich Scherf

Copyright © 2006 WILEY-VCH Verlag GmbH &amp; Co. KGaA, Weinheim

ISBN 3-527-31218-8

The intention of this article is to emphasize current aspects of the photophysics of emissive conjugated polymers paying particular attention to the spectroscopy of singlet and triplet excitations, their motion and their dissociation into coulombically bound electron-hole pairs and free charge carriers. Any discussion of physics of devices such as light-emitting diodes, photovoltaic cells and field effect transistors is outside the scope of this chapter and will be dealt with in different chapters of this book.

## 3.2

### Spectroscopy of Singlet States

#### 3.2.1

##### Conventional CW Spectroscopy

Upon optical excitation of a molecule in the UV/VIS spectral range an electron is promoted from the highest occupied molecular orbital (HOMO) to either the lowest unoccupied molecular orbital (LUMO) or to a higher lying empty orbital. Correspondingly the charge distribution of the molecule and, concomitantly, the molecular forces will change. As a response to that charge redistribution the molecular skeleton will vibrate and relax into a new equilibrium configuration. In accordance with the Franck-Condon principle this will give rise to vibronic replica in absorption as well as in emission spectra unless there is a competitive fast non-radiative decay channel for the excitation. In case of coupling to a single harmonic oscillator of reduced mass  $M$  and angular frequency  $\omega$  the strength of coupling is described by the Huang-Rhys factor  $S$

$$S = \frac{M\omega}{2\hbar}(\Delta Q)^2 \quad (3.1)$$

where  $\Delta Q$  is the displacement of the minima of the potential curve along the configurational coordinate upon electronic excitation [21]. Note that if there was no displacement of the potential energy curves due to the readjustment of the bond length, only a single absorption and emission line – corresponding to the  $S_1 \leftrightarrow S_0$  0–0 transition – would be allowed for reasons of orthogonality of the wavefunctions. In the harmonic approximation the intensity of the pure electronic  $S_1 \leftrightarrow S_0$  0–0 transition and the  $n$ -th vibronic satellite is

$$I_n = \frac{e^{-S}}{n!} S^n. \quad (3.2)$$

The value  $S$  can be inferred either from the fractional intensity of the 0–0 transition

$$I_{0-0} / \sum_{n=0}^{\infty} I_{n \leftarrow 0} = e^{-S} \quad (3.3)$$

or from

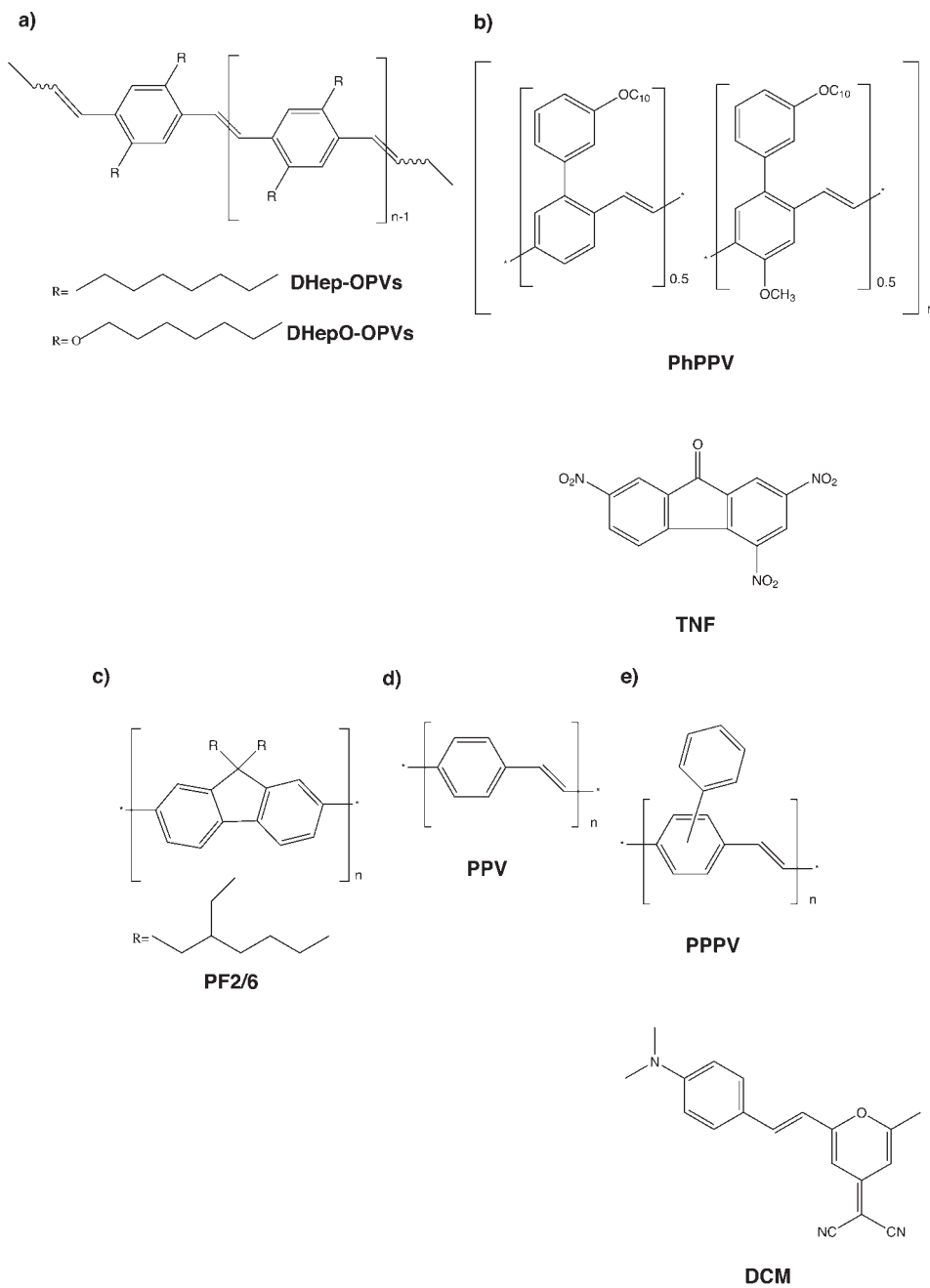
$$I_{1\leftarrow 0}/I_{0\leftarrow 0} = S \quad (3.4)$$

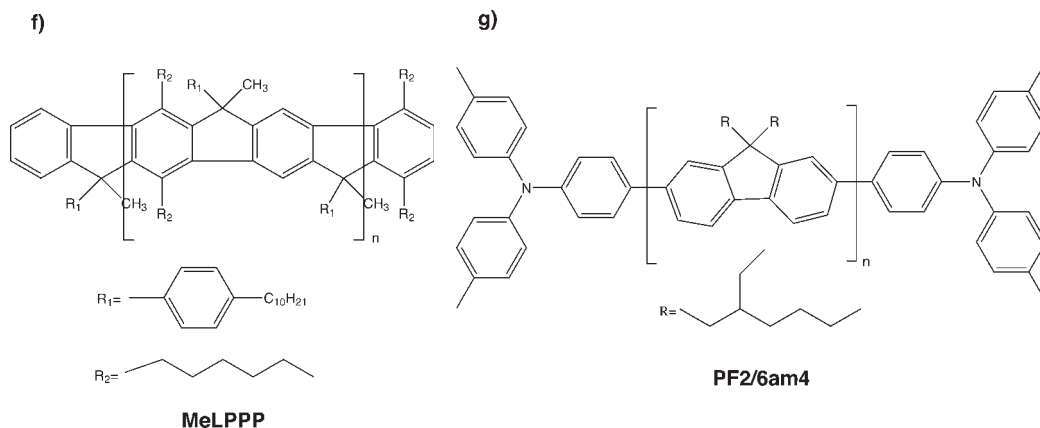
In reality there are several molecular vibrations that can couple to an electronic transition although the basic phenomenology is retained, namely the resonant character of the  $S_1\leftarrow S_0$  0–0 transition and the mirror symmetry of the vibronic satellites. In case of a  $\pi\rightarrow\pi^*$  transition the dominant vibrational modes are those of the polymer backbone, notably of the phenyl ring. An example is the absorption and fluorescence of  $\pi$ -conjugated molecules, such as tetracene, in the gas phase [22]. In fluid solution there is interaction between the transient dipole of the molecule with the permanent and induced dipoles of the solvent. It gives rise to (i) a bathochromic shift of the spectra, (ii) a Stokes shift between the 0–0 transition in absorption and emission that reflects the readjustment of the molecules in the solvent cage, and (iii) some spectral broadening. Employing line narrowing techniques, such as site-selective or hole-burning spectroscopy to chromophores isolated in frozen solution both the resonant and the narrow line character of the vibronic transitions can be recovered [23, 24].

However, the UV/VIS spectroscopy of conjugated polymers can, and often does, differ from that of conventional  $\pi$ -bonded small molecules, e. g. what simple molecular spectroscopy would predict. It turns out that most  $\pi$ -conjugated polymers, exceptions being unsubstituted polyacetylene and polydiacetylene, fluoresce. The fluorescence spectra of polymer films consist of a moderately broad  $S_0\leftarrow S_1$  0–0 transition accompanied by vibronic satellites. Different from small organic molecules they can feature an appreciable Stokes shift between absorption and emission. Often absorption spectra are not mirror symmetric with fluorescence spectra and show little if any vibronic splitting. Reasons are (i) major relaxation of the skeleton of an excited polymer chain can give rise to an concomitant change of the electronic excitation, (ii) intra and interchain energy transfer to intrinsic and extrinsic chromophores, and (iii) specific interchain coupling. Those features will be discussed below in an exemplary way employing a homologous series of oligomers of alkyl- and alkoxy-substituted phenylenevinylenes as test objects.

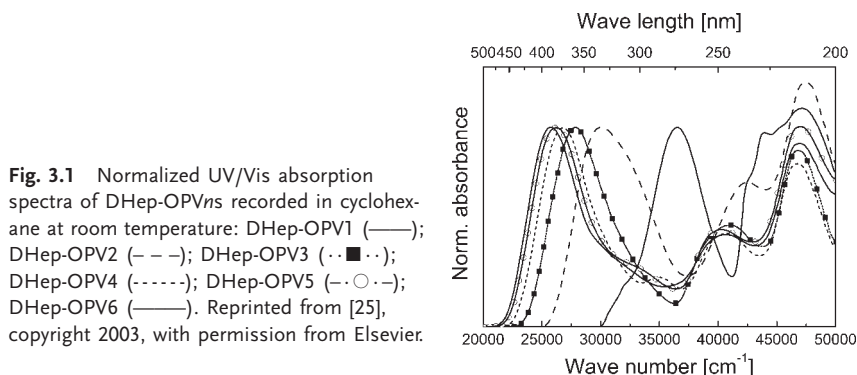
The compounds (see Scheme 3.1) were monodisperse all-trans oligomers 2,5-diheptyl-p-divinylbenzene, DHep-OPV $_n$  with  $n = 1$ –6 being the number of aromatic rings [25], and 2,5-diheptyloxy-p-divinylbenzene DHepO-OPV $_n$  with  $n = 1$ –7 [26], synthesized metathetically. They were investigated in 2-methyltetrahydrofuran (MTHF) or cyclohexane solution at either ambient temperature, matrix isolated in a MTHF glass at 10 K and 80 K, and as spin-coated thin films on quartz substrates, involving absorption and conventional fluorescence as well as site-selective fluorescence spectroscopy. Figure 3.1 shows that in cyclohexane solution at 295 K the low energy  $S_1\leftarrow S_0$  transition of DHep-OPV $_n$  in absorption shifts to lower energies as the chain length increases but vibronic fine structure is absent. Some vibronic structure appears as a MTHF solution of DHep-OPV3 is cooled down from 290 K to 80 K (Fig. 3.2). Low-temperature (80 K) absorption of DHep-OPV3 and DHep-OPV6 in MTHF and as spin-coated films at 295 K are







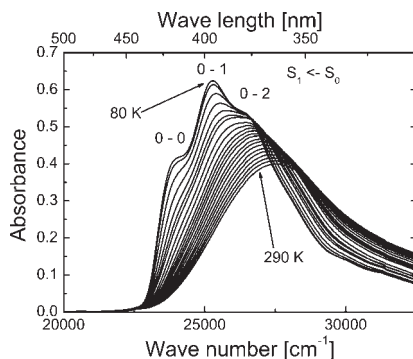
**Scheme 3.1** Chemical structures of compounds described in this chapter.



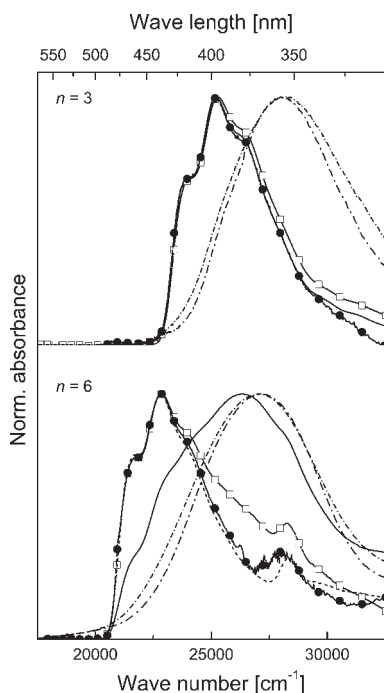
**Fig. 3.1** Normalized UV/Vis absorption spectra of DHep-OPVns recorded in cyclohexane at room temperature: DHep-OPV1 (—); DHep-OPV2 (---); DHep-OPV3 (··■··); DHep-OPV4 (-·-·-); DHep-OPV5 (-·○·-); DHep-OPV6 (—). Reprinted from [25], copyright 2003, with permission from Elsevier.

depicted in Fig. 3.3. The spectra in glassy matrix reveal a weak vibronic fine structure, albeit with system specific dependence on concentration, temperature and chain length. While spectra of DHep-OPV3 are independent of concentration, a hypsochromic shift in the DHep-OPV6 spectra is noted at a concentration of  $c = 10^{-5}$  mol/L. This trend continues at higher concentrations. In the films vibronic structure is completely lost, independent of temperature. On the other hand, conventionally recorded fluorescence spectra (not shown) do feature well-resolved vibronic structures.

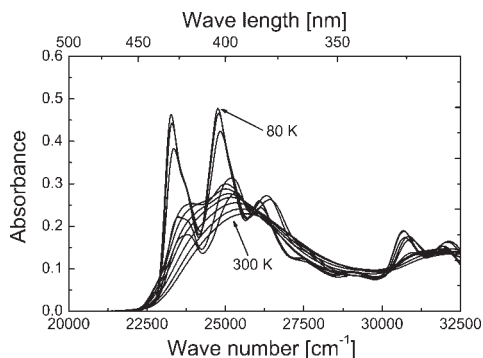
Figure 3.4 shows the absorption spectra of the alkoxy-derivative of DHep-OPV2 recorded in MTHF solution at different temperatures. While the general trend is similar to that of the alkyl-derivative (Fig. 3.2) the vibronic band splitting at lower temperatures is more pronounced. This is confirmed by Fig. 3.5 which indicates that, except for the DHepO-OPV1, there is a distinct dependence of the absorption spectra on concentration. At higher concentration the intensity of the  $S_1 \leftarrow S_0$  0-0 transition is diminished in favor of the higher-energy components.



**Fig. 3.2** UV/Vis absorption spectra of DHep-OPV3 recorded in 2MeTHF at different temperatures starting at 290 K in 10 K steps down to 80 K ( $c = 4 \times 10^{-5} \text{ mol} \cdot \text{L}^{-1}$ ). Reprinted from [25], copyright 2003, with permission from Elsevier.

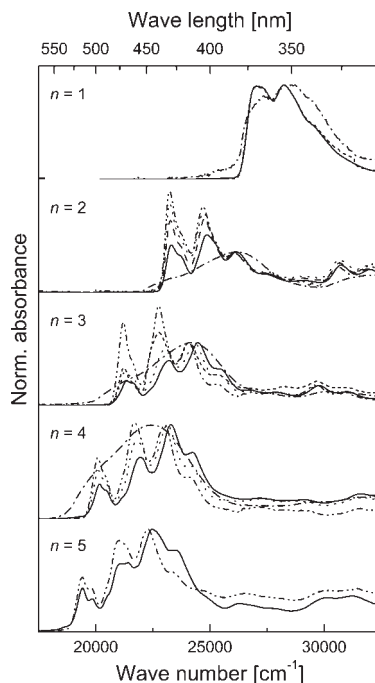


**Fig. 3.3** UV/Vis absorption spectra of DHep-OPV3 and DHep-OPV6 recorded in 2MeTHF at 80 K:  
 $c = 5 \times 10^{-7} \text{ mol} \cdot \text{L}^{-1}$  ( $-\bullet-\bullet-$ );  
 $c = 10^{-6} \text{ mol} \cdot \text{L}^{-1}$  ( $-\cdot-\cdot-$ );  
 $c = 10^{-5} \text{ mol} \cdot \text{L}^{-1}$  ( $\cdots\square\cdots$ );  
 $c = 4 \times 10^{-5} \text{ mol} \cdot \text{L}^{-1}$  ( $- - - -$ );  
 $c = 10^{-4} \text{ mol} \cdot \text{L}^{-1}$  ( $-\cdot-\cdot-$ ) and as thin layers at room temperature ( $-\cdot-\cdot-\cdot-$ ) as well as at 80 K ( $-\cdot-\cdot-\cdot-$ ). The spectra were normalized to the absorption maximum. Reprinted from [25], copyright 2003, with permission from Elsevier.



**Fig. 3.4** UV/Vis absorption spectra of DHepO-OPV2 recorded in 2MeTHF at different temperatures starting at 300 K in 20 K steps down to 80 K ( $c = 4 \times 10^{-5} \text{ mol} \cdot \text{L}^{-1}$ ). Reprinted from [26], copyright 2003, with permission from Elsevier.

**Fig. 3.5** Normalized UV/Vis absorption spectra of DHepO-OPVns recorded at 80 K in 2MeTHF ( $c = 5 \times 10^{-7} \text{ mol} \cdot \text{L}^{-1}$  (— · — · —);  $c = 10^{-6} \text{ mol} \cdot \text{L}^{-1}$  (-----);  $c = 10^{-5} \text{ mol} \cdot \text{L}^{-1}$  (·····);  $c = 4 \times 10^{-5} \text{ mol} \cdot \text{L}^{-1}$  (---);  $c = 10^{-4} \text{ mol} \cdot \text{L}^{-1}$  (—)) and as thin layer (— · — · —). Reprinted from [26], copyright 2003, with permission from Elsevier.



A key element for analyzing those observations is the dependence of the  $S_1 \leftarrow S_0$  transition as a function of chain length. It bears heavily on the particle in a box concept and predicts a linear dependence of the  $S_1 \leftrightarrow S_0$  0–0 transition on reciprocal chain length, or, equivalently, the number of repeat units of the chain. When extrapolating the predicted linear portion to  $n \rightarrow \infty$  one has to recognize, however, that the limiting value of that transition energy is finite because of bond alternation. The fact that the measured transition energy in a long polymer exceeds that hypothetical  $E_{n \rightarrow \infty}$  value has been considered as a signature of the effective chain being not infinite. Based upon an experimentally determined reciprocal energy–chain length relation the so-called effective conjugation length can be estimated. It is often considered to be limited by topological chain defects, such as cis–trans transformations or, more generally, the spatial extension of a chain deformation. A recent theoretical approach by Rissler [27] employing the density-matrix renormalization group theory, confirms that chain defects do lead to a linear dependence between the transition energy versus reciprocal distance between the defects on a chain. However, contrary to what the simple particle in the box model would predict, in the limit of weak or vanishing disorder the transition energy extrapolates to  $1/n^2$  rather than  $1/n$  as  $n$  extrapolates to infinity. This result is particularly important for weakly disordered polymers, such as the ladder-type poly(phenylene)s in which covalent bridging among the repeat units prohibits the formation of major topological defects. In this context it is important to recognize that even within a defect-controlled chain element the electron and hole compri-

ing an optical excitation do not move independently but in a correlated fashion. It is important to recognize that the excitation is a coulombically bound electron-hole pair with a typical 1 nm root-mean-square pair separation [28], i.e. much less than the effective conjugation length. Immediately after its generation an excitation suffers intrachain scattering as well as scattering on defects. This conclusion comes from independent theoretical approaches [14, 28] and from electroreflection spectroscopy [29].

The change of the absorption spectra of both DHep-OPVn as well as DHepO-OPVn in MTHF solution at different temperatures is a signature of temperature-dependent dynamic disorder. The loss of vibronic structure of the spectra can be explained in terms of twisting vibrations along the oligomer chain. It reduces the effective conjugation length to a value below the oligomer length in a statistical way and gives rise to a hypsochromic shift of the absorption spectra and any vibronic splitting is smeared out. At lower temperatures, torsional motion along the chain is frozen and, concomitantly, the effective conjugation length increases. In a film of oligomers or a polymer film this kind of disorder is static rather than dynamic.

Aggregation can also have a major effect on the spectroscopy of oligomers and polymers. It is known that aggregates of alkoxy-substituted PPVs such as poly(2-methoxy-5-2'-ethylhexyloxy-1,4-phenylene vinylene), or MEH-PPV play an important role in solution [30, 31, 32, 33, 34]. Cornil et al. [35] calculated the energy changes of complexes of PV-oligomers on top of one another with different separation distances. Below a critical distance of about 0.7 nm the molecular orbitals of a stilbene dimer start to delocalize over the two chains. As a result, excited-state splitting becomes important, i.e. the absorption is shifted to higher energies whereas the emission is red-shifted. Turning from the two-ring system to the higher oligomers the critical distance roughly corresponds to the oligomer length and saturates at around 14 nm. Therefore, the absorption spectra presented in Fig. 3.3 can be explained as a superposition of the spectrum of the isolated chains and the aggregated complexes.

Another important hint can be taken from the spectra of spin-coated layers. These exhibit a blue-shift compared with the spectra of isolated chains in solution, also. The analysis of the data obtained using grazing incidence X-ray diffraction (GIXD) techniques resulted in a morphology where the oligomers are assembled in a fashion as described above, starting with DHepO-OPV2 [36]. This is another important indication that in MTHF solution at low temperatures aggregation effects become important. In addition, the weak temperature dependence of the absorption maximum suggests a planar geometry, due to aggregation, even at room temperature. The tendency to form aggregates is strongly dependent on chain length. This is a result of the better polarizability of the longer oligomers and the larger critical distance.

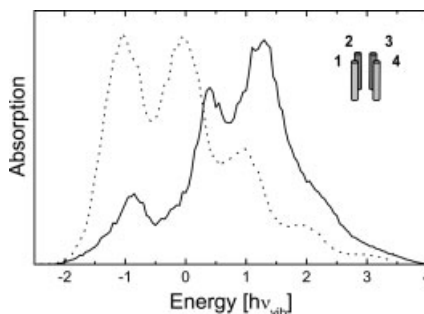
Theoretical models have been developed to describe the effect of interchromophoric coupling on the properties of the excited state. They have been used to describe the peculiar changes in band shape occurring upon aggregation of pseudo isocyanine dye molecules (formation of J- or Scheibe-aggregates) [37] and more

recently aggregates of  $\pi$ -conjugated oligomers. In the latter case both changes in absorption [38, 39, 40] and emission bands [41, 42, 43] were analyzed.

The main problem in the description of the changes in absorption and/or emission spectra of coupled chromophores is in the application of the Born–Oppenheimer (BO) approximation. Two limiting cases can be distinguished in which the BO approximation applies with certainty. One case is where the coupling between the chromophores is very weak. In this case, the BO can be applied to the individual chromophores and the coupling can be treated as a perturbation. The other extreme is where the interaction is so strong that the BO approximation can be applied to the aggregates as a whole. This means that the assembly of chromophores is treated as a supermolecule. In this case, the coupling between the excitation and the nuclear motion that gives rise to the Franck–Condon progression in the spectra of the isolated monomers, is treated as a perturbation. The intermediate case is not straightforward and can be treated by numerically diagonalizing a model Hamiltonian that includes both effects of interchromophoric coupling and the interaction between nuclear motion and the excitation. This method was employed to analyze the absorption spectra of DHepO-OPVn (see Fig. 3.5).

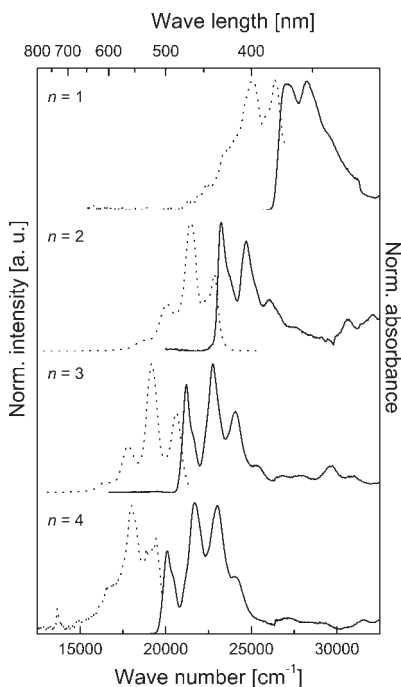
In these calculations, it was assumed that only one vibrational mode couples with the electronic excitation in the isolated chromophores. The Huang–Rhys parameter  $S$  for the isolated chromophores was taken to be 1. Furthermore, only clusters of four chromophores are studied. The transition dipole moments of the oligomers were aligned parallel. To include effects of disorder the zero excitation energies of these chromophores are taken at random from a Gaussian distribution. Also the matrix elements describing the through-space electromagnetic coupling between the chromophores were taken from a Gaussian distribution. The chromophores were arranged with their center positioned on the corners of a square and the transition dipole moments perpendicular to this fictitious square. To obtain a simulation of the absorption band shape the results of a thousand diagonalizations are averaged. The results are shown in Fig. 3.6. Here the dotted line shows results for uncoupled, isolated chromophores while the solid line shows the result for the quartet of coupled chromophores. As can be seen, the intensity of the 0–0 transition is strongly reduced by the interaction. For the cluster a new maximum in the absorption appears on the blue side of the monomer absorption band. This is in qualitative agreement with the expectation

**Fig. 3.6** Simulated UV/Vis absorption spectra of isolated (.....) and aggregated (——) DHepO-OPV3. Reprinted from [26], copyright 2003, with permission from Elsevier.



for an *H*-aggregate where the absorption maximum should show a blue-shift. For the cluster the simulated absorption spectrum still seems to have some residual vibronic fine structure although the energy separation between what appears to be the vibronic bands is no longer constant. Qualitatively, the reduction of the 0–0 band, the appearance of a new maximum at the blue side and the irregular spacing of the vibronic features observed for  $c = 10^{-4}$  mol/L can all be reproduced by the simulations. In reality, the experimental spectrum for  $c = 10^{-4}$  mol/L will, of course, always be a superposition of the spectra of aggregated and uncomplexed, free chromophores. However, since at  $c = 10^{-4}$  mol/L the contribution from unaggregated chromophores is rather small. This justifies the comparison between experimental and simulated band shapes.

Interestingly, 80 K fluorescence spectra of DHepO-OPV $n$ ,  $n = 1-4$ , (Fig. 3.7) are not mirror symmetric with absorption. At a temperature of 80 K, the 0–1 emission feature governs the spectrum for all investigated oligomers starting with DHepO-OPV2. This can be attributed to the superposition of emissions from isolated chains and aggregates. This conclusion is supported by investigations of Peeters et al. [44] on branched and therefore sterically hindered alkoxy side chains in a glassy MTHF matrix showing that, indeed the  $S_1 \leftarrow S_0$  0–0 transition is the dominant one. A similar behavior was found for the DHepO-OPV $n$ s at room temperature as described above. It is obvious [45, 36] that extracting the Huang–Rhys factor from spectra of a sample in which both nonaggregated and aggregated species coexist must give incorrect results.



**Fig. 3.7** UV/Vis absorption ( $c = 5 \times 10^{-7}$  mol  $\cdot$  L $^{-1}$ ; (—)) and photoluminescence ( $c = 10^{-6}$  mol  $\cdot$  L $^{-1}$ ; (·····)) spectra of DHepO-OPV $n$ s recorded in 2MeTHF at 80 K. The spectra were normalized to the maximum of the  $S_1 \leftarrow S_0$  absorption and  $S_1 \rightarrow S_0$  emission, respectively. Reprinted from [26], copyright 2003, with permission from Elsevier.

The tendency to form aggregates is strongly dependent on chain length and molecular constitution and, in solution, on concentration. By comparing the spectral features of DHep-OPVn [25] and DHepO-OPVn [26] indicates that the higher electron density caused by the electron-donating alkoxy group favors a more planar geometry and, concomitantly, reduced sterical hindrance over the alkyl substituted oligomers. At the same time improved ordering reduces the inhomogeneous width of the vibronic bands. However, one has to be cautious when pursuing this argument any further. Because of covalent bridging the ladder-type poly(phenylene)s (LPPPs) are the best ordered of all noncrystalline  $\pi$ -conjugated polymers. Nevertheless, this tendency to form aggregates is very weak as evidenced by the narrow vibronic bands in absorption and the pronounced  $S_1 \leftarrow S_0$  0–0 transition. The likely reason is random packing of the alkyl substituents [46].

The better-known type of aggregates are those that give rise to excimer emission. The steric requirement is a sandwich-like arrangement of the planes of the interacting elongated molecules in which the transition dipole moments are aligned parallel. When one of the molecules of the pair is excited to the  $S_1$  state the excitation oscillates within the pair. This gives rise to excited-state splitting into a parity-forbidden lower state and an upper state that carries most of the oscillator strength. Because of the attractive interaction in the excited state the pair relaxes into a new equilibrium configuration with reduced intermolecular spacing. It is repulsive in the electronic ground state. For this reason fluorescence emission becomes allowed only by vibronic coupling. Its spectrum is a featureless broad band red-shifted relative to absorption and the fluorescence lifetime is on the order of 100 ns. Textbook examples are the incipient molecular pairs in pyrene and perylene crystals [47] and the accidental parallel arrangement of the carbazole unit of adjacent polycarbazole chains [48, 49]. In the fluorescence spectra of conjugated polymers there is an occasional red-shifted component with little or no spectrally resolved vibronic structure featuring a lifetime extending into the ns range [50, 51, 52]. It can, but does not have to be assigned to emission from structural traps with excimer characteristics, i. e. whose structure is monomer-like in absorption but relaxes into a more strongly bound excimer state upon excitation. In a noncrystalline polymer structure it is conceivable that there are aggregates that are only weakly stabilized in the ground state but can further relax to a conformation with partial excimer character. An example is the site-selectively excited defect emission in (*not methylated*) LPPP [46]. Replacement of the hydrogen atoms by a methyl group more or less prevents this kind of aggregation. It seems plausible that in an amorphous polymer structure there is a variety of local structures in which the intermolecular interaction exceeds the average values and, accordingly, can act as traps for a singlet exciton. Depending on how well the conditions for genuine excimer formation are met, those aggregates will feature red-shifted fluorescence spectra ranging between monomer-like and excimer-like in character. Apart from contributing to the red portion of their intrinsic fluorescence spectra their emission is longer lived as compared to the lifetime of an isolated chromophore. The reason is that the oscillator strength and, concomitantly, their lifetime depend on the vectorial addition of the individual transition dipoles. De-



pending on the degree of parallelity of the transition dipole moments of the chromophores comprising the pair the lifetime of the excited state of the pair increases because the net transition dipole moments of the pair state decreases. Since, on the other hand, nonradiative decay of the  $S_1$  state is not affected by aggregation this lowers the fluorescence efficiency. Obviously, this is a detrimental effect in OLEDs. One way to avoid this situation is to choose polymer structures or appropriate polymer substituents that prevent the formation of incipient dimers. Site-selective fluorescence spectroscopy (see Section 3.2.2) is an experimental tool to distinguish whether an aggregate is more dimer- or excimer-like. In the case of dimers, the lowest excited state causes a finite oscillator strength in absorption and is red-shifted relative to the intrinsic absorption [46], while genuine excimer emission is generated via energy transfer among the nonaggregated chain segments. It is worth mentioning that defects that act as traps for singlets do so regarding charge carriers, too, because both HOMO and LUMO in the defect are off-set from those of the parent chromophore.

On the other hand, the red-shifted emission from conjugated polymers can originate also from chemically different moieties such as keto defects [53] created via accidental photochemical degradation or deliberate exciplex formation at the internal interface between conjugated polymers [54, 55, 56].

### 3.2.2

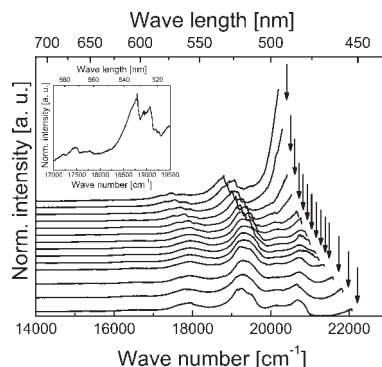
#### Site-selective Fluorescence (SSF) Spectroscopy

A generic feature of disordered systems, such as neat molecular glasses, matrix isolated molecules and polymers, is that any energy level is inhomogeneously broadened because of random packing and, accordingly, spatially random interactions. Because those interactions depend on a large number of internal coordinates the profiles of optical spectra are Gaussians [57] with a variance  $\sigma$  typically  $500\text{--}1000\text{ cm}^{-1}$  ( $\sim 60\text{--}120\text{ meV}$ ). To remove this kind of inhomogeneity requires the application of site-selective techniques [17, 23, 58]. They involve the use of a spectrally narrow laser that allows excitation of those chromophores from amongst a large ensemble contributing to an inhomogeneously broadened absorption. Only those chromophores whose transition energy is accidentally resonant with the laser are excited and, provided that excitation is into the  $S_1 \leftarrow S_0$  0–0 line, the resulting emission is homogeneously broadened and provides information on the true molecular Stokes shift, i.e. on any relaxation that might occur upon exciting a chromophore and coupling to energetically lower-lying phonons. Site-selectivity is eroded if one excites into higher-lying vibronic bands of the  $S_1 \leftarrow S_0$  transition and if energy transfer to lower-lying states can occur. In polymers that energy transfer can occur between different chromophores of a single chain or between adjacent chains. To identify whether or not site selectivity has been attained one scans the laser across the inhomogeneously broadened  $S_1 \leftarrow S_0$  0–0 transition towards lower energies and monitors the energy at which the emission spectrum shifts linearly with the laser energy. Unfortunately, stray light effects will obscure the  $S_1 \rightarrow S_0$  0–0 transition, if it is resonant with the

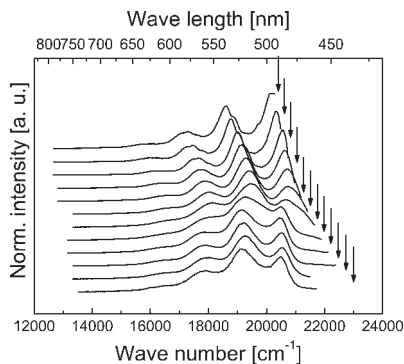
excitation. Probing vibronic emission lines, e.g. the  $S_1 \rightarrow S_0$  0–1 line avoids this problem.

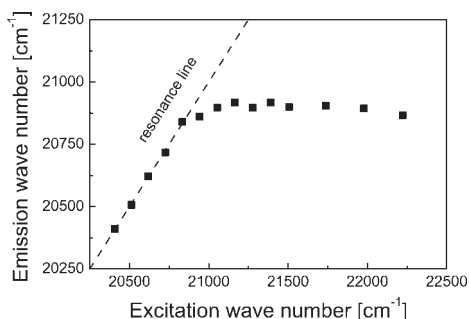
SSF spectroscopy was applied to alkyl- as well as alkoxy-substituted OPV oligomers (see Section 3.2.1) matrix isolated in a MTHF glass [25, 26]. Spectra recorded as a function of the excitation energy are presented in Figs. 3.8 and 3.9. As expected, above a critical energy the fluorescence spectra are independent of excitation energy and inhomogeneously broadened. Below this energy they become narrower and shift linearly with excitation energy (Figs. 3.10 and 3.11). Interestingly, for DHepO-OPV3 (Fig. 3.8) sharp zero-phonon features are observed and the  $S_1 \rightarrow S_0$  0–0 transition, inferred by adding the vibrational quantum energy of a relevant vibronic line, is resonant with the laser [26]. For DHep-OPV6 (Fig. 3.9), where the alkoxy-linking is missing, the SSF spectra reveal some residual line broadening and finite Stokes shift of  $260\text{ cm}^{-1}$  [25]. In principle, a finite Stokes shift can either be a signature of homogeneous coupling of the electronic excitation to a low-energy mode, such as a torsional mode of the chain, or of structural relaxation accompanied with a lowering of the energy of excitation. Since a phonon mode of the oligomer chain should not depend on the substituents the observed Stokes shift in the DHep-OPV6 is likely to be caused by optimizing the chain conformation thereby improving intrachain electronic coupling rather

**Fig. 3.8** A series of fluorescence spectra of DHepO-OPV3 with decreasing excitation energy. The inset depicts the zero-phonon lines, observed for an excitation energy of  $\tilde{\nu}_{\text{exc}} = 20\,410\text{ cm}^{-1}$ . The arrows mark the wave number of the corresponding laser energy. Reprinted from [26], copyright 2003, with permission from Elsevier.

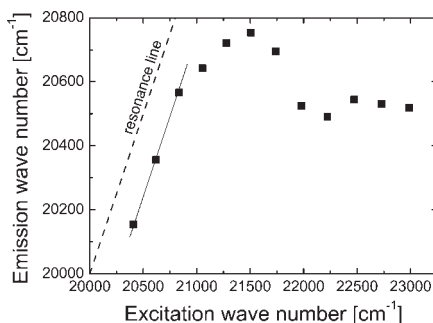


**Fig. 3.9** A series of fluorescence spectra of DHep-OPV6 with decreasing excitation energy ( $c = 10^{-5}\text{ mol} \cdot \text{L}^{-1}$ ). The arrows mark the wave number of the corresponding laser energy. Reprinted from [25], copyright 2003, with permission from Elsevier.





**Fig. 3.10** Wave number of the strongest zero-phonon line (corrected for the laser energy) is plotted versus the excitation wave number of DHepO-OPV3 in 2MeTHF at 10 K ( $c = 10^{-6} \text{ mol} \cdot \text{L}^{-1}$ ). The data (■) are taken from the site-selective fluorescence spectra. The resonance line is also shown. Reprinted from [26], copyright 2003, with permission from Elsevier.



**Fig. 3.11** Wave number of the  $S_1 \rightarrow S_0$  0–0 transition maxima of DHep-OPV6 in 2MeTHF at 10 K as a function of excitation wave number ( $c = 10^{-5} \text{ mol} \cdot \text{L}^{-1}$ ). The data (■) are taken from the site-selective fluorescence spectra. The resonance line is also shown. Reprinted from [25], copyright 2003, with permission from Elsevier.

than by phonon coupling. This type of Stokes shift is inhomogeneous in nature. In the alkoxy-substituted oligomer DHep-OPV3 this effect is absent suggesting the optimal intrachain ordering has been established in the ground state already because of side-chain ordering.

In  $\pi$ -conjugated polymers no zero-phonon lines have been observed in SSF spectra, indicating that there is always some chain relaxation in response to optical excitations [17, 59]. The magnitude of this effect should and, in fact, does depend on the rigidity of the chain. In PPV the residual Stokes shift is on the order of  $100 \text{ cm}^{-1}$ , while in MeLPPP it is  $\sim 20 \text{ cm}^{-1}$  only [21]. In the time domain the former value corresponds to a dephasing on the order of 100 fs as has been verified by experiments on fs-wave-packet fluorescence interferometry on tail states of PPV [60].

Interestingly, there has been a recent report on hole-burning spectra of MeLPPP matrix isolated in a MTHF glass at 4.2 K [61]. Hole burning is another method to remove inhomogeneous line broadening [23, 58]. It rests on the ability of an excited chromophore to undergo a photophysical or photochemical reaction thereby shifting its absorption line to a different spectral position. By this method a spectral hole could be burnt in the tail of the  $S_1 \leftarrow S_0$  0–0 transition of MeLPPP with a maximum linewidth of  $9 \text{ cm}^{-1}$ , i.e. less than the spectral width of the  $S_1 \rightarrow S_0$  0–0 transition inferred from a site-selectively measured fluorescence spectrum, which was the instrumental resolution. By making use of the uncertainty principle that relates the dephasing time  $T_2$  with the spectral width  $\Delta\nu$ ,  $T_2 =$

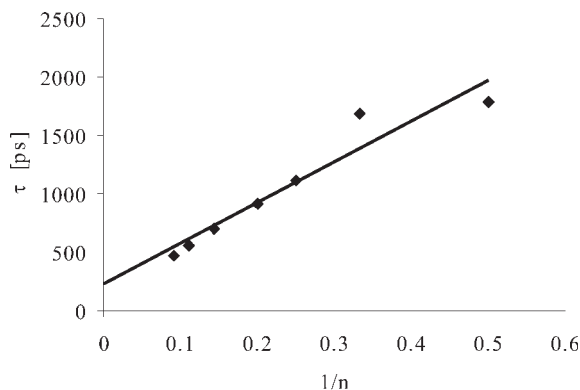
$(2\pi\Delta\nu)^{-1}$  this translates to a lower bound of 1.2 ps for the dephasing time. Since the efficiency of hole burning was unusually low,  $\sim 10^{-9}$ , one can conjecture that this is the true dephasing time of those few polymer chain segments that acquired their optimal conformation already, while the majority of chains suffer structural relaxation after excitation. This result may be related to cw-fluorescence of perfect polydiacetylene chains isolated in a monomer crystal. They are  $\pi$ -conjugated polymers, too, but in most cases they are nonfluorescent. At low temperature a single chain of a particular polydiacetylene, i.e. the red form of 3 BCMY-PDA, emits fluorescence and, interestingly, the  $S_1 \rightarrow S_0$  0–0 transition is a single line with a spectral width of  $3 \text{ cm}^{-1}$  [62]. This translates into a dephasing time of 3.6 ps, i.e. much longer than the dephasing time of an  $S_1$  exciton in PPV of  $\sim 150 \text{ fs}$  [63]. The implication being that the latter is determined by relaxation of a randomly packed polymer chain after optical excitation, absent if the chain is embedded within a perfect structural environment.

### 3.2.3

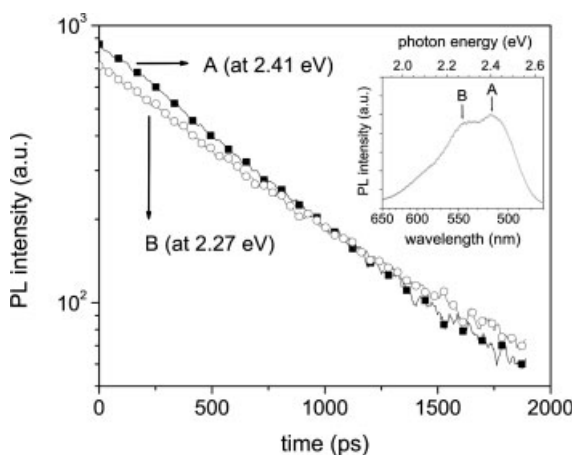
#### Excitation Dynamics

The decay of the lowest singlet excited state of a  $\pi$ -conjugated molecule is a first-order reaction with a decay rate on the order of  $1 \text{ ns}^{-1}$ . Measuring the decay of the photoluminescence from a film of a  $\pi$ -conjugated polymer one often observes a deviation from an exponential pattern. While at early times the extrapolated  $1/e$  decay time can be as short as 100 ps the long time emission decays more smoothly. This is a signature of intrachain and interchain energy transfer towards localized states of physical or chemical origin. It is obvious that unravelling the pathways by which an optical excitation can decay is crucial for any quantitative understanding of optoelectronic devices.

The radiative lifetime of the  $S_1$  state of  $\pi$ -conjugated oligomers depends on the chain length. Qualitatively, this is due to the superposition of coupled oscillators that form the excited state. Semiempirical quantum-chemical methods at the INDO/S level substantiate this reasoning [28]. In Fig. 3.12 the calculated radiative decays in oligomers of the ladder-type oligo(phenylene)s as a function of the reciprocal number of phenylene rings is depicted. When extrapolating the linear dependence to longer chains a lifetime of 300 ps is predicted. A similar dependence has been observed experimentally in oligo(flourene)s [64]. In that case the extrapolated value for the infinite chain is 400 ps. This is in quantitative agreement with the measured fluorescence decay of the MeLPPP polymer dispersed in a low-temperature MTHF glass [65]. Not only does this result confirm the validity of the theoretical approach but confirms that neither nonradiative intersystem crossing to the triplet manifold, nor energy transfer to nonradiative traps are important channels for deactivating the excited state of a isolated polymer chain. It is obvious that the shortening of the decay time in solid films must have extrinsic reasons. Figure 3.13 shows the fluorescence decay of a copolymer of phenyl-substituted poly(phenylene vinylene) (PhPPV) in dilute MTHF solution at 295 K measured with a streak camera [66]. The decay is almost single exponential although



**Fig. 3.12** Calculated fluorescence lifetimes as a function of the system size. Reprinted with permission from [28], copyright 2001 by the American Physical Society.



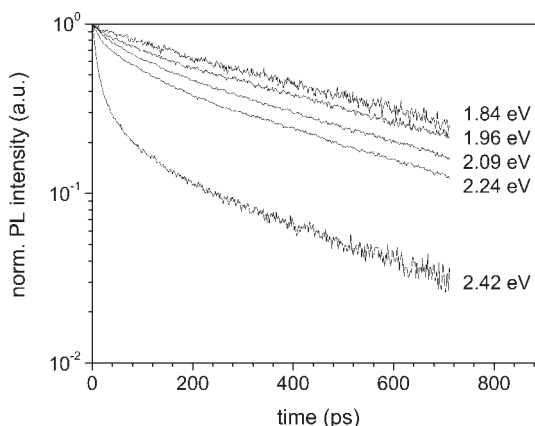
**Fig. 3.13** Transient photoluminescence of PhPPV in dilute MTHF solution at 295 K. Solid and open symbols refer to probing at spectral positions A and B in the inset, respectively. Reprinted from [66], copyright 2002, with permission from the American Institute of Physics.

the decay times are slightly different upon tuning the monochromator to the emission features A (650 ps) and B (750 ps), which are illustrated in the inset of Fig. 3.13, that are either due to two different conformations or to the neat and aggregated chain [66].

However, in the film the  $S_1$  lifetime is reduced to  $\sim 400$  ps if probed in the low-energy tail of the fluorescence spectra (Fig. 3.14). Upon probing at the high-energy wing the emission is highly nonexponential and features a fast initial decay. The reduction of the lifetime is a signature of excited-state quenching due to energy transfer to energy or charge acceptors involving interchain transport. The method of choice for delineating those processes is transient fluorescence spectroscopy.

Energy transfer is a ubiquitous phenomenon in molecular crystals in which singlet and triplet excitons with lifetimes of nanoseconds and up to 10–100 milliseconds, respectively, migrate incoherently via either dipole–dipole or exchange interaction. Typical intermolecular jump times are 1 ps for singlet excitons and 10 ps for triplets [2]. This implies that a singlet (triplet) exciton can visit some

**Fig. 3.14** Decay of the photoluminescence from a neat PhPPV film probed at different photon energies. Reprinted from [66], copyright 2002, with permission from the American Institute of Physics.



$10^4$  ( $10^8$ ) molecules before it decays intrinsically, the corresponding diffusion lengths being in the 10 nm (1  $\mu$ m) range. However, there is an important phenomenon specific for polymers and any other disordered solid. This is spectral diffusion. It originates from disorder-induced inhomogeneous broadening of the levels of the excited states. An inevitable consequence is that an exciton generated at an arbitrary site in the excitonic density of states (EDOS) distribution will tend to relax towards the tail states. As a consequence of the lower density of states in the tail the diffusivity of an exciton will decrease with time. The quantitative assessment of this phenomenon is currently a hot topic in the research of the physics of devices utilizing  $\pi$ -conjugated polymers. This includes color tuning of OLEDs with particular emphasis on the fabrication of white emitters and the energy channelling towards charge-transfer centers in photovoltaic cells.

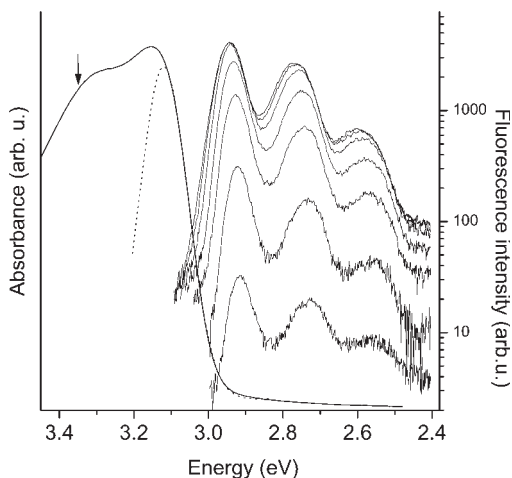
#### 3.2.3.1 Time-dependent Spectral Diffusion

When a photoexcitation is created within the inhomogeneously broadened density of states, it can relax by energy transfer to a neighboring chain segment with lower excitation energy. Once the excitation has moved to lower energy, absorption of a phonon is required for transfer to a site with higher energy. At very low temperature, thermal phonons are not available and the relaxation is energetically a downhill process. As the energy of the excitation decreases through successive transfer steps, the probability for the next jump decreases accordingly since the concentration of sites with an even lower energy gradually diminishes. This type of dynamics has been termed dispersive transport. Below a certain energy (which may be interpreted as a 'mobility threshold'), the probability for hopping of an excitation to a site with lower energy is so small that practically no jumps take place during the natural lifetime of the excitation.

Dispersive transport has been investigated both theoretically and experimentally. Theoretical studies [67, 68] predict that the average energy  $E$  of photoexcitations is proportional to  $\log(t)$ , with  $t$  the time after excitation [69]. This statement

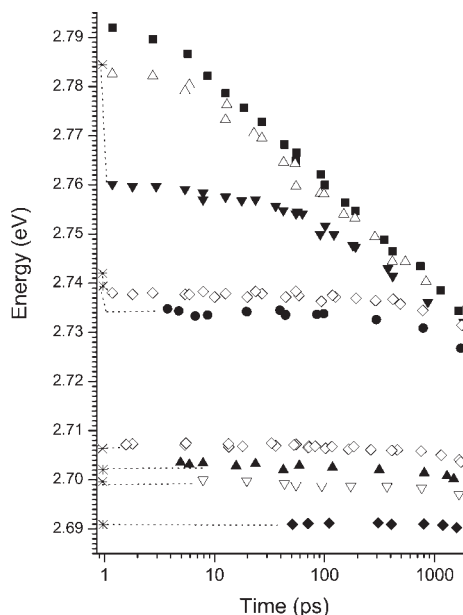
holds for excitations with high initial energy. For excitations with lower initial energy, a waiting time is predicted before the excitation makes its first jump. This waiting time becomes longer as the start energy of the excitation is lowered. After the time required for the first jump, the average energy follows the  $E \propto \log(t)$  behavior. This 'delay' in relaxation results from the fact that the mean distance to another site with lower energy depends on the initial energy of the excitation and becomes longer as this start energy is lowered. Correspondingly, the electronic coupling is weaker and the energy transfer takes place at a slower rate. Time-resolved fluorescence measurements with fixed excitation wavelength have indeed revealed a time-dependent red-shift of the fluorescence spectrum in accordance with a dispersive relaxation process [70, 71, 72]. For poly(para-phenylene vinylene) derivatives at low temperature, it has been observed that the maximum of the fluorescence spectrum shifts over 80 meV in the time window from 0 to 100 ps. The monotonic shift with time extends well into the nanosecond time domain [43, 73], and so it seems that at low temperature the photoexcitations do not reach a stationary energy during their lifetime. The bathochromic shift of the fluorescence has been interpreted in terms of migration of the photoexcitations to chain segments with longer effective conjugation length and thus lower excitation energy through transport of energy by, for example, the Förster mechanism. Fluorescence decay of  $\pi$ -conjugated polymer recorded for various detection wavelength upon excitation with a fixed photon energy can also be interpreted in terms of dispersive transport (Fig. 3.14) [70, 71].

In Fig. 3.15 the fluorescence spectra of a polyfluorene (PF2/6) film recorded in time windows covering ca. 10 ps to ca. 2 ns are presented. The film was held at 80 K and excited with 3.35 eV photons, i.e. well above the  $S_1 \leftarrow S_0$  0–0 absorption band [73, 74]. The vibronic components show a gradual bathochromic shift of roughly 100 meV, indicative of spectral diffusion. Further insight into the relaxation process is obtained by plotting the emission spectra as a function of the time



**Fig. 3.15** (Right) Time-gated fluorescence spectra of a film of polyfluorene PF2/6 after optical excitation at 3.35 eV at low temperature (15 K). The spectra were time integrated from 0–2, 8–10, 35–57, 134–136, 329–331, 822–824 and 1770–1850 ps, respectively. The arrow indicates the excitation energy. (Left) Low-temperature (80 K) absorption spectrum of the film. The dashed line is a fit of a Gaussian curve to the red edge of absorption spectrum. Reprinted from [73], copyright 2001, with permission from Elsevier.

**Fig. 3.16** Energy corresponding to the first moment of the 0–1 vibronic emission band of a polyfluorene film at low temperature (15 K) plotted as a function of time after excitation. The excitation energies are: ■: 3.081, △: 3.046, ▼: 2.997, ◇: 2.954, ●: 2.951, ◇: 2.918, ▲: 2.914, ▽: 2.911, ◆: 2.903 eV. The asterisks indicate the excitation energies corrected for the energy difference between the 0–0 transition and the first moment of the 0–1 vibronic band (0.209 eV). Reprinted from [73], copyright 2001, with permission from Elsevier.



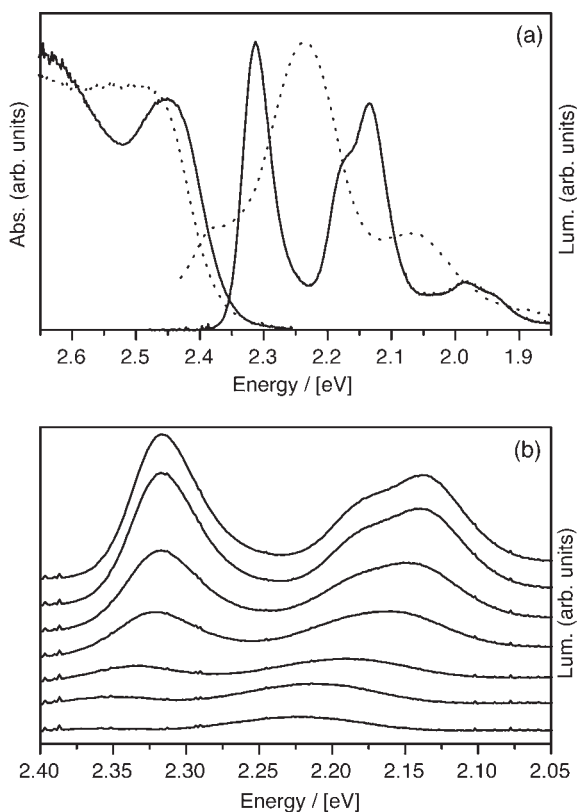
offset between excitation and temporal position of the detection window. (In order to eliminate stray light and reabsorption affects this bathochromic shift is monitored via the  $S_1 \rightarrow S_0$  0–1 transition (Fig. 3.16). The energy difference between the  $S_1 \rightarrow S_0$  0–0 transition and the first moment of the  $S_1 \rightarrow S_0$  0–1 vibronic band is 0.209 eV.) As the energy is scanned towards the low-energy tail of the absorption band, the relaxation process is delayed, as expected. Upon pumping at 2.95 eV the spectral position of the emission is time independent up to 300 ps. After this time some spectral broadening and small shifts are observed. At the lowest excitation energies used (2.92–2.90 eV) the emission bands remain almost stationary; for  $t > 1$  ns slight changes in the spectra indicate that limited relaxation can occur. Thus for excitation energies  $< 2.92$  eV the data strongly indicate that the excitations are essentially immobilized and cannot move to another chain segment with lower energy during their lifetime.

The asterisks in Fig. 3.16 depict the excitation energies, corrected for the vibrational energy associated with the 0–1 vibronic band. To calculate this energy (0.209 eV), it is assumed that for the lowest excitation energy (2.903 eV) the emission is resonant with the excitation and, on the spectral resolution of the experiment, there is no Stokes shift. Figure 3.16 also shows that additional relaxation channels open up for excitation energies  $> 2.94$  eV. These give rise to very rapid dissipation of excess energy through processes occurring on a time scale far beyond the temporal resolution of the experiment. These events can most likely be attributed to intrachromophoric vibrational relaxation following excitation through higher vibronic transitions, which is expected to be complete within a few hundred fs (see Section 3.2.1).



The experimental results can be modelled in terms of the Movaghar et al. Effective-medium approach [69, 73, 74] applied to hopping of either charged particles or excitonic states in a Gaussian DOS distribution. In the relevant time domain it predicts a logarithmic decay of the mean energy of an ensemble of excitations with a slope of  $0.3\sigma$  per decade where  $\sigma$  is the variance of the DOS. The latter can be inferred from the tail of the  $S_1 \leftarrow S_0$  0–0 absorption for excitons that yields  $\sigma = 70$  meV. Since in polyfluorene the experimental slope  $\Delta\epsilon$  per decade is 0.02 eV the agreement between theory and experiment is excellent. In passing we note that the energy versus  $\log t$  graphs for 3.05 eV and 3.08 eV excitation converge for  $t > 10$  ps. This implies that apparently the excess photon energy relative to the lowest singlet 0–0 transition has very little effect on the relaxation process taking place. This can be rationalized in terms of the excess energy being released into the vibrational heat bath on a time scale beyond the temporal resolution of the experiment and that temporal heating of the initially excited chain segment has little effect on the spectral diffusion.

Another example of the same phenomenon is the spectral diffusion of singlet excitons in a PPV film whose cw fluorescence at 293 K and 1.4 K are shown in Fig. 3.17 [75]. Upon lowering the temperature there is a significant bathochromic

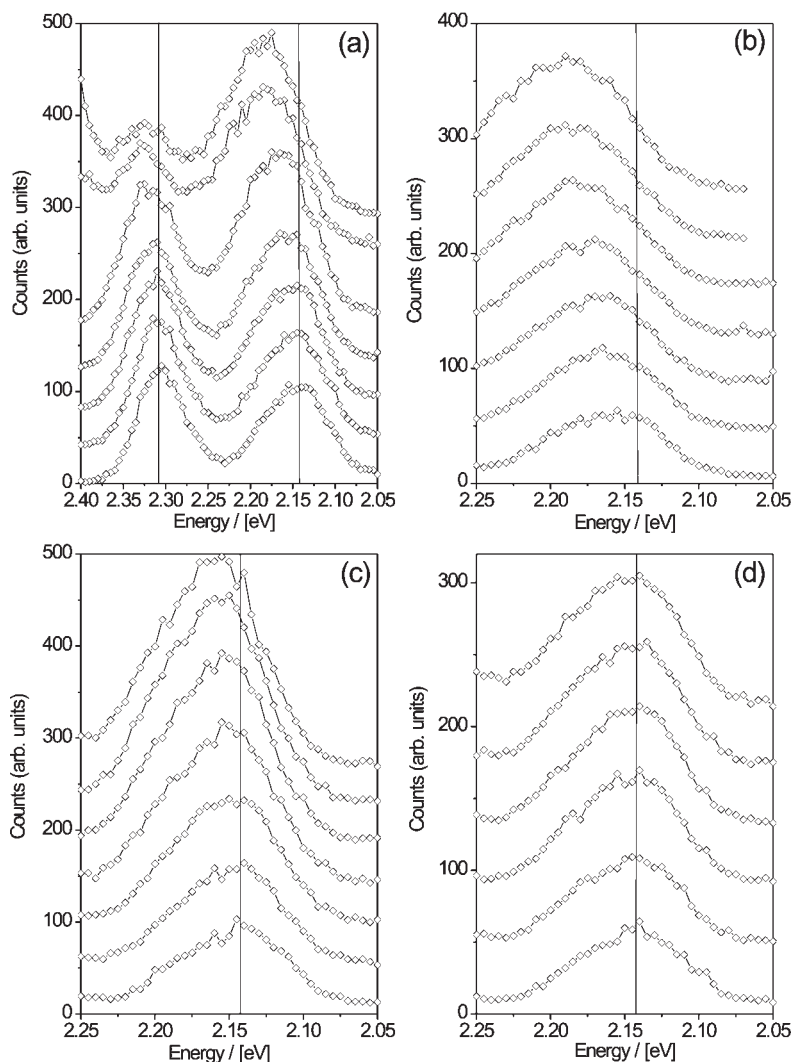


**Fig. 3.17** (a) Steady-state spectra of PPV at 1.4 K (solid lines) and at room temperature (dotted lines); (b) PPV fluorescence under temperature variation, from top to bottom: 40, 60, 100, 160, 220 and 280 K. Reprinted from [75], copyright 2004, with permission from Elsevier.

shift accompanied by spectral narrowing. In the 293 K fluorescence spectrum the prominent feature is a superposition of several vibronic 0–1 transitions. At the same time the fractional intensity of the  $S_1 \rightarrow S_0$  0–0 transition decreases as the temperature increases. This effect has been noted before and it has been argued that at higher temperatures emission originates from shorter chain segments with somewhat higher excited state energies [76, 77, 78]. The temperature induced fractional decrease of the  $S_1 \rightarrow S_0$  0–0 transition has been attributed to a site-dependent Huang–Rhys factor, i.e. for shorter chain segments the Huang–Rhys factor increases implying that the strength of the  $S_1 \rightarrow S_0$  0–1 transition emission increases. However, this interpretation cannot be correct because at the same time the apparent energy difference between the  $S_1 \rightarrow S_0$  0–0 and  $S_1 \rightarrow S_0$  0–1 emission decreases as the temperature increases. This is at variance with the fact that the frequency of molecular vibrations is essentially temperature independent. The above effect is a signature of reabsorption that becomes more important as temperature increases because the global fluorescence spectrum is blue-shifted as a result of a decreasing amount of spectral diffusion. Therefore, the  $S_1 \rightarrow S_0$  0–0 emission overlaps with the tail of the  $S_1 \leftarrow S_0$  0–0 absorption. This causes a fractional decrease of the intensity of the  $S_1 \rightarrow S_0$  0–0 band and a concomitant spectral distortion.

Figure 3.18 shows families of transient fluorescence spectra recorded at 1.4 K within short time windows covering the time domain from 200 fs to 20 ps and at selected excitation energies within the  $S_1 \leftarrow S_0$  0–0 transition whose spectral width is  $\sim 60$  meV (Gaussian width). There is significant spectral diffusion upon exciting into the central portion of the EDOS (excitonic density of states). If one were to plot the  $S_1 \rightarrow S_0$  0–1 emission spectra on a  $\log t$  axis the logarithmic decay pattern with a slope of  $0.35\sigma$  per decade would be recovered in good agreement with theoretical prediction, spectral relaxation is gradually eroded upon exciting into the absorption tail.

Detection of time-resolved spectral diffusion is thus a method to monitor energy transfer within an ensemble of chromophores not requiring an external fluorescent probe because the emitting states are only physically different but chemically identical. In a fluorescent system the energy transfer itself is a dipole-allowed transition with the coupling strength being determined by spectral overlap quantified by the Förster integral. For chemically identical chromophores the Förster radius is small, typically 1 to 1.5 nm only. It is further diminished if the excited state of a chromophore couples to, for instance, a torsional mode that gives rise to an additional conformationally determined Stokes shift. An example is spectral diffusion in a  $\pi$ -conjugated polymer whose chain element is a diphenylene vinylene unit [79]. In this case the relaxation process is retarded. In general, the method of monitoring spectral diffusion to assess the importance of relaxation of optically excited states allows to identify the different origins of the observed Stokes shift, such as genuine spectral diffusion versus conformational relaxation of a chromophore upon excitation. Extracting quantitative information on the excitation dynamics requires sophisticated theoretical data analysis.



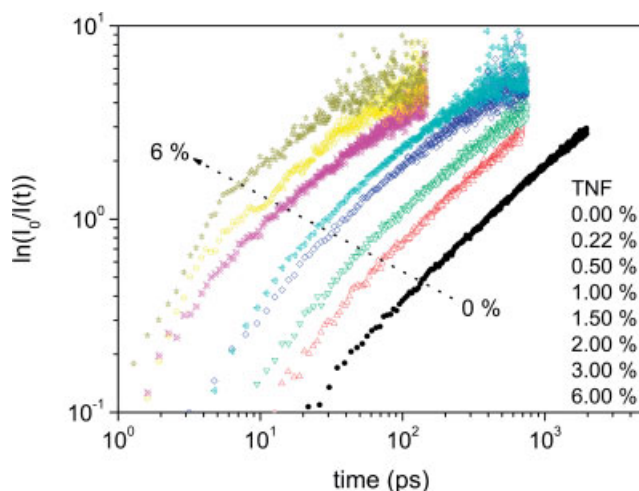
**Fig. 3.18** Fluorescence spectra (1.4 K) for central excitation energies at (a) 2.583 eV, (b) 2.480 eV, (c) 2.385 eV and (d) 2.384 eV, detected at a delay time (from top to bottom) of 200 fs, 400 fs, 1 ps, 2.5 ps, 5 ps, 10 ps and 20 ps (except (d), where the first record was taken at 800 fs). Because of stray light, the records are restricted to the  $1 \leftarrow 0$  vibron in (b–d); solid vertical lines are guidelines to the eye. Reprinted from [75], copyright 2004, with permission from Elsevier.

### 3.2.3.2 Fluorescence Decay in Doped Conjugated Polymers

In a molecular crystal the fluorescence decay reflects the sum of the rate constant for radiative and nonradiative decay of the excited state of the crystal. Information on energy transfer requires a fluorescent or nonfluorescent dopant that depletes the exciton reservoir. In a disordered system, in which the excited state is inhomogeneously broadened a fluorescence decay study does yield information without requiring an excitation scavenger provided that the emission is spectrally resolved [see Section 3.2.3.1]. When measuring the decay within a spectrally narrow detection window one monitors the relaxation across the spectrally assessed energy slice of the EDOS. Such experiments were first done on films of PPV [70]. They confirmed that the dwell time of excitations is significantly shortened as the detection window is scanned towards the high-energy tail of the fluorescence spectrum. A more recent example of this phenomenon is the spectrally resolved fluorescence decay from a neat PhPPV film, employing the streak-camera technique [66].

Doping an organic system with an energy-accepting species yields additional information on the efficiency of energy transfer. However, upon analyzing experimental results from disordered organic solids one has to take into account that there is a superposition of several processes that are not easily disentangled. For instance, if the dopant is a chromophore with both a lower excited-state energy relative to the host and significant oscillator strength there is a convolution of donor–donor transfer across the host and donor–acceptor transfer, usually featuring different transfer rates. The latter process is absent if the dopant quenches the excited state of the host only via short-range charge transfer rather than by energy transfer. However, energy transfer across the host matrix is always accompanied by spectral diffusion, implying that the rate of an individual transfer act is time dependent.

An example of transfer of singlet excitons in a copolymer of the PPV-type, PhPPV, doped with trinitrofluorene (TNF), which is a strong electron acceptor, will be analyzed in greater detail. As expected, the fluorescence from a PhPPV film decays more rapidly as TNF is added. Since the absorption spectrum of TNF does not overlap with the emission spectrum of PhPPV, the quenching of the PhPPV singlet excitation must be due to electron transfer from the singlet excitation rather than due to energy transfer. The generated electron–hole pair, i.e. charge transfer state, must decay nonradiatively because the energy of a geminate  $(PhPPV)^+$  and  $(TNF)^-$  pair is insufficient to generate an emissive state. For quantitative assessment of energy transfer in a donor–acceptor system one can measure fluorescence of donor and/or acceptor as a function of concentration under steady or time-resolved conditions. In a system devoid of disorder, such as a molecular crystal, transfer of an exciton among an ensemble of donor molecules is a first-order process associated with a well-defined rate constant that depends on the concentration of the acceptor [2]. This is no longer the case for an energetically or spatially random system because the rate of the individual transfer events features a distribution. The simplest case is that of single-step Förster transfer in a solution of donors and acceptors. In this case the distribution of rates

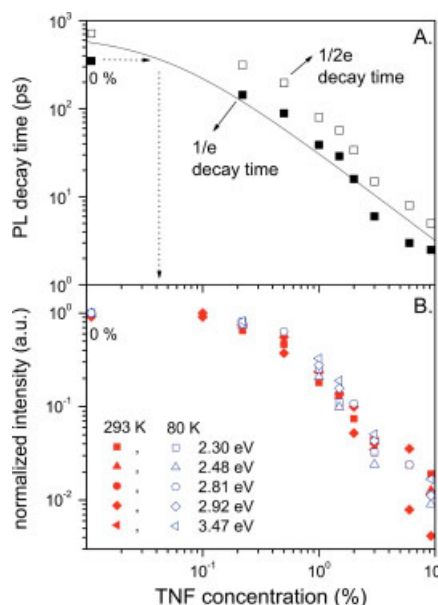


**Fig. 3.19**  
KWW (Kohlrausch–Williams–Watts) plots for PhPPV films with various TNF concentrations. Reprinted from [66], copyright 2002, with permission from the American Institute of Physics.

is solely determined by the random donor–acceptor distances. One operational way to characterize the fluorescence decay in a disordered system is to plot the time-dependent fluorescence intensity  $I(t)$  in terms of the Kohlrausch–Williams–Watt (KWW) function, i. e.  $I(t) = I_0 \exp[-(t/t_0)^\beta]$ , where  $0 < \beta < 1$  is a dispersion parameter. In a KWW-type data representation the slope of a linear  $\ln I_0/I(t)$  versus time dependence plotted on a double logarithmic scale is  $\beta$ . In classic Förster-type donor–acceptor transfer,  $\beta = 1/2$ . The  $1/e$  decay time is inferred from the ordinate value  $\ln I(t_{1/e}/t_0)/I_0 = 1$ . An example is the time-dependent fluorescence intensity of PhPPV doped with variable amounts of TNF (Fig. 3.19). It is noteworthy that on a  $\ln I(t)/I_0$  vs.  $\log t$  scale the decay pattern is merely shifted along the abscissa, maintaining its functional character except for a marginal change of  $\beta$  from  $\sim 0.7$  at the lowest concentration (0.22 %) to  $\sim 0.6$  at higher concentration (Fig. 3.19). Remarkably, the KWW plot for the undoped film features the same decay law and  $\beta$  exceeds the value expected for a single-step Förster process. This suggests that (i) in the undoped system the decay of singlet excitations is controlled by basically the same kind of stochastic process and (ii) the random process is multistep energy transfer among energetically disordered donor moieties. In Fig. 3.20 the  $1/e$  decay times as well as the  $1/2e$  decay times are shown as a function of concentration. They agree with the drop of steady-state fluorescence intensity as the concentration increases.

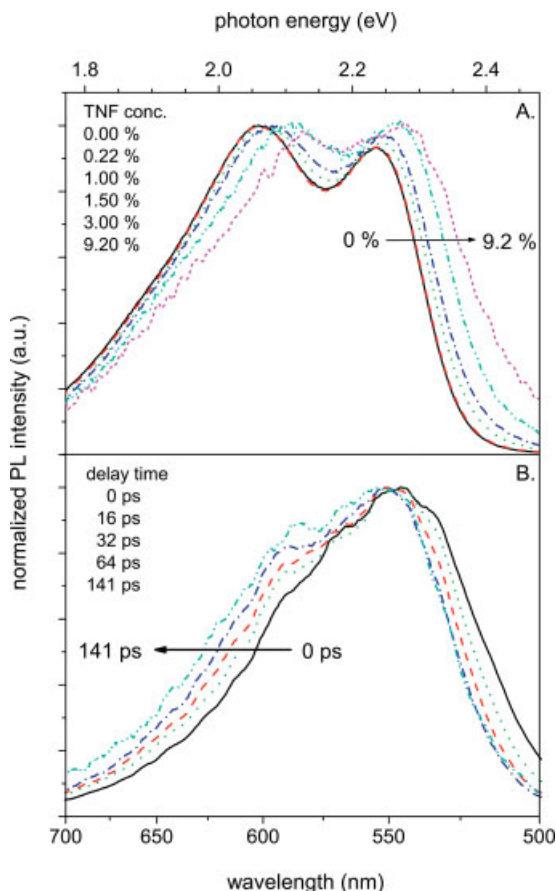
Upon recording the cw fluorescence spectra as a function of TNF concentration a continuous hypsochromic shift with increasing concentration is observed (Fig. 3.21). It is matched by an analogous bathochromic shift in the time-resolved spectra upon shifting the temporal detection window to later times. Both phenomena are related and can be attributed to the spectral diffusion of the PhPPV singlet excitation. The reason is that at increasing concentration of the dopants the host excitations have less time to relax spectrally. Therefore the fraction that will emit before energy transfer is completed must decay from higher states of

**Fig. 3.20** (A) TNF concentration dependence of PL decay times as 1/e (solid rectangle) and 1/2e (open rectangle). (B) TNF concentration dependence of cw photoluminescence (PL) intensity at 295 K and 80 K at various excitation energies. The solid line was calculated from  $\frac{d(s)}{dt} = -(k_0 + k_t c)[s]$  using a  $t_0 = 0.7$  ns and  $k_t = 3.18 \times 10^{12} \text{ s}^{-1}$ . Reprinted from [66], copyright 2002, with permission from the American Institute of Physics.



the EDOS. Since the intrinsic fluorescence decay pattern of the polymer in a bulk film or in MTHF solution ought to be virtually identical, the experimentally observed shortening of the decay time from  $700 \pm 50$  ps in solution to 400 ps in the film must be due to quenching by inadvertent impurities that are nonfluorescent, i.e. must act as charge-transfer centers like TNF. Based upon first-order quenching kinetics (see solid line in Fig. 3.20), one estimates, that their concentration has to be about 0.04 % only. By the way, it turns out that those impurities are responsible for cw photoconduction close to the absorption edge [80]. Obviously, roughly one impurity molecule per 2000 monomer repeat units is sufficient to quench 50 % of all primary excitations. On the other hand Monte Carlo simulations of the exciton relaxation within a Gaussian EDOS indicate that the number of jumps an exciton can make during its lifetime is roughly 5 only [81]. Both facts can only be rationalized by invoking delocalization of an excitation within chain segments comprising typically ten repeat units bearing in mind, however, that the delocalized entity is a coulombically tightly bound electron-hole pair migrating coherently or incoherently within a polymer segment. Based upon this notion the experimental results can be accounted for by analytic theory [82].

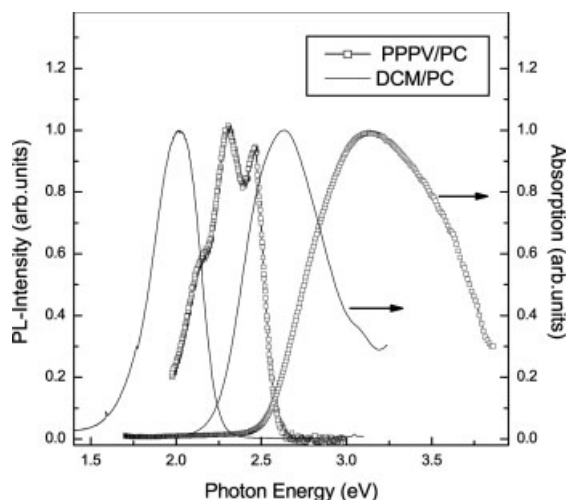
The other alternative for exciton quenching due to doping is Förster-type energy transfer towards a chromophore with bathochromatically shifted absorption spectrum so that the spectral overlap between the donor and acceptor absorption is larger. An example is fluorescence quenching in a film of poly(phenyl-phenylene-vinylene) (PPPV) blended with polycarbonate (PC) at a PPPV:PC ratio of 20:80 per weight and doped by the 4-dicyanomethylene-2-methyl-6-*p*-dimethylna-



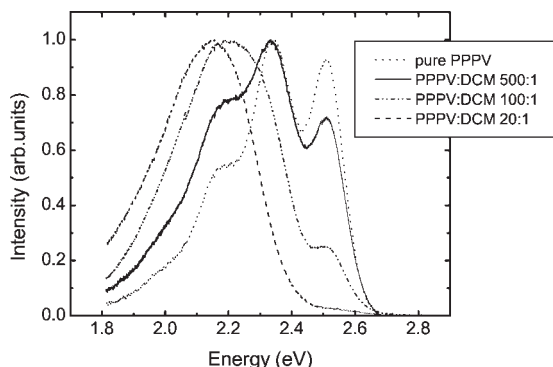
**Fig. 3.21** (A) cw photoluminescence spectra of a neat PhPPV film at 80 K ( $\lambda_{\text{exc}} = 425$  nm). (B) Time-resolved photoluminescence spectra of a neat PhPPV film at 290 K ( $\lambda_{\text{exc}} = 430$  nm). Reprinted from [66], copyright 2002, with permission from the American Institute of Physics.

minostyryl-4H-pyran (DCM) at weight ratios DCM:PPPV between  $10^{-3}$  and 0.25 [83]. The fluorescence was recorded in both the cw and transient mode at either 295 or 10 K. Figure 3.22 shows the absorption and fluorescence spectra of an undoped PPPV/PC film and a film of DCM dispersed in PC. The emission spectra of the doped samples are a superposition of the PPPV and DCM spectra, their relative intensities depending on the DCM concentration (Fig. 3.23). The occurrence of energy transfer from PPPV to DCM is obvious. This is further illustrated by Fig. 3.24, showing the temporal decay of the host emission detected at a photon energy of 2.53 eV at 10 K. Note that at 10 K the fluorescence decay is nonexponential while at 295 K (not shown) it is faster and almost exponential. The latter observation indicates that energy transfer is not a single-step donor-acceptor transfer tractable by Förster's theory but rather an almost time-independent exciton diffusion within the host matrix followed by a final transfer to the acceptor because single-step transfer should feature a KWW decay law with an exponent  $1/2$ . At lower temperatures donor-acceptor transfer is time dependent because of time-

**Fig. 3.22** Comparison of the time-integrated emission and absorption spectra of DCM and PPPV, both in a matrix of polycarbonate (PC). Reprinted from [83], copyright 1996, with permission from Elsevier.



**Fig. 3.23** Photoluminescence (PL) spectra of differently doped samples at  $T = 10$  K. The excitation photon energy is 3.1 eV. Reprinted from [83], copyright 1996, with permission from Elsevier.



dependent spectral diffusion. This process can be analyzed analytically employing time-dependent hopping theory as outlined below.

In the course of energy relaxation an exciton of energy  $E$  will, most probably, jump to a molecule in which its energy will be smaller than  $E$ . The density of accessible molecules will decrease after every exciton jump and, therefore, the distance to a next accessible target molecule will, on average, increase with time. The density of target molecules, accessible for an exciton of an energy  $E$ ,  $N(E)$ , is fully determined by the EDOS distribution  $g(E)$ :

$$N(E) = \int_{-\infty}^E dE' g(E') \quad (3.5)$$

where  $E'$  is the acceptor energy. The dependence of the energy transfer rate,  $\nu(r)$ , upon the distance  $r$  between an emitter chromophore of the energy  $E$  and an acceptor chromophore of the energy  $E'$  is described by the Förster formula as:



$$\nu(E - E', r) = \frac{1}{\tau} \left[ \frac{r_F(E, E')}{r} \right]^6 \quad (3.6)$$

where  $r_F$  is the Förster radius that generally depends upon the energies of both emitter and acceptor chromophores via the spectral overlap integral, and  $\tau$  the exciton lifetime. Since the widths of both the intrinsic and acceptor EDOS distribution ( $\sim 50$ – $100$  meV) are normally considerably smaller than the energy difference between them, it is possible to approximate the energy dependence of the Förster radius by two constants. The first,  $r_i$ , describes the energy transfer between chromophores within the intrinsic EDOS while the second,  $r_d$ , corresponds to exciton jumps from intrinsic states to acceptors.

As one can see from Eq. (3.6), the Förster jump rate strongly decreases with increasing distance between an emitter (starting site) and an acceptor (target site). Therefore, excitons will normally jump to the nearest accessible target sites. If the energy of an excited molecule is  $E$ , the probability densities are  $w_i(E, E', r)$  and  $w_d(E, E', r)$  of having such an either intrinsic or dopant target site, respectively, of the energy  $E' < E$  over the distance  $r$  is given by the Poisson distribution as

$$w_{i(d)}(E, E', r) = 4\pi r^2 g_{i(d)}(E') \exp \left[ -\frac{4\pi}{3} r^3 N_{i(d)}(E) \right], E < E' \quad (3.7)$$

where  $N_i$  and  $N_d$  are total densities of intrinsic,  $g_i(E)$ , and dopant,  $g_d(E)$ , sites of energies below  $E$ . If an exciton does have a nearest accessible intrinsic (dopant) target site over the distance  $r$ , the probability  $p_{i(d)}(r, t)$  that it has not yet jumped to this site until the time  $t$  is also described by the Poisson formula:

$$p_{i(d)}(r, t) = \exp[-\nu_{i(d)}(r)t] = \exp \left[ -\frac{t}{\tau} \left( \frac{r_{i(d)}}{r} \right)^6 \right] \quad (3.8)$$

An exciton still occupies an intrinsic starting molecule of the energy  $E$  at the time  $t$  if it jumped to neither host nor dopant molecules until this time. The respective probability,  $W_i(E, t)$ , can therefore be calculated as a product of the probabilities of having jumped to neither host nor guest molecules as

$$\begin{aligned} W_i(E, t) &= 4\pi N_i(E) \int_0^\infty dr r^2 \exp \left[ -\frac{4\pi}{3} r^3 N_i(E) \right] \exp \left[ -\frac{t}{\tau} \left( \frac{r_i}{r} \right)^6 \right] \\ &\times 4\pi N_d(E) \int_0^\infty dr r^2 \exp \left[ -\frac{4\pi}{3} r^3 N_d(E) \right] \exp \left[ -\frac{t}{\tau} \left( \frac{r_d}{r} \right)^6 \right] \end{aligned} \quad (3.9)$$

Equation (3.9) can be considerably simplified if one accounts for the very steep coordinate dependence of the Förster jump rate. Under these circumstances the second exponentials in the integrands of this equation can be written as

$$\exp\left[-\frac{t}{\tau}\left(\frac{r_{i(d)}}{r}\right)^6\right] \approx \begin{cases} 0, r < r_{i(d)}\left(\frac{t}{\tau}\right)^{1/6} \\ 1, r > r_{i(d)}\left(\frac{t}{\tau}\right)^{1/6} \end{cases} \quad (3.10)$$

Substituting Eq. (3.10) into Eq. (3.9) yields then

$$W_i(E, t) = \exp\left\{-\frac{4\pi}{3}\left(\frac{t}{\tau}\right)^{1/2} [r_i^3 N_i(E) + r_d^3 N_d(E)]\right\} \quad (3.11)$$

An exciton, occupying a host molecule, can jump to both intrinsic and dopant target sites independently. If this exciton has jumped to another host molecule, it is liable to further energy relaxation. However, if it has jumped to a dopant molecule it is quenched and cannot return to a host molecule. Although energy relaxation can further proceed within the manifold of dopants, its rate and, concomitantly, the value of the corresponding Förster radius do not affect the kinetics of exciton quenching. Assuming that all dopants are deeper in energy than any host molecule one can disregard energy transfer between dopant chromophores and Eq. (3.11) reduces to

$$W_i(E, t) = \exp\left[-\frac{4\pi}{3}r_d^3 N_d\right] \left(\frac{t}{\tau}\right)^{1/2} \exp\left[-\frac{4\pi}{3}r_i^3 N_i\left(\frac{t}{\tau}\right)^{1/2}\right] \quad (3.12)$$

In order to obtain the energy distribution functions of excitons, occupying the intrinsic sites,  $f_i(E, t)$ , one has to account for contributions from both excitons that still occupy molecules in which they have been initially generated and excitons that made one or more jumps within the manifold of intrinsic sites. The former contribution,  $p_0(t)$ , can be calculated by multiplying Eq. (3.12) by the intrinsic EDOS distribution and integrating the product over energy. The result reads:

$$p_0(t) = \left(\frac{3}{4\pi r_i^3 N_t}\right) \left(\frac{t}{\tau}\right)^{-1/2} \exp\left[-\frac{4\pi}{3}r_d^3 N_d\left(\frac{t}{\tau}\right)^{1/2}\right] \left\{1 - \exp\left[-\frac{4\pi}{3}r_i^3 N_t\left(\frac{t}{\tau}\right)^{1/2}\right]\right\} \quad (3.13)$$

where  $N_t$  is the total (energy-integrated) density of intrinsic sites. An exciton, currently occupying a host molecule, can jump to either a dopant molecule or a deeper intrinsic site. As one can see from Eq. (3.12) the relative probability of such jumps is determined by the products of the respective densities of states and Förster radii. Therefore, the occupational probability for intrinsic sites, occupied by excitons that made at least one jump by the time  $t$ ,  $f_i(E, t)$ , can be written as

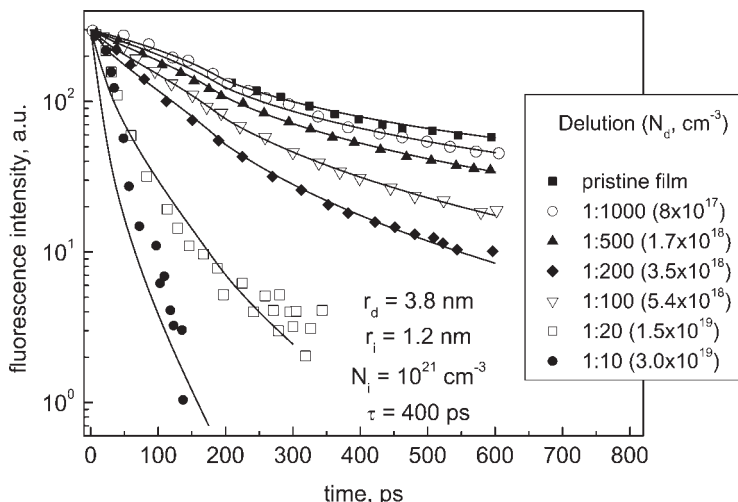
$$f_i(E, t) = [1 - p_0(t)] g_i(E) \exp \left[ -\frac{4\pi}{3} r_d^3 N_d \left( \frac{t}{\tau} \right)^{1/2} \right] \exp \left[ -\frac{4\pi}{3} r_i^3 N_i \left( \frac{t}{\tau} \right)^{1/2} \right] \\ \times \left( \frac{3}{4\pi r_i^3} \left( \frac{t}{\tau} \right)^{-1/2} \exp \left[ -\frac{4\pi}{3} r_d^3 N_d \left( \frac{t}{\tau} \right)^{1/2} \right] \left\{ 1 - \exp \left[ -\frac{4\pi}{3} r_i^3 N_i \left( \frac{t}{\tau} \right)^{1/2} \right] \right\} + \left( \frac{r_d}{r_i} \right)^3 N_d \right)^{-1} \quad (3.14)$$

Integrating this equation over energy, adding the density of excitons that still reside in ‘parent’ host molecules, and accounting for the radiative decay of excitons yields the total density  $p_i(t)$  of excitons occupying intrinsic sites at the time  $t$ :

$$p_i(t) = \exp \left( -\frac{t}{\tau} \right) p_0(t) + \exp \left( -\frac{t}{\tau} \right) [1 - p_0(t)] \\ \times \left( 1 + \frac{4\pi}{3} r_d^3 N_d \left( \frac{t}{\tau} \right)^{1/2} \exp \left[ \frac{4\pi}{3} r_d^3 N_d \left( \frac{t}{\tau} \right)^{1/2} \right] \left\{ 1 - \exp \left[ -\frac{4\pi}{3} r_i^3 N_i \left( \frac{t}{\tau} \right)^{1/2} \right] \right\}^{-1} \right)^{-1} \quad (3.15)$$

In the absence of the exciton energy diffusion within the intrinsic EDOS distribution, i. e. with  $r_i = 0$ , Eq. (3.15) reduces to the  $(t/\tau)^{1/2}$  dependence obtained by Klafter and Blumen [84] for the Förster-type donor photoluminescence quenching by randomly distributed exciton acceptors.

The theory has been used to analyze the experimental data in Fig. 3.24. Using the spectroscopically determined values for the Förster radii for donor–donor ( $r_i$ )



**Fig. 3.24** Photoluminescence (PL) transients of the different samples. The detection energy is 2.53 eV, corresponding to the  $S_1 \rightarrow S_0$  (0–0) emission band of PPPV [83]. The lines are fitting curves calculated from Eq. (3.15) – see text for further details. The inset shows experimental DCM:PPPV ratios and the dopant concentrations used in the calculations. Reprinted with permission from [82]. Copyright 2004 by the American Physical Society.

and donor–acceptor ( $r_d$ ) transfer ( $r_i = 1.2$  nm,  $r_d = 3.8$  nm) and using a fluorescence lifetime in the undoped sample of 400 ps the agreement between experiment and theory is excellent. A cautionary note is appropriate, though, because the theory has been formulated for point-like chromophores thus ignoring exciton delocalization within a polymer segment. In view of the large value of the Förster radius for dipole–dipole-type donor–acceptor transfer compared with charge transfer (see above) this can be justified. It is worth mentioning that in the original paper [83] energy transfer was analyzed in terms of single-step Förster theory. As expected, the inferred value for  $r_F$  turned out to be larger than the value based upon the spectral overlap integral because that analysis ignores donor–donor transfer prior to donor–acceptor transfer. The current theory takes proper account of this fact.

### 3.3

#### Optically Induced Charge Carrier Generation

Because the binding energy,  $E_b$ , of a singlet exciton in a conjugated polymer is about 0.5 eV or larger [18, 85, 86], its dissociation into a coulombically unbound electron and hole requires extra energy. In this respect classic molecular crystals behave in a similar fashion except  $E_b$  is even larger, i. e. 1 eV, because the “size” of the excitation residing on a molecule like anthracene is on the order of 0.1 nm only [2]. This precludes thermally or electric-field-induced dissociation because the rate constant for that process is vanishingly small relative to the rate constant for intrinsic decay. Therefore intrinsic photogeneration can only be accomplished via higher excited states. However, because in  $\pi$ -conjugated polymers the size of a singlet exciton, i. e. the rms separation of the electron–hole pair of a singlet exciton, is larger, i. e. typically 1 nm [14, 28], there can be exemptions to the above rule. Action spectra of photoconductivity in conjugated polymers do indicate that photoconduction starts right at the optical absorption edge implying that singlet excitons do have a finite chance for dissociation [87]. Meanwhile, it is well established, however, that most of this photoconductive response is due to either dissociation of relaxed singlet excitons at an electrode [88, 89] or via charge transfer to deliberate or inadvertent doping of strong electron acceptor or donors [80]. Intrinsic dissociation does occur but it requires a strong electric field and/or excess photon energy. These processes will be outlined briefly below. A more comprehensive treatise can be found in ref. [86].

#### 3.3.1

##### Intrinsic Photogeneration

Because radical ions feature red-shifted absorption spectra relative to those of the neutral parent molecules, transient absorption spectroscopy is the method of choice for monitoring dissociation of a neutral excited state into charged moieties [90]. Considering the fact that a high electric field is likely to be needed to disso-

ciate a relaxed singlet exciton a double modulation technique was applied to probe photogeneration of charges in a film of MeLPPP [91]. A periodic (5 kHz) electric field was applied to the sample and the transmittance of the sample in the spectral range in which radical cations/anions absorb was monitored via pump probe spectroscopy. When exciting the sample by moderately intense ( $\leq 14 \mu\text{J}$ ) 100-fs pulses of 3.1-eV photons the observed polaron signal increased smoothly featuring a stretched exponential law. Importantly, the number of generated polarons increased continuously within the time window between  $\approx 1$  ps and  $\approx 500$  ps. Note that the lifetime of a  $S_1$  exciton in MeLPPP is 300 ps. The intensity of the signal increased in a power-law fashion with the electric field. These two observations prove that (i) the dissociating species is the relaxed singlet exciton after its vibronic excess energy has been dissipated and (ii) dissociation requires extra energy. Using random walk theory the field dependence of dissociation can be rationalized in terms of an exciton binding energy of about 0.8 eV [86]. Note that a calculation by solving the Bethe–Salpeter equation for a two-body Green function of the electron–hole pair yielded  $E_b = 0.64$  eV [14]. Studies of the electric-field-induced fluorescence quenching on members of the PPV-family indicate that the value of  $E_b$  is more or less independent of the type of conjugated polymer [11, 92].

Similar experiments to those reported in ref. [91] had suggested that field-induced dissociation of the  $S_1$  exciton in MeLPPP is efficient only during the earlier stage of exciton dynamics [90]. Meanwhile, it has been recognized that it is due to annihilation of singlet excitons at higher photon dose [93, 94]. This process shortens the singlet exciton lifetime and at the same time increases the dissociation yield because the extra electronic energy of an excited state can be used to compensate the energy needed for dissociation. An early proof for the latter notion that the exciton binding energy  $E_b$  is  $\gg kT$  is the increase of the cw photoconduction yield at an energy roughly 1 eV above the  $S_1 \leftarrow S_0$  0–0 absorption edge [89, 95, 96, 97]. Extending their earlier work [91], Gulbinas et al. [98] meanwhile increased the photon energy to 4.6 eV and observed a fast onset of photodissociation of nonrelaxed excitons superimposed onto the slow dissociation signal due to relaxed singlet excitons. The former process resembles autoionization of a higher Franck–Condon state known to be a general phenomenon in molecular crystals [2, 99]. The extra energy required for generating an electron–hole pair can also be supplied by two-photon absorption [100], in the course of bimolecular annihilation of two excitons [93, 100, 101] and upon subsequent optical excitation of a relaxed singlet exciton [102, 103, 104]. The latter process bears some analogy to optical detrapping of a trapped charge carrier in a molecular crystal [105].

A model of photodissociation of a superexcited Franck–Condon state has been based upon the notion that the extra electronic energy is converted into vibrational energy of the originally excited segment of the polymer chain. Before dissipating the excess energy into the phonon bath its local temperature is higher [106] and the exciton can dissociate thermally in the course of a quasiequilibrium Boltzmann process. Both the weak temperature dependence and the field dependence of photoconduction at higher photon energies can be explained in terms of this model [97]. An alternative model assumes that the excess photon energy is

initially stored in a low number of discrete vibrational modes before vibrational coherence is lost ( $\sim 30$  fs) [107]. In order to discriminate between both mechanisms one has to monitor the appearance of the polaron signal on a sub-ps time scale. It appears plausible, though, that both processes contribute and on a ps time scale the slower process will win.

### 3.3.2

#### Geminate Electron–Hole Pairs

In view of the low dielectric constant of organic materials, coulombically bound electron–hole pairs or, synonymously, geminate pairs (GPs) play an important role in the photophysics of organic solids [2]. Since the oscillator strength for their direct optical generation decreases exponentially with intrapair distance they are not directly excited, the only exception being charge transfer (CT) states of adjacent molecules in acene crystals [108]. Their absorption spectra are hypsochromically shifted relative to the  $S_1 \leftarrow S_0$  0–0 transition and their oscillator strength is a few per cent of that of the latter transition [108]. Non-nearest-neighbour GPs are generated either via autoionization from a higher Franck–Condon state or of the bimolecular recombination of singlet or triplet excitons. Being metastable relative to the  $S_1$  exciton, GPs in molecular crystals and organic liquids are much shorter lived than the  $S_1$  state unless traps are involved [2]. Pursuing the latter argument further it is straightforward to conjecture that in disordered organic solids, e. g. molecular glasses or conjugated polymers [109], their lifetime should be greatly extended, because cascading towards the coulombic potential well requires intermediate thermally activated transport.

Striking evidence on the existence of GPs in conjugated polymers is the phenomenon of thermally stimulated luminescence at very low temperatures (5 K). Upon heating a MeLPPP film after photoexcitation at 5 K delayed luminescence is observed on a time scale of hours [110, 111]. This can only arise from the recombination of charges locally trapped in tail states of the densities of charge transporting states. Monitoring the decay of the delayed fluorescence (DF) is a probe of the first-order recombination of GPs at a given temperature, making sure, however, that the effect is in fact due to GPs rather than the bimolecular recombination of a pair of triplet excitons, which is the conventional origin of DF in molecular crystals [2]. Both processes can be disentangled by applying a strong electric field during or after optical excitation, because only GPs respond significantly to an electric field [112, 113]. Experiments on MeLPPP and on PhPPV revealed an order of magnitude effect on the DF intensity upon turning on/off a pulsed 2-MV/cm field. This effect greatly exceeds any field-assisted quenching of singlet excitons that might be created upon the fusion of few triplet excitons. It turns out that the recombination-limited DF decays in a power-law fashion,  $I_{\text{DF}}(t) \sim t^{-n}$  with  $n \sim 1$ , as expected for disordered systems where both the initial intrapair distance and the energy barriers that impede recombination are randomly distributed [114]. Even at room temperature DF can extend well into the microsecond range.

Another way to distinguish whether delayed fluorescence is caused by the fusion of two triplet excitons or by the recombination of geminate electron-hole pairs is to measure its action spectrum. Triplets are generated via intersystem crossing from vibrationally relaxed singlet excitons, while the formation of GPs commences only when the photon energy equals the  $S_1$  energy *plus* the coulombic energy required to expand the  $S_1$  state into a GP. Such an experiment was performed on single poly-chinoxalin polymer chains in which the repeat units are directly linked together. The polymer was embedded in a frozen MTHF matrix. Remarkably, DF has *not* been observed until the photon energy is 0.4 eV above the  $S_1 \leftarrow S_0$  0–0 transition [115]. On the contrary, in another type of polychinoxalin containing an ether linkage between the repeat units that weakens  $\pi$ -conjugation within the polymer chain, DF commenced right at the absorption edge. Combined with independent evidences this indicates that in this case DF originates from triplet–triplet fusion. The result for the experiment on the directly linked poly-chinoxalin polymers is the first direct spectroscopic probe of autoionization of an energetically hot Franck–Condon state in a single polymer chain. The value of 0.4 eV represents a lower bound for the exciton binding energy because the GPs are still coulombically bound. The fact that the effect is interrupted by an ether linkage proves that the degree of  $\pi$ -electron delocalization is crucial for the efficiency of autoionization. It is straightforward to conjecture even in a bulk polymer film the initial dissociation event is on-chain autoionization. Depending on the energy landscape inside the chain the majority of GPs will recombine quickly to form a relaxed  $S_1$  state. The remaining portion will transfer one of the constituted charges to an adjacent chain. It will be that portion of initially generated GPs that, e.g., give rise to photoconductivity. This is in accordance with experiments in which charge generation in MEH-PPV is probed on a sub-ps time scale employing terahertz radiation. It turned out that the dissociation efficiency is 100 times larger in the film as compared with dilute benzene solution at 295 K [116]. Apparently, at temperatures far beyond the glass transition the conformational dynamics of the polymer chain is ultrafast and erodes any local structure in the energy landscape that would be required for temporarily trapping a GP.

The question of how GPs are formed and how they decay is ultimately related to the photoconductivity. The general notion has always been that in molecular crystals and molecularly doped polymers photogeneration is a multistep process. The initial event is the field- and temperature-independent autoionization of a Franck–Condon state with sufficient energy. It generates a GP that can either recombine or fully dissociate in the course of field- and temperature-assisted Brownian motion as described by Onsager's theory [117]. Therefore the field and temperature dependence of intrinsic photogeneration is entirely due to the escape of the GP from the coulombic potential. In conjugated polymers the situation is fundamentally different because the rate-limiting step is the field-assisted dissociation of a more or less relaxed singlet exciton into a GP, rather than the subsequent full dissociation [11]. Analyzing such data in terms of Onsager's approach would yield incorrect numerical results.

## 3.3.3

**Sensitized Photogeneration**

Since dissociation of a relaxed singlet exciton in a conjugated polymer is an endothermic process, its efficiency is low, notably at moderate electric fields as are usually applied in photoconductivity. Within the spectral range of the  $S_1 \leftarrow S_0$  0–0 transition and at light intensities at which nonlinear effects are absent observed photocurrents are due to sensitization via exciton diffusion towards inadvertent or deliberately added dopants with large electron affinity or low ionization potential [118] (see Section 3.2.3.2). Recall that in PhPPV a relative dopant concentration (by weight) of  $5 \times 10^{-4}$  quenches 50 per cent of singlet excitons thereby creating GPs comprising a PhPPV radical cation and negatively charged dopant. It is not surprising that deliberate doping at moderate concentrations photoconduction is almost concentration independent because the number of singlet excitons that form sensitized GPs can only increase by a factor of two. This is confirmed by photoconductivity studies on PhPPV doped by trinitrofluorenone and perylenediimide. A significant increase of the photocarrier yield has only been observed upon increasing the perylenediimide concentration beyond  $\cong 20\%$  (by weight) [118]. However, it is not easy to understand why the photocarrier yield at moderate doping, i.e. when more than 50% of the singlet excitons form a donor–acceptor-type GP, is, depending on electric field, as low as  $10^{-4}$  to  $10^{-3}$ , while the temperature dependence is much weaker, as expected for a coulombically bound GP of intrachain separation of 1 nm, i.e. 0.4 eV. Attempts to solve this paradox involve (i) the random walk of the dissociating GP with statistically random start energy [119] and (ii) the notion that the charge on the polymer segment oscillates within the coulombic potential as in the Morse potential of a diatomic molecule and the associated kinetic energy can assist escape [120].

Photostimulated charge transfer towards an acceptor and the subsequent escape from the coulombic potential is the rate-limiting step in a photovoltaic cell [121, 122]. It is apparent that achieving high charge generation efficiency involves a solution of the problem of how to overcome coulombic attraction of the GP. A crucial role is played by the internal interface between donor and acceptor microphases [123, 124, 125]. A special strategy is appropriate tuning of the HOMO/LUMO levels of the donors and acceptors ensuring that electron–hole capture is barrier free [56, 126]. Another way to accomplish efficient GP dissociation involves the establishment of an interfacial weak dipole field between the donor and acceptor already existing in the dark that tends to inhibit geminate recombination [127]. These questions will be addressed in greater detail in other chapters of this book.



### 3.4

#### Triplet States

##### 3.4.1

#### Phosphorescence

Before discussing phosphorescence in conjugated polymers in detail it is appropriate to recall some basic knowledge about this phenomenon in low molecular weight organic materials, such as aromatic hydrocarbons [2, 128]. Phosphorescence is the radiative decay of triplet excitons in conjugated organic molecules. It involves the transition from the  $T_1$  excited state to the  $S_0$  ground state. The change of spin within this transition requires spin-orbit coupling to conserve total momentum. Since in aromatic hydrocarbons commonly electronic transitions of the  $\pi$ - $\pi^*$  type are involved, the spin-orbit coupling is very weak. Thus, this transition is spin forbidden and the intensity is orders of magnitude smaller than the intensity of fluorescence from the singlet excited state. For the same reason the lifetime of the triplet state is very long, up to milliseconds or even seconds, compared with nanoseconds for fluorescence. During the long lifetime of the triplet state the exciton is liable to diffusion to trap states or to bimolecular reactions with other excitations such as triplet excitons, singlet excitons or charge carriers. These competing processes often prevent the observation of phosphorescence especially at room temperature.

The triplet state is usually populated via intersystem crossing (ISC) from the optically excited singlet state. Since ISC requires vibrational coupling between the  $S_1$  and  $T_1$  levels, ISC is more efficient if the two states are close in energy. The ISC rate  $k_{ISC}$  depends exponentially on the energy gap ( $\Delta E_{ST}$ )  $k_{ISC} \sim \exp(-\Delta E_{ST}/E_0)$ ,  $E_0$  being an empirical parameter related to molecular vibrations. In aromatic hydrocarbons the  $\Delta E_{ST}$  is about 1 eV, as apparent from the red-shift of the phosphorescence spectrum relative to the fluorescence spectrum. The large energy separation is a manifestation of the importance of exchange interaction in organic molecules. The rates of ISC increase significantly, if a triplet level such as  $T_2$  is close to  $S_1$  in energy. This is realized in tetracene where ISC is much higher compared with anthracene. Typical ISC rates in aromatic hydrocarbons are on the order of  $10^6 \text{ s}^{-1}$  at least two orders of magnitude lower than the fluorescence rate. This results usually in low triplet quantum yields in acene crystals. The weak spin-orbit coupling in aromatic hydrocarbons can be achieved by vibration-induced mixing of  $\pi, \sigma$  orbitals. The bending vibration of C-H bonds induces a higher "S" character in the orbital and thus weak spin-orbit coupling. More efficient is the spin-orbit coupling in molecules with  $n \rightarrow \pi^*$  transitions, such as benzophenone, where significant phosphorescence can be observed. The rate of intersystem crossing in benzophenone increases to  $10^{11} \text{ s}^{-1}$ . Introducing heavy atoms such as Cl, Br, I into the molecular structure leads to higher ISC, because of higher spin-orbit coupling.

Contrary to the vast amount of experimental and theoretical studies on the photophysics of the singlet state of conjugated polymers there is still limited

information about the role of the triplet state in these materials. Despite the fact that understanding the role of  $T_1$  is crucial to gain a complete understanding of the photophysics of conjugated polymers. From an application point of view it is even more desirable to clarify the role of triplets, since in OLEDs the probability of formation of triplets under electrical excitation is more likely than under photo-excitation. This issue will be discussed in other chapters of this book.

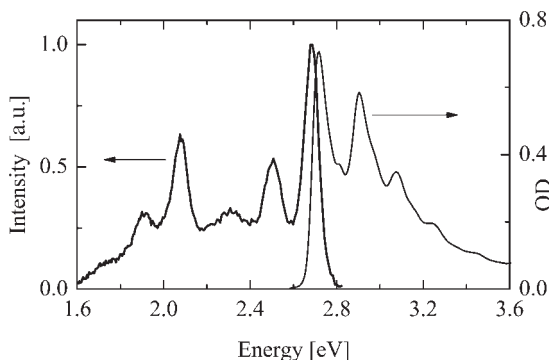
Information about the generation and decay of triplet states in conjugated polymers has been acquired mainly via indirect detection techniques such as transient photoinduced triplet-triplet absorption (PIA) [129, 130, 131, 132] and optically detected magnetic resonance (ODMR) [133, 134]. The advantage of the measurement of triplet-triplet absorption is that the measured quantity is directly proportional to the density of triplet states, thus yielding information about the formation and decay rates of triplets. In ODMR basically the same quantity as in PIA is measured, the only difference being that the signal is modulated by a magnetic field. The detection of delayed fluorescence has also been used to prove the existence of triplets and investigate their bimolecular decay in conjugated polymers [135, 136]. However, no information about the energetic position of the triplet state, the shape of the spectrum or radiative decay times of triplets can be inferred from these experiments. The energetic position of the triplet state in conjugated polymers has been located by pulse-radiolysis-induced energy-transfer experiments [8, 137, 138]. By applying a strong electron pulse from an accelerator to a benzene solution containing the polymer, triplet states in benzene are populated. If appropriate triplet sensitizers are present in solution the initially created benzene triplets are transferred to the polymer via the sensitizer with almost unit efficiency. This is monitored by PIA measurements of the triplet-triplet transition of the polymer. If the triplet energy of the sensitizer is below the triplet level of the polymer energy transfer is impeded and no triplet-triplet absorption can be detected. Thus, from variation of the triplet energy of the sensitizer the triplet state of the polymer can be estimated. For MeLPPP, a prototypical conjugated polymer of the PPP-type,  $T_1$  was located at 2.15 eV using this technique [137]. Pulse-radiolysis experiments on a variety of conjugated polymers led to the empirical formula  $E(T_1) = 1.13 E(S_1) - 1.43 (\pm 0.25)$  to estimate the triplet energy from the known energy of the singlet state [8]. Of further advantage of the pulse-radiolysis experiment is the possibility to estimate the quantum yield of triplet formation. Typical values for luminescent conjugated polymers such as polyfluorene are on the order of 3 % at most [139]. A serious drawback of the technique is the restriction to solution and room-temperature experiments.

Direct observation of phosphorescence from conjugated polymers has been achieved by the application of gated detection techniques. In these techniques the detection window of an intensified CCD is delayed with respect to the excitation laser pulse. Therefore the detector is blocked during the intense prompt fluorescence caused by the conjugated polymer and able to detect the delayed emission that is usually orders of magnitude lower than prompt fluorescence. Spectrally resolved detection allows for the observation of the shape and energetic position of the delayed emission. By varying the width of the detection window

and the delay between excitation and detection, the kinetics of the delayed emission can be investigated.

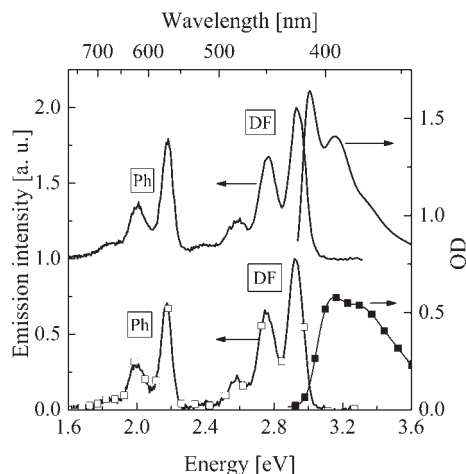
The first observation of phosphorescence with gated detection techniques from a conjugated polymer has been reported for films and frozen solutions of MeLPPP [7]. Figure 3.25 shows the absorption and delayed emission spectra of a thin solid film of MeLPPP. The emission was recorded 5  $\mu$ s after excitation with 5-ns laser pulses of 2.76 eV (450 nm) energy. Two contributions to the delayed emission are apparent. The position of the emission at 2.68 eV (463 nm) with a vibronic splitting of 180 meV is identical to the prompt fluorescence. It can be assigned to delayed fluorescence (DF) from the singlet state [7, 136]. In the low-energy part of the delayed emission a peak at 2.08 eV (596 nm) can be identified, the vibronic splitting to the second peak being again 180 meV characteristic of a C = C stretch vibration of the phenyl ring [29]. Since this emission is absent at room temperature, is long lived and has the same vibronic splitting as that of DF, it has to be assigned to phosphorescence [7, 136]. Taking into account the different experimental conditions, i. e. room temperature and liquid solution, the value of  $T_1$  is in good agreement with the estimated triplet energy obtained by pulse-radiolysis energy-transfer experiments (2.15 eV) [137]. Thus the  $\Delta E_{ST}$  amounts to 0.6 eV. For a similar PPP-derivative, namely Ph-LPPP, electrophosphorescence and phosphorescence, respectively, was found even at room temperature, although the polymer was contaminated with Pd, thus enhancing the ISC through spin-orbit coupling [140, 141].

Meanwhile, there have been several reports on phosphorescence of conjugated polymers of the PPP-type, such as dodecyloxy-poly(*p*-phenylene) (DDO-PPP), poly-2,8-indenofluorene (PIF), poly(2,7-(9,9-bis(2-ethylhexyl)fluorene)) (PF2/6) [20, 142, 143]. Figure 3.26 depicts dilute solution and thin film spectra of delayed emission of PF2/6 as a representative of materials that are used frequently for organic light-emitting diodes. The polymer was held at 80 K and excited by a laser pulse of energy 3.05 eV (406 nm). The emission was recorded with a delay time of 5 ms. For comparison the absorption of PF2/6 in dilute solution and film is shown as well. The absorption of PF2/6 in dilute solution (Fig. 3.26, upper half) is characterized by the inhomogeneously broadened  $S_1 \leftarrow S_0$  0-0 transition



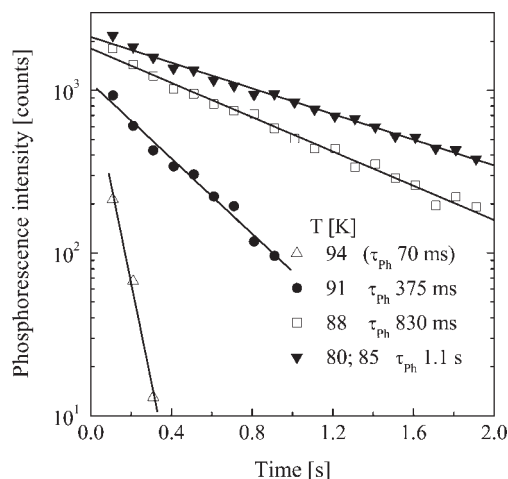
**Fig. 3.25** The absorption spectrum of a MeLPPP film at 80 K and delayed emission of a MeLPPP film at 80 K. The delay between excitation with 2.76 eV and detection was 5  $\mu$ s. Reprinted from [142], copyright 2002, with permission from the American Institute of Physics.

**Fig. 3.26** Absorption and delayed emission spectra of PF2/6 in MTHF at 80 K (upper half). The emission spectrum was taken 5 ms after optical excitation at 3.05 eV. DF corresponds to delayed fluorescence and Ph to phosphorescence. Absorption and delayed emission of a PF2/6 film at 80 K (lower half). The delay was 5 ms after excitation at 3.05 eV. Reprinted from [142], copyright 2002, with permission from the American Institute of Physics.



at 3.00 eV followed by a vibronic progression with a dominant splitting of about 160 meV probably due to a C=C stretch mode of the phenyl ring. Compared with dilute solution the absorption of the PF2/6 film is shifted to the blue spectral region with a maximum at 3.15 eV (Fig. 3.26, lower half). As a consequence of the decreased rigidity of the polymer backbone of PF2/6 with respect to MeLPPP, the absorption of the film is blue-shifted and inhomogeneous broadening of the transition is increased. For this reason the vibronic structure vanishes except for a shoulder on the high energy side of the absorption. In the delayed emission spectra of PF2/6 in both, dilute solution and film, two different contributions can be distinguished. The spectral position of the high energy part of the spectra is coincident with the prompt fluorescence at 2.93 eV and shows the same vibronic splitting of about 170 meV. This emission is due to delayed fluorescence from the  $S_1$  state of PF2/6. At lower energy the delayed emission at 2.18 eV can be assigned to the  $T_1 \rightarrow S_0$  0–0 transition bearing a vibronic splitting of 170 meV, identical to the prompt fluorescence. The singlet-triplet energy gap in PF2/6 amounts to  $\Delta E_{ST} \approx 0.75$  eV. The position of the  $T_1$  state of a similar polyfluorene has been investigated by means of pulse-radiolysis energy transfer, which locates the triplet state at  $2.3 \pm 0.1$  eV [8]. Keeping in mind that this corresponds to a room-temperature value in benzene solution and considering that a bathochromic shift upon cooling to 80 K can be expected for the energetic position of  $T_1$  comparable to that of the  $S_1 \rightarrow S_0$  transition (70 meV) the agreement between energy-transfer data and the direct measurement of  $T_1$  at 2.18 eV is very good [142, 143]. The lifetime of the phosphorescence emission of PF2/6 in MTHF solution at low temperature is presented in Fig. 3.27. The decay is monoexponential with a lifetime of about 1 s, characteristic of the PPP-type polymers mentioned above [20, 144].

The systematic variation of flexibility of the polymer backbone in the investigated PPP-type polymers allows to correlate the excited-state energy with conjugation length in this series. It is known from work on conjugated oligomers that the singlet energy varies with chain length as  $E(n, S_1) = E_\infty + E/n$ , where  $n$  is the num-



**Fig. 3.27** Time dependence of the phosphorescence intensity of PF2/6 in MTHF at various temperatures. Optical excitation was at 3.05 eV. Reprinted from [142], copyright 2002, with permission from the American Institute of Physics.

ber of phenyl rings at least for a small number of  $n$  [145] (see Section 3.2.1). This allows to estimate the effective conjugation length of the corresponding polymer. It may be shown that the relation holds for triplet-state energies of the PPP-type materials as well, although with a slope much weaker than for singlets [20]. This difference has been interpreted in terms of the extension of the optical excitation. A weaker slope implies that the triplet exciton is much more localized compared with the singlet exciton. This conclusion has been drawn from semiempirical calculations [146] and verified experimentally for the triplet state of polyynes earlier [147].

Another observation that concerns the effect of conjugation length on excited states in PPP polymers is the singlet-triplet energy gap. The  $\Delta E_{ST}$  in the PPP-type conjugated polymers varies little from 0.6 eV for MeLPPP, the most planar and rigid polymer, to about 0.75 eV for DDO-PPP, the latter having no bridged repeat units to restrict chain flexibility. The increasing torsional freedom in the series from MeLPPP to DDO-PPP leads to an increase in the energy gap  $\Delta E_{ST}$ . Recent theoretical investigations supported the observed trend with quantum mechanical calculations of triplet and singlet state energies as a function of the torsion angle between repeat units [148]. According to the calculations, the more delocalized singlet exciton is destabilized if the torsion angle is higher with respect to the planar conformation. The localized triplet exciton is less affected by the conformational confinement, thus the  $\Delta E_{ST}$  increases.

Despite the small dependence of the  $\Delta E_{ST}$  on the twisting angle between repeat units of the conjugated polymer there seems to be a more or less universal gap of  $\sim 0.7$  eV for a large variety of chemically very different polymers [148]. This differs from low molecular weight organic molecules where  $\Delta E_{ST}$  can vary from 0.3 to 1 eV depending on chemical structure [2]. There is comprehensive experimental confirmation of the above result from investigations of the phosphorescence of Pt containing conjugated polymers [9, 147, 149, 150]. In these polymers the effi-

ciency of phosphorescence is enhanced through increased spin-orbit coupling of the heavy metal atom Pt. The singlet-triplet energy gap  $\Delta E_{ST}$  is independent of the nature of the chemical spacer linking the Pt atoms, which were varied over a wide range [9, 149]. The value of the gap does not even depend on the delocalization of electrons along the spacer unit either [9], although the position of the singlet energy varies drastically depending on the structure of the spacer entity. For polymers of the polyethylene-type, that are analogous Pt-free materials, the  $\Delta E_{ST}$  remains unaltered at  $\sim 0.7$  eV [9]. In a soluble PPV derivative, PhPPV, the singlet-triplet gap was found to be  $\sim 0.8$  eV [151]. In this material phosphorescence could not be observed by direct excitation of the polymer [113]. The reason for this is its low  $T_1$  level of about 1.7 eV, estimated from pulse-radiolysis experiments [152]. Since the nonradiative deactivation increases exponentially with decreasing energy gap between  $T_1$  and  $S_0$  this explains why the direct observation is a challenge. Nevertheless, the triplet energy of PhPPV was located by sensitized phosphorescence at 1.63 eV [151]. The PhPPV film was blended with PtOEP, a platinum containing porphyrin, with a triplet energy of 1.9 eV and a singlet energy lower than that of PhPPV. The ISC of the PtOEP is nearly 100% increasing the population of the  $T_1$  of PhPPV more efficiently. Phosphorescence emission from PhPPV could be observed either by excitation of the polymer or of the dopant, implying efficient transfer of triplets from the dopant to the PhPPV.

From the phosphorescence studies on conjugated polymers of the PPP-type and PPV-type the common observation is the low-lying triplet energy with a comparatively long lifetime of the triplet state. This implies that these polymers are not suited as host materials for phosphorescent OLEDs using triplet harvesting. For this application short lifetimes of the triplet state and high triplet energies are mandatory to prevent nonradiative quenching and enable emission in the blue spectral range.

### 3.4.2

#### Decay, Annihilation and Migration of Triplet Excitons

To understand the kinetics of triplet excitons in conjugated polymers it is of advantage to recall the scenario of processes involving triplets in molecular crystals such as anthracene. If triplets are generated via ISC from the optical excited singlet state they can decay in a monomolecular or bimolecular fashion. The rate equation for the triplet concentration  $[T]$  can be expressed as [47]:

$$\frac{d[T]}{dt} = G_T - \beta_0[T] - \gamma_{TTA}[T]^2 - \sum \gamma_i[T][n_i] \quad (3.16)$$

$G_T$  being the generation rate of triplets,  $\beta_0$  is the sum of the radiative  $k_r$  and non-radiative  $k_{nr}$  decay, hence the inverse phosphorescence lifetime ( $\beta_0 = k_{nr} + k_r = 1/\tau_{phos}$ ).  $\gamma_{TTA}$  is the bimolecular triplet-triplet-annihilation (TTA) constant. The last term in Eq. (16) includes all losses due to bimolecular interaction of triplets with impurities such as paramagnetic quenchers and charge carriers.  $\gamma_i$  is the rate constant for this process and  $n_i$  the concentration of the impurity. For the present

discussion of triplet decay under photoexcitation the last term in Eq. (3.16) will be neglected. The annihilation of two triplet excitons leads to generation of a excited singlet state and thus to delayed fluorescence. The energetic position and shape of DF being identical to the prompt fluorescence, but emission occurs on a longer time scale. Thus the observation of DF yields information on the kinetics of triplets even if no phosphorescence is observed.

For low excitation conditions, i.e. where the monomolecular decay prevails  $\gamma_{\text{TTA}}[T]^2 < \beta_0[T]$ , the time dependence of the phosphorescence intensity derived from Eq. (16) is:

$$I_{\text{Ph}}(t) = k_r[T(t)] = k_r[T_0]\exp[-\beta_0 t] \quad (3.17)$$

$[T_0]$  refers to the initial triplet concentration. The corresponding intensity of the DF is:

$$I_{\text{DF}}(t) = \frac{1}{2}f\gamma_{\text{TTA}}[T(t)]^2 \quad (3.18)$$

where  $f$  is the fraction of triplet encounters leading to the formation of singlet excitons. Combination of Eq. (3.18) with Eq. (3.17) yields:

$$I_{\text{DF}}(t) = \frac{1}{2}f\gamma_{\text{TTA}}[T_0]^2\exp[-2\beta_0 t] \quad (3.19)$$

From Eq. (3.19) it is apparent that the DF intensity varies quadratically with the triplet concentration and hence with excitation light intensity as long as the singlet state is deactivated by monomolecular decay. The DF intensity decays exponentially with a lifetime half of the phosphorescence lifetime  $\tau_{\text{phos}}$ .

The situation is different under high excitation density, where TTA is the dominant process, i.e.  $\gamma_{\text{TTA}}[T]^2 > \beta_0[T]$ . Then the phosphorescence decay reads:

$$I_{\text{Ph}}(t) = k_r[T(t)] = \frac{k_r[T_0]}{(1 + \gamma_{\text{TTA}}[T_0]t)} \quad (3.20)$$

Combining Eq. (3.20) and Eq. (3.18) gives for the decay of the DF intensity:

$$I_{\text{DF}}(t) = \frac{1}{2}f\gamma_{\text{TTA}}[T_0]^2 \frac{1}{(1 + \gamma_{\text{TTA}}[T_0]t)^2} \quad (3.21)$$

In summary, the phosphorescence decays either exponentially or according to a power law, depending on which deactivation process prevails. Accordingly, decays the DF, although with half the phosphorescence lifetime and an exponent of two in the power law, respectively. If the DF intensity varies as  $I_{\text{DF}} \sim I_{\text{Ph}}^2$ , it is caused by TTA.

Before discussing TTA in conjugated polymers the quenching of triplets by paramagnetic impurities such as charge carriers should be addressed, since it is of major importance for application of the phosphorescence in devices such as light-emitting diodes. If one identifies the quenching species  $n_i$  in the last term of Eq. (3.16) with charge carriers  $n_h$ , i.e. holes in an unipolar device, and

the rate constant  $\gamma_i$  with the bimolecular constant for interaction of triplets with holes  $\gamma_{Th}$ , Eq. (3.16) reads:

$$\frac{d[T]}{dt} = G_T - \beta_0[T] - \gamma_{Th}[T][n_h] \quad (3.22)$$

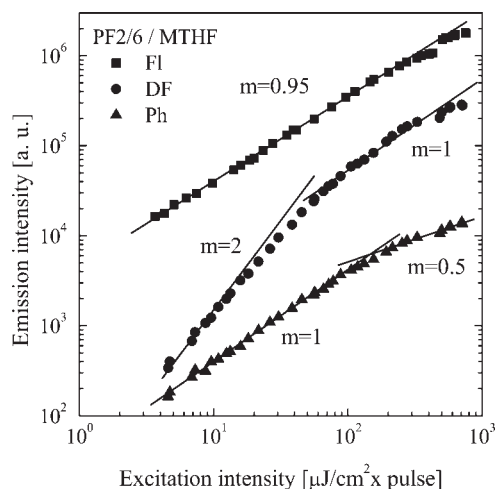
For simplicity the term for losses due to TTA has been neglected, implying low excitation intensity conditions. The rate constant for decay of triplets in the presence of charges  $\beta$  is then given by [2]:

$$\beta = \beta_0 + \gamma_{Th}[n_h]. \quad (3.23)$$

From Eq. (3.23) the density of charges necessary for triplet quenching can be estimated. If one assumes a decrease of the hole-induced triplet decay by an order of magnitude the rate constant  $\beta$  should be  $9 \text{ s}^{-1}$  for PF2/6, where the monomolecular triplet decay rate  $\beta_0$  is  $0.91 \text{ s}^{-1}$ . Adopting the rate constant  $\gamma_{Th}$  from a polyfluorene derivative with  $3 \times 10^{-14} \text{ cm}^3/\text{s}$  [153], yields a minimum charge density  $n_h$  of about  $3 \times 10^{14} \text{ cm}^{-3}$ . This is three orders of magnitude lower than the capacitor charge of a 100-nm thick device at 10 V applied voltage assuming a dielectric constant of 3.5. Thus quenching of triplets by charges is a major loss mechanism. The implication is that polymers with comparatively long triplet lifetimes are not suitable as host materials for triplet harvesting in OLEDs. One obvious way to circumvent the charge quenching of triplets is to use materials with short decay times. In heavy metal phosphorescent dyes such as  $\text{Ir(ppy)}_3$  [154] the phosphorescence lifetime is about  $1.2 \times 10^{-6} \text{ s}$ . According to Eq. (3.23) the charge density required for efficient quenching is about  $3 \times 10^{20} \text{ cm}^{-3}$ , implying negligible deactivation of triplets by the above mechanism.

In Fig. 3.28 the prompt fluorescence, DF and phosphorescence intensity as a function of laser intensity for a frozen solution of PF2/6 in MTHF are shown. The fluorescence intensity varies approximately linearly with laser power. The DF intensity increases quadratically with exciting laser intensity up to  $60 \text{ }\mu\text{J}/(\text{cm}^2 \times \text{pulse})$ , above this intensity it changes linearly with pump fluence. A linear dependence of phosphorescence intensity on pump light intensity up to  $150 \text{ }\mu\text{J}/(\text{cm}^2 \times \text{pulse})$  can be seen from Fig. 3.28, whereas for higher excitation intensities the phosphorescence intensity shows a square-root increase. From the data in Fig. 3.28 it can be concluded that the DF is caused by TTA. The deviation of the DF from the quadratic intensity dependence at higher pump intensities might be caused by the onset of singlet-singlet annihilation, thus reducing the number of triplets generated at high intensities [142]. In frozen solution a quadratic dependence of DF on excitation intensity has been observed for MeLPPP [144] and PhPPV [113] as well, and was shown to be the signature of occurrence of TTA. The situation in thin films of conjugated polymers is more complicated than in frozen solution, where the chains are supposed to be isolated. Whereas in molecular crystals the DF is entirely due to TTA, a study of DF in polyvinylcarbazole showed that in this material the recombination of geminate electron-hole pairs is important as a source of DF as well (see Section 3.3.2) [155]. In films of

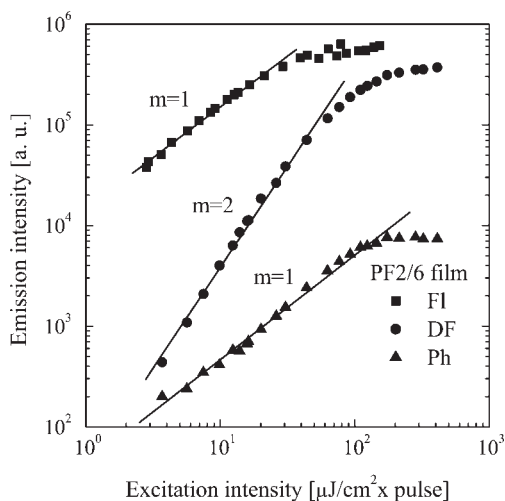




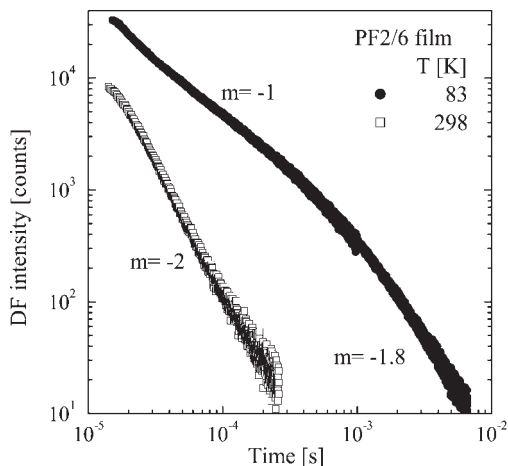
**Fig. 3.28** Dependence of fluorescence, delayed fluorescence and phosphorescence intensity of PF2/6 in MTHF on pump intensity at 80 K. The time delay for measurements of DF and Ph was 1  $\mu$ s. Excitation was at 3.05 eV. Reprinted from [142], copyright 2002, with permission from the American Institute of Physics.

MeLPPP the recombination of geminate pairs is the main source for DF [7, 94], although it is caused by TTA in solution. This was concluded from combined evidence of DF decay with time and the reduction of DF upon applying an electric field [94, 112]. The DF intensity in MeLPPP films decays with time as  $I(\text{DF}) \sim t^{-1}$ . The algebraic decay law of DF can be rationalized in terms of previous Monte Carlo simulations of GP recombination in random solids [114]. In that work the hopping-type random walk of an electron generated at a distance  $r_0$  away from a stationary positive charge was considered. The simulation system was a regular cubic lattice where the energies were taken from a Gaussian distribution with a variance of 100 meV. Parameters were the initial GP distance, the electronic intersite coupling and the temperature. The simulated quantities were the survival probability of the electron and the monomolecular recombination rate as a function of time normalized to the intersite jump time in a system without disorder. It turned out that the survival probability is a smoothly decay function of time. At 120 K and an intrapair distance of three lattice constants (1.8 nm) some 10 per cent of the pairs survive for more than 12 orders of magnitude in time. The recombination rate obeys a  $\propto t^{-1.3}$  law for short times and approaches a  $\propto t^{-1}$  law in the long time limit, the functional decay being virtually independent on the choice of parameters. The qualitative explanation is that those pairs that are generated at favorable hopping sites recombine quickly but the rest relaxes towards metastable tail states of the density of states from which escape is kinetically impeded. The experimental data on DF from a MeLPPP film are in full agreement with the simulation. The response of DF to an applied electric field is an order of magnitude effect, since geminate pairs are more liable to dissociate than singlet or even triplet excitons. On the basis of DF experiments of a PhPPV film in an electric field geminate-pair recombination was recognized as the main source of DF [113]. Compelling evidence for this conclusion was established using thermally stimulated luminescence experiments [110, 156].

However, the DF in PF2/6 is caused by TTA rather than geminate-pair recombination. This can be shown from the dependence of DF intensity on excitation intensity in Fig. 3.29. At low to moderate pump fluences the fluorescence as well as the phosphorescence intensity increase linearly with light flux until saturation occurs. The DF varies quadratically with laser power until saturation is observed as was the case in the PF2/6 solution (Fig. 3.28). The reason for the saturation of prompt fluorescence with excitation intensity is the dominance of singlet-singlet annihilation at higher pump fluence for the deactivation of the singlet state leading to a sublinear intensity dependence of phosphorescence accordingly. Further proof for TTA as the source of DF in films of PF2/6 comes from the time dependence of DF intensity (Fig. 3.30). The decay of DF proportional to  $t^{-2}$  is in accordance with Eq. (3.22) but limited to room temperature. One has to remember that Eq. (3.22) is only valid for the case of molecular crystals. In amorphous systems the situation is more complicated due to the influence of energetic and positional disorder on migration of excitations. In amorphous systems disorder is evidenced by inhomogeneous line broadening in absorption, fluorescence and phosphorescence spectra. Its effect on excitation transport has been extensively studied theoretically by Monte-Carlo simulation (MC) techniques [157] and analytic theory using the effective medium approximation (EMA) [69]. Although the majority of studies has been devoted to the transport of charges, migration of triplet excitons is virtually identical since intersite coupling is mediated by exchange interaction as well. Unfortunately, only the triplet exciton transport is amenable to spectroscopic probing. The elementary step of incoherent transport occurs via hopping from site  $\varepsilon_i$  to site  $\varepsilon_j$  described by the Miller–Abrahams equation [158]:



**Fig. 3.29** Dependence of fluorescence, delayed fluorescence and phosphorescence intensity of a PF2/6 film on pump intensity at 80 K. The time delay for measurements of DF and Ph was 1  $\mu$ s. The photon energy for optical excitation was 3.49 eV. Reprinted from [142], copyright 2002, with permission from the American Institute of Physics.



**Fig. 3.30** Delayed fluorescence intensity vs. time of a PF2/6 film at 83 K and 298 K. Excitation was at 3.49 eV. Reprinted from [142], copyright 2002, with permission from the American Institute of Physics.

$$\nu_{ij} = \begin{cases} \nu_0 \exp(-2\alpha R_{ij}) \exp - \left[ \frac{\varepsilon_j - \varepsilon_i}{kT} \right], & \varepsilon_j > \varepsilon_i \\ \nu_0 \exp(-2\alpha R_{ij}), & \varepsilon_j \leq \varepsilon_i \end{cases} \quad (3.24)$$

where  $\nu_{ij}$  is the hopping frequency,  $\nu_0$  the attempt-to-escape frequency, being on the order of a typical phonon frequency  $\sim 10^{-12} \text{ s}^{-1}$ .  $R$  is the distance between sites and  $\alpha$  is the inverse wave function localization radius.

In amorphous organic materials the site energies are modulated by fluctuations of van der Waals interactions of the excitations with its surrounding molecules. The density of states (DOS) consists of localized states and is best described by a Gaussian distribution with width  $\sigma$  and energy  $\varepsilon$  relative to the center of the DOS as:

$$\rho(\varepsilon) = (2 \Pi \sigma)^{-1/2} \exp - \left( \frac{\varepsilon^2}{2\sigma^2} \right) \quad (3.25)$$

Typical values for the energetic disorder characterized by the parameter  $\sigma$  are on the order of 50 to 100 meV in conjugated polymers. If an excitation is initially created at random within the DOS it will relax down in energy until dynamic equilibrium is reached, provided that the lifetime of the excitation is long enough. An inevitable consequence of this type of electronic relaxation is spectral diffusion and, most importantly, dispersion of excitation transport. According to MC simulation and EMA theory the excitation relaxation features a logarithmic decay law  $\varepsilon \sim \ln t$  with a characteristic energy-dependent waiting time before relaxation sets in [73, 159, 160, 161, 162]. The logarithmic decay law is a consequence of the shape of the density of states because the number of sites in a Gaussian-shaped DOS decreases rapidly in the tail states. Thus the number of sites available for energy relaxation without thermal activation decreases as well. Therefore the energy at which dynamic equilibrium is attained is dictated by the interplay of disorder and available thermal activation. For a Gaussian DOS the excitations tend to

settle at an energy  $\varepsilon_\infty = -\sigma^2/kT$  below the center of the DOS [157]. For strong disorder or very low temperature dynamic equilibrium will not be attained since  $\varepsilon_\infty$  is too far from the center of the DOS. Thus triplet excitons become immobilized in the very tail states of the DOS. As long as the excitation is close to the center of the DOS the relaxation proceeds fast before it is slowed down in the tail states of the DOS. This phenomenon causes dispersion of jump rates. Therefore the exciton diffusion “constant”  $D$  is no longer a constant but becomes time dependent as does the bimolecular reaction constant  $\gamma_{\text{TTA}}$  of triplets, because both quantities are related via:

$$\gamma_{\text{TTA}} = 8\pi DfR \quad (3.26)$$

$R$  being the interaction distance and  $f$  the fraction of encounters that lead to generation of singlets. Thus time-dependent diffusion renders  $\gamma_{\text{TTA}}$  also time dependent. The time dependence of diffusivity and  $\gamma_{\text{TTA}}$  are related to the hopping frequency via [159]:

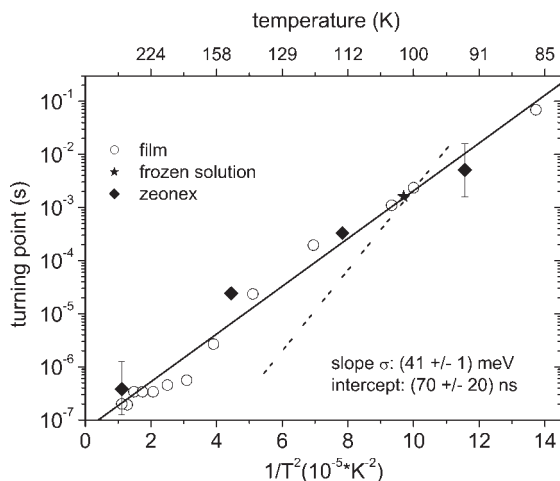
$$D(t) \sim \gamma_{\text{TTA}}(t) \sim \nu(t) \sim \frac{1}{t \ln(\nu_0 t)} \quad (3.27)$$

In the long time limit Eq. (3.27) can be approximated by  $\gamma_{\text{TTA}} \sim t^{1.04}$  [114]. This has been verified experimentally in a polyfluorene derivative [163]. In this study the DF as well as the triplet concentration was monitored as a function of time and temperature to investigate the influence of dispersion on triplet-triplet annihilation. Since the attainment of dynamic equilibrium of triplet relaxation is temperature and time dependent it can be monitored via time resolved detection of DF. According to theory [164] and MC simulation [165] the time  $t_s$  where the dispersive to nondispersive transition of relaxation occurs, is given by:

$$t_s = t_0 \exp - \left( \frac{c\sigma}{kT} \right)^2 \quad (3.28)$$

where  $c$  is an empirical constant depending on the dimensionality of the system. According to recent Monte Carlo simulations on transport on a one-dimensional chain [166] the coefficient  $c$  is close to 0.9. The inverse quadratic temperature dependence is a consequence of the Gaussian-shaped DOS, because the relaxation energy is itself temperature dependent (see above) and the elementary hopping step is thermal activated as well.  $t_0$  is the dwell time of the triplet exciton in a system without disorder. It is related to the attempt-to-escape frequency and wave function localization radius [161]. Following the above framework the power law decay of DF,  $\text{DF} \sim t^{-1}$ , in the PF2/6 film (Fig. 3.30) reflects the influence of dispersion on  $\gamma_{\text{TTA}}$  [142]. The turnover of DF decay to  $\text{DF} \sim t^{-2}$  is the signature of dynamic equilibrium in the transport of triplets.

Quantitative agreement between theoretical predictions of triplet migration in disordered solids and experiment was shown for an end-capped PF2/6 derivative [163]. The time-resolved DF of end-capped PF2/6 was investigated in the form of dense solid films, in dilute frozen solution and in an inert matrix polymer (zeo-



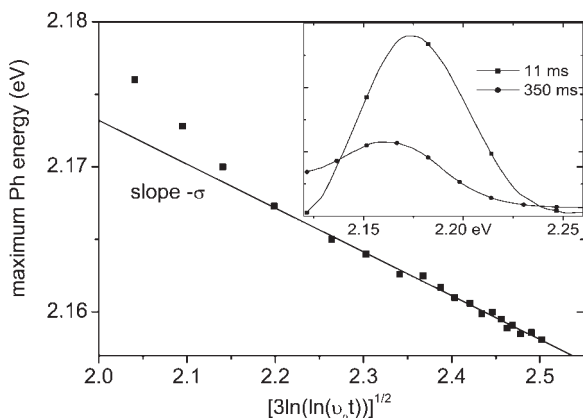
**Fig. 3.31** Turning point  $t_s$  as defined in Eq. (3.28) as a function of inverse squared temperature. Turning points were derived from DF decay vs. time of a polyfluorene PF2/6 derivative at different temperatures. The dashed line corresponds to data obtained with PF2/6 in frozen solution [142]. Reprinted with permission from [163]. Copyright 2003 by the American Physical Society.

nex). In all cases the DF decays according to a power law  $DF \sim t^{-n}$  with an exponent of  $n \sim 1$  in the dispersive regime and  $n \sim 2$  in the nondispersive regime. The turnover at  $t_s$  occurs faster as the temperature increases but is independent of the preparation method mentioned above. A plot of  $\log t_s$ , associated with the establishment of quasiequilibrium, is shown in Fig. 3.31 as function of reciprocal quadratic temperature. Fitting the data according to Eq. (3.28) yields a minimal dwell time of 70 ns. This value is in good agreement with the hopping time of triplets in benzophenone [161]. The slope yields a width of the DOS  $\sigma$  of 41 meV assuming  $c = 0.9$ , i.e. a one-dimensional relaxation process indicating that triplet diffusion is confined to a single chain. The width of the DOS can be obtained independently from the analysis of the band shape of the  $T_1 \rightarrow S_0$  transition in the low-temperature phosphorescence spectrum. The full width at half maximum (FWHM) of the 0–0 band of the 15 K phosphorescence spectrum is 61 meV, i.e. a variance of 26 meV [163]. Under the experimental conditions  $\sigma/kT > 20$  corresponding to strong disorder this value is not identical to the DOS distribution since the variance of the occupational DOS narrows in course of spectral diffusion. MC simulations indicated [167] that in the strong disorder case the variance of the occupied DOS distribution has narrowed to 70 % of its initial value. This yields  $\sigma \sim 30$  meV for the width of the DOS in good agreement with the value derived from Eq. (3.28). As mentioned above the energy relaxation follows a logarithmic decay law. In the long time limit at zero temperature  $T \rightarrow 0$  it adopts the form of [114, 159, 161]:

$$\varepsilon_\infty \sim \sigma \sqrt{3(\ln(\ln \nu_0 t))} \quad (3.29)$$

Under such conditions energy relaxation is slowed down because no thermal energy is available for excitons that are trapped and equilibrium cannot be attained (“frustrated energy relaxation”). Therefore the energy shift of phosphorescence

**Fig. 3.32** Maximum of the  $T_1 \rightarrow S_0$  0–0 transition of a polyfluorene PF2/6 derivative vs. time according to Eq. (3.29). Data points were derived from Gaussian fits to the 15 K phosphorescence spectrum. Reprinted with permission from [163]. Copyright 2003 by the American Physical Society.



spectra reflecting spectral diffusion should only be small at long times, since most relaxation proceeds at early times. The migration of triplets in benzophenone is in excellent agreement with these theoretical predictions [161]. To further show that energy relaxation in conjugated polymers in the strong-disorder case follows the same pattern one can plot the maximum energy of the  $T_1 \rightarrow S_0$  0–0 transition as function of time in the form of Eq. (3.29), using  $\nu_0$  as an adjustable parameter. This is illustrated in Fig. 3.32 for the PF2/6 derivative. The agreement between theory and experiment is very good. The center of the DOS for triplet excitations obtained from the fit is 2.26 eV, which is a reasonable value.

In the above study it could be shown that the relaxation of triplets in conjugated polymers is in *quantitative* agreement with predictions based on the concept of random walk in a disordered solid. Meanwhile, this theoretical framework for the description of migration of triplets in disordered solids has been applied to PFO (polyfluorene with octyl side chains) [168] as well. PFO contains liquid crystalline domains in the polymer that leads to the formation of highly ordered domains ( $\beta$  phase). This  $\beta$  phase plays an essential role in the photophysics of this polymer, notably on triplet migration.

### 3.5

#### Résumé

A central aspect of research into photophysics of luminescent conjugated polymers deals with the dynamics of singlet and triplet excitations. This is the topic of this chapter. The singlet excitation is the elementary excitation generated when a conjugated polymer absorbs a photon. This process is associated with an oscillator strength of roughly unity, which is characteristic of a dipole-allowed transition in a  $\pi$ -bonded large organic molecule. The onset of absorption, sometimes called the optical gap, is a purely electronic  $S_1 \leftarrow S_0$  0–0 transition in the terminology of molecular spectroscopy. At higher photon energies the electronic

transition couples with molecular vibrations forming a Franck–Condon state. The excess vibrational energy is funnelled into the vibrational heat bath of the chromophores and is dissipated on a time scale of less than 100 fs. Subsequently, a vibrationally cold singlet state can decay by (i) spontaneously emitting a fluorescence quantum, (ii) stimulated emission above a critical intensity, (iii) intersystem crossing to the triplet manifold, (iv) energy transfer to like or unlike chromophores, (v) undergo a photophysical reaction such as formation of an excimer, (vi) dissociation into a electron–hole pair, and (vii) radiationless decay to the ground state. A complementary way to generate both singlet and triplet excitations is by recombination of an electron and a hole, for instance, injected from electrodes.

A process that is specific for amorphous conjugated polymers and, more generally, for molecular glasses or molecularly doped polymers, is incoherent energy transfer among the manifold of donor chromophores, inevitably associated by spectral relaxation (spectral diffusion) of an excitation of either singlet or triplet character. The latter originates from inhomogeneous broadening of the transition energy of chromophores caused by random interchromophore packing and/or by local differences between the transition energies of more ordered subunits of a polymer chain comprising different repeat units. It causes both spectral broadening and the appearance of a Stokes shift between the electronic origin of absorption and emission unless fluorescence spectroscopy is performed under site-selective conditions. By the same token the efficiency of energy transfer decreases in time. The effect of spectral fluorescence broadening can profitably be used for extending the spectral emission range of organic LEDs into the entire visible spectrum. This requires chromophore blending or the use of copolymers.

A measure of the degree of disorder stored in a conjugated polymer below the glass transition temperature is the spectral width of the  $S_1 \leftarrow S_0$  0–0 transition in absorption. It contains intra as well as interchain contributions. Since both singlet and triplet excitations are coulombically bound electron–hole pairs with rms intra-pair distance,  $r_{eh}$ , typically 1 nm only, they are delocalized within ordered chain segments that are appreciably longer than  $r_{eh}$ , i.e. typically 5 to 6 nm. This leads to some motional narrowing of the intrachain contribution of the disorder potential an excitation experiences. The dominant disorder contribution is, therefore the variation of the length of the ordered chain segments that translates into inhomogeneous broadening of the  $S_1 \leftarrow S_0$  0–0 transition. Stiffening of the polymer backbone via covalent bridging, as in the ladder-type poly-phenylenes, as well as side-group-induced ordering within a given chain reduces this type of disorder as evidenced by the appearance of vibrational splitting within the  $S_1 \leftarrow S_0$  absorption spectrum.

An often harmful effect in conjugated polymers is aggregation via locally enhanced interchain interaction. It depresses the excited-state energy in the dimer/aggregate. If the oscillator strength of the lowest transition is lower than average this causes a prolongation of the fluorescence lifetime and, since nonradiative channels are not affected, a decrease of the fluorescence efficiency that is detrimental for OLEDs.

Optical generation of triplet excitations is via intersystem crossing from the  $S_1$  state. The intrinsic triplet lifetime measured in matrix-isolated polymers is no different from that of a  $\pi$ -bonded oligomer. It reaches 1 s for a phosphorescent  $T_1 \rightarrow S_0$  0–0 transition of quantum energy  $\geq 2.0$  eV and decreases exponentially with decreasing  $T_1$ – $S_0$  splitting because of nonradiative decay becomes important as the number of molecular vibrations required to release the electronic energy decreases. At least near room temperature there is virtually no phosphorescence emission from conjugated polymer films. The reason is that, owing to their long intrinsic lifetime and their mobility, they are easily quenched by (i) bimolecular triplet fusion, (ii) residual oxygen or spurious oxidation products and, (iii) charge carriers present, i. e. in a LED. Triplet excitations migrate via exchange interaction as charge carriers do. For this reason the phenomenology of the hopping motion of both is analogous. The only way to harvest triplets produced via electron–hole recombination is to use triplet emitters with short radiative lifetimes that any nonradiative pathways are overcompensated.

To dissociate a vibrationally relaxed  $S_1$  excitation into a coulombically unbound electron and hole requires an extra energy of  $\geq 0.5$  eV. It can only occur in the presence of a strong electron accepting (or donating) dopant, a strong electric field ( $> 1$  MV/cm), or a metallic interface. Hot Franck–Condon states, generated by (i) one quantum absorption at a photon energy at least 1 eV above the  $S_1 \leftarrow S_0$  0–0 transition, (ii) two-photon absorption, or (iii) bimolecular exciton annihilation, can autoionize, quite similarly to how they do in conventional molecular crystals. However, photoionization will initially always create an intermediate coulombically bound electron–hole pair that can either recombine geminately or fully separate albeit with finite yield. To avoid geminate recombination is a challenge in the fabrication of efficient photovoltaic cells in which the primary dissociation process occurs at a donor–acceptor couple/interface.

### Acknowledgement

We would like to thank Prof. V. I. Arkhipov for stimulating discussions and the Fond der Chemischen Industrie for financial support.



## References

- 1 A. J. Heeger, S. Kivelson, J. R. Schrieffer, W. P. Su, *Rev. Mod. Phys.* **1988**, *60*, 781–850.
- 2 M. Pope, C. E. Swenberg, *Electronic Processes in Organic Crystals and Polymers* Oxford University Press, New York **1999**.
- 3 D. J. Pinner, R. H. Friend, N. Tessler, *J. Appl. Phys.* **1999**, *86*, 5116–5130.
- 4 J. Staudigel, M. Stössel, F. Steuber, J. Simmerer, *J. Appl. Phys.* **1999**, *86*, 3895–3910.
- 5 B. E. Kohler, *J. Chem. Phys.* **1988**, *88*, 2788–2792.
- 6 B. E. Kohler, C. Spangler, C. Westerfield, *J. Chem. Phys.* **1988**, *89*, 5422–5428.
- 7 Yu. V. Romanovskii, A. Gerhard, B. Schweitzer, U. Scherf, R. I. Personov, H. Bässler, *Phys. Rev. Lett.* **2000**, *84*, 1027–1030.
- 8 A. P. Monkman, H. D. Burrows, L. J. Hartwell, L. E. Horsburgh, I. Hamblett, S. Navaratnam, *Phys. Rev. Lett.* **2001**, *86*, 1358–1361.
- 9 A. Köhler, J. S. Wilson, R. H. Friend, M. K. Al-Suti, M. S. Khan, A. Gerhard, H. Bässler, *J. Chem. Phys.* **2002**, *116*, 9457–9463.
- 10 R. Kersting, U. Lemmer, M. Deussen, H. J. Bakker, R. F. Mahrt, H. Kurz, V. I. Arkhipov, H. Bässler, E. O. Göbel, *Phys. Rev. Lett.* **1994**, *73*, 1440–1443.
- 11 D. Hertel, E. V. Soh, H. Bässler, L. J. Rothberg, *Chem. Phys. Lett.* **2002**, *361*, 99–105.
- 12 G. Weiser, *Phys. Rev. B* **1992**, *45*, 14076–14085.
- 13 M. Rohlfling, S. G. Louie, *Phys. Rev. Lett.* **1999**, *82*, 1959–1962.
- 14 J. W. van der Horst, P. A. Bobbert, M. A. J. Michels, H. Bässler, *J. Chem. Phys.* **2001**, *114*, 6950–6957.
- 15 M. Deussen, H. Bässler, *Synth. Met.* **1993**, *54*, 49–55.
- 16 K. Fesser, A. R. Bishop, D. K. Campbell, *Phys. Rev. B* **1983**, *27*, 4804–4825.
- 17 S. Heun, R. F. Mahrt, A. Greiner, U. Lemmer, H. Bässler, D. A. Halliday, D. D. C. Bradley, P. L. Burn, A. B. Holmes, *J. Phys. Condens. Matter* **1993**, *5*, 247–260.
- 18 R. Österbacka, M. Wohlgenannt, M. Shkunov, D. Chinn, Z. V. Vardeny, *J. Chem. Phys.* **2003**, *118*, 8905–8916.
- 19 G. Lanzani, G. Cerullo, D. Polli, A. Gambetti, M. Zavelani-Rossi, C. Gadermaier, *phys. stat. sol. (a)*, **2004**, *201*, 1116–1131.
- 20 D. Hertel, S. Setayesh, H. G. Nothofer, U. Scherf, K. Müllen, H. Bässler, *Adv. Mater.* **2001**, *13*, 65–70.
- 21 H. Bässler, B. Schweitzer, *Acc. Chem. Res.* **1999**, *32*, 173–182.
- 22 A. Amirav, U. Even, J. Jortner, *J. Chem. Phys.* **1981**, *75*, 3770–3793.
- 23 R. I. Personov in *Spectroscopy and Excitation Dynamics in Condensed Molecular Systems* (Ed.: V. M. Agranovich, R. M. Hochstrasser), North Holland, Amsterdam **1983**, p. 555.
- 24 H. Bässler in *Electronic Materials: The Oligomer Approach*, (Ed.: K. Müllen, G. Wegner), Wiley-VCH, Weinheim **1998**, chapter 7.
- 25 O. Narwak, A. Gerhard, S. C. J. Meskers, S. Brocke, E. Thorn-Csanyi, H. Bässler, *Chem. Phys.* **2003**, *294*, 17–30.
- 26 O. Narwak, S. C. J. Meskers, R. Peetz, E. Thorn-Csanyi, H. Bässler, *Chem. Phys.* **2003**, *294*, 1–15.
- 27 J. Rissler, *Chem. Phys. Lett.* **2004**, *395*, 92–96.
- 28 J. Rissler, H. Bässler, F. Gebhard, P. Schwerdtfeger, *Phys. Rev. B* **2001**, *64*, 045122.
- 29 M. G. Harrison, S. Möller, G. Weiser, G. Urbasch, R. F. Mahrt, H. Bässler, U. Scherf, *Phys. Rev. B* **1999**, *60*, 8650–8658.
- 30 T.-Q. Nguyen, V. Doan, B. J. Schwartz, *J. Chem. Phys.* **1999**, *110*, 4068–4078.
- 31 I. D. W. Samuel, G. Rumbles, C. J. Collison, S. C. Moratti, A. B. Holmes, *Chem. Phys.* **1998**, *227*, 75–82.
- 32 M. Zheng, F. Bai, D. Zhu, *J. Photochem. Photobiol. A* **1998**, *116*, 143–145.
- 33 J. H. Hsu, W. S. Fann, P. H. Tsao, K. R. Chuang, *J. Phys. Chem. A* **1999**, *103*, 2375–2380.
- 34 G. H. Gelinck, J. M. Warman, E. G. J. Staring, *J. Chem. Phys.* **1996**, *100*, 5485–5491.

- 35 J. Cornil, D. A. dos Santos, X. Crispin, R. Silbey, J. L. Bredas, *J. Am. Chem. Soc.* **1998**, *120*, 1289–1299.
- 36 O. Narwak, Ph. D. Thesis, University of Hamburg, Germany, **2002**. Available from <http://www.sub.uni-hamburg.de/disse/781/dissertation.pdf>.
- 37 T. Kobayashi, *J-aggregates*, World Scientific, Singapore **1996**.
- 38 E. S. Manas, F. C. Spano, *J. Chem. Phys.* **1998**, *109*, 8087–8101.
- 39 S. Siddiqui, F. C. Spano, *Chem. Phys. Lett.* **1999**, *308*, 99–105.
- 40 F. C. Spano, S. Siddiqui, *Chem. Phys. Lett.* **1999**, *314*, 481–487.
- 41 F. C. Spano, *Chem. Phys. Lett.* **2000**, *331*, 7–13.
- 42 F. C. Spano, *Synth. Met.* **2001**, *116*, 339–342.
- 43 S. C. J. Meskers, R. A. J. Janssen, J. E. M. Haverkort, J. H. Wolter, *Chem. Phys.* **2000**, *260*, 415–439.
- 44 E. Peeters, A. Marcos Ramos, S. C. J. Meskers, R. A. J. Janssen, *J. Chem. Phys.* **2000**, *112*, 9445–9454.
- 45 E. Thorn-Csanyi, P. Kraxner, *Macromol. Rapid Commun.* **1998**, *19*, 223–228.
- 46 R. F. Mahrt, T. Pauck, U. Lemmer, U. Siegner, M. Hopmeier, R. Henning, H. Bässler, E. O. Göbel, P. Haring Bolivar, G. Wegmann, H. Kurz, U. Scherf, K. Müllen, *Phys. Rev. B* **1996**, *54*, 1759–1765.
- 47 J. B. Birks, *Photophysics of Aromatic Molecules*, Wiley Interscience, London **1969**.
- 48 H. Masuhara, N. Tamai, N. Ikeda, N. Mataga, A. Itaya, K. Okamoto, S. Kusabayashi, *Chem. Phys. Lett.* **1982**, *91*, 113–116.
- 49 W. Klöpffer, G. Rippen, J. Kowal, *Macromol. Chem. Macromol. Symp.* **1986**, *5*, 187–196.
- 50 I. D. W. Samuel, G. Rumbles, C. J. Collison, *Phys. Rev. B* **1995**, *52*, 11573–11576.
- 51 R. Jakubiak, C. J. Collison, W. C. Wan, L. J. Rothberg, B. R. Hsieh, B. R., *J. Phys. Chem. A* **1999**, *103*, 2394–2398.
- 52 C. J. Collison, L. J. Rothberg, V. Treemanekarn, Y. Li, *Macromolecules* **2001**, *34*, 2346–2352.
- 53 L. Romaner, A. Pogantsch, P. S. de Freitas, U. Scherf, M. Gaal, E. Zojer, E. J. W. List, *Adv. Funct. Mater.* **2003**, *13*, 597–601.
- 54 A. C. Morteani, A. S. Dhoot, J. S. Kim, C. Silva, N. C. Greenham, C. Murphy, E. Moons, S. Cina, J. H. Burroughes, R. H. Friend, *Adv. Mater.* **2003**, *15*, 1708.
- 55 A. C. Morteani, P. Sreearunothai, L. M. Herz, R. H. Friend, C. Silva, *Phys. Rev. Lett.* **2004**, *92*, 247402.
- 56 A. P. Kulkarni, X. Kong, S. A. Jenekhe, *J. Phys. Chem. B* **2004**, *108*, 8689–8701.
- 57 L. Kador, *J. Chem. Phys.* **1991**, *95*, 5574–5581.
- 58 W. E. Moerner, *Persistent Spectral Hole Burning. Science and Applications*, Springer Verlag, Heidelberg **1988**.
- 59 T. Pauck, H. Bässler, J. Grimme, U. Scherf, K. Müllen, *Chem. Phys.* **1996**, *210*, 219–227.
- 60 F. Milota, J. Sperling, V. Szoecs, A. Tortschanoff, H. K. Kauffmann, *J. Chem. Phys.* **2004**, *120*, 9870–9885.
- 61 Yu. V. Romanovskii, H. Bässler, U. Scherf, *Chem. Phys. Lett.* **2004**, *383*, 89–94.
- 62 T. Guillet, J. Berrehar, R. Grousson, J. Kovensky, C. Lapersonne-Meyer, M. Schott, V. Voliotis, *Phys. Rev. Lett.* **2001**, *87*, 087401.
- 63 F. Milota, J. Sperling, V. Szöcs, A. Tortschanoff, H. F. Kauffmann, *J. Chem. Phys.* **2004**, *120*, 9870–9885.
- 64 C. Im, unpublished results.
- 65 Yu. V. Romanovskii, unpublished results.
- 66 C. Im, J. Lupton, P. Schouwink, S. Heun, H. Becker, H. Bässler, *J. Chem. Phys.* **2002**, *117*, 1395–1402.
- 67 J. R. Morgan, M. A. El-Sayed, *J. Chem. Phys.* **1983**, *87*, 200–202; *ibid.* 2178–2185.
- 68 R. Richert, H. Bässler, *Chem. Phys. Lett.* **1985**, *118*, 235–239.
- 69 B. Movaghar, M. Grünewald, B. Ries, H. Bässler, D. Würtz, *Phys. Rev. B* **1986**, *33*, 5545–5554.
- 70 R. Kersting, U. Lemmer, R. F. Mahrt, K. Leo, H. Kurz, H. Bässler, E. O. Göbel, *Phys. Rev. Lett.* **1993**, *70*, 3820–3823.
- 71 B. Mollay, U. Lemmer, R. Kersting, R. F. Mahrt, H. Kurz, H. F. Kauffmann, H. Bässler, *Phys. Rev. B* **1994**, *50*, 10769–10779.
- 72 G. R. Hayes, I. D. W. Samuel, R. T. Phillips, *Phys. Rev. B* **1997**, *56*, 3838–3843.
- 73 S. C. J. Meskers, J. Hübner, M. Oestreich, H. Bässler, *Chem. Phys. Lett.* **2001**, *339*, 223–328.

- 74 S. C. J. Meskers, J. Hübner, M. Oestreich, H. Bässler, *J. Phys. Chem.* **2001**, *105*, 9139–9149.
- 75 J. Sperling, C. Benesch, L. Kuna, H. F. Kauffmann, F. Milota, *Synth. Met.* **2004**, *143*, 315–322.
- 76 S. H. Lim, T. G. Bjorklund, C. J. Bardeen, *Chem. Phys. Lett.* **2001**, *342*, 555–562.
- 77 T. G. Bjorklund, S. H. Lim, C. J. Bardeen, *J. Phys. Chem. B* **2001**, *105*, 11970–11977.
- 78 S. P. Kennedy, N. Garro, R. T. Phillips, *Phys. Rev. B* **2001**, *64*, 115206.
- 79 K. Brunner, A. Tortschanoff, C. Warmuth, H. Bässler, H. F. Kauffmann, *J. Phys. Chem. B* **2000**, *104*, 3781–3790.
- 80 C. Im, E. V. Emelianova, H. Bässler, H. Spreitzer, H. Becker, *J. Chem. Phys.* **2002**, *117*, 2961–2967.
- 81 A. Elschner, R. F. Mahrt, L. Pautmeier, H. Bässler, M. Stolka, K. McGrane, *Chem. Phys.* **1991**, *150*, 81–91.
- 82 V. I. Arkhipov, E. V. Emelianova, H. Bässler, *Phys. Rev. B* **2004**, *70*, 205205.
- 83 U. Lemmer, A. Ochse, M. Deussen, R. F. Mahrt, E. O. Göbel, H. Bässler, P. Haring Bolivar, G. Wegmann, H. Kurz, *Synth. Met.* **1996**, *78*, 289–293.
- 84 J. Klafter, A. Blumen, *Chem. Phys.* **1985**, *119*, 377.
- 85 H. Bässler in *Primary Photoexcitations in Conjugated Polymers: Molecular Exciton versus Semiconductor Band Model*, (Ed.: N. S. Sariciftci), World Scientific, Singapore **1997**.
- 86 V. I. Arkhipov, H. Bässler, *phys. stat. sol. (a)* **2004**, *201*, 1152–1187.
- 87 A. J. Heeger in *Primary Photoexcitations in Conjugated Polymers: Molecular Exciton versus Semiconductor Band Model*, (Ed.: N. S. Sariciftci), World Scientific, Singapore **1997**.
- 88 B. J. Mulder, *Philips Res. Supp.* **1968**, *4*, 1.
- 89 S. Barth, H. Bässler, U. Scherf, K. Müllen, *Chem. Phys. Lett.* **1998**, *288*, 147–154.
- 90 W. Graupner, G. Cerullo, G. Lanzani, M. Nisoli, E. W. List, G. Leising, S. De-Silvestri, *Phys. Rev. Lett.* **1998**, *81*, 3259–3262.
- 91 V. Gulbinas, Y. Zaushitsyn, V. Sundström, D. Hertel, H. Bässler, A. Yartsev, *Phys. Rev. Lett.* **2002**, *89*, 107401.
- 92 M. Deussen, M. Scheidler, H. Bässler, *Synth. Met.* **1995**, *73*, 123–129.
- 93 A. Haugeneder, M. Neges, C. Kallinger, W. Spirkel, U. Lemmer, J. Feldmann, M. C. Amann, U. Scherf, *J. Appl. Phys.* **1999**, *85*, 1124–1130.
- 94 D. Hertel, Yu. V. Romanovskii, B. Schweitzer, U. Scherf, H. Bässler, *Synth. Met.* **2001**, *116*, 139–143.
- 95 M. Chandross, S. Mazumdar, S. Jeglinski, X. Wie, Z. V. Vardeny, E. W. Kwock, T. M. Miller, *Phys. Rev. B* **1994**, *50*, 14702–14705.
- 96 A. Köhler, D. A. dos Santos, D. Beljonne, Z. Shuai, J. L. Bredas, A. B. Holmes, A. Kraus, K. Müllen, R. H. Friend, *Nature* **1998**, *392*, 903–906.
- 97 V. I. Arkhipov, E. V. Emelianova, S. Barth, H. Bässler, *Phys. Rev. B* **2000**, *61*, 8207–8214.
- 98 V. Gulbinas, Y. Zaushitsyn, H. Bässler, A. Yartsev, V. Sundström, *Phys. Rev. B* **2004**, *70*, 035215.
- 99 N. E. Geacintov, M. Pope, *J. Chem. Phys.* **1967**, *50*, 814.
- 100 C. Silva, A. S. Dhoot, D. M. Russell, M. A. Stevens, A. C. Arias, J. D. Mackenzie, N. Greenham, R. H. Friend, *Phys. Rev. B* **2001**, *64*, 125211.
- 101 C. Lüer, H. J. Egelhaaf, D. Oelkrug, C. Gadermaier, G. Cerullo, G. Lanzani, *Phys. Rev. B* **2003**, *68*, 155313.
- 102 M. A. Stevens, C. Silva, D. M. Russell, R. H. Friend, *Phys. Rev. B* **2001**, *63*, 165213.
- 103 J. G. Müller, U. Lemmer, J. Feldmann, U. Scherf, *Phys. Rev. Lett.* **2002**, *88*, 147401.
- 104 C. Gadermaier, G. Cerullo, G. Sansone, G. Leising, U. Scherf, G. Lanzani, *Phys. Rev. Lett.* **2002**, *89*, 117402.
- 105 H. Rohrbacher, N. Karl, *phys. stat. sol. (a)* **1975**, *29*, 517–527.
- 106 V. I. Arkhipov, E. V. Emelianova, H. Bässler, *Phys. Rev. Lett.* **1999**, *82*, 1321–1324.
- 107 D. M. Basko, E. M. Conwell, *Phys. Rev. B* **2002**, *66*, 155210.
- 108 L. Sebastian, G. Weiser, G. Peter, H. Bässler, *Chem. Phys.* **1983**, *75*, 103–114.
- 109 E. Frankevich, Y. Nishihara, A. Fuiji, M. Ozaki, K. Yoshino, *Phys. Rev. B* **2002**, *66*, 155203.
- 110 A. Kadashchuk, Yu. Sbryshevskii, A. Vakhnin, N. Ostapenko, V. I. Arkhipov, E. V. Emelianova, H. Bässler, *Phys. Rev. B* **2001**, *63*, 115205.

- 111 A. Kadashchuk, A. Vakhnin, I. Blonski, D. Beljonne, Z. Shuai, J. L. Bredas, V. I. Arkhipov, P. Heremans, E. V. Emelianova, H. Bässler, *Phys. Rev. Lett.* **2004**, 93, 066803.
- 112 B. Schweitzer, V. I. Arkhipov, U. Scherf, H. Bässler, *Chem. Phys. Lett.* **1999**, 313, 57–62.
- 113 A. Gerhard, H. Bässler, *J. Chem. Phys.* **2002**, 117, 7350–7356.
- 114 B. Ries, H. Bässler, *J. Mol. Electron.* **1987**, 3, 15–24.
- 115 A. Hayer, H. Bässler, B. Falk, S. Schrader, *J. Chem. Phys. A* **2002**, 106, 11045–11053.
- 116 E. Hendry, M. Koeberg, J. M. Schins, L. D. A. Siebbeles, M. Bonn, *Phys. Rev. B* **2004**, 70, 033202.
- 117 L. Onsager, *Phys. Rev.* **1938**, 54, 554.
- 118 C. Im, W. Tian, H. Bässler, A. Fechtenkötter, M. D. Watson, K. Müllen, *J. Chem. Phys.* **2003**, 119, 3952–3957.
- 119 U. Albrecht, H. Bässler, *Chem. Phys. Lett.* **1995**, 235, 389–393.
- 120 V. I. Arkhipov, E. V. Emelianova, H. Bässler, *Chem. Phys. Lett.* **2003**, 372, 886–892.
- 121 N. S. Sariciftci, A. J. Heeger, *Int. J. Mod. Phys. B* **1994**, 8, 237–274.
- 122 J. J. M. Halls, C. A. Walsh, N. C. Greenham, E. A. Marseglia, R. H. Friend, A. C. Moratti, A. B. Holmes, *Nature* **1995**, 376, 498–500.
- 123 D. M. Russell, A. C. Arias, R. H. Friend, C. Silva, C. Ego, A. C. Grimsdale, K. Müllen, *Appl. Phys. Lett.* **2002**, 80, 2204–2206.
- 124 S. C. Veenstra, H. F. Jonkman, *J. Polym. Sci. Polym. Phys.* **2003**, 41, 2549–2560.
- 125 T. Kietzke, D. Neher, K. Landfester, R. Montenegro, R. Güntner, U. Scherf, *Nature Materials* **2003**, 2, 408–U7.
- 126 A. C. Morteani, A. S. Dhoot, J. S. Kim, C. Silva, N. Greenham, C. Murphy, E. Moons, S. Cina, J. H. Burroughes, R. H. Friend, *Adv. Mater.* **2003**, 15, 1708–1712.
- 127 V. I. Arkhipov, P. Heremans, H. Bässler, *J. Appl. Phys.* **2003**, 82, 4605–4607.
- 128 N. J. Turro, *Modern Molecular Photochemistry*, University Science Books, Sausalito, **1991**.
- 129 N. F. Colaneri, D. D. C. Bradley, R. H. Friend, P. L. Burn, A. B. Holmes, C. W. Spangler, *Phys. Rev. B* **1990**, 42, 11670–11681.
- 130 W. Graupner, S. Eder, K. Petritsch, G. Leising, U. Scherf, *Synth. Met.* **1997**, 84, 507–510.
- 131 M. Wohlgenannt, W. Graupner, G. Leising, Z. V. Vardeny, *Phys. Rev. B* **1999**, 60, 5321–5330.
- 132 E. J. W. List, C. H. Kim, A. K. Naik, U. Scherf, G. Leising, W. Graupner, J. Shinar, *Phys. Rev. B* **2001**, 64, 155204.
- 133 V. Dyakonov, G. Rösler, M. Schwörer, E. L. Frankevich, *Phys. Rev. B* **1997**, 56, 3852–3862.
- 134 P. A. Lane, S. V. Frolov, Z. V. Vardeny in *Semiconducting Polymers*, (Ed.: G. Hadziioannou, P. F. van Hutten), WILEY-VCH, Weinheim **2000**.
- 135 J. Partee, E. L. Frankevich, B. Uhlhorn, J. Shinar, Y. Ding, T. J. Barton, *Phys. Rev. Lett.* **1999**, 82, 3673–3676.
- 136 Yu. V. Romanovskii, A. Gerhard, B. Schweitzer, R. I. Personov, H. Bässler, *Chem. Phys.* **1999**, 249, 29–39.
- 137 A. P. Monkman, H. D. Burrows, I. Hamblett, S. Navaratnam, U. Scherf, C. Schmitt, *Chem. Phys. Lett.* **2000**, 327, 111–116.
- 138 A. P. Monkman, H. D. Burrows, I. Hamblett, S. Navaratnam, *Chem. Phys. Lett.* **2001**, 340, 467–472.
- 139 H. D. Burrows, J. S. de Melo, C. Serpa, L. G. Arnaut, A. P. Monkman, I. Hamblett, S. Navaratnam, *J. Chem. Phys.* **2001**, 115, 9601–9606.
- 140 J. M. Lupton, A. Pogantsch, T. Piok, E. J. W. List, S. Patil, U. Scherf, *Phys. Rev. Lett.* **2002**, 89, 167401.
- 141 M. Reufer, F. Schindler, S. Patil, U. Scherf, J. M. Lupton, *Chem. Phys. Lett.* **2003**, 381, 60–66.
- 142 D. Hertel, R. Guentner, U. Scherf, H. Bässler, *J. Chem. Phys.* **2001**, 115, 10007–10013.
- 143 C. Rothe, R. Guentner, U. Scherf, A. P. Monkman, *J. Chem. Phys.* **2001**, 115, 9557–9562.
- 144 Yu. V. Romanovskii, H. Bässler, *Chem. Phys. Lett.* **2000**, 326, 51–57.
- 145 *Electronic Materials: The Oligomer Approach*, (Ed.: K. Müllen und G. Wegner), Wiley-VCH Weinheim **1998**.
- 146 D. Beljonne, Z. Shuai, R. H. Friend, J. L. Brédas, *J. Chem. Phys.* **1995**, 102, 2042–2049.

- 147 N. Chawdhury, A. Köhler, R. H. Friend, W.-Y. Wong, J. Lewis, M. Younus, P. R. Raithby, T. C. Corcoran, M. R. A. Al-Mandhary, M. S. Khan, *J. Chem. Phys.* **1999**, *110*, 4963–4970.
- 148 A. Köhler, D. Beljonne, *Adv. Funct. Mater.* **2004**, *14*, 11–18.
- 149 J. S. Wilson, A. Köhler, R. H. Friend, M. K. Al-Suti, M. R. A. Al-Mandhary, M. S. Khan, P. R. Raithby, *J. Chem. Phys.* **2000**, *113*, 7627–7634.
- 150 N. Chawdhury, A. Köhler, R. H. Friend, M. Younus, P. R. Raithby, J. Lewis, *Macromolecules* **1998**, *31*, 722–727.
- 151 F. Laquai, C. Im, A. Kadashchuk, H. Bässler, *Chem. Phys. Lett.* **2003**, *375*, 286–291.
- 152 A. P. Monkman, H. D. Burrows, G. Miguel, I. Hamblett, S. Navaratnam, *Chem. Phys. Lett.* **1999**, *307*, 303–309.
- 153 A. S. Dhoot, D. S. Ginger, D. Beljonne, Z. Shuai, N. C. Greenham, *Chem. Phys. Lett.* **2002**, *360*, 195–201.
- 154 M. A. Baldo, M. E. Thompson, S. R. Forrest, *Nature* **2000**, *403*, 750–753.
- 155 F. Stolzenburg, H. Bässler, *Mol. Cryst. Liq. Cryst.* **1989**, *75*, 147–158.
- 156 A. Kadashchuk, Y. Skryshevski, Y. Piryatinski, A. Vakhnin, E. V. Emelianova, V. I. Arkhipov, H. Bässler, J. Shinar, *J. Appl. Phys.* **2002**, *91*, 5016–5023.
- 157 H. Bässler, *phys. stat. sol. (b)* **1993**, *175*, 15–56.
- 158 A. Miller, E. Abrahams, *Phys. Rev.* **1960**, *120*, 745–755.
- 159 B. Movaghar, B. Ries, M. Grünewald, *Phys. Rev. B* **1986**, *34*, 5574–5582.
- 160 B. Ries, H. Bassler, M. Grunewald, B. Movaghar, *Phys. Rev. B* **1988**, *37*, 5508–5517.
- 161 R. Richert, H. Bässler, B. Ries, B. Movaghar, M. Grünewald, *Philos. Mag. Lett.* **1989**, *59*, 95–102.
- 162 B. Movaghar, B. Ries, M. Grünewald, *Phys. Rev. B* **1986**, *34*, 5574–5582.
- 163 C. Rothe, A. P. Monkman, *Phys. Rev. B* **2003**, *68*, 075208.
- 164 M. Grünewald, B. Pohlmann, B. Movaghar, D. Würtz, *Philos. Mag. B* **1984**, *49*, 341–356.
- 165 M. Scheidler, B. Cleve, H. Bässler, P. Thomas, *Chem. Phys. Lett.* **1994**, *225*, 431–436.
- 166 K. Kohary, H. Cordes, S. D. Baranovskii, P. Thomas, S. Yamasaki, F. Hensel, J.-H. Wendorff, *Phys. Rev. B* **2001**, *63*, 094202.
- 167 G. Schönherr, H. Bässler, M. Silver, *Philos. Mag. B* **1981**, *44*, 369–381.
- 168 C. Rothe, S. M. King, F. Dias, A. P. Monkman, *Phys. Rev. B* **2004**, *70*, 195213.

## 4

## Polymer-Based Light-Emitting Diodes (PLEDs) and Displays Fabricated from Arrays of PLEDs

Xiong Gong, Daniel Moses and Alan J. Heeger\*

## 4.1

### Introduction

Semiconducting (conjugated) polymers are important as the active materials in a new generation of electronic and optical devices, including polymeric light-emitting diodes (PLEDs), photodetectors, photovoltaic cells, sensors, field effect transistors, and optical amplifiers/lasers [1–6]. Research carried out over the last decade has demonstrated the commercial opportunities associated with implementation of PLEDs in passive and active matrix displays. As a result, the development of PLEDs that show efficient, stable blue, green, and red emission is an active ongoing research effort in laboratories in Europe, Asia and the United States [7–11].

PLEDs that emit white light are of interest and potential importance for use as backlights in high-efficiency active matrix displays (with color filters) and because they might eventually be used for solid-state lighting. The development of large-area PLEDs that emit stable white light and that can be fabricated using low-cost solution processing will be of major importance to future solid-state lighting.

The purpose of this chapter is to summarize concepts and progress in the field of PLEDs. This review is organized as follows: Section 4.2 describes light-emitting diodes, LEDs, fabricated from semiconducting polymers (PLEDs). Following the discussion of the methods for accurate measurement of performance parameters of PLEDs (and OLEDs based on small molecules) in Section 4.3, we discuss the Fowler–Nordheim mechanism for carrier injection and the basic PLED operating mechanism in Section 4.4. Various approaches toward improvement of carrier injection and carrier balance are described in Section 4.5. Section 4.6 summarizes the progress on pixilated displays, both passively addressed displays and active matrix displays. After discussion of the limits on the electroluminescence efficiency in Section 4.7, recent progress on white-light emission from PLEDs in our labs at UCSB is summarized in Section 4.8. We conclude with a short summary of the remaining challenges.

## 4.2

## LEDs Fabricated from Semiconducting Polymers

Conventional light-emitting diodes (LEDs) are made of direct band gap inorganic crystals (e.g., GaAs or GaN). Although LEDs made from inorganic crystals work remarkably well for many applications, they are not well suited for applications that require large areas, arrays of different colored LEDs, or mechanical flexibility; crystals are brittle and must be grown by expensive epitaxial methods such as molecular beam epitaxy or chemical vapor deposition. LEDs fabricated from semiconducting polymers are therefore attractive because they can be easily patterned in large areas onto almost any type of substrate, they can emit a range of colors that span the entire visible spectrum, and they are flexible [12, 13].

Fig. 4.1 shows a schematic of the structure of a polymer LED. A photo of a thin-film flexible seven-segment display fabricated from a semiconducting polymer is shown in Fig. 4.2. The bottom electrode (the anode) of this flexible display was made by spin-casting a layer of metallic polyaniline onto a flexible plastic substrate [12].

For the demonstration device in Fig. 4.2, polyaniline was chosen as the anode material because it is flexible, conducts current, and is transparent to visible light (there is no indium-tin-oxide (ITO) layer in the device of Fig. 4.2). More generally,

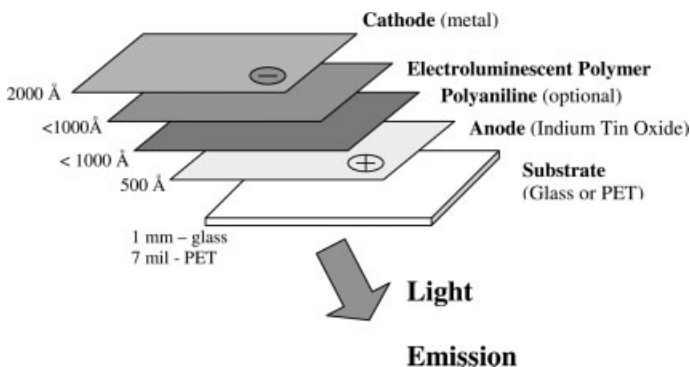


Fig. 4.1 Device structure of an LED fabricated from semiconducting and metallic polymers.



Fig. 4.2 Photo of a thin-film flexible seven-segment display fabricated from semiconducting and metallic polymers.

however, a bilayer electrode comprising a thin layer of metallic polymer cast onto ITO is used for the anode; the ITO carries the current and the metallic polymer layer serves to planarize the ITO and to improve the injection of holes into the luminescent semiconducting polymer. The emissive layer of the display shown in Fig. 4.2 was formed by spin casting a layer of MEH-PPV (poly(2-methoxy-5-(2-ethylhexyloxy)-1,4-phenylenevinylene) over the polyaniline. The top electrodes that define the seven-segment display were formed by evaporating calcium through a patterned shadow mask. Because of the low conductivity of undoped emissive polymers, it was not necessary to pattern the polymer or the bottom electrode to prevent current spreading between neighboring pixels.

Semiconducting polymers have been synthesized with different molecular structures and with an associated wide range of energy gaps. Consequently luminescent semiconducting polymers can be obtained with emission colors that span the full range of the visible spectrum. Side-chain functionalization of the same main chain (e.g. with alkoxy or alkyl groups) can be used to shift the color of the emitted light over a substantial portion of the visible spectrum. The use of synthesis to create homopolymers with different molecular structures and to create copolymers is the “band gap engineering” methodology for semiconducting polymers. Fig. 4.3 shows a few examples that demonstrate the range of different band gaps and emission colors that can be obtained through band gap engineering. The use of copolymers is particularly interesting. By using block-copolymers, well-defined quantum-well structures can be created.

Concentration quenching is not a major problem in semiconducting polymers. Typically, the quantum efficiency for photoluminescence from thin films is comparable to that from dilute solutions. The absence of strong concentration quenching is the result of the spatial delocalization of the excited states. Because the weakly bound excitons are spread over many repeat units, the Davydov splitting that results from interchain interactions is small. As a result, the disorder that is present in films cast from solution is sufficiently large to mix the “dark” and emissive Davydov-split states. Thus, quantum efficiencies in excess of 60–70 % can be obtained from thin solid films of luminescent semiconducting polymers.



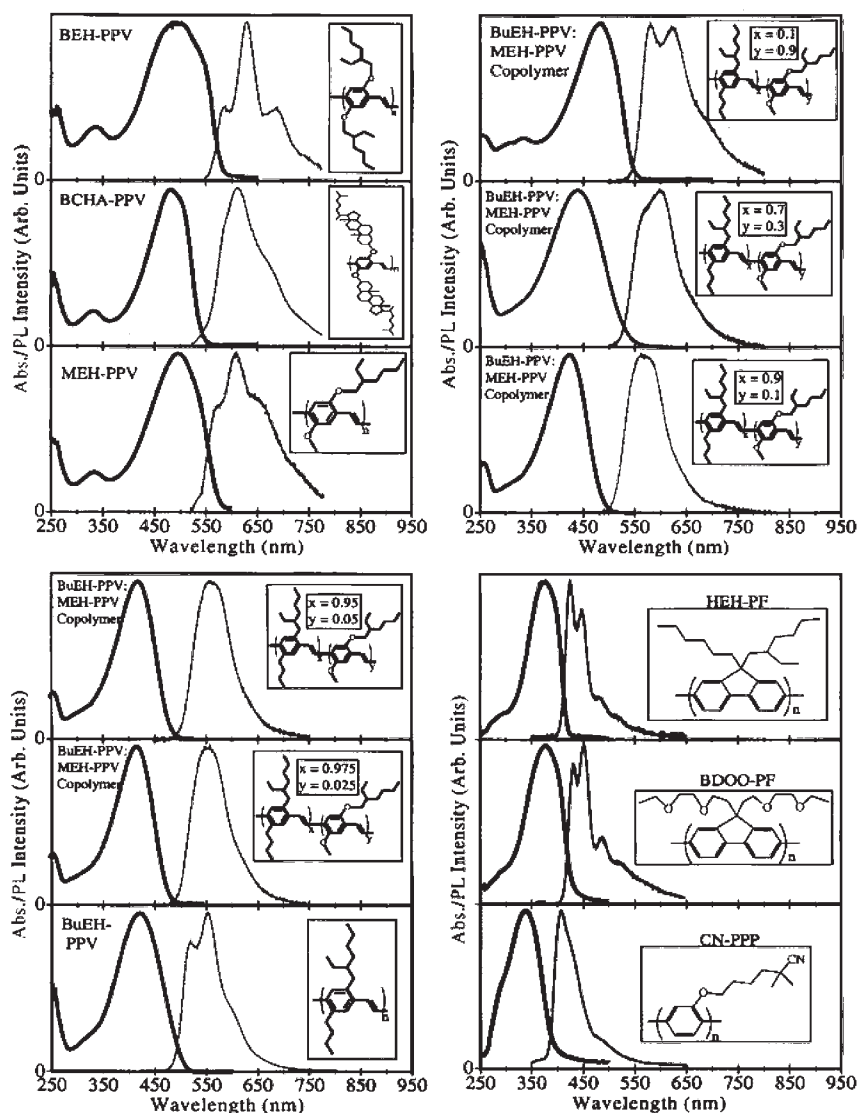


Fig. 4.3 Absorption and emission spectra of a number of semiconducting polymers with different molecular structures. The emission colors span the visible spectrum.

### 4.3

#### Accurate Measurement of OLED/PLED Device Parameters

A prime concern of the OLED/PLED community is the level of uncertainty and inconsistency of results found in published scientific literature. Here, we summarize an accurate method for measurement of OLED/PLED optical properties.

In addition to transmittance, absorbance, and color temperature, light is described by the following [14]:

Flux	the total luminous power (measured in lumens)
Intensity	the angular concentration of flux (candelas)
Illuminance	the surface density of incident flux (lux or lumen/m <sup>2</sup> )
Luminance	the intensity emitted per unit area (candelas/m <sup>2</sup> )

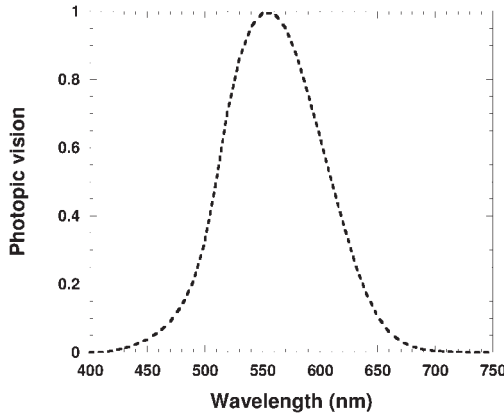
Table 4.I summarizes the various quantities, their units and the related measurement techniques.

Because the major application of OLEDs/PLEDs is for displays, the response of the human eye, described by the photopic luminosity function [15], must be taken into account. The photopic luminosity function is shown in Fig. 4.4. By using the photopic luminosity function, the radiance (watts/(sr m<sup>2</sup>)) is converted into the luminance (candela/m<sup>2</sup>, cd/m<sup>2</sup> or lumen/(sr m<sup>2</sup>)). Therefore, photometry is used to measure the forward viewing luminance at the surface of an OLED/PLED.

The luminous intensity (luminance) can be determined by measuring the flux in any given solid angle,  $\Omega$  (the ratio of the size of aperture divided by the square of the distance between the light and the aperture). Consider a flat emitting surface, each point of which emits light equally in all directions; i.e. a Lambertian source. A PLED/OLED is a Lambertian source if the luminous intensity follows

**Table 4.1** The quantity and unit of measurement.

Technique of measurement	Type of measurement	Quantity	Unit of measurement
Photometry	Total flux	Total luminous flux	lumens
Radiometry	Total flux	Total radiant flux	Watts
Spectroradiometry	Total flux	Total spectral flux	Watts/nm
Photometry	Angular intensity	Luminous intensity	candelas = lumen/sr
Radiometry	Angular intensity	Radiant intensity	Watts/sr
Spectroradiometry	Angular intensity	Spectroradiometric intensity	Watts/(sr nm)
Photometry	At a surface	Illuminance	Lux = lumen/m <sup>2</sup>
Radiometry	At a surface	Irradiance	Watts/m <sup>2</sup>
Spectroradiometry	At a surface	Spectral irradiance	Watts/(m <sup>2</sup> nm)
Photometry	At a surface	Luminance	candelas/m <sup>2</sup>
Radiometry	At a surface	Radiance	Watts/(sr m <sup>2</sup> )
Spectroradiometry	At a surface	Spectral radiance	Watts/(sr m <sup>2</sup> nm)



**Fig. 4.4** The photopic luminosity function.

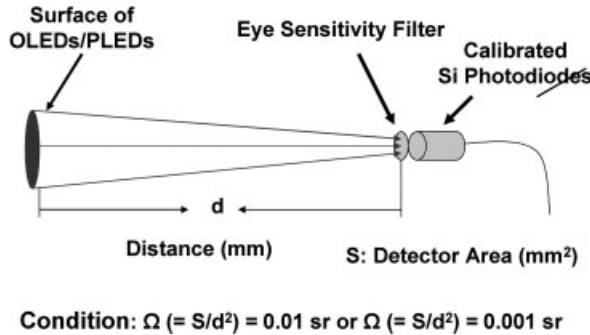
the cosine law when measured with a small-area detector placed far away from the surface (very small  $\Omega$ , see below) [16]. We will assume that for PLEDs/OLEDs, deviations from Lambertian emission are relatively small.

To measure the luminous intensity one must first choose a reference direction for the measurements, and one must then determine the solid angle to be used in the measurement. For display applications, the reference direction should be chosen as the forward viewing direction (along the direction perpendicular to the surface of the OLED/PLED). The luminous intensity is defined as the emission in  $\text{cd/m}^2$  from the emitting surface.

An accurate and convenient configuration for measuring luminous efficiency from OLEDs/PLEDs is shown in Fig. 4.5. Because the luminous efficiency strongly depends on the OLED/PLED emission spectrum (even for constant quantum efficiency), an eye-sensitivity filter is mounted directly onto the surface of the calibrated photodiode (see Fig. 4.4) [15].

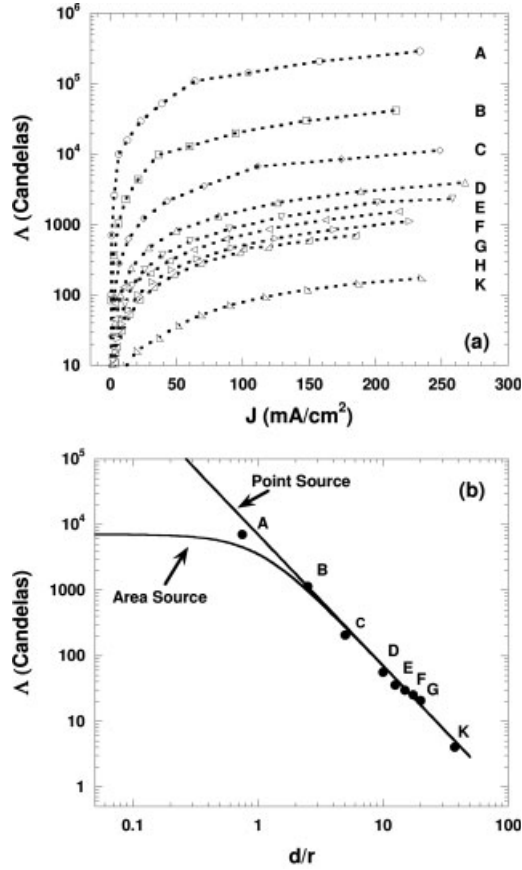
Assuming a Lambertian intensity profile and a disc-shaped source with radius  $r$ , the light intensity on a point detector placed a distance  $d$  away (see Fig. 4.5) can be expressed as follows [17, 18]:

$$I = I_0 (r^2 / r^2 + d^2) \quad (4.1)$$



**Fig. 4.5** Configuration for measuring OLED/PLED luminous intensity.

**Fig. 4.6** (a) The luminous intensity ( $\Lambda$ , cd) vs. current density ( $J$ , mA/cm<sup>2</sup>) measured at the different distances ( $d$ , mm) between the surface of the PLEDs and the calibrated photodiodes. (A):  $d = 3$  mm; (B)  $d = 10$  mm; (C)  $d = 20$  mm; (D)  $d = 40$  mm; (E)  $d = 50$  mm; (F)  $d = 60$  mm; (G)  $d = 70$  mm; (H)  $d = 80$  mm; and (K)  $d = 150$  mm. The PLEDs are made from MEH-PPV. The surface area of calibrated photodiodes is  $4 \times 4$  mm<sup>2</sup>. (b) Inverse square law approximation error.



For a detector with a finite area, this expression can be used provided the detector subtends a sufficiently small solid angle (see Fig. 4.5). The condition recommended by CIE [19] is that  $\Omega \leq 0.01$  sr. Under these conditions, the luminous intensity ( $\Lambda$ , in candelas) can be obtained by comparing the signal from the PLED to that obtained from a calibrated lamp. The brightness is then given by  $L = \Lambda / \pi r^2$ .

The data from a set of such measurements are shown in Fig. 4.6 (for these data,  $r = 2$  mm). As expected, the signal falls off as  $d^{-2}$ . Note that even for  $d/r = 1$ , there is no serious error from the finite area of the detector.

Once the luminance,  $L$  (cd/m<sup>2</sup>), is accurately measured the luminous efficiency, LE (cd/A), luminous power efficiency, PE (lm/W) and external quantum efficiency,  $\eta_{\text{ext}}$  (the ratio of the number of photons emitted by the OLED/PLED into the viewing direction of the number of electrons injected) can be determined using the following expressions [20]:

$$\begin{aligned}
\text{LE}(\text{cd/A}) &= \frac{L}{j} \\
\text{PE}(\text{lm/W}) &= \frac{\pi^* L}{jV} \\
\eta_{\text{ext}}(\%) &= \frac{5.0 \times 10^3}{(h\nu)\phi(\lambda)} \text{LE}
\end{aligned} \tag{4.2}$$

where  $j$  is the current density,  $V$  is the applied voltage,  $h\nu$  is the photon energy (in eV) of the emission, and  $\phi(\lambda)$  is the photopic luminosity function (Fig. 4.4).

Another option is to place the OLED/PLED into an integrating sphere containing a calibrated detector, and then to measure the total output from the device [16]. In an integrating sphere, all the emitted photons are collected, including those that are guided to the edge of the substrate. Note, however, that photons emitted from the edge of the substrate are not useful in display applications. Thus, the integrating sphere approach must be used with caution. If the edges of the OLED/PLED are sealed to absorb the waveguided and scattered light, the external quantum efficiency can be accurately obtained. Once the external quantum efficiency is measured,  $L$ , LE and PE can be calculated using above equations. The values obtained by using the integrating sphere are consistent with corresponding values obtained from the configuration shown in Fig. 4.5 [20].

The condition for measurement of PLEDs carried out in our labs at UC Santa Barbara are the following: the surface area ( $S$ ) of the calibrated photodiode with eye-sensitivity filter is  $4 \times 4$  mm; the distance ( $d$ ) between the photodiode and PLEDs is 4 cm; i.e.  $\Omega = 0.01$  sr ( $\Omega = S/d^2$ ).

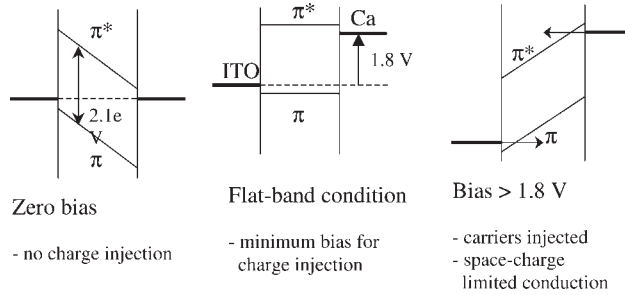
Note that, as indicated by Optronic Laboratories, the response of a diffuser/fiber combination is far from uniform or ideal [21]. Not only does the fiber/diffuser combination fail to provide the correct measurement area, but also the nonuniform spatial response makes the result highly sensitive to alignment. Therefore, the fiber/diffuser combination should be avoided if the OLED/PLED intensity is to be correctly measured.

#### 4.4

##### Fowler–Nordheim Tunneling in Semiconducting Polymer MIM Diodes

The operating mechanism of PLEDs is quite different from conventional p-n junction LEDs. In a PLED, a pure undoped film of luminescent semiconducting polymer is sandwiched between a high work function metal anode and a low work function metal cathode. The charge carrier concentration in such pure semiconducting films is sufficiently low ( $\approx 10^{14} - 10^{15} \text{ cm}^{-3}$ ) that any residual carriers introduced by impurities etc. are swept out by the built-in field that arises from the difference in work functions of the two electrodes. The depletion depth of pristine poly(phenylene vinylene) (PPV) is approximately 250  $\mu\text{m}$ , which is much larger than the thickness of the polymer layer in an LED (typically  $< 100$  nm). Consequently, the electronic structure of the LED can be approximated by the rigid band

**Fig. 4.7**  
The electronic structure of the LED.



model displayed in Fig. 4.7 [22]. The built-in field causes the uniform slope in the energies of the states in the bulk of the semiconducting polymer; there is negligible band bending.

The height of the barrier for hole injection is determined by the difference between the work function of the anode and the energy level of the  $\pi$  (valence) band; the height of the barrier for electron injection is determined by the energy difference between the work function of the cathode and the energy level of the  $\pi^*$  (conduction) band. The barrier height can be determined in this simple way because conjugated polymers do not have surface states that would pin the Fermi level.

- Zero bias with a common Fermi Level across the device (note that within the semiconducting polymer layer, the Fermi level moves across the energy gap on going from the anode to the cathode).
- A flat-band condition occurs when the applied voltage equals the difference in the work functions of the anode and the cathode. This is the minimum voltage required for injection of electrons and holes. Ideally, the electroluminescent emission should turn on at this voltage.
- Forward bias; carriers are injected through the triangular barriers at the anode (holes) and cathode (electrons) and meet within the polymer film where they radiatively recombine (electroluminescence).

When a positive bias is applied to the LED, the Fermi level of the cathode is raised relative to that of the anode, as shown in Fig. 4.7(c). Thus the thickness of the barrier is a function of the applied voltage; the barrier thickness decreases as the voltage is increased. Carriers tunnel through the barrier primarily by Fowler–Nordheim field emission tunneling from the anode and cathode into the  $\pi$ -band (holes from the anode) and the  $\pi^*$ -band (electrons from the cathode) of the semiconducting polymer. Thermionic emission over the barriers can also play a role if the barriers are small and the temperature is relatively high [22]. Since the rate of injection by Fowler–Nordheim tunneling is determined by the strength of the electric field, it is important for the polymer layer to be thin so that high electric fields can be obtained at low voltages.

To optimize the performance of PLEDs, it is important to minimize the barriers for charge injection by choosing electrodes with work functions that are well matched to the bands of the polymer. ITO, polyaniline, polypyrrole, and poly(3,4-ethyendioxthiophene) (PEDOT) are the most commonly used anode materials [23–25]. They also have the important property that they are transparent and therefore allow the emitted light to escape from the device. Calcium, barium, and magnesium are commonly chosen as the cathode because of their low work functions. Unfortunately, low work function metals are highly reactive. PLEDs must, therefore be hermetically sealed for long life. Improved electron injection from stable metals such as aluminum can be achieved by coating the electrode with a polar self-assembled monolayer. The dipole layer effectively shifts the electrode work function [26, 27].

If the electrodes are well matched to the bands of the polymer, then the barrier for charge injection is small and the current that passes through the LED is not limited by injection. Instead, the hole current is space-charge limited and the electron current is trap limited [28]. Space-charge limiting arises because the space charge that builds up near the anode due to the population of holes screens the field between the two electrodes and thereby limits the current. The traps that limit electron transport originate from defects that have energy levels just below the conduction band (due to disorder in the polymer).

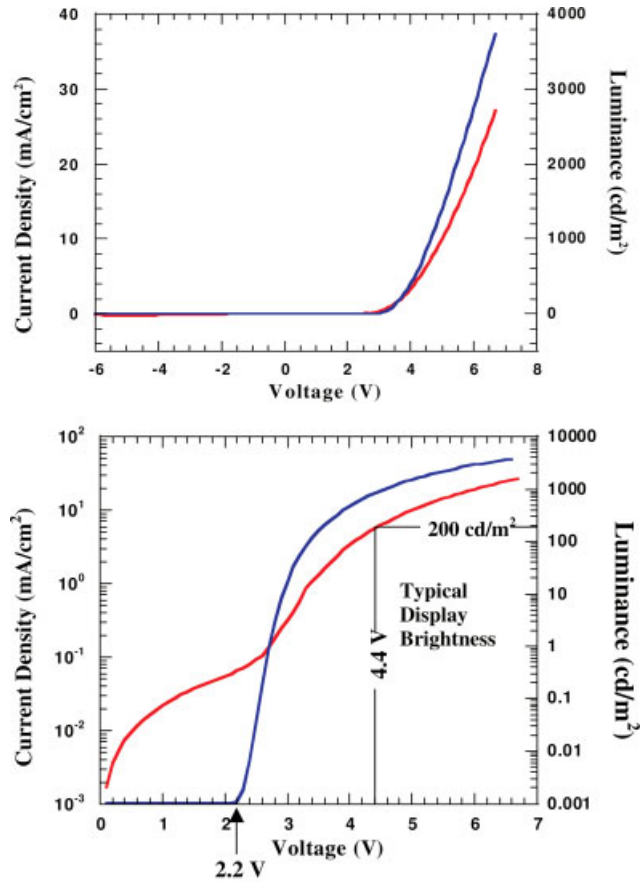
Once electrons and holes have been injected into the polymer, they must encounter each other and recombine radiatively to give off light. In this context, the low mobility of the charge carriers (polarons) in semiconducting polymers is helpful since the slow drift of the charge carriers across the thickness of the semiconducting polymer will allow enough time for the carriers to meet and recombine radiatively.

There are several factors that determine the efficiency of an LED. Maximum efficiency can only be achieved through balanced electron and hole currents. If one carrier type is injected much more efficiently and drifts in the applied electric field with higher mobility than the other, then many of the majority carriers will traverse the entire polymer layer without recombining with a minority carrier. As shown in Fig. 4.7, this problem can be minimized by carefully choosing appropriate electrodes so that the Fermi level of the anode is close in energy to the top of the  $\pi$ -band and the Fermi level of the cathode is close in energy to the bottom of the  $\pi^*$ -band. With such well-matched electrodes, both carriers are injected efficiently.

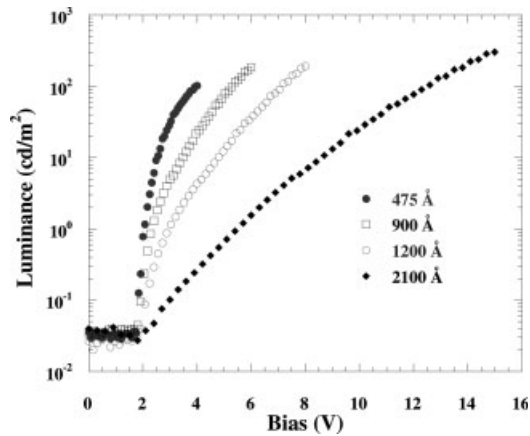
As demonstrated in Fig. 4.8, diodes fabricated as described above show excellent rectification ratios and strong electroluminescent light emission in forward bias. Light emission turns on close to the flat-band condition; i. e. when the applied voltage is greater than the difference between the work functions of the two electrodes (see Fig. 4.7). The current at voltages below 2 V in Fig. 4.7(b) is residual leakage current resulting from microshorts and imperfections.

Parker observed that the turn-on voltages for devices with different thicknesses of the semiconducting polymer layer are roughly the same and equal to the voltage required to reach the flat-band condition [22]. As shown in Fig. 4.9, however,

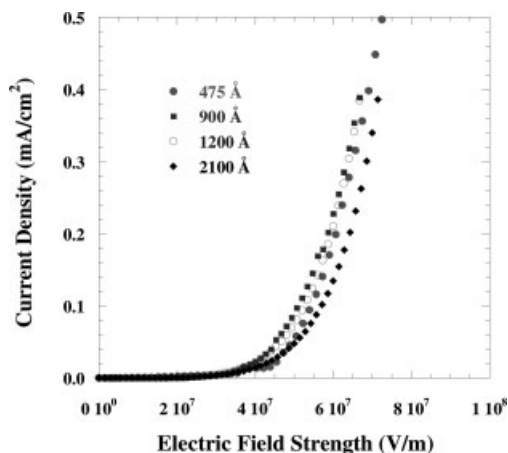
**Fig. 4.8** Current density (red) and luminance (blue) vs voltage for devices fabricated with MEH-PPV using polyaniline as the anode and calcium as the cathode.



**Fig. 4.9** Luminance vs voltage for ITO/MEH-PPV/Ca LEDs with semiconducting polymer layers of different thicknesses. Note that turn-on voltage is independent of thickness and equal to that needed to reach the flat-band condition (see Fig. 4.7(b)).







**Fig. 4.10** Current vs electric field for devices fabricated with MEH-PPV layers of different thicknesses.

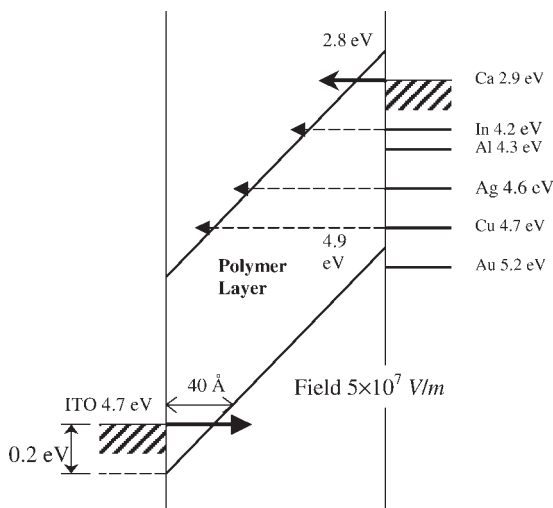
the current density is a strong function of the thickness. By replotting the data in Fig. 4.9 as a function of the electric field strength (rather than the voltage), all the data collapse onto a single curve; see Fig. 4.10. Thus PLEDs are electric-field driven rather than voltage driven.

Understanding the operating mechanism of PLEDs is complicated by the two-carrier nature of these diodes. In order to study the details of the carrier injection, single-carrier devices were fabricated in which the current density of one of the carriers was reduced to negligible levels.

#### 4.4.1

##### Single-carrier Devices

“Hole-only” devices were fabricated by replacing the low work function Ca cathode (2.9 eV) with higher work function metals such as In (4.2 eV), Al (4.4 eV), Ag (4.6 eV), Cu (4.7 eV) or Au (5.2 eV); see Fig. 4.11.



**Fig. 4.11** Band diagram (in forward bias) indicating the magnitudes of the triangular tunneling barrier for various cathode materials.

Increasing the work function of the cathode increases the offset between the Fermi energy of the cathode and the bottom of the  $\pi^*$ -band of MEH-PPV at 2.8 eV. This reduces the number of injected electrons to levels at which the injected holes dominate. Despite the fact that the work function of the cathode increases by more than 1 eV (from In to Au), the  $I$ – $V$  curves of the devices made with In, Al, Ag, Cu and Au cathodes are almost identical, indicating that electron injection has been shut off.

Fowler–Nordheim tunneling theory predicts that the tunneling current is an exponential function of  $1/F$  [29]

$$I \propto F^2 \exp(-\kappa/F) \quad (4.3)$$

where  $I$  is the current,  $F$  is the electric field strength and  $\kappa$  is a parameter that depends on the barrier shape. For a triangular barrier [30],

$$\kappa = 8\text{-}\Pi(2 m^*)^{1/2} \phi^{3/2} / 3\zeta\lambda \quad (4.4)$$

Here,  $\phi$  is the barrier height,  $m^*$  is the effective mass of holes in the semiconducting polymer,  $q$  is the electron charge and  $h$  is Planck's constant.

The  $I$ – $V$  data from a hole-only device fabricated from MEH-PPV with Au as the cathode and ITO as the anode are plotted as  $I/F^2$  vs  $1/F$  in Fig. 4.12. As predicted, the plot is close to linear particularly at high fields. The literal assumption of tunneling through a triangular barrier appears to be an excellent approximation. The deviation from linearity at lower fields probably indicates an additional contribution to the current from thermionic emission.

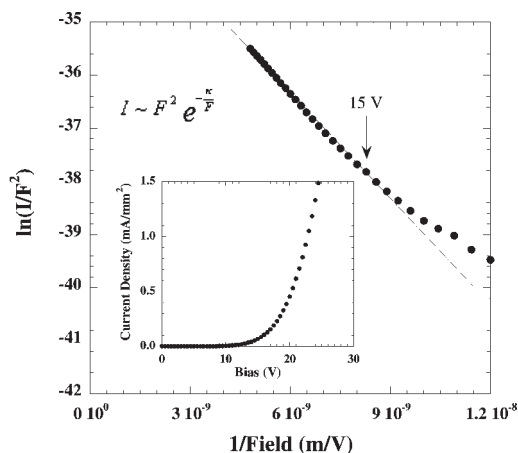
Assuming that the electric field is constant across the semiconducting polymer and that  $m^* = m$  (the free-electron mass), the calculated barrier heights are found to be 0.2–0.3 eV for all the hole-only devices indicated in Fig. 4.11. The fact that the inferred barrier height is unchanged despite the large variation in cathode work function indicates that the barrier must be at the ITO/polymer interface. Indeed,  $\phi = 0.2$ –0.3 eV is in agreement with the energy diagram in Fig. 4.11.

A similar approach can be taken to study electron injection. Replacing ITO with a lower work function metal (e. g. Nd or Mg) yields devices in which the carriers are almost exclusively electrons. A similar analysis of the data from a range of “electron-only” devices indicates that electrons tunnel into the  $\pi^*$ -band of MEH-PPV at 4.9 eV through a triangular barrier at the polymer/cathode interface. With Ca as the cathode, this barrier is 0.1 eV, again in agreement with the energy diagram in Fig. 4.11.

#### 4.4.2

#### LED Operating Voltage and Efficiency

The operating voltage is very sensitive to the barrier height. This sensitivity is predicted by the Fowler–Nordheim tunneling model. Equations (4.3) and (4.4) indicate that for the same tunneling current, the ratio  $\phi^{3/2}/V$  must be the same. Thus,

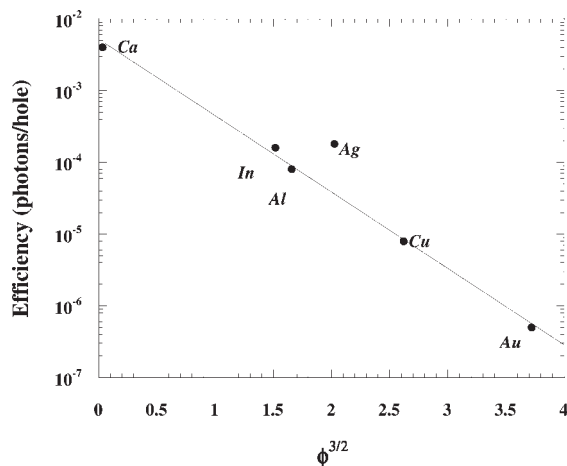


**Fig. 4.12** Fowler–Nordheim plot of  $\ln[I/F^2]$  vs  $1/F$  for a hole-only device fabricated using MEH-PPV with ITO as the anode and Au as the cathode.

increasing the barrier height from 0.1 eV (PANI) to 0.6 eV (Cr) should increase the operating voltage by a factor of 11. The experimentally determined increase was a factor of 9.

It is obvious that the device efficiency,  $\eta$ , must also be very sensitive to the barrier height, since the efficiency is limited by upon the minority carrier density. As suggested by Eqs. (4.3) and (4.4), Fig. 4.13 plots  $\ln(\eta)$  vs  $\phi^{3/2}$ . The excellent agreement between the theory and the data confirms the use of the Fowler–Nordheim tunneling model for describing the carrier injection into the band structure of the semiconducting polymer.

There is evidence of interface modification when metal films are deposited onto semiconducting polymers. However, since these interactions involve specific chemical reactions between the metal atoms and certain groups on the polymer, it is not clear how such chemical reactions could give rise to the systematic variation in the device efficiency with work function that is evident in Fig. 4.13.



**Fig. 4.13** Semilog plot of quantum efficiency (photons/electron) vs  $\phi^{3/2}$ .

## 4.4.3

**Limits of the Model**

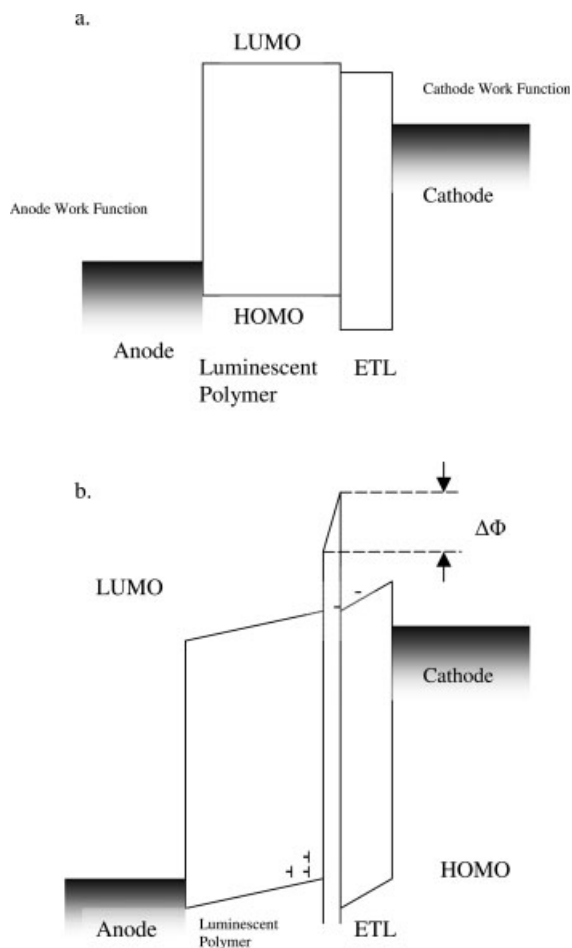
When the barrier heights are small, the simple comparison of work functions for the prediction of barrier heights is inappropriate; thermionic emission becomes important for barriers less than a few tenths of an eV. Moreover, the barrier will not be perfectly triangular as the model assumes, but must be somewhat ill-defined as a result of disorder-induced band tailing near the polymer band edges. In addition, the evaporated electrode materials are likely to be full of defects (possibly even amorphous) and are therefore not expected to have precisely the well-defined work function values listed in reference books. Other factors, such as the mobility of each charge species and space-charge limiting effects, may also have increasing influence over the performance for low barrier-height devices. Nevertheless, it is clear that an energy-band picture for the semiconducting polymer supplemented by Fowler–Nordheim tunneling theory provides an excellent starting point for understanding the operating mechanism of LEDs fabricated from semiconducting polymers.

## 4.4.4

**Approaches to Improved Carrier Injection:****Hole-blocking Layers, Electron-acceptors and Hole-acceptors**

It is not always possible to find electrode materials that are well matched to the electronic structure of an electroluminescent polymer. For example, for large bandgap blue-emitting polymers such as the polyfluorenes, the energy barrier at the cathode is typically too large for efficient injection of electrons via Fowler–Nordheim tunneling. Similarly, for more electronegative, stable semiconducting polymers, the barrier at the anode will be too large for efficient hole injection. In such cases, hole and/or electron-blocking layers can be added to improve the balance of electron and hole currents [31, 32]. Fig. 4.14 shows the electronic structure of an LED with a hole-blocking layer. The blocking layer creates a barrier at the interface of two polymers that blocks the flow of the majority carrier. As the density of the majority carrier increases at the blocking interface, the electric field at the minority carrier injecting electrode increases, thereby enhancing the minority carrier injection. As a result, the electron and hole currents will be more nearly balanced. The analogous diagram can be drawn for a device with an electron-blocking layer.

Improved injection can also be achieved through the addition of defects and impurities. End-capping with electron-accepting groups and/or hole-accepting groups is a useful example [33]. As shown in Fig. 4.15, such groups lead to the formation of localized states near the band edges. Thus in forward bias an electron can tunnel into the  $\pi^*$ -band in two steps; first from the cathode into a localized state on an electron-accepting site, and then from that site into the  $\pi^*$ -band. Since the tunneling probability decreases exponentially as  $\phi^{3/2}$ , the two-step injection can be more efficient than direct tunneling through the barrier into the

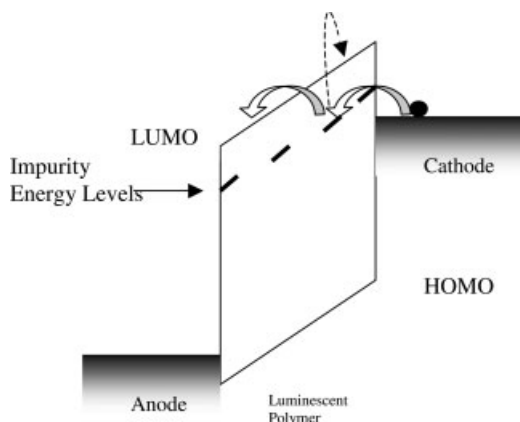


**Fig. 4.14** (a) Flat-band diagram of the electronic structure of an LED with a hole-blocking layer. (b) Electronic structure of an LED with a hole-blocking layer in forward bias. The electric field is primarily across the ETL; the field in the luminescent polymer is nearly zero.

$\pi^*$ -band. As sketched in Fig. 4.15 (dotted arrow), a two-step process involving tunneling followed by thermal excitation from the impurity acceptor state into the band can also help.

Electron-accepting and/or hole-accepting groups can also be incorporated into the chain (copolymers) or by addition of appropriate small molecules into the film. In the latter approach, however, clustering and phase separation are likely problems [34, 35].

**Fig. 4.15** End-capping with electron-accepting groups and/or hole-accepting groups leads to the formation of localized states near the band edges; electron accepting states are at energies just below the  $\pi^*$ -band, and hole-accepting states are at energies just above the  $\pi$ -band. Alternatively, such acceptor units can be inserted into the main chain as “dopants”. Small molecule acceptors can also be used.



## 4.5

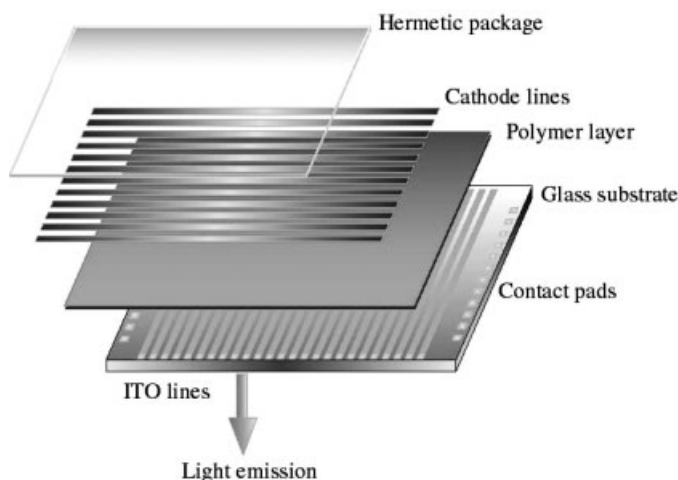
### Pixilated Displays

The ability to process the luminescent semiconducting polymer from solution enables the introduction of simple and potentially inexpensive methods for manufacturing pixilated displays. There are two general classes of pixilated displays that differ in the manner in which the individual pixels are switched on and off: passive matrix displays and active matrix displays.

Active matrix displays have a thin-film transistor (TFT) switching circuit embedded in the area of each individual pixel. Although the TFT backplanes needed for polymer emissive displays are similar to those developed for liquid crystal displays (LCDs), the TFT circuits must be capable of switching much higher currents than are required for LCDs. For active matrix displays, the luminescent semiconducting polymer and cathode, etc. are deposited directly onto the premanufactured TFT backplane (the anode for the LED pixel is built onto the TFT circuit). In an active matrix display, the pixels are held at constant brightness by the TFT circuit and the image is refreshed at video rates (e. g. 60 Hz).

Passively addressed displays utilize electrodes that are patterned into columns and rows as sketched in Fig. 4.16. In a passively addressed display, only the pixel defined by the intersection of a specific column of the anode and a specific row of the cathode that are simultaneously addressed will give off light. The image is produced by scanning the columns and rows with appropriate driver circuits. Because of the low duty cycle, each individual pixel is pulsed to high brightness when it is on; the viewer averages the intensity. For example, with a 64-column display, the duty cycle is 1/64. Thus to achieve an average brightness of 200  $\text{cd}/\text{m}^2$ , the pixels must be pulsed on to a brightness of 12 800  $\text{cd}/\text{m}^2$ .

For monochrome displays, a uniform film of the semiconducting polymer (as sketched in Fig. 4.16) can be spin-cast from solution. For full-color displays, both active matrix and passively addressed, individual red, green and blue pixels must be patterned and individually addressed.



**Fig. 4.16**  
Diagram of the  
structure of a  
passively ad-  
dressed display.

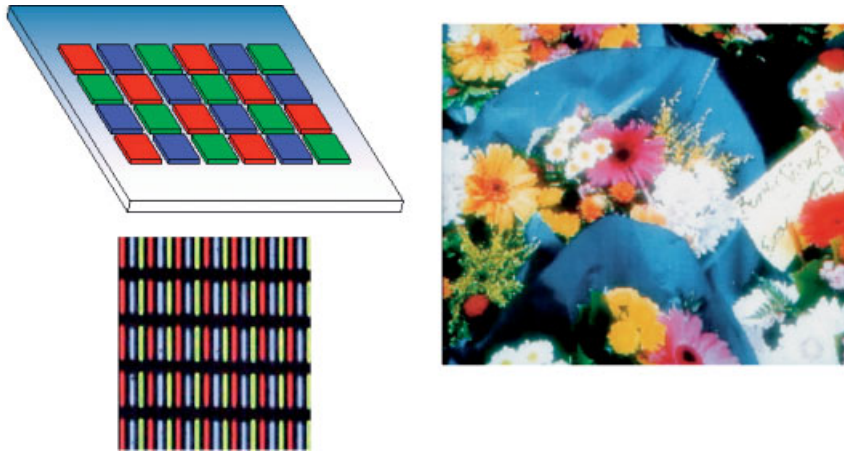


**Fig. 4.17** Examples of different semi-conducting polymers in solution. These colored solutions can be thought of as “functional inks” and applied to substrates using the methods of modern printing technology.

The colored liquids in Fig. 4.17 are examples of different semiconducting polymers in solution. These colored solutions can be thought of as “functional inks” and applied to substrates using the methods of modern printing technology. Ink-jet printing appears to be an ideal way to deposit the red, green and blue pixels of a full-color display. Fig. 4.18 illustrates this remarkable opportunity.

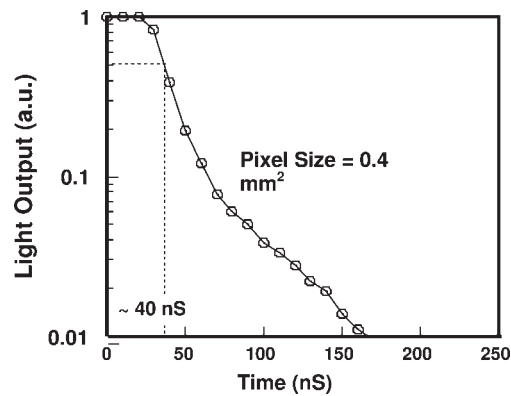
In display applications, fast (video rate) switching of the pixels is required. The intrinsic lifetime of the electroluminescence is the decay time of the photoluminescence; i.e. less than a nanosecond. Thus, for pixilated polymer emissive displays, the switching rate is limited only by the RC time constant of the device. For the small pixels of a full-color display,  $C$  is sufficiently small that the devices can be switched in times in the nanosecond regime. This fast switching is demonstrated for a single pixel in Fig. 4.19.

The possibility of using flexible substrates to fabricate fully flexible displays is particularly attractive (see Fig. 4.2). The critical limitation of the flexible LED technology is the permeability of most plastics to oxygen and water vapor. This permeability allows atmospheric oxygen and water vapor into the device and accelerates degradation. Water vapor is especially hazardous to the device operation since it will react with the low work function cathode. The development of technology



**Fig. 4.18** Sketch of a printed array of pixels is shown on the left. Below on the left is a photo of the colored pixels in an early device fabricated by ink-jet printing (defects evident). On the right is a color photo of a full-color display shown by Seiko-Epson in 2000.

**Fig. 4.19** Demonstration of fast in switching for a polymer LED pixel. In this figure a LED was fabricated on a strip-line configuration to minimize the stray input capacitance.



for making plastic substrates capable of forming a hermetic seal will be a critical step in the evolution of the field of polymer electronics. The flexibility offers advantages to the end user. More importantly, however, flexible substrates are required for roll-to-roll manufacturing.

A photo of a full-color polymer emissive active matrix display is shown in Fig. 4.20.





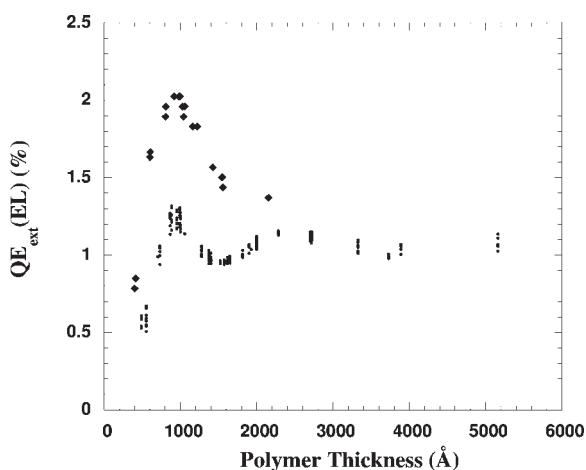
**Fig. 4.20** Full-color polymer emissive active matrix display showing a video image.

#### 4.6

##### Thickness Dependence of Electroluminescence Efficiency

Fig. 4.21 shows the thickness dependence of the external quantum efficiency for electroluminescence,  $QE_{\text{ext}}(\text{EL})$  as a function of the film thickness for two closely related PPV derivatives, OC1C10-PPV and MEH-PPV. The quantum efficiencies of these devices were measured using an integrating sphere.

The oscillatory dependence on the thickness ( $d$ ) of the polymer layer arises from the proximity of the metallic mirror electrode (the cathode); the emitting oscillator interacts with the virtual image oscillator “behind the mirror” [36, 37]. Because the radiation from the emitter and the retarded radiation from the image oscillator interfere, the PL decay rate is an oscillatory function of the distance from the mirror. Consequently, for a thin film, the quantum yields for photoluminescence and electroluminescence are oscillatory functions of  $d$ .



**Fig. 4.21** Thickness dependence of the external quantum efficiency of LEDs fabricated from OC1C10-PPV and MEH-PPV.

When the average distance from the mirror to the oscillator is too small ( $d \ll 100$  nm), the losses from the metallic electrode quench the luminescence. This is a particularly important limitation. Although thinner devices would have lower operating voltages (the PLED is electric-field driven), the efficiency decreases rapidly for thicknesses below 100 nm. As shown in Fig. 4.16, the optimum thickness is approximately 80 nm [38].

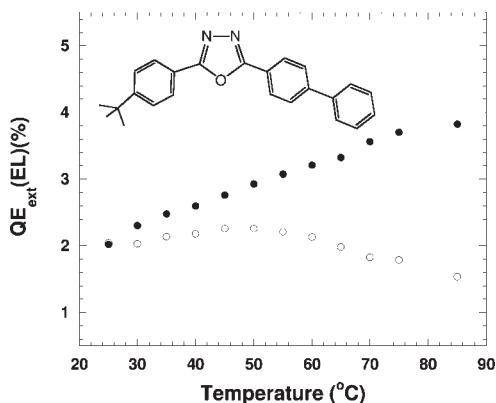
#### 4.7

##### Limits on the Electroluminescence Efficiency

The performance of PLEDs is ultimately limited by the quantum efficiency for photoluminescence. If, however, the lowest energy excited states are strongly bound excitons (electron-hole pairs in singlet or triplet states), the theoretical limit for the quantum efficiency of electroluminescence (EL) is 25 % of the corresponding quantum efficiency for photoluminescence (PL): an electron in the  $\pi^*$ -band and a hole in the  $\pi$ -band can form a triplet with multiplicity of three or a singlet with multiplicity of one, but only the singlet can decay radiatively. However, if the cross section for an electron-hole pair to form a singlet bound state is significantly higher than the cross section to form a triplet bound state, the ratio of EL quantum efficiency to PL quantum efficiency would be correspondingly larger than that predicted by the simple statistical argument given above (i.e.  $> 25\%$ ). Finally, if the electron-hole binding energy is sufficiently weak, the maximum quantum efficiencies can theoretically approach that of the PL. In the weak interaction limit, electron-hole pairs in a triplet configuration would simply scatter but not recombine. Eventually, the spin-orbit interaction would cause a spin-flip after which singlet formation and radiative recombination could occur.

Fig. 4.22 shows the temperature dependence of  $QE_{\text{ext}}(\text{EL})$  of a device fabricated from OC1C10-PPV containing 20 % (by weight) of (2-(4-biphenyl)-5-(4-tert-butylphenyl)1,3,4-oxadiazole (Bu-PBD) with a film thickness of 100 nm. The use of

**Fig. 4.22** Temperature dependence of  $QE_{\text{ext}}(\text{EL})$  and  $QE_{\text{ext}}(\text{PL})$ . Filled circles;  $QE_{\text{ext}}(\text{EL})$  of a device fabricated from OC1C10-PPV containing 20 % Bu-PBD. Data from an identical device with pure OC1C10-PP are shown for comparison (open circles).  $QE_{\text{ext}}(\text{PL}) = 8\%$  and temperature independent between room temperature and  $85^\circ\text{C}$ .



Bu-PBD (a well-known electron acceptor and transport molecule) was motivated by the need to achieve better-balanced electron and hole currents; see Fig. 4.15. The data from an identical device fabricated with pure OC1C10-PPV (without Bu-PBD) are shown for comparison. For devices containing Bu-PBD, the efficiency increases reversibly with temperature; at 85 °C,  $QE_{\text{ext}}(\text{EL}) = 4\%$ . The effect of the Bu-PBD is evidently to fine tune the balance of the electron and hole injection. The acceptor level in Bu-PBD is close to the bottom of the  $\pi$ -band of the luminescent polymer (see Fig. 4.15).

The increase in  $QE_{\text{ext}}(\text{EL})$  does not result from an increase in  $QE_{\text{ext}}(\text{PL})$ ; as shown in Fig. 4.22, the latter is temperature independent in devices with and without the Bu-PBD. The PL and EL efficiencies were carefully checked on each of a series of devices fabricated with films of different thickness (analogous to the data in Fig 21). The PL and EL efficiencies track one another as  $d$  is varied.

By using EL and PL data from the same devices to minimize the error,

$$QE_{\text{ext}}(\text{EL}) = 4.0 (\pm 0.2) \%, \text{ at operating voltages of } 3\text{--}4 \text{ V};$$

$$QE_{\text{ext}}(\text{PL}) = 8 (\pm 0.8) \% \text{ at zero field.}$$

These data demonstrate that  $QE_{\text{ext}}(\text{EL}) / QE_{\text{ext}}(\text{PL}) = 0.5$ . This is a lower limit for the ratio. Note that the EL data were obtained at electric fields of  $3\text{--}4 \times 10^5 \text{ V/cm}$ ; at these high electric fields, field-induced quenching measurements show a reduction in PL efficiency by 10% [39, 40]. Thus,  $QE_{\text{ext}}(\text{EL}) / QE_{\text{ext}}(\text{PL}) > 0.5$ .

The high value for  $QE_{\text{ext}}(\text{EL}) / QE_{\text{ext}}(\text{PL}) > 0.5$  indicates that either the exciton binding energy is small (of order  $k_B T$ ) or that the cross section for an electron-hole pair to form a singlet bound state is significantly higher than the cross sec-

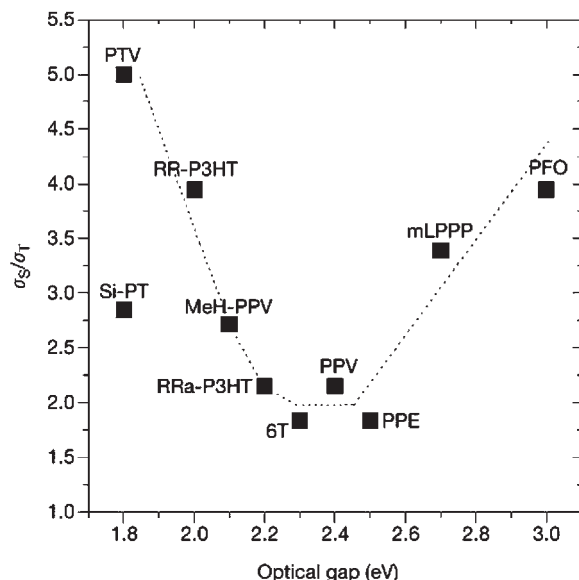


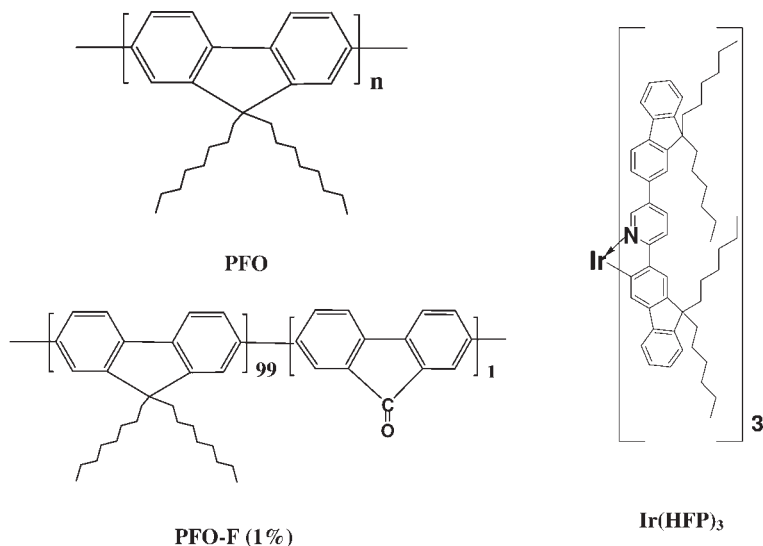
Fig. 4.23 Ratio of the singlet to triplet cross sections for a series of luminescent semiconducting polymers with different energy gaps (and thus different emission colors).

tion to form a triplet. There is experimental evidence that both of these alternatives are true. The exciton binding energy in PPV, as inferred from photoconductivity measurements, is approximately 60–70 meV; i.e. only  $2\text{--}3 k_B T$  at room temperature. Wohlgenannt et al. [41] were able to directly measure the ratio of singlet to triplet cross sections; their data are reproduced in Fig. 4.23. The singlet cross section is 3–4 times larger than the triplet cross section for all the luminescent semiconducting polymers; i.e. consistent with  $Q_{\text{ext}}(\text{EL}) / Q_{\text{ext}}(\text{PL}) > 0.5$ .

## 4.8

### White-light emission

PLEDs that emit white light are of interest for use as back-lights in high-efficiency active matrix displays (with color filters) and because they might eventually be used for solid-state lighting [42]. In such applications, manufacturing costs will be a major issue. The fabrication of PLEDs by processing the active materials from solution promises to be much less expensive than that of OLEDs where the active layers require high-vacuum deposition. Several approaches have been used to generate white light from PLEDs. As an illustrative example, we focus on the use of polyfluorene (PFO) as a host material containing small quantities of poly(9,9-dioctylfluorene-*co*-fluorenone) with 1% fluorenone, (PFO-F(1%)) and the Ir complex, tris[2,5-bis-2'-(9',9'-dihexylfluorene)pyridine- $\kappa^2$ NC<sub>3</sub>]Iridium(III), Ir(HFP)<sub>3</sub>. The PFO provides the blue component, the PFO-F(1%) provides the green component [43] and the Ir(HFP)<sub>3</sub> [44], provides the red component. The molecular structures of the various components are shown in Fig. 4.24.



**Fig. 4.24** Molecular structures of polyfluorene (PFO, polyfluorene containing 1% fluorenone, and the Ir metal-organic complex, Ir(HFP)<sub>3</sub>.

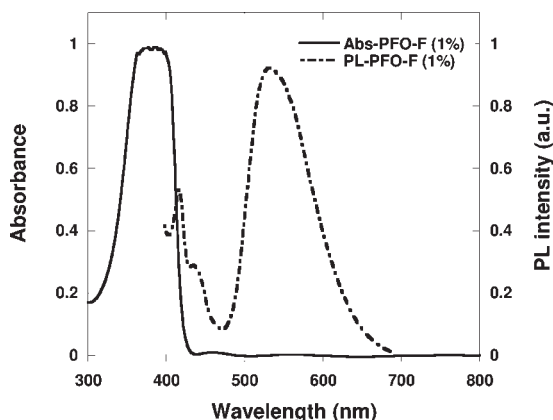


Fig. 4.25 Absorption and PL spectra of PFO-F (1%) thin films.

Polyfluorenes (PFs), as efficient blue emitters, have emerged as an important class of conjugated polymers. They exhibit high photoluminescence (PL) efficiency, good charge transport and thermal stability. As host materials, the PFs enable full-color (blue, green and red) emission via energy transfer to longer-wavelength emitters in blends with other conjugated polymers, phosphorescent dyes and organo-metallic emitters. Consequently, the PFs are interesting candidates as materials for use in the fabrication of PLEDs that emit white light. In such white-emitting PLEDs, the PFs can function both as the host and as the blue emitter.

Typically, however, a low-energy (2.2–2.4 eV) green PL band appears in the emission from PFs over time and degrades the blue emission. The green emission band originates from *fluorenone defects* (impurities) in the PF chain [7, 45]. Having identified the role of fluorenone defects in the PFs, one can take advantage of the fluorenone defect for creating materials with stable green emission [46].

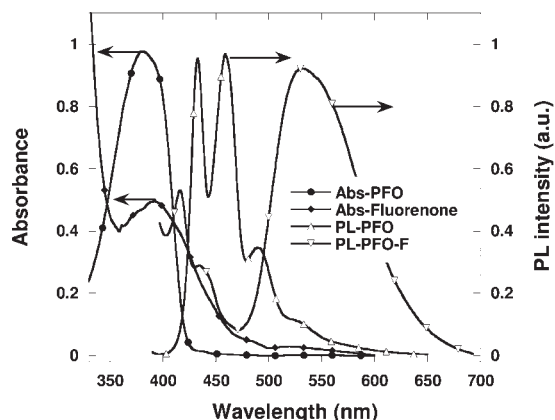
Fig. 4.25 shows the absorption and PL spectra of PFO-F (1%) thin films. For PFO-F (1%), the absorption onsets at approximately 430 nm (2.88 eV) with a maximum absorption at 384 nm (3.23 eV), corresponding to the expected  $\pi$ - $\pi^*$  transition from the fluorene backbone. When compared to PFO, however, an additional weak absorption band appears at  $\sim$ 420 nm, which is associated with the  $n$ - $\pi^*$  transition observed in the spectroscopy of fluorenone molecules. Under irradiation with light of 384 nm, the PL from PFO-F (1%) is green with a weak blue component; i.e. the same as the PL from oxidized PFO films. The green emission from PFO-F (1%) films thus originates from fluorenone units within the copolymer.

#### 4.8.1

##### Efficient Excitation Energy Transfer from PFO to the Fluorenone Defect

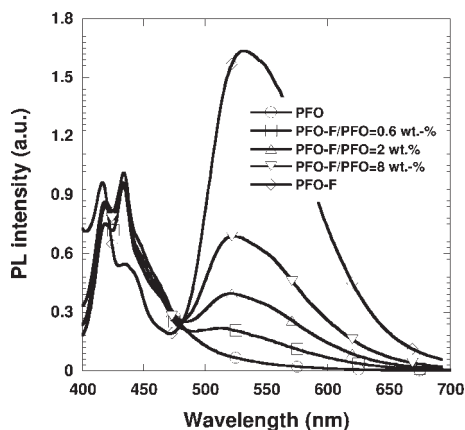
The absorption spectra of PFO and fluorenone thin films and the PL spectra of PFO and PFO-F (1%) thin films are shown in Fig. 4.26. The absorption maxima for PFO and fluorenone are at 384 nm and 415 nm, respectively. Under irradiation

**Fig. 4.26** Normalized thin-film absorption spectra of PFO and fluorenone and photoluminescence spectra of PFO and PFO-F (1 %).

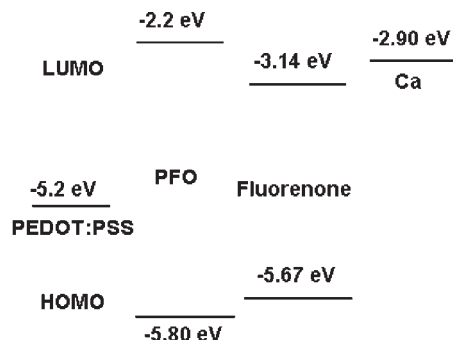


tion with 380-nm light, the PL shows well-defined vibronic features. A weaker long-wavelength emission ( $\sim 530$  nm) is also evident in the spectra. Fig. 4.26 demonstrates that there is a good overlap between the absorption spectrum of fluorenone and the emission spectrum of PFO implying efficient Förster energy transfer with subsequent emission from the fluorenone.

In order to test the efficiency of Förster energy transfer, thin films of pure PFO, PFO-F(1 %) and PFO with different concentrations of PFO-F(1 %) were prepared and excited optically with 380-nm radiation. Normalized thin-film PL spectra of PFO and PFO blended with the different concentrations of PFO-F (1 %) are shown in Fig. 4.27. The PL profile indicates two species. (1) The PL from PFO with maxima at 420 nm and 450 nm. (2) The PL from fluorenone with maximum at 530 nm. The blue emission (at 420 nm and 450 nm) decreases and the green emission (at 530 nm) increases as the concentration of PFO-F (1 %) is increased. Direct measurements of the optical absorption at 380 nm indicate that the absorption coefficient of PFO is 20 times greater than that of the fluorenone component.



**Fig. 4.27** Normalized thin-film photoluminescence spectra of PFO, PFO-F (1 %) and PFO blended with different concentrations of PFO-F (1 %).



**Fig. 4.28** HOMO and LUMO energy levels of fluorenone are compared to the  $\pi$ - and  $\pi^*$ -band edges of PFO.

Thus, for PFO-F(1 %), nearly all the incident photons are absorbed by the PFO. These data indicate efficient Förster energy transfer from PFO to the fluorenone defects.

The highest occupied molecular orbital (HOMO) and lowest unoccupied molecular orbital (LUMO) energy levels of fluorenone are shown in Fig. 4.28. Consistent with charge trapping, the fluorenone defects function as both a hole trap and an electron trap; the HOMO and LUMO of fluorenone fall within the  $\pi$ - $\pi^*$  gap of PFO [47]. In addition, the hole (electron) can be injected from the PEDOT:PSS (Ca) electrode directly into the HOMO (LUMO) of fluorenone because of the small energy barrier between PEDOT:PSS and the HOMO (or between Ca and the LUMO) of fluorenone.

Therefore, the more pronounced green emission from PFO containing fluorenone defects results from a combination of efficient energy transfer, charge carrier trapping and relatively easy injection (from the electrodes) of carriers into the fluorenone traps.

#### 4.8.2

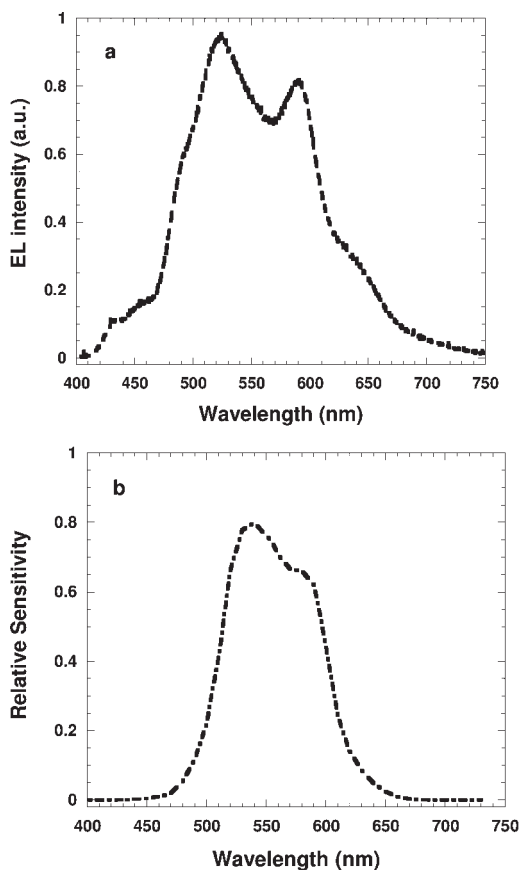
##### White Electrophorescent PLEDs

White-emitting PLEDs were fabricated using PFO, PFO-F and Ir(HFP)<sub>3</sub>. Fig. 4.29(a) shows the EL spectra obtained from devices with a configuration of (ITO)/PEDOT:PSS/emitting layer/Ba/Al. The emitting layer comprises Ir(HFP)<sub>3</sub>:PFO-F(1 %):PFO. The same spectra, renormalized to the sensitivity of the human eye, is shown in Fig. 4.29(b). The emission is well matched to the response of the human eye.

In the electrophosphorescent PLEDs made from the blends of Ir(HFP)<sub>3</sub>:PFO-F(1 %):PFO, injected holes and electrons recombine by two processes; direct recombination on the main chain (PFO) to produce blue emission in parallel with electron and hole trapping on the fluorenone units and on the Ir(HFP)<sub>3</sub> followed by radiative recombination, with green light from PFO-F (1 %) and red light from the triplet excited state of Ir(HFP)<sub>3</sub>.

The CIE (Commission International d'Eclairage) coordinates, color temperature (CT) and color rendering index (CRI) were quantitatively evaluated from EL spectra

**Fig. 4.29** (a) EL spectra obtained from white-emitting electrophosphorescent PLEDs and (b) the same spectra as in (a) but renormalized to the sensitivity of the human eye.

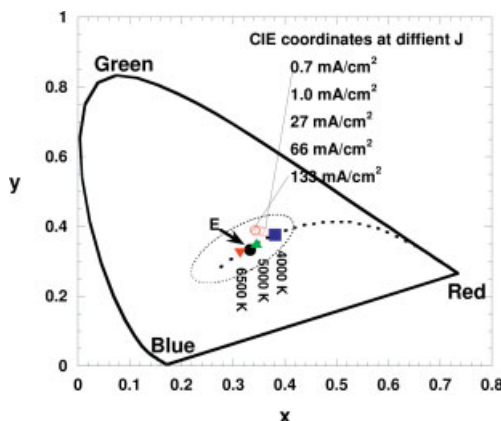


[48, 49]. Fig. 4.30 shows the 1931 CIE chromaticity diagram, with coordinates corresponding to the emission from electrophosphorescent PLEDs: data points are shown for devices (open circles) biased at different current densities. In Fig. 4.30, the dotted line indicates different color temperatures; the dotted oval indicates the approximate area where the human eye perceives the color as white. The CIE coordinates for the  $\text{Ir}(\text{HFP})_3$ :PFO-F(1%):PFO devices are (0.352, 0.388) at  $J = 1 \text{ mA/cm}^2$ , very close to the CIE coordinates for pure white light, (0.333, 0.333). The CIE coordinates show only minor shifts at different  $J$ . The stability of the CIE coordinates as a function of the brightness and applied voltage is much better than reported previously for PLEDs/OLEDs [11, 50–55].

The  $\text{Ir}(\text{HFP})_3$ :PFO-F(1%):PFO devices had CT  $\sim 4600 \text{ K}$  and CRI = 86; the CT  $\sim 4600 \text{ K}$  is very close to the CT of sunlight at  $20^\circ$  solar altitude (4700 K) [56]. The CTs and CRIs are insensitive to brightness and  $J$ .

The white emission turns on at approximately 5 V, with a luminance ( $L$ ) of  $L = 6100 \text{ cd/m}^2$  at 17 V. A Lambertian intensity profile was assumed to calculate the LE ( $\text{cd/A}$ ) and the PE ( $\text{lm/W}$ ) with the following results:  $\text{LE} = 3 \text{ cd/A}$  and  $L = 255 \text{ cd/m}^2$  at  $J = 8.5 \text{ mA/cm}^2$ . The PE was approximately  $1 \text{ lm/W}$ .





**Fig. 4.30** CIE (1931) chromaticity diagram, with coordinates corresponding to the emission from white-emitting devices (○ ○ ○) biased at different current densities. Also shown are the equienergy point (E) for pure white light (0.333, 0.333) (●) and the coordinates corresponding to color temperatures of 4000 K (■), 5000 K (▲) and 6500 K (▼). The dotted line indicates different color temperatures; the dotted oval indicates the approximate area where the human eye perceives the color as white.

Since the charge carriers are not balanced in the devices described in Figs. 4.29 and 4.30 [33], we anticipate that the LE and PE can be enhanced by using approaches described earlier in this chapter. Indeed, as noted in Fig. 4.16, the carrier injection and carrier balance can be improved through the use of hole-injection and electron-injection layers. Using this approach, at UC Santa Barbara we have achieved higher efficiency by fabricating multilayer white electrophosphorescent PLEDs. The multilayer white PLEDs are fabricated by using luminescent semiconducting polymers and organometallic complexes as the emission layer, water-soluble (or methanol-soluble) poly(vinylcarbazole) sulfonic lithium (PVK-SO<sub>3</sub>Li) as the HTL and water-soluble (or methanol-soluble) 4-(5-(4-*tert*-butyl-phenyl)-1,3,4-oxadiazole-2-yl)-biphenyl-4'-yl sulfonic sodium (*t*-Bu-PBD-SO<sub>3</sub>Na) as the ETL. All layers are spin-cast from solutions in the device configuration: ITO/PEDOT/HTL/emissive layer/ETL/Ba/Al. The results demonstrate that white-emitting PLEDs with both HTL and ETL have significantly enhanced luminance, luminous efficiency and power efficiency. The multilayer white electrophosphorescent PLEDs have LE = 10.4 cd/A, PE = 3 lm/W and  $L = 2391 \text{ cd/m}^2$  at  $J = 23 \text{ mA/cm}^2$  ( $V = 11 \text{ V}$ ) with  $L = 2.4 \times 10^4 \text{ cd/m}^2$  at 16 V. For solid-state lighting applications, the corresponding numbers are  $> 20 \text{ cd/A}$  and 5 lm/W [57].

#### 4.9

#### Conclusion

Research on PLEDs has demonstrated significant progress. Although the basic mechanisms of carrier injection, recombination and emission are understood, characterization of degradation mechanisms is less well developed. Moreover, challenges remain that must be resolved to enable the widespread application of PLEDs in commercial products. Among the most important challenges are achieving high materials purity, low-cost manufacturing, high brightness and

efficiency, and long operational lifetimes. Impurities in luminescent materials cause exciton quenching and hence decrease the emission efficiency, increase the device series resistance, and decrease operational stability.

The use of white-emitting PLEDs for solid-state lighting will require significant breakthroughs toward the development of low-cost manufacturing of large areas, improved electroluminescent efficiency, improved out-coupling efficiency, and long operational stability. Roll-to-roll manufacturing techniques offer an opportunity for mass production of low-cost, large-area white-emitting PLEDs; these processes may eventually make the cost of producing white PLEDs competitive. However, the process development of roll-to-roll manufacturing has not even seriously begun. Moreover, the luminous efficiency achieved from white-emitting PLEDs is still too low for most solid-state lighting applications [46]. Thus, the fabrication of multilayer white-emitting PLEDs using solution processable polymer systems must be expanded and developed [57].

#### Note:

The approach to improving the carrier injection outlined in Section 4.4.4 has recently been extended to a multilayer structure with the addition of both an electron injecting (hole-blocking) layer and a hole injecting (electron-blocking) layer; see X. Gong et al., *Adv. Mater.*, **2005**, 17, 2053.

#### Acknowledgement

The research results described in this review were supported by the Air Force Office of Scientific Research (F49620-02-01-0127 and F49620-99-01-0031) and Air Force Office of Scientific Research through the MURI Center at the University of Washington ("Polymeric Smart Skins")(AFOSR F 49620-01-10364), the National Science Foundation (NSF-DMR 0096820), and the Mitsubishi Center for Advanced Materials at UCSB.

#### References

- 1 A. J. Heeger, *Angew. Chem. Int. Ed.*, **2001**, 40, 2591; *Solid State Comm.*, **1998**, 107, 673 and *Rev. Mod. Phys.*, **2001**, 73, 681.
- 2 D. Braun, A. J. Heeger, *Appl. Phys. Lett.*, **1991**, 58, 1982.
- 3 G. Yu, J. Wang, J. McElvain, A. J. Heeger, *Adv. Mater.*, **1998**, 10, 1431.
- 4 P. S. Heeger, A. J. Heeger, *Proc. Nat. Aca. Sci. USA*, **1999**, 96, 12219.
- 5 C. D. Dimitrakopoulos, D. J. Masearo, *IBM J. Res. Dev.*, **2001**, 45, 11.
- 6 M. D. McGehee, A. J. Heeger, *Adv. Mater.*, **2000**, 12, 1655.
- 7 U. Scherf, E. J. W. List, *Adv. Mater.*, **2002**, 14, 477.
- 8 S. Setayesh, D. Marsitzky, K. Müllen, *Macromolecules*, **2000**, 33, 2016.
- 9 U. Scherf, *J. Mater. Chem.*, **1999**, 9, 1853.
- 10 J. Kido, H. Shionoya, K. Nagai, *Appl. Phys. Lett.*, **1995**, 67, 2281.
- 11 C. Zhang, A. J. Heeger, *J. Appl. Phys.*, **1998**, 84, 1579.

- 12 Y. Cao, G. M. Klavetter, N. Colaneri, A. J. Heeger, *Nature*, **1992**, 357, 477.
- 13 A. Dodabalapur, *Solid State Commun.*, **1997**, 102, 259.
- 14 J. G. Holmes, *Proc. SPIE*, **1978**, 146, 2.
- 15 J. C. Whitaker, "Video Display Engineering", McGraw-Hill Companies, Inc., p.52, **2001**.
- 16 N. C. Greenham, R. H. Friend, D. D. C. Bradley, *Adv. Mater.*, **1994**, 6, 491.
- 17 A. D. Ryer, "Light Measurement Handbook", International Light Inc., **1998**.
- 18 H. A. E. Keitz, "Light Calculations and Measurements", 2<sup>nd</sup> edition, Macmillan and Co Ltd, **1971**.
- 19 Commission International de l'Éclairage: *Measurement of LEDs*, CIE publication 127.
- 20 X. Gong, M. R. Robinson, J. C. Ostrowski, D. Moses, G. C. Bazan, A. J. Heeger, *Adv. Mater.*, **2002**, 14, 581.
- 21 <http://olinet.com>
- 22 I. D. Parker, *J. Appl. Phys.*, **1994**, 75, 1656.
- 23 J. Gao, A. J. Heeger, J. Y. Lee, C. Y. Kim, *Synth. Met.*, **1996**, 82, 221.
- 24 Y. Cao, G. Yu, C. Zhang, R. Menon, A. J. Heeger, *Synth. Met.*, **1997**, 87, 171.
- 25 Y. Yang, E. Westerweele, C. Zhang, P. Smith, A. J. Heeger, *J. Appl. Phys.*, **1995**, 77, 694.
- 26 I. Campbell, J. Kress, R. Martin, D. Smith, *Appl. Phys. Lett.*, **1997**, 71, 3228.
- 27 Y. Cao, G. Yu, A. J. Heeger, *Adv. Mater.*, **1998**, 10, 917.
- 28 P. W. M. Blom, M. J. M. de Jong, J. J. M. Vleggaar, *Appl. Phys. Lett.*, **1996**, 63, 3308.
- 29 R. H. Fowler, L. Nordheim, *Proc. R. Soc. London Ser.*, **1928**, A 119, 173.
- 30 S. M. Sze, "Physics of Semiconductor Devices", Wiley, New York, **1981**.
- 31 Y. Cao, G. M. Treacy, P. Smith, A. J. Heeger, *Appl. Phys. Lett.*, **1992**, 60, 2711.
- 32 S. Aratani, C. Zhang, K. Pakbaz, S. Hoyer, F. Wudl, A. J. Heeger, *J. Electron. Mater.*, **1993**, 22, 745.
- 33 X. Gong, W. L. Ma, J. C. Ostrowski, K. Bechgaard, G. C. Bazan, A. J. Heeger, S. Xiao, D. Moses, *Adv. Func. Mater.*, **2004**, 14, 393.
- 34 X. Zhan, Y. Liu, X. Wu, S. Wang, D. Zhu, *Macromolecules*, **2002**, 35, 2529.
- 35 A. J. Campbell, D. D. C. Bradley, H. Antoniadis, *J. Appl. Phys.*, **2001**, 89, 3343.
- 36 H. Kuhn, *J. Chem. Phys.*, **1997**, 53, 171.
- 37 N. C. Greenham, *Bull. Am. Phys. Soc.*, **1998**, 43, 14.
- 38 Y. Cao, I. D. Parker, G. Yu, C. Zhang, A. J. Heeger, *Nature*, **1999**, 397, 414.
- 39 R. Kersting, *Phys. Rev. Lett.*, **1994**, 73, 1440.
- 40 D. Moses, C. H. Lee, A. J. Heeger, *Phys. Rev. B.*, **1996**, 54, 4748.
- 41 M. Wohlgenannt, Kunj Tandon, S. Mazumdar, S. Ramasesha, Z. V. Vardeny, *Nature*, **2001**, 409, 494.
- 42 A. J. Heeger, *Solid State Commun.*, **1998**, 107, 673 & *Rev. Modern Phys.*, **2001**, 73, 681.
- 43 X. Gong, D. Moses, A. J. Heeger, *Synth. Met.*, **2004**, 141, 17.
- 44 X. Gong, J. C. Ostrowski, G. C. Bazan, D. Moses, A. J. Heeger, M. S. Liu, A. K.-Y. Jen, *Adv. Mater.*, **2003**, 15, 45.
- 45 X. Gong, P. K. Iyer, D. Moses, G. C. Bazan, A. J. Heeger, S. Xiao, *Adv. Func. Mater.*, **2003**, 13, 325.
- 46 X. Gong, W. L. Ma, J. C. Ostrowski, G. C. Bazan, D. Moses, A. J. Heeger, *Adv. Mater.*, **2004**, 16, 615.
- 47 S. E. Shaheen, B. Kippelen, N. Peyghambarian, J. F. Wang, J. D. Anderson, E. A. Mash, P. A. Lee, N. R. Armstrong, Y. Kawabe, *J. Appl. Phys.*, **1999**, 85, 7939.
- 48 G. Wyszelki, W. S. Stiles, *Color Science*, 2<sup>nd</sup> edition (Wiley, New York), pp. 117–232, **1982**.
- 49 D. B. Judd, G. Wyszecski, *Color in Business, Science and Industry*, 3<sup>rd</sup> edition (John Wiley & Sons), pp. 91–388, **1975**.
- 50 J. Kido, H. Shionoya, K. Nagai, *Appl. Phys. Lett.*, **1995**, 67, 2281.
- 51 Z. Shen, P. E. Burrows, V. Bulvić, S. R. Forrest, M. E. Thompson, *Science*, **1997**, 276, 2009..
- 52 Y. Hamada, T. Sano, H. Fujii, Y. Nishio, *Jpn. J. Appl. Phys.*, **1996**, 35, L1339.
- 53 Y. Z. Wang, R. G. Sun, F. Meghdadi, G. Leising, A. J. Epstein, *Appl. Phys. Lett.*, **1999**, 74, 3613.
- 54 M. Strukelj, R. H. Jordan, A. Dodabalapur, *J. Am. Chem. Soc.*, **1996**, 118, 1213.
- 55 T. Yamamoto, *Prog. Polym. Sci.*, **1992**, 17, 1153.
- 56 R. W. G. Hunt, *Measuring Color*, 2<sup>nd</sup> edition, Ellis Horwood, pp. 38–109, **1991**.
- 57 X. Gong, S. Wang, G. C. Bazan, A. J. Heeger, *Adv. Mater.*, **2005**, 17, 2053.

## 5

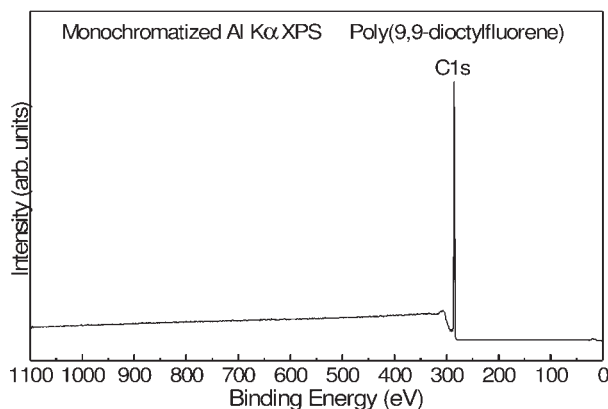
## Metal/Polymer Interface Studies for Organic Light-Emitting Devices

*Man-Keung Fung, Chun-Sing Lee, and Shuit-Tong Lee*

## 5.1

### Review of Organic Light-Emitting Diodes and their Fundamental Interface Studies

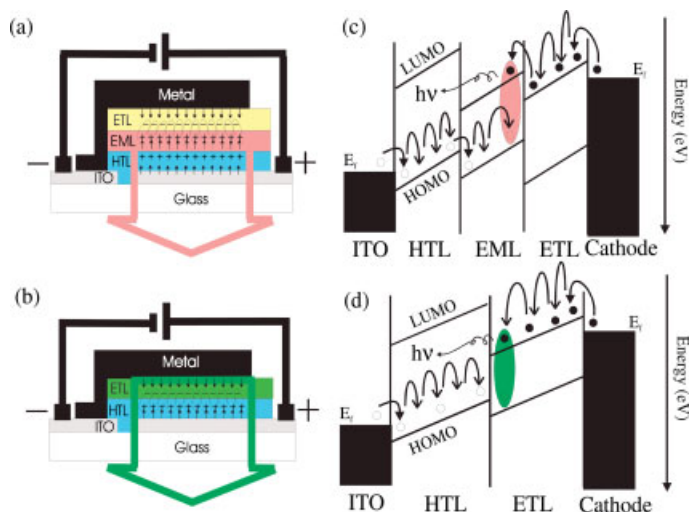
Organic materials have been traditionally considered as an insulator until a feeble electrical conductivity of organic molecules was reported in the late 1950s [1]. An epoch of using organics for electrical applications has begun since 1977, when Chiang et al. [2] discovered a gigantic increase of eleven orders of magnitude of electrical conductivity of a polymer when halogen was introduced into polyacetylene. A new term of ‘organic semiconductor’, which is commonly used today, was therefore coined specifically for this new class of conducting materials. This discovery, unveiling the mystery of plastic electronics, led to the award of a Nobel Prize in Chemistry in 2000 to Heeger, MacDermid and Shirakawa for their contributions in conducting polymers. Meanwhile, DC-driven electroluminescence from organic anthracene single crystal was manifested in the 1960s by Pope et al. [3] and Helfrich and Schneider [4], who were the pioneers on disclosing the phenomenon of organic electroluminescence. Nevertheless, the application of organic light-emitting diodes (OLEDs) was still unrealistic due to the high operating voltage (greater than 100 V to achieve reasonable luminance) needed for injecting charges into the organic crystal. A breakthrough was made in 1987 when Tang et al. [5] demonstrated that double-layered and vapor-deposited molecular films consisting of a hole-transporting layer of aromatic diamine and an emissive layer of 8-hydroxyquinolinealuminum ( $\text{Alq}_3$ ) could generate organic electroluminescence greater than  $1000 \text{ cd/m}^2$  at a driving voltage lower than 10 V. The double-layer design has become a landmark achievement and prototypical structure in OLEDs. The demonstration of electroluminescence in conjugated polymers by Burroughes et al. [6] in 1990 further heightened interest and nourished research and development in organic electroluminescence. In the last 15 years, organic semiconductors have developed rapidly from a topic of research interest into a wide range of applications, which include polymer light-emitting diodes (PLEDs) [6–14], small-molecule based OLEDs [5, 15–20], organic lasers [21–26], organic transistors [27–35] and solar cells [36–41], etc.



**Fig. 5.1** A survey spectrum of 1000 Å thick poly(9,9-dioctylfluorene) film as measured from XPS.

The main difference between PLEDs and small-molecule based LEDs, as a result of the use of either polymeric or small-molecular compounds respectively, is in the method of film preparation. Films of small molecules are usually prepared by vacuum evaporation, while polymer films are prepared by spin coating from solution in a nitrogen-filled glove box. Polymer films prepared by spin coating are often thought to be impurity-rich since the coatings are not vacuum-deposited. As organic synthesis becomes more mature, high purity of polymers can now be routinely obtained. A survey spectrum in Fig. 5.1 shows an X-ray photoelectron spectrum of a conjugated polymer film of poly(9,9-dioctylfluorene), which was obtained from the Dow Chemical Company and spun under ambient condition on ITO. This spectrum contains a single, intensive and narrow peak at a binding energy of 285 eV due to carbon 1s core level and no other peaks, thus showing that the polymer surface is highly pristine and free of contamination.

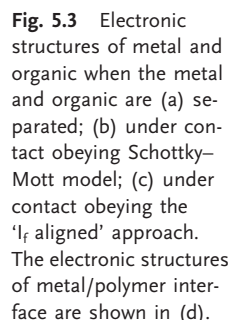
Aside from film preparation, the device configuration and working principle of both PLEDs and small-molecule based OLEDs are basically the same, as shown in Fig. 5.2. The device typically consists of a high work function anode (e. g. indium tin oxide) and a low work function cathode, and a hole-transporting layer (HTL), an emissive layer (EML) and an electron-transporting layer (ETL) sandwiched between (Fig. 5.2(a)). In most of the devices nowadays, double layers for charge transporting are commonly used, where one of them also functions as the emitting layer (Fig. 5.2(b)). Application of an external voltage across the two electrodes leads to injection of holes and electrons from the anode and cathode, respectively, into the organic layers. With appropriate energy-level alignment across each layer, electrons and holes migrating towards one other by a hopping transport mechanism recombine near one of the interfaces, as shown in Fig. 5.2(c) and 2(d), yielding light upon radiative decay of excitons. The carrier injection barrier heights at the various interfaces (so-called injection barrier) and the mobility of organic layers determine the location of the recombination zone and more critically device performance, such as turn-on voltage and luminescent efficiency. The chemistry between the electrode and organic also has a substantial influence on the electronic properties at the interface, which in turn dictates the properties of OLEDs.



**Fig. 5.2** Device configuration and working principle of OLEDs. (a) a triple-layer device showing a hole-transporting layer (HTL), emissive layer (EML) and electron-transporting layer (ETL) sandwiched between two electrodes; (b) a double-layer device. An energy diagram showing hopping transport of holes and electrons in (c) a triple-layer device and (d) a double-layer device. Light comes out upon radiative decay of excitons.

A study of interfaces between the organic and metal layers is thus of fundamental importance for improving the device performance of OLEDs.

The electronic properties of metal and organic, such as work function of metal ( $\phi_m$ ), work function of organic material ( $\phi_p$ ), ionization potential (IP), electron affinity (EA) and bandgap ( $E_g$ ), are determined by the vacuum level ( $E_{vac}$ ), Fermi Level ( $E_f$ ), highest occupied states (HOS) and lowest unoccupied states (LUS) (Fig. 5.3(a)). Two regimes are commonly used to describe the interface formation when two metal and organic layers are in contact. In the early days, it was believed that energy-level alignment is upheld at the metal/organic interface, or vice versa, so-called the Schottky–Mott limit [42]. In such a case, the metal and the organic layer have a common vacuum level (Fig. 5.3(b)). The hole-injection barrier  $E_v^f$  and electron-injection barrier  $E_f^c$  are therefore simply equal to  $IP - \phi_m$  and  $\phi_m - EA$ , respectively. Nevertheless, this rule was found to be invalid for most metal/organic interfaces [43–55]. A dipole layer (Fig. 5.3(c)) is often present at both the organic-on-metal and metal-on-organic interfaces (hereafter, the organic-on-metal interface is simply represented as organic/metal, and vice versa), and the  $E_f$  is always taken as a common level. Using this  $E_f$ -aligned approach and the nomenclature reported by Ishii et al. [44] for organic/metal interfaces, the  $E_v^f$  becomes  $IP - \Delta - \phi_m$  while  $E_f^c$  is equal to  $\phi_m - (EA - \Delta)$  or  $E_g - E_v^f$ . It should be noted that the sign of  $\Delta$  depends on the direction of the dipole moment. In the case shown in Fig. 5.3(c),  $\Delta$  is positive. In reality, it is more difficult to manifest an actual polymer/metal interface accurately, in contrast to the ideal organic/metal contact in Fig. 5.3(c), since preparation of polymer films with a



thickness in Å by a spin-coating technique is not an easy task. In polymer/metal interfaces, the interfacial dipole  $\Delta$  is therefore generally represented as  $\phi_m - \phi_p$  (Fig. 5.3(d)). The binding energy separation between the HOS and  $\phi_p$  of the polymer then represents the barrier height  $E_v^f$  for hole injection, giving  $IP = \phi_p + E_v^f$  and  $E_f^c = E_g - E_v^f$ . Using the above definitions,  $\Delta$  for a polymer/metal interface would always be null [56], in contrast to that observed in most organic/metal interfaces [44, 45]. The nonzero interfacial dipoles are often observed in the latter case because vapor-deposited molecular species tend to have an intimate contact, and thus interaction with the metal substrate, resulting in charge-transferring or interfacial chemical interactions between the metal and organic material. On the contrary, the presence of solvent in the spin-coated polymer was believed to passivate the above chemistry [57].

The insignificance of  $\Delta$  on the polymer/metal interface has been recently illustrated in a review of Salaneck et al. [58]. For PLEDs, numerous research groups have studied the interface formation between calcium and poly(p-phenylene vinylene) (PPV) (or substituted PPV), which is a prototypical emitting material used in PLEDs [59–68]. Recently, fluorene-based polymers like blue-emitting poly(9,9-dioctylfluorene) (PFO) and green-emitting poly(9,9-dioctylfluorene-co-benzothiadiazole) (F8BT) have been widely used in PLEDs with prominent luminescence characteristics [7, 69–75]. For example, highly efficient PLEDs of green color with low turn-on voltage (2 V), high brightness (1000 cd/m<sup>2</sup> at 3.1 V) and high efficiency (22 lm/W at 100 cd/m<sup>2</sup>) have been reported using fluorene-based polymers [7, 69]. Therefore, more fundamental studies on the polyfluorene-based polymers are necessary for further enhancing device performance. Towards this goal, Salaneck et al. [76–83] and our research group [84–88] have

recently reported a number of metal/PFO interface studies using photoelectron spectroscopic techniques. These metals include Ca [84, 85], Li [76, 78, 79, 83, 86], Na [77, 86], K [86–88], Cs [86–88], Al [76, 81, 82], LiF/Al [76, 78, 81, 82] and CsF/Al [80–82]. This chapter aims at giving a review of our recent results on: (i) metal/F8BT interfaces and (ii) the electrode selection for small-molecule-based OLEDs using representative metals and metal/metal fluoride as cathodes, so as to underscore the importance of interface study and its consequential applications in OLEDs and PLEDs.

The following section begins with a brief experimental description (Section 5.2). The analytical methods used in the present works are X-ray photoelectron spectroscopy (XPS) and ultraviolet photoelectron spectroscopy (UPS), the detailed working principles of which can be found in the literature [44, 57, 58]. In Section 5.3, we summarize the interface of F8BT with two commonly used metal electrodes, namely Ca and Cs, studied by using photoelectron spectroscopic techniques. The formation of bipolaron states upon doping is also discussed. In Section 5.4, the application of rare-earth metals as a cathode in PLEDs is discussed in terms of their interface formation with the F8BT, and the usage of rare-earth metal/cesium fluoride cathode for different OLED configurations is elucidated in Section 5.5. This chapter ends with the conclusions in Section 5.6.

## 5.2

### Polymer Materials, their Preparations, and Experimental Details

The primary object of this chapter is to show the importance of surface analysis and metal/organic interfaces in OLEDs. This is achieved by a review of the surface analysis of a promising green-emitting polymer, namely F8BT, from the polyfluorene family that has been widely used in light-emitting polymer technology [7, 69–75]. The polymer was obtained from the Dow Chemical Company. The structure of F8BT is shown in Fig. 5.4, where the side chains of  $C_8H_{17}$  increase the solubility of the polymer in most common organic solvents such as toluene and xylene. The photoluminescence (PL) spectrum of F8BT exhibits an emissive peak of 530 nm (Fig. 5.5). F8BT were spin coated from a toluene or xylene solution (0.15 wt. %) to form 5–10 nm thick films on ultraviolet ozone-treated indium tin oxide (ITO) substrates. The freshly spin-coated film was then loaded in a UHV chamber immediately for photoemission spectroscopic studies.

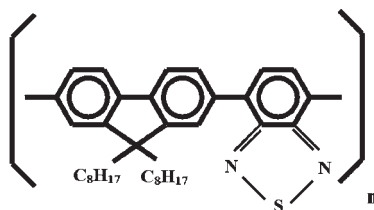
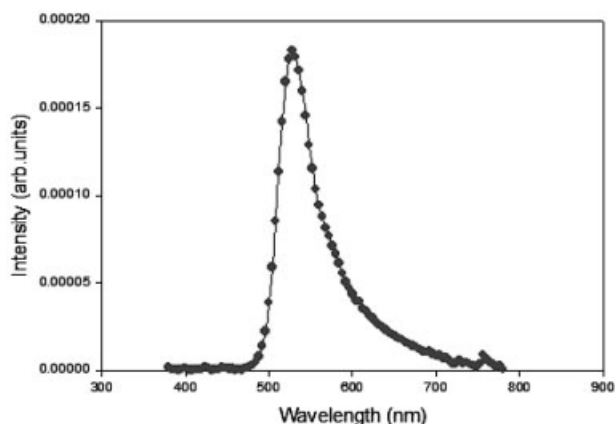


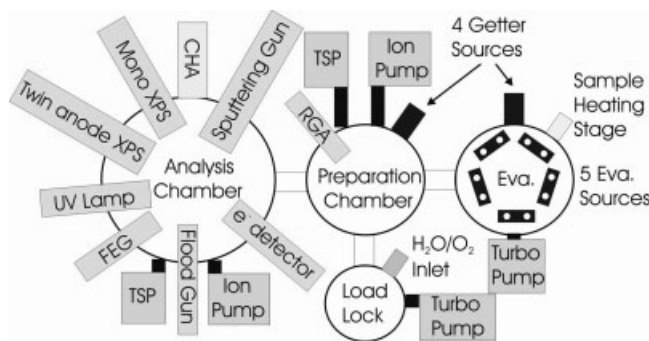
Fig. 5.4 Chemical structure of F8BT.





**Fig. 5.5** Photoluminescence (PL) spectrum of F8BT.

The photoemission studies were performed in a VG ESCALAB 220i-XL photoemission spectroscopy system with a monochromatic aluminum  $K\alpha$  source (1486.6 eV) for XPS analysis and an unfiltered He I (21.2 eV) and He II (40.8 eV) gas-discharge lamp for UPS analysis. The photoelectrons are collected by a CHA equipped with six channeltrons. Shown in Fig. 5.6 is a schematic drawing of the surface analysis system. This system consists of an analysis chamber, a multiport carousel chamber equipped with a residual gas analyzer (RGA), an evaporation chamber with substrate heating elements, and a sample load-lock chamber with an inlet for oxygen and water vapor exposure experiment. The base pressures in the analysis chamber, the multiport carousel chamber, the evaporation chamber and the load-lock chamber were  $5 \times 10^{-10}$ ,  $9 \times 10^{-10}$ ,  $6 \times 10^{-10}$  and  $2 \times 10^{-7}$  mbar, respectively. The absolute energy resolution of the analyzer was 0.018 eV for the UPS and 0.36 eV for the XPS measurements, thus obtaining a spectral resolution of approximately 0.1 eV as estimated from the Fermi edge of Au and a full width at half-maximum (FWHM) of 0.7 eV from Au  $4f_{7/2}$ . Before transferring the sample to the analysis chamber, F8BT samples were warmed slightly ( $< 300^\circ\text{C}$ ) in the evaporation chamber to remove the solvent and surface



**Fig. 5.6** A schematic drawing of the VG ESCALAB 220i-XL photoelectron spectroscopy system. An analysis chamber, a multiport carousel chamber, an evaporation chamber and a sample load-lock chamber are shown.

contaminants. UPS spectra were then recorded with a sample bias of  $-4.0$  V to allow the observation of the inelastic electron cut-off so that sharp cut-off edges were observed in all the He I UPS spectra.

In the present work, Ca, CsF, Al, Ag and ytterbium (Yb) were evaporated in the evaporation chamber using either tungsten baskets or tantalum cells. The amount of evaporants was monitored by a quartz crystal microbalance. It was calculated from the changes of the oscillation frequency of the crystal and in turn governed by the bulk densities of the evaporants where the densities of the Ca, CsF, Al, Ag and Yb are 1.55, 1.88, 2.70, 10.49 and  $6.57 \text{ g/cm}^3$ , respectively [89]. For alkali metal deposition, a SAES getter source of Cs was installed in the evaporation chamber, where the source has been degassed thoroughly before deposition. The alkali metal deposition was carried out with a specific current for 45 s.

High-resolution XPS of the Ca  $2p$ , Yb  $4d_{5/2}$ , Cs  $3d_{5/2}$ , F  $1s$ , Au  $4f_{7/2}$ , S  $2s$ , S  $2p$ , N  $1s$  and C  $1s$  core levels was performed with a pass energy of 20 eV and scanning step size of 0.05 eV. Part of the analysis was accomplished with a scanning step size of 0.1 eV, which will be specifically mentioned in the text. The amount of metal deposited in the present work was expressed either in terms of Å or atomic percentage. The latter was estimated from the integrated intensities of the XPS peaks.

The work function of the ITO substrate and ionization potential of the as-prepared polymer film were 4.9 eV and  $5.7 \pm 0.1$  eV, respectively. The work functions of the metals at different coverages on F8BT relative to that of the pristine polymer could be accurately measured by shifting the steep inelastic electron cut-off in the UPS He I spectra of the metal/polymer films so as to align with that of the as-prepared film. The shift values were recorded and they are exactly equal to the changes of the work function. Accordingly, interfacial dipole across the metal/polymer interface can be accurately measured. Angle-dependent XPS was also performed on selected samples to determine the distribution and thus diffusion of metals in F8BT.

For device fabrications as described in Section 5.3 and 5.5,  $30 \text{ } \Omega$  patterned ITO-coated glass substrate was cleaned with Decon 90, rinsed in deionized water, then dried in an oven, and finally treated in an ultraviolet (UV) ozone chamber. The OLEDs were fabricated by thermal evaporation at a vacuum of  $5 \times 10^{-7}$  mbar. An additional capping layer of Ag (100 nm) was then evaporated on top of the metal cathodes. The deposition rates were monitored with a quartz oscillating thickness monitor and controlled to be 1–2 Å/s for the organic materials and metals. The current density–voltage–luminance (J–V–L) characteristics were measured simultaneously with a programmable Keithley model 237 power source and a Photoresearch PR 650 spectrometer. For lifetime tests, devices were encapsulated in a glove box filled with purified dry nitrogen ( $< 1 \text{ ppm O}_2$ ). The initial luminance of the devices was measured using a Photoresearch PR 650 spectrometer. The devices were tested at a constant direct current density of  $20 \text{ mA/cm}^2$  and the relative light intensity of the devices was monitored using photodiodes and continuously recorded using a computer-controlled data-acquisition system. All measurements were carried out in air at room temperature.

### 5.3

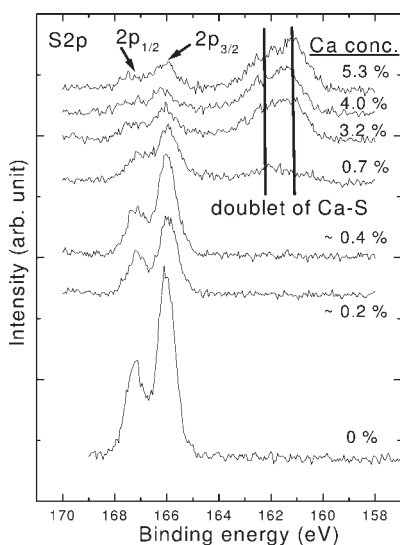
#### Chemistry and Electronic Properties of Metal/F8BT

The interfaces of F8BT with Ca and Cs are discussed in this section. Ca and Cs are chosen because Ca is commonly utilized as a cathode in PLEDs and the latter possesses a very low work function. We are interested in studying site specificity of the metal-doped system, by observing any formation of new chemical states with the carbon backbone, sulfur and nitrogen atoms of F8BT. We also demonstrate the differences of electronic structures of F8BT upon Ca and Cs doping. This aims at correlating the existing photoelectron spectroscopic results with the corresponding polymer devices.

##### 5.3.1

##### Ca on F8BT

Figure 5.7 shows the XPS spectra of S 2*p* core level with increasing Ca doping concentration. The pristine F8BT film exhibits two peaks at binding energies of 166.1 and 167.2 eV. This doublet with a separation of 1.1 eV corresponds to S 2*p*<sub>3/2</sub> and S 2*p*<sub>1/2</sub> core levels, respectively [90]. It can be seen that their intensities drop with increasing dopant concentration. At 5.3 % Ca doping, two new chemical states emerge at binding energies of 161.2 and 162.3 eV that are considered as the doublet of calcium sulfide [91], and the energy separation between the S 2*p*<sub>3/2</sub> (166.0 eV) and corresponding sulfide peak (161.2 eV) is 4.8 eV. This indicates that at the interface the metallic calcium transferred charges to the sulfur atoms of F8BT and most of the dopants were no longer in metallic states. The XPS spectra of N 1*s* core level with different concentrations of Ca is depicted in



**Fig. 5.7** Evolution of XPS S 2*p* spectra of F8BT with increasing Ca doping concentration in terms of atomic percentage.

**Fig. 5.8** Evolution of XPS N 1s spectra of F8BT with different Ca concentration.

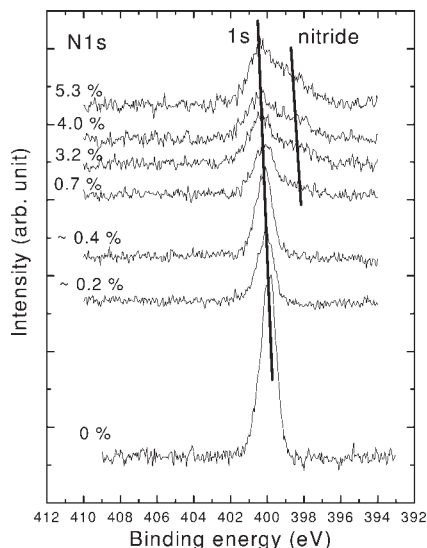
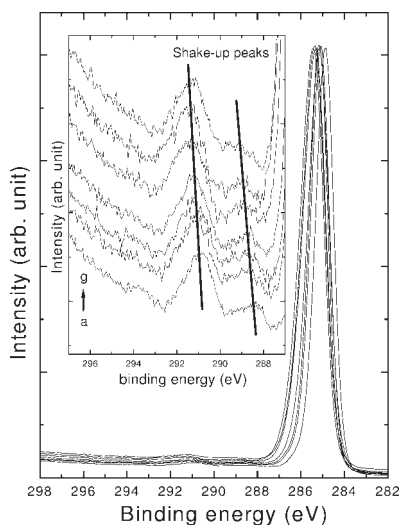


Fig. 5.8. The N1s core level at a binding energy near 399.8 eV progressively decreases in intensity upon Ca deposition since the overlayer suppressed the photoelectron yields derived from the original F8BT, and at the same time a vague peak appears at a lower binding energy around 398.2 eV. This later peak is assignable to nitride [92] and in the present case it should be Ca–N covalent bonds. Unlike in the case of S 2*p*, the peak related to the nitride does not grow proportionally with the dopant concentration and hence Ca only mildly interacts with the nitrogen atoms of F8BT. Since the doping concentration is relatively low in such a bulky polymer and other sulfur atoms or carbons in the polymer chain all compete for the incoming calcium, there are not enough Ca atoms to react with all the nitrogen atoms in the benzothiadiazole rings to form Ca–N covalent adducts.

Illustrated in Fig. 5.9 are the XPS of C 1s core level spectra of the pristine F8BT and Ca/F8BT with their enlarged shake-up features shown in the inset. The C 1s main peak of the pristine F8BT is located at a binding energy of 284.9 eV and possesses a FWHM of 0.98 eV. The FWHM in the present case is comparable with that in our previous study using PFO [93], indicating that the presence of S and N of the F8BT does not alter the intrinsic properties of the polymer. In all doping levels, no additional C 1s peak associated with reacted carbons could be resolved since the fraction of carbons involved in the carbon–metal reaction was insignificant in such a bulky polymer. With Ca concentration increasing up to 5.3 %, the binding energy and FWHM of the C 1s core level increase to 285.4 and 1.23 eV, respectively. The 0.5 and 0.25 eV increase in the binding energy and FWHM reflects a charge transfer from Ca to C atoms, but the extent is not so significant compared to the case when a similar Ca doping level was incorporated into PFO [93]. In such a case, the binding energy and FWHM were increased by 0.81 and 0.74 eV, respectively. Besides, two magnified satellite peaks at binding

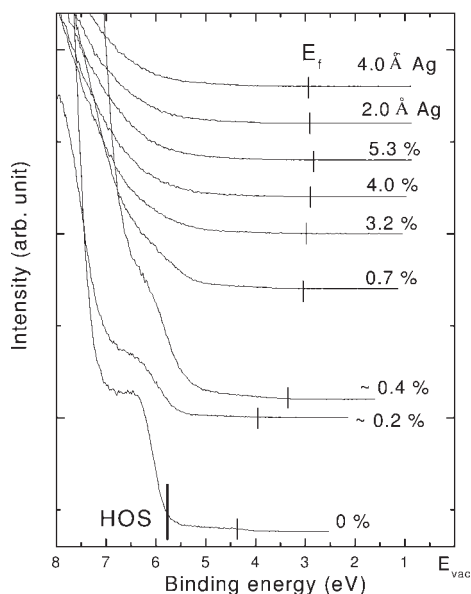


**Fig. 5.9** Evolution of XPS C 1s spectra of F8BT with increasing Ca concentration. The Ca concentration from the bottom to top is the same as that in Fig. 5.8. The two satellite peaks (peak  $\pi^*(1)$  and peak  $\pi^*(2)$ ) are shown in the inset.

energies of 288.5 and 291.0 eV of the pristine film in the present case are believed to be the shake-up peaks corresponding to  $\pi$  to  $\pi^*(1)$  and  $\pi$  to  $\pi^*(2)$  transitions, respectively. In the shake-up process, the valence electrons of the F8BT, i. e. electrons in the HOMO, are simultaneously excited to the lowest-unoccupied molecular orbital (LUMO) or unoccupied molecular orbital (UMO) states so that the transition of HOMO to LUMO and UMO ( $\pi$  to  $\pi^*(1)$  and  $\pi$  to  $\pi^*(2)$  respectively) can be observed. In fact, peak  $\pi^*(2)$  is commonly known as the shake-up peak for molecules with aromatic group and  $\pi^*(1)$  is for the phenylene chains [93]. Interestingly, the shake-up peaks do not change with increasing Ca concentration, in contrast to what was commonly observed at the Ca/PFO [93] and alkali-metal/PFO interfaces [86]. The shake-up features in those interfaces were gradually broadened and decreased in intensities. In the present case, we suggest that the UMOs of the F8BT are unaffected by the Ca deposition. Combining all the results from S 2p, N 1s, C 1s core levels and its shake-up features of the XPS, it is evident that the Ca preferentially interacts with the S atoms of F8BT; however, the carbon backbone, especially the aromatic and phenylene chains, is involved little in chemical reaction.

Figure 5.10 shows the He I UPS spectra of F8BT with increasing Ca concentration, with alignment of all  $E_{\text{vac}}$  at the origin, i. e. binding energy of  $E_{\text{vac}} = 0$  eV. The molecular orbitals of F8BT at higher binding energy are not depicted here. Vertical bars at the lower binding energy side indicate the Fermi level ( $E_f$ ) position referenced to Au. Accordingly, the ionization potential and work function of the pristine F8BT as determined from the bottom curve are 5.8 and 4.4 eV, respectively. With increasing Ca, the work function of Ca/F8BT gradually decreases and eventually shifts to 2.8 eV at higher metal coverage. However, the overall spectral characteristics do not change significantly and no polaron or bipolaron states, which are expected in most doped polymers, could be identified. This implies that the

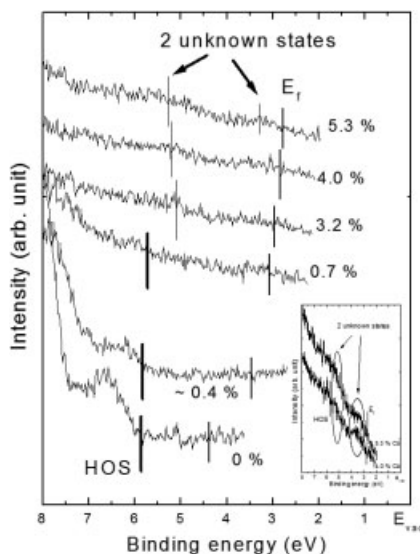
**Fig. 5.10** Enlarged UPS He I spectra showing regions near the F8BT HOMO. HOS and Fermi level ( $E_f$ ) are located. The spectra of 2.0 Å and 4.0 Å of Ag deposited on top of 5.3 % Ca/F8BT are depicted in the two topmost curves.



Ca-doped interface of F8BT is somewhat different compared with other common light-emitting polymers such as PFO and poly(*p*-phenylene vinylene) (PPV) [59, 64, 65]. These findings further confirm the XPS results that the added electrons originated from the Ca strongly localize at the sulfur sites of F8BT and have little effect on the carbon backbone. Ca then forms a stable interface with F8BT without significantly changing the electronic structures of the pristine polymer.

The two topmost UPS spectra in the same figure show the interface between Ag and Ca/F8BT. It is to clarify, as a general expectation, that the Ag coverage does not interact with the underlying interface when Ag is utilized as an encapsulating layer for the metal electrode in an actual device. Similarly, all the S 2p, N 1s and C 1s core levels acquired from the XPS spectra for films with the Ag coverage were also unchanged. These results are relevant to device fabrications. From the analytical point of view, it is not a principal issue to explain in detail and therefore we merely discuss some selected findings in Section 3.2 (Cs on F8BT).

The He II UPS spectra of F8BT at different Ca doping level are shown in Fig. 5.11, with alignment of all  $E_{vac}$  at the origin. Thick vertical bars in the three bottom curves denote the HOS positions of F8BT or Ca/F8BT and the bars pointing at the lower-energy region are the  $E_f$  positions determined from the He I UPS spectra. All spectra are generally consistent with those in Fig. 5.10. Magnifying the spectra of the 4.0 and 5.3 % doped films (as shown in the inset), we can observe two weak peaks that are located in the former forbidden gap with binding energies of 3.3 and 5.3 eV. The energy separation of 2.0 eV between these two peaks is similar to that of the bipolaron states in many common metal/PFO interfaces [86]. Nevertheless, it is unreliable to assign these two peaks as bipolarons because (i) the intensities of these peaks are trivial; (ii) they are unobservable in the enlarged He I UPS spectra;



**Fig. 5.11** UPS He II spectra showing regions near the F8BT HOMO. HOS, Fermi level ( $E_f$ ) and satellites are located. The satellites corresponding to 4.0% Cs/F8BT and 5.3% Cs/F8BT are enlarged and illustrated in the inset.

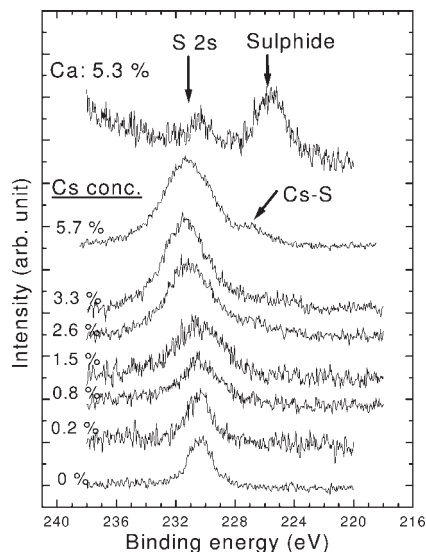
and (iii) these may be satellites arising from the He II $\beta$  source with excitation energy of 48.4 eV, which has about 10.0 % intensity of the pristine He II $\alpha$  excitation line at 40.8 eV. The third reason becomes more important on the UPS results when the Ca concentration is sufficiently high in F8BT. In such a case, the absolute intensities of the He II $\alpha$  excited peaks from the alkyl side chains, which locate at 11.0–13.0 eV, are increased (Since the alkyl side chains do not affect the electronic information, i. e. are not involved in the charge-transfer processes, it is immaterial to show their spectra in the present study), thus intensifying the satellite peaks at an apparent binding energy of 7.6 eV (48.4–40.8 eV) lower. As a result, it may cause complications in the interface information at a binding energy below 6 eV. We point out that care should be exercised in using He II UPS to obtain valence-band information near the low binding energy region at metal/polymer interfaces like metal/PFO and metal/F8BT.

### 5.3.2

#### Cs on F8BT

XPS spectra of the S 2s core level of F8BT with different Cs doping concentrations are shown in Fig. 5.12. S 2s peaks are shown here instead of S 2p core level because the strong Cs 4p<sub>3/2</sub> peak located at a binding energy of 161.3 eV [92] may overlap with the sulfide peak at about 161.0–162.0 eV, which is the region of interest. The S 2s core level of the pristine film is positioned at a binding energy of 230.3 eV. It can be seen that the main peak shifts to a higher binding energy with increasing Cs concentration. The shift is actually due to alteration of vacuum levels upon Cs deposition onto the polymer. With increasing doping level, the main peak and its intensity are broadened and increased, respectively. This is due to the

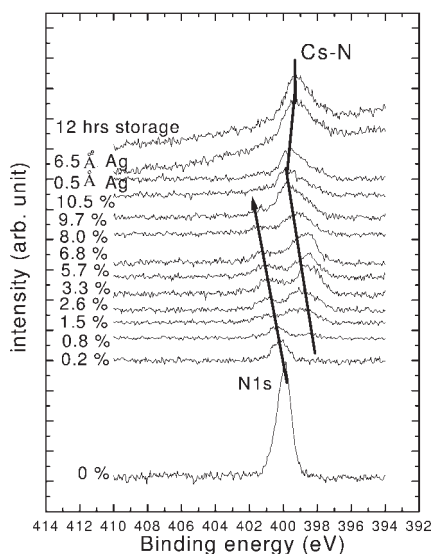
**Fig. 5.12** Evolution of XPS S 2s spectra of F8BT with increasing Cs doping concentration in terms of atomic percentage.



contribution of the photoelectron signal of the Cs 4s core level at the binding energy of 232.3 eV [92]. However, it does not drown the predicted sulfide peak position since it is 5.0 eV away from the Cs 4s. A weak shoulder emerges at a binding energy of 226.7 eV when the Cs is 5.7%. It is considered as a sulfide bond in an organometallic complex, e.g. Cs-S, since the approximate energy separation of 4.8 eV between the S 2s (231.5 eV) and new shoulder (226.7 eV) is consistent with that observed in the S 2p core level as mentioned earlier and the reproduced S 2s peak at the Ca/F8BT interface as shown in the topmost spectrum of Fig. 5.12. Although the metal doping levels are similar in the top two spectra, the capability to form sulfide in both cases is definitely different. In the case of Cs, it only reacts mildly with the sulfur group. Instead, it may chemically weaken the N double bonds connected to the aromatic backbone. This can be manifested in Fig. 5.13, which shows the XPS spectra of the N 1s core level with different nitrogen concentrations. With increasing Cs concentration to 10.5%, in addition to a decrease of intensities and a shift of binding energies of the N 1s core levels, it is also clear that an extra component built up at a binding energy of 2.3 eV lower than the original N 1s peak. The new peak becomes much stronger than the original peak at a Cs concentration of 5.7% and entirely replaces it at 10.5%. The energy separation of 2.3 eV between the original N 1s core level and the new component indicates that the new peak is a nitride peak [92, 94]. This suggests that Cs would preferably bond to the N atom instead of the S atom in the case of Ca deposition.

To investigate the effect of a Ag encapsulating layer in an actual device on the Cs/F8BT system and clarify the stability of Cs-N complexes with Ag encapsulation, XPS spectra of N 1s core level as influenced by two selected Ag coverages on the Cs/F8BT after residual gases exposed at a background pressure of





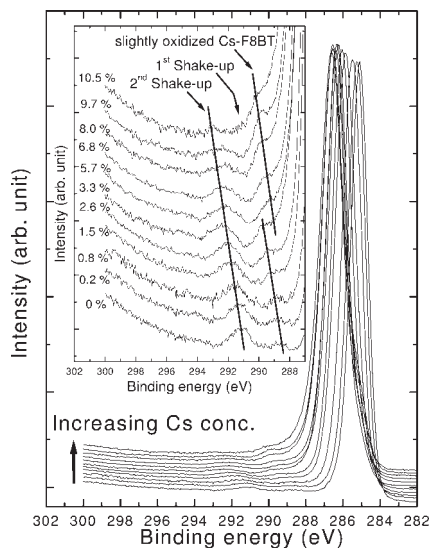
**Fig. 5.13** Evolution of XPS N 1s spectra of F8BT with different Cs concentration up to 10.5 %. The spectra of 10.5 % Cs/F8BT film deposited with 0.5 and 6.5 Å of Ag and the latter film exposed with residual gases at a background pressure of  $2 \times 10^{-9}$  mbar for 12 h are shown in the top three curves.

$2 \times 10^{-9}$  mbar for 12 h are shown in the top three spectra of Fig. 5.13. It can be seen that the affected core levels are unchanged in all the cases and they are also chemically stable against the residual gases. We also note that the nitride peak shifts 0.3 eV back to a lower binding energy for a Ag coverage of 6.5 Å. It is understandable since the Ag coverage, with a higher work function than Cs, would decrease the vacuum level of the entire Ag/Cs/F8BT interfaces and hence shifts the entire XPS spectra to low binding energy region.

Figure 5.14 is the XPS spectra showing the C 1s core level of the Cs-doped F8BT and the enlarged shake-up peaks are depicted in the inset. The C 1s main peak of the pristine F8BT is positioned at a binding energy of 284.9 eV and possesses a FWHM of 0.99 eV. The binding energy and FWHM of the C 1s core level increase to 286.4 and 1.22 eV, respectively, when the Cs concentration is 5.7 %. The increase of the FWHM illustrates that a charge transfer occurs from the Cs to C atoms. Nevertheless, the differences in chemistry between the Ca/F8BT and Cs/F8BT are not the only contributing factor to the energy shifts since these shifts, to a certain extent, are also work-function dependent.

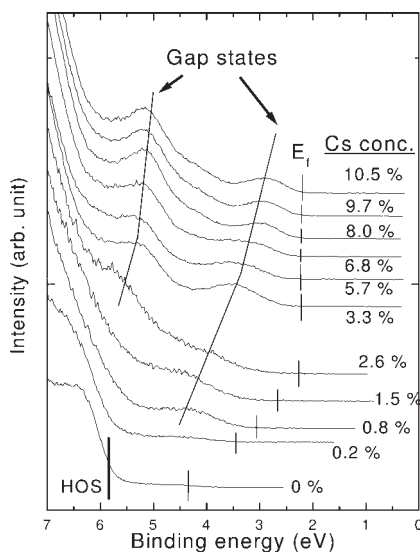
It can be seen from the inset that the shake-up peak at the higher binding energy, which corresponds to the  $\pi$  to  $\pi^*(2)$  or HOMO to UMO transition, broadens and diminishes with increasing Cs concentration. This suggests that the UMO of the F8BT was affected and broadened by Cs deposition and the trend in the shake-up peaks is similar to that of Ca [93] and a number of alkali metals deposited on the PFO [86]. The other shake-up peak related to the  $\pi$  to  $\pi^*(1)$  transition at the lower binding energy, with an energy separation of 2.5 eV relative to the second shake-up peak and 3.6 eV to the C 1s main peak, follows the same trend for Cs concentrations below 3.3 %. At a Cs concentration of 3.3 %, a new peak evolves at the first shake-up peak position. The energy separation of the new peak

**Fig. 5.14** Evolution of XPS C 1s spectra of F8BT with increasing Cs coverage. The two shake-up peaks (peak  $\pi^*(1)$  and peak  $\pi^*(2)$ ) and an extra peak that may be related to oxide, are depicted in the inset.



from the second shake-up peak and C 1s main peak alters to 2.8 and 3.3 eV, respectively, though the second shake-up peak still keeps a separation of 6.1 eV relative to the C 1s core level. At the same time, the intensity of this new peak gradually increases. This experiment has been repeated several times with the same results. It is still unclear whether the new peak corresponds to a new chemical state, extra shake-up peak or the original one with a modified structure. It may be the former because the Cs-F8BT complex can be easily oxidized due to the high reactivity of Cs. After the XPS and UPS analysis that took several hours, a new chemical state related to oxide at a binding energy of 3.3 eV higher than the original C 1s main peak was observed. Similar chemical shifts as observed in many polymers support this scenario [95]. Since it could not be further substantiated from the Cs  $3d_{5/2}$  core level of the XPS because of the proximity of the binding energies between the reacted Cs and  $\text{Cs}_2\text{O}$  [92] and there is no considerable increase of oxygen level from the O 1s peak, further work is needed to clarify the cause.

Figure 5.15 shows the UPS He I spectra with increasing Cs coverage on F8BT. Three clear changes were observed. First,  $\phi$  of Cs/F8BT shifts to a lower binding energy of 2.2 eV at higher metal coverage. Secondly, a new electronic state evolves in the previously forbidden bandgap and a transition of one gap state to two gap states can be identified. The two electronic features emerging at Cs coverage higher than 2.6 % are believed to be bipolaron states. One is at a lower binding energy near the Fermi level, while the other emerges clearly above the HOS of F8BT. The results are similar to those in the PFO films deposited with Ca [85] and different alkali metals [86], and the PPV films covered with Na [59, 64] and Rb [65]. Although Cs preferably interacts with N atoms in the F8BT, the evidences from the existing UPS spectra and behavior of shake-up peaks of C 1s core level as



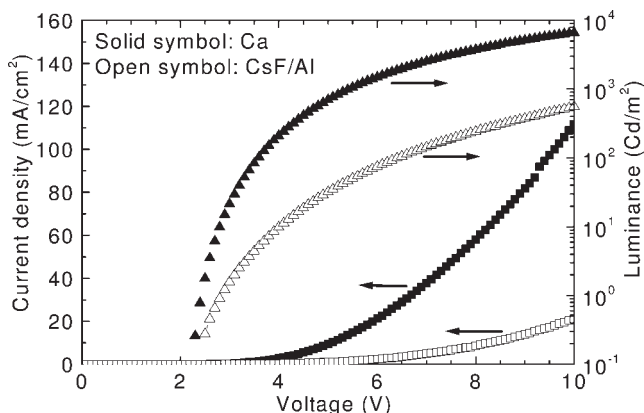
**Fig. 5.15** Enlarged UPS He I spectra with increasing Cs coverage showing regions near the F8BT HOMO. HOS, Fermi level ( $E_f$ ) and gap states are located.

seen from the XPS C 1s spectra shows that Cs also donates negative charges, induces two interbandgap states and broadens the HOMO of the polymer. However, the bipolaron formation may be detrimental to the radiative recombination of holes and electrons and result in luminescence quenching in the PLEDs, since any excitons approaching these gap states, or negative bipolarons, are likely to dissociate and contribute their holes to them [73, 96]. Thirdly, the energy difference between the two gap states is roughly constant at 1.8–2.0 eV, which is also similar in magnitude to those in the previous studies [59, 64, 65, 85–87]. The similar separation observed here indicates that confinement of charge carriers in F8BT is about the same as that in PFO and PPV [59, 66], and hence the phenyl rings in PPV, F8 and F8BT accept nearly the same charges.

Combining all the results from the UPS, S 2p, N 1s, C 1s core levels and its shake-up features of the XPS, it is manifested that Cs favorably interacts with the N atoms of the F8BT and at the same time it brings electronic modification to the polymer that may be undesirable in PLED fabrication. Our findings also suggest that the F8BT possesses two distinct interfaces when interacted with Cs and Ca, which have never been observed in the case of PFO.

Before ending this section, the current density–voltage–luminance characteristics of two PLEDs using Ag/Ca (solid symbol) and Ag/Al/CsF (open symbol) as a cathode, respectively, with 40 nm of poly(3,4-ethylene dioxythiophene) (PEDOT): poly(styrene sulfonate) (PSS) as a polymer anode and 100 nm of F8BT as a green-emitting layer are depicted in Fig. 5.16. The thickness of the Ca, CsF, Al and Ag layers is 50, 5, 80 and 100 nm, respectively. The Al/CsF instead of Cs was used as the cathode since the role of Al on CsF is known to release Cs into the polymer [80]. It can be seen that the Ca device shows much larger current density than the CsF/Al device, in contrast to the common belief that the lower work function of

**Fig. 5.16**  $J$ - $V$ - $B$  characteristics of the devices ITO/PEDOT:PSS (40 nm)/F8BT (100 nm)/Ca (50 nm)/Ag (100 nm) (solid symbol) and ITO/PEDOT:PSS (40 nm)/F8BT (100 nm)/CsF (5 nm)/Al (8 nm)/Ag (100 nm) (open symbol).



Cs ( $\phi = 2.2$  eV) more effectively injects electrons to the polymer layer than the Ca ( $\phi = 2.8$  eV). At an operating voltage of 8 V, the current density in the Ca device ( $60 \text{ mA/cm}^2$ ) is six times higher than that in the Al/CsF device ( $9 \text{ mA/cm}^2$ ), and the Ca device exhibits a luminance of  $4000 \text{ cd/m}^2$  and a current efficiency of  $6.7 \text{ cd/A}$  compared to the corresponding values of  $300 \text{ cd/m}^2$  and  $3.3 \text{ cd/A}$  in the CsF/Al device. The results shown here using Ca as a cathode are analogous to those in another study [73].

## 5.4

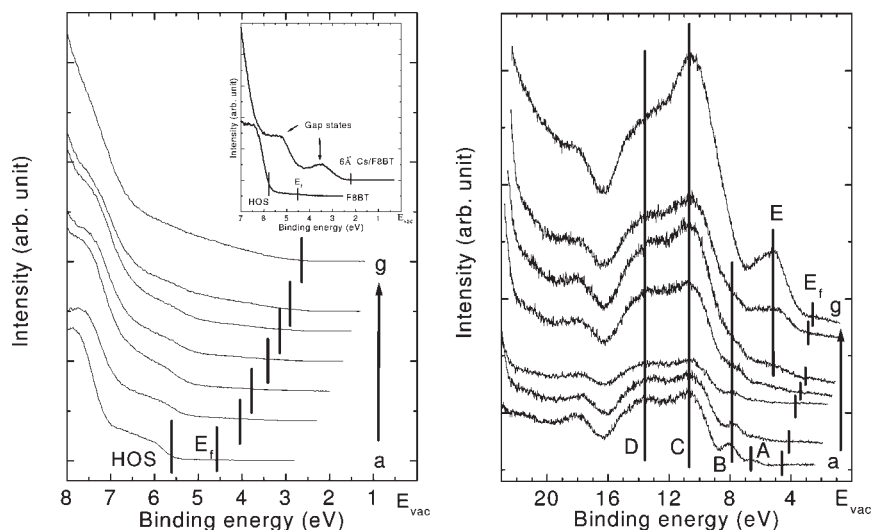
### Role of Ytterbium and Ytterbium/Cesium Fluoride on the Chemistry of F8BT

In this section, we discuss the interfaces of ytterbium (Yb)/F8BT, Yb/CsF/F8BT and Yb/CsF/Au. Yb is of interest since this rare-earth metal has a low work function ( $\phi = 2.6$  eV) and a high negative heat of formation for its fluoride formation ( $\Delta_f H = \sim 1700 \text{ kJ/mol}$  [97]) compared to those of Al ( $\phi = 4.3$  eV,  $\Delta_f H = -1510.4 \text{ kJ/mol}$  [97]) and Ca ( $\phi = 2.9$  eV,  $\Delta_f H = -1228.0 \text{ kJ/mol}$  [97]). These features can not only enhance electron injection (in the case of Yb/F8BT) or facilitate metal fluoride dissociation (in the case of Yb/CsF/F8BT or Yb/CsF/Au), but also can form a stable alloy with Ag that is often used as an encapsulating layer on top of the cathode, i.e. Ag/Yb/F8BT or Ag/Yb/CsF/F8BT. CsF is chosen since the dissociated alkali metal itself has a low work function of 2.2 eV, which in principle further enhances the electron injection into the polymer. Though the configuration of CsF/metal could not be successfully applied to the F8BT device as mentioned above, the use of F8BT in the present work allows us to examine the dissociation process directly by observing the changes of the N, S or C core levels of F8BT. Understanding the chemistry of these metal fluoride/metal interactions can also be useful for application to other OLED devices. Besides, it is worth investigating the interface formation in the Yb/CsF/Au system to understand whether the dissociation of Yb/CsF is polymer dependent or not.

## 5.4.1

## Electronic and Chemical Properties at the Interface of Yb/F8BT

The evolution of UPS He I spectra of F8BT with increasing Yb coverage is depicted in Fig. 5.17(a), with alignment of  $E_{\text{vac}}$  at the origin. The valence structure of the pristine polymer is shown in curve a, and curves b to g correspond to 0.25, 0.5, 1.0, 2.0, 4.0 and 6.0 Å of Yb deposited on top of the F8BT. The molecular orbitals of the F8BT at higher binding energy are not illustrated. The  $E_f$  position and HOS are indicated by vertical bars. With increasing Yb coverage, the work function of Yb/F8BT gradually decreases and eventually shifts to 2.6 eV at high Yb coverages. The intensity of the HOMO of F8BT also gradually decreases with doping, and it is largely swamped out at a Yb coverage of 6 Å. At this coverage, a background emission between binding energies of 3 to 7 eV consists of a residual intensity arising from the deformed HOMO that was also observed in the case of PFO doped with Al [76], and Yb 4*f* core level which occurred at a binding energy of 3 eV above the  $E_f$  [92]. Obviously, no doping induced gap states were observed at the Yb/F8BT interface, in contrast to the case when alkali metals were incorporated into the same polymer. The corresponding spectrum is reproduced in the inset of Fig. 5.17a. The absence of bipolaron states in the present case, which is expected in most doped polymers, implies that the Yb-doped interface of F8BT is somewhat different compared with other common light-emitting polymers such as PFO and poly(*p*-phenylene vinylene) (PPV) [59, 64, 65].



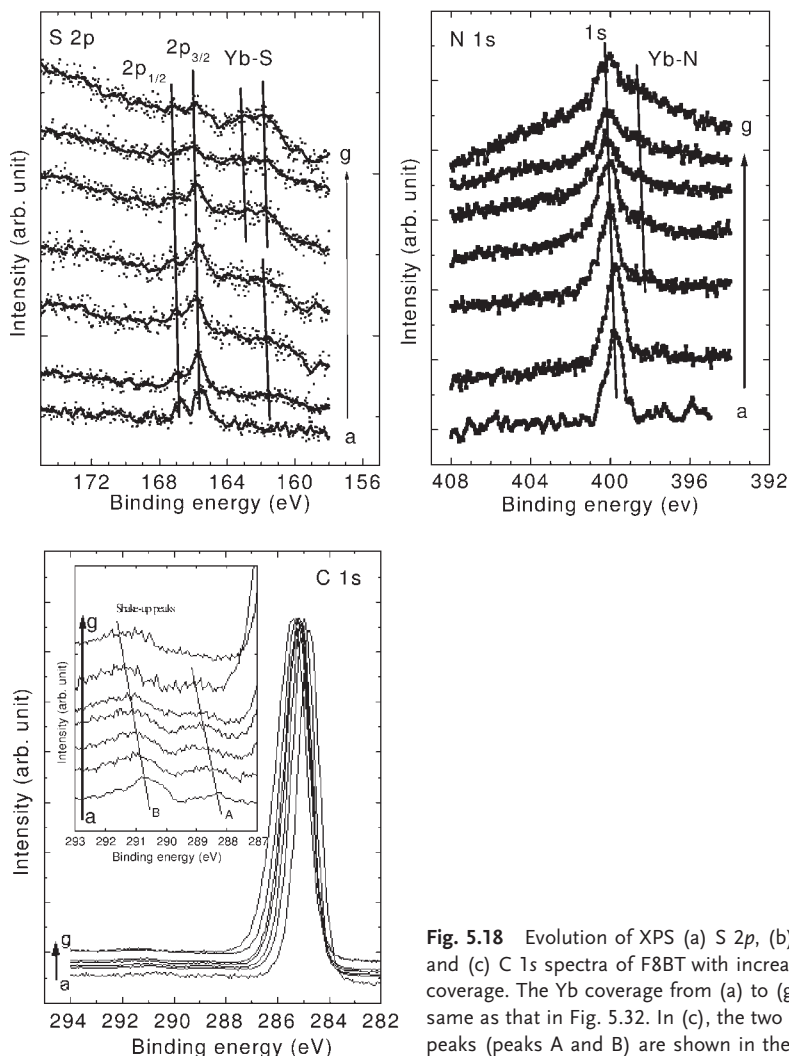
**Fig. 5.17** (a) Enlarged UPS He I spectra showing regions near the F8BT HOMO. The Yb coverage from a to g correspond to 0, 0.25, 0.5, 1.0, 2.0, 4.0 and 6.0 Å, respectively. Fermi level  $E_f$  and HOS are located. The inset shows the same valence band regions on Cs/F8BT.

(b) Evolution of UPS He II spectra of F8BT with increasing Yb coverage. The Yb coverage from a to g is the same as that in (a). The vertical bars pointing at the lowest binding energy side locate the  $E_f$  positions, and peaks A to E correspond to different valence band features.

The UPS He II spectra of F8BT with different coverages of Yb are shown in Fig. 5.17(b). The vertical bar pointing at the lowest binding energy of each curve represents the  $E_f$  positions. Peaks at position A and B, with energy of 1.55 eV apart, are attributed to the maximum of the HOMO and HOMO-1, respectively, derived from the delocalized  $\pi$ -states of the phenyl backbone, which were also observed in other conjugated polymers like PFO and poly(p-phenylene), while C and D located at binding energies of 10.7 and 13.6 eV, respectively, in the pristine film indicate the valence band features originated from the alkyl side chains [58, 78]. With increasing Yb coverage, the HOMO and HOMO-1 intensities diminish gradually, and at the same time peak C and another new peak at position E emerge. The increase of peak C intensity together with the disappearance of peaks A and B implies that some of the  $\pi$ -bonds were broken upon Yb deposition. The destructive behavior of Yb deposited on F8BT in the present case may also be the reason to account for the high operating voltage and low device efficiency of the poly(2-methoxy,5-(2'-ethyl-hexoxy)-1,4-phenylene-vinylene) (MEH-PPV) based LEDs using rare-earth metals such as Yb and samarium (Sm) as a cathode, which was previously reported by Parker [98]. The emergence of peak E is actually a combined intensity arising from the Yb 4f and unresolved satellite peaks of the alkyl side chains (peaks C and D) due to the He II  $\beta$  source as mentioned earlier.

To better understand the reactivity of Yb towards F8BT, the chemistry at the Yb/F8BT interface was studied with XPS, and the corresponding S 2p, N 1s and C 1s core level spectra are shown in Fig. 5.18(a)–(c). Curve a of Fig. 5.18 represents the S 2p peaks of the pristine polymer and the remaining curves from (b) to (g) correspond to Yb coverage of 0.25, 0.5, 1.0, 2.0, 4.0, and 6.0 Å, respectively. The pristine F8BT film exhibits a doublet at binding energies of 165.6 and 166.7 eV, which corresponds to S 2p<sub>3/2</sub> and S 2p<sub>1/2</sub> core levels, respectively [99]. A new doublet at a lower binding energy is evolved upon Yb deposition, and this can be clearly resolved into two chemical states with binding energies of 162.0 and 163.1 eV when the Yb is 6 Å thick. These two new peaks, with 1.1 eV apart and a 4.0 eV difference compared with the original S 2p doublet, are related to Yb–S bonding [92]. Figure 5.18(b) depicts the evolution of N 1s core level of the XPS spectra with different Yb coverage. The N 1s core level of the neat film is positioned at a binding energy of 399.7 eV. With increasing Yb, a new peak at a binding energy of 1.6 eV lower than the main peak emerges. This is specifically for nitride [92] and in the present case it should be a Yb–N covalent bond. Unlike in the case of S 2p, the peak related to the nitride does not grow apparently with the Yb coverage and hence the Yb merely mildly reacts with the nitrogen atoms in the benzothiadiazole rings to form Yb–N covalent adducts.

The evolution of C 1s core level of the XPS spectra of F8BT with increasing Yb coverage is illustrated in Fig. 5.18(c). Their enlarged satellite features are depicted in the inset. The C 1s main peak of the pristine F8BT is located at a binding energy of 284.7 eV and possesses a FWHM of 0.93 eV. With increasing Yb coverage to 6.0 Å, the binding energy and FWHM increases to 285.4 and 1.39 eV, respectively. The higher shift of the C 1s binding energy is derived from the decrease of the work function upon Yb deposition. Nevertheless, the 0.46 eV increase in the



**Fig. 5.18** Evolution of XPS (a) S 2p, (b) N 1s, and (c) C 1s spectra of F8BT with increasing Yb coverage. The Yb coverage from (a) to (g) is the same as that in Fig. 5.32. In (c), the two satellite peaks (peaks A and B) are shown in the inset.

FWHM is relatively large compared with that at the Ca/F8BT (0.25 eV) and Cs/F8BT (0.23 eV) interfaces as mentioned in Section 5.3, assuring that the topmost coverage in all these cases is most likely the same. This may be due to either an immense charge-transfer process between Yb and F8BT or an emergence of a covalently bonded Yb–C complex. The XPS could not resolve the latter from the C 1s core level since the fraction of carbons involved in the Yb–C reaction was insignificant in such a bulky polymer. However, the cause for the C 1s broadening can be realized by correlating the two satellite features in the inset of Fig. 5.18(c) as mentioned below and the corresponding UPS He I spectra as shown in Fig. 5.17(a).

From the inset of Fig. 5.18(c), the pristine film exhibits two magnified satellite peaks at binding energies of 288.4 and 291.2 eV. It can be seen that increasing the Yb coverage broadens and diminishes the satellite peaks, and eventually the one with a lower binding energy (peak B) disappears. These two satellite peaks at A and B are believed to be the shake-up peaks corresponding to  $\pi$  to  $\pi^*(1)$  and  $\pi$  to  $\pi^*(2)$  transitions, respectively. Detailed descriptions of this shake-up process can be found in the previous section. To recall this process in short, peak  $\pi^*(2)$  is known as the shake-up peak for molecules with aromatic group and  $\pi^*(1)$  is for the phenylene chains. These XPS results suggest that part of the LUMOs of the F8BT, particularly the phenylene chains, is affected by the Yb deposition. It is still unclear whether the deterioration of the shake-up peak is due to an electron transfer from the Yb to F8BT or a modification of the phenylene chains by forming Yb–C complexes. We consider that the former case is less likely since we could not observe any formation of new electronic states from the UPS He I spectra as shown in Fig. 5.17(a), which are often presented in other several metal/PFO or metal/F8BT interfaces where charge-transfer processes are taking place. Combining all the photoemission results as mentioned here, it is evident that the Yb favorably and chemically reacts with the S atoms and phenylene chains of the F8BT, but interacts to a lesser extent with the N atoms.

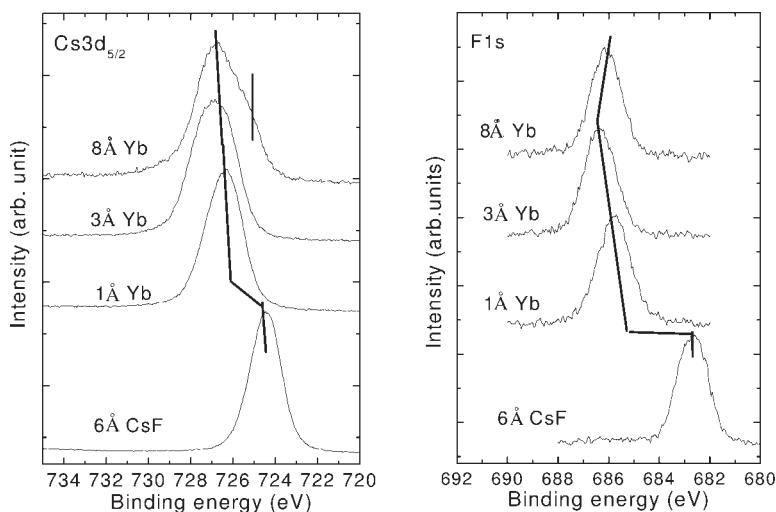
From an ‘ultrahigh-vacuum’ point of view, direct utilization of Yb as a cathode in PLEDs may form an organometallic complex with the polymer backbone that can inhibit the charge-transfer process between the electrode and  $\pi$ -conjugated carbon. However, in an actual device fabrication environment, i.e.  $10^{-6}$  mbar, the evaporated Yb may be in oxide states. Nevertheless, Yb should still be a promising electrode when used in combination with metal fluoride giving the high negative heat of formation typically found in rare-earth metals [97]. In the following sections, it is of interest to know that whether the Yb can dissociate the CsF in the presence of sputter-cleaned Au substrate and F8BT film. UPS spectra will not be presented since deposition of metal on top of CsF may induce charging due to the high photoelectron yield of Cs [80].

#### 5.4.2

##### Chemistry at the Yb/CsF/Au Interface

Figure 5.19 shows the XPS spectra of Cs  $3d_{5/2}$  and F 1s core levels with different coverages of Yb (1, 3 and 8 Å) deposited on top of 6 Å thick CsF/Au. The binding energy of Cs 3d peak of the neat CsF film is positioned at 724.4 eV with a FWHM of 1.73 eV. 1 Å of Yb deposition immediately shifts the Cs  $3d_{5/2}$  core level to 726.3 eV and increases the FWHM to 2.06 eV. The broadening of the Cs main peak indicates that a chemical reaction between the Yb and CsF occurs at the interface, resulting in two or more chemical states that could not be resolved from the XPS. The FWHM continuously increases to 2.78 eV with the Yb coverage, and eventually an extra peak can be clearly resolved at the lower binding energy side. Similar shifts were also observed from the F 1s XPS spectra as shown in Fig. 5.19(b). It is interesting to note that the FWHM of the F 1s first broadens to





**Fig. 5.19** Evolution of XPS (a) Cs 3d<sub>5/2</sub> and (b) F 1s spectra on Yb/CsF/Au. The coverage of the CsF and Yb is indicated in the figure.

1.55 eV at a Yb coverage of 1 Å and then reduces to 1.39 eV at 8 Å Yb coverage, while the binding energy of the main peak position increases from 682.7 to 686.1 eV. The reason for the initial increase of the FWHM of the F 1s is due to the existence of two chemical states, i.e. CsF and YbF<sub>3</sub>. The cause of the reduction at higher Yb coverages will be illustrated in the following paragraph. Besides, the Cs 3d<sub>5/2</sub> and F 1s core levels shifting to higher binding energies are the results of decreasing  $\phi_p$  upon deposition of Yb and charging, as mentioned earlier due to the Yb covered onto the Cs with a high photoemission cross section. Their combined effects possibly overshadow the ‘actual’ shifts related to the chemical interactions between Yb and CsF.

To obtain the ‘actual’ chemical shifts, the differences of binding energies between the Cs 3d<sub>5/2</sub> and F 1s are recorded, as shown in Table 5.1. The binding energy positions and FWHMs upon Yb deposition and the corresponding possible reaction products at each deposition step are also summarized in this table. For the pristine CsF film, the binding energy difference between the Cs and F peaks ( $\Delta\text{Cs-F}$ ) is 41.7 eV, which agrees very well with the typical value [92, 100]. This validates the absence of chemical interaction at the CsF/Au surface. The 0.33 (2.06–1.73 eV) and 0.1 eV (1.55–1.45 eV) broadening of the Cs and F peaks, respectively, and alteration of the  $\Delta\text{Cs-F}$  to 40.5 eV for a 1-Å deposition of Yb reflects an occurrence of chemical reaction that possibly gives the reaction products of dissociated Cs and YbF<sub>3</sub>. The  $\Delta\text{Cs-F}$  remains in the range of 40.5 to 40.7 eV upon Yb deposition. This illustrates that the final reaction products are most likely identical to the previous deposition steps. When the Yb is 8 Å, the FWHM of the Cs 3d<sub>5/2</sub> continuously increases to 2.78 eV while that of F 1s drops to 1.39 eV. This suggest that the CsF largely converts to Cs and YbF<sub>3</sub>, and

**Table 5.1** A summary showing (i) the binding energy position, (ii) the binding energy shift relative to the pristine CsF film ( $\Delta$ ) and (iii) the FWHM corresponding to the Cs  $3d_{5/2}$  and F 1s core levels. The energy differences between the Cs  $3d_{5/2}$  and F 1s ( $\Delta\text{Cs-F}$ ) are recorded in each deposition step, and the corresponding possible reaction products are suggested.

Energy (eV)	Amount of Yb deposited onto the CsF/Au (Å)			
	0	1	3	8
Cs $3d_{5/2}$	724.4	726.3	726.8	726.8 (725.4)
$\Delta$	N/A	+1.9	+2.4	+2.4 (1.0)
FWHM	1.73	2.06	2.52	2.78
F 1s	682.7	685.8	686.3	686.1
$\Delta$	N/A	+3.1	+3.6	+3.4
FWHM	1.45	1.55	1.46	1.39
$\Delta\text{Cs-F}$	41.7	40.5	40.5	40.7 (39.3)
Possible reaction products	CsF	CsF, YbF <sub>3</sub> , Cs	CsF, YbF <sub>3</sub> , Cs	YbF <sub>3</sub> , Cs, (Cs <sub>2</sub> O)

Note:

- (1) The positive sign means a higher binding energy shift.
- (2) The value in the brackets represents information from the extra Cs peak positioned at a lower binding energy as observed in Fig. 5.19(a).

hence the YbF<sub>3</sub> dominates the spectral intensity related to the F 1s core level. If a portion of the CsF is consumed, a similar reduction of the FWHM should be observed in the Cs  $3d_{5/2}$  core level spectra. However, we could not see such a decrease since an extra peak grows up in the proximity of that of the metallic Cs at a lower binding energy of 1.4 eV. If the lower binding energy component of the Cs  $3d_{5/2}$  core level is utilized to determine the  $\Delta\text{Cs-F}$ , it becomes 39.3 eV. This new peak is mostly attributed to the Cs<sub>2</sub>O as the dissociated Cs can be oxidized quickly even in vacuum.

It can be seen that as little as 1 Å of Yb can activate the CsF dissociation. This chemical reaction is driven by the large negative heat of formation of YbF<sub>3</sub>. Table 5.2 summarizes the dissociation energy or heat of formation of CsF, YbF<sub>3</sub> and some representative metal fluorides commonly used in OLEDs. Based on a 'bulk' chemical reaction of  $M_1 + M_2F \rightarrow M_1F + M_2$  and neglecting the changes of entropy energy, the free energy to form M<sub>2</sub> as the final product was estimated, as shown in the same table. It can be calculated that an exothermic reaction occurs upon Yb deposited on CsF, giving an overall heat of formation ( $\Delta_f H_{\text{OA}}$ ) of -9.4 kcal/mol (or -39.5 kJ/mol). This brings up a crucial point that the chemical reaction between the Yb and CsF takes place spontaneously, regardless of the type of substrates. Our calculation agrees well with the experimental results as mentioned earlier. Comparing to the case of  $\text{Al} + 3\text{CsF} \rightarrow \text{AlF}_3 + 3\text{Cs}$ , which

**Table 5.2** Heat of formations (single bond dissociation energy),  $\Delta_f H_2$ , corresponding to different metal fluorides [97] are shown. Based on a 'bulk' chemical reaction of  $M_1 + M_2F \rightarrow M_1F + M_2$  and neglecting the changes of entropy energy, the overall heat of formations (or free energy to form  $M_2$ ),  $\Delta_f H_{OA}$ , are estimated.

$M_1$	$M_2F$ ( $\Delta_f H_2$ , in kJ/mol)	$M_1F$ ( $\Delta_f H_1$ , in kJ/mol)	Chemical reaction	$\Delta_f H_{OA}$ (kJ/mol)
Yb	CsF (−553.5)	YbF <sub>3</sub> (−1700)	Yb + 3CsF $\rightarrow$ YbF <sub>3</sub> + 3Cs	−39.5
Al	CsF (−553.5)	AlF <sub>3</sub> (−1510.4)	Al + 3CsF $\rightarrow$ AlF <sub>3</sub> + 3Cs	+150.1
Al	LiF (−616)	AlF <sub>3</sub> (−1510.4)	Al + 3LiF $\rightarrow$ AlF <sub>3</sub> + 3Li	+337.6
Ca	LiF (−616)	CaF <sub>2</sub> (−1228)	Ca + 2LiF $\rightarrow$ CaF <sub>2</sub> + 2Li	+4.0
Ca	CsF (−553.5)	CaF <sub>2</sub> (−1228)	Ca + 2CsF $\rightarrow$ CaF <sub>2</sub> + 2Cs	−121.0

has an  $\Delta_f H_{OA}$  of +35.9 kcal/mol (or +150.1 kJ/mol), Al + 3LiF  $\rightarrow$  AlF<sub>3</sub> + 3Li which has an  $\Delta_f H_{OA}$  of +80.8 kcal/mol (or +337.6 kJ/mol) and Ca + 2LiF  $\rightarrow$  CaF<sub>2</sub> + 2Ca, which holds an  $\Delta_f H_{OA}$  of +1.0 kcal/mol (or +4.0 kJ/mol), Yb is a promising electrode to assist the metal fluoride dissociation that leads to a better electron injection to many small molecules or polymers in the OLEDs. Moreover, recent studies demonstrated that Li could be liberated from the Al/LiF on Alq<sub>3</sub> [101] but not on PFO [76]. These results further substantiate that the dissociation of Al/LiF is substrate dependent (e. g. the  $\Delta_f H_{OA}$  is negative in a combined reaction of Al + 3LiF + 3Alq<sub>3</sub>  $\rightarrow$  AlF<sub>3</sub> + 3Li<sup>+</sup>Alq<sub>3</sub><sup>−</sup>, while the reaction is endothermic in Al + 3LiF + 3PFO  $\rightarrow$  AlF<sub>3</sub> + 3Li<sup>+</sup>PFO<sup>−</sup>), in contrast to that of Yb/CsF.

However, it has to be pointed out that the predicted trends using the thermodynamic approach should be used with care. For example, it might not be able to consider the derivation caused by various experimental details such as the methods of preparing the thin films. To cite an example, an experimental study [80] showed that Cs could dissociate at the Al/CsF interface though the calculated free energy is endothermic. Therefore, the calculation based on the bulk thermodynamic data may overestimate the true free energy because the vapor-deposited species arrival on the surface are expected to be much more thermally reactive than that of the bulk components [101].

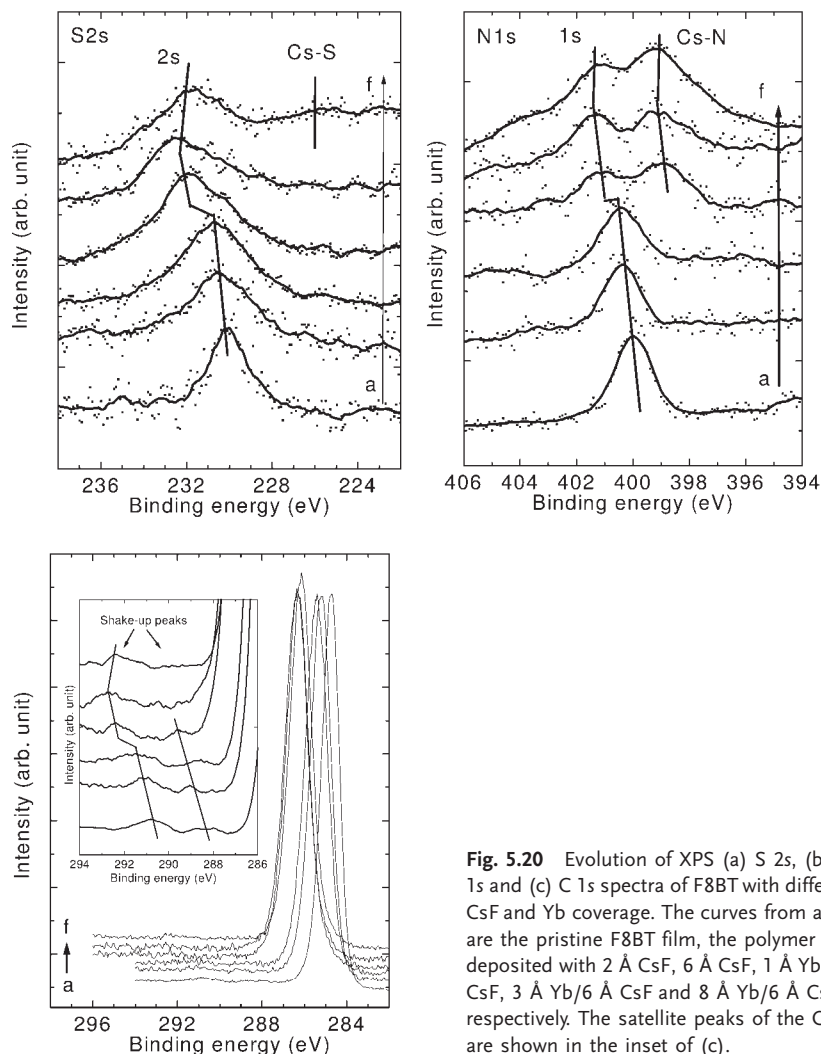
Another interesting finding based on the thermodynamic data is the low  $\Delta_f H_{OA}$  (−28.9 kcal/mol or −121.0 kJ/mol) of the Ca/CsF system. The combined used of Ca and CsF should conceptually construct a novel cathode configuration in OLEDs. Our device studies in Section 5.5 have clarified this presumption. The device performances are also dependent of other factors, e. g. they may be deteriorated by exciton quenching that arise from the gap-state formation over a rather thick interface region due to the highly exothermic reaction between the Ca and CsF.

## 5.4.3

**Chemistry at the Yb/CsF/F8BT Interfaces**

In order to understand the interface formation on the Yb/CsF/F8BT system, interface studies of Cs/F8BT and Yb/F8BT as shown in Sections 5.3 and 5.4 are compared. In short, it was found that the tendency to form sulfide and nitride in both cases is definitely different. For Cs/F8BT, the highly reactive Cs may not sufficiently destroy the rigid sulfur groups, but chemically weakens the N double bonds connected to the aromatic backbone. In contrast, the Yb preferably interacts with the S atoms. Therefore, by looking into the S and N sites on the Yb/CsF/F8BT system by XPS, which will be mentioned in the following, two important events can be identified, i. e. dissociation of CsF and diffusion of Yb.

Figure 5.20 shows the XPS S 2s, N 1s and C 1s spectra with increasing CsF and Yb coverage on F8BT. The curves in alphabetical order are the pristine F8BT film, the polymer film deposited with 2 Å CsF, 6 Å CsF, 1 Å Yb/6 Å CsF, 3 Å Yb/6 Å CsF and 8 Å Yb/6 Å CsF. In the XPS spectra of S 2s and N 1s, a step size of 0.1 eV was used so as to reduce the noise level, since the photoelectron signals related to the S and N may be submerged by the topmost layer of Yb. This does not seriously alter the spectral resolution as the peaks of interest, e. g. sulfide and nitride, are located at least 2 eV far away from the main peaks. However, the settings of the analyzer were still the same as those mentioned before (step size = 0.05 eV, pass energy = 20 eV) for the Cs 3d<sub>5/2</sub>, F 1s, and C 1s core levels, and their energy positions at each deposition step are recorded, as shown in Table 5.3. The possible reaction products are also suggested. In Fig. 5.20(a), it can be seen that the S 2s broadens and shifts to higher binding energy with increasing the CsF coverage. This does not imply a chemical interaction between the CsF and F8BT. As mentioned earlier, the photoelectron signal derived from the Cs 4s core level located at a binding energy of 232.3 eV [92] and charging due to the high photoelectron yield of Cs may contribute to the spectral broadening and shifting, respectively. The  $\Delta\text{Cs-F}$  equal to 41.7–41.9 eV (see Table 5.3) further verifies that the evaporant is still in a state of CsF, compared with that in a recent report [80]. Figures 5.20(a) and (b) present a distinct result when Yb/CsF was deposited onto the polymer, and two significant findings. First, a stable interface is observed from the S 2s spectra when 8 Å of Yb was deposited on top of the 6 Å CsF/F8BT, as shown in Fig. 5.20(a). The 5.0 eV energy difference between the S 2s core level and the broadened small shoulder suggests that the new peak may correspond to the formation of Cs–S complex at a higher Yb coverage, since the energy separation as shown in Fig. 5.18(a) and Fig. 5.12 is 4.0 and 4.8 eV for Yb–S and Cs–S, respectively. No strong component at a lower binding energy is seen, illustrating that the Yb does not diffuse deep into the polymer layer, which is in contrast to the case of Yb/F8BT (Fig. 5.18(a)) that a relatively large peak was found at a binding energy of 4.0 eV below the S main peak. This in turn suggests that the CsF layer can function as a barrier to stop the metal diffusion. Secondly, a clear evolution of a new peak at a lower binding energy in Fig. 5.20(b) shows that the CsF was dissociated upon Yb deposition and hence Cs was liberated, based on the fact that the Cs could strongly interact with the N atoms in



**Fig. 5.20** Evolution of XPS (a) S 2s, (b) N 1s and (c) C 1s spectra of F8BT with different CsF and Yb coverage. The curves from a to f are the pristine F8BT film, the polymer film deposited with 2 Å CsF, 6 Å CsF, 1 Å Yb/6 Å CsF, 3 Å Yb/6 Å CsF and 8 Å Yb/6 Å CsF, respectively. The satellite peaks of the C 1s are shown in the inset of (c).

the F8BT as mentioned in Fig. 5.13. After the Yb deposition, the  $\Delta\text{Cs-F}$  reduces from 41.7 to 39.9 eV. The change of the  $\Delta\text{Cs-F}$  is entirely consistent with the case of Al/CsF/PFO [80] where the CsF was dissociated and  $\text{AlF}_3$  was formed.

From the inset of Fig. 5.20(c), we observe clearly the alternation of the shake-up features of the C 1s core level upon CsF and Yb deposition. The CsF deposition does not affect the shake-up peaks, but 3 Å of Yb immediately destroys one of them at a lower binding energy. This result is analogous to that obtained at the Cs/PFO and Cs/F8BT interfaces, indicating that the LUMO is broadened by the metal deposition by a charge-transfer process. Therefore, unlike the case of Yb/CsF/Au, the liberated Cs is not in the metallic state and instead it immediately

**Table 5.3** A summary showing (i) the binding energy position, (ii) the binding energy shift relative to the pristine CsF or F8BT film ( $\Delta$ ) and (iii) the FWHM corresponding to the Cs  $3d_{5/2}$ , F 1s and C 1s core levels. The energy differences between the Cs  $3d_{5/2}$  and F 1s ( $\Delta$ Cs–F) are recorded in each deposition step, and the corresponding possible reaction products are suggested.

Energy (eV)	Amount of CsF or Yb deposited on F8BT					
	(a) F8BT	(b) 2 Å CsF	(c) 6 Å CsF	(d) 1 Å Yb on b	(e) 3 Å on b	(f) 8 Å on b
Cs $3d_{5/2}$	N/A	724.7	724.9	726.5	726.5	726.4
$\Delta$	N/A	N/A	+0.2	+1.8	+1.8	+1.7
FWHM	N/A	1.61	1.66	1.68	1.71	1.72
F 1s	N/A	682.8	683.2	686.1	686.4	686.5
$\Delta$	N/A	N/A	+0.4	+3.3	+3.6	+3.7
FWHM	N/A	0.87	1.11	1.92	1.55	1.53
C 1s	284.8	285.2	285.4	286.4	286.4	286.2
$\Delta$	N/A	+0.4	+0.6	+1.6	+1.6	+1.4
FWHM	0.96	1.12	1.22	1.23	1.24	1.24
$\Delta$ Cs–F	N/A	41.9	41.7	40.4	40.1	39.9
Major reaction products	F8BT	CsF, F8BT	CsF, F8BT	CsF, YbF <sub>3</sub> , Cs–N, Cs <sup>+</sup> ·F8BT <sup>−</sup>	YbF <sub>3</sub> , Cs–N, Cs <sup>+</sup> ·F8BT <sup>−</sup>	YbF <sub>3</sub> , Cs–N, Cs–S, Cs <sup>+</sup> ·F8BT <sup>−</sup>

Note: The positive sign means a higher binding energy shift.

reacts with the N atoms of the F8BT (to form Cs–N complex) and the polymer backbone (in the form of Cs<sup>+</sup>·F8BT<sup>−</sup>). Since the doped Cs is still in an ionic state, we could not observe an enormous change of the FWHM upon Yb deposition onto the CsF layer. Comparing the FWHMs of the Cs  $3d_{5/2}$  in Table 5.1 and Table 5.3 that correspond to the liberated Cs in metallic (and also oxide) and ionic form, respectively, the former table gives a broadening of 1.05 eV (2.78–1.73 eV) and the latter shows a shift of only 0.06 eV (1.72–1.66 eV).

It should also be noted that Cs–C complex was not formed in the case of Yb/CsF/F8BT since we merely observed a 0.28 eV augment in the FWHM of the C 1s (see Table 5.3), in contrast to the 0.46 eV as observed at the Yb/F8BT interface where the formation of the organometallic complex of Yb–C was expected.

## 5.5

### Highly Efficient and Substrate-Independent Ytterbium/Cesium Fluoride Cathodes

The above interface studies have demonstrated that the application of a bilayer cathode consisting of an ultrathin CsF and a Yb metal leads to the liberation of low  $\phi_m$  Cs (2.2 eV) metal atoms that would act as n-type dopants in the polymer

layer at the interface. In this section, the applications of this Yb/CsF bilayer cathode system for OLEDs based on both small-molecular and polymeric electron-transporting materials are discussed. The motivation is to verify that the CsF dissociation is a substrate-independent process and can be used in combination with most small-molecular or polymeric films.

Figure 5.21 shows the organic materials used in this study; hole-transporting materials:  $\alpha$ -naphthylphenylbiphenyl diamine (NPB) or PEDOT:PSS, electron-transporting and light-emitting materials: tris-(8-hydroxyquinoline) aluminum ( $\text{Alq}_3$ ), 9,10-di-(2-naphthyl) anthracene (DNA), and PFO. Three different types of devices covered with CsF/Yb/Ag were fabricated with configurations as follows,

**Set 1:** ITO/NPB (72 nm)/ $\text{Alq}_3$  (48 nm)/CsF (1.3 nm)/Yb (14.5 nm)/Ag (200 nm)  
 ITO/NPB (72 nm)/ $\text{Alq}_3$  (48 nm)/Yb (14.5 nm)/Ag (200 nm)  
 ITO/NPB (72 nm)/ $\text{Alq}_3$  (48 nm)/Mg:Ag (200 nm)

**Set 2:** ITO/NPB (72 nm)/DNA (48 nm)/CsF (1.3 nm)/Yb (14.5 nm)/Ag (200 nm)  
 ITO/NPB (72 nm)/DNA (48 nm)/Mg:Ag (200 nm)

**Set 3:** ITO/PEDOT:PSS (60 nm)/PFO (70 nm)/CsF (1.3 nm)/Yb (14.5 nm)/Ag (200 nm)  
 ITO/PEDOT:PSS(60 nm)/PFO(70 nm)/Ca(50 nm)/Ag(200 nm)

Control devices with conventional Mg:Ag, Ag/Yb or Ag/Ca were also fabricated for comparison. Figure 5.22 shows the current density and luminance as a function of operating voltage for the  $\text{Alq}_3$ -, DNA-, PFO-based devices, respectively. Figure 5.22(a) shows the current density and luminance as a function of operating voltage for the devices. Apparently, the insertion of the CsF layer significantly improves the device performance. Both  $J$ - $V$  and  $L$ - $V$  curves shift to a lower driving voltage. For instance, the driving voltage at a current densities of  $100 \text{ mA/cm}^2$  of devices with the Yb/CsF, Yb, and Mg:Ag cathodes are 7.15, 7.65 and 11.7 V, respectively. Similarly, the voltages to obtain a luminance of  $1000 \text{ cd/m}^2$  for the

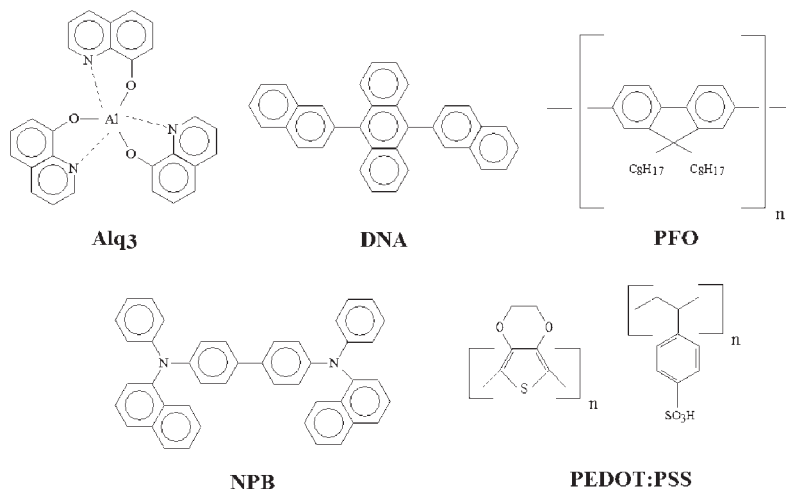
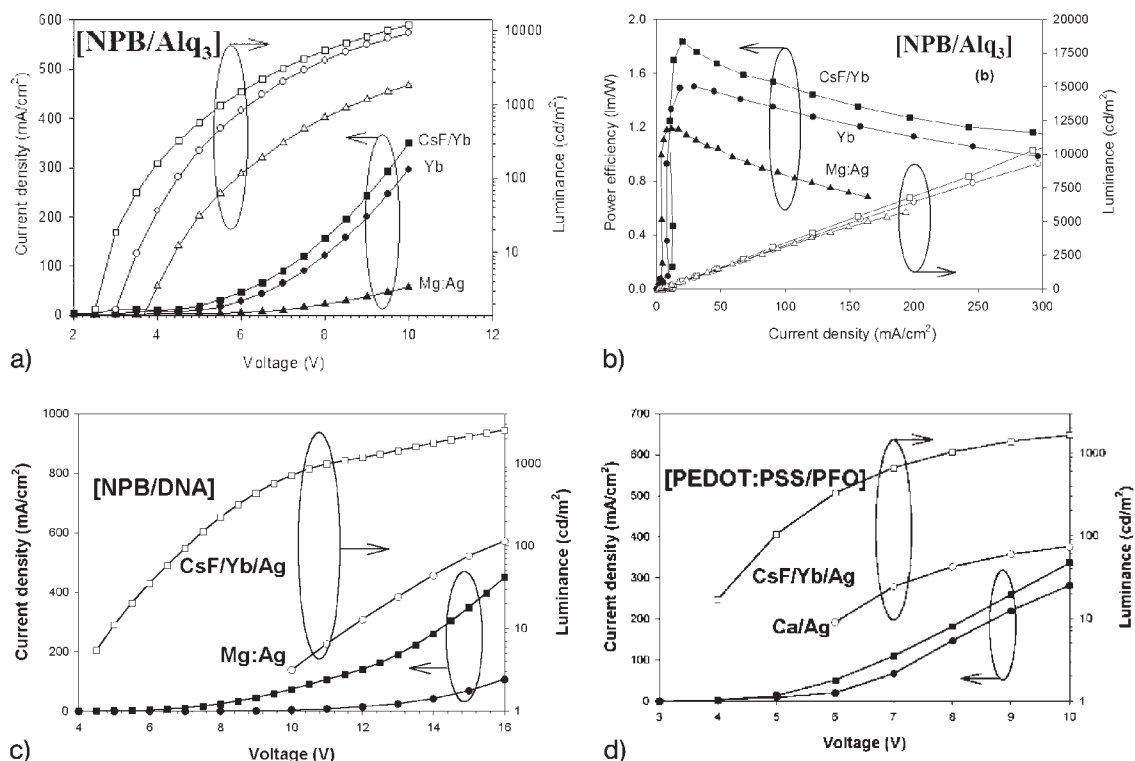


Fig. 5.21 Chemical structures of organic materials.



**Fig. 5.22**  $J$ - $V$ - $L$  characteristics of devices using CsF/Yb/Ag (■) and conventional Mg:Ag or Ca/Ag (●) cathodes with the following configurations: (a) NPB/Alq<sub>3</sub>, while the power efficiency and luminance as a function of current density is shown in (b); (c) NPB/DNA; and (d) PEDOT:PSS/PFO.

three devices are 5.55, 6.20 and 8.60 V, respectively. In addition, the turn-on voltage (defined as the voltage required to obtain a luminance of 1 cd/m<sup>2</sup>) for the device with the Yb/CsF cathode is reduced to 2.42 V, while that for Yb and Mg:Ag cathodes are at 2.95 and 3.75 V, respectively.

A low device operating voltage can also be achieved by reducing the thickness of Alq<sub>3</sub> layer; however, unavoidably, it will lead to a higher leakage current and a lower EL efficiency. In our present approach, the Alq<sub>3</sub> thickness is not reduced. Instead, a better electron-injecting cathode was used to reduce the device-operating voltage. The current and power efficiencies of devices using the Yb/CsF, Yb and Mg:Ag cathodes are shown in Fig. 5.22(b). The efficiency of the standard Mg:Ag device is 2.88 cd/A or 0.61 lm/W, while that of the device using Yb cathode is 3.23 cd/A or 1.13 lm/W at a current density of 200 mA/cm<sup>2</sup>. The efficiency further increases to 3.45 cd/A or 1.27 lm/W for the device with Yb/CsF cathode.

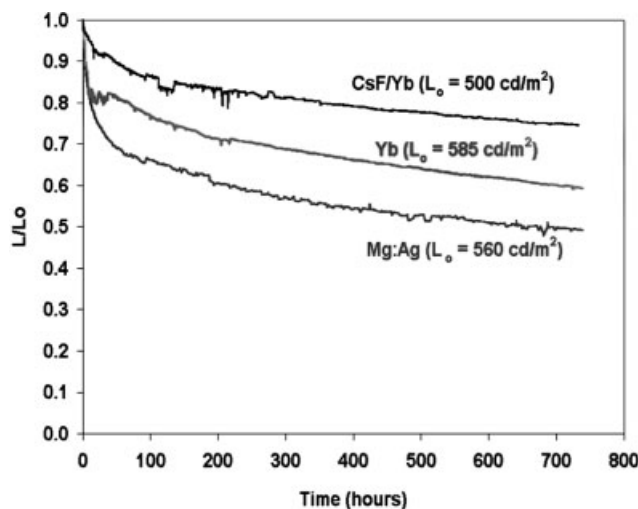
The DNA devices (set 2) give the expected blue emission at 448 nm. The device with the conventional Mg:Ag cathode exhibits poor electrical and optical characteristics, in which only a light output of 75 cd/m<sup>2</sup> and a current density of 70 mA/



$\text{cm}^2$  can be achieved at 15 V (Fig. 5.22(c)), corresponding to a current efficiency of only 0.1 cd/A. Such poor performance is attributed to low electron affinity of DNA, resulting in a large electron injection barrier at the metal/organic interface (see discussion below). By employing the Yb/CsF cathode, device performance is dramatically improved. For example, a luminance of  $2100 \text{ cd/m}^2$  and a current density of  $350 \text{ mA/cm}^2$  were obtained at 15 V. The current efficiency increases by almost six times comparing with that of the device using the Mg:Ag cathode.

Polymer-based devices (set 3) also demonstrate such significant improvement employing the Yb/CsF cathode system. Figure 5.22(d) shows that the operating voltage for devices drastically decreases when Yb/CsF cathode is used; while both the current and the power efficiencies increase, compared to those using the conventional Ag/Ca cathode. The above results illustrate that due to the liberation of the very low  $\phi_m$  of Cs ( $\phi_m$  of Cs, Mg and Ca are 2.2, 3.7 and 2.9 eV, respectively) via the dissociation of CsF at the metal/organic contact, the electron injection barriers at either Yb/CsF/small-molecule or Yb/CsF/polymer interface are dramatically reduced, leading to an enhancement of electron injection and resulting in a better balance of electron and hole currents at the emissive layer for achieving higher device efficiency. It should be noted that the CsF dissociation occurs spontaneously and exothermically upon Yb deposition, regardless of the types of substrates or organic media used. This gives strong evidence that the presented Yb/CsF cathode system can be applicable generally to all types of organic media, either small-molecular or polymeric materials.

A standard NPB/Alq<sub>3</sub> device with the presented Yb/CsF cathode also shows high operational stability. Figure 5.23 exhibits the operational stability of encapsulated device with a configuration of NPB/Alq<sub>3</sub>/CsF/Yb/Ag operated at  $20 \text{ mA/cm}^2$  and room temperature. The stability results for devices using Yb and Mg:Ag as the cathode are also shown for comparison. The initial luminance,  $L_0$ , for the



**Fig. 5.23** Electro-luminescence vs. operating time of standard NPB/Alq<sub>3</sub> encapsulated device with a cathode of CsF/Yb/Ag, using dc driving at a constant current density of  $20 \text{ mA/cm}^2$ .  $L_0$  values are in  $\text{cd/m}^2$ , and the time values are in hours.

Yb/CsF device is  $500 \text{ cd/m}^2$ . The luminance of the device loses only about 33 % after 1600 h. The reason behind this long lifetime may be attributed to the reduced oxygen diffusion at the Yb/CsF interface, which thus significantly suppresses the degradation of devices and suppresses the growth of dark spots, as in the case of Al/CsF/PFO or Al/LiF/Alq<sub>3</sub> [80, 102].

## 5.6

### Conclusions

In this chapter, we review our recent interface studies between F8BT and low work function metals. Through such studies, we show that the combination of XPS and UPS is a powerful approach for unveiling the electronic structure and chemistry of light-emitting polymers and metal/polymer interfaces. In Section 5.3, we report that F8BT shows two distinct interfaces when contacting with Ca and Cs. From the UPS study, Ca formed a stable interface with F8BT without significantly changing the electronic structures of the polymer, which is in contrast to the Cs/F8BT interface where bipolaron states occurred in the previously forbidden gap. XPS revealed that Ca covalently bonded with the sulfur atoms, whereas Cs preferably interacted with the nitrogen in the F8BT. These results are useful to account for the inferior device performance using CsF/Al as a cathode in the F8BT-based polymer light-emitting device. The results in Section 5.4 illustrate the use of low work function rare-earth metals in PLEDs. Direct deposition of Yb onto the polymer ruined the valence band features and formed organometallic complexes with sulfur and carbon atoms. The results show that the Yb may not be a good electron injector in the PLEDs. In addition to the device results in Section 5.5, we show that Yb/CsF is a promising electrode for both small-molecule-based and polymeric OLEDs, because of the negative heat of formation of YbF<sub>3</sub> and substrate-independent dissociation.

### Acknowledgements

We acknowledge Dow Chemical for the supply of chemicals. This work is supported by the Research Grants Council of Hong Kong (CityU 2/02C) and the Chinese Academy of Sciences, P. R. China. Technical support from Prof. S. N. Bao, Dr. S. L. Lai, Dr. M. Y. Chan and Ms. S. W. Tong is greatly appreciated.

## References

- 1 D. D. Eley, *Nature* **1948**, 162, p. 819.
- 2 C. K. Chiang, C. R. Fincher, Y. W. Park, A. J. Heeger, H. Shirakawa, E. J. Louis, S. C. Gau, and A. G. MacDiarmid, *Phys. Rev. Lett.* **1977**, 39, p. 1098.
- 3 M. Pope, H. P. Kallmann, and P. Magnante, *J. Chem. Phys.* **1963**, 38, p. 2042.
- 4 W. Helfrich and W. G. Schneider, *Phys. Rev. Lett.* **1965**, 14, p. 229.
- 5 C. W. Tang and S. A. Van Slyke, *Appl. Phys. Lett.* **1987**, 51, p. 913.
- 6 J. H. Burroughes, D. D. C. Bradley, A. R. Brown, R. N. Marks, K. Mackay, R. H. Friend, P. L. Burns, and A. B. Holmes, *Nature* **1990**, 347, p. 539.
- 7 R. H. Friend, R. W. Gymer, A. B. Holmes, J. H. Burroughes, R. N. Marks, C. Taliani, D. D. C. Bradley, D. A. Dos Santos, J. L. Brédas, M. Lögdlund, and W. R. Salaneck, *Nature* **1999**, 397, p. 121.
- 8 Y. Cao, I. D. Parker, G. Yu, C. Zhang, and A. J. Heeger, *Nature* **1999**, 397, p. 414.
- 9 M. Gross, D. C. Müller, H. G. Nothofer, U. Scherf, D. Neher, C. Bräuchle, and K. Meerholz, *Nature* **2000**, 405, p. 661.
- 10 P. L. Burn et al., *Nature* **1992**, 356, p. 47.
- 11 N. C. Greenham, S. C. Moratti, D. D. C. Bradley, R. H. Friend, and A. B. Holmes, *Nature* **1993**, 365, p. 628.
- 12 D. Braun and A. J. Heeger, *Appl. Phys. Lett.* **1991**, 58, p. 1982.
- 13 G. Gustafsson et al., *Nature* **1992**, 357, p. 477.
- 14 N. Tessler, N. T. Harrison, and R. H. Friend, *Adv. Mater.* **1998**, 10, p. 64.
- 15 C. W. Tang, S. A. Van Slyke, and C. H. Chen, *J. Appl. Phys.* **1999**, 65, p. 3610.
- 16 Z. Shen, P. E. Burrows, V. Bulović, S. R. Forrest, and M. E. Thompson, *Science* **1997**, 276, p. 2009.
- 17 M. A. Baldo, M. E. Thompson, and S. R. Forrest, *Nature* **2000**, 403, p. 750.
- 18 M. A. Baldo, D. F. O'Brien, Y. You, A. Shoustikov, S. Sibley, M. E. Thompson, and S. R. Forrest, *Nature* **1998**, 395, p. 151.
- 19 J. R. Sheats et al., *Science* **1996**, 273, p. 884.
- 20 S. R. Forrest, P. E. Burrows, and M. E. Thompson, *Laser Focus World* **1995**, 31, p. 99.
- 21 J. H. Schön, Ch. Kloc, A. Dodabalapur, and B. Batlogg, *Science* **2000**, 289, p. 599.
- 22 U. Vietze, O. Krauß, F. Laeri, G. Ihlein, F. Schüth, B. Limburg, and M. Braham, *Phys. Rev. Lett.* **1998**, 81, p. 4628.
- 23 S. R. Forrest, *Nature* **1999**, 397, p. 294.
- 24 V. G. Kozlov, V. Bulović, P. E. Burrows, and S. R. Forrest, *Nature* **1997**, 389, p. 362.
- 25 N. Tessler, G. J. Denton, and R. H. Friend, *Nature* **1996**, 382, p. 695.
- 26 F. Hide et al., *Science* **1996**, 273, p. 1833.
- 27 J. H. Schön, Ch. Kloc, A. Dodabalapur, and B. Batlogg, *Science* **2000**, 290, p. 963.
- 28 J. H. Schön, H. Meng, and Z. Bao, *Nature* **2001**, 413, p. 713.
- 29 H. Sirringhaus, T. Kawase, R. H. Friend, T. Shimoda, M. Inbasekaran, W. Wu, E. P. Woo, *Science* **2000**, 290, p. 2163.
- 30 H. Sirringhaus, N. Tessler, R. H. Friend, *Science* **1998**, 280, p. 1741.
- 31 F. Garnier, R. Hajlaoui, A. Yassar, and P. Srivastava, *Science* **1994**, 265, p. 1684.
- 32 L. Torsi, A. Dodabalapur, L. J. Rothberg, A. W. P. Fung, and H. E. Katz, *Science* **1996**, 272, p. 1462.
- 33 Y. Yang, and A. J. Heeger, *Nature* **1994**, 372, p. 344.
- 34 A. R. Brown, A. Pomp, C. M. Hart, and D. M. Deleeuw, *Science* **1995**, 270, p. 972.
- 35 Z. Bao, A. Dodabalapur, and A. J. Lovinger, *Appl. Phys. Lett.* **1996**, 69, p. 4108.
- 36 W. U. Huynh, J. J. Dittmer, and A. P. Alivisatos, *Science* **2002**, 295, p. 2425.
- 37 L. Schmidt-Mende, A. Fechtenkötter, K. Müllen, E. Moons, R. H. Friend, and J. D. MacKenzie, *Science* **2001**, 293, p. 1119.
- 38 M. Granström, K. Petritsch, A. C. Arias, A. Lux, M. R. Andersson, and R. H. Friend, *Nature* **1998**, 395, p. 257.
- 39 C. W. Tang, *Appl. Phys. Lett.* **1986**, 48, p. 183–185.
- 40 J. J. M. Halls et al., *Nature* **1995**, 376, p. 498.
- 41 G. Yu, J. Gao, J. C. Hummelen, F. Wudl, and A. J. Heeger, *Science* **1995**, 270, p. 1789.
- 42 W. Schottky, Halbleitertheorie der Sperrschicht, *Naturwissenschaften* **1938**, 26, p. 843.
- 43 S. Narioka, H. Ishii, D. Yoshimura, M. Sei, Y. Ouchi, K. Seki, S. Hasegawa, T. Miyazaki, Y. Harima, and K. Yamashita, *Appl. Phys. Lett.* **1995**, 67, p. 1899.

- 44 H. Ishii, K. Sugiyama, E. Ito, and K. Seki, *Adv. Mater.* **1999**, *11*, p. 605.
- 45 H. Ishii, K. Sugiyama, D. Yoshimura, E. Ito, Y. Ouchi and K. Seki, *IEEE J. Sel. Top. Quantum Electron.* **1998**, *4*, p. 24.
- 46 K. Seki, E. Ito and H. Ishii, *Synth. Met.* **1997**, *91*, p. 137.
- 47 A. Rajagopal, C. I. Wu, and A. Kahn, *J. Appl. Phys.* **1998**, *83*, p. 2649.
- 48 I. G. Hill, A. Rajagopal, and A. Kahn, *J. Appl. Phys.* **1998**, *84*, p. 3236.
- 49 T. Chassé, C. I. Wu, I. G. Hill, and A. Kahn, *J. Appl. Phys.* **1999**, *85*, p. 6589.
- 50 R. Schlaf, C. D. Merritt, L. A. Crisafuli, and Z. H. Kafafi, *J. Appl. Phys.* **1999**, *86*, p. 5678.
- 51 R. Schlaf, P. G. Schroeder, M. W. Nelson, B. A. Parkinson, P. A. Lee, K. W. Nebesny, and N. R. Armstrong, *J. Appl. Phys.* **1999**, *86*, p. 1499.
- 52 S. T. Lee, X. Y. Hou, M. G. Mason, and C. W. Tang, *Appl. Phys. Lett.* **2000**, *72*, p. 1593.
- 53 S. T. Lee, Y. M. Wang, X. Y. Hou, and C. W. Tang, *Appl. Phys. Lett.* **1999**, *74*, p. 670.
- 54 Y. Park, V. Choong, E. Ettegui, Y. Gao, B. R. Hsieh, T. Wehrmeister, and K. Müllen, *Appl. Phys. Lett.* **1996**, *69*, p. 1080.
- 55 Q. T. Le, F. Nüesch, L. J. Rothberg, E. W. Forsythe, and Y. Gao, *Appl. Phys. Lett.* **1999**, *75*, p. 1357.
- 56 T. Kugler, W. R. Salaneck, H. Rost, A. B. Holmes, *Chem. Phys. Lett.* **1999**, *310*, p. 391.
- 57 M. Lögdlund, T. Kugler, G. Greczynski, A. Crispin, W. R. Salaneck, M. Fahlman, in *Conjugated Polymer and Molecular Interfaces: Science and Technology for Photonic and Optoelectronic Application* (Ed: W. R. Salaneck, K. Seki, A. Kahn and J. J. Piroux), Marcel Dekker Inc., **2002**, p. 73.
- 58 W. R. Salaneck, M. Lögdlund, M. Fahlman, G. Greczynski, and Th. Kugler, *Mater. Sci. Eng. R* **2001**, *34*, p. 121.
- 59 W. R. Salaneck and M. Lögdlund, *Polym. Adv. Technol.* **1998**, *9*, p. 419.
- 60 W. R. Salaneck, S. Stafström, and J. L. Brédas, *Conjugated Polymer Science and Interfaces*, Cambridge University Press, Cambridge, **1996**, p. 150, p. 123 and p. 147.
- 61 Y. Gao, K. T. Park and B. R. Hsieh, *J. Appl. Phys.* **1993**, *73*, p. 7894.
- 62 P. Bröms, J. Birgersson, N. Johansson, M. Lögdlund, and S. R. Salaneck, *Synth. Met.* **1995**, *74*, p. 179.
- 63 Th. Kugler, M. Lögdlund, and W. R. Salaneck, *IEEE J. Selec. Top. Quantum Electron.* **1998**, *4*, p. 14.
- 64 M. Fahlman, D. Beljonne, M. Lögdlund, R. H. Friend, A. B. Holmes, J. L. Brédas, and W. R. Salaneck, *Chem. Phys. Lett.* **1993**, *214*, p. 327.
- 65 G. Iucci, K. Xing, M. Lögdlund, M. Fahlman, and W. R. Salaneck, *Chem. Phys. Lett.* **1995**, *244*, p. 139.
- 66 M. Fahlman, J. L. Brédas, and W. R. Salaneck, *Synth. Met.* **1996**, *78*, p. 237.
- 67 W. R. Salaneck, R. H. Friend, and J. L. Brédas, *Phys. Rep.* **1999**, *319*, p. 231.
- 68 S. Li, E. T. Kang, Z. H. Ma, and K. L. Tan, *Surf. Interface Anal.* **2000**, *29*, p. 95.
- 69 D. Lacey, *9<sup>th</sup> International Workshop on Inorganic and Organic Electroluminescence*, Oregon, Bend, USA, 13–17 September 1998.
- 70 A. W. Grice, D. D. C. Bradley, M. T. Bernius, M. Inbasekaran, W. W. Wu, and E. P. Woo, *Appl. Phys. Lett.* **1998**, *73*, p. 629.
- 71 R. B. Fletcher, D. G. Lidzey, D. D. C. Bradley, S. Walker, M. Inbasekaran, and E. P. Woo, *Synth. Met.* **2000**, *111–112*, p. 151.
- 72 Wang-Lin Yu, Yong Cao, and Alan J. Heeger, *Appl. Phys. Lett.* **1999**, *75*, p. 3270.
- 73 M. Stoessel, G. Wittmann, J. Staudigel, F. Steuber, J. Blässing, W. Roth, H. Klausmann, W. Rogler, J. Simmerer, A. Winnacker, M. Inbasekaran and E. P. Woo, *J. Appl. Phys.* **2000**, *87*, p. 4467.
- 74 I. S. Millard, *Synth. Met.* **2000**, *111–112*, p. 119.
- 75 Y. He, S. Gong, R. Hattori and J. Kanicki, *Appl. Phys. Lett.* **1999**, *74*, p. 2265.
- 76 G. Greczynski, M. Fahlman, and W. R. Salaneck, *J. Chem. Phys.* **2000**, *113*, p. 2407.
- 77 G. Greczynski, M. Fahlman, and W. R. Salaneck, *Chem. Phys. Lett.* **2000**, *321*, p. 379.
- 78 G. Greczynski, M. Fahlman, and W. R. Salaneck, *Appl. Surf. Sci.* **2000**, *166*, p. 380.
- 79 G. Greczynski, M. Fahlman, W. R. Salaneck, N. Johansson, D. A. dos Santos, and J. L. Brédas, *Thin Solid Films* **2000**, *363*, p. 322.

- 80 G. Greczynski, M. Fahlman, and W. R. Salaneck, *J. Chem. Phys.* **2001**, *114*, p. 8628.
- 81 G. Greczynski, W. R. Salaneck, and M. Fahlman, *Synth. Met.* **2001**, *121*, p. 1625.
- 82 G. Greczynski, M. Fahlman, and W. R. Salaneck, *Appl. Surf. Sci.* **2001**, *175*, p. 319.
- 83 G. Greczynski, M. Fahlman, W. R. Salaneck, N. Johansson, D. A. dos Santos, A. Dkhissi and J. L. Brédas, *J. Chem. Phys.* **2002**, *116*, p. 1700.
- 84 L. S. Liao, L. F. Cheng, M. K. Fung, C. S. Lee, S. T. Lee, M. Inbasekaran, E. P. Woo, and W. W. Wu, *Phys. Rev. B* **2000**, *62*, p. 10004.
- 85 L. S. Liao, L. F. Cheng, M. K. Fung, C. S. Lee, S. T. Lee, M. Inbasekaran, E. P. Woo, and W. W. Wu, *Chem. Phys. Lett.* **2000**, *325*, p. 405.
- 86 M. K. Fung, S. L. Lai, S. N. Bao, C. S. Lee, S. T. Lee, W. W. Wu, M. Inbasekaran and J. J. O'Brien, *J. Vac. Sci. Technol. A* **2002**, *20*, p. 911.
- 87 M. K. Fung, S. L. Lai, S. N. Bao, C. S. Lee, J. J. O'Brien, M. Inbasekaran, W. W. Wu and S. T. Lee, *Synth. Met.* **2002**, *128*, p. 97.
- 88 M. K. Fung, S. L. Lai, S. N. Bao, C. S. Lee, J. J. O'Brien, M. Inbasekaran, W. W. Wu and S. T. Lee, *Proc. SPIE* **2002**, *4464*, p. 85.
- 89 [www.webelements.com](http://www.webelements.com)
- 90 A. Barrie, I. W. Drummond and Q. C. Herd, *J. Electron Spectrosc. Relat. Phenom.* **1974**, *5*, p. 217.
- 91 H. F. Franzen, M. X. Umana, J. R. McCreary, R. J. Thorn, *J. Solid State Chem.* **1976**, *18*, p. 363.
- 92 J. F. Moulder, W. F. Stickle, P. E. Sobol and K. D. Bomben, in *Handbook of X-ray Photoelectron Spectroscopy* (Ed: J. Chastain), Perkin-Elmer Corporation, Physical Electronics Division, **1992**.
- 93 L. S. Liao, L. F. Cheng, M. K. Fung, C. S. Lee, S. T. Lee, M. Inbasekaran, E. P. Woo, and W. W. Wu, *Phys. Rev. B* **2000**, *62*, p. 10004.
- 94 J. Sharma, T. Gora, J. D. Rimstidt, R. Staley, *Chem. Phys. Lett.* **1972**, *15*, p. 233.
- 95 G. Beamson and D. Briggs, in *High Resolution XPS of Organic Polymers*, Wiley, Chichester, **1992**.
- 96 Y. Park, V.-E. Choong, B. R. Hsieh, C. W. Tang, and Y. Gao, *Phys. Rev. Lett.* **1997**, *78*, p. 3955.
- 97 D. D. Wagman, W. H. Evans, V. B. Parker, R. H. Schumm, S. M. Baily, I. Halow, K. L. Churney, and R. L. Nuttall, in *Handbook of Chemistry and Physics 67th edn.* (Eds: R. C. Weast, M. J. Astle, and W. H. Beyer), Chemical Rubber Corp., Boca Raton, **1986**, p. 5-5.
- 98 I. D. Parker, *J. Appl. Phys.* **1994**, *75*, p. 1656.
- 99 A. Barrie, I. W. Drummond and Q. C. Herd, *J. Electron Spectrosc. Relat. Phenom.* **1974**, *5*, p. 217.
- 100 W. E. Morgan, J. R. V. Wazer, W. J. Stec, *J. Am. Chem. Soc.* **1973**, *95*, p. 751.
- 101 M. G. Mason, C. W. Tang, L.-S. Hung, P. Raychaudhuri, J. Madathil, D. J. Giesen, L. Yan, Q. T. Le, Y. Gao, S.-T. Lee, L. S. Liao, L. F. Cheng, W. R. Salaneck, D. A. dos Santos, and J. L. Brédas, *J. Appl. Phys.* **2001**, *89*, p. 2756.
- 102 M. Schaer, F. Nüesch, D. Berner, W. Leo, L. Zuppiroli, *Adv. Mater.* **2001**, *11*, p. 116.

## 6

# The Synthesis of Electroluminescent Polymers

Andrew C. Grimsdale

### 6.1

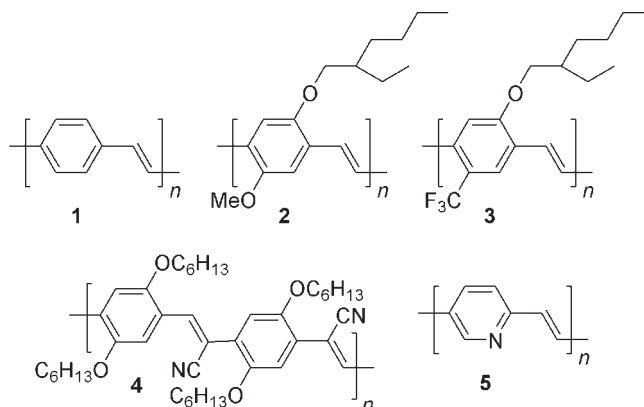
#### Introduction

Since the discovery by Holmes, Friend and coworkers of electroluminescence from conjugated polymers [1], there has been considerable industrial and academic interest in electroluminescent polymers for use as the active materials in light-emitting devices (LEDs) [2, 3] or polymer lasers [4]. Obviously if one is to make commercially viable devices then one needs materials that can produce the desired emission colors, with high emission intensity and efficiency, and show good stability. This presents a challenge to synthetic chemists to design and make polymers that meet these criteria. In particular the control of the emission color, of the charge-accepting and transporting properties, which are important for optimizing device efficiency, and of electrical and optical stability, which are vital factors in determining device lifetimes must be addressed. In this chapter an overview is presented of the main methods by which the most important types of electroluminescent polymers can be prepared with an emphasis on how synthetic design can contribute to the meeting of the above-mentioned device-performance criteria. Space does not permit a comprehensive review of all structures or methods, for which the reader is referred to existing reviews [2, 3], but instead representative structures and syntheses are shown.

### 6.2

#### Poly(arylene vinylene)s

Poly(arylene vinylene)s (PAVs) represent the most widely studied group of electroluminescent polymers. The parent compound poly(*para*-phenylene vinylene) (PPV, 1, Fig. 6.1) [5] is insoluble and so must be processed as a precursor polymer but derivatives such as MEH-PPV (2) [6] with solubilizing alkyl, aryl, silyl, or alkoxy chains show good solubility in organic solvents and so can be readily processed by techniques such as spin casting. By appropriate choice of substituents



**Fig. 6.1**  
Representative  
PAVs.

the emission color of PAVs can be varied between blue-green and red and even into the near infrared. The charge-accepting and transporting properties can be modified by incorporation of electron-withdrawing groups onto the ring as in **3**, or onto the vinylene moiety as in CN-PPV (**4**) [7], or by incorporating heterocycles instead of benzenes as in PPyV (**5**) [8].

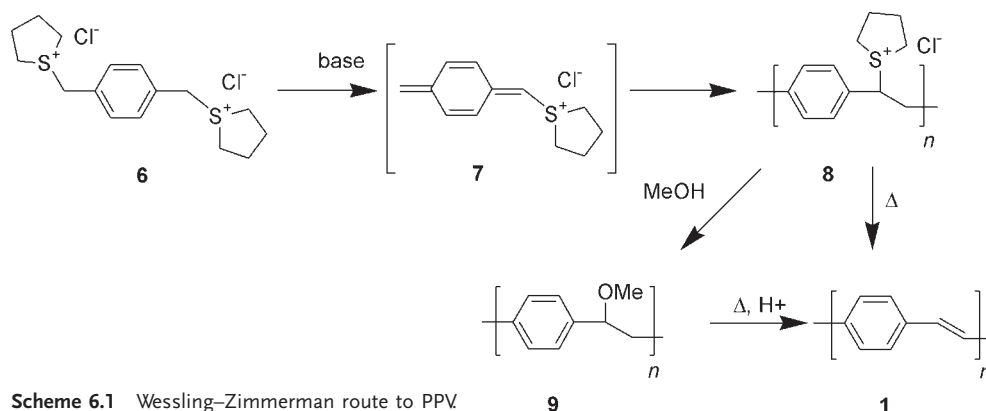
There are four main routes to the synthesis of PAVs [9]: polymerizations via quinodimethane intermediates, polycondensations, transition-metal-mediated polycouplings, and metathesis polymerizations. Other methods such as chemical vapor deposition and electropolymerization have also been used on occasion but generally give poorer quality polymers.

### 6.2.1

#### PAVs via Quinodimethane Polymerizations

These are the most widely used routes to PAVs. The first to be developed was the Wessling–Zimmerman route to PPV as shown in Scheme 6.1 [5]. Here the starting material is a *p*-xylenyl bis(sulfonium salt) **6**, which on treatment with 1 equivalent of base generates a quinodimethane **7**, which then polymerizes to produce the sulfonium precursor polymer **8**. This is water soluble and can be used to make thin films that are thermally converted to the final films of PPV by heating at 220–250 °C under vacuum. Alternatively the sulfonium groups can be displaced by methanol to give the more stable methoxy-precursor **9**, which requires a combination of heat and hydrochloric acid vapor for efficient conversion to **1**.

The mechanism of the Wessling polymerization has been the subject of considerable debate [10]. The intermediacy of the quinodimethane has been established by UV-Vis spectroscopy but there has been much disagreement as to whether the polymerization follows a radical or an anionic pathway. The presence of radical-trapping agents (including oxygen) has been shown to drastically reduce the molecular weight of the PPV formed which suggests that the dominant mechanism is radical [5, 11], but the formation of low molecular mass material by a competing anionic process cannot be totally excluded.

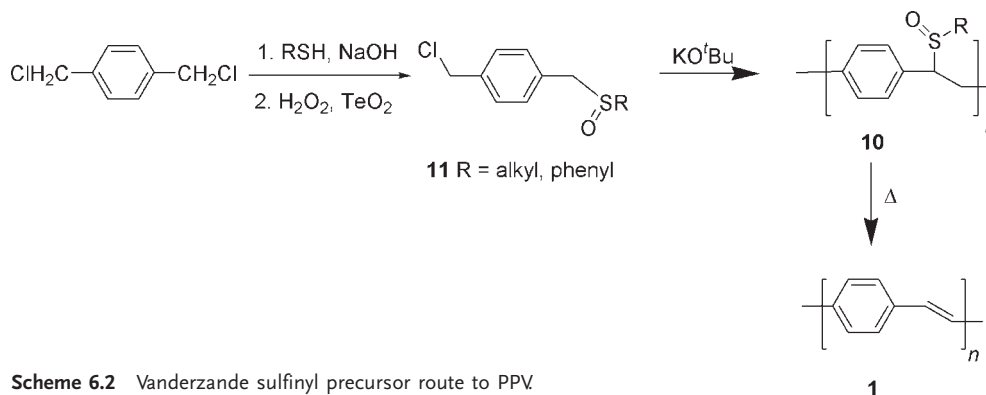


Scheme 6.1 Wessling-Zimmerman route to PPV

There has been considerable effort devoted to optimizing the conditions for the polymerization and the final conversion step [2, 10]. The temperature for the conversion can be dramatically lowered to 100–115 °C by using a bromide [12] or a dodecylphenylsulfonate counterion [13] instead of a chloride. Performing the conversion under an inert atmosphere improves the optical properties of the PPV as traces of oxygen have been shown to induce formation of carbonyl defects during the conversion [14].

The Wessling sulfonium precursor route has also been used to make a variety of other PAVs, including MEH-PPV (2) [15] but in view of the environmentally undesirable properties of the sulfur reagents used (toxicity, stench) other routes are generally preferred for polymers other than PPV.

A number of variations on the Wessling route using other sulfur-based leaving groups have been examined. Vanderzande and coworkers have developed a modified Wessling procedure using a sulfinyl or sulfonyl precursor polymer 10 (Scheme 6.2) [16–18]. The disadvantage of this route is that the synthesis of the monomer 11 is more complicated, despite recent improvements [19–21], but the final PPV is reported to possess fewer defects. Here also a radical mechanism has been demonstrated as leading to the high molar mass polymers [22].

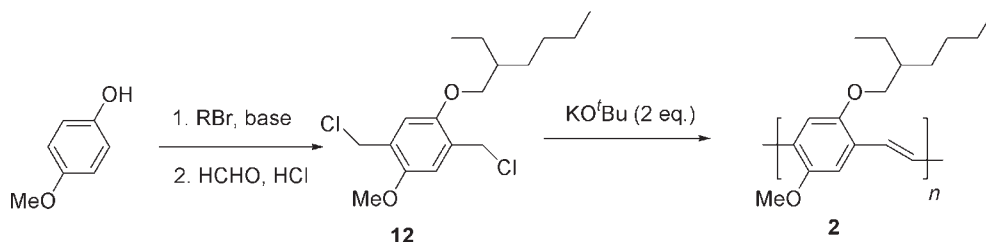


Scheme 6.2 Vanderzande sulfinyl precursor route to PPV



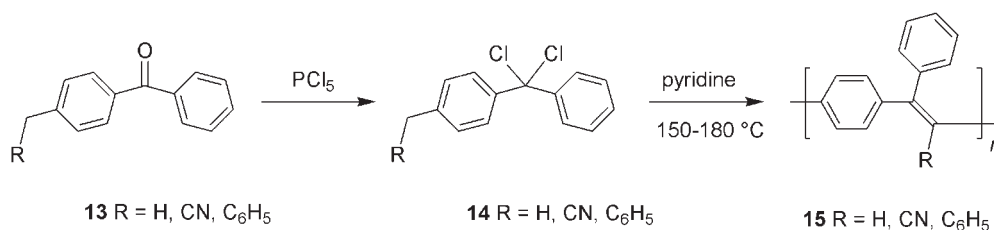
Xanthates have also been used as leaving groups in modified Wessling syntheses of PAVs [23–26].

By far the most popular method for making PAVs is the Gilch synthesis [27], illustrated in Scheme 6.3 for the synthesis of MEH-PPV (**2**). [28] Here a dihalo-methyl **12** monomer (both chloro- and bromo-monomers are used) is converted directly to the PAV by means of an excess of base. If only 1 equivalent of base is used a halo-precursor polymer can be obtained that is then convertible to the conjugated material by treatment with base or by thermal elimination in vacuum. Since the molecular weight of materials in Gilch syntheses can be controlled by addition of benzyl bromide as a chain stopper [29], or of 4-methoxyphenol, [30] a known anionic initiator, an anionic mechanism has been proposed, but the most recent study by Vanderzande and coworkers [31, 32] suggests that, as for the Wessling synthesis, the primary mechanism is a radical pathway, with only low molecular weight materials arising from anionic routes.



**Scheme 6.3** Gilch route to MEH-PPV (**2**).

A related method for preparing PAVs with cyano and/or aryl substituents on the vinylene moieties was developed by Hörhold and coworkers (Scheme 6.4) [33, 34]. Here a benzophenone **13** is converted to a gem-dichloride **14**, which then undergoes base-induced self-condensation to produce the polymers **15**.



**Scheme 6.4** Hörhold route to PPVs with substituents on the vinylene.

There are two major limitations to the quinodimethane-based polymerization methods for making PAVs. First they do not work for all aromatic systems. For example poly(9,10-anthracenyl vinylene) (**16**) cannot be made by these routes as the quinodimethane **17** does not polymerize (Fig. 6.2). [35] A study by Garay et al. [36] determined that the polymerizability of an arylene bissulfonium salt

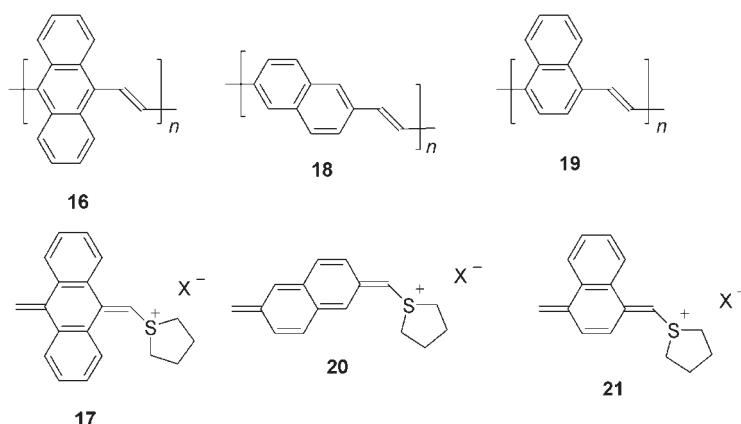
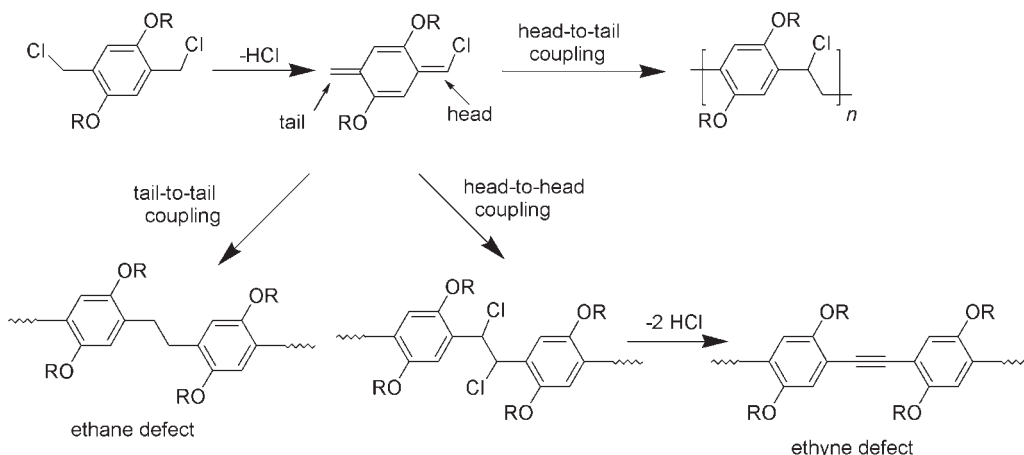


Fig. 6.2 PAVs from quinodimethanes with different degrees of polymerizability.

was determined by the enthalpy of formation of the quinodimethane intermediate, thus enabling one to successfully predict whether a given structure was accessible by the Wessling route. The yield of the reaction is also dependent upon the properties of the quinodimethane. Thus the yield and molecular weight of the 2,6-naphthalene polymer **18** are much lower than for the 1,4-naphthalene polymer **19** made under the same conditions. This is explained by the quinodimethane **20** being less stable than **21** due to the loss of aromaticity in the former and its retention in the latter [37].

A second problem is that the formation of defects that lower the emission efficiency is intrinsic in the polymerization process due to nonregular coupling of the quinodimethane intermediates, as illustrated in Scheme 6.5 for the Gilch synthesis. This has been demonstrated by NMR studies on a  $^{13}\text{C}$ -labelled PPV derivative, in which the ethyne and ethane moieties could be detected in 1.5–2.2% amount [38–40]. By appropriate choice of substituents the levels of these defects can be minimized to obtain high-efficiency polymers [41].

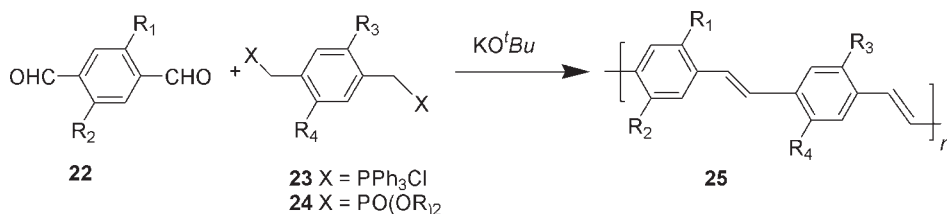


Scheme 6.5 Formation of defects during Gilch synthesis.

## 6.2.2

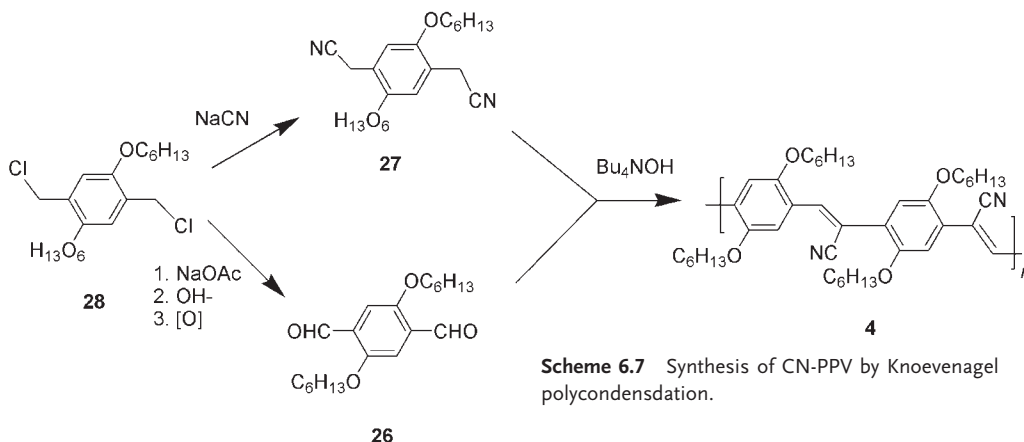
## PAVs via Polycondensations

Both Wittig and Horner condensations of arylbisaldehydes (**22**) with, respectively, aryl bisphosphonium salts (**23**) and bisphosphonates (**24**) have been used to make PAVs (Scheme 6.6). One advantage of these methods is that alternating copolymers (**25**) are accessible that could not be made by the quinodimethane methods. The polymers so obtained are generally of much lower molecular weight than the materials obtained from the Gilch route, but lack the ethane and ethyne defects discussed above and so may show better optical properties. Comparative studies have shown the Horner condensation to be the superior method as it produces higher molecular weight materials with virtually all the double bonds being *trans*, whereas the Wittig condensation results in a high proportion of *cis*-vinylene units, so that the latter material has poorer optical properties [42–44]. Hörhold and coworker [45] have used a Horner polycondensation route to prepare MEH-PPV (**2**) that is much more soluble than the material obtained by the Gilch route, due to its lower molar mass, but whose EL and PL properties match those of the higher mass polymer.



**Scheme 6.6** Wittig and Horner routes to PAVs.

PAVs with nitrile substituents on the vinylene moieties can be prepared by Knoevenagel condensation of a dialdehyde **26** with a bisnitrile **27** as illustrated for the synthesis of CN-PPV (**4**) in Scheme 6.7 [7]. Both monomer components are readily prepared from the bischloromethyl compound **28** otherwise used as a monomer for a Gilch synthesis. Here also, molecular masses are lower than from Gilch synthesis.



**Scheme 6.7** Synthesis of CN-PPV by Knoevenagel polycondensation.

## 6.2.3

## Heck Coupling and other Transition-metal-mediated Methods

Heck coupling of a dihaloarene with a divinylarene offers a direct route to PAVs, either homopolymers or alternating copolymers. As with the condensation methods discussed above, the molecular weights are generally lower than those obtained by the Gilch route, but the materials are relatively defect free. Examples of materials made by this method are the copolymer **29** with *ortho*-phenylene units made using a 1,2-dialkoxy-4,5-diiodobenzene, [46] the regioregular poly(2-dodecyloxyphenylene vinylene) (**30**) obtained by self-polymerization of the vinylbromobenzene **31** [47], and the pyrazine-containing copolymer **32**, prepared from a bis(4-bromostyryl)pyrazine [48]. All of these would be difficult or impossible to synthesize by previously discussed methods.

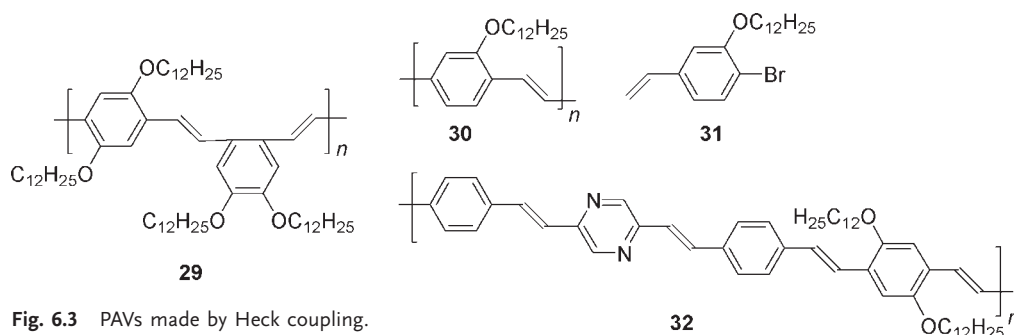
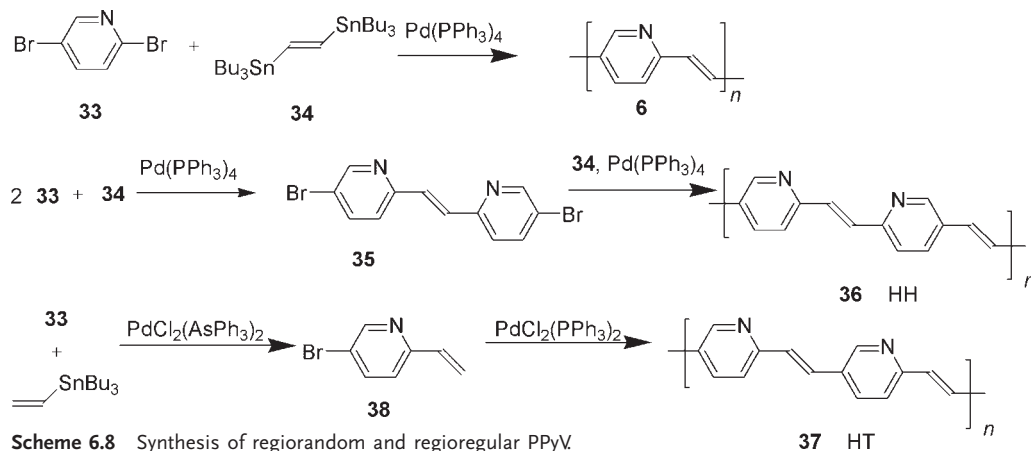
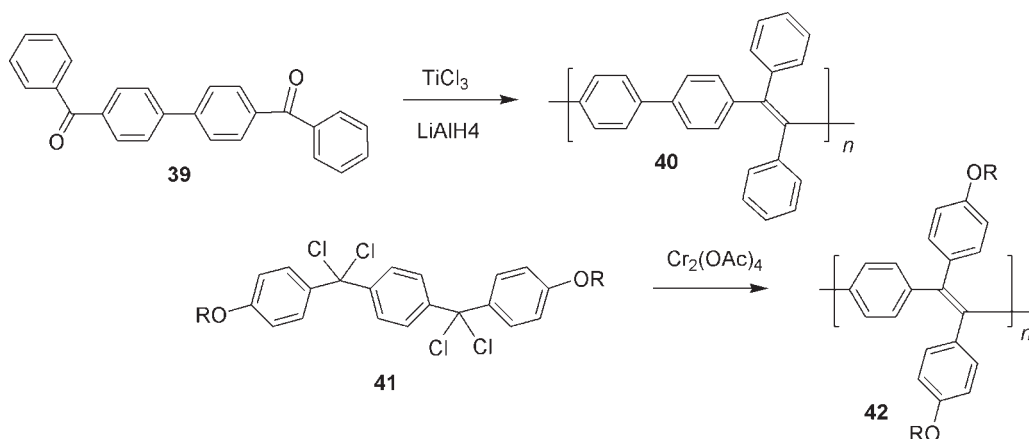


Fig. 6.3 PAVs made by Heck coupling.

Stille coupling of haloarenes with bisstannyl ethene has occasionally been used to make PAVs, but the yields and molecular weights are usually low. Swager and coworkers utilized it to make PPyV (**6**) in both regiorandom and regioregular forms (Scheme 6.8) [8]. Coupling a 1:1 ratio of the halide **33** and stannane **34** produces regiorandom **6**. If a twofold excess of **33** is used then coupling occurs preferentially at the 2-position to give **35** that upon reaction with more **34** produces the head-to-head polymer **36**. The head-to-tail polymer **37** was obtained by selective coupling of a vinylstannane with the 2-position of **33**, followed by Heck homocoupling of the resulting 2-vinyl-5-bromopyridine **38**.



Scheme 6.8 Synthesis of regiorandom and regioregular PPyV



**Scheme 6.9** McMurry and H rhold condensation routes to PAVs with two aryl groups on the vinylene moieties.

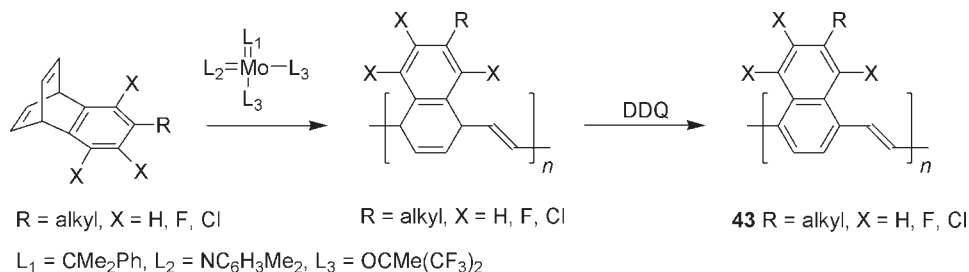
Low-valent transition-metal reagents have been used to make PPVs with two aryl substituents on the vinylene units. Thus Feast and coworkers [49,50] used McMurry coupling of the diketone **39** to make the polymer **40** with a 1:1 ratio of *cis:trans* double bonds (Scheme 6.9). This high amount of *cis*-bonds is a problem with the McMurry method. The H rhold group have utilized a Cr(II) reagent to reductively couple the bis(*gem*-dihalide) **41** (prepared from the diketone using phosphorus pentachloride) to produce similar polymers **42** [51, 52]. These methods generally give much lower molecular weights than the Gilch method, but are useful for making otherwise inaccessible structures.

#### 6.2.4

##### PAVs by Metathesis Polymerization

Two types of methathesis polymerization have been used to make PAVs. Thorn-Cs nyi and coworkers have used transition-metal-mediated metathesis of divinyl-benzenes to make alkyl- and alkoxy-substituted PPVs, but the products are primarily oligomers [53,54].

Ring-opening metathesis polymerization (ROMP) has been used to make precursor polymers to PAVs as shown in Scheme 6.10 for the synthesis of poly(naphthalene vinylene)s **43** by Grubbs and coworkers [55, 56]. ROMP has also



**Scheme 6.10** Synthesis of soluble PNVs by ROMP.

been used to make precursors to PPV [57, 58]. The advantage of ROMP is that it is a living polymerization method, which permits very precise control of the molecular weight of the polymer and is also applicable to synthesis of block copolymers. The disadvantages are that the monomers required may be difficult to prepare, and it cannot be used for a direct synthesis of PAVs.

### 6.2.5

#### Structure–Property Relationships in PAVs

The emission color and efficiency of PAVs is primarily affected by two structural elements – the effects of substituents, and the degree of conjugation along the backbone. Intermolecular effects such as aggregation of polymer chains in the solid state can also affect the emission spectrum (aggregation generally produces a red-shift) as well as the photoluminescence efficiency (aggregation tends to enhance nonradiative decay pathways).

##### 6.2.5.1 Substituent Effects on Emission Color of PPVs

Unsubstituted PPV (**1**) is a yellow-green emitter with emission maxima at 520 and 551 nm [1]. Attachment of alkoxy groups leads to a red-shift in the emission so that the 2-methoxy derivative **44** is a yellow emitter ( $\lambda_{\text{max}} = 550$  nm) [59], and a 2,5-dialkoxy derivative such as MEH-PPV (**2**) displays orange-red emission ( $\lambda_{\text{max}} = 603, 650$  nm) [6]. The size and position of the substituents affects the chain packing and thus the luminescence efficiency. Bulkier side-chains reduce the efficiency of nonradiative decay pathways due to interchain interactions and so increase the PL and EL efficiency [60]. Such interactions can lead to the formation of aggregates that produce a red-shift in the solid-state emission, as has been demonstrated for MEH-PPV (**2**) [61,62]. Extremely large substituents as in **45** seem to dilute the semiconducting properties of the polymer, and so reduce the EL efficiency [63]. Steric effects also produce a blue-shift in the emission maximum ( $\lambda_{\text{max}} = 567$  nm) of **45** due to out-of-plane twisting of the polymer backbone to reduce the steric interactions between the cholestanyloxy groups that reduces the effective conjugation. [63] Similar steric effects explain why green emission is observed from 2,3-dialkoxy-derivatives such as **46** ( $\lambda_{\text{max}} = 530$  nm) or **47** ( $\lambda_{\text{max}} = 513$  nm), and why the PL efficiency of **46** is notably higher than for **2** (40 % cf. 15–20 %) [64, 65].

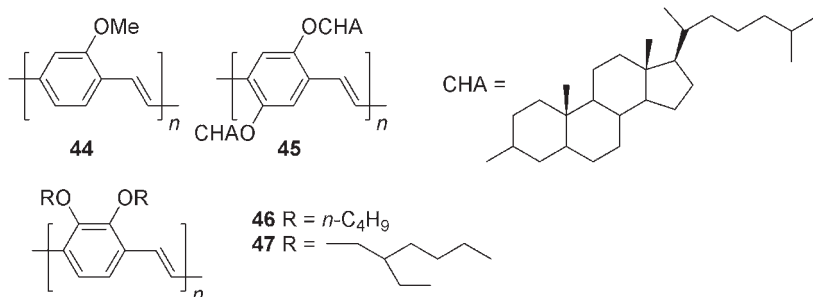
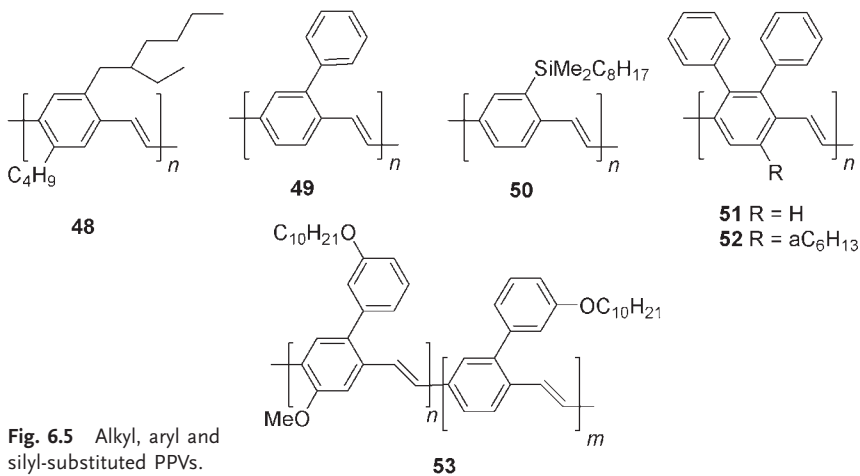


Fig. 6.4 Alkoxy-substituted PPVs.



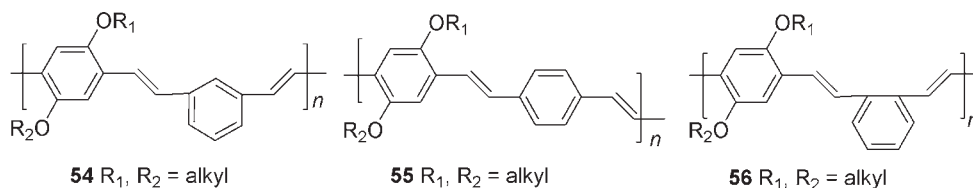
**Fig. 6.5** Alkyl, aryl and silyl-substituted PPVs.

Unlike alkoxy groups, alkyl, aryl and silyl groups do not induce a red-shift in the emission so that for example, BuEH-PPV **48**, [63] PPPV **49** [66], and DMOS-PPV **50** [67], are all green-emitting polymers. The increased steric bulk of the 2,3-phenyl groups in **51** and **52** produces a marked blue-shift in the emission so that these materials show blue-green EL ( $\lambda_{\text{max}}$  = 500 and 490 nm, respectively). A group at Covion have shown that 2-phenyl-PPVs made by the Gilch route have much higher defect levels and thus shorter device lifetimes than 2,5-dialkoxy-PPVs, but that monomers bearing both aryl and alkoxy substituents produce much lower defect levels [37,39]. The copolymer **53** ( $\lambda_{\text{max}}$  = 548–575 nm depending upon *m:n*) thus displays the longest device lifetimes of all reported PPV derivatives [39].

The effect of substituents on the vinylene unit depends upon their steric bulk, so that the cyano groups in CN-PPV (**22**) seem to have no effect upon the position of the emission maxima, whereas the bulky aryl substituents in **40** or **42** produce a marked blue-shift.

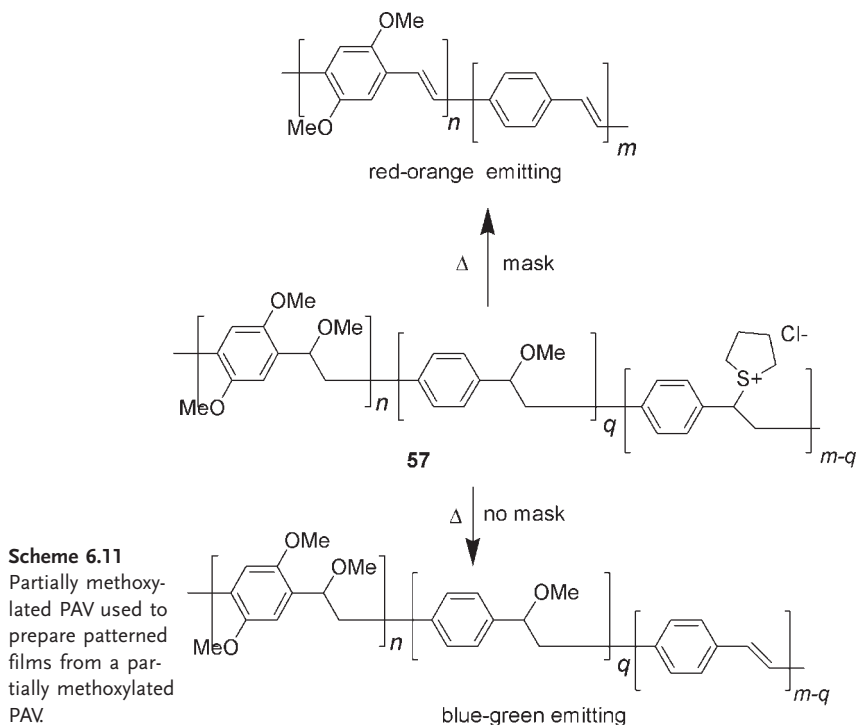
#### 6.2.5.2 Controlling Emission Color via the Degree of Conjugation in PPVs

An obvious way to control the emission color from a conjugated polymer is to control the conjugation length of chromophores within it, by the introduction of units that disrupt the conjugation, and so induce a blue-shift in the emission color. For example *meta*-phenylene units as in **54** break the through conjugation so that the emission maximum is at 490 nm as compared with 550 nm for the all-*para* copolymer **55**. The *ortho*-phenylene units in **56** also produce a blue-shift ( $\lambda_{\text{max}} = 500$  nm), but in this case it is because of out-of-plane twisting of the backbone due to steric interactions between the *ortho*-substituents rather than an interruption of through conjugation [68].



**Fig. 6.6** PAVs with *meta*-, *para*- and *ortho*-phenylene units.

Another way to control the conjugation length is to deliberately introduce non-conjugated units into the polymer chain. This is readily done in precursor-polymer synthesis, e. g. Wessling synthesis, by selectively replacing some of the substituents on the precursor with groups, e. g. acetates that will not eliminate to give the vinylene double bond under the standard conversion conditions. This has been performed by a variety of methods and shown to be an efficient way to control the emission color of PPV [69] and alkoxy-PPVs such as MEH-PPV [15]. The presence of a small fraction of nonconjugated units enhances the EL efficiency due to exciton confinement, while high levels of nonconjugated units reduce the efficiency due to poorer charge transport. Partial replacement of the sulfonium groups with methoxy groups has also been used as a way of patterning films of a dialkoxy-PPV/PPV copolymer (Scheme 6.11) [70]. Methoxylation occurs preferentially at sites adjacent to the dialkoxaphenylenes to produce a copolymer **57** with methoxy groups next to all dialkoxaphenylene units and sulfonium





groups next to most phenylene units. When a film of **57** was heated under a mask the areas under the mask underwent complete elimination as the HCl produced was trapped under the mask where it induced elimination of the methoxy groups to give a red-orange emitting copolymer, whereas in the unmasked areas only elimination of the sulfonium groups occurred to produce a blue-green emitting material.

#### 6.2.5.3 Effect of the Aryl Group on the Emission from PAVs

The emission color of PAVs depends crucially on the nature of the arylene unit. Replacement of a phenylene with an oligophenylene unit produces a blue-shift in the emission, e.g. the poly(pentaphenylene vinylene) **58** is a blue emitter ( $\lambda_{\text{max}} = 446 \text{ nm}$ ) [71], while heterocycles induce red-shifts. This is particularly marked in the case of thiophene so that the polymer **59** actually emits in the near-infrared ( $\lambda_{\text{max}} = 740 \text{ nm}$ ) [72]. The picture with fused polycyclic aromatics is more complicated with the 1,4-naphthalene **19** [73] and 9,10-anthracene **60** [74] polymers both being markedly red-shifted in emission compared with PPV (**1**), while the 2,6-naphthalene **18** [75] and 3,6-phenanthrene **61** [58] materials are slightly blue-shifted.

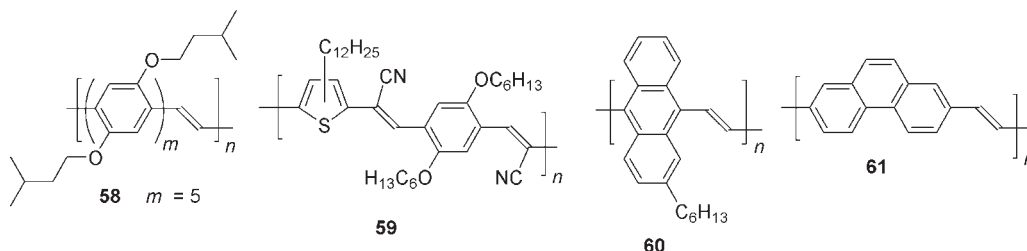


Fig. 6.7 PAVs with units other than benzene.

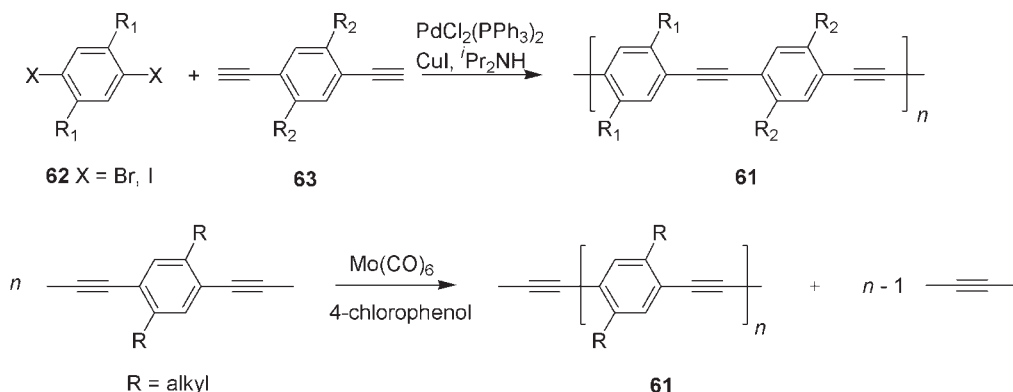
#### 6.2.5.4 Substituent Effects on Charge Injection

Most conjugated organic materials are better hole acceptors than electron acceptors, i.e. they are more readily oxidized than reduced. Thus to obtain efficient EL emission a low work function cathode such as calcium is required, which leads to problems as such materials are sensitive to air and moisture. The use of charge-transporting layers is one solution to this. Another approach is to improve the electron affinity of the material, by incorporating electronegative heteroatoms or substituents. Thus PPV derivatives such as **3** [76] or **4** [7] bearing electron-withdrawing groups, or **5** [8] or **29** [48] containing heterocycles, display better electron-accepting properties, and often higher device efficiencies, than PPV.

## 6.3

## Poly(arylene ethynylene)s

Poly(arylene ethynylene)s (PAEs, **61**) [77] are more rigid than PAVs and show a greater tendency towards aggregation, which produces marked red-shifts in their solid-state luminescence. They have been less utilized in LEDs than PAVs, largely due to the lack of good-quality polymers. Two routes (Scheme 6.12) have been used to prepare them: Hagihara–Sonogashira coupling and alkyne metathesis. The former involves the polycoupling of an aryldiyne **62** with a dihaloarene **63** – either bromo or iodoarenes can be used with the latter being much more reactive. The advantages of this method are the wide range of substrates it is applicable to, and the ability to make alternating copolymers. Disadvantages are the need for exact stoichiometry to obtain high molecular weight, the presence of potentially fluorescence-quenching halogens as endgroups, and the formation of diyne defects due to alkyne homocoupling. Much of the early materials made by this route were of poor quality, leading to inefficient EL emission.



**Scheme 6.12** Synthesis of PAEs.

The metathesis procedure has been developed by Bunz [77] and has the advantage of producing defect-free materials with well-defined endgroups. These materials are of much higher quality than those from the polycoupling method and so produce better results in LEDs. The disadvantages of this method include the greater experimental difficulty, which it is not applicable to all alkynes, and that it is useful only for homopolymers or statistical copolymers.

The substituent effects in PAEs match those seen in PAVs [77]. Most PAEs investigated to date have been poly(p-phenylene ethynylenes) (PPEs) with alkoxy- (red-orange emitting) or alkyl substituents (green emitting). Blue emission has been seen from PPEs with *meta* – or *ortho*-phenylene units [78,79], or with bulky substituents that reduce interchain interactions [80].

## 6.4

## Polyarylenes

Polyarylenes form the second most studied group of electroluminescent polymers. The most important classes are polyphenylenes, e.g. poly(*para*-phenylene)(PPP, **64**) [81], which are of particular importance as blue-emitting materials, and poly(3-alkylthiophene)s (P3ATs, **65**), [82] which are generally orange-red emitters. Polymers containing nitrogen-heterocycles, e.g. poly(2,7-carbazoles) (**66**) [83], are of interest because of their better charge-transporting properties. By controlling the steric interactions between substituents the planarity of the polymer main chain and thus the degree of conjugation and the emission color can be controlled. In P3ATs the degree of head-to-tail (HT) coupling (regioregularity) of the thiophene units is thus important in determining the polymer properties [82]. For polyphenylenes the planarity of the polyphenylene backbone can be controlled by means of methine bridges e.g. in ladder-type PPP (**67**) [84]. The use of copolymers enables one to tune the properties by incorporating low-bandgap units as in the green-emitting copolymer **68** [85], while charge transport can be controlled by incorporation of charge-transporting units, e.g. oxadiazoles or triaryl amines, either within the main chain (**69**) [86] or as side chains (**70**) [87].

A wide variety of synthetic methods have been used to prepare polyarylenes [9]. The main methods are arene couplings that fall into three classes: oxidative couplings, reductive couplings, and transition-metal-mediated crosscouplings. Precursor methods are used for the insoluble PPP, while polymers containing heterocycles such as oxadiazoles or quinolines can be made by efficient polymer analogous heterocyclic synthesis reactions. One advantage of polyarylenes over PAVs is these synthetic methods generally preclude the incorporation of defects that are a major problem with many of the routes to PAVs.

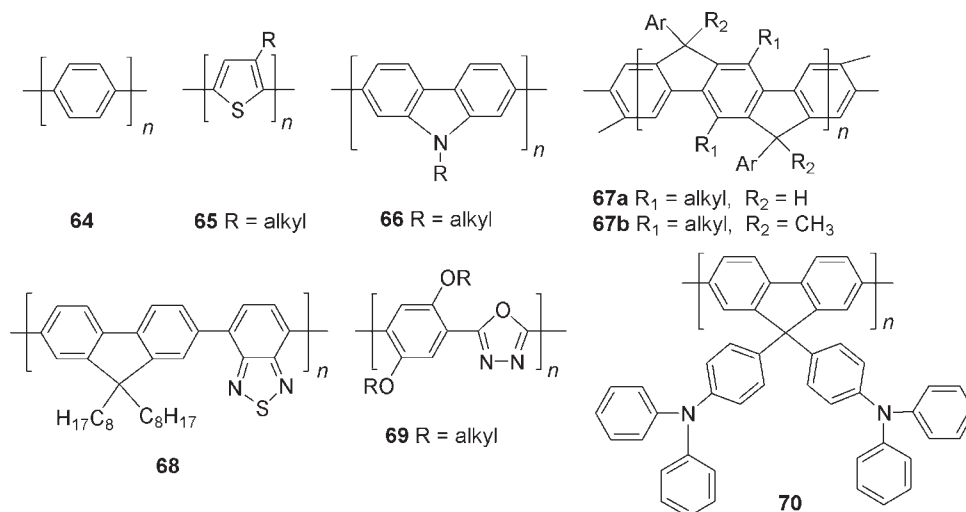
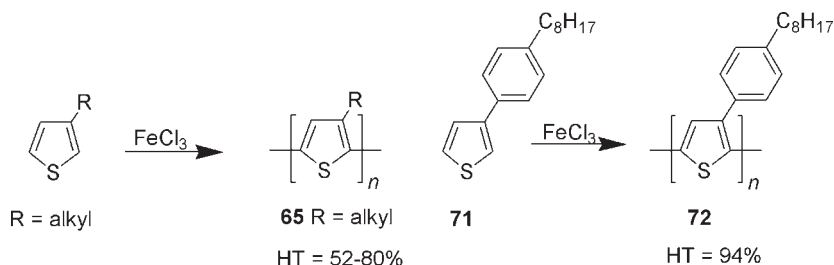


Fig. 6.8 Some representative polyarylenes.

## 6.4.1

**Oxidative Coupling of Arenes**

Oxidative coupling of 3-alkylthiophenes with iron(III) chloride to give soluble poly(3-alkylthiophene)s (P3ATs, **65**) (Scheme 6.13) was introduced by the group of Wegner [88]. Since then it has been used to make a wide range of substituted polythiophenes. This method, however, produces regiorandom polymers with a proportion of 2,5- (head-to-tail, HT) coupling of between 52 and 80 % depending upon the reaction conditions and the substrate [89, 90]. Andersson and coworkers [91] have shown that oxidation of 3-arylthiophenes **71** in which the aryl substituent stabilizes the 2-cation and hinders 2,2-coupling by its bulk produces regioregular (94 % HT) polymers **72**. While the oxidative coupling of thiophenes produces good yields and high molecular weights, generally only low molecular weight polymers are obtained from oxidation of other aromatic materials.

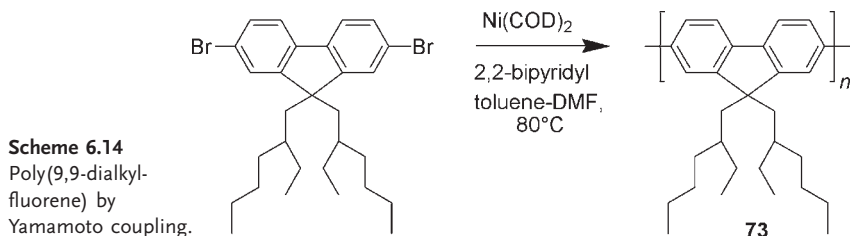


**Scheme 6.13** Polythiophenes by oxidative polymerization.

## 6.4.2

**Reductive Coupling of Arenes (Yamamoto Coupling)**

The reductive coupling of arenes is one of the most important methods for preparing polyarenes. A number of methods have been used, but the most widely used is that developed by Yamamoto [92] using bis(cyclooctadiene)nickel(0) ( $\text{Ni}(\text{COD})_2$ ) and 2,2'-bipyridyl as illustrated in Scheme 6.14 for the synthesis of a polyfluorene **73** [93].



This coupling is usually performed using dibromoarene monomers but chloro- and iodo- monomers can also be used. Percec and coworkers have prepared polyphenylenes by nickel(0) coupling of bistriflates and bismesylates [94, 95]. A disadvantage of the Yamamoto procedure is that the expensive nickel reagent must be used stoichiometrically but other procedures using inexpensive nickel(II) and a reducing agent such as zinc do not give as good results [92]. Limitations of this method are that it can only be used for homopolymers or statistical copolymers and that it is incompatible with some functional groups, e. g. alkynes that bind to (and thus deactivate) the reagent.

#### 6.4.3

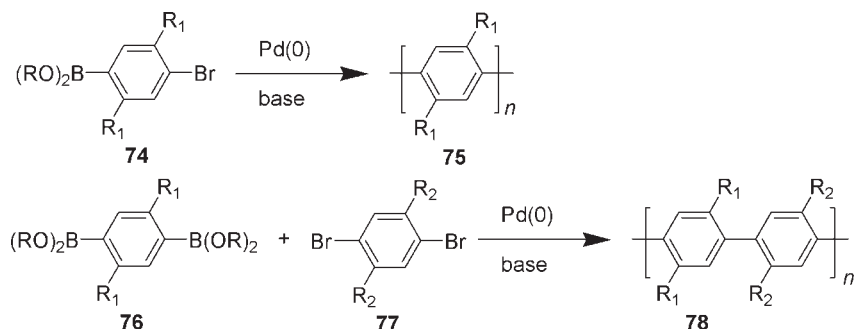
##### Transition-metal-mediated Crosscoupling Reactions

Transition-metal-mediated crosscoupling reactions are the most important and widely used methods for coupling arenes [96] so that it is natural that they have become equally important for the synthesis of polyarenes. All of the major crosscoupling reactions have been used in polymerizations, but the most important is Suzuki coupling, which generally gives the highest yields and molecular weights. Other methods such as Stille coupling generally give much lower yields and molecular weights than Suzuki polycondensation, but Kumada and Negishi coupling are used for the synthesis of high molecular weight regioregular polythiophenes.

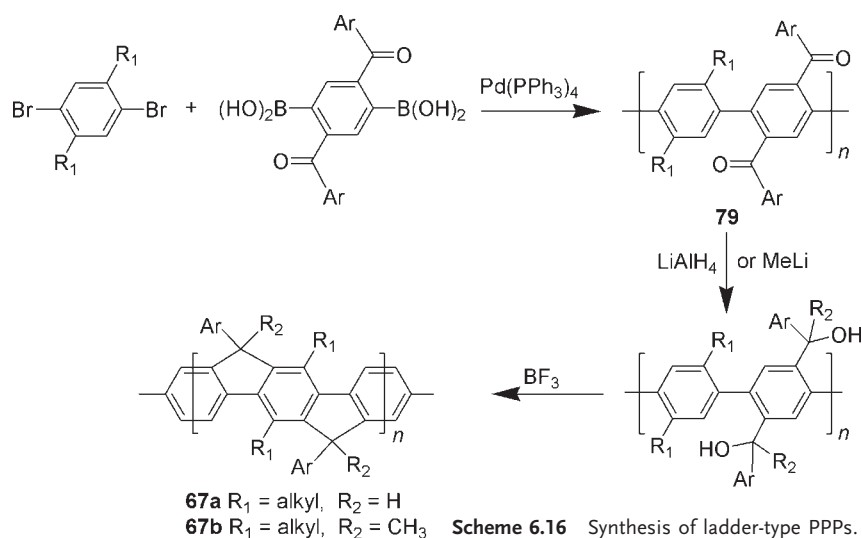
##### 6.4.3.1 Suzuki Polycondensation

Suzuki polycondensation [97] is the most widely used method for making polyarenes. Two variations are used: AB coupling and AA–BB coupling, which are illustrated for the synthesis of polyphenylenes in Scheme 6.15. In the former a monomer **74** containing one boronic acid and one halide functional group is self-condensed to give the homopolymer **75**. Statistical copolymers are also possible by this route. In the latter a bisboronate **76** is condensed with a bishalide **77** to produce a polymer **78** that may be either a homopolymer ( $R_1 = R_2$ ) or an alternating copolymer ( $R_1, R_2$  different). The main problem with the AA–BB method is that an exact 1:1 stoichiometry of the two components is required to obtain high molecular weights that can be difficult to achieve experimentally. On the other hand the monomers **76** and **77** are generally much easier to prepare and purify than **74**. For this reason, the AA–BB method is the more widely used. Since deboronation can be a problem with electron-rich systems such as thiophenes, usually such units are used as the dihalide in Suzuki polycondensations.

An excellent example of the use of Suzuki polycondensation is the synthesis of ladder-type PPPs (**67**) (see Scheme 6.16) [84]. A precursor polymer **79** is prepared by AA–BB coupling and then converted to the ladder polymers by polymer analogous reactions. Reduction followed by ring closure with boron trifluoride produces a polymer (**67a**) with bridgehead hydrogens, while addition of methyl lithium instead of reduction leads to Me-LPPP (**67b**) with methyls at the bridgeheads.



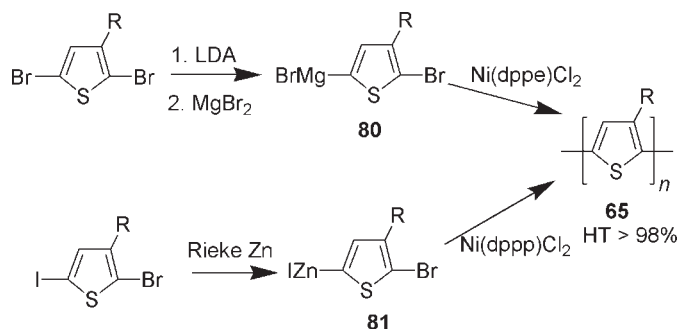
**Scheme 6.15** Suzuki polycondensation by AB (above) and AA-BB (below) methods.



**Scheme 6.16** Synthesis of ladder-type PPPs.

#### 6.4.3.2 Regioregular Polythiophenes by Crosscoupling

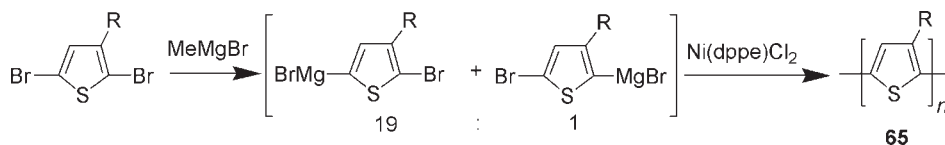
Efficient routes (Scheme 6.17) to regioregular P3ATs **65** (HT >98%) were developed almost simultaneously by McCullough [98, 99] and Rieke and coworkers [100,101]. The former used a regioselective metal-halogen exchange to make the thienyl Grignard **80** that underwent Kumada coupling to produce **65**. The latter used a selective insertion of activated zinc into the iodide of a 5-iodo-2-bromo-



**Scheme 6.17**  
McCullough and  
Rieke routes to  
regioregular P3ATs.

mothiophene to make the thienyl zinc compound **81**, which gave **65** by Negishi coupling. Both methods give similar yields, molecular weights, and regioregularities.

In both cases high molecular weights depend upon obtaining very pure intermediates which is not experimentally trivial. McCullough and coworkers [102] have since developed a simpler Grignard metathesis (GRIM) method to regioregular polythiophenes (Scheme 6.18), which can be performed on a large scale. Here, a mixture of the 5- (95 %) and 2-magnesium (5 %) compounds is obtained from the metathesis, but the product is still highly regioregular (> 95 % HT), which they showed is due to a mixture of kinetic and thermodynamic factors [103].



**Scheme 6.18** Grignard metathesis (GRIM) route to regioregular P3ATs.

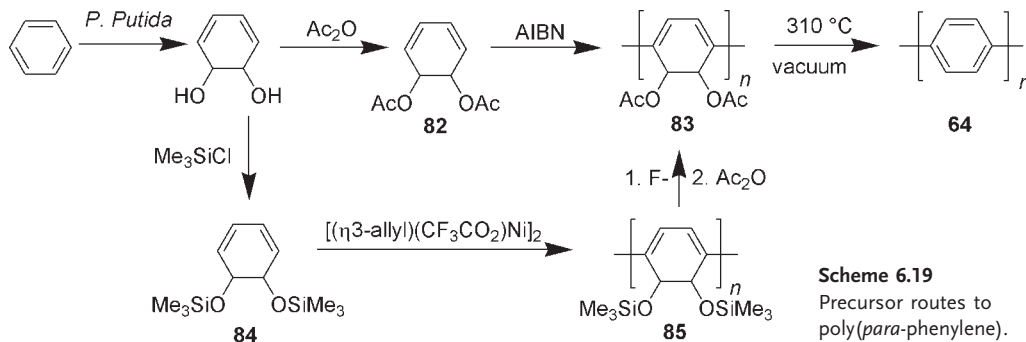
HT > 95%

Other methods, e. g. Stille coupling [104], have also been used to make regioregular polythiophenes, but the yields and molecular masses are significantly lower than for the methods described above.

#### 6.4.4

##### Precursor Routes to Poly(*para*-phenylene)

Poly(*para*-phenylene) (PPP, **64**) is insoluble and infusible and so films of PPP must be made by precursor routes (Scheme 6.19) [105]. The first of these, which was developed at ICI [106, 107], utilizes a radical polymerization of the diacetate **82** to produce a precursor polymer **83** that is thermally converted to PPP. This method produces PPP containing about 15 % 1,2-linkages. A totally *para*-polymer can be made by the method of Grubbs involving the stereoregular nickel-catalyzed living polymerization of the bis(silyl ether) **84** to **85**, and then its conversion to **83** [108–110].

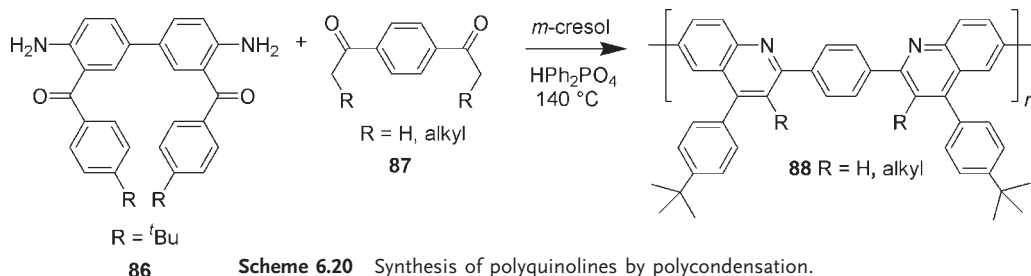


**Scheme 6.19**  
Precursor routes to poly(*para*-phenylene).

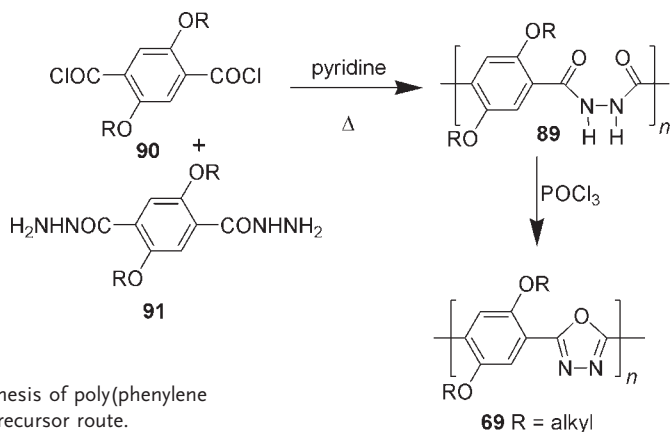
## 6.4.5

## Polyarylenes by Heterocyclic Polysynthesis

The existence of highly efficient heterocyclic ring-forming reactions allows polymers containing such rings to be made by polycondensations. For example, condensation of the diamine **86** with the diketone **87** gives the polyquinoline **88** [111]. The yields of these condensations are generally high but the molecular weights of the resulting polymers are usually only moderate.



Polyheterocycles can even be made by polymer analogous reactions. A good example of this is the formation of oxadiazole-containing polymers. Thus, Janietz et al. [86] prepared the precursor polymers **89** by the polycondensation of **90** with **91** and then dehydrated it with phosphorus oxychloride to give the phenylene oxadiazole copolymers **69** (Scheme 6.21).





## 6.4.6

## Structure–Property Relationships

As with PAVs, the properties of polyarylenes are dependent in many ways upon their structures. First, the nature of the arene unit affects the emission. For example, phenylene-based materials have large bandgaps and so are blue emitters, whereas materials based on heteroarenes such as thiophene have much smaller bandgaps and so emit at longer wavelengths. Thus by varying the composition of copolymers one can tune their emission. Secondly, the relative planarity of the system affects the color as more planar materials have better conjugation and thus smaller bandgaps. Substituents also affect the color as steric interactions can produce out-of-plane twisting of the polymer backbone that produces blue-shifts in the emission. Since aggregation can lead to red-shifts in emission, or enhance nonradiative decay pathways, attaching bulky side chains to increase inter-chain separation can be used to control the emission color and enhance the PL efficiency. As with PAVs the charge-accepting and transporting properties of polyarylenes can be manipulated by incorporation of suitable units in the main chain or as sidechains.

## 6.4.6.1 Bridged versus Nonbridged Polyphenylenes

Polyphenylenes are an excellent example of how one may control the emission color of a polymer by its planarity. PPP (**64**) is nearly planar with torsion angles between adjacent benzene rings of  $23^\circ$  [112]. Substitution of PPP with solubilizing alkyl or alkoxy groups leads to a marked increase in the torsion angle to  $\sim 70^\circ$  due to steric interactions between the sidechains [112]. This produces a major blue-shift in the emission so that whereas PPP is a blue emitter ( $\lambda_{\text{max}} = 459$  nm), [81] poly(2,5-dialkoxy-1,4-phenylene)s, e.g. **92** mainly emit in the violet ( $\lambda_{\text{max}} = \text{ca. } 410$  nm) in solution, although the formation of aggregates may lead to markedly red-shifted emission in the solid state [113]. As a result, the EL may be green, yellow, or even white in color. The methine bridges in ladder-type PPPs (**67**) keep the polymer planar so that the emission from Me-LPPP (**67a**) is blue-green ( $\lambda_{\text{max}} = 470$  nm). Polymers in which only some of the pheny-

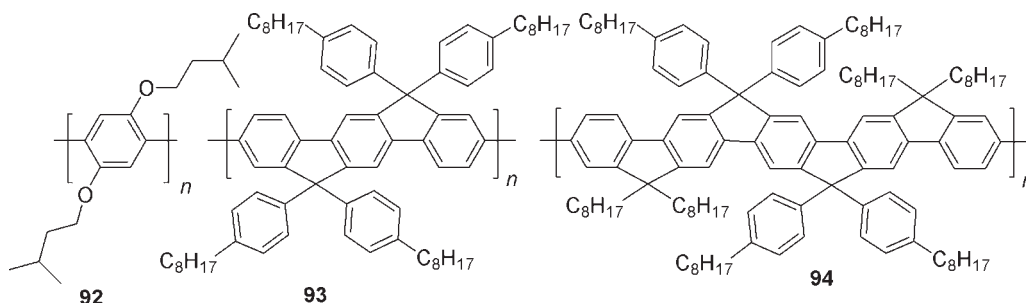


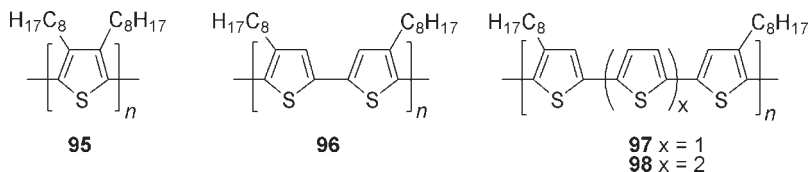
Fig. 6.9 Polyphenylenes with varying degrees of bridging.

lenes are linked by methine bridges show emission properties intermediate between **92** and **67**. With increasing ladder quality the emission maximum red-shifts from 420 nm for polyfluorenes such as **73** [93] through 430 nm for polyindenofluorenes, e. g. **93**, [114] to 445 nm for the polypentaphenylene **94** [115].

The aryl substituents in **93** and **94** above also serve to improve the color purity of their emission as they reduce interchain interactions, which, as mentioned above, can produce marked red-shifts in the emission from phenylene-based materials due either to formation of emissive aggregates or to enhanced exciton migration to emissive defect sites.

#### 6.4.6.2 Effect of Alkyl Substituents in Polythiophenes

The asymmetry of 3-substituted thiophenes means that there exist three regioisomeric ways for them to couple: 2,2'- (head-to-head, HH), 2,5'- (head-to-tail, HT) and 5,5'- (tail-to-tail, TT). Head-to-head linkages produce out-of-plane twisting of the polymer chain about the interthiophene bond due to the large steric interactions between the substituents, with a concomitant blue-shift in the emission spectrum. Thus, Hadzioannou and coworkers [116] showed that the emission maximum of a series of alkylated polythiophenes **95**–**98** could be tuned from 460 nm for **95** to 550 nm to **98** by increasing the distance between the HH-linkages. Similar effects are induced by using bulky substituents [117]. Regioregular P3AT that have no HH dyads thus show red-shifted absorption and emission compared with the corresponding regiorandom materials. Their EL efficiencies are also higher that may in part reflect better charge transport due to more efficient chain packing [118, 119].

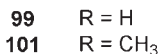


**Fig. 6.10** Polythiophenes with varying distances between head-to-head dyads.

The solid-state PL efficiency of polythiophenes can be optimized by varying the substituents. This is generally low for P3ATs due to efficient nonradiative decay pathways produced by strong interchain interactions. However, the regioregular poly(3-arylthiophene)s **72** show similar PL efficiencies in solution but much higher solid-state values than their alkyl counterparts, which is attributed to the bulky aryl groups producing greater interchain separation [120].

#### 6.4.6.3 Homo- versus Copolymers

The previous two sections showed how the emission from a class of polymer can be fine tuned by varying the substituents and substitution patterns. The most fun-



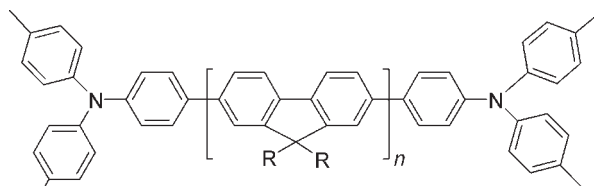
**Fig. 6.11** Fluorene-thiophene copolymers.

in its emission ( $\lambda_{\text{max}} = 468 \text{ nm}$ ) due to steric interactions inducing increased torsion between the thiophene and fluorene units [121, 122].

tune the emission color across the whole visible spectrum.

#### 6.4.6.4 Optimizing Charge Injection into Polyarylenes

polymer.



**Fig. 6.12** A polyfluorene endcapped with a hole-transporting group.

**102** R = 2-ethylhexyl

## 6.5

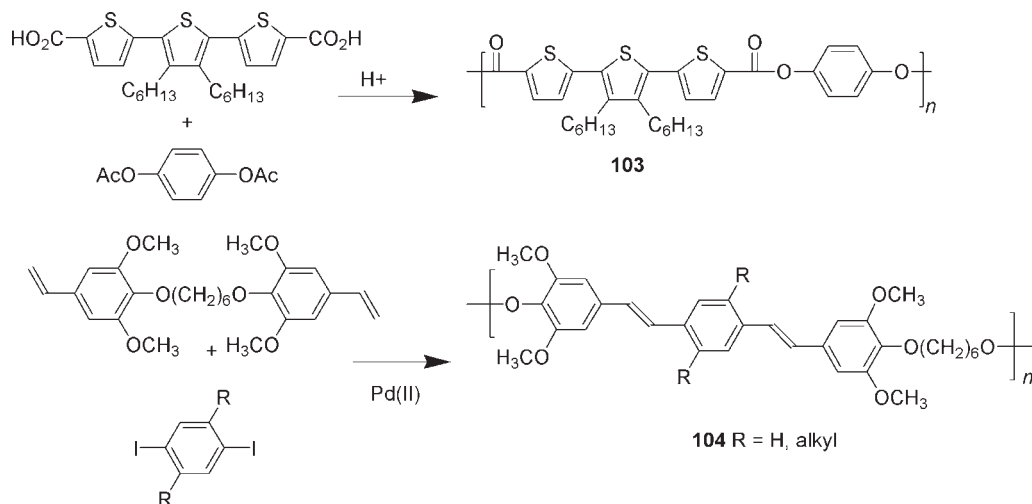
### EL Polymers with Isolated Chromophores

Polymers with chromophores linked by nonconjugated units, e.g. alkyl chains, or as pendant groups on nonconjugated chains such as polystyrene, can in principle combine the advantageous physical properties of polymers – easy processability, good film-forming properties, etc. – with the desirable optical properties of molecular chromophores such as well-defined spectra, and high fluorescence quantum yields. The second approach also enables one to utilize the huge body of knowledge classical polymer synthesis to make materials with well-defined physical properties, e.g. molecular weight. A disadvantage of these approaches is that the nonconjugated units hinder charge transport and so adversely affect the EL efficiency, although incorporation of charge-transporting moieties can alleviate this.

#### 6.5.1

##### Polymers with Isolated Chromophores in the Main Chain

There are two ways to prepare materials with emissive chromophores linked by nonconjugated spacers: a) suitably functionalized emissive units can be incorporated into polymers, usually by polycondensation reactions, for example the copolymer **103** is prepared by condensation of a terthiophene biscarboxylic acid with *p*-diacetyloxybenzene [125]; b) the conjugated emissive unit can be prepared in the polymerization step as illustrated in Scheme 6.22 by the synthesis of the polyether **104** with emissive oligo-phenylene vinylene units by Heck coupling [126]. Wittig, Horner, and Knoevenagel condensations have also been used to such polymers, while polymers with oligoarylene units have been made by Suzuki or Yamamoto coupling.

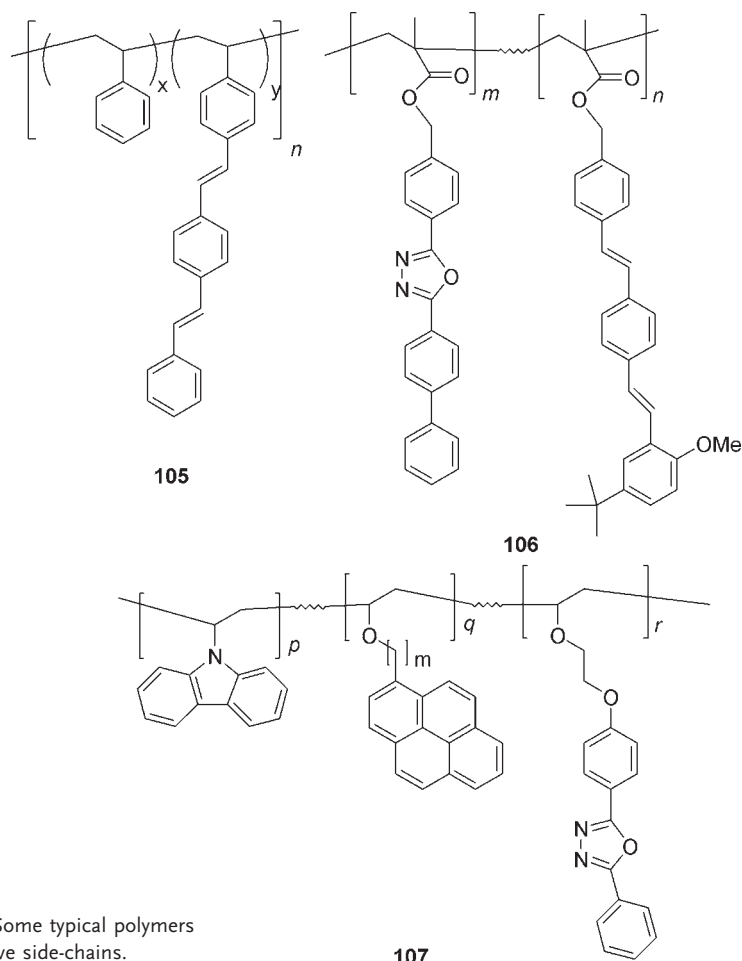


**Scheme 6.22** Synthesis of polymers with isolated chromophores in the main chain.

### 6.5.2

#### Polymers with Emissive Sidechains

Polymers bearing emissive side-chains can be prepared by attaching chromophores to suitably functionalized polymers. For example the copolymer **105** has been made by Heck coupling of 4-vinyl-stilbene to a partially brominated polystyrene [127]. Alternatively, monomers bearing suitable side-chains can be incorporated into standard polymer syntheses. This approach is of particular value in the preparation of materials bearing a mixture of emissive and charge transporting units, e. g. the polymethacrylate **106**, made by Holmes and coworkers [128] by radical polymerization of a mixture of methacrylate monomers. If living polymerization techniques are used then block copolymers with emissive and charge-transporting blocks are accessible, e. g. the triblock copolymer **107** made by a living radical polymerization of three successive vinyl monomers followed by attachment of the oxadiazoles by Williamson condensation [129].



**Fig. 6.13** Some typical polymers with emissive side-chains.

## 6.6

### Stability of EL Polymers

A critical criterion for emissive polymers for LEDs is their stability, which determines the device lifetime. The major problem is the susceptibility of extended conjugated systems to attack by oxygen and/or water, which cannot be totally excluded even by the best device encapsulation techniques [130]. In PAVs, the most vulnerable sites are the vinylene moieties. These could be protected by direct attachment of electron-withdrawing groups to them, but this is not always possible and may have undesirable effects upon the emission color. Generally speaking the use of less electron-rich arylene units seems to be the best approach so that the aryl-substituted PPV **53** is stable enough to be used commercially in LEDs. This material is also one of the most defect-free PPVs known, which also

seems to assist in extending its lifetime. In polyarylenes, electron-rich units such as thiophenes appear to be susceptible to direct attack by oxygen while in bridged polyphenylenes such as polyfluorenes the main problem is oxidation at the bridgeheads to give emissive ketones that act as traps and so red-shift the emission [131]. Here, the use of aryl substituents improves the stability, mainly because their synthesis does not allow the formation of bridgeheads with residual hydrogen substituents that are much more susceptible to oxidation than disubstituted bridges.

## 6.7

### Conclusion

A large variety of methods have been demonstrated for the efficient synthesis of a wide range of luminescent polymers. By varying the main chain and substituents, emission can be achieved in any desired color of the visible spectrum. Appropriate choices of substituents can be used to minimize formation of defects during synthesis or by aerial oxidation, to control interchain interactions and to assist charge injection and transport, all of which help to improve efficiency and device lifetime.

### References

- 1 J. H. Burroughes, D. D. C. Bradley, A. R. Brown, R. N. Marks, K. MacKay, R. H. Friend, P. L. Burn, A. B. Holmes, *Nature* **1990**, *347*, 539–541.
- 2 A. Kraft, A. C. Grimsdale, A. B. Holmes, *Angew. Chem. Intl. Ed.* **1998**, *37*, 403–428.
- 3 U. Mitschke, P. Bäuerle, *J. Mater. Chem.* **2000**, *10*, 1471–1507.
- 4 M. D. McGehee, A. J. Heeger, *Adv. Mater.* **2000**, *12*, 1655–1668.
- 5 R. A. Wessling, *J. Polym. Sci., Polym. Symp.* **1985**, *72*, 55–66.
- 6 D. Braun, A. J. Heeger, *Appl. Phys. Lett.* **1991**, *58*, 1982–1984.
- 7 N. C. Greenham, S. C. Moratti, D. D. C. Bradley, R. H. Friend, A. B. Holmes, *Nature* **1993**, *365*, 628–630.
- 8 M. J. Marsella, D.-K. Fu, T. M. Swager, *Adv. Mater.* **1995**, *7*, 145–147.
- 9 U. Scherf, *Topics Curr. Chem.* **1999**, *201*, 163–222.
- 10 F. R. Denton, P. M. Lahti, *Plast. Eng.* **1998**, *48*, 61–102.
- 11 F. R. Denton, P. M. Lahti, F. E. Karasz, *J. Polym. Sci., Part A: Polym. Chem.* **1992**, *30*, 2223–2231.
- 12 R. O. Garay, U. Baier, C. Bubeck, K. Müllen, *Adv. Mater.* **1993**, *5*, 561–564.
- 13 A. Marletta, D. Goncalves, O. N. Oliveira Jr., R. M. Faria, F. E. G. Guimaraes, *Adv. Mater.* **2000**, *12*, 69–74.
- 14 F. Papadimitrakopoulos, K. Konstadinidis, T. M. Miller, R. L. Opila, E. A. Chandross, M. E. Galvin, *Chem. Mater.* **1994**, *6*, 1563–1568.
- 15 G. Padmanaban, S. Ramakrishnan, *J. Am. Chem. Soc.* **2000**, *122*, 2244–2251.
- 16 F. Louwet, D. Vanderzande, J. Gelan, J. Mullens, *Macromolecules* **1995**, *28*, 1330–1331.
- 17 M. M. de Kok, A. J. J. M. van Breeman, R. A. A. Corlear, P. J. Adriaenssens, J. M. Gelan, D. Vanderzande, *Acta Polym.* **1999**, *50*, 28–34.
- 18 L. Lutsen, P. Adriaenssens, H. Becker, A. J. Van Breemen, D. Vanderzande, J. Gelan, *Macromolecules* **1999**, *32*, 6517–6525.

- 19 A. J. J. M. van Breemen, D. J. M. Vanderzande, P. J. Adriaenssens, J. M. J. V. Gelan, *J. Org. Chem.* **1999**, *64*, 3106–3112.
- 20 M. Van Der Borgh, D. Vanderzande, P. Adriaenssens, J. Gelan, *J. Org. Chem.* **2000**, *65*, 284–289.
- 21 L. J. Lutsen, A. J. van Breemen, W. Kreuder, D. Vanderzande, J. M. J. V. Gelan, *Helv. Chim. Acta* **2000**, *83*, 3113–3121.
- 22 A. Issaris, D. Vanderzande, J. Gelan, *Polymer* **1997**, *38*, 2571–2574.
- 23 S. Son, A. Dodabalapur, A. J. Lovinger, M. E. Galvin, *Science* **1995**, *269*, 376–378.
- 24 S.-C. Lo, A. K. Sheridan, I. D. W. Samuel, P. L. Burn, *J. Mater. Chem.* **2000**, *10*, 275–281.
- 25 G. Padmanaban, S. Ramakrishnan, *Synth. Met.* **2001**, *119*, 533–534.
- 26 S. C. Lo, L. O. Pålsson, M. Kilitziraki, P. L. Burn, I. D. W. Samuel, *J. Mater. Chem.* **2001**, *11*, 2228–2231.
- 27 H. G. Gilch, W. L. Wheelwright, *J. Polym. Sci.:A-1* **1966**, *4*, 1337–1349.
- 28 A. J. Heeger, D. Braun, PCT Intl. Patent Appl. WO 92/16,023, **1992**; *Chem. Abstr.* **1992**, *118*, 157401j.
- 29 B. R. Hsieh, Y. Yu, A. C. Van Laeken, H. Lee, *Macromolecules* **1997**, *30*, 8094–8095.
- 30 C. J. Neef, J. P. Ferraris, *Macromolecules* **2000**, *33*, 2311–2314.
- 31 L. Hontis, V. Vrindts, L. Lutsen, D. Vanderzande, J. Gelan, *Polymer* **2001**, *42*, 5793–5799.
- 32 L. Hontis, L. Lutsen, D. Vanderzande, J. Gelan, *Synth. Met.* **2001**, *119*, 135–136.
- 33 D. Raabe, H.-H. Hörhold, U. Scherf, *Makromol. Chem. Rapid Commun.* **1986**, *7*, 613–619.
- 34 D. Raabe, H.-H. Hörhold, *Acta Polymer.* **1992**, *43*, 275–278.
- 35 H.-P. Weitzel, A. Bohnen, K. Müllen, *Makromol. Chem.* **1990**, *191*, 2815–2835.
- 36 R. O. Garay, M. N. Sarimalis, R. S. Maontni, S. A. Hernandez, *Des. Monomers Polym.* **2000**, *3*, 231–244.
- 37 J. D. Capistran, D. R. Gagnon, S. Antoun, R. W. Lenz, F. E. Karasz, *Polym. Prepr.* **1984**, *25*(2), 282–283.
- 38 H. Becker, H. Spreitzer, K. Ibrom, W. Kreuder, *Macromolecules* **1999**, *32*, 4925–4932.
- 39 H. Becker, O. Gelsen, E. Kluge, W. Kreuder, H. Schenk, H. Spreitzer, *Synth. Met.* **2000**, *111–112*, 145–149.
- 40 H. Becker, H. Spreitzer, W. Kreuder, E. Kluge, H. Vestweber, H. Schenk, K. Treacher, *Synth. Met.* **2001**, *122*, 105–110.
- 41 H. Becker, H. Spreitzer, W. Kreuder, E. Kluge, H. Schenk, I. Parker, Y. Cao, *Adv. Mater.* **2000**, *12*, 42–48.
- 42 K. L. Brandon, P. G. Bentley, D. D. C. Bradley, D. A. Dunmer, *Synth. Met.* **1997**, *91*, 305–306.
- 43 A. Drury, S. Maier, A. P. Davey, A. B. Dalton, J. N. Coleman, H. J. Byrne, W. J. Blau, *Synth. Met.* **2001**, *119*, 150–151.
- 44 A. B. Dalton, J. N. Coleman, M. in het Panhuis, B. McCarthy, A. Drury, W. J. Blau, J.-M. Nunzi, H. J. Byrne, *J. Photochem. Photobiol. A* **2001**, *144*, 31–41.
- 45 S. Pfeiffer, H.-H. Hörhold, *Macromol. Chem. Phys.* **1999**, *200*, 1870–1878.
- 46 B. Xu, J. Zhang, Y. Pan, Z. Peng, *Synth. Met.* **1999**, *107*, 47–51.
- 47 Y. Liu, P. Lahti, F. La, *Polymer* **1998**, *39*, 5241–5244.
- 48 Z. Peng, M. E. Galvin, *Chem. Mater.* **1998**, *10*, 1785–1788.
- 49 W. J. Feast, I. S. Millichamp, R. H. Friend, M. E. Horton, D. Phillips, S. D. D. V. Rughooputh, *Synth. Met.* **1985**, *10*, 181–191.
- 50 W. J. Feast, I. S. Millichamp, *Polym. Commun.* **1983**, *24*, 102–103.
- 51 H.-H. Hörhold, J. Gottschaldt, J. Opfermann, *J. Prakt. Chem.*, **1977**, *319*, 611–621; *Chem. Abs.*, **1977**, *87*, 152616q.
- 52 H.-H. Hörhold, A. Bleyer, E. Birkner, S. Heinze, F. Leonhardt, *Synth. Met.* **1995**, *69*, 525–528.
- 53 E. Thorn-Csányi, P. Kraxner, *Macromol. Chem. Phys.* **1997**, *198*, 3827–3843.
- 54 R. Reetz, O. Norwark, O. Herzog, S. Brocke, E. Thorn-Csányi, *Synth. Met.* **2001**, *119*, 539–540.
- 55 S. Tasch, W. Graupner, G. Leising, L. Pu, M. P. Wagaman, R. H. Grubbs, *Adv. Mater.* **1995**, *7*, 903–906.
- 56 L. Pu, M. Wagaman, R. H. Grubbs, *Macromolecules* **1996**, *29*, 1138–1143.
- 57 V. P. Conticello, D. L. Gin, R. H. Grubbs, *J. Am. Chem. Soc.* **1992**, *114*, 9708–9710.
- 58 Y.-J. Miao, G. C. Bazan, *J. Am. Chem. Soc.* **1994**, *116*, 9379–9380.
- 59 T. Zyung, J.-J. Kim, W.-Y. Hwang, D. H. Hwang, H. K. Shim, *Synth. Met.* **1995**, *71*, 2167–2169.



- 60 S. Doi, M. Kuwabara, T. Noguchi, T. Ohnishi, *Synth. Met.* **1993**, 57, 4174–4179.
- 61 T.-Q. Nguyen, V. Doan, B. J. Schwartz, *J. Chem. Phys.* **1999**, 110, 4068–4078.
- 62 T.-Q. Nguyen, I. B. Martini, J. Liu, B. J. Schwartz, *J. Phys. Chem. B* **2000**, 104, 237–255.
- 63 M. R. Andersson, G. Yu, A. J. Heeger, *Synth. Met.* **1997**, 85, 1275–1276.
- 64 R. E. Martin, F. Geneste, R. Riehn, B. S. Chuah, F. Cacialli, R. H. Friend, A. B. Holmes, *Chem. Commun.* **2000**, 291–292.
- 65 R. E. Martin, F. Geneste, B. S. Chuah, C. Fischmeister, Y. Ma, A. B. Holmes, R. Riehn, *Synth. Met.* **2001**, 122, 1–6.
- 66 H. Vestweber, A. Greiner, U. Lemmer, R. F. Mahrt, R. Richert, W. Heitz, H. Bässler, *Adv. Mater.* **1992**, 4, 661–662.
- 67 S. T. Kim, D.-H. Hwang, X.-C. Li, J. Grüner, R. H. Friend, A. B. Holmes, H.-K. Shim, *Adv. Mater.* **1996**, 8, 979–982.
- 68 T. Ahn, M. S. Jang, H.-K. Shim, D.-H. Hwang, T. Zyung, *Macromolecules* **1999**, 32, 3279–3285.
- 69 J. C. Carter, I. Grizzi, S. K. Hecks, D. J. Lacey, S. G. Latham, P. G. May, O. Ruiz de los Panos, K. Pichler, C. R. Towns, H. F. Wittmann, *Appl. Phys. Lett.* **1997**, 71, 34–36.
- 70 P. L. Burn, A. B. Holmes, A. Kraft, D. D. C. Bradley, A. R. Brown, R. H. Friend, R. W. Gymer, *Nature* **1992**, 356, 47–49.
- 71 M. Remmers, D. Neher, J. Grüner, R. H. Friend, G. H. Gelinck, J. M. Warman, C. Quattrocchi, D. A. dos Santos, J.-L. Brédas, *Macromolecules* **1996**, 29, 7432–7445.
- 72 D. R. Baigent, P. J. Hamer, R. H. Friend, S. C. Moratti, A. B. Holmes, *Synth. Met.* **1995**, 71, 2175–2176.
- 73 M. Onoda, Y. Ohmori, T. Kawai, K. Yoshino, *Synth. Met.* **1995**, 71, 2181–2182.
- 74 R. Mülher, A. Cravino, J. Williams, F. Stelzer, G. Jakopic, G. Leising, *Synth. Met.* **2001**, 119, 193–194.
- 75 M. Van Der Borght, D. Vanderzande, J. Gelan, *Polymer* **1998**, 39, 4171–4174.
- 76 A. C. Grimsdale, X.-C. Li, F. Cacialli, J. Grüner, A. B. Holmes, S. C. Moratti, R. H. Friend, *Synth. Met.* **1996**, 76, 165–167.
- 77 U. H. F. Bunz, *Chem. Rev.* **2000**, 100, 1605–1644.
- 78 K. Yoshino, K. Tada, M. Onoda, *Jpn. J. Appl. Phys.* **1994**, 33, L1785–1788.
- 79 B. S. Kang, D. H. Kim, S. M. Lim, J. Kim, M.-L. Seo, K.-M. Bark, S.-C. Shin, K. Nahm, *Macromolecules* **1997**, 30, 7196–7201.
- 80 V. E. Williams, T. M. Swager, *Macromolecules* **2000**, 31, 4069–4073.
- 81 G. Grem, G. Leditzky, B. Ullrich, G. Leising, *Adv. Mater.* **1992**, 4, 36–37.
- 82 M. Leclerc, K. Faid, *Adv. Mater.* **1997**, 9, 1087–1094.
- 83 J.-F. Morin, M. Leclerc, *Macromolecules* **2001**, 34, 4680–4682.
- 84 U. Scherf, *J. Mater. Chem.* **1999**, 9, 1853–1864.
- 85 P. K. H. Ho, D. S. Thomas, R. H. Friend, N. Tessler, *Science* **1999**, 285, 233–237.
- 86 S. Janietz, A. Wedel, R. Friedrich, S. Anlauf, *Polym. Prep.* **1999**, 40(2), 1219–1220.
- 87 C. Ego, A. C. Grimsdale, F. Uckert, G. Yu, G. Srdanov, K. Müllen, *Adv. Mater.* **2002**, 14, 809–811.
- 88 M. Leclerc, F. Martinez Diaz, G. Wegner, *Makromol. Chem.* **1989**, 190, 3105–3116.
- 89 H. Mao, B. Xu, S. Holdcroft, *Macromolecules* **1993**, 26, 1163–1169.
- 90 S. Amou, O. Haba, M. Ueda, K. Takeuchi, M. Asai, *Polym. Prep.* **1999**, 40(1), 93–94.
- 91 M. R. Andersson, D. Selse, M. Berggren, H. Järvinen, T. Hjertberg, O. Inganäs, O. Wennerström, J. E. Österholm, *Macromolecules* **1994**, 27, 6503–6.
- 92 T. Yamamoto, *Prog. Polym. Sci.* **1992**, 17, 1153–1205.
- 93 M. Grell, W. Knoll, D. Lupo, A. Meisel, T. Miteva, D. Neher, H.-G. Nothofer, U. Scherf, A. Yasuda, *Adv. Mater.* **1999**, 11, 671–675.
- 94 V. Percec, S. Okita, R. Weiss, *Macromolecules* **1992**, 25, 1816–1823.
- 95 V. Percec, M. Zhao, J.-Y. Bae, D. H. Hill, *Macromolecules* **1996**, 29, 3727–3735.
- 96 *Metal-Catalysed Crosscoupling Reactions*, A. De Meijere, F. Diederich, Eds., Wiley-VCH, Weinheim, Germany, **2004**.
- 97 A. D. Schlüter, *J. Polym. Sci. A: Polym. Chem.* **2001**, 39, 1533–1556.
- 98 R. D. McCullough, R. D. Lowe, *J. Chem. Soc., Chem. Commun.* **1992**, 70–72.
- 99 R. D. McCullough, R. D. Lowe, M. Jayaraman, D. L. Anderson, *J. Org. Chem.* **1993**, 58, 904–912.
- 100 T.-A. Chen, R. D. Rieke, *J. Am. Chem. Soc.* **1992**, 114, 10087–10088.

- 101 T.-A. Chen, X. Wu, R. D. Rieke, *J. Am. Chem. Soc.* **1995**, *117*, 233–244.
- 102 R. S. Loewe, S. M. Khersonsky, R. D. McCullough, *Adv. Mater.* **1999**, *11*, 127–130.
- 103 R. S. Loewe, P. C. Ewbank, J. Liu, L. Zhai, R. D. McCullough, *Macromolecules* **2001**, *34*, 4324–4333.
- 104 J.-P. Lère-Porte, J. J. E. Moreau, C. Torrelles, *Eur. J. Org. Chem.* **2001**, 1249–1258.
- 105 D. L. Gin, V. P. Conticello, *Trends Polym. Sci.* **1996**, *4*, 217–223.
- 106 D. G. H. Ballard, A. Courtis, I. M. Shirley, S. C. Taylor, *J. Chem. Soc., Chem. Commun.* **1983**, 954–955.
- 107 D. G. H. Ballard, A. Courtis, I. M. Shirley, S. C. Taylor, *Macromolecules* **1988**, *21*, 294–304.
- 108 D. L. Gin, V. P. Conticello, R. H. Grubbs, *J. Am. Chem. Soc.* **1992**, *114*, 3167–3169.
- 109 D. L. Gin, V. P. Conticello, R. H. Grubbs, *J. Am. Chem. Soc.* **1994**, *116*, 10507–10519.
- 110 D. L. Gin, V. P. Conticello, R. H. Grubbs, *J. Am. Chem. Soc.* **1994**, *116*, 10934–10947.
- 111 X. Zhang, A. S. Shetty, S. A. Jenekhe, *Acta Polym.* **1998**, *49*, 52–55.
- 112 K. C. Park, L. R. Dodd, K. Levon, T. K. Kwei, *Macromolecules* **1996**, *29*, 7149–7154.
- 113 V. Cimrová, M. Remmers, D. Neher, G. Wegner, *Adv. Mater.* **1996**, *8*, 146–149.
- 114 J. Jacob, J. Zhang, A. C. Grimsdale, K. Müllen, M. Gaal, E. J. W. List, *Macromolecules* **2003**, *36*, 8240–8245.
- 115 J. Jacob, S. Sax, T. Piok, E. J. W. List, A. C. Grimsdale, K. Müllen, *J. Am. Chem. Soc.* **2004**, *126*, 6987–6995.
- 116 R. E. Gill, G. E. Malliaras, J. Wildeman, G. Hadziioannou, *Adv. Mater.* **1994**, *6*, 132–135.
- 117 M. R. Andersson, M. Berggren, O. Inganäs, G. Gustafsson, J. C. Gustafsson-Carlberg, D. Selse, T. Hjertberg, O. Wennerström, *Macromolecules* **1995**, *28*, 7525–7529.
- 118 F. Chen, P. G. Mehta, L. Takiff, R. D. McCullough, *J. Mater. Chem.* **1996**, *6*, 1763–1767.
- 119 R. D. McCullough, *Adv. Mater.* **1998**, *10*, 93–116.
- 120 M. R. Andersson, O. Thomas, W. Mamma, M. Svensson, M. Theander, O. Inganäs, *J. Mater. Chem.* **1999**, *9*, 1933–1940.
- 121 A. Donat-Bouillud, I. Lévesque, Y. Tao, M. D'Iorio, S. Beaupré, P. Blondin, M. Ranger, J. Bouchard, M. Leclerc, *Chem. Mater.* **2000**, *12*, 1931–1936.
- 122 I. Lévesque, A. Donat-Bouillud, Y. Tao, M. D'Iorio, S. Beaupré, P. Blondin, M. Ranger, J. Bouchard, M. Leclerc, *Synth. Met.* **2001**, *122*, 79–81.
- 123 C. Ego, D. Marsitzky, S. Becker, J. Zhang, A. C. Grimsdale, K. Müllen, J. D. MacKenzie, C. Silva, R. H. Friend, *J. Am. Chem. Soc.* **2003**, *125*, 437–443.
- 124 T. Miteva, A. Meisel, W. Knoll, H. G. Nothofer, U. Scherf, D. C. Müller, K. Meerholz, A. Yasuda, D. Neher, *Adv. Mater.* **2001**, *13*, 565–570.
- 125 M. Belletête, L. Mazerolle, N. Desrosiers, M. Leclerc, G. Durocher, *Macromolecules* **1995**, *28*, 8587–8597.
- 126 S. T. Pasco, P. M. Lahti, F. E. Karasz, *Macromolecules* **1999**, *32*, 6933–6937.
- 127 P. Hesemann, H. Vestweber, J. Pommeröhne, R. F. Mahrt, A. Greiner, *Adv. Mater.* **1995**, *7*, 388–390.
- 128 X.-C. Li, F. Cacialli, M. Giles, J. Grüner, R. H. Friend, A. B. Holmes, S. C. Moratti, T. M. Yong, *Adv. Mater.* **1995**, *7*, 898–900.
- 129 Y. Heischkel, H.-W. Schmidt, *Macromol. Chem. Phys.* **1998**, *199*, 869–880.
- 130 B. K. Cumpston, K. F. Jensen, *Trends Polym. Sci.* **1996**, *4*, 151–157.
- 131 U. Scherf, E. W. J. List, *Adv. Mater.* **2002**, *14*, 477–487.

## 7

# Charge-transporting and Charge-blocking Amorphous Molecular Materials for Organic Light-emitting Diodes

Yasuhiko Shirota

### 7.1

#### Introduction

The operation of organic light-emitting diodes (OLEDs) involves charge injection from electrodes, transport of charge carriers, recombination of holes and electrons to generate electronically excited states or excitons, followed by their deactivation by emission of either fluorescence or phosphorescence. The main factors that determine luminous and external quantum efficiencies are the following:

- efficiency of charge injection from the electrodes,
- charge balance,
- spin multiplicity of the luminescent state,
- emission quantum yield, and
- light output coupling factor.

In order to attain high quantum efficiency for electroluminescence (EL), it is necessary to achieve three things: efficient charge injection from the electrodes at low drive voltage, good charge balance, and confinement of the injected charge carriers within the emitting layer to increase the probability of the desired emissive recombination. Layered devices consisting of an emitting layer and additional charge-transporting and charge-blocking layers usually exhibit better performance than single-layer devices consisting of only the emitting layer because of the following reasons. The presence of hole-transport and electron-transport layers reduces the energy barriers for the injection of charge carriers from electrodes, hence facilitating charge injection from the electrodes and leading to a better balance in the number of holes and electrons. At the same time, both layers block charge carriers from escaping from the emitting layer, confining injected holes and electrons to it.

The performance of OLEDs therefore depends upon various materials functioning in specialized roles such as emitting, charge-transporting, and charge-blocking (Fig. 7.1). Consequently, it is of crucial importance to develop high-perfor-

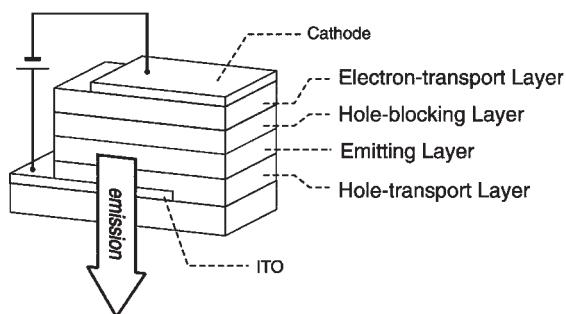


Fig. 7.1 Multilayer OLEDs.

mance materials in all these categories in order to achieve overall high performance from the device. Generally, the following criteria are required of materials if they are to find application in OLEDs. Materials should

- possess suitable ionization potentials and electron affinities, i. e., well-matched energy levels for the injection of charge carriers from the electrodes and adjacent organic layers
- be capable of forming smooth, uniform films without pinholes
- be both morphologically and thermally stable.

In addition to these general requirements, materials should meet further specialized needs depending upon the roles that they play in devices.

Since the pioneering studies on OLEDs using small molecules and polymers [1, 2], both small molecules and polymers have been studied for use as materials in OLEDs. Small organic molecules that readily form stable amorphous glasses above room temperature, i. e., amorphous molecular materials [3], and polymers containing  $\pi$ -electron systems in the main chain, i. e.,  $\pi$ -conjugated polymers, have been proven to be promising candidates for materials for OLEDs.

Polymers containing  $\pi$ -electron systems as pendant groups have also been investigated.

This chapter describes first the general aspects of amorphous molecular materials and then hole-transporting, electron-transporting, and hole-blocking amorphous molecular materials for use in OLEDs.

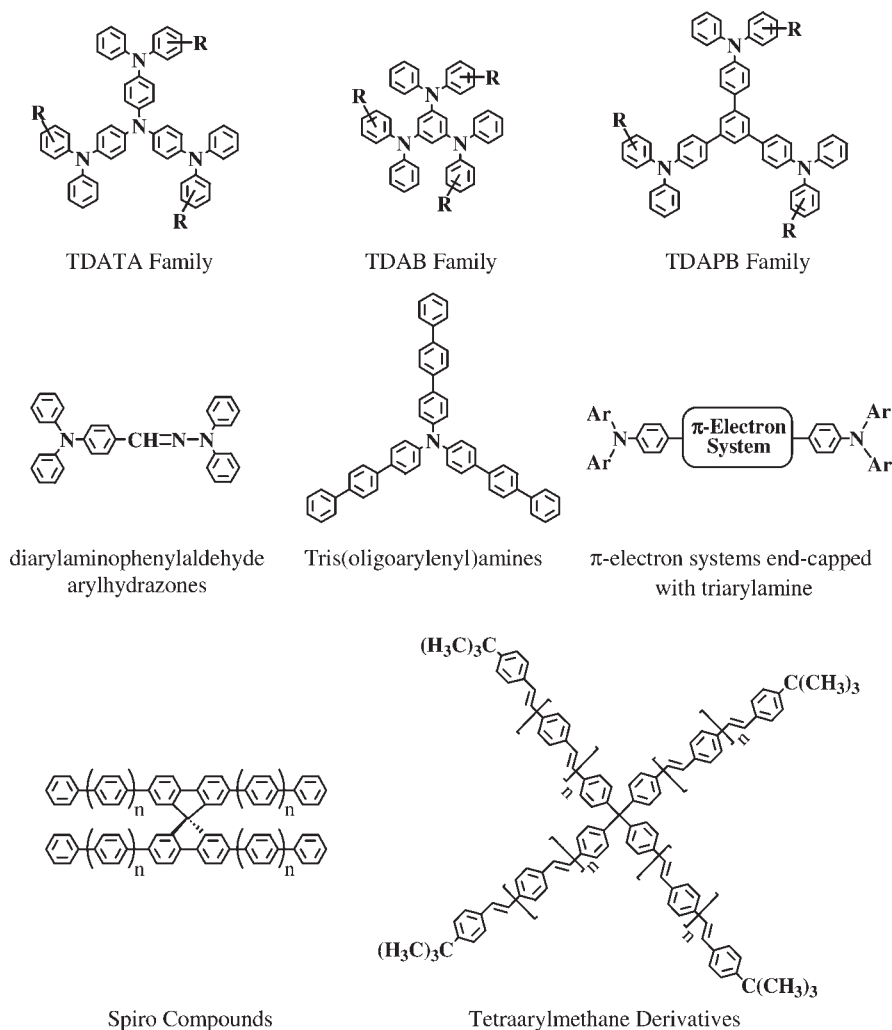
## 7.2

### Amorphous Molecular Materials

Generally, small organic molecules tend to crystallize readily, and hence, they usually exist as crystals below their melting temperatures. However, recent extensive studies have revealed that like polymers, small organic molecules can also readily form stable amorphous glasses above room temperature if their molecular structures are properly designed [3]. Such amorphous molecular materials have

received a great deal of attention as a new class of functional materials, in particular from the standpoint of applications as materials for OLEDs. A number of reports have been published since the mid-1990s, and a new field of organic materials science that deals with amorphous molecular glasses has been opened up [4].

Formation of the amorphous glassy state is confirmed by polarizing optical microscopy, X-ray diffraction, and differential scanning calorimetry. Amorphous molecular materials are characterized by well-defined glass-transition phenomena usually associated with polymers and ready formation of uniform amorphous thin films by vacuum deposition or spin coating from solution. Amorphous molecular materials contrast polymers in that they are pure materials with well-defined molecular structures and definite molecular weights without any distribu-



Structures 1

tion. They can usually be purified by column chromatography, followed by recrystallization or vacuum sublimation [3].

A variety of amorphous molecular materials have been created. Typical key compounds that readily form amorphous glasses are  $\pi$ -electron starburst molecules, e. g., the families of 4,4',4''-tris(diphenylamino)triphenylamine (TDATA) [5, 6], 1,3,5-tris(diphenylamino)benzene (TDAB) [7, 8], and 1,3,5-tris[4-(diphenylamino)phenyl]benzene (TDAPB) [9], diarylaminophenylaldehyde arylhydrazones [10], tris(oligoarylenyl)amines [11],  $\pi$ -electron systems end-capped with triarylamine [12, 13, 14], spiro-compounds [15], tetraarylmethane derivatives [16], and macrocycle-based compounds [17] (Structures 7.1). A number of structural modifications of these key compounds have been made, including the replacement of the phenyl group by biphenyl, naphthyl, fluorenyl, phenanthryl, and oxadiazolyl groups, the replacement of the diphenylamino group by the carbazolyl or benzo-carbazolyl group, and the enlargement of the molecular size leading to dendrimers [18, 19].

### 7.3

#### Requirements for Materials in OLEDs

Amorphous molecular materials function as hole-transporting, hole-blocking, electron-transporting, or emitting materials, mainly depending upon their ionization potentials and electron affinities. Materials having low ionization potentials together with low electron affinities usually function as hole-transporting materials by accepting hole carriers with a positive charge and transporting them, while materials having high electron affinities together with high ionization potentials usually function as electron-transporting materials by accepting negative charges and allowing them to move through the molecules. In other words, materials with electron-donating properties and materials with electron-accepting properties serve in OLEDs as hole-transporting and electron-transporting materials, respectively. Hole-blocking materials should possess weakly electron-accepting properties with high ionization potentials so that they accept electrons from the electron-transport layer and transport them to the emitting layer, but at the same time block hole carriers from escaping from the emitting layer. The emitting layer functions as the recombination center for injected holes and electrons to generate electronically excited states or excitons, which either emit luminescence or transfer their excitation energies to a luminescent dopant dispersed in a host material in the emitting layer. Therefore, materials for use in the emitting layer should have both electron-donating and electron-accepting properties since they need to accept both holes and electrons, that is, bipolar character.

## 7.4

### Amorphous Molecular Materials for Use in OLEDs

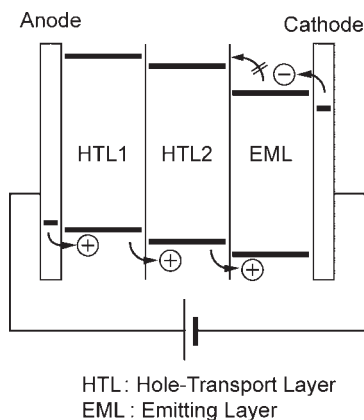
#### 7.4.1

##### Hole-transporting Amorphous Molecular Materials

The hole-transport layer in layered OLEDs generally plays the roles of facilitating hole injection from the anode, accepting holes, and transporting injected holes to the emitting layer. The hole-transport layer also functions as the electron-blocking layer that stops electrons from escaping from the emitting layer and recombining undesirably elsewhere or completely traversing the device as lost current. Therefore, hole-transporting materials should undergo reversible anodic oxidation to form stable cation radicals. The materials should possess high hole drift mobilities to be capable of swiftly transporting the holes through them. N,N'-Bis(3-methylphenyl)-N,N'-diphenyl-[1,1'-biphenyl]-4,4'-diamine (TPD), which was originally used as a charge-carrier transport material dispersed in a polymer binder in photoreceptors in electrophotography [20], was used as a good hole transporter for OLEDs [21]. More recently, N,N'-di(1-naphthyl)-N,N'-diphenyl-[1,1'-biphenyl]-4,4'-diamine ( $\alpha$ -NPD) has been most widely used as a hole transporter in combination with tris(8-quinolinolato)aluminum (Alq<sub>3</sub>) as a green-emitting material or as a host material in which a luminescent dopant is dispersed [22].

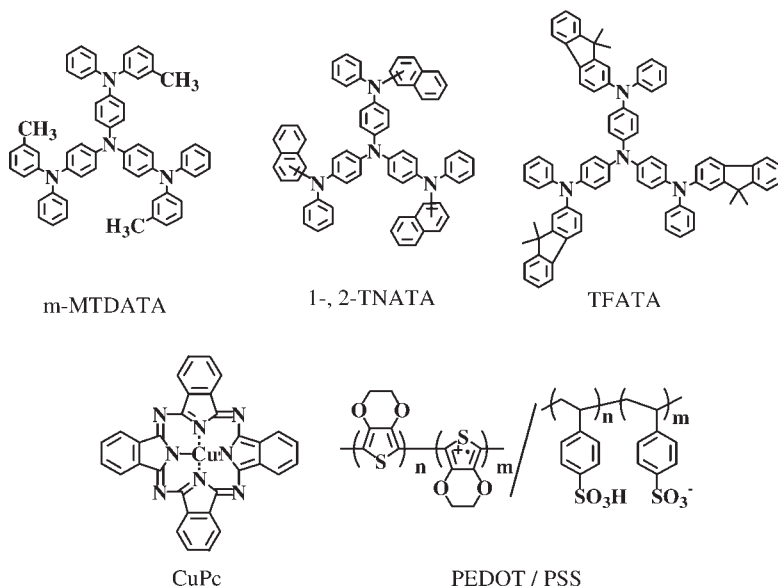
Fine tuning all the desirable properties of one single hole-transporting material as listed above is a challenging task, and reaching the optimum for all electronic traits may even be impossible, or come with other drawbacks. An efficient strategy is therefore to create the desired behavior and function as a sum of properties of more than one material and layer.

One important aspect of high-quality OLEDs is efficient hole injection from the anode, which is usually a thin, transparent layer of indium tin oxide (ITO), at low drive voltage. Therefore, materials with very low solid-state ionization potentials are used as the hole-transporting layer that facilitates hole injection from the anode, which is referred to as a hole-injection buffer layer. Often, this layer will not be a perfect match for passing the holes directly into the desired emitting layer of the particular device in question, and it is elaborate to insert a second hole-transport layer with a higher ionization potential between the hole injection buffer layer and the emitting layer to reduce the energy barrier for hole injection from the hole-injection buffer layer into the emitting layer. A three-layer OLED consisting of the double hole-transport layers of 4,4',4''-tris[3-methylphenyl(phenyl)amino]triphenylamine (m-MTDATA) [5] (HTL1) and TPD [20] (HTL2) and an emitting layer of Alq<sub>3</sub> was found to exhibit higher luminous and external quantum efficiencies and in particular, enhanced durability than the corresponding double-layer device without the m-MTDATA layer [23]. The analysis of the current density–voltage characteristics of hole-only devices using m-MTDATA showed that the ITO/m-MTDATA interface is capable of providing trap-free space-charge-limited current and that m-MTDATA forms an almost ohmic contact with the ITO electrode [24, 25].



**Fig. 7.2** Side view of the organic EL device consisting of double hole-transport layers.

m-MTDATA and its family, e. g., 4,4',4''-tris[1,2-naphthyl(phenyl)amino]triphenylamine (1- and 2-TNATA) [26] and 4,4',4''-tris[9,9-dimethylfluoren-2-yl(phenyl)amino]triphenylamine (TFATA) [27], are characterized by their very low solid-state ionization potentials and the good quality of their amorphous films. They have proven to serve as good materials for the hole-injection buffer layer (HTL1) that facilitates hole injection from the ITO electrode in layered devices consisting of double hole-transport layers (Fig. 7.2). Copper phthalocyanine (CuPc) has also been widely used as a hole-injection buffer layer (HTL1) that facilitates hole injection [22]. In OLEDs using polymer films, an electrically conducting polymer, poly(3,4-ethylenedioxythiophene) doped with poly(styrene sulfonic acid) (PEDOT: PSS), has been widely used as a hole-injection buffer layer (Structures 7.2).



Structures 2



As for materials for use in the second hole-transport layer (HTL2), materials with higher ionization potentials than those of materials employed in the first hole-injection buffer layer (HTL1) are used to reduce the energy barrier for hole injection into the emitting layer. TPD and  $\alpha$ -NPD have been widely used as good hole-transporting materials with suitable ionization potentials for use in HTL2. However, both TPD and  $\alpha$ -NPD are not thermally stable. TPD is not morphologically stable either, tending to crystallize readily. A number of thermally stable hole-transporting amorphous molecular materials with higher  $T_g$ s than those of TPD and  $\alpha$ -NPD have been developed (Table 7.1).

**Table 7.1** Hole-transporting amorphous molecular materials.

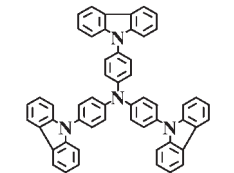
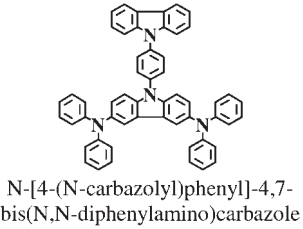
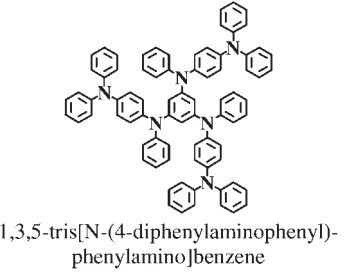
Family	Abbreviation	Compound Structure and Name	Ref.
TDATA Family	TCTA	 4,4',4''-tri(N-carbazolyl)-triphenylamine	28
	DCB	 N-[4-(N-carbazolyl)phenyl]-4,7-bis(N,N-diphenylamino)carbazole	29
TDAB Family	p-DPA-TDAB	 1,3,5-tris[N-(4-diphenylaminophenyl)-phenylamino]benzene	30

Table 7.1 Continued.

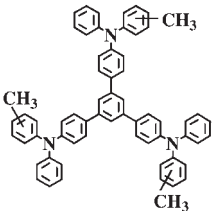
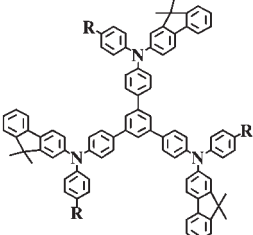
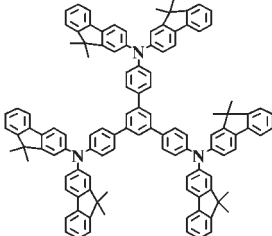
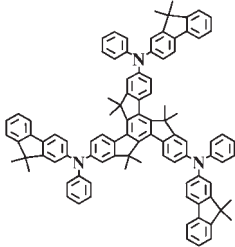
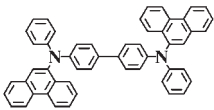
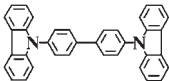
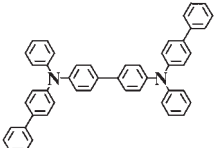
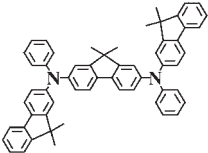
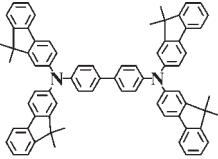
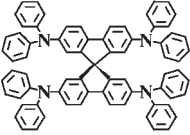
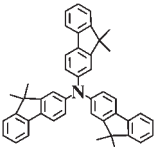
Family	Abbreviation	Compound Structure and Name	Ref.
TDAPB Family	o-, m-, p-MTDAPB	 <p>1,3,5-tris[4-(methylphenyl)phenyl]benzenes</p>	9
	R = H: TFAPB R = CH <sub>3</sub> : MTFAPB	 <p>4,4',4''-tris[9,9-dimethylfluoren-2-yl-(phenyl)amino]triphenylbenzenes</p>	31
TBFAPB		 <p>4,4',4''-tris[bis(9,9-dimethylfluoren-2-yl)amino]triphenylbenzene</p>	31
TFATr		 <p>2,7,12-tris[9,9-dimethylfluoren-2-yl-(phenyl)amino]-5,5,10,10,15,15-hexamethyltruxene</p>	32

Table 7.1 Continued.

Family	Abbreviation	Compound Structure and Name	Ref.
TPD Derivatives	PPD	 N,N'-diphenyl-N,N'-bis(9-phenanthryl)benzidine	33
	CBP	 4,4'-di(N-carbazole)biphenyl	34
	p-BPD	 N,N'-di(biphenyl-4-yl)-N,N'-diphenyl-[1,1'-biphenyl]-4,4'-diamine	35
	PFFA	 N,N'-bis(9,9-dimethylfluoren-2-yl)-N,N'-diphenyl-9,9-dimethylfluorene-2,7-diamine	36
	FFD	 N,N,N',N'-tetrakis(9,9-dimethylfluoren-2-yl)-[1,1'-biphenyl]-4,4'-biamine	27
	spiro-TAD	 2,2',7,7'-tetrakis-(N,N-diphenylamino)-9,9'-spirobifluorene	15
	Tris(oligo-arylenyl)amine	 tris(9,9-dimethylfluoren-2-yl)amine	37

**Table 7.2** Glass-transition temperatures ( $T_g$ s) and oxidation potentials ( $E_{1/2}^{\text{ox}}$ ) of hole-transporting amorphous molecular materials.

Material	$T_g$ [°C]	$E_{1/2}^{\text{ox}}$ [a]	Material	$T_g$ [°C]	$E_{1/2}^{\text{ox}}$ [a]
m-MTDATA	75	0.06	TBFAPB	189	0.51
1-TNATA	113	0.08	TFATr	208	0.48
2-TNATA	110	0.11	TPD	61	0.48
TFATA	131	0.08	$\alpha$ -NPD	96	0.51
TCTA	151	0.69	PPD	152	–
TDCTA	212	0.92 [b]	CBP	–	1.041 [c]
DCB	–	0.78 [c]	p-BPD	102	0.50
p-DPA-TDAB	108	0.23	PFFA	135	0.32
o-MTDAPB	109	0.72 [d]	FFD	165	0.40
m-MTDAPB	105	0.66 [d]	Spiro-TAD	133	–
p-MTDAPB	110	0.64	F <sub>2</sub> PA	82	0.51
TFAPB	150	0.61	TF1A	125	0.44

[a] V vs Ag/AgNO<sub>3</sub> (0.01 mol dm<sup>-3</sup>) in CH<sub>2</sub>Cl<sub>2</sub>.

[b] V vs. ferrocene/ferrocenium in acetonitrile (irreversible anodic oxidation process).

[c] V vs Ag/AgCl.

[d]  $E_{p/2}^{\text{ox}}$  (irreversible anodic oxidation process).

Many of these materials fulfill the requirements of reversible anodic oxidation to form stable cation radicals and the capability of transporting holes (Table 7.2). Some of these materials with relatively low ionization potentials can be used as a single hole-transport layer in OLEDs.

These high- $T_g$  materials have enabled the fabrication of thermally stable OLEDs. The luminance usually decreased with the increasing temperature for Alq<sub>3</sub>-based OLEDs; however, doping of luminescent dyes in Alq<sub>3</sub> tended to prevent such phenomena. Thermally stable Alq<sub>3</sub>-based OLEDs using TCTA [28], TFATA and FFD [27] as hole transporters have been reported to operate at 150–170 °C [27, 28]. In particular, an OLED consisting of quinacridone-doped Alq<sub>3</sub> as an emitting layer and TFATr as a hole-transport layer was shown to operate even at 200 °C [32].

#### 7.4.2

##### Electron-transporting Amorphous Molecular Materials

Analogous to the hole-transport layer, the electron-transport layer in layered devices generally plays the roles of facilitating electron injection from the cathode, accepting electrons, and transporting them to the emitting layer. The electron-

transport layer functions at the same time as the hole-blocking layer that blocks holes from escaping from the emitting layer. The electron-transporting materials should therefore undergo reversible cathodic reduction to form stable anion radicals. The materials should be able to transport electron carriers with desirably high electron drift mobilities.

As compared with hole-transporting materials, fewer electron-transporting materials have been reported. A well-known green emitter, Alq<sub>3</sub>, has been used as a good electron transporter. Other reported electron-transporting materials include oxadiazole derivatives, a dendrimer-type oxadiazole, a triazole derivative, tris(phe-nylquinoxaline), silole derivatives, benzimidazole derivative, and boron-contain-ing compounds (Table 7.3).

**Table 7.3** Electron-transporting amorphous molecular materials.


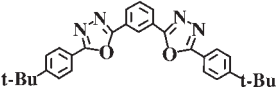
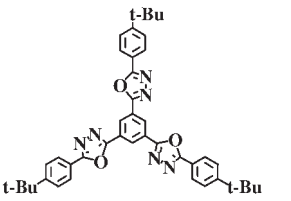
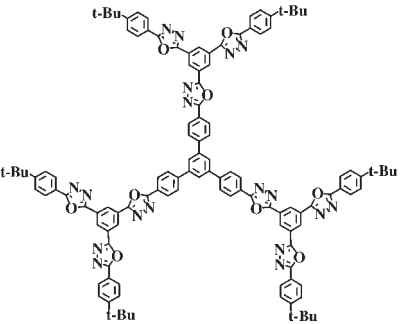
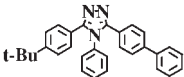
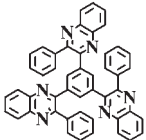
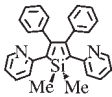
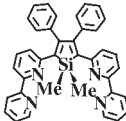
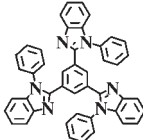
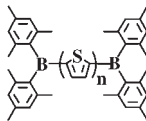
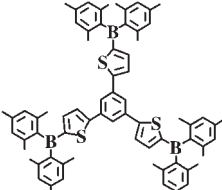
Family	Abbreviation	Compound Structure and Name	Ref.
Oxiadiazole Derivatives	t-Bu-PBD	 2-(biphenyl-4-yl)-5-(tert-butylphenyl)-1,3,4-oxadiazole	21
	OXD-7	 1,3-bis[5-(p-tert-butylphenyl)-1,3,4-oxadiazol-2-yl]benzene	38
	TPOB	 1,3,5-tris(4-tert-butylphenyl-1,3,4-oxadiazolyl)benzene	39, 40
		 dendrimer type oxiadiazole	41

Table 7.3 Continued.

Family	Abbreviation	Compound Structure and Name	Ref.
Triazole Derivative	TAZ	 3-(biphenyl-4-yl)-4-phenyl-5-(4-tert-butylphenyl)-1,2,4-triazole	42
Tris(phenylquinoxaline)	TPQ	 1,3,5-tris(3-phenylquinoxaline-2-yl)benzene	43
Silole Derivatives	PYSPY	 2,5-bis[(2,2'-bipyridin-6-yl)]-1,1-dimethyl-3,4-diphenylsilole	44
	PyPySPyPy	 2,5-bis[(2,2'-bipyridin-6-yl)]-1,1-dimethyl-3,4-diphenylsilole	45
Benzimidazole Derivative	TPBI	 2,2',2''-(1,3,5-benzenetriyl)tris-[1-phenyl-1H-benzimidazole]	46
Boron- containing Compounds	BMB-nT	 $\alpha,\omega$ -bis(dimesitylboryl)oligothiophene	47–49
	TMB-TB	 1,3,5-tris[5-(dimesitylboryl)thiophen-2-yl]benzene	50

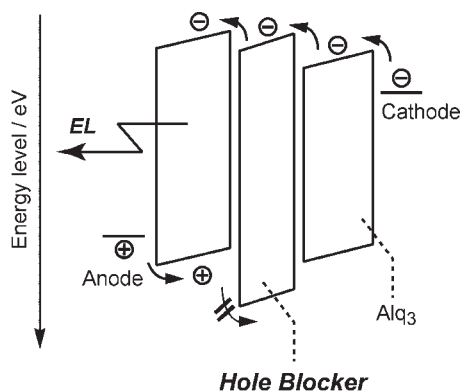
## 7.4.3

**Hole-blocking Amorphous Molecular Materials**

One of the requirements for the fabrication of high-performance OLEDs is to confine injected charge carriers in the emitting layer to lead to efficient recombination of holes and electrons. Apart from their obvious role of facilitating charge injection from the electrodes, the hole-transport and electron-transport layers in OLEDs also function as the blockers of electrons and holes, respectively, to stop them from escaping from the emitting layer instead of recombining emissively there. However, there are only a few electron-transporting materials that function as effective hole-blocking materials at the same time. A well-known emitter and electron transporter,  $\text{Alq}_3$ , does not necessarily function well as an effective hole blocker. For example, when materials with hole-transporting properties, e.g., TPD and  $\alpha$ -NPD, are used as blue or blue-violet emitters instead of as hole transporters, hole injection from these emitting materials into  $\text{Alq}_3$  takes place to give the emission resulting from  $\text{Alq}_3$ .

A promising approach is the separation of the two functions of the facilitation of electron injection from the cathode and the blocking of hole carriers from escaping from the emitting layer. A separate hole-blocking layer is inserted additionally between the emitting layer and the insufficiently hole-blocking electron-transport layer. They then play their respective roles of blocking holes from escaping from the emitting layer and facilitating electron injection from the cathode (Fig. 7.3).

Hole-blocking materials for use in OLEDs should fulfill several requirements. They should possess weak electron-accepting properties together with high ionization potentials to be able to accept electrons from the electron-transport layer and to pass them to the emitting layer, but to block hole carriers from entering it. That is, the difference in the highest occupied molecular orbital (HOMO) energy levels between the emitting material and the hole-blocking material should be much larger than that in their lowest unoccupied molecular orbital (LUMO) energy levels. The cathodic reduction processes of hole blockers should be reversible to form stable anion radicals. In addition, they should not form exciplexes with emitting materials with electron-donating properties.



**Fig. 7.3** Role of hole-blocking materials.

Bathocuproine (BCP) has been used as a hole-blocking material. However, it tends to form exciplexes with a number of emitting materials with hole-transporting properties, e.g., TPD and m-MTDATA, and emits exciplex emission in the longer wavelength region [51]. Its morphological and thermal stability have not been made clear.

New classes of hole-blocking amorphous molecular materials have recently been developed, which include the families of triarylbenzenes and triarylboranes (Table 7.4). These compounds readily form amorphous glasses with well-defined  $T_g$ s and possess weakly electron-accepting properties. These hole-blocking materials enabled fabrication of high-performance blue- and blue-violet-emitting OLEDs using  $\alpha$ -NPD, p-TTA and TPD as emitters. The performance of some devices is summarized in Table 7.5.

**Table 7.4** Hole-blocking amorphous molecular materials.

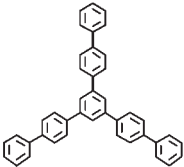
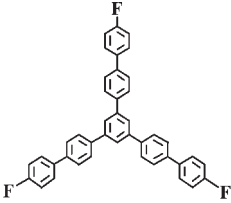
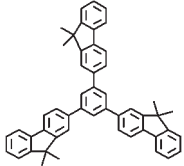
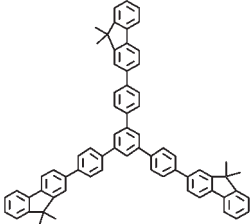
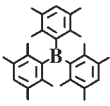
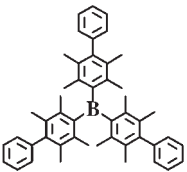
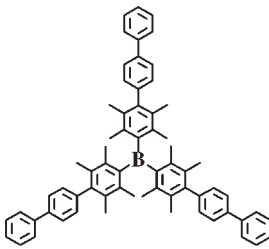
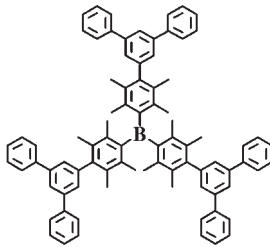
Family	Abbreviation	Compound Structure and Name	Ref.
Triarylbenzenes	TBB	 1,3,5-tris(biphenyl-4-yl)benzene	51, 52
	F-TBB	 1,3,5-tris(4-fluorobiphenyl-4'-yl)benzene	51–53
	TFB	 1,3,5-tris(9,9-dimethylfluoren-2-yl)benzene	51, 52
	TFPB	 1,3,5-tris[4-(9,9-dimethylfluoren-2-yl)phenyl]benzene	51, 52



Table 7.4 Continued.

Family	Abbreviation	Compound Structure and Name	Ref.
Triarylboranes	TPhB	 tris(2,3,5,6-tetramethylphenyl)borane	54
	TBPhB	 tris(2,3,5,6-tetramethylbiphenyl-4-yl)borane	54
	TTPhB	 tris(2,3,5,6-tetramethyl-1,1':4',1''-terphenyl-4-yl)borane	54
	TTPhPhB	 tris[2,3,5,6-tetramethyl-4-(1,1':3',1''-terphenyl-5'-yl)phenyl]borane	54

**Table 7.5** Performance of blue- and blue-violet-emitting OLEDs.

Device	EL Peak Wavelength [nm]	Maximum Luminance [ $\text{cd m}^{-2}$ ]	Luminous Efficiency [a] [ $\text{lm W}^{-1}$ ]	External Quantum Efficiency [a] [%]
A	404	3,960 (at 15.0 V)	–	1.40
B	435	7,400 (at 11.0 V)	0.78	2.8
C	444	9,100 (at 11.0 V)	1.0	2.5

Device A: ITO/m-MTDATA (50 nm)/TPD (20 nm)/F-TBB (10 nm)/Alq<sub>3</sub> (20 nm)/MAG

Device B: ITO/m-MTDATA (40 nm)/p-TTA (20 nm)/TTPhPhB (10 nm)/Alq<sub>3</sub> (30 nm)/LiF/Al

Device C: ITO/m-MTDATA (40 nm)/ $\alpha$ -NPD (20 nm)/TTPhPhB (10 nm)/Alq<sub>3</sub> (30 nm)/LiF/Al

[a] At a luminance of 300  $\text{cd m}^{-2}$ .

$\alpha,\omega$ -Bis(dimesitylboryl)oligothiophenes (BMB-nT) function as good electron-transporting materials with stronger electron accepting properties than those of Alq<sub>3</sub> and at the same time as good hole blockers [55].

## 7.5

### Charge Transport in Amorphous Molecular Materials

Since charge transport is a central phenomenon in the operation processes of OLEDs, the charge-transport properties of amorphous molecular materials need to be elucidated in detail. Extensive studies of charge transport in organic disordered systems have been performed on polymers and molecularly doped polymers, where small organic molecules are dispersed in a polymer binder. In the latter system, hole drift mobilities have been reported to vary by two orders of magnitude depending upon the binder polymer. Creation of amorphous molecular materials has enabled the investigation of charge transport in the glassy state of small organic molecules.

Charge carrier drift mobilities of a number of amorphous molecular materials have been determined by a time-of-flight method, and their electric-field and temperature dependencies have been analyzed in terms of the disorder formalism [56, 57]:

$$\mu = \mu_0 \exp \left[ - \left( \frac{2\sigma}{3kT} \right)^2 \right] \exp \left\{ C \left[ \left( \frac{\sigma}{kT} \right)^2 - \Sigma^2 \right] E^{1/2} \right\} \quad (7.1)$$

where  $\sigma$  and  $\Sigma$  are the parameters that characterize the energetic and positional disorder, respectively,  $\mu_0$  represents a hypothetical mobility in the energetic disorder free system,  $E$  is the electric field,  $k$  is the Boltzmann constant,  $T$  is the temperature, and  $C$  is an empirical constant.

**Table 7.6** Hole drift mobilities of amorphous molecular materials [a].

Material	$\mu_{\text{h}}/[\text{cm}^2 \text{ V}^{-1} \text{ s}^{-1}]$	Ref.	Material	$\mu_{\text{h}}/[\text{cm}^2 \text{ V}^{-1} \text{ s}^{-1}]$	Ref.
m-MTDATA	$2.7 \times 10^{-5}$	24	TPD	$1.1 \times 10^{-3}$	20
1-TNATA	$1.9 \times 10^{-5}$	37	$\alpha$ -NPD	$8.8 \times 10^{-4}$	59
2-TNATA	$5.2 \times 10^{-5}$	37	p-BPD	$1.0 \times 10^{-3}$	35
TFATA	$1.8 \times 10^{-5}$	27	PFFA	$1.1 \times 10^{-3}$	36
TCTA	$2.0 \times 10^{-5}$	37	FFD	$4.1 \times 10^{-3}$	27
p-DPA-TDAB	$1.4 \times 10^{-4}$	58	Spiro-TAD	$2.5 \times 10^{-4}$	60
TFAPB	$6.4 \times 10^{-3}$	31	TPTPA	$1.0 \times 10^{-2}$	61
TFIA	$8.1 \times 10^{-3}$	37	TPSePA	$1.1 \times 10^{-2}$	61

[a] Measured at an electric field of  $10^5 \text{ V cm}^{-1}$  at r. t.

Numerous studies of charge transport in amorphous molecular materials have shown that hole drift mobilities of amorphous molecular materials vary widely from  $10^{-6}$  to  $10^{-2} \text{ cm}^2 \text{ V}^{-1} \text{ s}^{-1}$  at an electric field of  $1.0 \times 10^5 \text{ V cm}^{-1}$  at room temperature, greatly depending upon their molecular structures. Table 7.6 lists hole drift mobilities of some amorphous molecular materials that function as hole-transporting materials in OLEDs.

## 7.6

### Outlook

Amorphous molecular materials have found successful application as materials for use in OLEDs, constituting a new class of functional organic materials. A new field of organic materials science that deals with amorphous molecular glasses has been opened up.

A number of hole-transporting, electron-transporting, charge-blocking, and emitting amorphous molecular materials that are of great interest and significance from scientific viewpoints have been reported up to this time. However, the materials that have been actually used in commercial devices are still very limited in number. Many factors should be taken into consideration for practical use, including facile synthesis, low cost, and others as well as the performance, the morphological and thermal stability of materials. The development of new materials with potential technological applications still remains to be a challenging subject.

## References

- 1 C. W. Tang, S. A. VanSlyke, *Appl. Phys. Lett.* **1987**, *51*, 913–915.
- 2 J. H. Burroughes, D. D. C. Bradley, A. R. Brown, R. N. Marks, K. Mackay, R. H. Friend, P. L. Burns, A. B. Holmes, *Nature* **1990**, *347*, 539–541.
- 3 Y. Shirota, *J. Mater. Chem.* **2000**, *10*, 1–25.
- 4 Y. Shirota, *J. Mater. Chem.* **2005**, *15*, 75–93.
- 5 Y. Shirota, T. Kobata, N. Noma, *Chem. Lett.* **1989**, 1145–1148.
- 6 A. Higuchi, H. Inada, T. Kobata, Y. Shirota, *Adv. Mater.* **1991**, *3*, 549–550.
- 7 W. Ishikawa, H. Inada, H. Nakano, Y. Shirota, *Chem. Lett.*, **1991**, 1731–1734.
- 8 W. Ishikawa, H. Inada, H. Nakano, Y. Shirota, *Mol. Cryst. Liq. Cryst.* **1992**, *211*, 431–438.
- 9 H. Inada, Y. Shirota, *J. Mater. Chem.* **1993**, *3*, 319–320.
- 10 K. Nishimura, T. Kobata, H. Inada, Y. Shirota, *J. Mater. Chem.* **1991**, *1*, 897–898.
- 11 A. Higuchi, K. Ohnishi, S. Nomura, H. Inada, Y. Shirota, *J. Mater. Chem.* **1992**, *2*, 1109–1110.
- 12 T. Noda, I. Imae, N. Noma, Y. Shirota, *Adv. Mater.* **1997**, *9*, 239–241.
- 13 T. Noda, H. Ogawa, N. Noma, Y. Shirota, *Adv. Mater.* **1997**, *9*, 720–722.
- 14 T. Noda, H. Ogawa, N. Noma, Y. Shirota, *J. Mater. Chem.* **1999**, *9*, 2177–2181.
- 15 J. Salbeck, N. Yu, J. Bauer, F. Weissörtel, H. Bestgen, *Synth. Met.* **1997**, *91*, 209–215.
- 16 W. J. Oldham, Jr., R. J. Lachicotte, G. C. Bazan, *J. Am. Chem. Soc.* **1998**, *120*, 2987–2988.
- 17 M. Ottmar, T. Ichisaka, L. R. Subramanian, M. Hanack, Y. Shirota, *Chem. Lett.* **2001**, 788–789.
- 18 K. Katsuma, Y. Shirota, *Adv. Mater.* **1998**, *10*, 223–226.
- 19 M. Thelakkat, *Macromol. Mater. Eng.* **2002**, *287*, 442–461.
- 20 M. Stolka, J. F. Yanus, D. M. Pai, *J. Phys. Chem.* **1984**, *88*, 4707–4714.
- 21 C. Adachi, T. Tsutsui, S. Saito, *Appl. Phys. Lett.* **1989**, *55*, 1489–1491.
- 22 S. A. Van Slyke, C. H. Chen, C. W. Tang, *Appl. Phys. Lett.* **1996**, *69*, 2160–2162.
- 23 Y. Shirota, Y. Kuwabara, H. Inada, T. Wakimoto, H. Nakada, Y. Yonemoto, S. Kawami, K. Imai, *Appl. Phys. Lett.* **1994**, *65*, 807–809.
- 24 C. Giebeler, H. Antoniadis, D. D. C. Bradley, Y. Shirota, *Appl. Phys. Lett.* **1998**, *72*, 2448–2450.
- 25 C. Giebeler, H. Antoniadis, D. D. C. Bradley, Y. Shirota, *J. Appl. Phys.* **1999**, *85*, 608–615.
- 26 Y. Shirota, Y. Kuwabara, D. Okuda, R. Okuda, H. Ogawa, H. Inada, T. Wakimoto, H. Nakada, Y. Yonemoto, S. Kawami, K. Imai, *J. Lumin.* **1997**, *72–74*, 985–991.
- 27 K. Okumoto, Y. Shirota, *Chem. Lett.* **2000**, 1034–1035.
- 28 Y. Kuwabara, H. Ogawa, H. Inada, N. Noma, Y. Shirota, *Adv. Mater.* **1994**, *6*, 677–679.
- 29 Q. Zhang, J. Chen, Y. Cheng, L. Wang, D. Ma, X. Jing, F. Wang, *J. Mater. Chem.* **2004**, *14*, 895–900.
- 30 W. Ishikawa, K. Noguchi, Y. Kuwabara, Y. Shirota, *Adv. Mater.* **1993**, *5*, 559–561.
- 31 K. Okumoto, H. Doi, Y. Shirota, *J. Photopolym. Sci. Technol.* **2002**, *15*, 239–242.
- 32 K. Okumoto, Y. Shirota, Jpn. Kokai Tokkyo Koho, **2003**, 261473.
- 33 D. F. O'Brien, P. E. Burrows, S. R. Forrest, B. E. Koene, D. E. Loy, M. E. Thompson, *Adv. Mater.* **1998**, *10*, 1108–1112.
- 34 B. E. Koene, D. E. Loy, M. E. Thompson, *Chem. Mater.* **1998**, *10*, 2235–2250.
- 35 K. Okumoto, K. Wayaku, T. Noda, H. Kageyama, Y. Shirota, *Synth. Met.* **2000**, *111–112*, 473–476.
- 36 K. Okumoto, Y. Shirota, *Mater. Sci. Eng. B* **2001**, *85*, 135–139.
- 37 M. Tanaka, M. Maeda, K. Okumoto, A. Mozer, H. Kageyama, Y. Shirota, to be submitted for publication.
- 38 D. O'Brien, A. Bleyer, D. G. Lidzey, D. D. C. Bradley, *J. Appl. Phys.* **1997**, *82*, 2662–2670.
- 39 J. Bettenhausen, P. Strohhriegl, *Adv. Mater.* **1996**, *8*, 507–510.
- 40 H. Ogawa, R. Okuda, Y. Shirota, *Mol. Cryst. Liq. Cryst.* **1998**, *315*, 187–192.
- 41 J. Bettenhausen, M. Greczmiel, M. Jandke, P. Strohhriegl, *Synth. Met.* **1997**, *91*, 223–228.

- 42 J. Kido, C. Ohtaki, K. Hongawa, K. OKuyama, K. Nagai, *Jpn. J. Appl. Phys.* **1993**, 32, L917–L920.
- 43 M. Jandke, P. Strohrriegel, S. Berleb, E. Werner, W. Brutting, *Macromolecules* **1998**, 31, 6434–6443.
- 44 K. Tamao, M. Uchida, T. Izumikawa, K. Furukawa, S. Yamaguchi, *J. Am. Chem. Soc.* **1996**, 118, 11974–11975.
- 45 L. C. Palilis, H. Murata, M. Uchida, Z. Kafafi, *Org. Electron.* **2003**, 4, 113–121.
- 46 Z. Gao, C. S. Lee, I. Bello, S. T. Lee, R.-M. Chen, T.-Y. Luh, J. Shi, C. W. Tang, *Appl. Phys. Lett.* **1999**, 74, 865–867.
- 47 T. Noda, Y. Shirota, *J. Am. Chem. Soc.* **1998**, 120, 9714–9715.
- 48 A. J. Makinen, I. G. Hill, T. Noda, Y. Shirota, Z. H. Kafafi, *Appl. Phys. Lett.* **2001**, 78, 670–672.
- 49 A. J. Makinen, I. G. Hill, M. Kinoshita, T. Noda, Y. Shirota, Z. H. Kafafi, *J. Appl. Phys.* **2002**, 91, 5456–5461.
- 50 M. Kinoshita, Y. Shirota, *Chem. Lett.* **2001**, 614–615.
- 51 Y. Shirota, M. Kinoshita, K. Okumoto, *Proc. SPIE-Int. Soc. Opt. Eng.* **2002**, 4464, 203–210.
- 52 K. Okumoto, Y. Shirota, *Chem. Mater.* **2003**, 15, 699–707.
- 53 K. Okumoto, Y. Shirota, *Appl. Phys. Lett.* **2001**, 79, 1231–1233.
- 54 M. Kinoshita, H. Kita, Y. Shirota, *Adv. Funct. Mater.* **2002**, 12, 780–786.
- 55 T. Noda, H. Ogawa, Y. Shirota, *Adv. Mater.* **1999**, 11, 283–285.
- 56 H. Bässler, *phys. stat. sol. B*, **1981**, 107, 9–53.
- 57 H. Bässler, *phys. stat. sol. B*; **1993**, 175, 15–56.
- 58 Y. Shirota, S. Nomura, H. Kageyama, *Proc. SPIE-Int. Soc. Opt. Eng.* **1998**, 3476, 132–141.
- 59 Z. Peng, S. T. Lee, D. P. Webb, Y. C. Chen, W. A. Gambling, *Synth. Met.* **1999**, 107, 107.
- 60 U. Bach, K. De Cloedt, H. Spreitzer, and Grätzel, *Adv. Mater.* **2000**, 12, 1060.
- 61 H. Ohishi, M. Tanaka, H. Kageyama, and Y. Shirota, *Chem. Lett.* **2004**, 33, 1266–1267.

## 8

# Dendrimer Light-Emitting Diodes

*John M. Lupton*

### 8.1

#### Introduction

Organic electroluminescent materials are generally categorized into two classes, small molecular [1] or polymeric [2]. Whereas small molecules such as aluminum tris(8-hydroxyquinoline) (Alq<sub>3</sub>) are conventionally deposited under high-vacuum conditions by evaporation, high molecular weight polymeric materials can be processed under ambient conditions from solution and can even be printed using ink-jet techniques. Much of the research into organic electroluminescence (EL) over the past 15 years has focused on either rather low or extremely high molecular weight materials [3]. A natural intermediate to these two classes of materials are dendritic structures, fractal-like molecules containing self-similar subunits. These materials can combine the benefits of both worlds, i. e. high molecular weight, solution processability, tuneability and functionalizability with well-defined monodisperse structural properties [4].

Dendritic systems, and in particular conjugated dendrimers, have recently attracted considerable attention from the synthetic organic chemistry community [5–22], as well as from photophysicists, particularly in view of the search for synthetic model analogies to biological compounds to study biophysical processes [23–25], and even more basic areas of research such as topology, rheology and statistical physics [26–30]. Geometrically, dendrimers are unique systems, as the number of atoms grows exponentially with the branching – or generation – of the dendrimer, rather than to the power of  $n$  as in  $n$ -dimensional space. This exponential growth is a characteristic of an infinite-dimensional system [25]. In contrast, there is only one unique connecting path across the structure between two lattice sites, i. e. units of the molecule, making the connectivity or the path of an excitation one-dimensional. This results in unusual optical properties of these macromolecules such as geometrical energy funnelling [31]. Dendritic molecules have been synthesized and studied as a comparison to biological [32] light-harvesting complexes, and a body of both theoretical and experimental work exists on these artificial light-harvesting antennae [23, 33–47]. In these complexes excita-

tions are generated optically in the dendron periphery of the molecule and transferred through incoherent exciton hopping via the Förster mechanism or via strong coherent dipole-dipole coupling into the central region of the molecule, leading to a certain degree of exciton confinement. Excitonic effects due to this strong degree of localization have attracted considerable attention and charge-transfer complexes have been observed as well as strong coherences and Davidov-like excitonic splittings [24, 25, 33, 48–50]. A number of investigations of intramolecular interchromophoric couplings exist both in the time [51–55] and in the frequency domain, right down to the level of single light-harvesting molecules [56].

In addition to the similarities with light-harvesting complexes, dendrimers may also be used as light-emitting materials [6, 8–11, 17, 18]. The exciton confinement at the center of the dendrimer allows the emitting region to be modified independently of the dendron architecture, which can be tuned to give the desired interactions with the environment such as neighboring molecules or solvent [9, 11, 33]. Emissive excitations can hence be shielded from the environment through the periphery of the dendrimer [19, 20]. This can reduce parasitic perturbations such as solvation effects in the condensed phase or luminescence quenching through interaction with the environment or surrounding chromophores [9, 20, 57–61] in the solid film. Dendrimers or starbursts were proposed as emitting or transport layers in organic LEDs in the mid-1990s [8–11, 17–19, 62–68] and combine a number of advantageous electronic and processing properties: they possess a well-defined molecular weight and can hence be synthesized reproducibly to a high purity; they are solution processable in most cases and, in contrast to conjugated polymers with potentially very high molecular weight and viscosity, may be ideally suited for inkjet printing of LED structures, as has previously been demonstrated with polymer-based materials [69]. In addition, it has been shown that the emission color of the core region may be tuned independently of the dendron architecture across the entire visible spectrum [11]. This provides a novel tool for controlling the emission color of organic LEDs. Such facile tuneability is not accessible with either conventional small molecule and particularly not with polymeric organic semiconductors, where substitutions to control the processability usually also lead to an alteration of the photophysical properties. A well-known example of this is the comparison of precursor poly(phenylene-vinylene) (PPV) with the soluble variant MEH-PPV. Whereas the precursor-derived material is insoluble and emits in the green part of the spectrum, substitution of the side chains to ensure solubility results in a considerable red-shift of the electronic transition. Processability and electronic properties are therefore intimately coupled.

A further interest in dendrimers for EL applications is the possibility of assigning different functional properties to the individual components of the macromolecular structure. For instance, it is conceivable to attach moieties with hole-transporting properties to the core region and electron-transporting properties to the dendrons, or even to integrate bipolar transport functionality in one molecule by virtue of asymmetric dendronization [41, 70]. Many of the fundamental aspects relating to the physical structure and architecture of dendrimers can be mapped

directly to the requirements of sophisticated EL materials. The initial interest in dendrimers was in using them as transporting and shielding units, such as intelligent drug-delivery systems [71, 72], where the macromolecule or even supramolecular dendritic assembly acts as a cage for a particular reagent that is released following an external stimulus [73]. Likewise, chromophores can be integrated into the dendritic cage, which dramatically reduces concentration quenching and solvent interactions [20]. The highly nonlinear structure of dendrimers also lends itself to light-harvesting applications and the construction of excitonic funnels to facilitate color tuning in EL devices. A number of these interesting aspects have been addressed in the context of LEDs. The benefit of dendrimers is thus threefold. Firstly, these materials provide a unique material system to study the optical and electrical properties of organic semiconductors in a well-defined environment, thus enabling the development of elaborate structure–property relationships, which are of particular relevance to organic semiconductors [61]. These can in turn feed into material design and provide valuable information on the influence of morphology and intermolecular packing on, for example, charge carrier mobility and intermolecular interactions [58]. Dendrimers also provide a natural environment for studying organic semiconductor blend systems with a minimum of phase separation due to matching surface groups [70, 74]. Secondly, dendrimers offer an exciting playing field for constructing the next generation of organic devices using supramolecular assembly techniques. With macromolecular organic electronics approaching maturity, exploitation of self-assembly techniques to combine chemical with device functionality is becoming an increasingly important aspect in materials and device design (for an example of molecular-scale engineering in devices see [75]). Thirdly, and most importantly, the demonstration of exceptionally efficient electrophosphorescence from dendrimers containing transition-metal complexes means that these material systems are amongst the most promising solution-processable organic EL complexes known to date. The ease of processability united with the synthetic flexibility and diversity such as the control of surface functionality of the macromolecule imply that electroluminescent dendrimers now pose a very real alternative to small molecular and polymeric organic semiconductors [76].

This chapter aims at reviewing the development of dendrimers for organic EL applications. Dendrimers as interesting macromolecular structures have been actively studied now for the past 20 years, and it would be impossible to provide an entirely balanced overview of the highly diverse development of dendritic structures within this framework. Where appropriate, parallels are drawn from recent advances in electroluminescent dendrimers to issues previously discussed in the general context of the physical properties of dendrimers. After highlighting the basic concept of using dendrimers as EL materials, different classes of fluorescent and phosphorescent materials studied to date are presented. The electronic properties of dendrimers are discussed subsequently with particular attention paid to the tuneability availed by the decoupling of different functional units constituting the macromolecule. Intramolecular excitations within dendrimers can be tuned independently of intermolecular interactions between molecules, thus enabling



independent tuneability of the emission color, charge transport, and the level of interchromophoric coupling and aggregation. It is shown that even materials whose EL performance is not particularly outstanding can provide unique insight into subtle structure–property correlations in organic semiconductors and allow an extrapolation to other material systems. Finally, comparisons are drawn with attempts to dendronize conjugated polymers in order to control the interchain packing behavior.

## 8.2

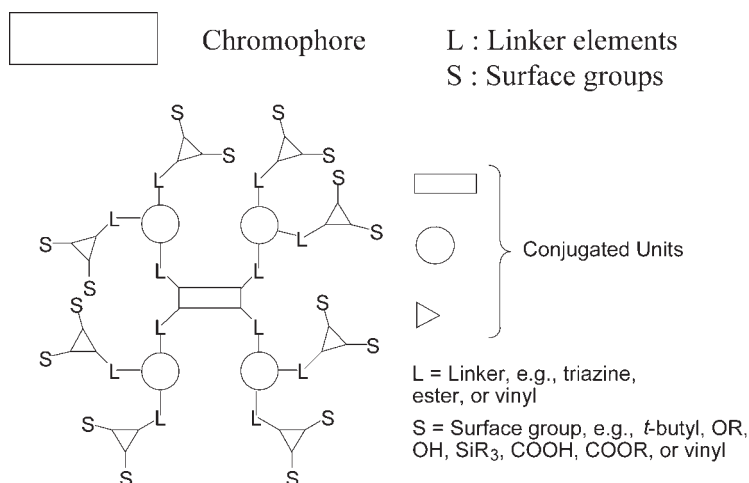
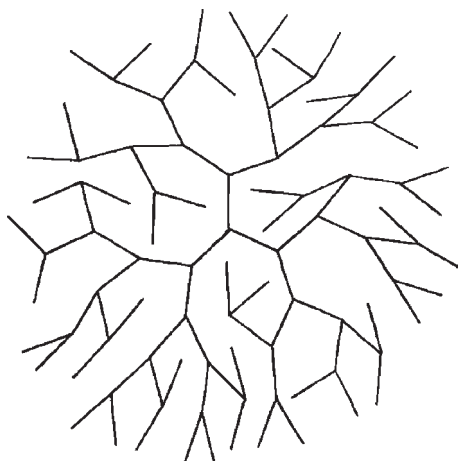
### The Dendrimer Concept

Organic semiconductors can generally be divided into two classes of materials: small organic molecules and polymeric materials. There is an interesting class of macromolecular materials in between, however, with a branching exponential rather than an iterative linear geometry. These materials are known as dendrimers, derived from the Greek for tree (*dendros*) and parts (*meros*). Over the past decade there has been rapidly increasing interest in dendritic molecules from a large variety of research areas [5, 6, 9, 13, 15, 16, 19, 33, 71, 77, 78]. A sizeable number of publications and patents were produced by Tomalia and coworkers [70, 71], who identified dendrimers as materials suitable to imitate naturally occurring light-harvesting complexes important to photosynthesis. Further interest in dendrimers has been as molecular drug-delivery systems, employing molecular recognition features incorporated in the branches (termed *dendrons*) [19, 71]. A remarkable feature of dendrimers is the ability to localize energy at the center of the molecule through correct choice of the energy gradient between core and dendrons [33, 79]. The simplest conceivable dendrimer structure is a regularly branched molecule formed by the complete reaction of multifunctional monomer units. Such structures, as shown schematically in Fig. 8.1, can be grown either convergently by synthesizing branched arms and attaching these to a core unit, or divergently, by initiating the branching reaction from the core and growing subsequent generations in much the same way as linear polymerization occurs. The units constituting the dendrimer may be either conjugated, nonconjugated or partially conjugated.

Dendrimers can be constructed to contain different functional elements, e. g. to consist of a luminescent conjugated core region – either monomeric, polymeric or molecular – surrounded by hyperbranched, conjugated side groups or dendrons. This is shown schematically in Fig. 8.2. In this general structure, all units are conjugated, but the conjugation is broken between the different constituents. This can be achieved by *meta*-conjugations or carbonyl linkers, for example. Excitations are therefore not delocalized across the entire molecule.

Energy localization at and funnelling to the center of dendrimers has been demonstrated in a number of systems [14, 33, 77, 78, 81], although to date immediate practical applications are still under consideration. The fact that the dendrons of each branching level (referred to as the generation *G*) possess three contact

**Fig. 8.1** Schematic representation of a trifunctional fifth generation self-similar starburst dendrimer following Boris and Rubinstein [80].



**Fig. 8.2** Schematic structure of conjugated dendrimers. A conjugated core is surrounded by doubly branched conjugated dendrons, forming a second-generation dendrimer. The different conjugated groups are linked through linker units (L). The dendrimer is surrounded by surface groups (S), which control the interaction with the environment.

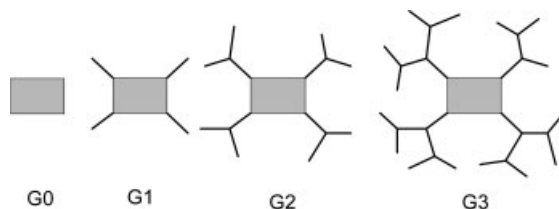
points within the dendrimer, two of which point away from the core, suggests from a mere statistical argument that excitation energy should diffuse from the core to the periphery. Indeed, such systems, where the emissive centers are localized on the dendron periphery, have been demonstrated [19]. However, dendrimers can also possess a unique shielding effect, which protects excitations from interactions with the environment. This has been demonstrated conclusively by the encapsulation of emissive centers in a dendrimer architecture. In work carried out by Meijer and coworkers, a reduction in aggregate emission was observed for Bengal Rose shielded in this way [20]. A most remarkable effect of energy

localization has been demonstrated by Aida and coworkers [78, 81], who found that their dendritic macromolecules could be photoisomerized by the absorption of a number of infrared photons rather than a single ultraviolet photon. This result, which is yet to be reproduced in the literature, suggests that the dendrimer architecture inhibits all radiative and nonradiative decay modes for excitations at the core, so that quanta of infrared radiation accumulate, finally leading to photoisomerization.

Although dendrimers are optically fascinating systems and may well find applications in artificial light-harvesting devices, few direct applications have been demonstrated as yet. A further area of interest has been in electroactive dendrimers [7, 12] and the effect of the dendritic architecture on oxidation and reduction of the macromolecule. Dendritic or starburst materials have also been used as charge-transporting materials [17, 64–68, 82], in particular for organic LEDs. However, the possibility to independently control the emissive core and the dendrimer architecture, the potential shielding and localization of excitations as well as the possibility for energy funnelling, make conjugated dendrimers extremely interesting as emissive materials for organic LEDs [8, 10, 11, 18]. In effect, conjugated dendrimers allow a nanoscale control of the electronic properties of organic semiconductors. The wide range of emission colors available to organic LEDs has frequently been cited as a key benefit of these devices over conventional LEDs. Using conjugated dendrimers, Halim et al. [11] demonstrated that the emission spectrum of dendrimers in a common architecture can be tuned throughout the visible spectrum. The dendrons provide a means of controlling the ordering and microscopic packing of the emissive chromophores, which is extremely important in the operation of LEDs, as it affects both charge transport and interchromophore coupling of the emissive dipoles. Finally, the interaction of the molecule with the environment is of great importance. The surface groups of the dendrimers provide a method of controlling the solubility, which can be extremely useful in the fabrication of solution processed multilayer devices.

One particular strength of dendrimers when compared to polymeric systems is their monodispersity, which greatly simplifies structural characterization and generally facilitates a convergent and iterative synthetic procedure. Standard spectroscopic tools such as UV/VIS and FTIR absorption can be used to monitor the progress of reactions between stages. Flash silica column chromatography is readily employed to purify the compounds, which are then quality checked by thin-layer chromatography (TLC) and combustion analysis (e. g. inductively coupled plasma optical emission spectroscopy, ICP-EOS). Gel permeation chromatography (GPC) gives further insight into the purity of the compound and may also be used to estimate the molecular radii by studying the diffusivity.  $^1\text{H}$  NMR provides insight into the distribution of different isomers in the product, but also indicates contamination by hydrogen-containing impurities. An important tool employed to characterize dendrimers is mass spectrometry, the most commonly used form of which is matrix-assisted laser desorption/ionization-time-of-flight (MALDI-TOF). MALDI-TOF is particularly suited to characterize dendrimers as it minimizes fragmentation of large molecules and provides an accurate idea of the

**Fig. 8.3** Schematic diagram of a dendrimer core chromophore surrounded by dendron branches of varying generation  $G = 0$  to 3.



chemical purity of the final product. It also gives an isotope distribution, which can be used to confirm the molecular formula and weight. Such detailed diagnostic techniques are generally not readily available in polymer synthesis, where purification of the final product can become an important issue.

Dendrimers uphold a close connection between physical shape and property. Chromophores can be situated either at the end of the dendrons or at the core of the macromolecule, akin to biological light-harvesting complexes. A structure of such a molecule surrounded by branching dendron arms of increasing generation is sketched in Fig. 8.3. The effect of the dendrons on the core can be twofold. Firstly, it is noted that the schematic structures of the molecules directly resemble an antenna. By careful design of an intramolecular energy gradient it is thus possible to funnel energy absorbed in the arms to the emissive core, where radiative decay can occur. Secondly, the dendrons act as a protective box or shield around the core. This is particularly important in organic semiconductor applications, where solid-state quenching effects due to pronounced intermolecular  $\pi$ -orbital overlap as well as efficient exciton diffusion to low-energy quenching sites is prevalent [61]. Surrounding the emissive core with dendrons can thus reduce both nonradiative decay in the solid state as well as minimizing the diffusivity of excitons. This site-isolation effect has been demonstrated in a number of dendritic structures [41, 60, 70]. A particularly interesting example is aggregation control in solutions of laser dyes, where it has been shown that much higher concentrations can be achieved upon dendronization than without [83]. Optical gain from fluorene-based conjugated dendrimers has also been demonstrated [84]. The considerably increased solution concentration achievable with dendrimers substantially reduces the optical path lengths required for optical gain, which in turn is significant for the development of optical amplifiers.

A further motivation for dendrimers is the fact that thermal crystallization can be a serious problem in small-molecule thin-film devices and indeed many low molecular weight materials form poor-quality polycrystalline solid phases. Controlling and minimizing attractive intermolecular forces by exploiting the globular structure of dendrimers should allow the formation of stable amorphous phases required for high-quality thin films [18]. This could be demonstrated impressively in a nearfield scanning microscope investigation of films of different dendrimer generation [35]. Higher-generation films were seen to become more amorphous, which could also be related directly to the aggregation signature in the photophysical properties. Generation dependent aggregation, crystallization and morphology control has also been observed in iridium-based dendrimers [85].

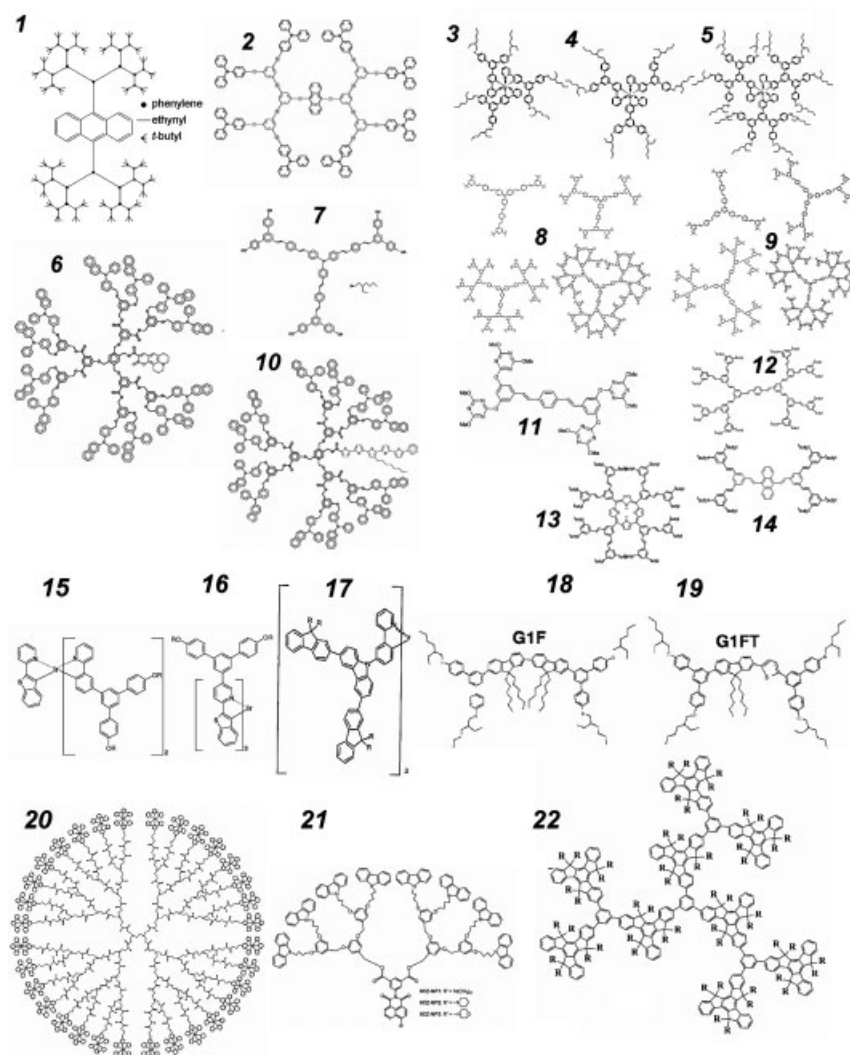
The dendrimer concept is principally modular in nature, i. e. the synthesis can be built up from different blocks to construct potentially vast macromolecular complexes of well-defined physical shape and ensemble properties. A substantial amount of work has been directed towards the basic issues of nanoscale synthetic engineering. Both single-particle measurements, such as atomic force microscopy [86, 87], as well as ensemble measurements, such as dynamic light-scattering [88], have unravelled interesting physical behavior, which is expected to have implications for future EL device design. The modularity of dendritic synthesis should be stressed particularly in the context of supramolecular electronically active aggregates [89, 90] and the possibility of facile blending of individual dendritic species to perform particular functions in the ensemble [74].

### 8.3

#### Electroluminescent Dendritic Materials

A wide range of cores and dendrons have been explored in past years, and depending on the application envisaged more attention has been paid either to the precise nature of the emissive species or the dendritic periphery enclosing the emissive unit. Figure 8.4 lists examples of electroluminescent dendrimers previously discussed in the literature. Most of the materials (except for **20**) contain a single chromophore at the center of the structure, from which emission occurs. The emissive unit may be either fluorescent or phosphorescent in nature, such as the transition-metal complexes **3**–**5**, **13** (with platinum porphyrin) and **15**–**17**. The dendron units perform different functionalities and can be either conjugated (such as stilbene, biphenyl, phenylacetylene, fluorene, truxene) or nonconjugated (such as Fréchet-type poly(aryl-ether) or polyamidoamine). Whereas the dendrons form passive units in most of the molecules, triphenylamines are explicitly employed as surface groups of **2**, **6**, **10** to ensure a high degree of hole conductivity. Electron-transporting oxadiazole periphery groups have also been explored [91]. Most of the dendrimer structures are symmetric in nature. Asymmetric dendronization is possible using iridium-based chemistry, as demonstrated in **15**. At least partial site isolation has been demonstrated in all of the structures except **20**.

**Fig. 8.4** Examples of electroluminescent dendrimers studied to date. **1**: fourth-generation anthracene core phenylacetylene [18]; **2**: second-generation anthracene core dendrimer with triphenylamine surface functionalization [18]; first-generation fac-tris(2-phenylpyridyl)Ir(III) cored dendrimer with biphenyl dendrons in the para (**3**) and meta (**4**) position [76, 92–96]; **5**: second-generation iridium centered dendrimer [93–97]; **6**: coumarin centered poly(benzyl-ethyl) dendrimer with naphthyl diphenylamine termination [41, 98]; **7**: tris(distyrylbenzyl)amine centered dendrimer with first-generation meta-linked biphenyl dendrons terminated by alkoxy surface groups [99]; **8**: four generations of a tris(distyrylbenzyl)amine centered dendrimer with stilbene dendrons in the meta substitution terminated by *t*-butyl surface groups [58–59, 100, 101]; **9**: four generations of a 1,3,5-tris(distyrylbenzyl)-benzene cored stilbene dendrimer [102, 103]; **10**: pentathiophene lumophore attached to poly(benzyl-ethyl) arms terminated by naphthyl diphenylamine groups [70, 104]; **11**: first-gen-



eration triazine dendrimer with a distyrylbenzene core [10]; stilbene-based dendrimers [8, 9, 11, 105, 106] with cores of distyrylbenzene (12, second-generation), porphyrin (13, first-generation) and platinum-porphyrin [74] and anthracene (14, first-generation); 15: first-generation asymmetric dendrimer with two dendronized 2-phenylpyridyl and one benzothienylpyridyl ligand and ethylhexyl surface groups [107, 108]; 16: symmetric iridium centered benzothienylpyridyl dendrimer [107]; 17: first-generation iridium-centered fluorene dendrimer, with the fluorene linking to a carbazole

group of the dendrons [109]; 18: first-generation bis-fluorene dendrimer with biphenyl dendrons [110–112]; 19: first-generation fluorene-thiophene dendrimer with biphenyl dendrons [111]; 20: third generation polyamidoamine dendrimer containing 32 ruthenium bipyridine chromophores located at the surface of the dendrimer [113]; 21: third-generation naphthalimide cored dendrimer with Fréchet-type poly(aryl-ether) dendrons and carbazole peripheral groups [91]; 22: first-generation dihydro-diindenofluorene (truxene) dendrimer [114].

## 8.4

### Electronic Properties

#### 8.4.1

##### Control of Emission Color

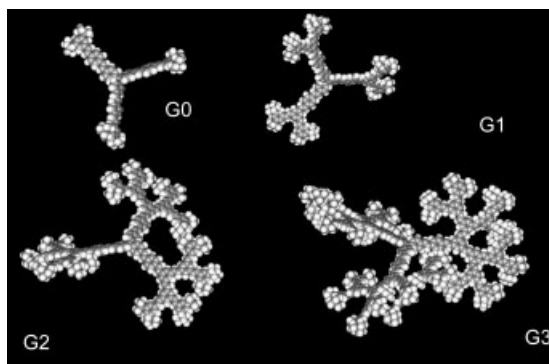
One of the first aspects that was addressed using dendrimers with conjugated dendrons and conjugated core units was the question of whether the emission color of the material can be tuned without substantially modifying the molecular architecture and in particular the macromolecular surface properties, which control solubility. Dendrimers **12–14** present such a class of material, where the dendron periphery could be maintained independently of the core structure. Varying the core from a porphyrin over an anthracene to a distyrylbenzene unit allowed spectral tuneability from the deep red ( $\sim 670$  nm) to the blue ( $\sim 440$  nm) [11], which was readily observed in photoluminescence (PL) and EL measurements. Energy transfer from the conjugated stilbene dendrons to the core unit could be verified using PL excitation spectroscopy. Although the EL properties of these materials were initially rather rudimentary, they did provide a substantial motivation to pursue further studies into dendrimers as EL materials. Initial device efficiencies ranged between 0.01 % and 0.1 % [8], depending on the dendron generation. This appeared promising considering the comparable values that polymeric LEDs started off from [2] and the rapid progress in terms of efficiency achieved with the help of guided device optimization. Color tuneability could also be achieved with the dendrimers **8** and **9**, which also consist of distyrylbenzene based cores surrounded by stilbene dendrons of generation 1 to 3 [102]. In this case, the core unit is made up of three isolated distyrylbenzene units linked by a central phenyl ring, which does not allow conjugation between branches. The almost identical structure of the nitrogen-centered molecule results in a considerably red-shifted emission due to strong electronic delocalization between the distyrylbenzene units facilitated by the lone electron pair on the nitrogen atom. Although electrochemical measurements and solid-state aggregation behavior did suggest that in this case the rather large core unit can have a considerable impact on the overall physical structure of the macromolecule [102, 115], the surface functionality remained intact.

#### 8.4.2

##### Control of Intermolecular Interactions

The dendron periphery and the dendrimer generation provide a unique method of investigating the effect of chromophore spacing on the emission and transport properties of LEDs. There is considerable interest in understanding the nature of the emissive species responsible for EL in organic materials, as well as the basic processes involved in charge transport. It is commonly assumed that good charge-transporting properties are a result of close chromophore proximity and a strong level of interaction between transport sites. In contrast, this proximity has been

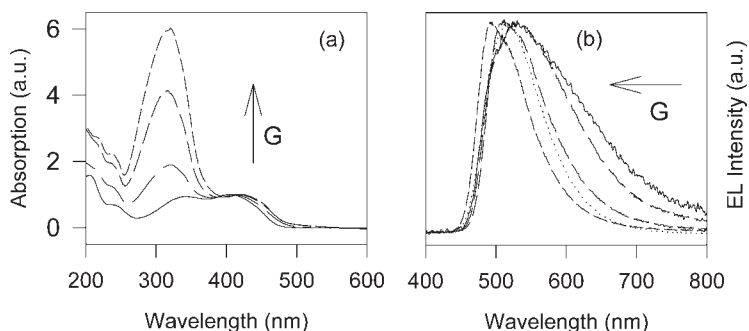
**Fig. 8.5** Space-filling representation of the four generations of the nitrogen-centered distyrylbenzene-stilbene dendrimer **8**.



shown to lead to luminescence quenching and an overall reduction in emission efficiency [116]. By using the dendrons as microscopic spacers between chromophores, the trade-off between efficient luminescence and good charge transport can be investigated. In contrast to blend systems, the problem is much better defined in the case of dendrimers, as there is only one molecule involved in the investigation and there is no danger of phase separation. Figure 8.5 shows a space-filling representation of the nitrogen-centered distyrylbenzene dendrimer with stilbene dendrons (**8**). The number of dendron units in the molecules increases as  $6 \times (2^G - 1)$  with generation number  $G$ . As the stilbene has a wider energy gap than the tris(distyrylbenzenyl) amine core, the dendrons act both as excitonic funnels but also as localizers of charge and excitation energy in the solid state. This is both a result of the energetic landscape that the excitations on the core of the dendrimer experience, as well as of the physical structure of the macromolecule. As is apparent from Fig. 8.5, increasing the generation results in the molecule becoming more and more bulky. The closest proximity that two core units (i. e. the G0-complex) can be situated in is therefore expected to increase with increasing generation number. Also, the core isolation should evolve from a more two-dimensional to a three-dimensional topological problem, as steric hindrance between the dendron units leads to space filling of the molecule, ideally approaching a globular structure.

The effect of exciton localization and shielding of the emissive species in the dendrimer from undesirable intermolecular interactions is readily visible in the absorption and EL properties [59]. Figure 8.6(a) shows the absorption spectra of neat thin films of the four generations of dendrimer **8**. Two features are apparent, peaking at 420 nm and 320 nm. The high-energy feature displays a substantial increase with increasing generation, whereas the low-energy feature remains virtually unchanged. The effect is even more pronounced in solutions of the material, where quantum-chemical calculations could clearly demonstrate that the low-energy feature arises solely from the core lumophore of the dendrimer and the high-energy absorption is attributable to the stilbene dendrons [117]. Indeed, besides providing a real space visualization of the molecular electronic modes involved in absorption, semiempirical calculations could also explain the exponen-

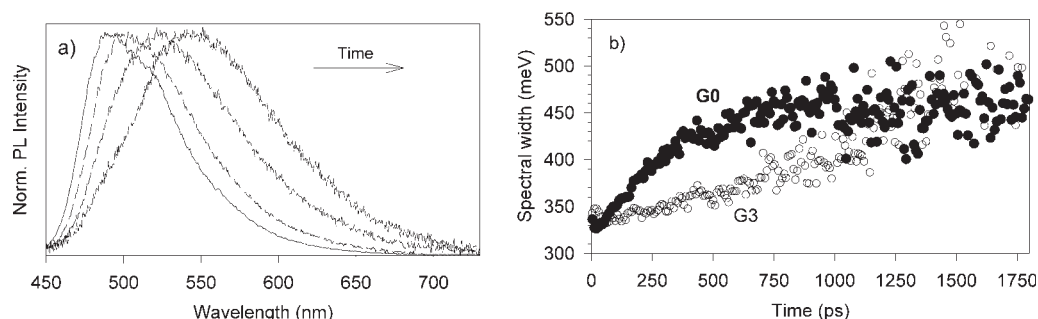




**Fig. 8.6** (a) Absorption spectra of films of the dendrimer generations G0 to G3 normalized to the feature at 420 nm. (b) EL spectra of devices made with dendrimers of generations 0 to 3 (solid and dashed lines) together with the solution PL spectrum (dotted line) [59].

tial increase in the high-energy absorption strength with generation [103]. The fact that the absorption features of the dendrimer barely shift with increasing molecular size can be taken as evidence for excitonic localization at the center of the molecule. This effect was first observed by Kopelman et al. [33] in a family of phenyl-acetylene dendrimers. The case of emission from bulk films is somewhat different, as shown in Fig. 8.6(b). Whereas the absorption effectively broadens with increasing generation, the EL spectra narrow. Comparison with the solution PL spectra (dotted line), which are identical for all generations due to the exciton funnelling and localization effect, shows that pronounced emission occurs from a red-shifted tail state for low generations. This emission can be substantially reduced with increasing generation, until the EL spectra in the solid state become very similar to the solution PL spectra. Increasing the dendrimer generation thus allows a reduction of intermolecular interactions, which tend to lead to emission from red-shifted, aggregated species arising from interchromophoric coupling [61]. This also results in an increase in the overall PL quantum yield in the solid state with generation, although it remained comparatively low at a maximum of 12 % [100]. This is in contrast to the solution yield, which was found to be independent of generation at 60 %.

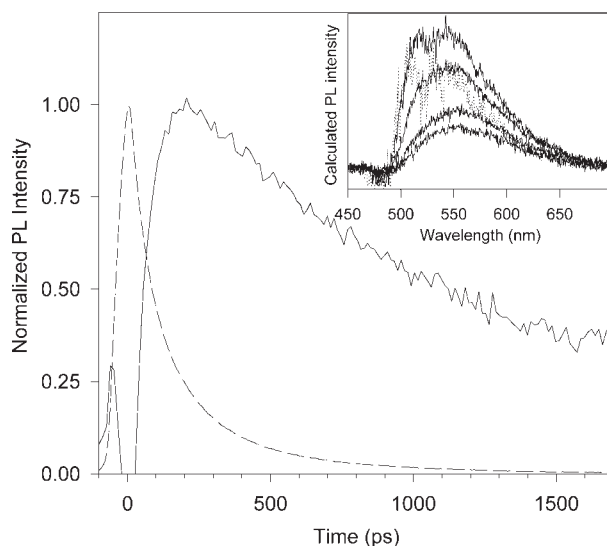
Aggregation is, however, not the only physical phenomenon that affects the solid-state emission properties of organic semiconductors and gives rise to spectral changes when going from the condensed to the solid phase. As soon as the lumophores are deposited in the solid state, excitation energy may be exchanged between adjacent molecules by means of energy transfer [116]. This exciton hopping depends sensitively on the intermolecular separation, which can in turn be tuned using the dendrimer generation. Figure 8.7(a) shows time-resolved PL spectra of the G0 core of **8** [60]. Little change is observed in the spectra within the first 100 ps, except for a pronounced red-shift by 5 nm. At longer times, however, a substantial red tail develops, which dominates the emission 1.5 ns after excitation. It is straightforward to show by means of comparing different generations that the rapid red-shift observed on short timescales is purely due to exciton



**Fig. 8.7** (a) Time-dependent PL spectra of the zeroth-generation dendrimer **8** measured at 290 K. The spectra evolve to the red with increasing delay after excitation. The time windows chosen are (spectra from left to right): 0 ps (5 ps integration window), 100 ps (5 ps window), 500 ps (50 ps window) and 1500 ps (400 ps window). (b) Evolution of the spectral width of dendrimer film PL as a function of time for G0 and G3 [60].

hopping between adjacent molecules. Increasing the dendron branching and thus the intercore separation substantially slows down the migration rate and consequently the rate at which the spectra red-shift. The spectral broadening, on the other hand, at longer timescales arises due to exciton diffusion to and trapping in intermolecular sites with particularly strong interchromophoric coupling, which facilitate excimer formation. The red component in Fig. 8.7(a) almost vanishes when the same measurement is carried out for the third-generation dendrimer. Besides exhibiting a slowed exciton diffusion rate (i.e. a slower red-shift) [60], the high-generation dendrimer also efficiently inhibits intermolecular coupling and delocalization. Figure 8.7(b) displays this effect in a plot of spectral width as a function of time. Whereas the G0 spectra broaden after 100 ps, the G3 spectra remain virtually unperturbed for half a nanosecond. The enhanced spectral purity and similarity to the solution PL in Fig. 8.6 can thus also be taken as a signature of the much slower migration of excitons to excimer traps [60]. In contrast to polymers, where both intramolecular and intermolecular energy transfer and aggregation phenomena are important [61, 116], intramolecular processes can be excluded from these dendritic systems. They therefore provide a model framework to study the formation of intermolecular species, which have attracted considerable attention in the field of organic semiconductors.

As the evolution of the red-tail aggregate or excimer emission occurs on much longer timescales than the spectral red-shift due to energy transfer, the rapidly relaxed dendrimer core spectrum (i.e. the spectrum in Fig. 8.7 taken at 100 ps delay) can be taken as the emission arising from the lowest-energy conformation of the molecules within their disorder broadened density of states. Subtracting this lowest-order electronic emission from subsequent emission spectra yields the pure intermolecular spectral component, as shown in the inset of Fig. 8.8. The rise and decay of the excitonic and intermolecular emission can be clearly resolved using this technique, which demonstrates directly the tendency for phenylene-vinylene units to form intermolecular excited state species [116]. Rather than



**Fig. 8.8** Calculated excimer component in delayed G0 spectra of **8** at 290 K. The excimer spectra deduced by subtracting the molecular PL are shown in the inset for 80 ps delay (dotted) and 200 ps, 500 ps, 1000 ps, and 1500 ps delay (from top to bottom). Note that the spectra do not change with time but are broadened and red-shifted by 50 nm when compared to the steady-state spectra in Fig. 8.6(b). The rise and decay of the excimer component (solid line) is compared to the main emission band (dashed line) [60].

using polymeric or oligomeric systems, which do not provide a single, independent parameter to tune the level of interaction, dendrimers afford a direct demonstration of the control over intermolecular delocalization using the generation as the only freely tunable variable.

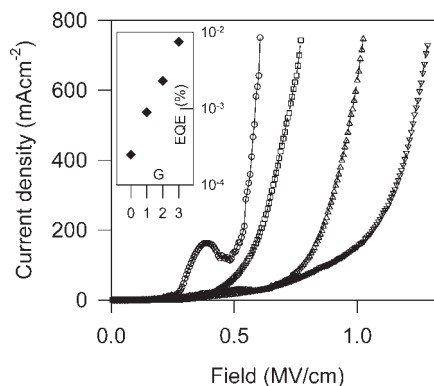
Control over concentration quenching and aggregation has been demonstrated in a variety of material systems using this technique of dendritic encapsulation both in solution phase and in the solid state [20, 118–121]. A noteworthy example of the benefit of encapsulation is the demonstration of optical gain from dendritically protected chromophores [83, 84]. Aggregation quenching is generally a major problem with laser dyes, which restricts the dye concentrations usable and thus poses limits on the minimal optical path lengths. Increasing the dye concentration while maintaining the quantum yield is possible using dendritic architectures, and also suggests novel routes to highly compact solid-state lasing materials following on from the success of conjugated polymers.

#### 8.4.3

##### Control of Charge Transport

Charge transport in disordered organic semiconductors generally occurs by hopping between adjacent conjugated segments. This process has been investigated in detail in molecularly doped polymers and even in doped crystalline materials

**Fig. 8.9** Current–voltage characteristics of devices made with dendrimers of generations 0 to 3 (from left to right,  $G = 0$  ( $\circ$ ),  $G = 1$  ( $\square$ ),  $G = 2$  ( $\Delta$ ),  $G = 3$  ( $\nabla$ )). Inset is the external quantum efficiency as a function of generation [59].



[116]. Typically, the average hopping distance can be tuned by varying the concentration of a guest species in a host material, with the known problems of change of morphology and composition, which may be rather detrimental to the operation of an actual device. In organic LEDs it is often desirable to be able to tune charge transport so as to balance electron and hole currents. The dendron-controlled interlumophore spacing indicated in Fig. 8.3 and supported by the space-filling representations in Fig. 8.5 suggests that a facile procedure for tuning charge transport in dendritic systems is to simply vary the dendrimer generation, providing the dendrons do not participate in charge transport. Figure 8.9 displays current–voltage characteristics recorded for single-layer LEDs containing the four different generations of material **8** sandwiched between indium tin oxide (ITO) and aluminum electrodes [59]. The resistance of the layer increases monotonically with increasing generation and the devices turn on at higher fields. This is in agreement with the dendrons forcing the cores further apart and the average separation between the lower energy gap central lumophores of the dendrimer increasing. Interestingly, the dark current prior to turn-on of the diode also increases substantially with generation (whereas the current post turn-on decreases), which may be taken as a signature of enhanced charge trapping on the dendrimer cores due to increased spatial isolation [122].

The inset in Fig. 8.9 also shows the LED external quantum efficiency of the single-layer device as a function of generation. It increases exponentially with generation. The fact that the single-layer device efficiency rises with increasing intermolecular spacing arises due to the imbalance between hole and electron currents in the device. Whereas ITO forms a reasonable electrode for hole injection into the dendrimer layer, there is a substantial barrier to electron injection from the aluminum electrode. Balancing the minority and majority charge carrier currents can be achieved in two ways: by either changing one of the two barriers or by tuning the mobility. Whereas the device current–voltage characteristics are dominated by the hole majority carrier current, the light output is determined by the electron minority carrier current, which thus also controls the overall efficiency. Increasing the intermolecular spacing evidently results in a stronger re-

duction of the hole current than in the electron current, thereby leading to current balancing and more efficient recombination. This also results in the device efficiency becoming almost independent of the electron injection barrier for high generations, so that equally efficient devices could be realized using gold cathodes [59]. Apparently, hole and electron currents respond somewhat differently to the change in intermolecular spacing, which is most likely due to preferential trapping of electrons on the conjugated units [123]. Both transient photocurrents, which are sensitive to the majority carriers, and transient EL, which is dominated by the minority carriers, were investigated for device structures containing **8** [58]. Whereas the hole mobility determined from time-of-flight decreases by almost two orders of magnitude with increasing generation and provides values of an effective (although dispersion limited) hole mobility within the semiconductor layer, transient EL shows little effect on generation [58]. Interestingly, mobility values extracted from time-of-flight data can be used to model the current–voltage characteristics both of the devices shown in Fig. 8.9 [58] and of more recent phosphorescent dendrimer structures [97], demonstrating the validity of controlling charge transport, i. e. mobility, by generation-controlled intermolecular packing.

Tuning the transport properties of the dendrimer layers can be particularly useful in bilayer configurations. Although materials **8** were primarily conceived as emissive layers, they may also function as charge transporting materials in conjunction with an electron-transporting layer. Device efficiencies in such bilayer structures containing PBD as electron transporter were shown to depend sensitively on the hole mobility within the dendrimer and reached values of up to 10 cd/A at low brightnesses of a few cd/m<sup>2</sup> [58]. Quantum efficiencies of 0.4 % were attainable at brightnesses approaching 100 cd/m<sup>2</sup>. Similar results were also observed for bilayer structures comprising Alq<sub>3</sub> as an electron-transporting layer, although in this case emission from the Alq<sub>3</sub> predominated [58].

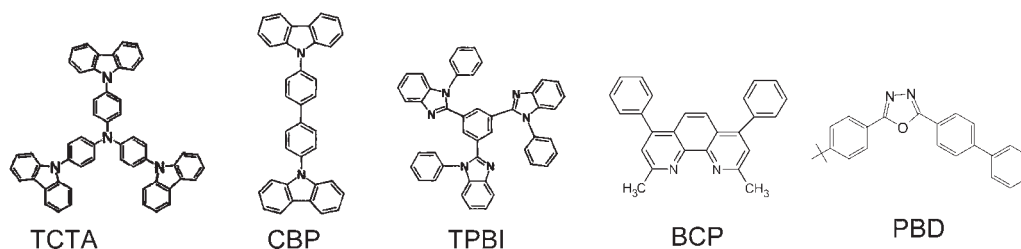
## 8.5 Dendrimer Devices

The first dendrimer LEDs reported by Wang et al. [18] based on **1** and **2** were rather rudimentary in their device characteristics. The quantum efficiencies could not be determined but were supposedly rather low, operating voltages were high and consequently the device operational stability was limited. The EL and PL exhibited a pronounced red-shift with respect to the solution spectra, indicating that the site-isolation effect did not grip satisfactorily in the solid state although the anticipated excitonic funnelling to the core of the structure occurred in the condensed phase. Efficiencies in subsequent reports by Halim et al. on material **12** remained relatively low (< 0.1 %) and driving voltages high [8], although the site isolation effect was conclusively demonstrated in structures **12–14** [11]. Most importantly, it was shown for the first time that materials with otherwise poor solution-processing properties such as distyrylbenzene, which constitutes a phenylene-vinylene trimer, could be deposited in high-quality films with only

minimal aggregation effects. Due to the continued interest in blue-emitting organic semiconductors, this demonstration of employing rather short conjugated elements to achieve blue emission is significant. Site isolation and color purity in the solid state has since been demonstrated in most of the materials shown in Fig. 8.4. A first substantial increase in efficiency was reported for dendrimers **8**, where up to 10 cd/A could be reached at low current densities in bilayer configurations [58]. Besides the considerable color purity achieved, materials **8** also allowed a detailed study of the influence of dendronization on the photophysics and charge-transporting properties of  $\pi$ -conjugated molecules as described above.

Functionalization of the surface groups to aid charge transport was explored in materials **11** [10] containing electron-transporting triazine units and in dendrimers **2** [18], **6** and **10** [41, 70, 98, 104] that incorporated hole transporting triphenylamines and naphthyl diphenylamine terminations, respectively. Although blue EL could be observed from material **11** with a very low efficiency of 0.003 %, devices were found to be rather unstable. Improved quantum efficiencies of up to 0.76 % and power efficiencies approaching 1 lm/W could be achieved in devices containing **10** and BCP/Alq<sub>3</sub> hole-blocking/electron-injecting layers [70]. Blends of **6** and **10** were also explored, although this was found to lower the efficiency somewhat to 0.2 % [70] due to charge-trapping effects. Respectable efficiencies of up to 0.5 % could also be achieved for low generations of the carbazole functionalized naphthalimide dendrimers [91]. Interestingly, the third-generation structure **21** had a much lower efficiency and stability and much greater turn-on voltage than the first-generation material. Novel truxene-based dendrimers **22** were also recently explored [114]. These materials exhibited a strong PL broadening upon going from solution – where emission occurs in the UV at 360 nm – to the solid state. In contrast, the EL was found to be blue-green with up to 0.15 % efficiency and peaked around 530 nm. This is very reminiscent of ketonic defects in polyfluorenes [124, 125], which are particularly prominent in EL [126], suggesting that emission in these materials occurs solely from defects. Interestingly, in contrast to the influence of site isolation on charge transport reported for the group of materials **8**, the conductivity was found to increase dramatically upon dendronization, suggesting that in this case the dendrons participate actively in transport [114].

One of the motivations for using dendrimers is the facility of creating blends of different materials by ensuring compatibility of surface groups [127]. This was initially explored using the first phosphorescent dendrimers based on platinum-porphyrins **13** blended into **8** and **9** [74]. High-quality mixed films could be obtained, which exhibited intriguing properties due to simultaneous emission from the singlet and triplet state in the blue and the red region of the visible spectrum. Charge trapping on the guest phosphorescent emitter was found to be a dominant process, but triplet-triplet or triplet-charge interactions also strongly influenced the device properties, resulting in a strong spectral dependence of the driving conditions such as current and duty cycle. Blends of **6** and **10** were also explored for balancing charge transport. Substantial charge-trapping effects were again observed in the blend, which was concluded to reduce the effectiveness



**Fig. 8.10** Structures of electron- and hole-transporting materials commonly used in combination with dendrimers. TCTA: 4,4',4''-tris(N-carbazolyl)triphenylamine; CBP: 4,4'-bis-(N-carbazolyl)biphenyl; TPBI: 1,3,5-tris(2-N-phenylbenzimidazolyl)benzene; BCP: Bathocuproine; PBD: 2-(4-biphenyl)-5-(4-tert-butylphenyl)-1,3,4-oxadiazole.

of elaborate charge-transporting surface groups [70]. More recently, dendrimer blending has been explored in fluorene-containing biphenyl dendrimers **18** and **19** to achieve effective color tuning from the blue-green to the near UV, maintaining respectable quantum and power efficiencies of 1 % and 1.5 lm/W, respectively [111]. Dendrimers can also readily be blended with charge-transporting materials, which are usually evaporated in conventional devices. This allows a direct deposition of multicomponent single layers from solution. Figure 8.10 lists some of the commonly used charge-transport materials, which are either used as matrices or as dopants. TCTA [128] and CBP are bipolar organic conductors, which are used as host matrices for the dendrimers. The dendritic structure of TCTA makes it particularly appealing for blending with dendrimers. PBD, BCP and TPBI [129] are electron-transporting/hole-blocking materials, where the star-like architecture of TPBI is again rather favorable. Interestingly, although a hole-injection layer of poly(3,4-ethylenedioxythiophene):poly(styrenesulfonate) on top of the ITO anode is often used in polymeric solution-processed devices and was employed in initial investigations on electrofluorescent dendrimers, it appears not to be necessary or beneficial in electrophosphorescent dendrimers.

Substantial improvements in the device efficiency by almost two orders of magnitude could be achieved by blending the second-generation dendrimer **8** with PBD [130]. Whereas a simple bilayer structure containing a dendrimer layer and a PBD:poly(methylmethacrylate) layer only resulted in a small increase in overall efficiency, the optimal structures were found to consist of a graded interlayer. This was fabricated by spin coating a doped dendrimer layer on top of a neat dendrimer layer from the same solvent, which resulted in partial but not complete dissolution [130]. Brightnesses of up to 900 cd/m<sup>2</sup> could be achieved. A similar approach was also pursued for the first-generation distyrylbenzene-cored biphenyl dendrimer **7**, which exhibited a comparable efficiency and peak brightnesses of up to 4500 cd/m<sup>2</sup>, again emitting in the blue-green part of the spectrum [99]. The solid-state PL quantum efficiency remained comparatively low at 9 %, which implicitly limits the maximal achievable EL quantum efficiency of these materials to below 1 % taking into account the triplet-generation fraction and nonoptimized photonic outcoupling efficiency.

Although impressive achievements have been made with fluorescent organic dendrimers, the true power of dendrimer LED technology is manifested in metal-containing phosphorescent complexes. Triplet formation upon electrical injection is the most serious loss channel in organic LEDs. This can be overcome efficiently by incorporating phosphorescent triplet emitters into the organic layer [131], which has allowed the fabrication of devices with up to 20 % external quantum efficiency and exceeding 70 lm/W power efficiency [132]. Phosphorescent emitter technology has been most successful in evaporated small molecule LEDs, as polymeric hosts typically have low-lying triplet levels that interact unfavorably with the phosphorescent guest, quenching the triplet emission. Promising results with power efficiencies of up to 24 lm/W from solution-processed materials have, however, also recently been achieved with nonconjugated polymer matrices such as poly(vinyl-carbazole) doped with PBD and an iridium-based phosphorescent complex [133].

The first electrophosphorescent dendrimer reported was a platinum-porphyrin **13** [74]. In these materials, the metallic atom enables strong spin-orbit coupling, which leads to spin-mixing of the singlet and triplet states and radiative emission from the otherwise dark triplet level. The efficiency of this material blended into a dendritic host was low, but the devices exhibited a number of intriguing transient properties due to the long-lived triplet state, such as a duty-cycle dependent emission color [74]. However, the triplet lifetime of platinum-porphyrins, which controls the degree of emissive-site saturation, is almost two orders of magnitude greater than that of iridium-based complexes, which is why the research focus soon shifted to these materials [134]. An alternative approach to phosphorescent dendritic materials are polyamidoamine dendrimers decorated with ruthenium bipyridine groups **20** [113]. These orange-red emitting materials exhibited a decrease in EL quantum efficiency from 0.22 % for the zeroth-generation chromophore to 0.05 % for **20** containing 32 chromophores, which also correlated with a decrease in solution PL efficiency. Interestingly, these transition-metal complexes are thought to lead to a considerable ionic mobility in the solid state, which also substantially affects the device stability and leads to an initial increase in efficiency with time [113].

The most successful dendrimer structures are based on transition-metal complexes [135] comprising an iridium coordination atom and phenylpyridine ligands [76]. Figure 8.11 shows luminance–efficiency curves for three device structures based on the first-generation dendrimer **4**. Whereas a single-layer device of **4** reaches a maximal quantum efficiency of 0.2 % [97], the efficiency can be increased by almost two orders of magnitude by blending the material in a suitable transport matrix and employing an additional electron-transport layer [76, 94]. The first structure characterized in Fig. 8.11 contains a spin-coated blend of **4** and CBP, covered by a BCP electron-transport layer and a LiF/Al cathode. The efficiency of the green-emitting device of over 20 cd/A is already impressive. It can be enhanced by switching to the more dendritic TCTA matrix, which yields a substantial improvement to over 55 cd/A and 40 lm/W at the for dendrimers comparatively low driving bias of 4.5 V required for a brightness of 400 cd/m<sup>2</sup>.



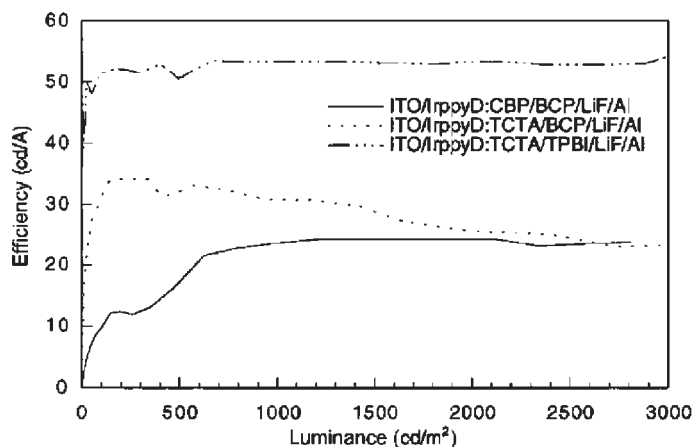


Fig. 8.11 Efficiency versus luminance of devices containing dendrimer 4 ( $\text{Ir}(\text{ppy})_3$ ). The electron-transporting BCP, respectively, TPBI layers were evaporated onto the spin-coated dendrimer:CBP/TCTA blend. Reproduced from [76] with permission of Wiley-VCH Verlag GmbH.

Besides the impressive efficiencies achieved in phosphorescent dendrimer LEDs, a further aspect is particularly noteworthy. Whereas the power efficiency naturally decreases with increasing driving current as the driving voltage rises simultaneously, both the quantum efficiency and the luminance efficiency are virtually independent of the driving current. This is surprising, as the efficiency in all previous phosphorescent organic devices was found to decrease strongly with increasing excitation density [136]. The conventionally observed decrease in efficiency with driving current is attributed to strong triplet-triplet annihilation due to the long lifetime of the triplet excitons [136]. Figure 8.11 clearly shows that a change of the triplet density by over an order of magnitude has no influence on the luminance efficiency. This suggests that interactions between the long-lived triplets may not be a performance-limiting problem. Alternatively, the metal-ligand charge-transfer state may be susceptible to electric-field induced dissociation [137]. This effect depends on the energy-level offsets to the surrounding medium, i. e. the matrix. Surrounding the triplet emitter in a large bandgap dendritic shell may substantially reduce this dissociation effect, but potentially also limit triplet-triplet and triplet-charge interactions, thus providing an explanation for the impressive device performance.

Although the highest efficiencies have been demonstrated for devices containing a spin-coated blend of transport and emitter materials covered by an evaporated transport layer, very high efficiencies of up to 10.4 % (35 cd/A) have also been reported from purely solution-processed devices containing only one single-blended layer [94]. Both the hole-transporter CBP and the electron-transporter TPBI can be mixed with 4 to form high-quality films. In comparison to the partially evaporated devices, this results in an increase in operating bias, so that the maximum power efficiency of 12.8 lm/W at a brightness of 550  $\text{cd/m}^2$  is not

reached until a bias of 8.1 V. Nevertheless, it may be possible to improve this further in the future by employing additional injection layers. In either case the peak brightnesses reported approach  $10^4$  cd/m<sup>2</sup>, which should be sufficient for most applications.

The effect of meta and para substitution of the biphenyl dendrons has also been explored in Ir(ppy)<sub>3</sub> dendrimers [93, 97]. For a given generation, para (3) rather than meta (4) linking of the dendrons increases the resistance of the organic layer. An even more substantial decrease in mobility is observed upon increasing dendrimer generation [97], comparable to the initial demonstration of mobility control in the fluorescent dendrimers 8 [58]. The greater resistivity in this case also leads to an increase of the single-layer device efficiency when compared to the meta-linked dendrons, which indicates more balanced charge transport, in analogy to the case discussed for 8 earlier on. The device efficiency can be substantially enhanced by blending with CBP, in which case the meta-linked dendrimer exhibits superior properties [93]. In the blend devices, the second-generation dendrimer was found to exhibit the lowest resistivity, in contrast to the neat devices. This was proposed to arise from preferential film formation properties of the higher-generation dendrimer due to the globular structure and decreased intermolecular attractive forces. However, atomic force microscopy images of blend systems containing the different dendrimers 3–5 displayed no systematic difference but excellent amorphous surfaces with a root mean square roughness of  $\sim 2.5$  nm [93].

The beauty of the transition-metal complexes is that small substitutions in the ligands can substantially alter the emission color. Choosing two phenylpyridyl ligands and one benzothienylpyridyl ligand in 15 leads to orange-red rather than green emission with an efficiency of 5.7 % (4.5 lm/W) [107]. Substitution with three benzothienylpyridyl ligands in 16 results in a deep red emission with a slightly lower efficiency of 4.25 % (1 lm/W) due to the lower PL quantum yield. In both cases devices were fabricated by blending the active material with CBP and subsequently covering the film with a TPBI layer. Substitution of the dendrons by electronically active fluorene units attached to the Ir(ppy)<sub>3</sub> core in structure 17 has also been reported [109]. Such devices also exhibited very high luminance efficiencies of up to 50 cd/A and 30 lm/W in optimized device structures comprising a blend of CBP and TPBI containing the active dendrimer and covered with an electron-transporting TPBI layer. As in the case of the truxene dendrimers 22 it appears that the fluorene units actively participate in charge transport [114]. As both polyfluorenes [138] and dendritic bifluorenes [110] exhibit excellent nondispersive charge-transporting properties, they appear to be very promising materials for inclusion in the dendrimer structure.

## 8.6

### Dendronized Polymers

In parallel with the development of dendrimers as novel EL materials, there has been considerable interest in controlling the bulk photophysical and transport properties of conjugated polymers by using spacer structures. Intermolecular interactions play an important role in the photophysics of conjugated polymers, so that controlling the microscopic packing by careful sidegroup substitution appears a reasonable way to alleviate potential problems. In addition, the on-chain mobility of charge carriers is typically orders of magnitude greater than the interchain mobility, so that an ideal polymeric semiconductor should facilitate charge transport between chain ends rather than between chromophore units located within the polymer. Although some interesting chemical structures have been reported in the context of dendronized polymers, it is important to realize that the interpretation of physical data becomes somewhat more complex than when dealing with well-defined monodisperse dendritic macromolecules. A particular issue that has attracted widespread attention was the suppression of long-wavelength emission in otherwise blue-emitting polyfluorenes. The long-wavelength band was initially attributed to aggregate or excimer emission, although it could later be conclusively demonstrated that it is primarily due to a localized chemical defect on the polymer backbone [124, 125]. Initial studies of dendronized polyfluorenes indeed suggested that the long-wavelength emission could be suppressed by dendronization with polyphenylene sidechains [139], with no or little detrimental influence on charge transport [140]. Alternative approaches to dendronization of polyfluorenes included decoration with poly(benzyl-ether) dendritic wedges [141]. Detailed studies of both long-lived (polarons and triplets) and short-lived (singlets) photoexcitations were carried out. Whereas the dynamics particularly of the triplets was found to be consistent with increased intermolecular spacing [142], the influence of dendronization on the photophysics of the singlet is much more subtle [143]. Contrary to expectation, no change in the delayed fluorescence from dendronized polyfluorenes was observed when compared to nondendronized analogous compounds [143]. A substantial spectral broadening was, however, detected for the prompt fluorescence upon dendronization, which was interpreted as a signature of considerable steric frustration of the molecule. In contrast to monodisperse macromolecular dendrimers, where the influence of dendronization is very clear cut [60], the correlation between structural modification through dendronization and photophysical properties in polymeric systems is somewhat more complicated. An impressive demonstration of the benefit of dendritic encapsulation was a drastic reduction in concentration quenching of rod-like poly(phenyleneethynylene) covered with poly(benzyl-ether) [144]. This investigation proved that the site-isolation effect can also occur in polymers. Time-resolved PL measurements on dendronized PPVs also suggested a reduction in aggregation [145]. However, in contrast to monodisperse dendrimers, dendronized polymers have yet to achieve a substantial gain in comparison to nondendronized analogs in terms of operational stability and efficiency.

A considerable motivation for dendronizing conjugated polymers is to enhance the light-collection efficiency in photovoltaic applications. As the polymer backbone can potentially exhibit rather efficient intramolecular excitation-energy transfer [146], surrounding the backbone with light-harvesting dendrons is expected to be beneficial. This concept has been explored in the context of hyper-branched polymers [17, 147]. Although the efficiencies reported are still subject to improvement, the concept may become of interest when designing more sophisticated multifunctional materials combining, for example, both hole- and electron-transporting properties. As efficient photovoltaic applications require both rapid exciton dissociation as well as balanced transport of electrons and holes away from the reaction center to avoid recombination, considerable work will have to be invested to prevent dendronization from inhibiting transport of either carrier.

Finally, an interesting approach to spatially insulating conjugated segments of polymers akin to the overall theme of dendronization is to exploit supramolecular architectures by threading cyclodextrane units onto polymer chains to form polyrotaxanes [148]. Whereas virtually all of the dendronization processes discussed thus far are purely covalent in nature, such a supramolecular assembly actually closely mimics nature by relying on noncovalent interactions such as hydrogen bonds. Natural light-harvesting complexes, after all, are highly complex systems that are predominantly assembled through comparatively weak intramolecular forces. Covering a hydrophobic conjugated polymer with hydrophilic cyclodextranes allows the fabrication of well-defined molecular wires with increased physical dimensions [148]. Although the spectral shifts observed when compared to neat polymeric materials most likely arise due to steric effects, as in the case of covalently bonded spacers [139], encapsulation of the polymer chain does improve the physical properties. Surprisingly, encapsulation by electrically insulating spacers was not found to be overly detrimental to charge transport, and EL could be observed from single-layer devices containing the polyrotaxane [148]. Dilution allows the identification of isolated molecular wires using atomic force microscopy, which opens up a pathway to direct mechanical manipulation of the polymer chain. As the method can be applied to various organic syntheses, it may constitute a route to designing more complex three-dimensional organic supramolecular structures.

## 8.7

### Conclusions

Dendrimers as active materials for LEDs have been researched now for almost eight years and enormous progress has been made in this time both in terms of synthetic procedures as well as and in particular with respect to device performance. Research into dendrimer-containing LEDs combines fundamental aspects of organic semiconductor physics, novel and highly sophisticated organic synthetic chemistry and elaborate device technology. Dendrimers provide a model ex-

ample of the methodology of scientific research. Starting out from mere curiosity, they have developed into a key technology and now constitute one of the most efficient electrical light sources known. This is surely an impressive feat, considering the sheer volume of input generated into organic and metallorganic chemistry by the systematic research into dendrimers. Dendrimer LED technology is now actively being researched in an industrial environment and forms an integral part of the materials strategy of Cambridge Display Technology [149]. There remains, however, plenty to do. Thus far, reports on the operational stability of dendrimer LEDs have been few, and – although there is no reason to doubt that this will be successful – it has yet to be demonstrated that the technology can compete with existing material classes in terms of operational lifetime requirements. Also, blue phosphorescent emitters are still actively sought [150], and only a few concepts are available of how to achieve this, the main problem being the requirement of the host matrix to have a very high-lying triplet level to prevent triplet quenching. It remains to be seen whether the route to blue dendritic phosphorescent emitters will follow the iridium chemistry currently pursued or whether alternative metallic complexes can be developed. A substantial role of dendrimers in developing wide gap hosts is also to be anticipated.

As Matthews, Shipway and Stoddart put it in their review “Dendrimers – Branching out from curiosities into new technologies” a mere 6 years ago: “There must somewhere be a dendrimer ‘El Dorado’ waiting to be discovered” [151]. Although it indeed looks like the key to this magic chest has now been turned, the rapid development of dendrimer technology holds promise for even more sophisticated applications in the future. The intrinsically modular conception of dendrimers, together with the increasingly exploited power of molecular self-assembly, allow the prediction that dendrimer technology will further the construction of ever more sophisticated electronically active supramolecular units for future generations of molecular electronics.

## References

- 1 C. W. Tang, S. A. Vanslyke, *Appl. Phys. Lett.* **1987**, 51, 913–915.
- 2 J. H. Burroughes, D. D. C. Bradley, A. R. Brown, R. N. Marks, K. Mackay, R. H. Friend, P. L. Burn, A. B. Holmes, *Nature* **1990**, 347, 539–541.
- 3 W. E. Howard, *Sci. Am.* **2004**, 290, 76–81.
- 4 P. L. Burn, I. D. W. Samuel, *Mater. Today* **1998**, 1, 3.
- 5 J. M. J. Fréchet, *Science* **1994**, 263, 1710.
- 6 S. K. Deb, T. M. Maddux, L. P. Yu, *J. Am. Chem. Soc.* **1997**, 119, 9079.
- 7 P. J. Dandliker, F. Diederich, M. Gross, C. B. Knobler, A. Louati, E. M. Sanford, *Angew. Chem.-Int. Ed.* **1994**, 33, 1739.
- 8 M. Halim, J. N. G. Pillow, I. D. W. Samuel, P. L. Burn, *Adv. Mater.* **1999**, 11, 371.
- 9 J. N. G. Pillow, M. Halim, J. M. Lupton, P. L. Burn, I. D. W. Samuel, *Macromolecules* **1999**, 32, 5985.
- 10 J. M. Lupton, L. R. Hemingway, I. D. W. Samuel, P. L. Burn, *J. Mater. Chem.* **2000**, 10, 867.
- 11 M. Halim, I. D. W. Samuel, J. N. G. Pillow, P. L. Burn, *Synth. Met.* **1999**, 102, 1113.
- 12 J. Issberner, R. Moors, F. Vögtle, *Angew. Chem.-Int. Ed.* **1995**, 33, 2413.
- 13 L. L. Miller, R. G. Duan, D. C. Tully, D. A. Tomalia, *J. Am. Chem. Soc.* **1997**, 119, 1005.

- 14 J. S. Moore, *Acc. Chem. Res.* **1997**, 30, 402.
- 15 V. V. Narayanan, G. R. Newkome, *Top. Curr. Chem.* **1998**, 197, 19.
- 16 A. D. Schluter, *Top. Cur. Chem.* **1998**, 197, 165.
- 17 X. T. Tao, Y. D. Zhang, T. Wada, H. Sasabe, H. Suzuki, T. Watanabe, S. Miyata, I. P. Riken, *Adv. Mater.* **1998**, 10, 226.
- 18 P. W. Wang, Y. J. Liu, C. Devadoss, P. Bharathi, J. S. Moore, *Adv. Mater.* **1996**, 8, 237.
- 19 A. W. Bosman, H. M. Janssen, E. W. Meijer, *Chem. Rev.* **1999**, 99, 1665.
- 20 J. F. G. A. Jansen, E. M. M. DeBrabanderVandenberg, E. W. Meijer, *Science* **1994**, 266, 1226.
- 21 J. M. J. Frechet, *J. Polym. Sci. A* **2003**, 41, 3713–3725.
- 22 J. M. J. Frechet, *Macromol. Symp.* **2003**, 201, 11–22.
- 23 W. Carl, *J. Chem. Soc.-Farad. Trans.* **1996**, 92, 4151.
- 24 E. Y. Poliakov, V. Chernyak, S. Tretiak, S. Mukamel, *J. Chem. Phys.* **1999**, 110, 8161.
- 25 S. Tretiak, V. Chernyak, S. Mukamel, *J. Phys. Chem. B* **1998**, 102, 3310.
- 26 Z. Y. Chen, S. M. Cui, *Macromolecules* **1996**, 29, 7943.
- 27 B. Derrida, H. Spohn, *J. Stat. Phys.* **1988**, 51, 817–840.
- 28 P. G. Degennes, H. Hervet, *J. Phys. Lett.* **1983**, 44, L351–L360.
- 29 T. C. Zook, G. T. Pickett, *Phys. Rev. Lett.* **2003**, 90.
- 30 M. Gauthier, L. Tichagwa, J. S. Downey, S. Gao, *Macromolecules* **1996**, 29, 519–527.
- 31 A. Bar-Haim, J. Klafter, *J. Phys. Chem. B* **1998**, 102, 1662–1664.
- 32 W. Kuhlbrandt, *Nature* **1995**, 374, 497–498.
- 33 R. Kopelman, M. Shortreed, Z. Y. Shi, W. H. Tan, Z. F. Xu, J. S. Moore, A. Bar-Haim, J. Klafter, *Phys. Rev. Lett.* **1997**, 78, 1239.
- 34 A. BarHaim, J. Klafter, R. Kopelman, *J. Am. Chem. Soc.* **1997**, 119, 6197.
- 35 L. F. Lee, A. Adronov, R. D. Schaller, J. M. J. Frechet, R. J. Saykally, *J. Am. Chem. Soc.* **2003**, 125, 536–540.
- 36 T. H. Ghaddar, J. F. Wishart, D. W. Thompson, J. K. Whitesell, M. A. Fox, *J. Am. Chem. Soc.* **2002**, 124, 8285–8289.
- 37 J. Hofkens, W. Schroevers, D. Loos, M. Cotlet, F. Kohn, T. Vosch, M. Maus, A. Herrmann, K. Mullen, T. Gensch, F. C. De Schryver, *Spectrochim. Acta A* **2001**, 57, 2093–2107.
- 38 J. Hofkens, M. Maus, T. Gensch, T. Vosch, M. Cotlet, F. Kohn, A. Herrmann, K. Müllen, F. De Schryver, *J. Am. Chem. Soc.* **2000**, 122, 9278–9288.
- 39 A. Adronov, J. M. J. Frechet, *Chem. Commun.* **2000**, 1701–1710.
- 40 G. M. Stewart, M. A. Fox, *J. Am. Chem. Soc.* **1996**, 118, 4354–4360.
- 41 S. Hecht, J. M. J. Frechet, *Angew. Chem. Int. Ed.* **2001**, 40, 74–91.
- 42 J. L. Bentz, F. N. Hosseini, J. J. Kozak, *Chem. Phys. Lett.* **2003**, 370, 319–326.
- 43 R. D. Jenkins, D. L. Andrews, *J. Chem. Phys.* **2003**, 118, 3470–3479.
- 44 X. L. Zhou, D. S. Tyson, F. N. Castellano, *Angew. Chem. Int. Ed.* **2000**, 39, 4301.
- 45 A. Bar-Haim, J. Klafter, *J. Lumin.* **1998**, 76–7, 197–200.
- 46 C. Devadoss, P. Bharathi, J. S. Moore, *J. Am. Chem. Soc.* **1996**, 118, 9635–9644.
- 47 V. Balzani, P. Ceroni, M. Maestri, V. Vicinelli, *Curr. Op. Chem. Biol.* **2003**, 7, 657–665.
- 48 T. Minami, S. Tretiak, V. Chernyak, S. Mukamel, *J. Lumin.* **2000**, 87, 115.
- 49 S. Tretiak, W. M. Zhang, V. Chernyak, S. Mukamel, *Proc. Natl. Acad. Sci. USA* **1999**, 96, 13003.
- 50 G. C. Bazan, W. J. Oldham, R. J. Lachicotte, S. Tretiak, V. Chernyak, S. Mukamel, *J. Am. Chem. Soc.* **1998**, 120, 9188.
- 51 O. Varnavski, G. Menkir, T. Goodson, J. M. Lupton, I. D. W. Samuel, P. L. Burn, *Appl. Phys. Lett.* **2000**, 77, 1120–1122.
- 52 O. Varnavski, I. D. W. Samuel, L. O. Palsson, R. Beavington, P. L. Burn, T. Goodson, *J. Chem. Phys.* **2002**, 116, 8893–8903.
- 53 D. J. Liu, S. De Feyter, M. Cotlet, A. Stefan, U. M. Wiesler, A. Herrmann, D. Grebel-Koehler, J. Q. Qu, K. Mullen, F. C. De Schryver, *Macromolecules* **2003**, 36, 5918–5925.
- 54 M. I. Ranasinghe, M. W. Hager, C. B. Gorman, T. Goodson, *J. Phys. Chem. B* **2004**, 108, 8543–8549.
- 55 S. C. J. Meskers, M. Bender, J. Hubner, Y. V. Romanovskii, M. Oestreich, A. Schenning, E. W. Meijer, H. Bassler, *J. Phys. Chem. A* **2001**, 105, 10220–10229.

- 56 T. Vosch, M. Cotlet, J. Hofkens, K. Van der Biest, M. Lor, K. Weston, P. Tinnefeld, M. Sauer, L. Latterini, K. Mullen, F. C. De Schryver, *J. Phys. Chem. A* **2003**, *107*, 6920–6931.
- 57 R. Jakubiak, Z. Bao, L. Rothberg, *Synth. Met.* **2000**, *114*, 61.
- 58 J. M. Lupton, I. D. W. Samuel, R. Beavington, M. J. Frampton, P. L. Burn, H. Bassler, *Phys. Rev. B* **2001**, *63*, 155206.
- 59 J. M. Lupton, I. D. W. Samuel, R. Beavington, P. L. Burn, H. Bassler, *Adv. Mater.* **2001**, *13*, 258.
- 60 J. M. Lupton, I. D. W. Samuel, P. L. Burn, *Phys. Rev. B* **2002**, *66*, 155206.
- 61 B. J. Schwartz, *Annu. Rev. Phys. Chem.* **2003**, *54*, 141.
- 62 C. Giebeler, H. Antoniadis, D. D. C. Bradley, Y. Shirota, *Appl. Phys. Lett.* **1998**, *72*, 2448.
- 63 K. Itano, T. Tsuzuki, H. Ogawa, S. Appleyard, M. R. Willis, Y. Shirota, *IEEE Trans. Electron. Devices* **1997**, *44*, 1218.
- 64 Y. Kuwabara, H. Ogawa, H. Inada, N. Noma, Y. Shirota, *Adv. Mater.* **1994**, *6*, 677.
- 65 Y. Shirota, Y. Kuwabara, H. Inada, T. Wakimoto, H. Nakada, Y. Yonemoto, S. Kawami, K. Imai, *Appl. Phys. Lett.* **1994**, *65*, 807.
- 66 Y. Shirota, Y. Kuwabara, D. Okuda, R. Okuda, H. Ogawa, H. Inada, T. Wakimoto, H. Nakada, Y. Yonemoto, S. Kawami, K. Imai, *J. Lumin.* **1997**, *72*, 985.
- 67 M. Thelakkat, R. Fink, F. Haubner, H. W. Schmidt, *Macromol. Symp.* **1998**, *125*, 157.
- 68 J. Bettenhausen, P. Stroehriegel, *Adv. Mater.* **1996**, *8*, 507.
- 69 S. C. Chang, J. Bharathan, Y. Yang, R. Helgeson, F. Wudl, M. B. Ramey, J. R. Reynolds, *Appl. Phys. Lett.* **1998**, *73*, 2561; T. Shimoda, S. Kanbe, H. Kobayashi, S. Seki, H. Kiguchi, I. Yudasaka, M. Kimura, S. Miyashita, R. H. Friend, J. H. Burroughes, C. R. Towns, *SID Proc.* **1999**, 26.3.
- 70 P. Furuta, J. Brooks, M. E. Thompson, J. M. J. Frechet, *J. Am. Chem. Soc.* **2003**, *125*, 13165–13172.
- 71 D. A. Tomalia, *Adv. Mater.* **1994**, *6*, 529.
- 72 D. A. Tomalia, A. M. Naylor, W. A. Goddard, *Angew. Chem. Int. Ed.* **1990**, *29*, 138–175.
- 73 E. W. Meijer, M. H. P. van Genderen, *Nature* **2003**, *426*, 128–129.
- 74 J. M. Lupton, I. D. W. Samuel, M. J. Frampton, R. Beavington, P. L. Burn, *Adv. Funct. Mater.* **2001**, *11*, 287–294.
- 75 P. K. H. Ho, J. S. Kim, J. H. Burroughes, H. Becker, S. F. Y. Li, T. M. Brown, F. Cacialli, R. H. Friend, *Nature* **2000**, 404, 481.
- 76 S. C. Lo, N. A. H. Male, J. P. J. Markham, S. W. Magennis, P. L. Burn, O. V. Salata, I. D. W. Samuel, *Adv. Mater.* **2002**, *14*, 975.
- 77 D. Gust, *Nature* **1997**, 386, 21.
- 78 D. L. Jiang, T. Aida, *Nature* **1997**, 388, 454.
- 79 S. Raychaudhuri, Y. Shapir, V. Chernyak, S. Mukamel, *Phys. Rev. Lett.* **2000**, *85*, 282–285.
- 80 D. Boris, M. Rubinstein, *Macromolecules* **1996**, *29*, 7251.
- 81 S. Mukamel, *Nature* **1997**, 388, 425.
- 82 A. Kimoto, J. S. Cho, M. Higuchi, K. Yamamoto, *Macromol. Symp.* **2004**, *209*, 51–65.
- 83 S. Yokoyama, A. Otomo, S. Mashiko, *Appl. Phys. Lett.* **2002**, *80*, 7–9; S. Yokoyama, A. Otomo, T. Nakahama, Y. Okuno, S. Mashiko, in *Dendrimers V: Functional and Hyperbranched Building Blocks, Photophysical Properties, Applications in Materials and Life Sciences*, **2003**, 288, 205–226.
- 84 J. R. Lawrence, G. A. Turnbull, I. D. W. Samuel, G. J. Richards, P. L. Burn, *Opt. Lett.* **2004**, *29*, 869–871.
- 85 E. B. Namdas, A. Ruseckas, I. D. W. Samuel, S. C. Lo, P. L. Burn, *J. Phys. Chem. B* **2004**, *108*, 1570–1577.
- 86 A. J. Berresheim, M. Muller, K. Mullen, *Chem. Rev.* **1999**, *99*, 1747–1785.
- 87 S. Rosenfeldt, N. Dingenouts, D. Potschke, M. Ballauff, A. J. Berresheim, K. Mullen, P. Lindner, *Angew. Chem. Int. Ed.* **2004**, *43*, 109–112.
- 88 J. C. M. Vanhest, D. A. P. Delnoye, M. Baars, M. H. P. Vangenderen, E. W. Meijer, *Science* **1995**, *268*, 1592–1595.
- 89 F. S. Precup-Blaga, J. C. Garcia-Martinez, A. Schenning, E. W. Meijer, *J. Am. Chem. Soc.* **2003**, *125*, 12953–12960; A. Schenning, P. Jonkheijm, J. Hofkens, S. De Feyter, T. Asavei, M. Cotlet, F. C. De Schryver, E. W. Meijer, *Chem. Commun.* **2002**, 1264–1265.
- 90 V. Balzani, P. Ceroni, M. Maestri, C. Saudan, V. Vicinelli, in *Dendrimers V: Functional and Hyperbranched Building Blocks, Photophysical Properties, Applica-*



- tions in *Materials and Life Sciences*, **2003**, 288, 159–191.
- 91 P. Du, W. H. Zhu, Y. Q. Xie, F. Zhao, C. F. Ku, Y. Cao, C. P. Chang, H. Tian, *Macromolecules* **2004**, 37, 4387–4398.
  - 92 J. P. J. Markham, S. C. Lo, S. W. Magennis, P. L. Burn, I. D. W. Samuel, *Appl. Phys. Lett.* **2002**, 80, 2645–2647.
  - 93 T. D. Anthopoulos, J. P. J. Markham, E. B. Namdas, J. R. Lawrence, I. D. W. Samuel, S. C. Lo, P. L. Burn, *Org. Electron.* **2003**, 4, 71–76.
  - 94 T. D. Anthopoulos, J. P. J. Markham, E. B. Namdas, I. D. W. Samuel, S. C. Lo, P. L. Burn, *Appl. Phys. Lett.* **2003**, 82, 4824–4826.
  - 95 S. C. Lo, E. B. Namdas, P. L. Burn, I. D. W. Samuel, *Macromolecules* **2003**, 36, 9721–9730.
  - 96 J. M. Lupton, I. D. W. Samuel, V. Christou, S. C. Lo, J. N. G. Pillow, P. L. Burn, *Metal-containing dendrimers*, US Patent application US2004137263.
  - 97 J. P. J. Markham, I. D. W. Samuel, S. C. Lo, P. L. Burn, M. Weiter, H. Bassler, *J. Appl. Phys.* **2004**, 95, 438–445.
  - 98 A. W. Freeman, S. C. Koene, P. R. L. Malenfant, M. E. Thompson, J. M. J. Frechet, *J. Am. Chem. Soc.* **2000**, 122, 12385–12386.
  - 99 D. G. Ma, J. M. Lupton, I. D. W. Samuel, S. C. Lo, P. L. Burn, *Appl. Phys. Lett.* **2002**, 81, 2285–2287; *ibid.* **2002**, 81, 4476.
  - 100 L. O. Palsson, R. Beavington, M. J. Frampton, J. M. Lupton, S. W. Magennis, J. P. J. Markham, J. N. G. Pillow, P. L. Burn, I. D. W. Samuel, *Macromolecules* **2002**, 35, 7891–7901.
  - 101 I. D. W. Samuel, R. Beavington, P. L. Burn, J. M. Lupton, *Dendrimers*, US Patent application US2003134147.
  - 102 R. Beavington, M. J. Frampton, J. M. Lupton, P. L. Burn, I. D. W. Samuel, *Adv. Funct. Mater.* **2003**, 13, 211–218.
  - 103 J. M. Lupton, I. D. W. Samuel, P. L. Burn, S. Mukamel, *J. Chem. Phys.* **2002**, 116, 455–459.
  - 104 A. Freeman, J. Frechet, S. Koene, M. Thompson, *Macromol. Symp.* **2000**, 154, 163–169.
  - 105 J. N. G. Pillow, I. D. W. Samuel, M. Halim, P. L. Burn, *Light-emitting dendrimers and devices*, US Patent US6558818.
  - 106 I. D. W. Samuel, M. Halim, J. N. G. Pillow, P. L. Burn, *Light-emitting dendrimers*, US Patent US6720093.
  - 107 T. D. Anthopoulos, M. J. Frampton, E. B. Namdas, P. L. Burn, I. D. W. Samuel, *Adv. Mater.* **2004**, 16, 557.
  - 108 I. D. W. Samuel, S. C. Lo, P. L. Burn, *Asymmetric dendrimers*, US Patent application US2004110029.
  - 109 I. D. W. Samuel, S. C. Lo, P. L. Burn, *Fluorene-containing dendrimers*, Patent application WO2004029134.
  - 110 J. P. J. Markham, T. D. Anthopoulos, I. D. W. Samuel, G. J. Richards, P. L. Burn, C. Im, H. Bassler, *Appl. Phys. Lett.* **2002**, 81, 3266–3268.
  - 111 J. P. J. Markham, E. B. Namdas, T. D. Anthopoulos, I. D. W. Samuel, G. J. Richards, P. L. Burn, *Appl. Phys. Lett.* **2004**, 85, 1463.
  - 112 I. D. W. Samuel, S. C. Lo, P. L. Burn, *Aryl-aryl dendrimers*, US Patent application US2004169463.
  - 113 J. A. Barron, S. Bernhard, P. L. Houston, H. D. Abruna, J. L. Ruglovsky, G. G. Malliaras, *J. Phys. Chem. A* **2003**, 107, 8130–8133.
  - 114 X. Y. Cao, X. H. Liu, X. H. Zhou, Y. Zhang, Y. Jiang, Y. Cao, Y. X. Cui, J. Pei, *J. Org. Chem.* **2004**, 69, 6050.
  - 115 P. L. Burn, R. Beavington, M. J. Frampton, J. N. G. Pillow, M. Halim, J. M. Lupton, I. D. W. Samuel, *Mater. Sci. Eng. B* **2001**, 85, 190–194.
  - 116 M. Pope, C. E. Swenberg, *Electronic Processes in Organic Crystals and Polymers*, 2<sup>nd</sup> edition, Oxford University Press, **1999**.
  - 117 J. M. Lupton, I. D. W. Samuel, P. L. Burn, S. Mukamel, *J. Phys. Chem. B* **2002**, 106, 7647–7653.
  - 118 S. Hecht, *J. Polym. Sci. a-Poly. Chem.* **2003**, 41, 1047–1058.
  - 119 K. Sooklal, L. H. Hanus, H. J. Ploehn, C. J. Murphy, *Adv. Mater.* **1998**, 10, 1083.
  - 120 S. F. Swallen, R. Kopelman, J. S. Moore, C. Devadoss, *J. Mol. Struct.* **1999**, 486, 585–597.
  - 121 M. Kawa, in *Dendrimers V: Functional and Hyperbranched Building Blocks, Photophysical Properties, Applications in Materials and Life Sciences*, **2003**, 228, 193–204.
  - 122 J. M. Lupton, I. D. W. Samuel, R. Beavington, P. L. Burn, H. Bässler, *Synth. Met.* **2001**, 116, 375.



- 123 P. W. M. Blom, M. J. M. Dejong, J. J. M. Vleggaar, *Appl. Phys. Lett.* **1996**, 68, 3308.
- 124 J. M. Lupton, M. R. Craig, E. W. Meijer, *Appl. Phys. Lett.* **2002**, 80, 4489.
- 125 U. Scherf, E. J. W. List, *Adv. Mater.* **2002**, 14, 477.
- 126 J. M. Lupton, J. Klein, *Phys. Rev. B* **2002**, 65, 193202.
- 127 I. D. W. Samuel, P. L. Burn, *Blended dendrimers*, Patent application WO2004020504.
- 128 M. Ikai, S. Tokito, Y. Sakamoto, T. Suzuki, Y. Taga, *Appl. Phys. Lett.* **2001**, 79, 156.
- 129 Z. Gao, C. S. Lee, I. Bello, S. T. Lee, R. M. Chen, T. Y. Luh, J. Shi, C. W. Tang, *Appl. Phys. Lett.* **1999**, 74, 865.
- 130 D. G. Ma, J. M. Lupton, R. Beavington, P. L. Burn, I. D. W. Samuel, *Adv. Funct. Mater.* **2002**, 12, 507–511.
- 131 M. A. Baldo, D. F. O'Brien, Y. You, A. Shoustikov, S. Sibley, M. E. Thompson, S. R. Forrest, *Nature* **1998**, 395, 151–154.
- 132 G. He, M. Pfeiffer, K. Leo, M. Hofmann, J. Birnstock, R. Pudzich, J. Salbeck, *Appl. Phys. Lett.* **2004**, 85, 3911.
- 133 X. H. Yang, D. Neher, *Appl. Phys. Lett.* **2004**, 84, 2476.
- 134 M. A. Baldo, S. Lamansky, P. E. Burrows, M. E. Thompson, S. R. Forrest, *Appl. Phys. Lett.* **1999**, 75, 4.
- 135 I. D. W. Samuel, S. C. Lo, P. L. Burn, *Neutral metallic dendrimer complexes*, Patent application WO2004020448.
- 136 M. A. Baldo, S. R. Forrest, *Phys. Rev. B* **2000**, 62, 10958.
- 137 J. Kalinowski, W. Stampor, J. Mezyk, M. Cocchi, D. Virgili, V. Fattori, P. Di-Marco, *Phys. Rev. B* **2002**, 66, 235321.
- 138 M. Redecker, D. D. C. Bradley, M. Inbasekaran, E. P. Woo, *Appl. Phys. Lett.* **1998**, 73, 1565.
- 139 S. Setayesh, A. C. Grimsdale, T. Weil, V. Enkelmann, K. Mullen, F. Meghdadi, E. J. W. List, G. Leising, *J. Am. Chem. Soc.* **2001**, 123, 946–953.
- 140 A. Pogantsch, F. P. Wenzl, E. J. W. List, G. Leising, A. C. Grimsdale, K. Mullen, *Adv. Mater.* **2002**, 14, 1061.
- 141 C. H. Chou, C. F. Shu, *Macromolecules* **2002**, 35, 9673–9677.
- 142 A. Pogantsch, F. P. Wenzl, U. Scherf, A. C. Grimsdale, K. Mullen, E. J. W. List, *J. Chem. Phys.* **2003**, 119, 6904–6910.
- 143 J. M. Lupton, P. Schouwink, P. E. Keivanidis, A. C. Grimsdale, K. Mullen, *Adv. Funct. Mater.* **2003**, 13, 154–158.
- 144 T. Sato, D. L. Jiang, T. Aida, *J. Am. Chem. Soc.* **1999**, 121, 10658–10659.
- 145 R. Jakubiak, Z. Bao, L. J. Rothberg, *Synth. Met.* **2001**, 116, 41–44.
- 146 J. G. Müller, U. Lemmer, G. Raschke, M. Anni, U. Scherf, J. M. Lupton, J. Feldmann, *Phys. Rev. Lett.* **2003**, 91, 267403.
- 147 J. Qiao, C. H. Yang, Q. G. He, F. L. Bai, Y. F. Li, *J. Appl. Polym. Sci.* **2004**, 92, 1459–1466.
- 148 F. Cacialli, J. S. Wilson, J. J. Michels, C. Daniel, C. Silva, R. H. Friend, N. Severin, P. Samori, J. P. Rabe, M. J. O'Connell, P. N. Taylor, H. L. Anderson, *Nat. Mater.* **2002**, 1, 160–164.
- 149 <http://www.cdtltd.co.uk/technology/40.asp>
- 150 R. J. Holmes, B. W. D'Andrade, S. R. Forrest, X. Ren, J. Li, M. E. Thompson, *Appl. Phys. Lett.* **2003**, 83, 3818.
- 151 O. A. Matthews, A. N. Shipway, J. F. Stoddart, *Prog. Polym. Sci.* **1998**, 23, 1–56.

## 9

## Crosslinkable Organic Semiconductors for Use in Organic Light-Emitting Diodes (OLEDs)

Klaus Meerholz, Christoph-David Müller, Oskar Nuyken

## 9.1

### Introduction

The display market is currently one of the fastest growing high-tech areas, driven by novel developments in the areas of digital cameras, cellular phones or similar portable electronic devices. A relatively young technology are *organic light-emitting diodes* (OLED), which may become a strong competitor for traditional liquid-crystal technology (LCD) in the near future. The attractive features of this novel technology are the thin device structure, low weight, the possibility to fabricate on flexible substrates, high brightness even at low energy consumption, large viewing angle, and potentially low production cost, promising innovative products for display and lighting applications.

Today, monochrome OLED displays are integrated in many commercial products, such as shavers (Phillips), car stereo (Pioneer) and cellular phones (Samsung). Recently, Kodak presented a digital camera featuring a 2-inch diagonal RGB OLED display. Larger displays have been fabricated in the labs of the leading display companies. Although they are currently still too expensive this technology will certainly make its way and become a commercial success.

**The fabrication of OLEDs** involves the deposition of one or more layers of organic semiconductors onto the transparent anode, indium tin oxide (ITO) in most cases, often coated with a hole-injection layer. Generally, two classes of devices are distinguished, according to the materials involved and – as a result of this – the fabrication process:

- 1) vacuum sublimation of small molecules;
- 2) wet-chemical deposition of conjugated oligomers and polymers.

Finally, a low work function metal is vacuum deposited as the cathode for electron injection. Upon application of a voltage, both types of charge carriers (electrons and holes) are injected and move towards each other by hopping [1]. Once a hole and an electron meet on an active site they combine to form an exciton, which can relax to

its ground state by emitting a photon. According to basic quantum-mechanical spin statistics the excitons are 25 % singlets and 75 % triplets. This is why recently much effort is being devoted to developing triplet-emitting devices [2].

Overall, the vacuum-deposited small-molecule OLED have advantages in some device-performance aspects, in particular when it comes to device lifetime. However, the sophisticated instruments lead to relatively high production cost, which increase superlinearly with the area to be coated. By contrast, due to the simplicity of the solution processing and the reduced instrumental cost, deposition from solution by spin- or dip-coating, screen and inkjet printing, etc. appears more attractive than vacuum techniques. Two issues are of particular importance:

**Multilayer capability:** Until now, the brightest and most efficient organic light-emitting devices (OLEDs) were realized using multilayer structures, consisting of an emission layer (EML) sandwiched between hole- and electron-transport layers (HTL and ETL, respectively). This general structure serves three main purposes: (1) it facilitates carrier injection into the devices by reducing the respective injection barriers, (2) one type of carrier (e. g. holes) is blocked by the opposite transport layer (in this case the ETL) after passing through the EML, thereby enhancing the recombination efficiency; and (3) quenching reactions of excitons at the electrodes are avoided. The most common method for building such multilayer OLED structures is successive vacuum deposition of the compounds. By contrast, the fabrication of multiple-layer structures from solution is not that simple: it is of crucial importance that previously deposited layers are absolutely resistant against the solvent used to deposit an additional layer.

**Full-color capability:** The main target for OLED technology is the field of full-color displays (red/green/blue, RGB). Thus, means to deposit the materials with high local resolution on the pixels of an active-matrix substrate are required. Using vacuum deposition, this is commonly obtained using shadow masks. Another technique for the controlled deposition of small molecules and certain polymers is laser-induced thermal imaging (LITI) [3, 4]. For the wet-chemical fabrication of RGB devices current research efforts are directed towards adaptation of well-established printing techniques such as screen and ink-jet printing. Due to its simplicity, conventional lithography using photoresists (compare fabrication of integrated circuits) could be a powerful technique to achieve high resolution.

This chapter is focused on solution-processible materials and discusses vacuum-deposited approaches for qualitative comparison only. It is organized as follows: in Section 9.2, we first lay out general considerations about producing multiple-layer devices by solution processing. This is followed by reviewing the various routes towards developing crosslinkable materials. Section 9.3 reviews the patterning methods to create RGB(W)-displays, emphasizing the lithographic application of photochemically crosslinkable materials discussed earlier. Finally, we draw some general conclusions (Section 9.4).

## 9.2

### Multiple-Layer Deposition

For the fabrication of multiple-layer structures from solution it is of crucial importance that previously deposited layers are absolutely resistant against the solvent(s) used to deposit the subsequent layer(s). One distinguishes three approaches: (1) orthogonal solvents, (2) change of polarity, and (3) polymerization/crosslinking. In the following, we briefly discuss some aspects relevant to these three approaches.

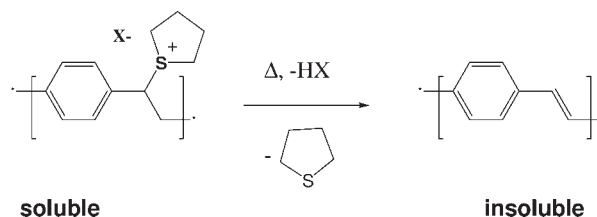
- 1) The simplest idea is to use “orthogonal” solvents for the individual layers, i. e., such that the solvent used in a deposition does not dissolve the previous layer(s). The most prominent example of such an approach is the conductive polymer PEDOT, which is commonly used as a hole-injecting anode and is deposited from an aqueous suspension. Organic layers can be deposited on top of the PEDOT layer without problem.

When it comes to depositing several layers from organic solvents, however, very often complete nonsolubility cannot be reached, leading to intermixing of the components at the interface. Furthermore, the number of layers is very limited, since only very few solvents can be used to dissolve typical OLED materials.

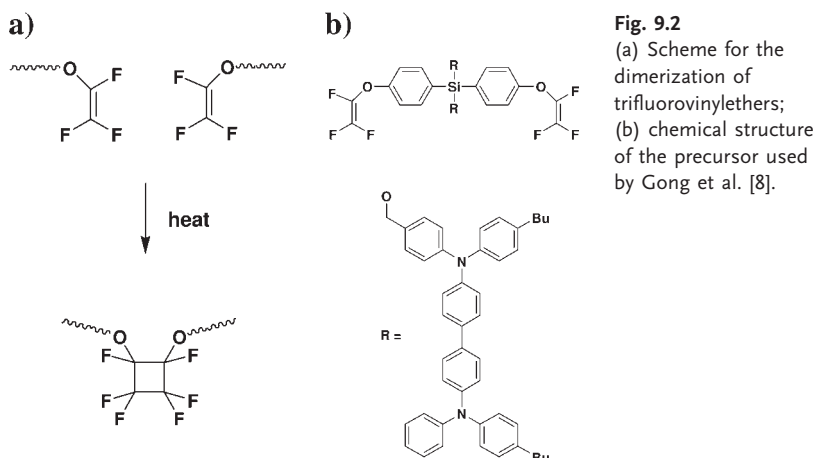
- 2) Secondly, the polarity/solubility of the material can be changed. This approach has barely been followed. One prominent example, however, is the first luminescent polymer, poly(p-phenylenevinylene) (PPV), which was obtained via a polar sulfonium precursor [5]. Here, the ionic precursor can be transformed thermally into a nonpolar polymer, which is insoluble in all organic solvents (Fig. 9.1).

Another example is the use of polyimides as inert binder for low-molecular-weight semiconductors. Upon thermal curing, the soluble polyimide precursors (polyamic acids) form insoluble polyimides. This concept was used as an alignment layer in OLEDs exhibiting polarized emission [6].

- 3) Finally, reactive (polymerizable) moieties can be introduced that can be polymerized after deposition. For this purpose soluble precursors, low-molecular weight as well as polymeric ones, with one (polymerization reactions) or two (polycondensation and polyaddition reactions) such reactive groups are required. After evaporation of the solvent the reaction is initiated, yielding a linear polymer (side-chain for polymerizations; main-chain for polycondensa-



**Fig. 9.1** Formation of PPV via sulfonium precursor route.



**Fig. 9.2**  
(a) Scheme for the dimerization of trifluorovinylethers; (b) chemical structure of the precursor used by Gong et al. [8].

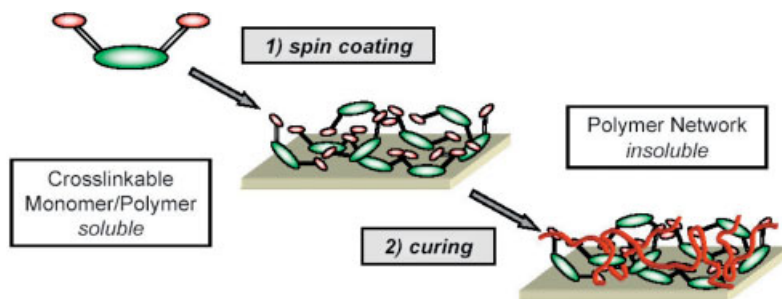
tion and polyaddition) with increased molecular weight. Thus, by selecting the right monomers the solubility of the resulting polymer will be significantly reduced, allowing, in principle, deposition of multiple layers. However, problems of intermixing cannot be entirely excluded.

An example of this material class was given by Jiang et al. [7] and Gong et al. [8], who reported on the use of trifluorovinylethers with two pendent triarylamine units per repeat unit (see Fig. 9.2). These materials can be cured thermally at 225°C via cyclopolymerization (polyaddition reaction). The introduction of this layer into AlQ<sub>3</sub> bilayer devices reduced the onset voltage, while keeping the efficiency unaffected [7]. In a yellow-emitting PPV-based device the same performance as in the PEDOT reference was obtained. In a blue-emitting device, the efficiency was improved by about one order of magnitude [8].

Ideally, more reactive groups are introduced, at least two (polymerization reactions) or three (polycondensation and polyaddition reactions), to yield absolutely insoluble crosslinked layers (Fig. 9.3). The next layer can then be prepared without negative impact on the underlying one, and the process can in principle be repeated without limitation.

The technically important criteria for the use of polymerizable or crosslinkable materials, respectively, are:

- 1) The precursors syntheses have to be compatible with the synthetic routes commonly used for the preparation of state-of-the-art materials, i. e., the reactive group has to be stable under the conditions to prepare the precursor and only become reactive upon initiation.
- 2) Generally, the polymerization is accompanied by a volume shrinkage of the materials, which may lead to mechanical stress in the film. This has been



**Fig. 9.3** Cartoon of the fabrication of crosslinked layers. The functional unit (i. e. the semi-conductive unit) is shown in green, the reactive unit in red. The spacer between them is shown as a black line. The material is dissolved in a suitable solvent, spin coated on the top of the substrate, and finally cured to yield an insoluble polymer network (red line). Multiple-layer structures are obtained by repeated deposition and curing.

speculated to be responsible for rather low lifetime of OLED devices. Thus, the volume reduction upon curing should be as low as possible in order to avoid this problem.

- 3) The electrical and optical properties as well as the device lifetime should not be negatively affected by the curing procedure.
- 4) Byproducts of the polymerization should have no influence on the performance of the devices.

In the following sections, we give an overview of the various attempts to fabricate crosslinked layers for use in multilayer OLEDs categorized by the reactive group used in the precursor materials. We start with the [2+2] cycloaddition of cinnamates and the radical polymerization of acrylates and styrene derivatives. The emphasis of the chapter is on our own work, which is focused on the cationic ring-opening polymerization (CROP) of oxetane-functionalized materials. Finally, we summarize the less-frequently employed synthetic routes.

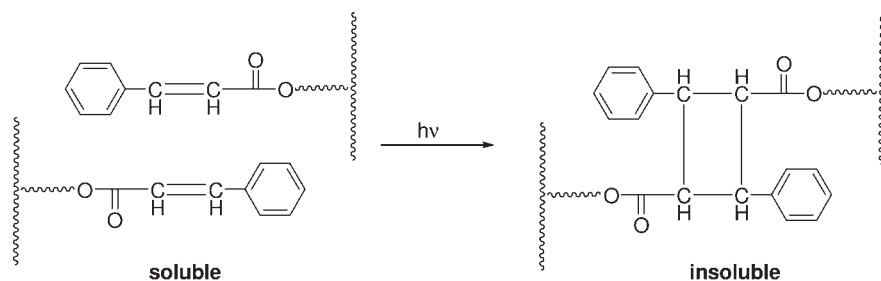
#### 9.2.1

##### [2+2] Cycloaddition of Cinnamates

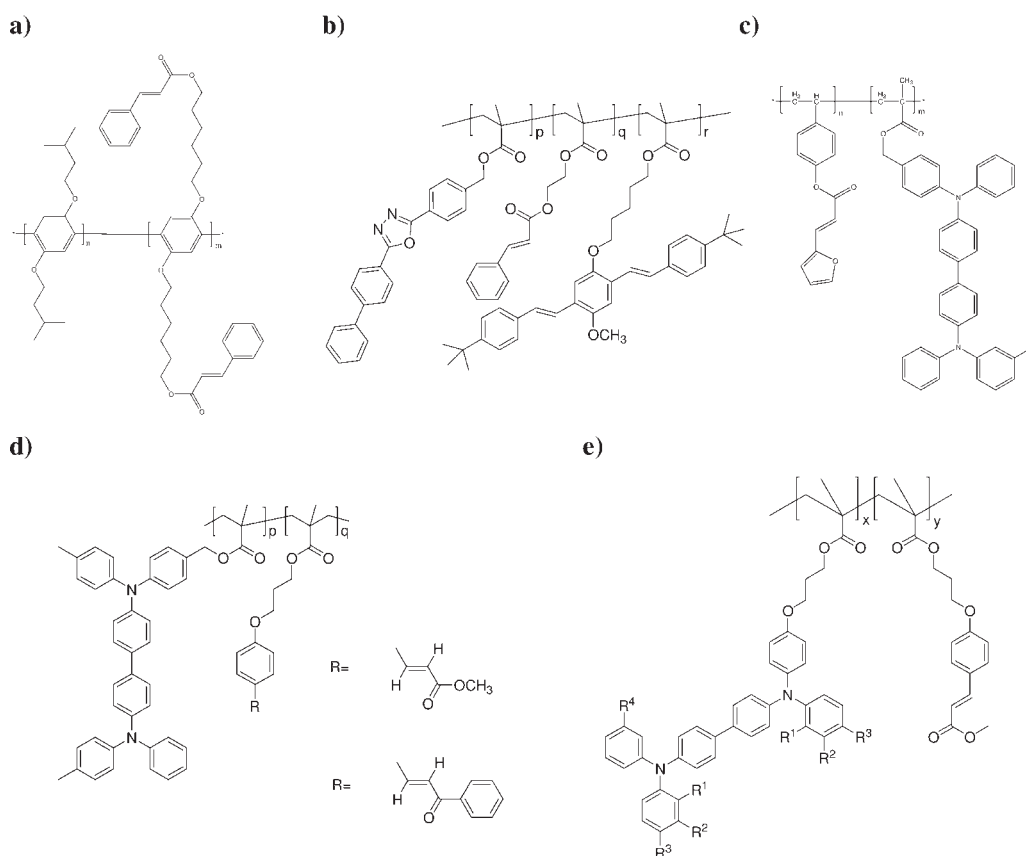
The [2+2] cycloaddition of cinnamates and related compounds was frequently used in conventional photoresist technology [9]. The general reaction scheme is shown in Fig. 9.4.

The first example of using the [2+2] cycloaddition for crosslinking of organic semiconductor layers was reported in 1997 by Remmers et al. [10]. It was a derivative of poly-p-phenylene (PP) deposited by the Langmiur-Blodgett (LB) technique (Fig. 9.5(a)). Polarized absorption and fluorescence of the films was reported, but no OLED devices were fabricated.

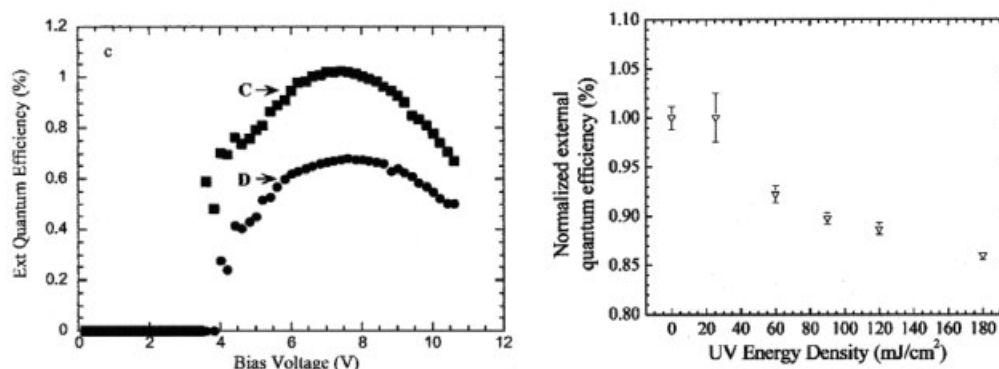
The next two examples were (meth-) acrylates. Li et al. [11] found that the PPV oligomer used as emitting unit (Fig. 9.5(b), right-hand side) was partially decom-



**Fig. 9.4** Scheme for the [2+2] cycloaddition of cinnamates.



**Fig. 9.5** Chemical structures of the precursors used in the [2+2]-cycloaddition approach: (a) Remmers et al. [10], (b) Li et al. [11], (c) Le Barry et al. [12], (d) Zhang et al. [13], and (e) Domerq et al. [14].



**Fig. 9.6** Influence of UV-irradiation on the OLED performance in side-chain hole-conducting polymers containing cinnamic acid groups. Left: External quantum efficiency of UV-irradiated (D) and nonirradiated (C) devices based on a material shown in Fig. 9.5(d) (adopted from Zhang et al. [13]); Right: Normalized quantum efficiency as a function of the UV energy for a series of devices based on a material shown in Fig. 9.5(e) (adopted from Dömerq et al. [14]).

posed during UV-illumination used to initiate the cycloaddition, as evidenced by reduced photoluminescence. The solubility was not tested after curing. Single-layer devices were fabricated. Le Barny et al. [12] fabricated bilayer devices using their crosslinkable TPD-based hole-conducting material (Fig. 9.5(c)) and 4-amino-naphthalaminides as the emitter.

In another [2+2]-approach, Zhang et al. [13] also reported the partial decomposition of the hole-transport units (Fig. 9.5(d)) during UV-exposure. As a result, the current throughput, the light output and the efficiency of devices using vacuum-deposited AlQ3 as the emitter all decrease upon crosslinking (see Fig. 9.6(a)).

Finally, Dömerq et al. [14] found that the external quantum efficiency of OLEDs using AlQ3 as the emitting material depended on the ionization potential of the hole-transport units (Fig. 9.5(e)), in agreement with previous reports on TPD-type materials in small-molecule OLEDs. By optimization of the UV exposure dose (see Fig. 9.6(b)) no loss of either the device efficiency or the lifetime was observed upon crosslinking the hole-transport polymer. However, the lifetime of the cross-linked devices was much shorter than for the vapor-deposited devices. An all-spin-coated 3-layer device using two hole-transport layers with graded ionization potential and an emission layer consisting of AlQ3 in polystyrene was fabricated.

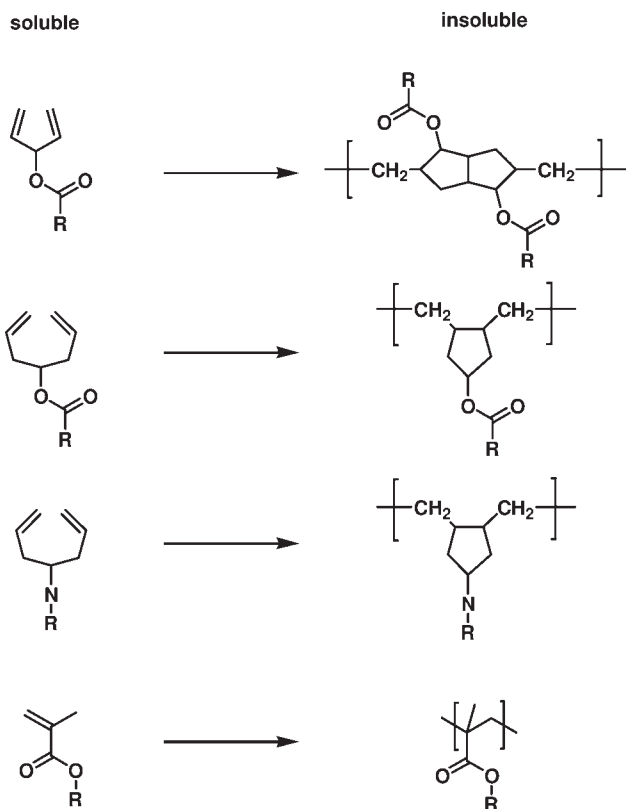
### 9.2.2

#### Radical Polymerization

The general polymerization schemes of dienes and acrylates are shown in Fig. 9.7:

Bacher et al. [15] reported on a series of triphenylene derivatives with one, two or three reactive acrylate units for crosslinking (Fig. 9.8(a)). No influence of the number of acrylate units on the degree of crosslinking was reported. Bi-layer OLEDs with the triphenylene as hole-transport agent and vapor-deposited AlQ3



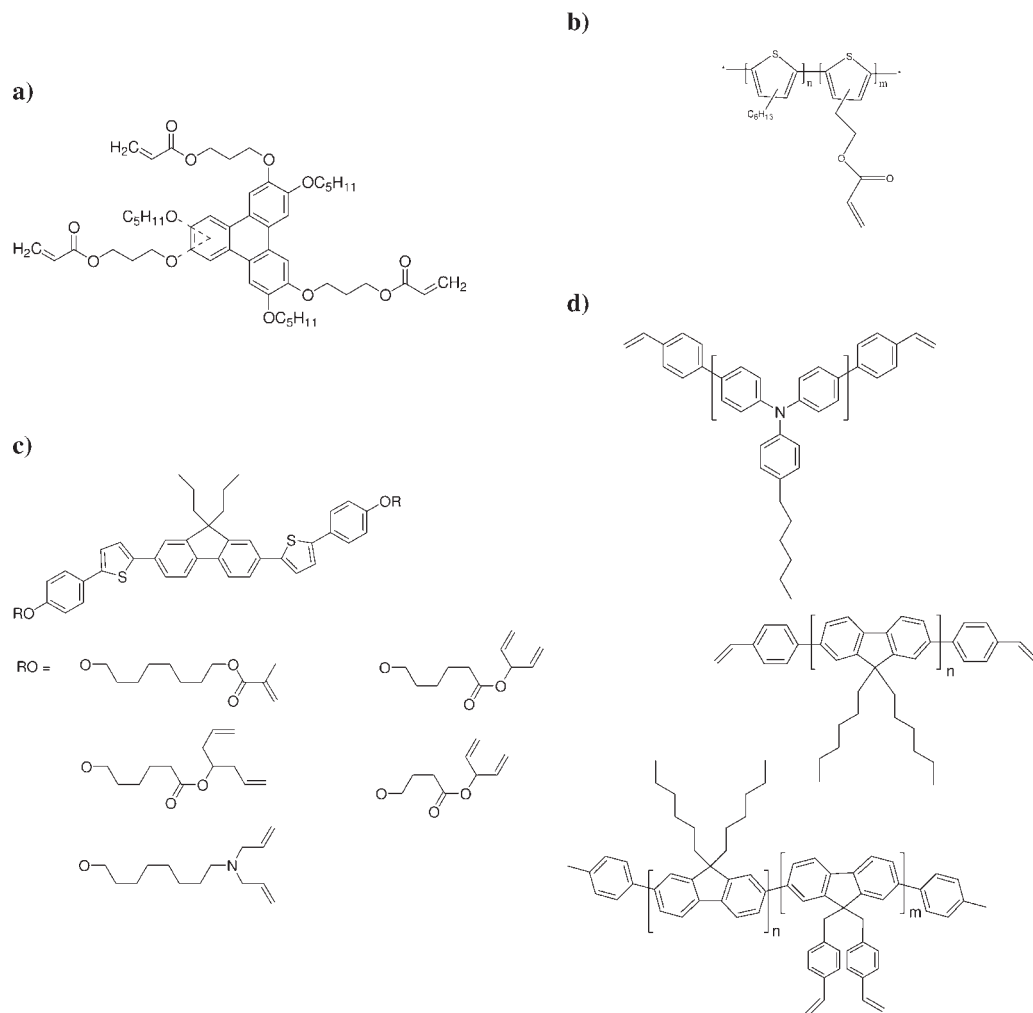


**Fig. 9.7** Schemes for the polymerization of dienes and methacrylates.

as the emitter were fabricated. Kock and de Ruiter [16] used a polythiophene derivative with pending acrylate groups as a negative resist for preparation of EB lithographic conductive patterns (Fig. 9.8(b)).

Contoret et al. [17, 18, 19, 20] prepared a series of fluorene-based liquid crystalline (nematic) fluorophores with a variety of reactive groups on both ends (Fig. 9.8(c)). After crosslinking the films yielded polarized emission. In some cases, crosslinking was found to increase the PL efficiency [18]. Probably as a result of this, crosslinked OLED devices showed stronger EL than noncrosslinked ones under the same drive voltage (Fig. 9.9, right). These findings were explained with a reduced number density of traps or a decreased exciton diffusion length. The current throughput in the crosslinked device was increased by two orders of magnitude after crosslinking (Fig. 9.9, left), indicating that the efficiency was reduced.

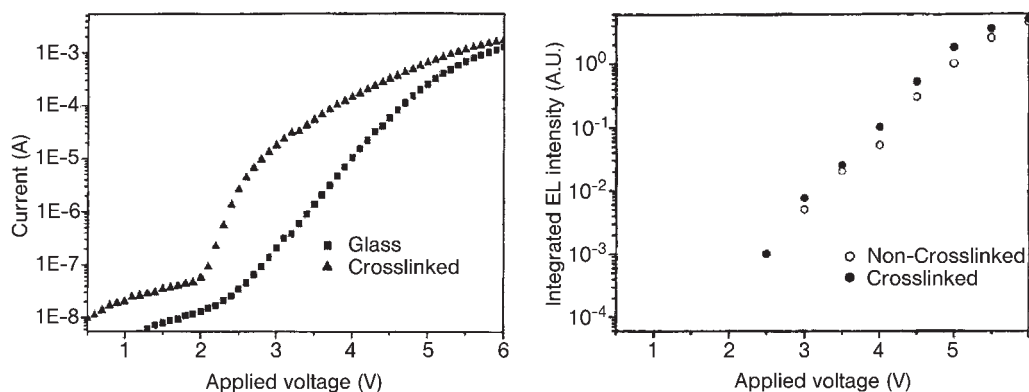
Chen et al. [21] and Klärner et al. [22] reported on a class of triphenylamines and polyfluorenes (Fig. 9.8(d)) with reactive styrene groups for crosslinking. Curing was performed thermally at 175–200 °C for 10–60 min. Network formation within the emitter was found to inhibit subsequent excimer formation. Triple-layer OLEDs, comprising a crosslinked hole-transporter, crosslinked emitter,



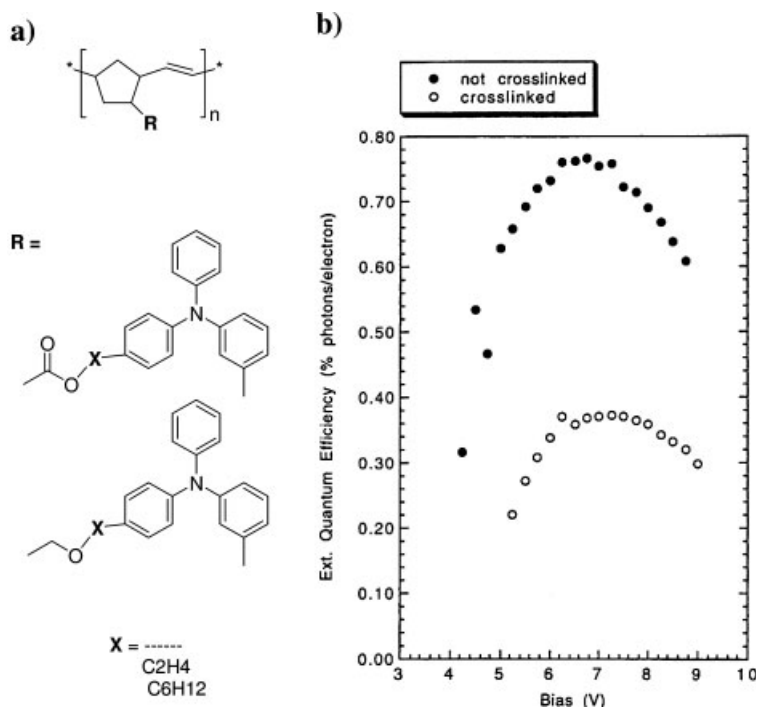
**Fig. 9.8** Chemical structures of the precursors used in the radical polymerization approach: (a) Bacher et al. [15], (b) Kock et al. [16], (c) Contoret et al. [17–19], and (d) Klärner & Chen et al. [21, 22].

and noncrosslinked electron conductor, show the highest efficiency, brightness and saturation of blue emission [21].

Bellmann et al. [23] reported on a series of hole-transporting triphenylamines based on polynorbornenes. The polymer, formed by ring-opening metathesis polymerization, contains double bonds, which are crosslinked by UV irradiation via a mechanism not fully investigated. However, in their best case crosslinking reduced the efficiency based on the emitter AlQ3 by factor of two approximately (Fig. 9.10).



**Fig. 9.9** Performance of an OLED based on a material class shown in Fig. 9.8(c): current-voltage characteristics (left) and light output (right) for a crosslinked (solid symbols) and noncrosslinked device (open symbols; adopted from Contoret et al. [18]).



**Fig. 9.10** Study of UV-curable polynorbornenes: (a) Chemical structures of the precursor polymers; (b) effect of UV-crosslinking of the polynorbornene-based HTL on the external quantum efficiency of OLEDs of the structure ITO/HTL/AIQ3/Mg.

## 9.2.3

**Cationic Ring-Opening Polymerization (CROP) of Oxetanes**

Oxetane-bearing organic semiconductors are the most successfully used group of materials used so far in crosslinked OLEDs. By simple functionalization the oxetane group can be introduced into almost all traditional materials commonly used in the OLED field. One unique feature of the oxetane group is that it is inert under the strongly basic conditions of transition-metal-catalyzed coupling reactions, which are most often the essential step in realizing high-performance OLED materials (e.g. Suzuki or Hartwig–Buchwald coupling). Chemical side reactions caused by the presence of oxetanes are thus not expected, so an easy integration in the commonly used synthetic routes is possible. Furthermore, oxetanes are well-known for their low volume shrinkage (< 5 %) upon polymerization [24].

Figure 9.11 shows the reaction scheme that is generally accepted for the cationic ring-opening polymerization (CROP) of oxetanes [25, 26, 27, 28]. Usually, so-called photoacids are employed to start the polymerization [29, 30]. Typical examples are onium compounds ( $Y^+(\text{Ar})_n X^-$ ) such as iodonium ( $n = 2$ ) and sulfonium ( $n = 3$ ).  $X^-$  are non-nucleophilic counter ions such as  $\text{BF}_4^-$ ,  $\text{PF}_6^-$ ,  $\text{AsF}_6^-$  and  $\text{SbF}_6^-$ . The nature of the compensating anion strongly influences the reactivity and the yield by complexing the reactive site [29], while leaving the decomposition rate of the initiator unaffected. There is no formal termination step of the CROP polymerization under the conditions used to process OLEDs (inert atmosphere, i. e. in the absence of water and oxygen).

In the presence of conjugated aromatic units such as in typical semiconductive organic materials the reaction may be sensitized by the active compound [31, 32]. This applies in particular, when light of a wavelength longer than the absorption band of the photoacid ( $\lambda > 350 \text{ nm}$ ) is utilized. The key step of photosensitization is the photoinduced electron transfer (PET) from the organic semiconductor to the photoacid, leading to the formation of a radical cation (organic semiconduc-

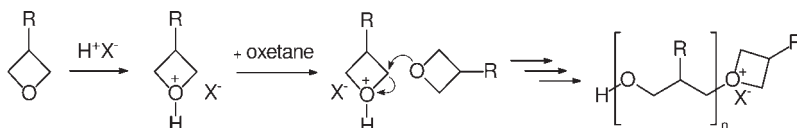


Fig. 9.11 Scheme of the cationic ring-opening polymerization of oxetanes.

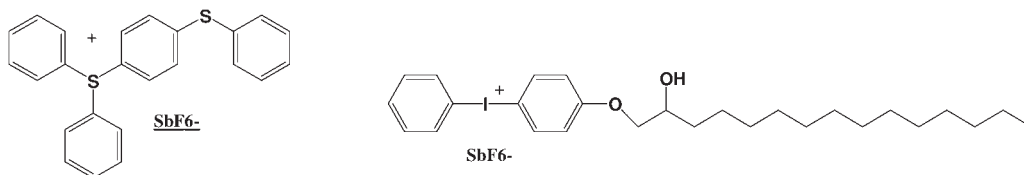
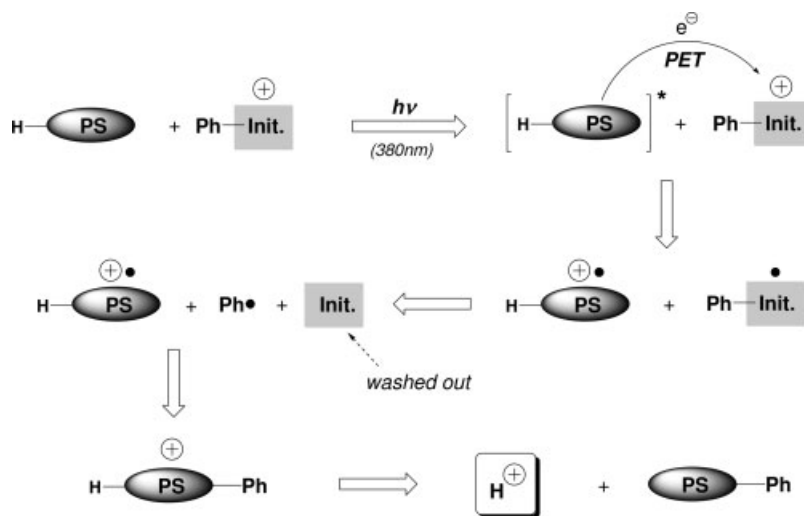


Fig. 9.12 Chemical structures of photoinitiators used in the CROP of oxetanes.



**Fig. 9.13** Scheme for the generation of protons via photoinduced electron transfer (PET). **PS** refers to a generic photosensitizer, e.g. a TPD-unit in a hole-transport material. **Ph** indicates the phenyl units in the photosensitizer (compare Fig. 9.12).

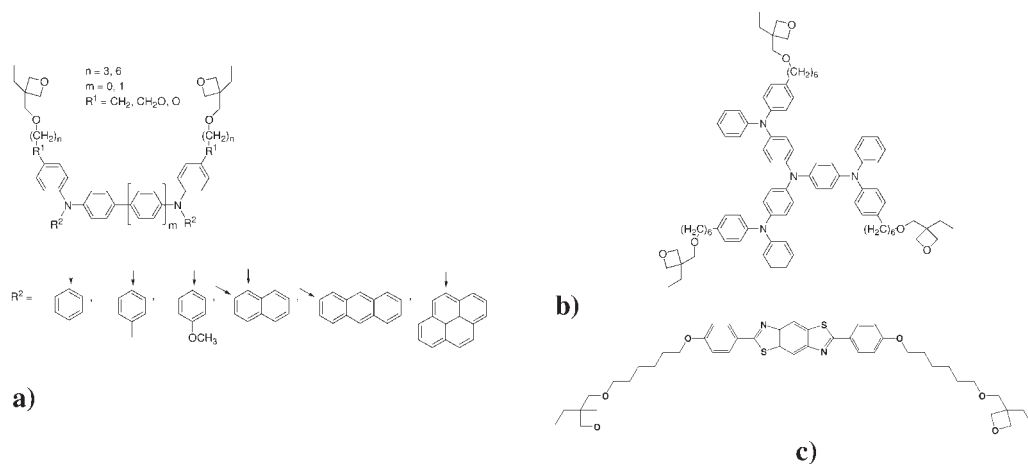
tor) and the reduction of the formerly positive charged initiator, yielding a neutral radical (Fig. 9.13). The initiator radical is highly unstable (estimated lifetime  $\sim 200$  ps) and decomposes irreversibly to form a neutral fragment, which can be removed by washing with a solvent, and a highly reactive phenyl radical. The latter reacts predominantly by combination with the aromatic radical cation, finally leading to the abstraction of a proton and initiation of the CROP.

Alternatively, undesirable side reactions may lead to persistent cation radicals. Due to these side reactions doping (p-type) of the organic semiconductor may occur, leading to a higher conductivity, but lower luminescence efficiency (photo and electroluminescence). However, by chemical or thermal (post-bake step at  $180^\circ\text{C}$ ) treatment, complete dedoping is possible and the luminescence efficiency is fully recovered. Additionally, in some cases the cation radical is able to attack the oxetane through nucleophilic reaction and ultimately start the same chain reaction as above [33].

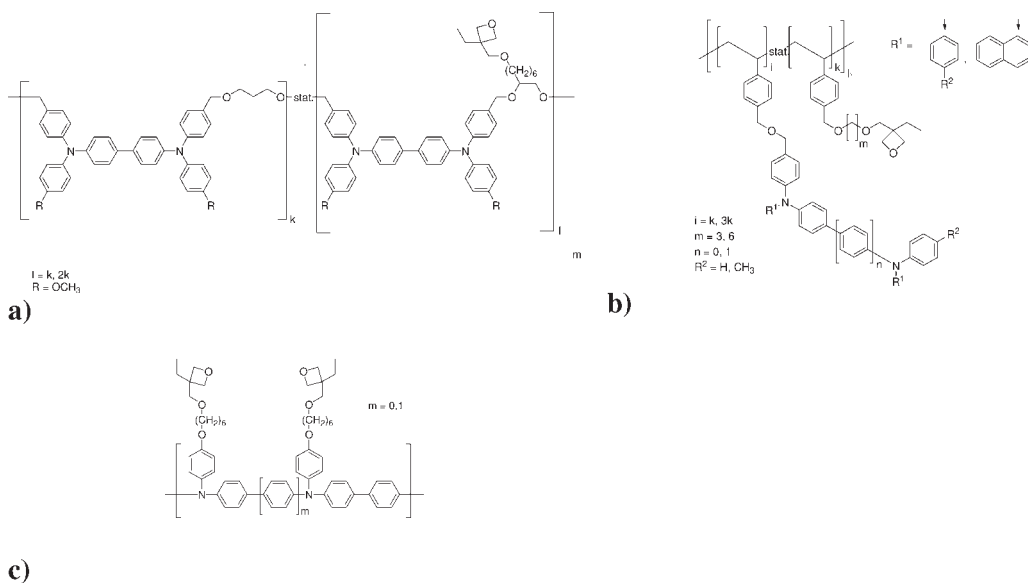
#### 9.2.3.1 Hole Conductors

A large variety of low molecular weight (Fig. 9.14) and polymeric (Fig. 9.15) oxetane-functionalized hole conductors has been synthesized.

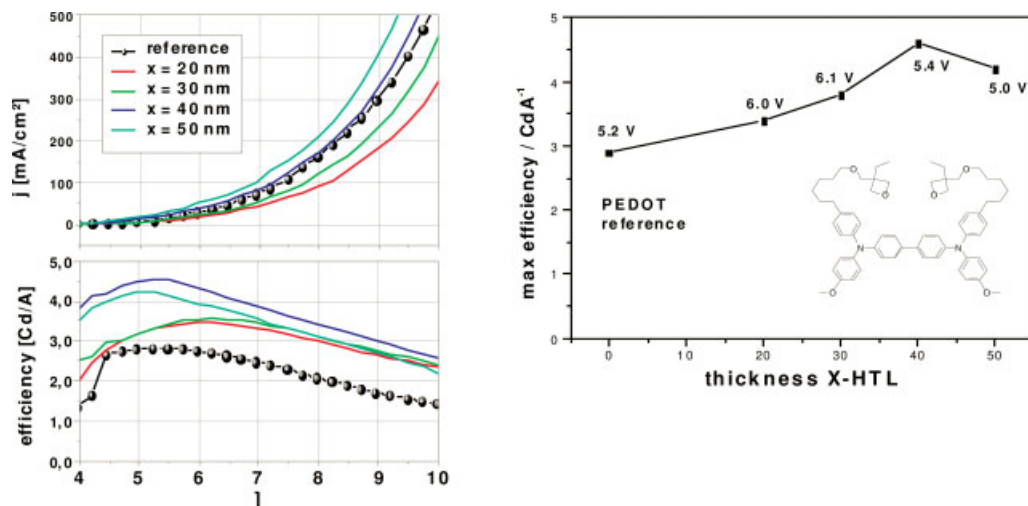
The oxetane-derivatized hole conductors span a broad range of redox potentials between 0.0 and 0.5 V vs. the ferrocene/ferrocenium redox couple, which is a standard reference in organic electrochemistry. Thus, this class of materials is ideally suited to bridge the gap to low-lying HOMO levels of an emitter polymer. This becomes particularly important for blue-emitting polymers such as polyfluorenes.



**Fig. 9.14** Chemical structures of oxetane-functionalized low-molecular-weight hole conductors: a) derivatives of TPD [34, 35, 36], b) hyperbranched triarylamine [35], and c) liquid-crystalline bisbenzthiazole derivative [64].



**Fig. 9.15** Chemical structures of oxetane-functionalized polymeric hole conductors: (a) non-conjugated main-chain polymers including TPD-type units [37], (b) polystyrene-based side-chain polymers with pendant TPD-type units [38], and (c) conjugated poly-TPD-type main-chain polymers [39].

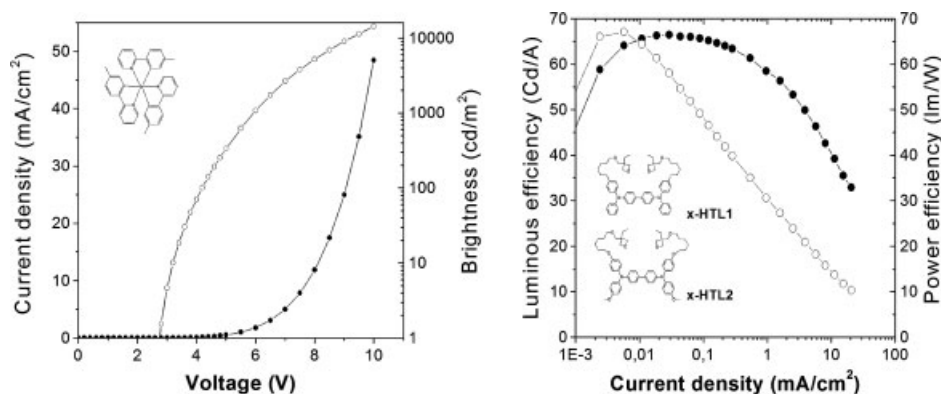


**Fig. 9.16** Performance of blue-emitting OLEDs based on crosslinked hole-transport layers (X-HTL) and a spirobifluorene-cofluorene derivative (**P1** [41]). The devices had the general structure ITO/X-HTL ( $x$  nm)/**P1** ( $80-x$  nm)/Ca (100 nm), the reference device ITO/PEDOT (30 nm)/**P1** (80 nm)/Ca (100 nm). *Left:* voltage dependency of the current and the efficiency. *Right:* Dependence of the maximum efficiency on the thickness of the X-HTL. The numbers indicate the voltage at which the maximum occurs. The chemical structure of the crosslinkable hole conductor used in this study is shown as an inset.

By subsequent deposition of crosslinked hole conductors with increasing redox potential, so-called “electronic stairs” can easily be fabricated. Those “electronic stairs”, introduced underneath HTLs between the anode and an endcapped polyfluorene derivative lead to an increase in efficiency by a factor of three [40].

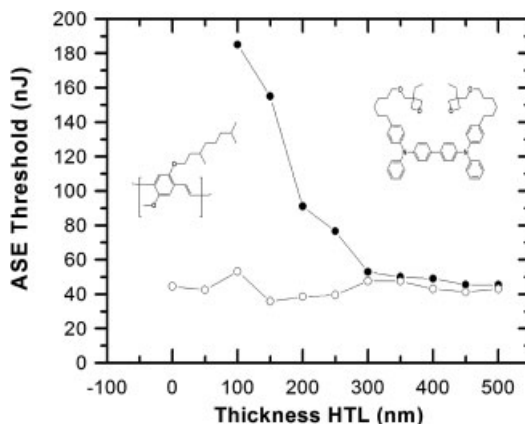
Figure 9.16 shows the effect of replacing the commonly used PEDOT layer by a crosslinked hole-transport layer (X-HTL) underneath HTLs between the anode and the blue-emitting spirobifluorene-cofluorene (Fig. 9.19(c)). In comparison with the reference device, which uses PEDOT as the anode (absent in the X-HTL devices) the efficiency is improved, but the onset voltage is slightly increased, due to the increased layer thickness. By variation of the thickness ratio of the hole-conducting and the emitting layer while maintaining an overall thickness of 100 nm, the onset voltage could be decreased dramatically. This arises with a further increase of efficiency (up to a factor of 1.5), and an overall device performance superior to the PEDOT reference device.

Similar improvements by introducing a hole-conductive interlayer have been obtained with many other emitting polymers [42]. Recently, record efficiencies of 67  $\text{Cd}/\text{A}$  (65  $\text{lm}/\text{W}$ , respectively) were achieved with a green phosphorescent system using a double injection layer (Fig. 9.17), in which the internal quantum efficiency approached unity [43]. This performance is similar to those obtained with small molecules [2].



**Fig. 9.17** Performance of a device ITO/PEDOT (30 nm)/x-HTL1 (20 nm)/x-HTL2 (20 nm)/PVK:PBD: Ir(mppy)<sub>3</sub>/LiF/Al. The chemical structures of the green-emitting phosphor and both crosslinkable hole conductors are shown as inserts, respectively [43].

The last example of this section deals with the optical function of hole-transport layers. In OLEDs some light is waveguided in the combined anode/organic layers due to total internal reflection [44]. By increasing the thickness of the hole conductor the emitter can be optically decoupled from the contact. In a series of devices with increasing thickness of the hole conductor, deposited subsequently from solution, it was shown that a HTL thickness larger than 300 nm was necessary to accomplish this. As a very sensitive measure the threshold of amplified spontaneous emission (ASE) was used (Fig. 9.18, [45]). This is an important result with respect to a potential electrically driven organic laser diode.



**Fig. 9.18** ASE threshold of a 200-nm thick MDMO-PPV layer as a function of the x-HTL layer thickness for samples on ITO (solid symbols) and on glass only (open symbols; for details see Ref. [45]). The chemical structures of the emitter and the hole conductor used for this study are shown as inserts.

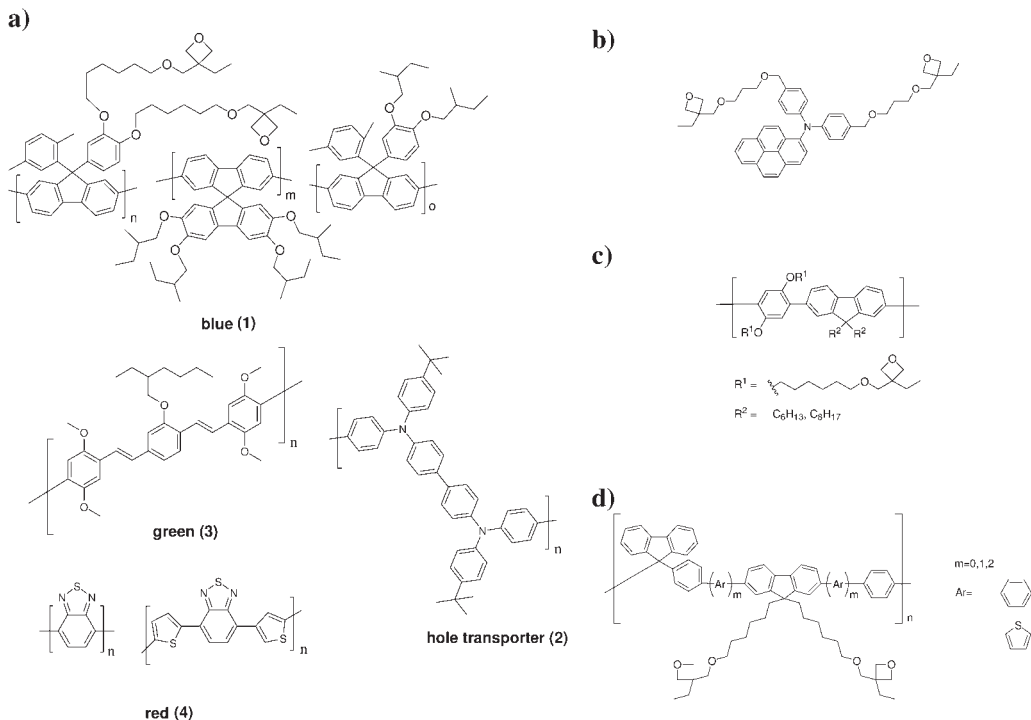


#### 9.2.3.2 Emitters

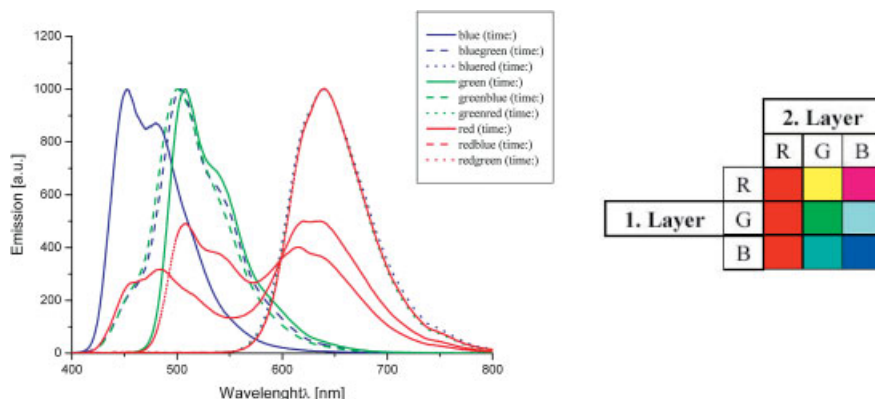
The first oxetane-functionalized emitter were pyrene derivatives (Fig. 9.19(b), [46]), however, with very limited performance in OLEDs. Later, a poly(phenylene-fluorene)-copolymer was reported, however, without any electroluminescence data (Fig. 9.19(c), [47]). The breakthrough came with a recent report on a crosslinkable class of state-of-the-art spirofluorenes (Fig. 9.19(a), [48, 49]). By incorporating a green- and red-emitting comonomer, it was possible to generate the three primary colors (RGB) necessary for color-display applications. More recent concepts use sterically hindered 9,9'-diarylfuorene blocks to link conjugated oligomers (Fig. 9.19(d), [50]).

Generally, OLEDs made from the crosslinked emitter polymers exhibit some important advantages over their noncrosslinked references [49]: (1) they exhibit identical, if not even slightly improved maximum efficiency  $\eta_{\text{max}}$ . (2) the turn-on voltage for light emission is slightly reduced. (3) The efficiency at high luminance is slightly higher. (4) Finally, crosslinked devices can be operated at higher current density before breakdown occurs.

If the emissive polymers were deposited on top of each other, simple additive color mixing is possible (Fig. 9.20).



**Fig. 9.19** Chemical structures of oxetane-functionalized emitters: (a) low molecular weight pyrene-based emitter [46], (b) poly(fluorene-phenylene) copolymer [47], (c) spirobifluorene-cofluorene RGB emitter polymers [48], and (d) fluorene-bridged co-oligomers [50].

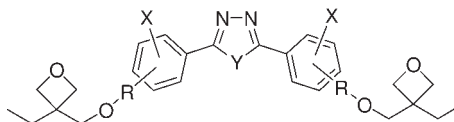


**Fig. 9.20** Emission spectra (left) of OLEDs of the general structure ITO/PEDOT/1. Layer/2. Layer/Ba/Ag. For both layers, which had identical thickness, the three primary colors RGB were varied. The color impression is shown on the right-hand side.

### 9.2.3.3 Electron Conductors

The number of crosslinkable electron conductors is relatively small compared to the number of hole-conducting materials. A series of oxetane-functionalized oxadiazoles was synthesized [51]. Unfortunately, due to the relatively strong basicity of the two nitrogen atoms in the oxadiazole ring, the reaction was strongly inhibited. An excess of more than 50wt% of the initiator was necessary to start polymerization in solution. This is of course unacceptable for application in OLEDs.

**Fig. 9.21** Chemical structures of oxetane-functionalized electron conductors: oxadiazole derivatives ( $Y = O$ , [51, 64]) and thiadiazole derivatives ( $Y = S$  [64])

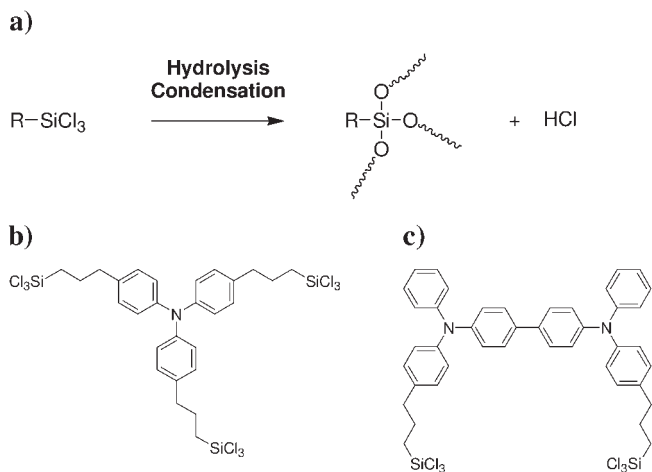


### 9.2.4

#### Alternative Approaches

Li et al. [52] reported on a derivative of tritolylamine (TTA) with three trichlorosilane groups as reactive units (Fig. 9.22(a)). In the presence of water, 3-dimensional silica networks exhibiting hole-conductive properties were formed.

Recently, Yan et al. [53] reported on a similar bis(trichlorosilyl)-derivatized TPD (Fig. 9.22(c)). This was used to form thin, self-assembled layers of 1.8 nm on ITO. The introduction of this layer improved the efficiency compared with a reference device using bare ITO as the anode and a green-emissive polymer. They also crosslinked the compound within a blend with a hole-conducting polymer onto PEDOT/PSS. Overall, a factor of about two improvement was achieved, yielding very efficient green-emitting diodes (17 Cd/A).

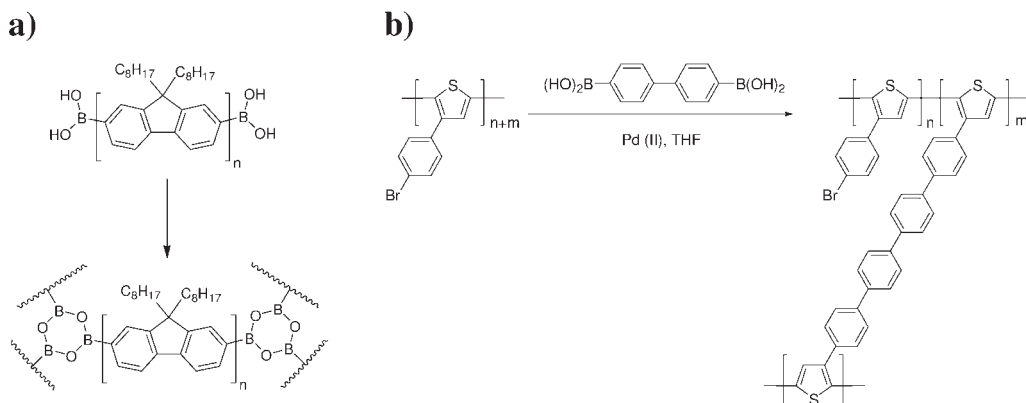


**Fig. 9.22**  
(a) Scheme for the hydrolysis of tri-chlorosilanes; (b), (c) Chemical structures of the precursors used by Li et al. [52] and Yan et al. [53].

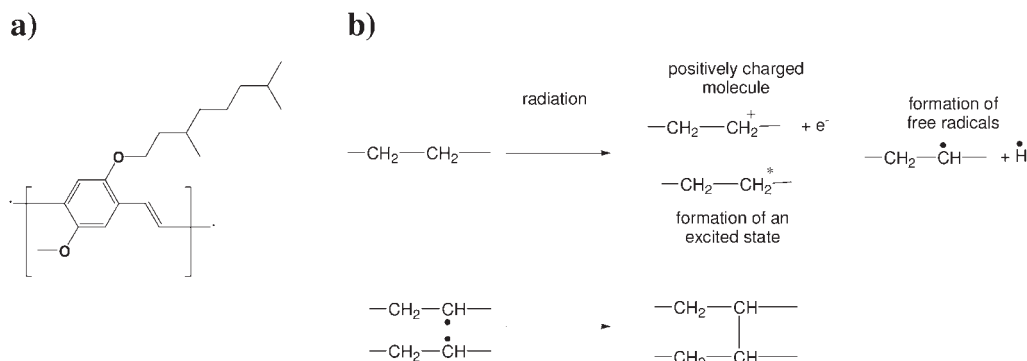
Li et al. studied the thermal dehydration of boronic acids (Fig. 9.23(a), [54]). Crosslinking considerably improved the photoluminescence stability. Multilayer capabilities were demonstrated.

Davidson and Ponsonby [55] studied the influence of the degree of crosslinking in a polythiophene derivative on its conductivity (Fig. 9.23(b),). With increasing degree of crosslinking they found an oscillatory behavior of the conductivity. This was explained by a tradeoff between more conductive pathways (good) and less intrachain planarity (bad).

Hikmet and Thomassen [56] studied the crosslinking of two widely used PPV-derivatives, Super Yellow and Super Orange (also known as MDMO-PPV or OC1C10; both from Covion/Frankfurt; Fig. 9.24(a)) by application of an electron beam. The proposed mechanism for crosslinking is shown in Fig. 9.24(b). They



**Fig. 9.23** Chemical structures of the precursors used by (a) Li et al. [54]; (b) Davidson and Ponsonby [55].



**Fig. 9.24** (a) Chemical structure of MDMO-PPV (or OC1C10-PPV, respectively) used in [56]; (b) proposed crosslinking mechanism.

found that e-beam treatment led to a reduction of the hole mobility by a factor of three. The EL is reduced after crosslinking, however, the EL spectrum remains unchanged.

### 9.3 Patterning

This section is intended to give an overview of the deposition techniques applied to achieve RGB and RGBW displays.

Today, fine metal **shadow masks** with features in range of 50–100  $\mu\text{m}$  (pixel size) are the most common method for patterning color primaries in the fabrication of small-molecule OLEDs. Since the materials are deposited through the gas phase, this technology has multilayer stack capability. Full-color displays of up to 20 inches have been realized, however, there are still issues regarding scalability of the method to very large mother glass formats. Furthermore, during continuous use of a mask, material accumulates on the mask, and reduces the resolution and accuracy of deposition. Therefore, the masks have to be cleaned or even replaced relatively often. To avoid these problems, for large-size applications, approaches that do not require individual patterning of OLED, such as the color-conversion method (CCM) similar to liquid-crystal display (LCD) technology are being developed.

**Laser-induced thermal imaging (LITI)** technology [3, 4] also referred to as dry or thermal printing could be an important alternative. Hereby, the light-emitting materials are first deposited on a flexible donor sheet, which is coated with a “light-to-heat-conversion” (LTHC) layer. This donor sheet is then brought into intimate contact with the receptor surface. By local heating using a strong laser pulse incident on the LTHC layer the donor is released and transfers to the target substrate (see Fig. 9.25). Finally, the used donor sheet is peeled off and discarded. The smallest feature size is given by the laser spot size, and a resolution of a



**Fig. 9.25** Illustration of the LITI printing process (adopted from Blanchet et al. [4]).

few micrometers has been demonstrated [4]. Obviously, for LITI the adhesion properties between the various layers is of paramount importance. To achieve adequate patterning the molecular weight cannot exceed a certain limit (ca.  $MW = 20\,000$  g/mole), which basically excludes most commercially available polymeric light-emitting materials. Since it is a dry process, LITI transfer is not affected by the solubility properties of the transfer layer, i. e., it has multilayer stack ability. Finally, LITI is scalable to large mother glasses and has reel-to-reel capability.

For the wet-chemical fabrication of RGB(W) devices, current research efforts are directed towards adaptation of well-established **printing techniques**. The ink-jet technology is considered the most promising, since it is capable of placing small amounts of solution (droplets) with high accuracy and reproducibility. However, even though this technique has the distinct advantage of simple manufacturing, and large-area displays were presented at international trade shows, it still has not proven its maturity in mass-production settings with large-format substrates. The main technological hurdle is the necessity to precondition the wetting properties of the substrate to define “microwells”. But only accurate adjustment of further parameters such as drop size, solvent formulation and drop velocity finally leads to the desired flat film of high quality.

Finally, another patterning method is conventional **photolithography**, utilizing materials that become insoluble upon illumination (“negative” photoresists). Due to its simplicity (compare fabrication of integrated circuits), a photolithographic process would be highly preferable over the printing techniques mentioned above: The lateral resolution would be much better (few micrometers compared to several tens of micrometers), and the coating of large substrates could be much faster. Preconditioning of the substrate is not required. If a crosslinking strategy is followed (“negative” photoresist) the deposition of multiple layers also becomes possible. The combination of organic semiconductors and photoresist technology will bring forward added values, which neither of the two alone would exhibit. Such materials will have a strong impact on the development of future OLED devices and architectures.

All material classes discussed in the previous section, which can be cured photochemically, can in principle be used in this process. Except for the necessity of good film-forming properties there are no other material limitations, such as for the molecular weight (SM and LITI), the thermal stability (SM) and/or the adhesion properties (LITI). The only concern is that the curing should leave the materials’ optical and electrical properties unaffected, which has been demonstrated in principle by several teams (see previous section).

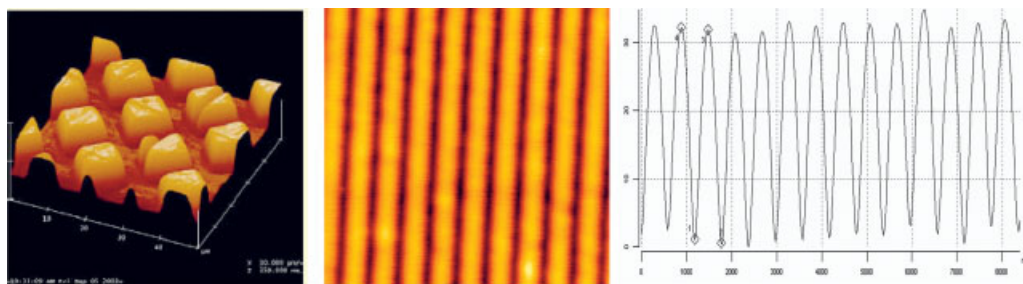
Most papers on crosslinkable organic semiconductors focus on the insolubility and multilayer capability. There are only few instances where the lithographic re-

solution is addressed [14, 33, 57]. The spatial resolution of photoprocess, independent of the chemistry involved, is basically limited by the accuracy one is able to image the pattern onto the film. The highest resolution is, therefore, obtained by e-beam structuring [56]. The second limitation depends on whether or not there is a termination reaction in the polymerization:

- In [2+2] cycloadditions (e.g. derivatives of the cinnamic acid), the reaction strictly occurs in the illuminated areas only.
- By contrast, in radical polymerization (e.g. acrylates and styrenes) the chain can grow beyond the illuminated areas, however, chain termination due to recombination and/or radical transfer will limit this relatively efficiently. Therefore, the resolution will not degrade by too much.
- In the case of ionic polymerizations, (e.g. CROP of oxetanes), under the conditions used for fabrication of OLED devices (inert gas atmosphere), there is no explicit termination step. Thus in the end of the polymerization, the chain ends remain positively charged. This could lead to a reduced lithographic resolution (and blurring of the image).

A very simple method to test the lithographic resolution of a material is to use TEM grids (TEM = transmission electron microscopy) as a contact-shadow masks [57]. AFM investigations of crosslinked layers, structured by using the method described above, show, that the used grids have been nicely reproduced. The achievable lithographic resolution is submicrometer as was demonstrated by recording a holographic grating. Such gratings might serve as distributed feedback structures in a future organic laser diode. This is more than sufficient concerning the requirements for RGB displays.

Finally, we review two attempts in which multicolor OLEDs were obtained by subsequent deposition on the entire substrate, patterned illumination, development (removal of polymer in nonilluminated areas), and finally curing (Fig. 9.27).



**Fig. 9.26** AFM images of photopatterned crosslinked hole-transport layers: *Left*: illuminated through a mesh-1500 TEM grid, yielding squared features of 8  $\mu\text{m}$  size separated by channels 5.6  $\mu\text{m}$  wide [57] (in addition scratches from placing the mask on the mate-

rial can be seen). *Middle*: illuminated by a holographic interference pattern with a period of 590 nm. *Right*: Cross section of the holographic surface relief grating, indicating a modulation depth of about 30 nm [58].



**Fig. 9.27** Photograph of a solution-processed multicolor devices: a) RGB device obtained by common lithography [48] and two-color device obtained by e-beam lithography [56].

An alternative route to process full-color OLEDs is to use a procedure similar to “normal” semiconductor manufacturing [59]. In this process the active layers are coated with a photoresist and then etched. Another, more exotic approach is reductive photopatterning [60]. Here, a single emissive layer of a blue-emitting host and red- and green-emitting guest molecules is used. The energy transfer between the host and the dopants is tuned via a reductive photoinitiated process in the presence of gaseous hydrazine. The color is “selected” by the hydrazine exposure time. Finally, several attempts to use microcontact printing ( $\mu$ CT) or micro-injection molding in capillaries (MIMIC) for patterning OLEDs was reported [62]. Despite an excellent resolution between several 10s of micrometers down to 500 nm [63] this process has not had a technical breakthrough, probably due to the well-known difficulties in repeatedly using a stamp.

## 9.4

### Conclusion and Outlook

This chapter focused on solution-processable materials with multilayer capability. In previous years, a large variety of approaches has been proposed, the most promising being oxetanes, styrenes, dienes, and trifluorovinylethers. Most examples are hole-transporting materials. Incorporation into OLEDs improved the efficiency of the devices relative to the reference devices using bare ITO or PEDOT as anode in many cases. In the latter case, besides improved hole injection the “interlayer” also functions as a barrier towards ion and proton migration from the PEDOT layer, which is thought to be responsible for the reduced lifetime of the devices. Crosslinked HTLs might also replace PEDOT as an injection layer all together.

The most efficient devices were obtained using a multilayer approach, i.e. using several transport layers, emitter, and blocking layer. Thus, ultimately, device optimization can be done similarly to small-molecule devices by selecting the best materials for their function rather than by generating materials, which fulfill all functions at once, but with limited performance (“single-layer” approach).

It is a distinct advantage of this approach that it makes small molecules applicable to solution processing. Due to their tendency to aggregate and/or crystallize “normal” low-molecular-weight semiconductors such as TPD, which are usually deposited by vapor deposition, are not well suited for processing by spincoating,

since recrystallization occurs. However, the combined spacer/reactive unit acts as an internal plasticizer, preventing the material from crystallization. Thus, these compounds are amorphous, highly viscous materials, which can easily be processed by spin coating. Films of these materials are surprisingly stable, i. e., dewetting is rarely observed at room temperature. However, due the relatively low viscosity the films do not withstand “stress” such as thermal treatment or electrical current for very long. This changes dramatically after the films are cured, yielding excellent morphological stability beyond that of small molecules and even polymers. This is an important fact, considering the thermal stress during long-duration operation. Thus, thermally induced morphological changes, like (re)crystallization and dewetting, which are assumed to be one of the factors limiting lifetime, are completely reduced. Furthermore, when various monomers and polymers are copolymerized, no phase separation can occur after the network formation, resulting in absolutely stable multicomponent films.

By contrast, crosslinking by nature is a disturbance of the highly sensitive system of an organic semiconductor. Even small changes of the chemical structure of a given organic semiconductor, e. g. when attaching the crosslinkable group(s), can have a strong impact on its electrical and optical properties. Furthermore, the crosslinking reaction itself proceeds via highly reactive intermediates, and undesired side reactions are likely to occur. Therefore, extreme care has to be taken when choosing the crosslinkable group or the curing method. The impact of the various parameters has to be studied individually, in particular by long-term measurements.

Thus, in order to optimize the conditions of the crosslinking reaction a detailed understanding of the role and the potential reaction pathways of the formed intermediates is necessary. It should be noted that the strong light interaction and the high presence of the organic semiconductor (close to unity) heavily influence all kinds of photoinduced crosslinking reactions. Therefore, an extended and complex range of potential reaction pathways must be considered.

In the area of the oxetane-derivatized semiconductors, successive optimization and fine tuning accomplished with a deeper understanding of the crosslinking process lead to significant reduction of undesired side reactions. By repeated modification of both materials and curing procedures, it was possible to reduce the initiator content from 3 % [40] to below 0.2 % [49]. Thus, the amount of reactive intermediates and side reactions could be reduced to a level, where their impact is by far compensated by the benefits of crosslinking. The latest versions of crosslinkable oxetane-derivatized RGB polymers all show significantly improved performance after crosslinking, both regarding efficiency and lifetime [42].

The second focus of this chapter is the full-color capability. The combination with the crosslinking strategy led to a novel class of semiconductive materials: smart (negative) photoresists. In addition to the fabrication of multilayer structures the layers could be simply patterned laterally by the use of a photolithographic process. In the few cases where the lithographic resolution was tested, it was easily sufficient for RGB pixilated deposition. In addition, these materials come with additional new features (“added values”).



Organic semiconducting photoresists exhibiting a lithographic resolution in the submicrometer scale are suited for an *on-chip* integration of optical functions. Waveguide structures could be realized directly into the active materials itself. In particular, integrated distributed feedback gratings (DFB, Fig. 9.26) are of high interest in the field of electrically pumped organic solid state lasers.

On the other hand, smart photoresists have strong competition from alternative technologies, e. g. inkjet and LITI. In order to be competitive, the synthesis of the crosslinkable materials must be based on the highly developed synthetic routes for the preparation of state-of-the-art materials. Integration of the crosslinkable group from the beginning is mandatory for the synthesis of conjugated polymers, since protective group chemistry or polymer analogous reactions generally lead to significant and thus expensive complications. In particular, the strong basic, transition-metal-catalyzed coupling reactions, predominantly used in synthesis of organic semiconductors, lead to severe restraints concerning the crosslinkable group. So far, this applies to oxetanes only.

### Acknowledgements

We would like to acknowledge the members of our research groups (Dr. Erwin Bacher, Dr. Michael Bayerl, Florian Bielefeldt, Dr. Thomas Braig, Dr. Markus Gross, Steffen Jungermann, Dr. Erwin Mecher, Dr. Felix Mielke, Nina Riegel, Dr. Markus Rojahn, Paula Rudati, and Dr. Valerie Wiederhorn) and Dr. Heinrich Becker, Dr. Aurelie Falcou, and Dr. Frank Meier from *Covion Organic Semiconductors* (Frankfurt, Germany) for the excellent collaboration.

### References

- 1 a) P. M. Borsenberger, D. S. Weiss, "Organic Photoreceptors for Imaging Systems" (Marcel Dekker, New York), 1993; b) H. Bässler, *Phys. Stat. Sol.* **175**, 15 (1993).
- 2 M. A. Baldo, D. F. O'Brien, Y. You, A. Shoustikov, S. Sibley, M. E. Thompson, S. R. Forrest, *Nature* **395**, 151–154 (1998).
- 3 M. C. Suh, B. D. Chin, M.-H. Kim, T. M. Kang, S. T. Lee, *Adv. Mater.* **15**, 1254–1258 (2003).
- 4 G. B. Blanchet, Y.-L. Loo, J. A. Rogers, F. Gao, C. R. Fincher, *Appl. Phys. Lett.* **82**, 463–465 (2003).
- 5 H. Burroughes, D. D. C. Bradley, A. R. Brown, R. N. Marks, K. Nakay, R. H. Friend, P. L. Burns, A. B. Holmes, *Nature*, **374**, 539 (1990).
- 6 A. Meisel, T. Miteva, G. Glaser, V. Scheumann, D. Neher, *Polymer*, **43** 5235 (2002).
- 7 X. Jiang, S. Liu, M. S. Liu, H. Ma, A. K. Jen, *Appl. Phys. Lett.* **76**, 2985 (2000).
- 8 X. Gong, D. Moses, A. J. Heeger, S. Liu, A. K. Jen, *Appl. Phys. Lett.* **83**, 183 (2003).
- 9 L. F. Thompson, R. E. Kerwin, in "Polymer Resist Systems for Photo- And Electron Lithography" *Ann Rev. Mater. Sci.*, **6**, 267 (1976).
- 10 M. Remmers, D. Neher, G. Wegner, *Macromol. Chem. Phys.* **198**, 2551 (1997).
- 11 X.-C. Li, T.-M. Yong, J. Grüner, A. B. Holmes, S. C. Moratti, F. Cacialli, R. H. Friend, *Synth. Met.* **84**, 437 (1997).
- 12 P. Le Barny, C. Bouche, H. Facoetti, F. Soyer, P. Robin, *Proc. SPIE* **3148**, 160 (1997).
- 13 Y.-D. Zhang, R. D. Hreha, G. E. Jabbour, B. Kippelen, N. Peyghambarian, S. R. Marder, *J. Mater. Chem.* **12**, 1703 (2002).

- 14 B. Domercq, R. D. Hrehla, Y.-D. Zhang, N. Larribeau, J. N. Haddock, S. Schultz, S. R. Marder, B. Kippelen, *Chem. Mater.* **15**, 1491 (2003).
- 15 A. Bacher, C. H. Erdelen, W. Paulus, H. Ringsdorf, H.-W. Schmidt, P. Schumacher, *Macromolecules* **32**, 4551 (1999).
- 16 T. J. J. M. Kock, B. de Ruiter, *Synth. Met.*, **79**, 215 (1996).
- 17 A. E. A. Contoret, S. R. Farrar, P. O. Jackson, S. M. Khan, L. May, M. O'Neill, J. E. Nicholls, S. M. Kelly, G. J. Richards, *Adv. Mater.* **12**, 971 (2000).
- 18 A. E. A. Contoret, S. R. Farrar, M. O'Neill, J. E. Nicholls, *Chem. Mater.* **14**, 1477 (2002).
- 19 A. E. A. Contoret, S. R. Farrar, S. M. Khan, M. O'Neill, G. J. Richards, M. P. Aldred, S. M. Kelly, *J. Appl. Phys* **93**(3), 1465 (2003).
- 20 M. P. Aldred, A. J. Eastwood, S. M. Kelly, P. Vlachos, A. E. A. Contoret, S. R. Farrar, B. Mansoor, M. O'Neill, W. C. Tsoi, *Chem. Mater.* **16**, 4928–4936 (2004).
- 21 J.-P. Chen, G. Klärner, J.-I. Lee, D. Markiewicz, V. Y. Lee, R. D. Miller, J. C. Scott, *Synth. Met.* **107**, 129 (1999).
- 22 G. Klärner, J.-I. Lee, V. Y. Lee, E. Chan, J.-P. Chen, A. Nelson, D. Markiewicz, R. Siemens, J. C. Scott, R. D. Miller, *Chem. Mater.* **11**, 1800 (1999).
- 23 E. Bellmann, S. E. Shaheen, S. Thayumanavan, S. Barlow, R. H. Grubbs, S. R. Marder, B. Kippelen, N. Peyghambarian, *Chem. Mater.* **10**, 1668 (1998).
- 24 R. Böhner, C. Erdmann, O. Nuyken, *Macromol. Symp.* **107**, 125 (1996).
- 25 S. Inoue, T. Aida, in: *Ring-Opening-Polymerisation*, K. J. Ivin, T. Saegusa, Eds., Elsevier Applied Science Publishers, New York, 1984, Bd. 1, Kap. 4, S. 185 ff.
- 26 S. Penczek, P. Kubisa, Cationic Ring-opening Polymerisation: Ethers, in: *Comprehensive Polymer Science*, edited by G. Allen, III, 751–786 (Pergamon Press, Oxford, 1989).
- 27 T. Saegusa, *J. Macromol. Sci. Chem. A* **6**, 997 (1972).
- 28 H. Sasaki, J. V. Crivello, *J. Macromol. Sci. Chem. A* **29**, 915 (1992).
- 29 *Chemistry and Technology of UV & EB Formulation for Coatings, Inks & Paints*, G. Webster, (ed.), Band 3: V. Crivello & K. Dietliker: *Photoinitiators for free radical, cationic & anionic photopolymerisation*, 2. edn, Wiley, 1998.
- 30 J.-P. Fouassier: *Photoinitiation, Photopolymerization, and Photocuring: Fundamentals and Applications*, München, Hanser 1995.
- 31 R. J. Devoe, M. R. V. Sahyun, N. Serpone, D. K. Sharma, *Canad. J. Chem.* **65**(10), 2342–9 (1987).
- 32 S. Fung, S. C. Moratti, S. C. Graham, R. H. Friend, *Synth. Met.* **102**, 1167 (1999).
- 33 D. Müller, N. Riegel, P. Rudati, M. Rojahn, O. Nuyken, K. Meerholz, in preparation.
- 34 M. S. Bayerl, T. Braig, O. Nuyken, C. D. Müller, M. Gross, K. Meerholz, *Macromol. Rapid Commun.* **20**, 224 (1999).
- 35 M. Rojahn, PhD thesis, Technical University of Munich, 2003.
- 36 C. D. Müller, M. Gross, K. Meerholz, T. Braig, M. Bayerl, F. Bielefeldt, O. Nuyken, *Synth. Met.* **111–112**, 31 (2000).
- 37 T. Braig, C. D. Müller, M. Gross, K. Meerholz, O. Nuyken, *Macromol. Rapid Commun.*, **21**, 583 (2000).
- 38 E. Bacher, M. Bayerl, P. Rudati, N. Riegel, D. Müller, K. Meerholz, O. Nuyken, *Macromolecules* **38**, 1640 (2005).
- 39 S. Jungermann, O. Nuyken, N. Riegel, D. Müller, K. Meerholz, in preparation.
- 40 C. D. Müller, T. Braig, H. Nothofer, M. Arnoldi, M. Gross, U. Scherf, O. Nuyken, K. Meerholz, *Chem. Phys. Chem.* **1**, 207 (2000).
- 41 Becker, H., Heun, S., Treacher, K., Büsing, A. Falcou, A. *SID, Dig. Tech. Papers* **33**, 780–782 (2002).
- 42 C. D. Müller, N. Reckefuss, A. Falcou, H. Becker, K. Meerholz, unpublished results.
- 43 X. Yang, D. C. Müller, D. Neher, K. Meerholz, *Adv. Mater.*, in press.
- 44 K. Meerholz, D. C. Müller, *Adv. Funct. Mater.*, **11**, 251 (2001).
- 45 M. Reufer, J. Feldmann, P. Rudati, A. Rühl, D. Müller, K. Meerholz, C. Kar-nutsch, M. Gerken, U. Lemmer, *Appl. Phys. Lett.* **86**, 221102 (2005).
- 46 T. Braig, M. S. Bayerl, O. Nuyken, D. C. Müller, M. Gross, K. Meerholz, *Polym. Mater. Sci. Eng.* **80**, 122 (1999).
- 47 R. Faber, A. Stasko, O. Nuyken, *J. Macromol. Sci. – Pure Appl. Chem. A* **38**, 353 (2001).

- 48 H. Becker, S. Heun, K. Treacher, A. Büsing, A. Falcou, *SID, Dig. Tech. Papers* **33**, 780–782 (2002).
- 49 C. D. Müller, A. Falcou, N. Reckefuss, M. Rohjan, V. Wiederhirn, P. Rudati, H. Frohne, O. Nuyken, H. Becker, K. Meerholz, *Nature* **421**, 829 (2003).
- 50 V. Wiederhirn, O. Nuyken, N. Reckefuss, P. Rudati, D. Müller, K. Meerholz, in preparation.
- 51 F. Bielefeld, diploma thesis Technical University of Munich, 1998.
- 52 W. Li, Q. Wang, J. Cui, H. Chou, S. E. Shaheen, G. E. Jabbour, J. Anderson, P. Lee, B. Kippelen, N. Peyghambarian, N. R. Armstrong, T. J. Marks, *Adv. Mater.* **11**(9), 730 (1999).
- 53 H. Yan, P. Lee, N. R. Armstrong, A. Graham, G. A. Evmenenko, P. Dutta, T. J. Marks, *J. Am. Chem. Soc.* **127**, 3172 (2005).
- 54 Y. Li, J. Ding, M. Day, Y. Tao, J. Lu, M. D'iorio, *Chem. Mater.* **15**, 4936 (2003).
- 55 K. Davidson, A. M. Ponsonby, *Synth. Met.* **102**, 1512 (1999).
- 56 R. A. M. Hikmet, R. Thomassen, *Adv. Mater.* **15**, 115 (2003).
- 57 E. Bacher, S. Jungermann, M. Rojahn, V. Wiederhirn, O. Nuyken, *Macromol. Rapid Commun.* **25**, 1191 (2004).
- 58 M. de la Rosa, K. Meerholz, unpublished results.
- 59 T. Tachikawa, N. Itoh, S. Handa, T. Miyake, *SID '04 Dig.*, 2004.
- 60 G. Trätting, A. Pogantsch, G. Langer, W. Kern, E. Zojer, *Appl. Phys. Lett.*, **81**, 4269 (2002).
- 61 Y. Koide, Q. Wang, J. Cui, D. Benson, T. J. Marks, *J. Am. Chem. Soc.* **122**, 11266 (2002).
- 62 T. Grandlund, T. Nyberg, L. Stolz-Raman, M. Svensson, O. Inganäs, *Adv. Mater.* **12**, 269 (2002).
- 63 S. Allard, L. Braun, M. Brehmer, R. Zentel, *Macromol. Chem. Phys.* **204**, 68 (2003).
- 64 J. Barche, S. Janietz, M. Ahles, R. Schmechel, H. von Seggern, *Chem. Mater.* **16**, 4286 (2004).

## 10

### Hybrid OLEDs with Semiconductor Nanocrystals

*Andrey L. Rogach and John M. Lupton*

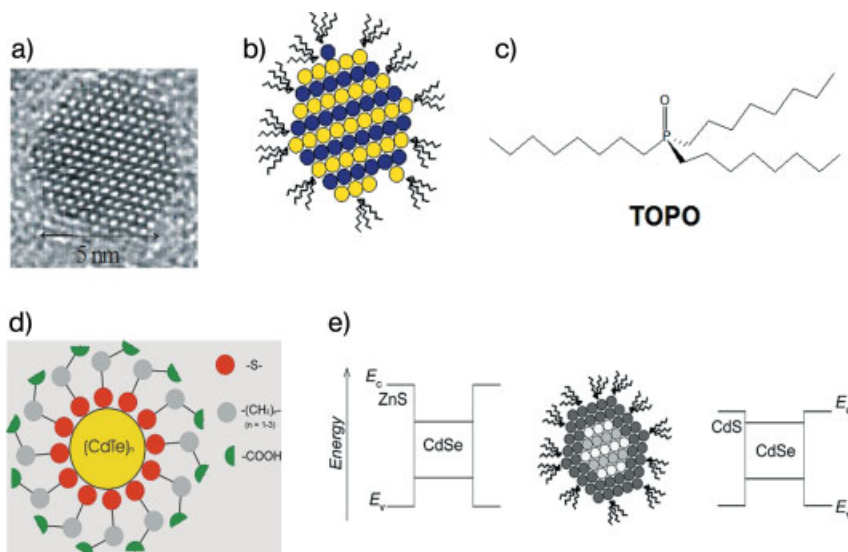
#### 10.1

##### Introduction

The advantages of the rapidly developing organic light-emitting diode (OLED) technology [1] can be combined with attractive properties of semiconductor nanocrystals (NCs). Optical properties of this class of lumophores are determined by the quantum-confinement effect [2], so that their emission color (Fig. 10.1) and the electron affinity can be finely controlled not only by the material choice but also by size within a single synthetic route. A typical semiconductor NC, which can also be thought of as a colloidal quantum dot, consists of an inorganic core, which is comparable to or smaller in size than the Bohr exciton diameter of the corresponding bulk material (Fig. 10.2(a)), surrounded ("passivated") by an organic shell of ligands (Fig. 10.2(b)–(d)). State-of-the-art syntheses, which can be carried out either in organic solvents or in water, provide different II–VI and III–V NCs with variable size and a narrow size distribution leading to the narrow emission spectra – 25–35 nm full width at half maximum (FWHM) in solution – tunable from the UV to the near-infrared spectral region [5]. Proper surface passivation leads to improved chemical stability and high photoluminescence (PL) quantum yields of > 50% for so-called core-shell NCs like CdSe/ZnS or CdSe/CdS [6, 7], where the large bandgap semiconductors (ZnS or CdS) epitaxially overgrow the core material (CdSe) and the band edges of the core material lie inside the bandgap of the outer material (Fig. 10.2(e)). Variable surface chemistry of NCs allows for the ease of their processability from different solvents and of their incorporation into different organic matrices. On the other hand, the conduction properties of NC-only films are poor [8], and it is difficult to achieve an electrical contact to single NCs because of their small size. An impressive exception to this was, however, the demonstration of Coulomb-blockade effects in single-electron transistors incorporating CdSe NCs [9]. Taking these aspects together, these particularities of NCs make them attractive materials for fabrication of hybrid semiconductor NC/organic LEDs with highly saturated emission color, which is of importance to the development of full-color large-area flat-panel displays. The basic



**Fig. 10.1** Size-dependent photoluminescence of CdTe NCs synthesized in water (2–5 nm size range, the smallest particles emit green, the largest red, quantum yield is up to 40 % [3]).



**Fig. 10.2** (a) High-resolution transmission electron microscopy image of a CdSe NC demonstrating the quality of a single-crystal semiconductor core. (b) Schematic representation of a NC consisting of a semiconductor core coated by “TOPO” ligand molecules and (c) one of the organic molecules typically used as a ligand in the organometallic synthesis [4]

of CdSe NCs – tri-n-octylphosphine oxide (TOPO). (d) Schematic representation of a water-soluble CdTe NC coated by short-chain mercapto-acid molecules [3]. (e) Schematic representation of a core/shell NC and the band structures for the typical materials CdSe/ZnS and CdSe/CdS.

idea behind NC-based OLEDs is to achieve full color tunability in a single host material. Although organic molecules span the entire visible spectrum in terms of emission wavelength, a change of material required to tune the color of emission can result in a dramatic modification of the charge-transport properties and thus of the device characteristics. A key goal of research into OLEDs is therefore a separate optimization of charge-transport and emission properties, which can be achieved in certain hybrid devices. Whereas organic semiconductors are typically

hole-transporting materials, NC solids generally display a strongly n-type behavior [10], i. e. preferentially conduct electrons, which make the two classes of materials a natural choice of partners. NC electroluminescence (EL) was first demonstrated ten years ago and has received a vast amount of attention since then, with the original paper on hybrid organic-inorganic LEDs [11] topping 600 citations. Interestingly, subsequent endeavors to employ and perfect the technology have been far and few and stand in no relation to the flurry of the field of all-organic LEDs. There is thus plenty of scope for future research and development activity in this field, and indeed ample potential to design novel, nanoscale device structures.

This chapter provides an overview on hybrid semiconductor NCs/organic LEDs, and is divided into two parts describing the devices operating in the visible and near-infrared spectral regions. The subsection on the visible LEDs is in turn divided into two parts describing composites processed from organic solvents and from aqueous solutions. The organic component of the hybrid LEDs is either (and mainly) a conjugated polymer, such as poly(para-phenylenevinylene) (PPV), a nonconjugated polymer, such as polyvinylcarbazole (PVK), or a small organic molecular material such as aluminum-tris-(8-hydroxyquinoline) (Alq<sub>3</sub>).

## 10.2

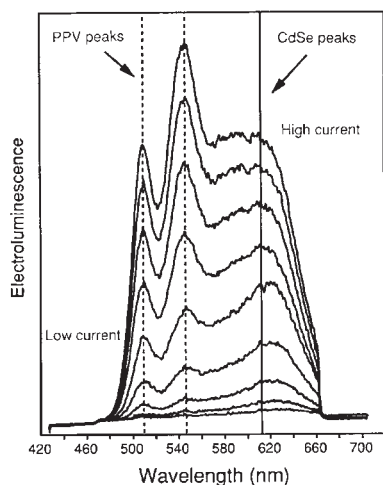
### LEDs in the Visible based on Composites of Semiconductor Nanocrystals and Polymers or Nanocrystals and Small Organic Molecules

#### 10.2.1

##### Devices Processed from Nanocrystals in Organic Solvents

The first paper on hybrid NC/polymer LEDs from the Berkeley group appeared in 1994 [11] and reported on a bilayer device comprising a thin (few tens of nm) layer of CdSe NCs deposited on a conducting support with the help of a bifunctional linker hexane dithiol, and a 100-nm thick layer of a soluble PPV derivative. The structure was sandwiched between an ITO-coated glass and a Mg/Ag electrode, which functioned as anode and cathode, respectively. The device with a hole-transporting PPV layer close to the ITO, with electrons injected into a layer of NCs and holes injected into a layer of polymer (forward bias) exhibited an emission characteristic of the CdSe NCs at the operating voltage of only 4 V, with an EL band tunable from yellow to red by changing the NC size. The *I*-*V* characteristics were determined by electron injection at the Mg/CdSe NC interface, which constituted the current-limiting mechanism. The recombination zone most likely lay within the CdSe NC layer close to the CdSe/PPV interface. At higher voltages, green emission from the PPV layer predominated, giving rise to a voltage-dependent color of this device (Fig. 10.3).

A subsequent paper from two MIT groups [12] reported on a single-layer device where CdSe NCs were homogeneously distributed within a polymer layer (70–120 nm thick) of PVK as a hole-conducting component that additionally contained an oxadiazole derivative (butyl-PBD) as an electron-transporting molecular species.



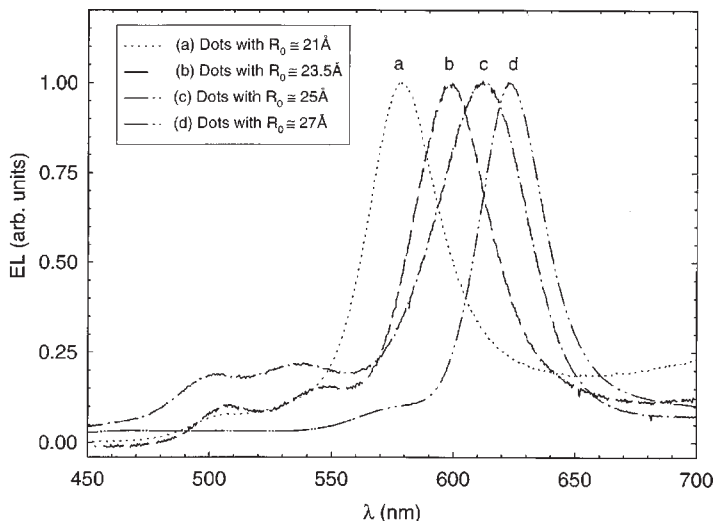
**Fig. 10.3** Voltage-dependent color of a CdSe NC/PPV device. Reprinted from [11], Copyright 1994, with permission from Nature Publishing Group.

The resulting volume fraction of CdSe NCs in a film sandwiched between ITO and Al electrodes was 5–10 %, below the percolation threshold for charge transport to occur between the NCs. The PL and EL spectra of the devices were reasonably narrow ( $< 40$  nm FWHM) and nearly identical, and were tunable from 530 to 650 nm by varying the NC size. The  $I$ - $V$  traces showed nearly inversion symmetry, and the EL in reverse bias (negative terminal on ITO) showed no change in the spectral line shape in comparison to that at the forward bias, indicating that NCs were not directly involved in carrier transport. Both the injection of electrons and holes by tunneling through the organic ligands were considered as excitation mechanisms of the NCs as well as Förster energy transfer from excitations formed in the organic host.

While the external quantum efficiencies of these first, unoptimized devices were low, on the order of 0.001 %, these studies showed a principal possibility of generating a spectrally pure EL from semiconductor NCs in hybrid devices. In this case, the EL is tunable by changing the physical size of the NC without the need for changing the actual chemistry of the material as is often the case for organic chromophores. Subsequent papers of the same groups reported on bilayer devices based on core-shell NCs [13, 14]. The devices of ref. [13] consisting of a spin-deposited layer of PPV on an ITO support and a spin-deposited layer of core/shell CdSe/CdS NCs adjacent to a Mg/Ag electrode showed sufficient improvements over the core-only CdSe-based devices, namely a factor of 20 increase in efficiency and a factor of 100 in lifetime. These devices could be tuned to emit from the green to the red with external quantum efficiencies of up to 0.22 % at brightnesses of  $600 \text{ cd/m}^2$  and current densities of  $1 \text{ A/cm}^2$ , with operating voltages of 4 V and lifetimes under direct current of hundreds of hours. In CdSe/CdS NCs, the hole is effectively confined to the core leading to a decreased probability of NC oxidation, while the combination of a small potential barrier between the core and shell conduction band (Fig. 10.2(e)) and a small electron effec-

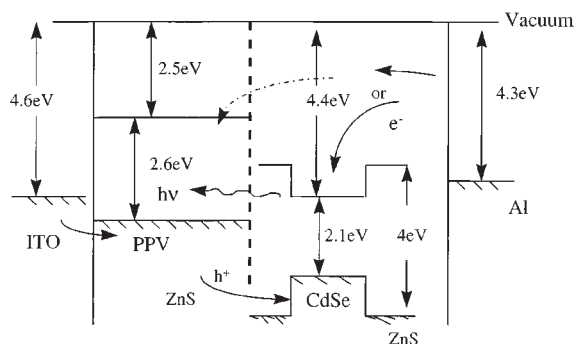
tive mass leads to a delocalization of the electron wavefunction over the whole NC that facilitates electron capture and transport [13]. Thus, the behavior of these LEDs was consistent with the picture of a field-dependent range of electron migration distance in the NC layer, which is limited by carrier trapping. Charge transport in densely packed solids of semiconductor NCs is a particularly intriguing process due to the large distribution of trapping times observed in charge-transport and photocurrent measurements [15]. Very recently it was demonstrated that the transport can be accurately described by the model of variable-range hopping conduction [16]. Such an accurate knowledge of charge injection and transport in the NC layer is imperative to designing and optimizing hybrid device operation.

Similar characteristics were reported in ref. [14] on a comparable bilayer device made of bare CdSe or core-shell CdSe/ZnS NCs spin cast from toluene solution on a PPV layer, which in turn was built up from aqueous solution by the layer-by-layer deposition technique in combination with polymethacrylic acid (PMA) (more on the layer-by-layer technique in Section 10.2.2). The PPV/PMA film served as a hole-transport layer and reduced the flow of electrons, thereby moving the electron-hole recombination zone away from the anode. The neat film of NCs was the electron transport layer that also served as the exciton recombination zone. Figure 10.4 shows size-dependent EL spectra of these devices employing bare CdSe NCs, demonstrating color tunability over a range of 80 nm. Evidently, there is still a considerable amount of PPV emission. This is due to the fact that direct recombination can also occur in the PPV layer. Figure 10.5 shows the energy-level diagram of the structure. The CdSe NC conduction band is substantially lower in energy than the lowest unoccupied molecular orbital (LUMO) of the



**Fig. 10.4** Size-dependent color of a CdSe NC/PPV device. Reprinted from [14], Copyright 1998, with permission from the American Institute of Physics.



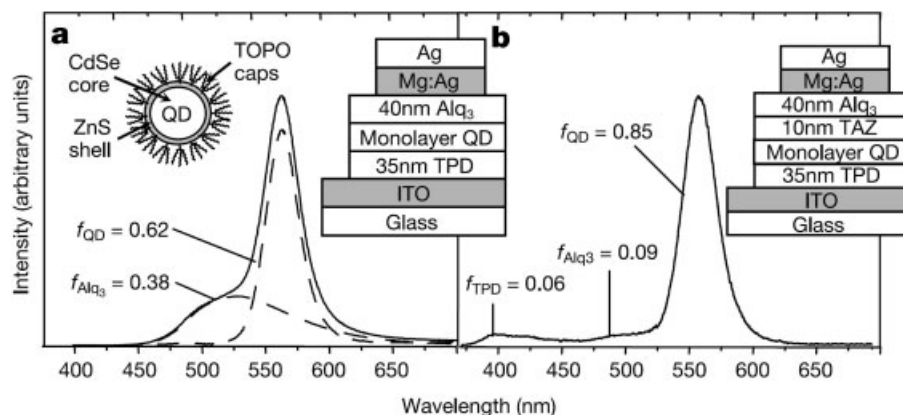


**Fig. 10.5** Energy diagram of a CdSe/ZnS NC/PPV device. Whereas the NC acts as an acceptor of electrons, there is a substantial barrier to be overcome for hole injection into the NC. An additional barrier to both electron and hole injection occurs due to the presence of the organic ligands. Reprinted from [14], Copyright 1998, with permission from the American Institute of Physics.

polymer. Conversely, the highest occupied molecular orbital (HOMO) of the polymer is substantially higher than the valence band of the NC. Consequently, there are rather large barriers for electron injection from the NC into the polymer ( $\sim 1.9$  eV) and for hole injection from the polymer into the NC ( $\sim 1.4$  eV). NCs can therefore be thought of as both electron acceptors and hole injectors in hybrids with conjugated polymers, as was demonstrated in photoinduced absorption measurements on blend systems [17]. Recombination in the electron-transporting NC layer is therefore preferable to recombination in the hole-transporting polymer in the case of the bilayer device, as the barrier to hole injection from the polymer to the NC layer is smaller than the barrier to electron injection from the NCs into the polymer. Following this reasoning, emission from the NCs dominates. This simple picture neglects the influence of the organic ligands, which are wide-gap insulators posing extremely large barriers for both electrons and holes. In addition, NCs capped with a ZnS overlayer will yield a modification of the relevant injection barrier, i. e. a substantial increase in the barrier to hole injection from the polymer. As the electrons are localized in the CdSe core of the NC, raising the valence band of the NC surface through ZnS capping should not have a dramatic effect on the barrier to electron injection into the polymer, as the overall energetic difference between the CdSe core conduction band and the polymer LUMO remains the same.

Further examples of hybrid NC/polymer LEDs emitting in the visible include single-layer devices constituting ZnS NCs synthesized in situ in a PMA-polystyrene (PS) matrix doped with tetraphenylbenzidine as a hole-transport material [18]; CdSe/ZnS-based LEDs, where the NC layers of different thicknesses (in the range of 30–250 nm) were deposited by spin-coating on a poly(3,4-ethylenedioxythiophene):polystyrenesulfonate (PEDOT:PSS) coated ITO substrate followed by deposition of various metal electrodes (Ba, Al, or Au) [19]; and multilayer LEDs made from ITO/PEDOT:PSS/PVK and a neat film of Mn-doped ZnS NCs, with an Al electrode on top [20]. The latter device showed EL both from the blue-emitting PVK and the yellow-emitting ZnS:Mn NCs, with an increasing contribution of PVK emission with rising voltage.

Trilayer hybrid NC/organic molecule LEDs with a single monolayer of CdSe/ZnS NCs sandwiched between two organic thin films have been introduced recently by two MIT groups [21, 22]. In these devices, the luminescence function of NCs was isolated from their participation in charge conduction, so that the organic layers transported charge carriers to the vicinity of the NC monolayer from which the narrow band EL originated. This differs from all previously reported concepts where the NCs had the dual function of both transporting electrons and serving as the emissive layer. An elegant phase-separation approach utilizing self-segregation of TOPO-capped NCs from the aromatic molecules of the hole-transporting material *N,N'*-diphenyl-*N,N'*-bis(3-methylphenyl)-(1,1'-biphenyl)-4,4'-diamine (TPD) spin-coated from their mixture in chloroform onto ITO substrates led to the formation of a complete single NC monolayer on top of a 35-nm thick TPD film. The final device was formed by thermal evaporation of a 10-nm thick layer of 3-(4-biphenyl)-4-phenyl-5-tert-butylphenyl-1,2,4-triazole (TAZ), followed by a 40-nm thick layer of Alq<sub>3</sub> and a Mg/Ag electrode. The function of TAZ was to block the holes and confine the excitons, leading to a narrower emission band with lower contributions from the TPD and Alq<sub>3</sub> EL in comparison to similar devices without the TAZ layer (Fig. 10.6). The external quantum efficiency of the device without TAZ was approx. 50% higher than in the presence of TAZ and exceeded 0.4% for a broad range of luminances. At 125 mA/cm<sup>2</sup>, the brightness of the three-layer device was 2000 cd/m<sup>2</sup> (i. e. 1.6 cd/A), which constitutes a 25-fold improvement over the best previously reported NC-based LEDs [13]. Although these devices exhibited a much faster response time than previous implementations, further studies are required to establish whether the exceptionally high switching speeds observed in all-organic LEDs can be matched by hybrid device structures. Charge trapping even at the monolayer thin QD layer will most likely limit the applicability to the sub-MHz region, whereas EL switching on the ns timescale has been demonstrated for all organic devices. In ref. [22], additional



**Fig. 10.6** EL spectra and schematic structures of two kinds of trilayer hybrid NC/organic molecule LEDs (with and without TAZ layer). Reprinted from [21], Copyright 2002, with kind permission of V. Bulovic.

studies on the devices utilizing CdSe NCs with variable ZnS shell thickness have shown that Förster energy transfer of excitons from organic materials to the NCs dominates the EL process, rather than direct charge injection into NCs. For the CdSe/ZnS-based devices with increased shell thickness of ZnS (2.5 monolayers ZnS on a CdSe core, which lead to a substantially improved passivation of surface quenching states and thus to a higher PL quantum yield), external quantum efficiencies of 1.1 % were achieved. The ZnS shell should pose a large barrier for hole injection from the organic into the CdSe core, thereby reducing the electron–hole capture probability on the NCs. This is not observed, and indeed the capture probability and quantum efficiency actually increase with shell thickness. The rise in EL efficiency is identical to the increase in PL efficiency upon capping, providing direct evidence for a predominant NC exciton generation channel through Förster transfer from the organic semiconductor. This is a further impressive illustration of how the NC and organic electronic properties can be modified and tuned independently of each other. The emission from the host was found to increase somewhat with increasing current density, which is a consequence of a broadening of the recombination region and thus a loss in Förster transfer efficiency. There is an intriguing issue that remains to be addressed using NC monolayers in organic LEDs, namely the role of triplet excitons. As these form the dominant excited-state species under electrical pumping due to spin statistics and the substantial exchange interaction in organic materials of order 1 eV, a vast amount of research effort over the past five years has been directed towards developing materials to harvest triplet excitations and enable radiative recombination through the phosphorescence channel. Spin is not a good quantum number in semiconductor NCs due to strong spin-orbit coupling arising from the presence of many atoms with large atomic order numbers. The exchange splitting is typically of the order of a few meV, so that singlet and triplets levels are effectively degenerate at room temperature. NCs could therefore potentially act as triplet harvesters, and it is a highly intriguing question whether the energy-transfer activation of the NCs in ref. [22] is indeed purely due to singlets or whether triplets can also be transferred, and subsequently decay radiatively on the NC. As the only competing relaxation channel for triplets in Alq<sub>3</sub> is comparatively slow nonradiative decay, migration distances are substantially larger than for singlets, so that they could potentially be harvested by a NC monolayer from a much broader recombination zone. Future research using phosphorescent organic compounds should be directed towards establishing whether triplet transfer from an organic semiconductor to a NC can indeed occur, or whether the opposite process may even be possible, i.e. triplet sensitization of the organic using semiconductor NCs.

A final interesting point in the monolayer device structure is the possibility of generating very high excitation densities at a well-defined position. This could prove useful to achieving the long sort-after goal of electrically pumped lasing in an organic semiconductor. The authors of ref. [22] propose that at the highest excitation densities employed at most 1 % of the NCs are excited. By employing NCs with substantially longer lifetimes, this ratio could be raised substantially, which may enable the observation of interesting collective effects.

Following these recent successful developments, trilayer hybrid NC/polymer devices were reported, constituting a film of CdSe/ZnS NCs a few monolayers thick sandwiched between films of PVK (hole transporter) and butyl-PBD (electron transporter) [23]. All the layers were deposited by a spin-coating technique from dissimilar solvents (either organics or water). These devices showed 20 times the external quantum efficiency (0.2%) and less than half the threshold voltage of a single-layer device based on the PVK/NC/PBD blend. These improvements upon going from a blend to a trilayer structure were attributed to more balanced carrier conduction to and enhanced recombination in the NC layer.

### 10.2.2

#### **Devices Processed from Nanocrystals in Aqueous Solutions**

NCs synthesized in aqueous solutions can be rendered charged at specific pH because of the free functional groups of ligand molecules (typically  $-\text{COOH}$  or  $-\text{NH}_2$  in the case of thioacids and thioamines). This allows processing of NCs following the layer-by-layer assembly approach [24]. This technique, which is based on alternating adsorption of oppositely charged species, was originally developed for positively and negatively charged polyelectrolyte pairs, either insulating [25] or conducting [26], and was later extended to the assembly of polymer-linked NCs. The methodology is very general and produces large-area high-quality homogeneous films almost irrespective of the substrate or NC materials, and with controllable thickness and composition.

The first hybrid NC-based LED made by layer-by-layer assembly was reported in ref. [27]. It was built up from 20 alternating double layers of a precursor of PPV (pre-PPV) and CdSe NCs capped by thiolactic acid, followed by thermal conversion of pre-PPV to PPV. The device emitted white light originating mainly from recombination through NC trap sites, with a turn-on voltage of 3.5–5 V and an external quantum efficiency of 0.0015%. The subsequent paper from the same group [28] compared single-layer CdSe NC-based devices utilizing conducting (PPV) or nonconducting (poly(allylamine hydrochloride)) (PAH) polymers and demonstrated the possibility to build up vertically structured bilayer CdSe NC/PAH – PPV/PAH LEDs. These devices showed a predominant emission either from the preferentially hole-transporting PPV or from the preferentially electron-transporting CdSe NCs, depending on the polarity of the applied field and the effective position of the recombination zone. The lifetime of the PPV emission in the bilayer device was found to be strongly increased, which may be due to the consumption of trace oxygen by CdSe NCs. It is interesting to note that the fact that CdSe can bind oxygen in dangling bonds on its surface may thus prove beneficial in two ways. First, NCs could help reduce the level of oxygen in organic semiconductors, which is detrimental to operation, and secondly, molecular oxygen can actually lead to a dramatic enhancement in fluorescence efficiency from NCs due to more efficient neutralization following an undesired photochemical charging event [29].

EL of different colors (from green to red) was obtained from layer-by-layer assembled LEDs based on thioglycolic acid capped CdTe NCs of different sizes and poly(diallyldimethylammonium chloride) (PDDA) [30]. In spite of the use of an insulating polymer, external quantum efficiencies of 0.1 % were achieved. Light emission was observed at current densities of 10 mA/cm<sup>2</sup> and at exceptionally low onset voltages of 2.5–3.5 V (i. e. only just above the bandgap of the CdTe NCs). The EL onset showed a dependence on the thickness of the film, indicating field-dependent current injection. The internal charge transport in these devices can be considered as a hopping transport between NCs acting as an electron-transporting material, which is driven by the external electric field. The EL of bi-layer devices, where each layer consisted of 20 alternating double layers of CdTe NCs (with a bimodal size distribution) and PDDA, showed emission from the NCs close to the ITO electrode. Layer-by-layer assembled LEDs based on water-soluble CdTe NCs and PPV were also reported [31]. Water-soluble CdTe NCs have also been incorporated into preformed films of electrochemically polymerized polyaniline by soaking [32]. Alternatively, polypyrrole has been electrochemically deposited from aqueous solution within the pores of drop-cast CdTe NC films [33]. Both of these device geometries led to visible-light emission at low biases of 2.5–3 V.

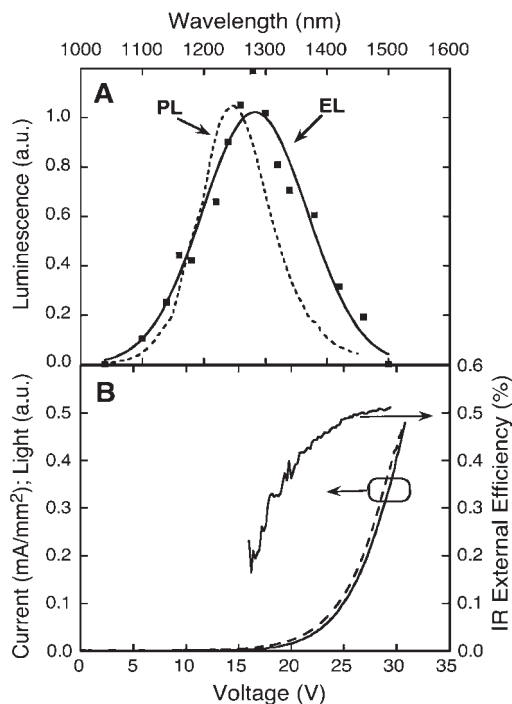
### 10.3

#### Near-infrared LEDs based on Composites of Semiconductor Nanocrystals and Polymers or Small Organic Molecules

Because of the limited choice of polymers and organic dyes emitting in the range of telecommunications windows (1.3 and 1.55  $\mu\text{m}$ ), the use of the near-infrared (NIR) emitting NCs in hybrid organic-inorganic LEDs provides a particularly attractive application window. The first paper on such LEDs appeared in 2002 and reported on single-layer blend devices [34]. They were based on composite mixed films of core-shell InAs/ZnSe NCs and a conducting polymer – either poly[2-methoxy-5-(2-ethylhexyloxy)-1,4-phenylenevinylene] (MEH-PPV) or poly[9,9-dehexylfluorenyl-2,7-diyl]-co-(1,4-{benzo-[2,1',3]thiadiazole})] (F6BT) spin cast from toluene solutions. The devices showed broad emission in the range of 1.3  $\mu\text{m}$ , which was attributed to the inhomogeneously broadened spectrum of the ensemble of differently sized NCs, with a rather high turn-on voltage of 15 V and a remarkably high external quantum efficiency reaching 0.5 % at high operating voltages (Fig. 10.7). The turn-on voltage increased in a series of LEDs with increasing volume fraction of NCs in the polymer, which is consistent with trapping of carriers at the NC sites and thus trap-limited transport in the blend. The quenching of both the PL and the EL of the host polymer matrix, however, also pointed to a possible role of energy transfer from the polymer host to the NCs.

In a subsequent report, EL spectra of single-layer devices based on the mixtures of PbS NCs with MEH-PPV or poly(2-(6-cyano-6'-methylheptyloxy)-1,4-phenyl-

**Fig. 10.7** (A) The PL spectrum of InAs/ZnS NCs in solution (dashed line) and the EL spectrum of a InAs/ZnS NCs/MEH-PPV LED (squares and solid line). (B) Current (dashed line), light (solid line) and external quantum efficiency (solid line, right axis) of the LED as a function of applied voltage. Reprinted from [34], Copyright 2002 AAAS.



ene) (CN-PPP) were shown to be potentially tunable across the range of 1000 to 1600 nm in ref. [35]. The EL intensity of the PbS NCs capped with octylamine (8 carbon atoms in the chain) was much higher than those capped with oleic acid (18 carbon atoms in the chain), which was explained by the suppression of either Förster energy transfer or direct carrier transfer from the polymer to the NCs in the case of the longer ligands.

Single-layer devices based on the blend of a methyl-substituted ladder-type poly(para-phenylene) (MeLPPP) and HgTe NCs synthesized in water and transferred to toluene, whose emission wavelength is tunable between 900 nm and 2000 nm by changing the NC size, were fabricated by spin coating from toluene solution and sandwiching between ITO and Al electrodes [36]. They showed both blue-green emission from MeLPPP and a near-IR emission from HgTe NCs, the latter with a turn-on voltage of 10 V and an external quantum efficiency of the unoptimized device of roughly 0.001 %.

Following the developments of trilayer hybrid visible NC-based LEDs [21, 22], trilayer NC/organic molecule NIR LEDs with a single monolayer of PbSe NCs sandwiched between two organic thin films were presented in ref. [37]. The fabrication was similar to the visible CdSe/ZnS-based LEDs and utilized the self-segregation process of the PbSe NCs (capped by oleic acid) from the hole-transporting organic molecules TPD or 4,4-bis[N-(1-naphthyl)-N-phenylamino]biphenyl (a-NPD) in chloroform. The electron-transporting layer of Alq<sub>3</sub> and/or bathocu-

proine was thermally evaporated on top. The NIR EL spectra of the devices fabricated were tunable from 1.33 to 1.56  $\mu\text{m}$  by changing the size of the PbSe NCs from 4 to 5 nm, with a FWHM of  $< 160$  nm ( $< 0.11$  eV). The external quantum efficiency of the NIR EL of these devices was measured to be 0.001 %, which was limited by the reduced PL quantum efficiency of closely packed PbSe NCs in the solid state as well as the unoptimized spectral overlap of the organic components and NIR-emitting NCs.

#### 10.4

##### Concluding Remarks

Research on hybrid semiconductor NC/organic LEDs has achieved a remarkable development in the span of one decade, involving more than two orders of magnitude improvement in the external quantum efficiency and providing highly saturated color emission. Although the device efficiencies are still over an order of magnitude lower than those of the purely organic counterparts, there are a number of potential advantages associated with NC-based devices, which will certainly merit future research. A variety of device configurations have become available including the promising sandwich architecture comprising only one monolayer of NCs serving exclusively as emitters. Further technological improvements of NC/organic LEDs are bound to follow, aimed at optimizing charge injection and transport. New concepts are also being explored, such as a current-in-plane architecture with a lateral configuration of electrodes relying on electronic tunneling through a mesoscopic metal layer with embedded semiconductor NCs [38]. Hybrid NC/organic LEDs emitting in the near-IR may become highly competitive with organic-only LEDs, which are hard to realize in the IR. The combination of the particle-size-dependent tunability of the spectral properties with the ease of processability and beneficial charge-transport properties of the organic counterparts has already demonstrated the fruitful synthesis of organic and inorganic materials science. A particularly promising avenue for the cooperation between organic and inorganic synthetic chemists is the rich spectrum of functionality attainable through tuning the stabilizing surface ligands of the NCs. One elegant approach to systematically do this has been to encage the NCs in complex organic star-shaped dendrimer structures, or indeed even synthesize the NCs directly in dendritic nanoreactors [39–43]. As dendrimers on their own are very promising materials for display applications, the high level of control of processability attainable with dendritic functionality of semiconductor NCs yields promise that both the vertical as well as the lateral positioning of NCs in OLEDs can be improved dramatically. Microcontact printing of dendrimer functionalized NCs was recently demonstrated [44]. As this is a key technology in OLEDs, it is only a matter of time before microcontact-printed full-color pixilated displays based on the hybrid organic/inorganic technology are developed. Future applications of the hybrid technology will also build on the demonstrations of efficient photovoltaic devices [45] and could be as diverse as laser diodes and electrically pumped single-photon



on-demand sources. A substantial development both in terms of the fundamental scientific impact, such as the underlying interaction mechanisms between delocalized inorganic and localized organic charges and excitations, as well as from a purely technological viewpoint are to be anticipated in the coming years.

## References

- 1 S. R. Forrest, *Nature* **2004**, 428, 911.
- 2 A. L. Efros, A. L. Efros, *Sov. Phys. Semicond.* **1982**, 16, 772.
- 3 N. Gaponik, D. V. Talapin, A. L. Rogach, K. Hoppe, E. V. Shevchenko, A. Kornowski, A. Eychmüller, H. Weller, *J. Phys. Chem. B* **2002**, 106, 7177.
- 4 C. B. Murray, D. J. Norris, M. G. Bawendi, *J. Am. Chem. Soc.* **1993**, 115, 8706.
- 5 A. L. Rogach, D. V. Talapin, H. Weller, *Semiconductor Nanoparticles*. In "Colloids and Colloid Assemblies", Ed. F. Caruso. WILEY-VCH, Weinheim, **2004**, pp. 52–95.
- 6 B. O. Dabbousi, J. Rodriguez-Viejo, F. V. Mikulec, J. R. Heine, H. Mattoussi, R. Ober, K. F. Jensen, M. G. Bawendi, *J. Phys. Chem. B* **1997**, 101, 9463.
- 7 X. Peng, M. C. Schlamp, A. V. Kadavanich, A. P. Alivisatos, *J. Am. Chem. Soc.* **1997**, 119, 7019.
- 8 C. A. Leatherdale, C. R. Kagan, N. Y. Morgan, S. A. Empedocles, M. A. Kastner, M. G. Bawendi, *Phys. Rev. B* **2000**, 62, 2669.
- 9 D. L. Klein, R. Roth, A. K. L. Lim, A. P. Alivisatos, P. L. McEuen, *Nature* **1997**, 389, 699.
- 10 D. Yu, C. Wang, P. Guyot-Sionnest, *Science* **2003**, 300, 1277.
- 11 V. L. Colvin, M. C. Schlamp, A. P. Alivisatos, *Nature* **1994**, 370, 354.
- 12 B. O. Dabbousi, M. G. Bawendi, O. Onitsuka, M. F. Rubner, *Appl. Phys. Lett.* **1995**, 66, 1316.
- 13 M. C. Schlamp, X. Peng, A. P. Alivisatos, *J. Appl. Phys.* **1997**, 82, 5837.
- 14 H. Mattoussi, L. H. Radzilowski, B. O. Dabbousi, E. L. Thomas, M. G. Bawendi, M. F. Rubner, *J. Appl. Phys.* **1998**, 83, 7965.
- 15 D. S. Ginger, N. C. Greenham, *J. Appl. Phys.* **2000**, 87, 1361.
- 16 D. Yu, C. Wang, B. L. Wehrenberg, P. Guyot-Sionnest, *Phys. Rev. Lett.* **2004**, 92, 216802.
- 17 Y. C. Tseng, M. Tzolov, E. H. Sargent, P. W. Cyr, M. A. Hines, *Appl. Phys. Lett.* **2002**, 81, 3446.
- 18 Y. Yang, S. Xue, S. Liu, J. Huang, J. Shen, *Appl. Phys. Lett.* **1996**, 69, 377.
- 19 R. A. M. Hikmet, D. V. Talapin, H. Weller, *J. Appl. Phys.* **2003**, 93, 3509.
- 20 H. Yang, P. H. Holloway, B. B. Ratna, *J. Appl. Phys.* **2003**, 93, 586.
- 21 S. Coe, W.-K. Woo, M. Bawendi, V. Bulovic, *Nature* **2002**, 420, 800.
- 22 S. Coe, W.-K. Woo, J. S. Steckel, M. Bawendi, V. Bulovic, *Org. Electr.* **2003**, 4, 123.
- 23 S. Chaudhary, M. Ozkan, W. C. W. Chan, *Appl. Phys. Lett.* **2004**, 84, 2925.
- 24 N. A. Kotov, I. Dekany, J. H. Fendler, *J. Phys. Chem.* **1995**, 99, 13065.
- 25 G. Decher, J.-D. Hong, J. Schmitt, *Thin Solid Films* **1992**, 210–211, 831.
- 26 J. H. Cheung, A. F. Fou, M. F. Rubner, *Thin Solid Films* **1994**, 244, 985.
- 27 M. Gao, B. Richter, S. Kirstein, *Adv. Mater.* **1997**, 9, 803.
- 28 M. Gao, B. Richter, S. Kirstein, H. Möhwal, *J. Phys. Chem. B* **1998**, 102, 4096.
- 29 J. Müller, J. M. Lupton, A. L. Rogach, J. Feldmann, D. V. Talapin, H. Weller, *Appl. Phys. Lett.* **2004**, 85, 381.
- 30 M. Y. Gao, C. Lesser, S. Kirstein, H. Möhwal, A. L. Rogach, H. Weller, *J. Appl. Phys.* **2000**, 87, 2297.
- 31 W. Chen, D. Grouquist, J. Roark, *J. Nanosci. Nanotechnol.* **2002**, 2, 47.
- 32 N. P. Gaponik, D. V. Talapin, A. L. Rogach, A. Eychmüller, *Phys. Chem. Chem. Phys.* **1999**, 1, 1787.
- 33 N. P. Gaponik, D. V. Talapin, A. L. Rogach, *J. Mater. Chem.* **2000**, 10, 2163.



- 34 N. Tessler, V. Medvedev, M. Kazes, S. H. Kan, U. Banin, *Science*, **2002**, 295, 1506.
- 35 L. Bakueva, S. Musikhin, M. A. Hines, T.-W. F. Chang, M. Tzolov, G. D. Scholes, E. H. Sargent, *Appl. Phys. Lett.* **2003**, 82, 2895.
- 36 D. S. Koktysh, N. Gaponik, M. Reufer, J. Crewett, U. Scherf, A. Eychmüller, J. M. Lupton, A. L. Rogach, J. Feldmann, *Chem. Phys. Chem.* **2004**, 5, 1435.
- 37 J. S. Steckel, S. Coe-Sullivan, V. Bulovic, M. G. Bawendi, *Adv. Mater.* **2003**, 15, 1862.
- 38 EU project IST-2002-38195 FUNLIGHT. "Functional Nanoscale Materials and Devices for Light Emission".
- 39 K. Sooklal, L. H. Hanus, H. J. Ploehn, C. J. Murphy, *Adv. Mater.* **1998**, 10, 14.
- 40 B. I. Lemon, R. M. Crooks, *J. Am. Chem. Soc.* **2000**, 122, 12886.
- 41 J. J. M. Donners, R. Hoogenboom, A. P. H. J. Schenning, P. A. van Hal, R. J. M. Nolte, E. W. Meijer, N. A. J. M. Sommerdijk, *Langmuir* **2002**, 18, 2571.
- 42 R. C. Hedden, B. J. Bauer, A. P. Smith, F. Gröhn, E. Amis, *Polymer* **2002**, 43, 5473.
- 43 W. Guo, J. Jack Li, A. Wang, X. Peng, *J. Am. Chem. Soc.* **2003**, 125, 3901.
- 44 X. C. Wu, A. M. Bittner, K. Kern, *Adv. Mater.* **2004**, 5, 413.
- 45 W. U. Huynh, J. J. Dittmer, A. P. Alivisatos, *Science* **2002**, 295, 2425.

## 11

### Polymer Electrophosphorescence Devices

*Xiaohui Yang and Dieter Neher*

#### 11.1

##### Introduction

Electroluminescence from  $\pi$ -conjugated polymers was first reported in 1990 by Burroughes et al. [1]. Compared to inorganic materials and small molecules, polymers promise easy fabrication of large-area displays and illumination devices. In fact, the first flexible polymer light-emitting diode (LED) was demonstrated by Gustafsson et al. in 1992 [2].

Besides the cost of production and long-term stability, color purity and device efficiency are the crucial parameters concerning the applicability of light-emitting polymer systems in commercial devices. While the color of an organic LED is closely related to the electronic structure of the emitting electronic system, the device efficiency is determined by the complicated interplay between various physical processes. Nevertheless, certain limits can be given based on simple considerations. In particular, when assuming that balanced injection of charges is possible and assuring that all injected charges recombine, the external quantum efficiency (EQE) is simply the product of the radiative quantum efficiency  $\eta_{\text{R}}$  of the emitter (the probability that the excited state formed by the recombination of charges emits a photon) and the probability  $\varphi_{\text{ex}}$  that photons generated in the emission layer leave the device. Based on ray-optics considerations, Greenham et al. [3] have predicted  $\varphi_{\text{ex}}$  to range between 15 and 25 %, depending on the refractive index of the active layer. For the determination of the radiative quantum efficiency both fluorescence and phosphorescence have to be taken into account. Quantum statistics predicts that the recombination of uncorrelated electrons and holes in organic media forms triplet states with a 3-fold higher probability than singlet states [4]. The ground state of the vast majority of luminescent materials is a singlet state. Since most luminescent polymers such as poly(p-phenylene)s (PPPs), polyfluorenes (PFs) and poly(p-phenylenevinylene)s (PPVs), contain only low-Z elements, spin-orbit coupling is weak. Therefore, these compounds exhibit very small radiative rates for phosphorescence from excited triplet states. For example, the phosphorescent lifetime of an oligomer of a ladder-type PPP was determined

to be around 250 ms at 77 K [5]. Consequently, competing nonradiative processes such as triplet-triplet annihilation or vibronic relaxation processes effectively quench the phosphorescence. In fact, the phosphorescence of a solid layer of a ladder-type PPP (MeLPPP) decayed on a time scale of 10–100  $\mu$ s, equivalent to a phosphorescent quantum efficiency of only  $10^{-4}$  [5]. Electrically driven phosphorescence from pure hydrocarbon conjugated polymers has only been observed at very low temperatures [6]. Though it has been demonstrated that metallic impurities [7] or even the inclusion of high-Z elements into the polymer structure [8] can lead to electrically driven phosphorescence, no efficient LED has yet been reported based on these approaches. Thus, for most conjugated polymers, only the relaxation of the excited singlet state contributes to the radiative emission, setting the limit for the external quantum efficiency to ca. 5 %. Recent results have, however, questioned the assumption that the quantum statistics outlined above is also true for conjugated polymer samples [9–12]. On the other hand, to the best of our knowledge, only a few LEDs based on single-component active polymer layers exceeded the quantum limit of 5 %. [13, 14].

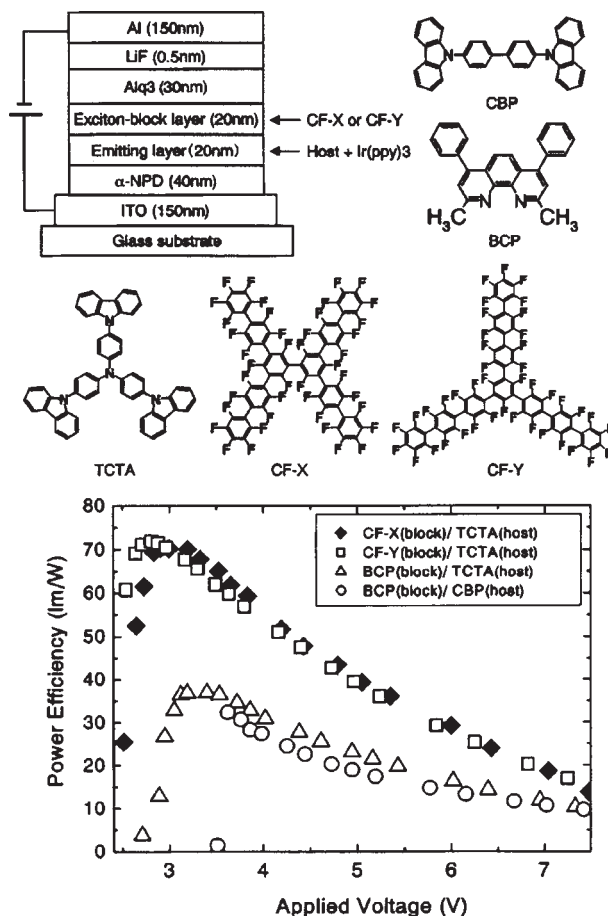


Fig. 11.1 The electrophosphorescent device structure used by Ikai et al. [17]. Also shown are the chemical structures of CBP, BCP, TCTA, CF-X and CF-Y. The power efficiency of the organic electrophosphorescent devices is shown in the lower graph.

In 1998, Baldo et al. [15] showed that the efficiency of organic LEDs can be improved by using phosphorescent dyes. In their device, the phosphorescent octaethyl-porphine platinum (PtEOP) dye was doped into an appropriate small molecule host at a low concentration. This electrophosphorescent device emitted red light with an external quantum efficiency of 4 %.

In the following years, the efficiencies of electrophosphorescent devices based on small molecules have been considerably improved, reaching impressive external quantum efficiencies of 11.6 % [16], 19.2 % [17, 18] and 10.3 % [19, 20] for blue, green and red emission, respectively. However, all of these devices consist of elaborate multilayer structures, including several charge-transporting and exciton-blocking layers (see Fig. 11.1 for an example of a highly efficient green-emitting device). Also, all these layers were deposited by thermal evaporation under high-vacuum condition, a process that might be relatively costly and time consuming for large-area production. Thus, considerable effort has been undertaken to fabricate highly efficient polymer electrophosphorescent devices.

This chapter is divided into six sections. Section 11.2 gives a short introduction into the optical and electronic properties of mostly used phosphorescent dyes. In Section 11.3, mechanisms of excitation of these dyes in polymer hosts will be discussed. The optimization of green, red, blue and white devices based on a PVK host is the subject of Section 11.4. The following two sections present selected examples of devices with conjugated polymer hosts or using fully functionalized polymers. Finally, a short conclusion and outlook summarize the current status of phosphorescent polymer LEDs.

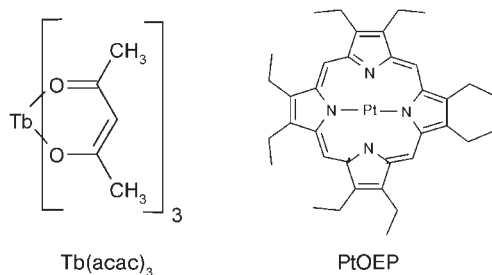
## 11.2

### Phosphorescent Dyes

In phosphorescent dyes, strong spin-orbit coupling leads to efficient intersystem crossing of the singlet excited states to the triplet manifold, and also mixes the singlet and triplet excited states, removing the spin-forbidden nature of the radiative transition of the triplet state to the ground state. Various kinds of phosphorescent dyes have been tested in OLEDs. We will focus here on three types of complexes, which are widely studied in OLEDs.

The first dye used in an electrophosphorescent LED was the terbium-complex  $\text{Tb}(\text{acetylacetonate})_3$  ( $\text{Tb}(\text{acac})_3$ , see Fig. 11.2) [21]. LEDs based on complexes with rare-earth central metals such as terbium or europium are very interesting for display applications, because they emit light with a very small spectral line width. These sharp emission lines are due to f-f transitions located on the central metal ion. Disadvantages of these complexes are, however, that color tuning via the chemical modification of the ligand is not possible and that the radiative lifetime of phosphorescence is rather long.

Baldo and coworkers [22, 23] were the first to use the red-emitting dye 2,3,7,8,12,13,17,18-octaethyl-21H,23H-porphine platinum (PtOEP, see Fig. 11.2) in an OLED. The absorption of this compound consists of a Soret band (at ca.

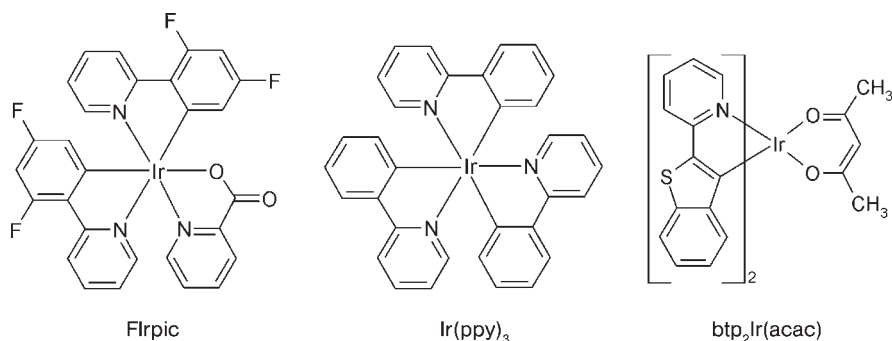


**Fig. 11.2** Chemical structure of Tb(acac)<sub>3</sub> and PtOEP.

390 nm) and a Q-band (500–540 nm), while the emission peaks at ca. 650 nm. The luminescence quantum efficiency measured for the dye in a deoxygenated toluene/DMF solution at room temperature is ca. 50 % [22]. The emission is largely ligand based and possesses a relatively long lifetime (83  $\mu$ s in toluene/DMF solution, 37  $\mu$ s in Alq<sub>3</sub> [22]). The triplet state of PtOEP lies at ca. 1.9 eV, which is similar to that of Alq<sub>3</sub> [23]. HOMO and LUMO levels are at 5.3 eV and 2.8 eV, respectively. It is, therefore, expected that PtOEP constitutes a carrier trap in many small molecule and polymer hosts. Unfortunately, the long radiative lifetime of PtOEP limits the performance of OLEDs particularly at high driving currents.

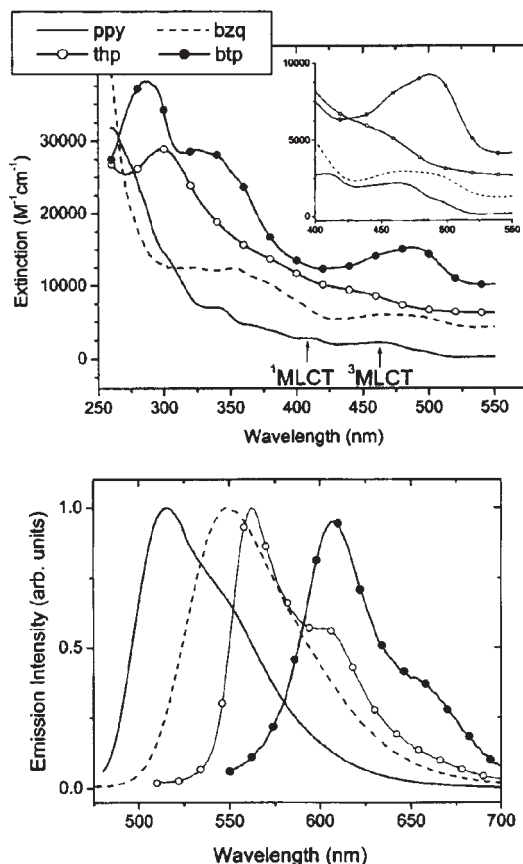
Today, the mostly used phosphorescent emitters are iridium complexes. Figure 11.3 shows the chemical structures of some popular iridium dyes.

The absorption spectra of the green-emitting ppy<sub>2</sub>Ir(acac) and the red-emitting btp<sub>2</sub>Ir(acac) complexes are shown in Fig. 11.4, together with those of two other complexes with intermediate emission wavelengths (with *bzq* and *thp*-ligands) [24]. The extinction coefficients for these bands are in the ranges expected for ligand-centered  $\pi\pi^*$  and metal-to-ligand charge-transfer (MLCT) bands, of about 30 000 and 6000 M<sup>-1</sup> cm<sup>-1</sup>, respectively. Strong spin-orbit coupling induced by Ir<sup>3+</sup> gives the formally spin-forbidden transition from the <sup>3</sup>MLCT to the singlet ground state a significant radiative allowedness. Note that, in Ir(ppy)<sub>3</sub> or ppy<sub>2</sub>-Ir(acac), the <sup>3</sup> $\pi\pi^*$  level is at an energy of 2.7 eV (corresponding to a wavelength



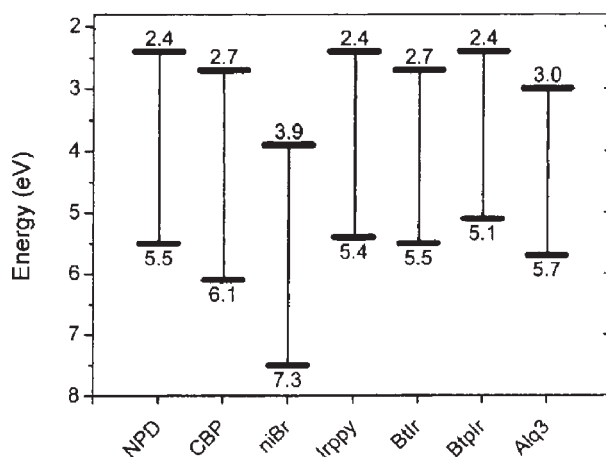
**Fig. 11.3** Chemical structures of commonly used Ir-dyes with blue, green and red emission: bis(2-(4,6-difluorophenyl)pyridyl-N,C<sup>2'</sup>)iridiumpicolinate (FIrpic), *fac*-tris(2-phenylpyridine) iridium Ir(ppy)<sub>3</sub> and bis(2-(2'-benzothieryl)-pyridinato-N,C<sup>3'</sup>)iridium(acetylacetonate) btp<sub>2</sub>Ir(acac).

**Fig. 11.4** The absorption and luminescence properties of various Ir(acac) dyes. Top: absorption spectra for dyes with different ligands. The spectra have been offset for clarity. Bottom: the corresponding photoluminescence spectra [24].



of 460 nm), so the  $^3\text{MLCT}$  is the lowest excited states. In contrast, the  $^3\pi\pi^*$  state of the thp-ligand is at 2.21 eV (564 nm), which is below the  $^3\text{MLCT}$  state, so a predominantly ligand-based state is the lowest-energy excited states in Ir(thp)<sub>3</sub>. A blue-shift of the emission from the triplet excited state is observed when adding fluorine atoms to the 4,6-positions of the 2-phenylpyridine ligand, as in bis(2-(4,6-difluorophenyl)pyridyl-N,C<sup>2'</sup>) iridium(acetylacetonate) (FIr(acac)) [25]. Replacement of the acetylacetonate ligand in FIr(acac) with picolinate (as in FIrp-pic) results in an additional blue-shift of 20 nm. This latter dye has been extensively studied as a blue-emitting phosphorescent dye in OLEDs. For more detailed discussions concerning the relative positions of  $^3\text{MLCT}$  and  $^3\pi\pi^*$  states in different Ir(III) complexes see [26].

Changing the chemical nature of the ligand strongly affects the HOMO and LUMO positions of the complexes (see Fig. 11.5). For example, Ir(ppy)<sub>3</sub> has the HOMO at 5.4 eV and will thus constitute a hole trap in most organic hosts [27]. The HOMO and LUMO level of FIrp-pic are at 5.8 eV and 2.9 eV, respectively [28]. Thus, this blue-emitting dye will predominantly act as an electron trap in many wide-bandgap matrices.

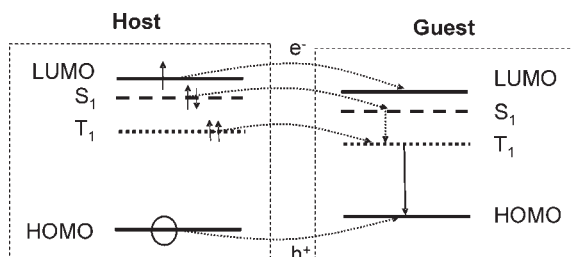


**Fig. 11.5** Positions of the HOMO and LUMO levels for various Ir-dyes, compared to some charge-transporting materials frequently used in OLEDs [27]. Here, niBr stands for N-2,6-dibromophenyl-1,8-naphthalimide, Irppy for Ir(ppy)<sub>3</sub>, Btrr for bis(2-phenylbenzothiazolato-n,C<sup>2'</sup>)iridium(acetyl-acetonate), Btp(Ir) for btp<sub>2</sub>Ir(acac), Alq<sub>3</sub> for Aluminium(III)-tris(8-hydroxyquinoline), NPD for 4,4'-bis(N-(1-naphthyl)-N-phenylamino)-biphenyl and CBP for 4,4'-N,N'-dicarbazolebiphenyl.

### 11.3

#### Transfer Processes in Polymer Hosts Doped with Phosphorescent Dyes

Unfortunately, the efficiency of pure layers of most phosphorescent dyes is very low, due to severe concentration-quenching (see, e.g., [29]). Therefore, the commonly used concept is to blend a low-molecular weight phosphorescent dye into a proper matrix. Transfer of excitation to the guest is then promoted by three processes (Fig. 11.6): Förster transfer of singlet excitons generated on the matrix to the guest, Dexter transfer of both singlet and triplet excitons generated on the host to the dopant as well as direct generation of singlet and triplet excitons on the guest. In the latter case, the host only functions as the charge-transporting matrix, while in the former cases excitons are first generated on the host and then transferred to the dopant. Förster transfer requires significant overlap of the emission spectrum of the matrix and the absorption spectrum of the guest.



**Fig. 11.6** Scheme illustrating various transfer processes from the host to the guest: electron (hole) transfer from the host LUMO (HOMO) to the guest LUMO (HOMO), Förster-type energy transfer between singlet states and Dexter-type energy transfer from the host to the guest triplet state. The nature of the excitonic state is simplified for better clarity.

Because most phosphorescent dyes used in LED applications have the most prominent absorption in the blue/deep blue wavelength region, wide bandgap materials have been used as hosts to insure efficient energy transfer in electrophosphorescent devices. Efficient Dexter transfer, in contrast, only requires that the energies of the (singlet and triplet) excitons on the host match the exciton energies on the guest. Finally, the phosphorescent dopant itself might function as a carrier trap and recombination site if there is a significant offset between the HOMO (or LUMO) positions of the host and the guest.

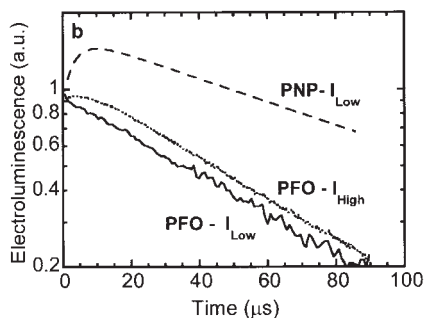
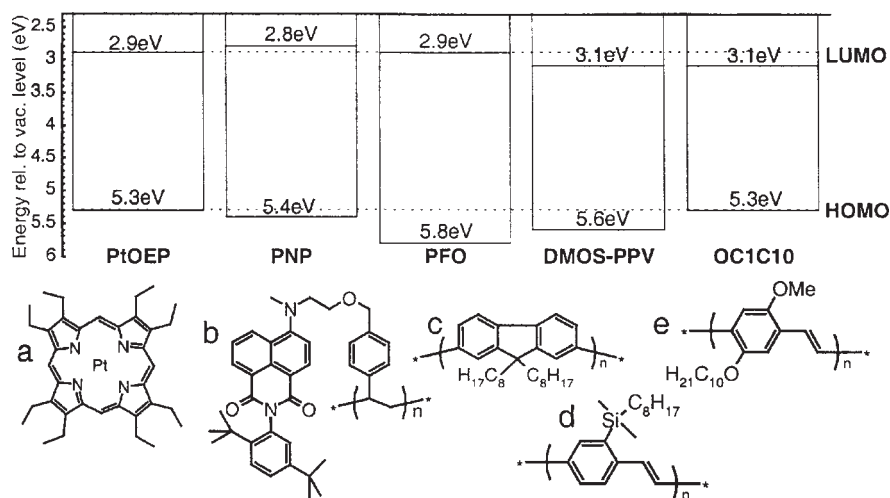
Irrespective of the process leading to the excitation of the dye, confinement of the triplet exciton on the dye is only guaranteed if the  $T_1$ - $S_0$  energy of the guest is smaller than that of the host. This limits the choice of polymer host materials, depending on the emission color of the dye. At this point one has to remember that the singlet-triplet splitting in conjugated polymers is quite significant.

Monkman et al. [30] have used pulse radiolysis and triplet energy transfer to measure the triplet energies in a broad range of different  $\pi$ -conjugated polymers. According to these results, the energy of the lowest triplet state  $T_1$  varies with the energy of the lowest singlet excited state  $S_1$  via  $E(T_1) = 1.13 \times E(S_1) - 1.45$  eV. This implies that for most conjugated polymers, the lowest excited singlet state is ca. 1 eV higher than  $T_1$ . Though others reported a slightly smaller singlet-triplet splitting of ca. 0.7 eV [8, 31], these results imply that only wide bandgap polymers are applicable as host materials for phosphorescent dyes. Nevertheless, a large variety of polymers with charge-transporting moieties in the sidechains [32–34] or fully conjugated polymers [35–42] have been demonstrated to function as hosts in electrophosphorescent devices.

Cleave et al. [35] have studied in detail the transfer processes between several polymer hosts and PtOEP. Figure 11.7(a) displays the chemical structures of the used compounds as well as their HOMO and LUMO positions. Four different situations were identified: If the offset of the HOMO (and LUMO) levels of the host and guest is small, carrier trapping is not significant and energy transfer dominates the excitation of the guest. An example of this case is provided by the blend of PtOEP and PNP. In fact, evidence for Dexter transfer was provided by transient electroluminescence. As shown by Fig. 11.7(b), the transient of the PNP:PtOEP blend exhibits a well-resolved initial growth, attributed to the migration of triplet excitons formed on the PNP host to the phosphorescent dye. On the other hand, if a large energy offset between the energy levels of the host and guest favors charge-carrier trapping, direct recombination of charges on the dye is the dominant process (as in the case of PtOEP doped into PFO). If both HOMO and LUMO levels are offset in the same direction, as for the DMOS-PPV blend, the excited states on both the host and the guest are unstable due to charge transfer. Finally, triplet energy transfer from the guest to the host has been observed for OC1C10-PPV doped with PtOEP.

In general, several transfer processes will be “active” in a dye-doped polymer layer. In the following paragraphs, we will discuss some selected examples in more detail to illustrate the benefits of the relevant processes.





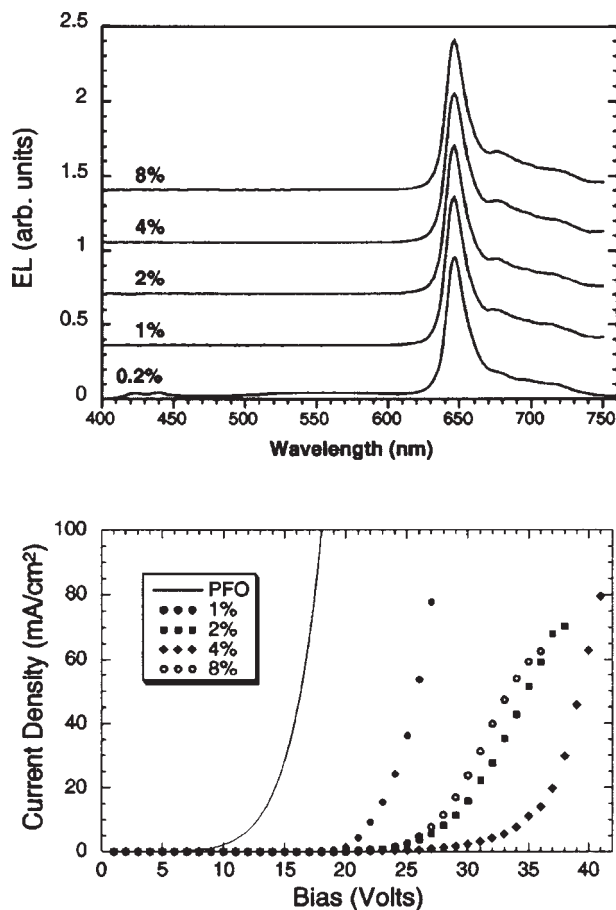
**Fig. 11.7** (a) HOMO and LUMO levels for the polymers and PtOEP studied in [35]. Oxidation potentials were determined using cyclic voltammetry, using a Ag/AgCl standard reference. LUMO levels were obtained from combination of the CV-determined HOMO energy and the optical bandgap for each material. The chemical structures of the materials are also shown. (b) transient electroluminescence of blends of PtOEP with PFO or PNP, following excitation with an electrical pulse of a few hundred ns length. For PFO blends, transients were recorded with low and high current densities [35].

### 11.3.1

#### Charge-Carrier Trapping

As pointed out above, a nice example for the dominant excitation of the dye via charge trapping is poly(9,9-dioctylfluorene) doped with PtOEP. Polyfluorene is a wide bandgap blue-emitting polymer, which has been widely studied with respect to efficient blue-emitting diodes [43–46]. Evidence that charge trapping is the dominate excitation mechanism came from several observations [37]: First, the host emission in the EL spectra is suppressed already at very low dye concentrations, as low as 1 wt. % of PtOEP in PFO (Fig. 11.8(a)). Secondly, there is a significant shift of the driving voltage (for a given current density or brightness) with increasing dye concentration (Fig. 11.8(b)). For example, the voltage to drive the LED at a current density of  $5 \text{ mA/cm}^2$  shifted from ca. 12 V for a pure PFO layer to 33 V for a layer containing 4 wt. % PtOEP. Note, that the driving voltage decreased on increasing the PtOEP concentration further to 8 wt. %.

**Fig. 11.8** upper graph: The electroluminescence spectra of PtOEP/PFO LEDs. The spectra are normalized to the phosphorescence peak at 646 nm and offset for comparison. Lower graph: Current density as a function of applied bias of a PFO LED and PtOEP/PFO LEDs with PtOEP concentrations of 1%, 2%, 4% and 8% by weight [37].



Most likely, the direct hopping of holes between PtOEP becomes possible at higher concentrations, without the need for detrapping to the PFO host. On the other hand, the decay time measured in transient electroluminescence (after excitation with an electrical pulse of 4  $\mu$ s duration) varied only slightly with concentration. Apparently, back transfer of excitons or charges to the host is not significant. Also, even though Förster transfer from PFO was clearly proven by the decrease of the host PL intensity with increasing dye concentration, the PFO PL efficiency was still 28% (ca. half of the efficiency of a pure PFO layer) at a PtOEP concentration of 1 wt.%. At this concentration, no PFO emission could be detected in the EL spectra. Finally, photoinduced absorption has been used to estimate the degree of Dexter transfer from the host to the dye. Surprisingly, the lifetime of the host triplet exciton (being 0.3–3.2 ms in the pure PFO layer) was not affected by the presence of the dye. Thus, Dexter transfer must be very inefficient even at a dye concentration of 8 wt. %.

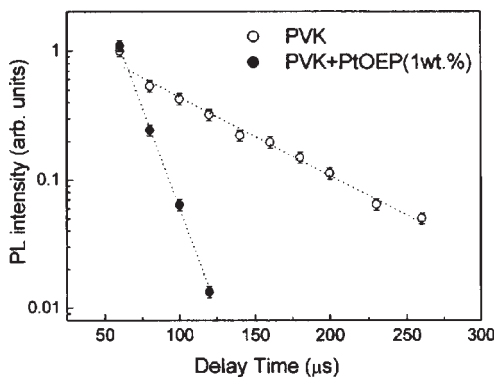
## 11.3.2

**Dexter Transfer**

Besides direct charge recombination on the dye, transfer of singlet and triplet excitons initially formed in the host constitutes a possible way to excite the phosphorescent dye. Occurrence of Förster transfer of singlet excitons has been proven for most dye-doped polymers by analyzing the decay of the host fluorescence intensity, accompanied by an increase of the guest emission intensity with increasing guest concentration. In contrast, acquiring evidence for Dexter transfer from the polymer host to the phosphorescent dye is far more difficult for several reasons. As pointed out above, transient electroluminescent experiments have been performed to provide evidence for Dexter transfer in a working device. However, the EL dynamics in a dye-doped system also involves the dynamics of charge carriers and an unambiguous interpretation of the EL transients might be difficult in some cases. Therefore, several experiments have studied the dynamics of the host and guest triplet exciton upon photoexcitation [37, 39, 47–49]. For example, Noh et al. [47] have measured the phosphorescence decay kinetics of pure polyvinylcarbazole (PVK) and PVK doped with PtOEP. As shown in Fig. 11.9, the PVK triplet lifetime was clearly shortened upon addition of 1 wt. % of the phosphorescent dye. This has been taken as evidence for efficient triplet-triplet energy transfer from the polymer host to the guest.

The study of the triplet dynamics in fully conjugated polymer hosts turned out to be difficult, because the intrinsic phosphorescence is barely observed from these polymers. The main reason is the lack of spin-orbit coupling in these carbon-based conjugated polymers, resulting in low intersystem-crossing (ISC) rates. Consequently, the polymer triplet state is only weakly populated after photoexcitation and the quantum yield of phosphorescence is low.

An elegant approach to populate the triplet state of a conjugated polymer after excitation of its singlet has been reported by Rothe et al. [50]: A solid layer of poly(9,9-bis(2-ethylhexyl)fluorene-2,7-diyl) (PF2/6) was mixed with benzil, which efficiently converted the singlet excitation of the polymer to triplet excitons. Benzil has a very low fluorescence quantum yield ( $\sim 0$ ), due to  $n \rightarrow \pi^*$  nature of

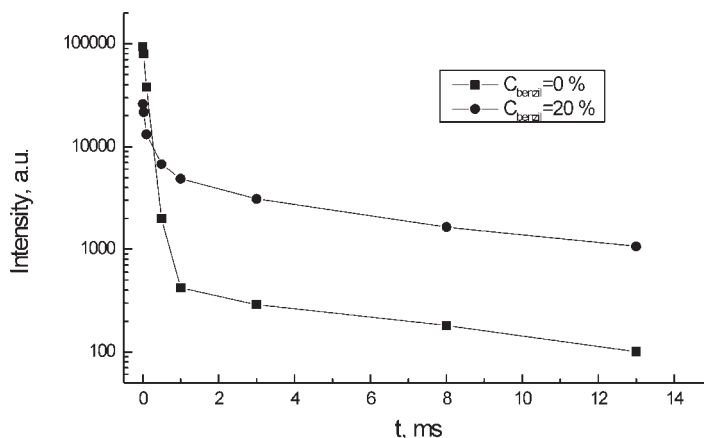


**Fig. 11.9** Decay profiles of the  $T_1$  state of PVK (opened circles) and PtOEP doped PVK (filled circles) films at 502 nm measured at 5.5 K. The triplet lifetime of PVK at 502 nm was clearly shortened by doping of PtOEP [47].

the lowest singlet state [51]. On the other hand, the quantum yield for ISC is very high (0.92). Because the singlet state of PF2/6 is ca. 0.28 eV higher than that of benzil and the polymer triplet state is ca. 0.17 eV below that of benzil, this compound should act as a very efficient singlet-triplet converter when blended into PF2/6. These authors further studied the photophysics of layers doped with PtOEP to provide evidence for triplet-triplet energy transfer. One important advantage of this approach is that the fluorescence of the polymer host is effectively quenched by the addition of benzil. Thus, the probability for energy transfer from the polymer host to the phosphorescent dye via Förster-type singlet exciton transfer is greatly reduced.

Bagnich et al. [49] have studied the photophysics of a ladder-type PPP (MeLPPP) doped with PtOEP and benzil. Upon addition of benzil at a concentration of ca. 20 wt. % the prompt fluorescence of MeLPPP is largely quenched, by a factor of more than 30. In order to prove that triplet-triplet transfer takes place between the polymer host and PtOEP, a blend system with 0.001 % by weight of PtOEP added to MeLPPP was studied. This amount of PtOEP does not lead to significant quenching of the polymer fluorescence. Most importantly, adding 20 wt. % of benzil to the MeLPPP:PtOEP layer reduced the phosphorescence intensity of PtOEP by a factor of only 3.5, while the prompt fluorescence of the polymer host decreased by a factor of 30. This provides strong evidence that in addition to Förster-type singlet-singlet transfer, other channels for exciting the phosphorescent dye must exist in the doped system. Since the quantum yield of fluorescence of benzil is close to zero, and no strong benzil phosphorescence is observed from the MeLPPP:benzil layers, direct transfer from a singlet or triplet exciton on the benzil to the phosphorescent dye can be neglected. Thus, the main channel for populating the triplet state of PtOEP in the benzil-doped system must involve (a) the benzil-sensitized conversion of polymer singlet excitons to triplet excitons, (b) the triplet exciton migration within the polymer matrix and (c) triplet-triplet energy transfer to the dye.

Further confirmation of this assignment comes from time-resolved phosphorescence measurements. Figure 11.10 shows the phosphorescence decay curves of the PtOEP in MeLPPP, without and with benzil codoped at a concentration of 20 wt. %. In both cases, fast and slow components are observed. The decay time of the fast component agrees with the intrinsic lifetime of the triplet state of PtOEP (70–100  $\mu$ s). Obviously, the fast component is due to porphyrin molecules excited as a result of the singlet-singlet energy transfer from the polymer. The introduction of benzil sharply decreases this fast contribution. At the same time, there is a marked increase of the long-lived component, with a lifetime comparable to that of the polymer (ca. 15 ms). This proves that the main energy donor for the PtOEP triplet state in the benzil-sensitized system is the triplet state of the polymer.

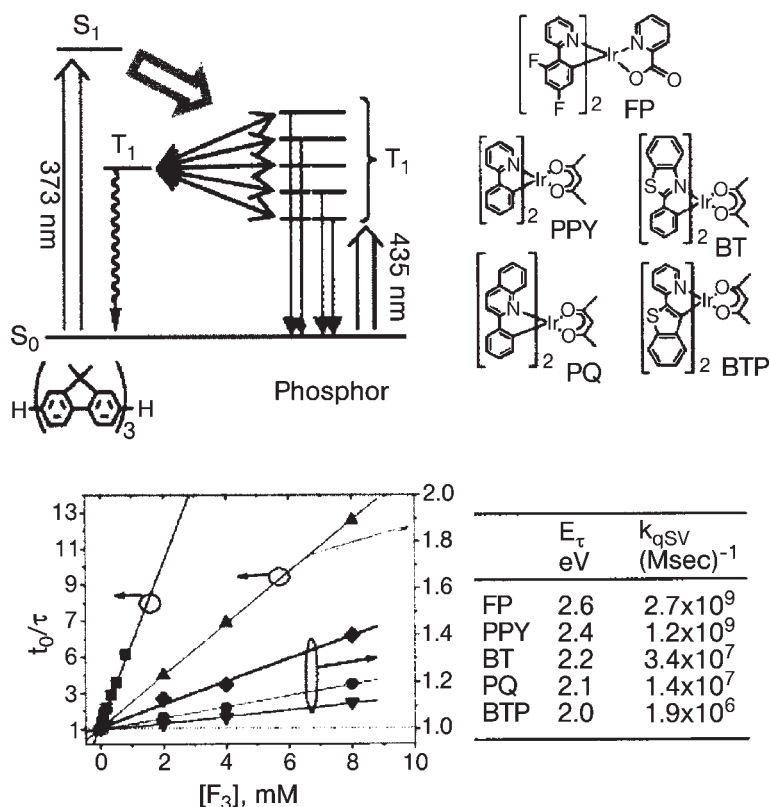


**Fig. 11.10** Decay of the PtOEP phosphorescence in a MeLPPP film without and with 20 wt.% of benzil at 77 K. The curves were recorded with a gate width of 10 ms (taken from [49]).

### 11.3.3

#### Energy Back Transfer

A very nice and illustrative example for triplet quenching via triplet energy back transfer between the guest and the host molecules was published recently by Sudhakar et al. [52]. Luminescent-quenching studies were carried out by measuring the phosphorescent lifetimes of various phosphorescent dyes in the presence of a model oligofluorene ( $F_3$ ) (see Fig. 11.11(a)). The oligomer was chosen instead of the polymer for several reasons, one being that the oligomer is fully transparent in the wavelength region where the phosphorescent dyes absorb. Figure 11.11(b) shows Stern–Volmer plots illustrating the quenching of the dye emission upon addition of  $F_3$  with increasing concentration. Excitation was at 435 nm, which excites only the iridium complexes. Apparently, rapid quenching of the phosphorescence of the blue-emitting FP (= FIrpic) and the green-emitting PPY (= Ir(ppy)<sub>3</sub>) occurs in the presence of  $F_3$  due to Dexter back transfer. On the contrary, quenching was far less efficient for the complexes with the triplet energy below 2.2 eV. It was concluded that  $F_3$  has its lowest triplet state at 2.3 eV, slightly above the  $T_1$  energy of the polymer (2.1 eV, [31]). Consequently, polyfluorene can be considered to be a suitable host only for red-emitting phosphors such as (btp)<sub>2</sub>Ir(acac).



**Fig. 11.11** Upper graph: Schematic energy-level diagram showing energy transfer between F<sub>3</sub> (left) and the iridium complexes studied by Thompson and coworkers (right). Lower graph: Stern-Volmer plot for quenching of the five phosphors by F<sub>3</sub>. (Legend: ■ FP, ▲ PPY, ◆ BT, ● PQ, ▼ BTP). The table shows the triplet energies of the phosphors and their Stern-Volmer quenching constants [52].

## 11.4

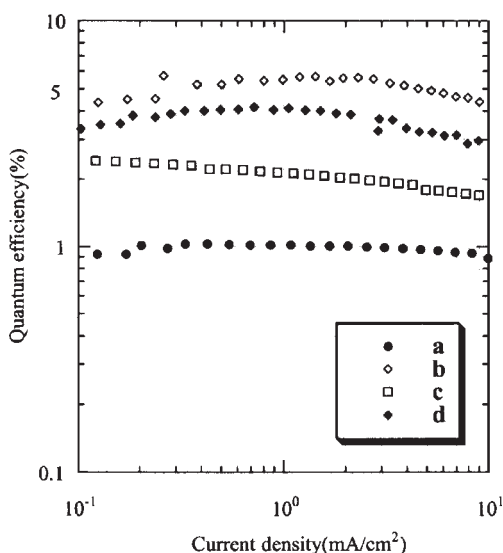
### Polymer Phosphorescence Devices based on PVK

PVK is a very suitable polymer host for phosphorescent dyes. The PVK T<sub>1</sub> state is at ca. 2.5 eV [53], so the polymer is suited to host green- and red-emitting dyes. HOMO and LUMO positions are at 5.8 eV and 2.2 eV, respectively [53]. Therefore, most dyes will constitute charge-carrier traps in PVK. The room-temperature emission of PVK is from an excimer, with a rather low quantum efficiency of ca. 9% (for PVK blended with PBD at a ratio 1:0.4) [54]. Consequently, good color purity can be easily achieved. By now, a large variety of dyes have been tested as emitting species in a PVK matrix. For historical reasons, we will first discuss devices using the green-emitting dye Ir(ppy)<sub>3</sub> and chemically related phosphors.

## 11.4.1

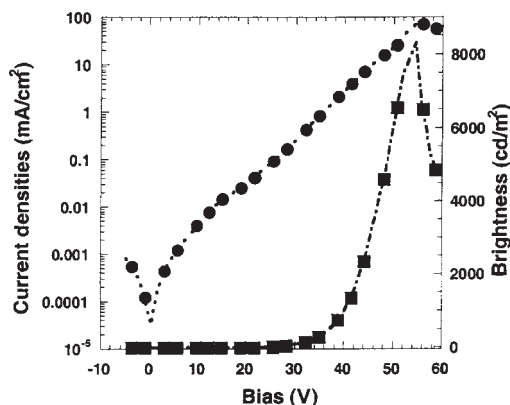
## Green PVK-based Devices

The first example of a LED based on PVK:Ir(ppy)<sub>3</sub> was published by Yang and Tsutsui [33]. These devices consisted of a PVK:Ir(ppy)<sub>3</sub> layer with a dye concentration of 4.8 or 6.8 wt. % and an electron-transporting layer, sandwiched between ITO and MgAg. As shown in Fig. 11.12, the external efficiency of the devices depended strongly on the choice of the electron-transporting component. The highest efficiency (peak efficiency of 7.5 %) was reported for the structure with an 1,3-bis[(4-tert-butylphenyl)-1,3,4-oxadiazolyl]phenylene (OXD-7) layer, but without a BCP blocking layer. Shortly afterwards, Lee et al. [55] published a polymer phosphorescent device with a similar device structure but with lower efficiency. However, all these devices included one or few additional electron-transporting layer deposited by thermal evaporation on top of the spin-coated polymer emission layer, the reason being that the electron mobility of PVK is rather poor [56]. Lamanski et al. [34, 57] were the first to show that efficient single layer polymer electrophosphorescent devices can be constructed when adding the electron-transporting compound 2-(4-biphenyl)-5-(4-tert-butylphenyl)-1,3,4-oxadiazole (PBD) to the PVK host to facilitate electron transport. Devices with a ca. 130-nm layer composed of PVK (67 wt. %), PBD (30 wt. %) and Ir(ppy)<sub>3</sub> (3 wt. %), sandwiched between an ITO anode and a MgAg cathode, exhibited an EQE of 3.4 % (corresponding to a peak current efficiency of 12.3 cd/A) and a turn-on voltage of 8 V [57]. Based on the complete absence of PVK or PBD emission, these authors noted that excitons must be exclusively formed on the phosphorescent dopant. The efficiency of devices based on a PVK:PBD:Ir(ppy)<sub>3</sub> emission layer were further improved to 8.5 % (30.1 cd/A) by adding a 5-nm thick 2,2',2''-(1,3,5-bezenetriyl)tris(1-phenyl)-1H-benzimidazole (TPBI) hole-blocking layer and a 30-nm



**Fig. 11.12** External quantum efficiency plotted against current for four different devices containing an PVK:Ir(ppy)<sub>3</sub> emission layer. The electron-transporting layer is (a) Alq<sub>3</sub>, (b) OXD-7. Also, devices were fabricated with an additional BCP hole-blocking layer (c) BCP/Alq<sub>3</sub>, (d) BCP/OXD-7 [33].

**Fig. 11.13** Brightness (■) and current density (●) characteristics of a ITO/PEDOT/[Ir(DPF)<sub>3</sub>]:PVK-PBD/Ca/Ag device with a Ir(DPF)<sub>3</sub> concentration of 1 wt. % as function of applied voltage [59].



thick Alq<sub>3</sub> electron-transporting layer [58]. Apparently, adding a hole-blocking layer improved the charge balance in these devices with Mg/Ag electrodes. This indicates that upon appropriate design of the device, highly efficient electrophosphorescence can be achieved from dye-doped polymer emission layers.

In the same year, Gong et al. [59] demonstrated that single-layer devices can exhibit efficiencies close to 10 %, corresponding to 36 cd/A. Their devices differed in several points from those reported by Lamanski et al. First, a more suitable Ca-electrode was used instead of the Mg/Ag cathode employed in former reports. Secondly, a green-emitting Ir-complex with fluorene-ligands, tris[9,9-dihexyl-2-(pyridinyl-2')fluorene] iridium (Ir(DPF)<sub>3</sub>), was used, which is expected to be slightly more electron-rich than the corresponding Ir(ppy)<sub>3</sub>.

In fact, the driving voltage of diodes with Ir(DPF)<sub>3</sub> doped into a PVK:PBD matrix increased dramatically with dye concentration. This gave strong evidence that the dye constitutes a deep charge trap (most likely a hole trap) in the PVK:PBD matrix. For an Ir(DPF)<sub>3</sub> concentration of 5 %, a voltage as high as 37 V needed to be applied to drive the device at 1 mA/cm<sup>2</sup>. It was also shown that the dye concentration affects the quantum efficiency and best values were obtained for devices with 0.3–1 wt % Ir(DPF)<sub>3</sub>. Figure 11.13 shows the voltage dependence of the current density and brightness for a device containing 1 wt. % of the dye. Due to severe charge-carrier trapping, accompanied by the build-up of a space-charge field, high current densities and high brightness were only achieved at very high voltages. As a consequence, the power efficiency of the most efficient device (with 0.3 wt. % dye concentration) was 2.5 lm/W, only. Nevertheless, this important work demonstrated that very efficient single-layer electrophosphorescent devices can be made with dye-doped polymers.

#### 11.4.1.1 Excitation of the Dye in the PVK Matrix

As pointed out above, the significant increase in driving voltage with increasing dye concentration already indicates that carrier trapping is severe in these PVK:PBD:Ir(DPF)<sub>3</sub> layers. Further evidence for the predominant excitation of



the dye via charge-carrier trapping and recombination on the dopant comes from the comparison between PL and EL spectra. In PL (with excitation of the matrix at 330 nm) a dye concentration of 8 wt. % is needed to completely quench the emission of the host via Förster and Dexter transfer to the dye [59]. A more detailed analysis of the PL as a function of dye concentration showed that the dependence of the energy-transfer efficiency on the Ir(DPF)<sub>3</sub> concentration is consistent with a Förster-type transfer of singlet excitons from the matrix to the dye [48, 60]. Nevertheless, LEDs with a dye concentration as small as 0.1 wt. % yielded pure dye emission, indicative of charge-carrier trapping [59]. However, these experiments could not rule out that Dexter transfer (which is not significant in PL experiments) contributes to the excitation of the dopant in the EL experiments. Evidence for efficient Dexter energy transfer comes from transient EL measurements performed by Noh et al. [47] on Ir(ppy)<sub>3</sub> doped at 8 wt. % into PVK. Nevertheless, there is little doubt that neither Förster nor Dexter transfer dominates the excitation of the dye in electroluminescence devices.

#### 11.4.1.2 Optimizing the Devices

Even though the formation of the guest triplet excited state via carrier trapping and subsequent direct carrier recombination on the guest molecule is an elegant way to achieve good color purity and high efficiency, as pointed out above, it is often accompanied by a high operating voltage due to the build-up of a space-charge field. We have, therefore, conducted a detailed study on the processes governing the efficiency and driving voltage in these dye-doped PVK LEDs [61]. In a first step, the preparation conditions of layers containing ca. 1 % of a methyl-substituted iridium complex, Ir(mppy)<sub>3</sub>, in a PVK:PBD matrix were optimized with respect to device performance. Most noticeable, annealing the active layer prior to the deposition of the Ca cathode significantly reduced the driving voltage, accompanied by a ca. 20 % increase of the luminance efficiency. In total, annealing led to a ca. 37 % improvement of the PCE, resulting in ca. 7.5 lm/W at a brightness of 600 cd/m<sup>2</sup>. At the moment we can only speculate about the reason for this improvement. Nguyen et al. [62] reported a ca. 50 % higher EQE for devices based on annealed poly(2-methoxy-5-(2'-ethylhexyloxy)-1,4-phenylenevinylene) (MEH-PPV) layers. This was explained by an improved interfacial contact to the cathode, due to the smooth surface of the annealed MEH-PPV film. A significant improvement in device efficiency has also been observed when annealing a multicomponent polymer emission layer prior to the deposition of the cathode. In this case, AFM studies revealed significant morphological changes, including the formation of phase-separated structures [63]. However, our AFM studies on the annealed PVK:PBD:Ir(mppy)<sub>3</sub> layers did not provide any evidence for phase separation. Evidence for the crucial role of electron injection comes from the significant improvement of device efficiency when inserting a thin LiF layer between the Ca-cathode and the emission layer [61]. It is well established that introducing a thin metal fluoride layer between an organic layer and low work function metals

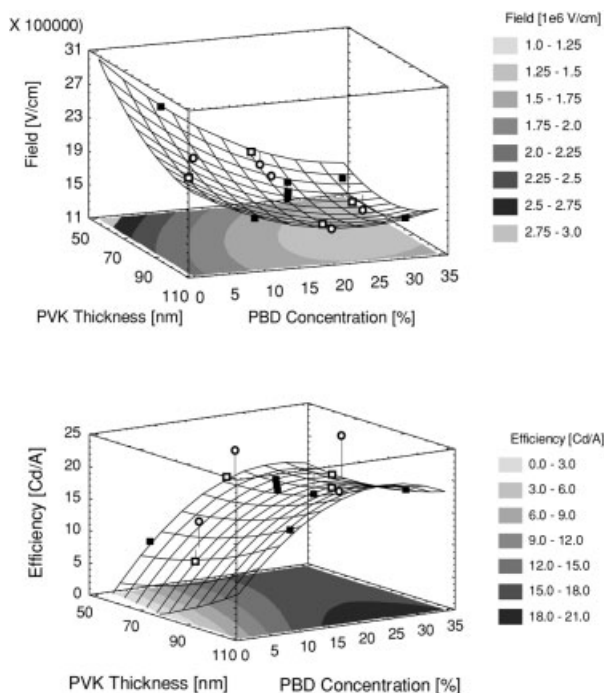
such as Ca or Yb improves the performance of organic light-emitting devices via improved electron injection [64].

Further information on how charge transport and charge-carrier trapping affect the device properties could be obtained by studying devices with different concentrations of the electron-transporting moiety PBD and of the hole-trapping Ir(mppy)<sub>3</sub> complex. As a third crucial parameter, the layer thickness was varied over a wide range. In order to minimize the number of devices, a statistical approach was utilized [65]. In short, 13 different devices with PBD concentrations  $c_{\text{PBD}}$  ranging between ca. 10 and 35 wt.%, Ir(mppy)<sub>3</sub> concentrations  $c_{\text{Ir}}$  between ca. 0.3 and 7 wt.% and PVK layer thicknesses  $d_{\text{PVK}}$  between 50 and 110 nm were examined. In all cases, the emissive layers were annealed and an interfacial LiF layer was added before deposition of the Ca/Al cathode. Current–brightness–voltage characteristics of the different devices were recorded and, in the analysis of the data, various device properties such as the luminance efficiency and the driving voltage were compared at certain current densities. Then, each of these device properties (denoted here as  $P(c_{\text{PBD}}, c_{\text{Ir}}, d_{\text{PVK}})$ ) was separately fit to a 2<sup>nd</sup>-order polynomial function of the variables  $c_{\text{PBD}}$ ,  $c_{\text{Ir}}$  and  $d_{\text{PVK}}$ :

$$P(c_{\text{PBD}}, c_{\text{Ir}}, d_{\text{PVK}}) = A_1 c_{\text{PBD}} + A_2 c_{\text{PBD}}^2 + B_1 c_{\text{Ir}} + B_2 c_{\text{Ir}}^2 + C_1 d_{\text{PVK}} + C_2 d_{\text{PVK}}^2 + D c_{\text{PBD}} c_{\text{Ir}} + E c_{\text{PBD}} d_{\text{PVK}} + F c_{\text{Ir}} d_{\text{PVK}} \quad (11.1)$$

This results in 9 fitting coefficients A–F for each device property. However, for the devices studied, only very few of these coefficients had values with statistical significance. Most importantly, both the efficiency and the driving field depended strongly on the concentration of PBD, while they were only weakly affected by the concentration of the Ir-dye. Figure 11.14(a) shows the resulting multiparameter fitting function to the electric field at a constant current density of 5 mA/cm<sup>2</sup>, plotted as a function of  $c_{\text{PBD}}$  and  $d_{\text{PVK}}$  for a fixed value of  $c_{\text{Ir}} = 3.5$  wt.%. Also shown are the measured data points (symbols). Even though these data were measured for devices with very different Ir(mppy)<sub>3</sub> concentration, most data points lie close to the response surface plot of the multiparameter fitting function, calculated for a constant Ir(mppy)<sub>3</sub> concentration. This illustrates that varying the Ir(mppy)<sub>3</sub> concentration does not significantly influence the driving field. We, therefore, presume that the space-charge formed by hole trapping on the Ir(mppy)<sub>3</sub> can be effectively neutralized by efficient electron injection and transport in our devices.

The corresponding response surface plot of the fit to the luminance efficiency (Fig. 11.14(b)) also shows that the concentration of the electron-transporting moiety in the layer is the major parameter controlling the device performance. In fact, increasing the PBD concentration from 10 to 35 wt.% doubles the luminance efficiency. Also, the rather small scatter of the experimental data around the fitting function (calculated for a constant value of  $c_{\text{Ir}}$ ) suggests, that the Ir(mppy)<sub>3</sub> concentration has only a weak influence on the device efficiency. However, there are few data points situated well above the fit, which were all measured for devices with Ir(mppy)<sub>3</sub> concentrations less than 0.5 wt.%. Apparently,



**Fig. 11.14** Results of the statistical analysis of the dependence of the electric field (upper graph) and the luminance efficiency (lower graph) of PEDT:PSS/PVK:PBD:Ir(mppy)<sub>3</sub> / LiF/Ca devices on the PBD concentration, the PVK layer thickness and the Ir(mppy)<sub>3</sub> concentration. Symbols show the experimental data measured at a constant current density of 5 mA/cm<sup>2</sup> for devices with Ir(mppy)<sub>3</sub> concentrations of 0.3–0.5 wt. % (open circles), 2.5–4 wt. % (solid squares) and 5–7 wt. % (open squares). The response surface and contour plots present the corresponding multiparameter functions according to Eq. (11.1), obtained from the best fit to the experimental data, plotted for a fixed Ir(mppy)<sub>3</sub> concentration  $c_{Ir}$  of 3.5 wt. % ([61]).

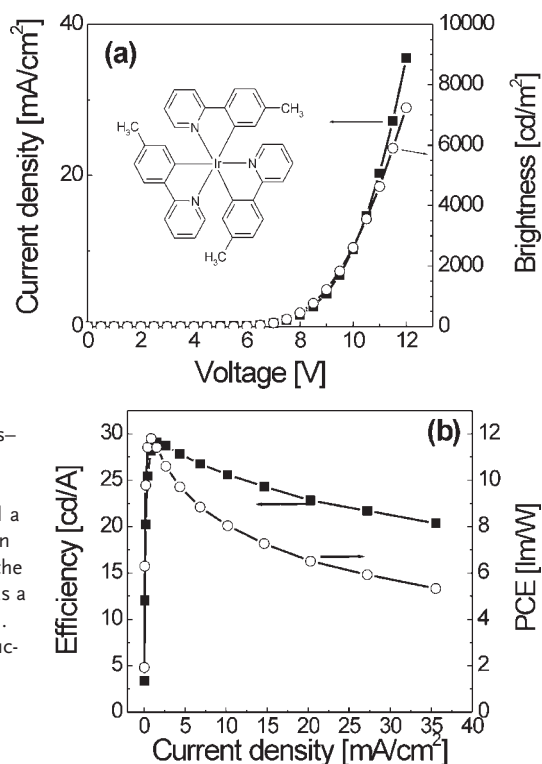
higher dye concentrations introduce additional nonradiative channels, either due to the formation of aggregates or by triplet-triplet annihilation between triplet excitons situated on adjacent dyes.

Taking into account this effect, the data shown in Fig. 11.14(b) suggest that the total number of guest triplet excitons formed in the emission layer per unit time and unit area at a given current density is rather independent of the concentration of the hole-trapping Ir-complex. This observation provides clear evidence that the transfer of excitons initially formed on the matrix plays a minor role for the excitation of the dye. The result also suggests that the capture of charges by the individual guest molecules is not the main step limiting the kinetics of triplet formation on the phosphorescent Ir-complex. Furthermore, at high PBD concentrations, there is no dependence of the driving field on the layer thickness. Apparently, the current is neither transport limited nor influenced by the build-up of a space-charge field at these PBD concentrations.

### 11.4.1.3 Optimizing Charge Injection

The device efficiency could be further improved by replacing the LiF/Ca cathode with a CsF/Al cathode [61]. Earlier works on devices with fluorescent and phosphorescent organic layers have shown that a thin CsF layer in combination with a Ca, Al or MgAg electrode greatly improves electron injection [66–68]. Figure 11.15(a) shows the current–brightness–voltage characteristics of a device with a PBD concentration of 30 wt. %, an Ir(mppy)<sub>3</sub> concentration of 1 wt. % and CsF/Al cathode. Figure 11.15(b) displays the dependence of the luminance efficiency and the PCE on the current density of the devices. The turn-on voltage (0.1 cd/m<sup>2</sup>) of the device was 3.5 V. The maximum luminance efficiency was 27 cd/A at a current density of 2.3 mA/cm<sup>2</sup> and a brightness of 610 cd/m<sup>2</sup>, corresponding to an EQE of 7.6 %. Even though the luminance efficiency and power efficiency decreased gradually with increasing current density, the luminance efficiency was 23.4 cd/A at a current density of 20 mA/cm<sup>2</sup>, an operating voltage of 8.9 V and a brightness of 4680 cd/m<sup>2</sup>, corresponding to an EQE of 6.6 % and a PCE of 8.3 lm/W.

On the anode side, even the utilization of PEDT:PSS (with a work function of ca. 5.2 eV) leaves a ca. 0.6-eV barrier for hole injection to PVK (HOMO at 5.8 eV [53]). It can thus be expected that the reduction of the barrier height for hole injection will significantly improve the power efficiency of the PVK-based devices.



**Fig. 11.15** (a) Current–brightness–voltage characteristics of a green-emitting PVK-based device with a 70-nm thick PEDOT:PSS layer and a CsF(1 nm)/Al cathode. Also shown are the corresponding curves for the luminance efficiency and the PCE as a function of the current density (b). The inset shows the chemical structure of Ir(mppy)<sub>3</sub>. The absolute Ir(mppy)<sub>3</sub> concentration in the PVK(70):PBD(30) host was 0.7 wt. % ([61]).

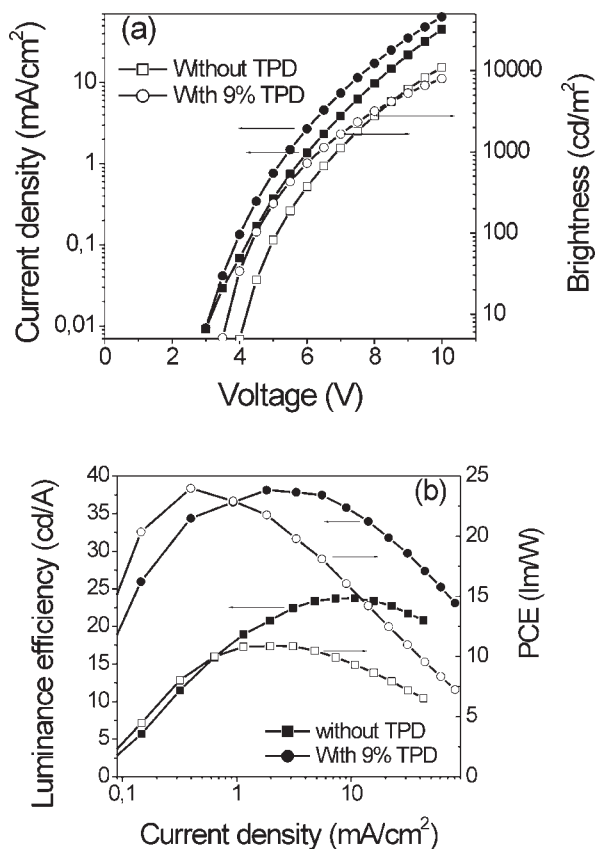
Recently, we have demonstrated that adding the hole-transporting molecule TPD significantly improved device performance, without any further modification of the charge-injection electrodes [69]. TPD is particularly suitable because the HOMO level of TPD at 5.5 eV [70] is similar to that of Ir(ppy)<sub>3</sub> (5.4 eV) [27] but significantly higher than that of PVK. In fact, TPD was earlier shown to function as a hole trap at low concentration and a hole-transporting moiety at high loading when doped into PVK [71]. In the latter case, charge transport was proposed to occur by hopping between adjacent TPD molecules, without the need for thermally assisted back transfer to the PVK matrix. In our devices, the optimum TPD concentration was determined by two processes: On one hand, the TPD concentration needed to be high enough to guarantee that holes are injected directly into the TPD-HOMO. Work by Adachi [18] has shown that direct hole injection onto the dopant becomes efficient at dopant concentrations above ca. 6 wt. %. On the other hand, if the TPD concentration was raised to 19 wt. %, the efficiency dropped again (though the driving voltage decreased further), which is indicative of the formation of TPD-percolation pathways for holes. Based on these consideration we presumed that at intermediate doping levels, charges are predominately injected from the PEDT:PSS anode onto the TPD molecules. Then, transport of holes occurs mainly by hopping between TPD and Ir(mppy)<sub>3</sub> molecules. This is confirmed by the data shown in Table 11.1.

Interestingly, EL spectra of devices with a low Ir(mppy)<sub>3</sub> concentration in the PVK:PBD:TPD matrix exhibited a well-resolved blue component, which we attributed to the emission from a TPD:PBD exciplex. Note that the emission from an undoped PVK:PBD matrix has been assigned to originate from an exciplex between PVK and PBD, as mentioned above [72]. Therefore, the question arises as to why the PVK:PBD exciplex emission is efficiently suppressed in the EL of the PVK:PBD:Ir(mppy)<sub>3</sub> layer even at low dye concentration. Based on the large offset between the HOMO positions of PVK and the dye we presume that the probability to form the exciplex on the matrix is very low, due to hole trapping on the dye. In contrast, the HOMO positions of TPD and Ir(mppy)<sub>3</sub> are almost identical. In addition, the LUMO level of TPD (−2.4 eV) [70] is similar to that

**Table 11.1** Performances of PVK:PBD based single-layer devices with ca. 6 % Ir(mppy)<sub>3</sub> and different TPD concentrations [69].

TPD concentration	Peak luminous efficiency	Voltages at 10 <sup>2</sup> , 10 <sup>3</sup> , 10 <sup>4</sup> cd/m <sup>2</sup>	PCE at 1000 cd/m <sup>2</sup>	Brightness at 10 V
0 %	23.7 cd/A	5.0 V, 6.9 V, >10 V	10.5 lm/W	8920 cd/m <sup>2</sup>
6 %	35.5 cd/A	4.4 V, 5.9 V, 8.8 V	17.6 lm/W	17900 cd/m <sup>2</sup>
9 %	38.1 cd/A	4.3 V, 5.8 V, 8.6 V	19.8 lm/W	18600 cd/m <sup>2</sup>
12.5 %	37.1 cd/A	4.2 V, 5.6 V, 8.4 V	19.8 lm/W	21400 cd/m <sup>2</sup>
19 %	27.6 cd/A	4.1 V, 5.4 V, 8.2 V	15.2 lm/W	22100 cd/m <sup>2</sup>

**Fig. 11.16** (a) Current-density (solid symbols) – brightness (open symbols) – voltage characteristics of a device containing PVK (0.61) + PBD (0.24) + Ir(mppy)<sub>3</sub> (0.06) + TPD (0.09) (circles) and of a control device without TPD (squares); (b) the corresponding luminance efficiency (solid symbols) and power conversion efficiency (open symbols) curves as a function of current density (data taken from [69]).



of the dye ( $-2.4$  eV) [27] and, correspondingly, the electron confinement on the dye is weak. Thus, exciplexes should form easily on the PVK:PBD:TPD matrix, with almost the same probability as excitons form on the dye. Consequently, efficient devices with pure dye emission require Ir(mppy)<sub>3</sub> concentrations significantly higher than the optimum concentration in layers without TPD.

Figure 11.16 shows the current density–brightness–voltage properties of a device with ca. 6 wt. % Ir(mppy)<sub>3</sub> and 9 wt. % TPD, compared to that of a control device without TPD. The peak luminance efficiency of the TPD-doped device is 38 cd/A at a current density of 1.8 mA/cm<sup>2</sup>, a voltage of 5.5 V and a brightness of 700 cd/m<sup>2</sup>, corresponding to an external quantum efficiency of 10.7%. Moreover, the maximum PCE is 24 lm/W, with a current density of 0.4 mA/cm<sup>2</sup>, a voltage of 4.4 V and a brightness of 136 cd/m<sup>2</sup>. The operating voltages for 10<sup>2</sup>, 10<sup>3</sup>, 10<sup>4</sup> cd/m<sup>2</sup> were 4.3 V, 5.8 V, 8.6 V, respectively. These performances are approaching those of multilayer devices based on 4,4'-N,N'-dicarbazole-biphenyl (CBP) host, the low molecular weight counterpart host to PVK [73–75].

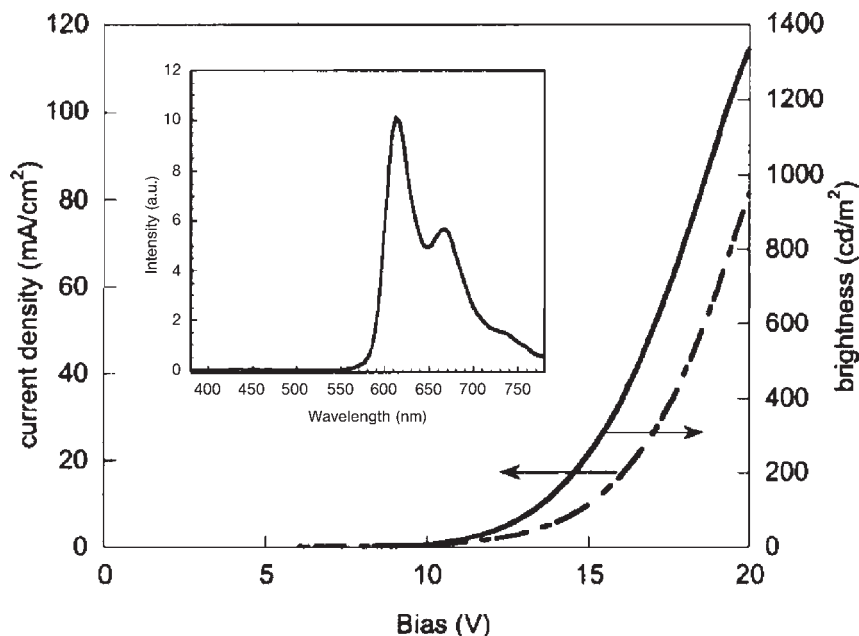
#### 11.4.2 PVK-based Devices with Red Emission

Most work related to red phosphorescence with a PVK host has been performed with  $\text{Btp}_2\text{Ir}(\text{acac})$  (see Fig. 11.3 for the chemical structure). This dye has an emission wavelength of ca. 620 nm (note that emission maxima lower and higher in wavelength are frequently reported for this dye). With the HOMO at 5.1 eV and the LUMO at 2.4 eV, this dye constitutes a deep hole and a weak electron trap in PVK. In addition, red-emitting devices have been made with platinum-based complexes such as 2,8,12,17-tetraethyl-3,7,13,18-tetramethyl porphyrin (PtOX), *cis*-bis[2-(2-thienyl)pyridine- $\text{N},\text{C}^3$ ] platinum ( $\text{Pt}(\text{thpy})_2$ ) [34], europium [76–78] and ruthenium complexes [79]. For devices containing PtOX (or the chemically related PtOEP) in PVK, a peak external quantum efficiency of 2.5 % (corresponding to 1.4 cd/A) was reported [80]. Note that the emission of PtOX originates from a  $^3\pi\pi^*$  transition located on the ligand, which becomes partially allowed by the presence of the heavy-metal atom in the center of the porphyrin ring. As a consequence, this compound exhibits a rather long phosphorescence lifetime of ca. 70–100  $\mu\text{s}$  and nonradiative decay processes in the bulk can significantly lower the fraction of triplets decaying radiatively to the ground state. In fact, work by Monkman and coworkers [41] has nicely demonstrated a strong relation between the phosphorescence lifetime of a dopant and the external electrophosphorescence efficiency. This might explain why, despite the high PL quantum efficiency of PtOX in solution (44 % in toluene [34]), the performance of PtOX- (and PtOEP-) based devices is quite disappointing. On the other hand,  $\text{Pt}(\text{thpy})_2$  possesses a short emission lifetime (2  $\mu\text{s}$  in toluene) but the quantum efficiency is low (18 %) [34]. As a consequence, the performance of devices based on PVK:PBD: $\text{Pt}(\text{thpy})_2$ , as reported by Lamansky, is also poor.

LEDs based on europium complexes are interesting for applications, because they emit red light with a very small spectral line width, as small as 3.5 nm. However, the corresponding  $^5\text{D}_0 - ^7\text{F}_2$  transition of the  $\text{Eu}^{3+}$  ion is parity forbidden and the emission lifetime is extremely long (hundreds of microseconds). This might explain why the EQE of devices based on europium complexes doped into PVK (or other conjugated polymer matrixes) is rather low and decreases rapidly with increasing driving current.

Xia et al. [79] reported a rather efficient red-emitting diode (peak wavelength 612 nm) based on the ionic ruthenium-complex  $[\text{Ru}(4,7\text{-Ph}_2\text{-phen}_3)]^{2+}$ . The most efficient device comprised an ITO anode, a PVK layer doped at 5 wt. % with a dye, a PBD hole-blocking layer, an  $\text{Alq}_3$  electron-injecting layer and a LiF/Al cathode. The maximum luminance efficiency was 8.6 cd/A (at a brightness of 4  $\text{cd}/\text{m}^2$ ). However, the efficiency dropped significantly to 2.6 cd/A at 100  $\text{cd}/\text{m}^2$ . Moreover, the driving voltage was very high (21 V for a brightness of 100  $\text{cd}/\text{m}^2$ ), which might be indicative of severe charge trapping.

Red emission from  $\text{btp}_2\text{Ir}(\text{acac})$  in a PVK matrix was first reported by Chen et al. [80]. The devices consisted of a PVK:PBD (1:1) matrix, doped with 4 wt. % of the dye. ITO/PEDT:PSS and Ca/Al were used as the anode and cathode, respectively. The diode emitted pure red light with the maximum at 614 nm (see Fig. 11.17). The peak EQE was 3.3 % (corresponding to 2.6 cd/A) at a brightness of

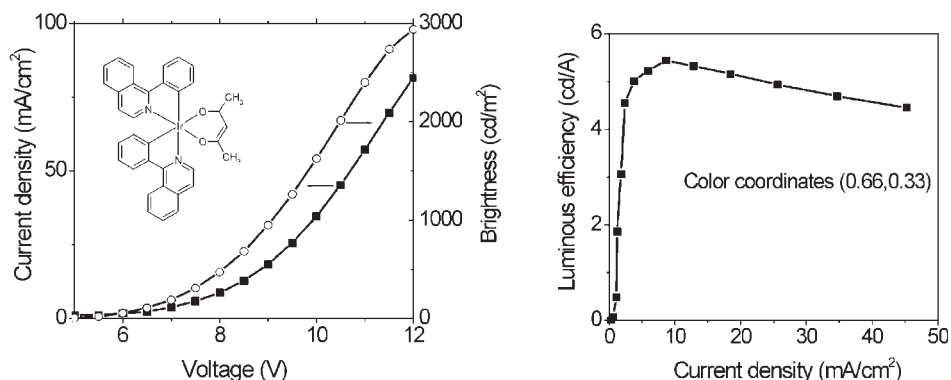


**Fig. 11.17** Current–light–voltage curves of PLEDs with 4 % btp<sub>2</sub>Ir(acac)-doped PVK:PBO matrix as the emitting medium. The inset shows electroluminescence from the same device [80].

147 cd/m<sup>2</sup>. Interestingly, the efficiency decayed only gradually with increasing current density, in clear contrast to the sharp drop of the efficiency for the same devices doped with PtOX. It was presumed that the short phosphorescence lifetime (ca. 5  $\mu$ s) reduces the probability of quenching via triplet-triplet or triplet-polaron annihilation. Note that the voltage needed to drive the device at ca. 150 cd/cm<sup>2</sup> was rather large, 13 V, leading to a PCE of only 0.6 lm/W. In the same year, Kawamura reported a red-emitting diode based on a PVK:btp<sub>2</sub>Ir(acac) emission layer in combination with a BCP exciton blocking and a Alq<sub>3</sub> electron-transporting layer [53]. Even though the device structure was more complicated than that used by Chen et al., the device performance was inferior (peak EQE of ca. 1.9 % and PCE = 0.32 lm/W at 100 cd/m<sup>2</sup>). Here we note that the emission layer in the device published by Kawamura et al. [53] did not contain any additional electron-transporting moieties such as PBD. This highlights the importance of guaranteeing a balanced injection and transport of electrons and holes through the emission layer by optimizing its constituents.

Slightly higher efficiencies were reported by Gong et al. [81], using tris(2,5-bis-2'-(9',9'-dihexylfluorene) pyridine) iridium (Ir(HFP)<sub>3</sub>) blended into a PVK:PBD (60:40) matrix. These devices emitted reddish light with the peak at 600 nm, even at a dye concentration of 0.05 wt. %. The maximum EQE (5 % corresponding to 7.2 cd/A at a brightness of 169 cd/m<sup>2</sup>) was reported for a dye concentration of 3 wt. %. Unfortunately, the voltage to drive the device was rather high, resulting in a low PCE of 1.3 lm/W. The highest efficiency reported so far for btp<sub>2</sub>Ir(acac) was





**Fig. 11.18** left: Current–brightness–voltage characteristics of a single-layer red-emitting device based on (1-(phenyl)isoquinoline)<sub>2</sub>Ir(acetylacetonate)  $\text{piq}_2\text{Ir}(\text{acac})$  (see inset for the chemical structure). The structure of the device was PEDT/PVK:PBD: $\text{piq}_2\text{Ir}(\text{acac})$ /CsF/Al. The right graph displays the efficiency of the device as function of current density (X. H. Yang and D. Neher, unpublished data).

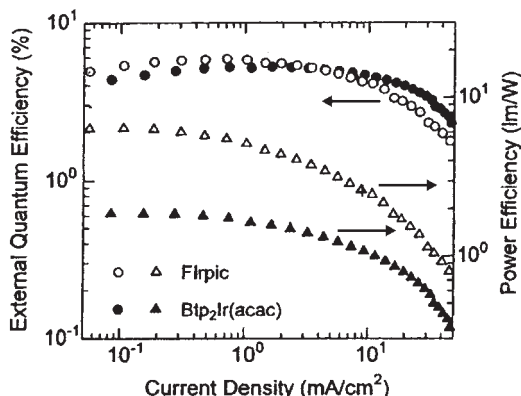
reported recently by Nakamura et al. [82]. Compared to earlier reports, these authors used OXD-7 instead of PBD and Ca was replaced by Cs. Cs has been reported to act as an efficient electron-injecting electrode due to its low work function (2.1 eV compared to ca. 2.9 eV for Ca). The maximum luminance efficiency was 4.3 cd/A (corresponding to  $\text{EQE} = 5.5\%$ ). Unfortunately, no data on the driving conditions and/or on the PCE were provided. Finally, iridium isoquinoline complexes have been shown to emit red light with significant shorter lifetime compared to, e.g., the red-emitting dye  $\text{btp}_2\text{Ir}(\text{acac})$  [83]. Figure 11.18 shows the current–brightness–voltage characteristics of red-emitting single-layer devices with the structure PEDT/PVK:PBD: $\text{piq}_2\text{Ir}(\text{acac})$ /CsF/Al. At 100 cd/m<sup>2</sup>, the efficiency was 4.3 cd/A ( $\text{EQE} = 5.1\%$ ) and the PCE was 2.1 lm/W (6.4 V). This is among the highest PCE values reported for red-emitting phosphor-doped PVK devices.

#### 11.4.3

##### PVK Devices with Blue Emission

Unfortunately, only few phosphorescent dyes emit blue light. The most studied blue-emitting Ir-complex is bis[(4,6-difluorophenyl)-pyridinato- $\text{N},\text{C}^2$ ](picolinato)Ir(III) (FIrpic, see Fig. 11.3 for the chemical structure). The emission spectrum of this dye is broad with the maximum at ca. 470 nm. As mentioned earlier, the HOMO and LUMO level of FIrpic is at 5.8 eV and 2.9 eV, so the dye should constitute a rather deep electron trap but not a hole trap in PVK. Also, the triplet energy is 2.62 eV [25], comparable to or even larger than the PVK triplet energy as determined from the peak wavelength of the PVK phosphorescence of 500 nm [47]. It has, therefore, been proposed that the transfer of excitons from the host to the dye is an endothermic process [53].

**Fig. 11.19** External quantum efficiency and luminous power efficiency as functions of the current density for the PLEDs doped with Firpic (12 wt.%) or  $\text{btp}_2\text{Ir}(\text{acac})$  (1 wt.%) [84].



The first devices using Firpic doped into PVK have been published by Kawamura et al. [53]. Interestingly, the device properties changed only slightly when increasing the dye concentration in PVK from 2.5 wt. % to 10 wt. %. The highest efficiency was 1.3 % (corresponding to 2.9 cd/A) at a dye concentration of 10 wt. % Also, the quantum efficiency varied only slightly with current density over a wide range. This result is surprising, as the triplet exciton should not be well confined on the dye, leading to TT annihilation at higher current densities.

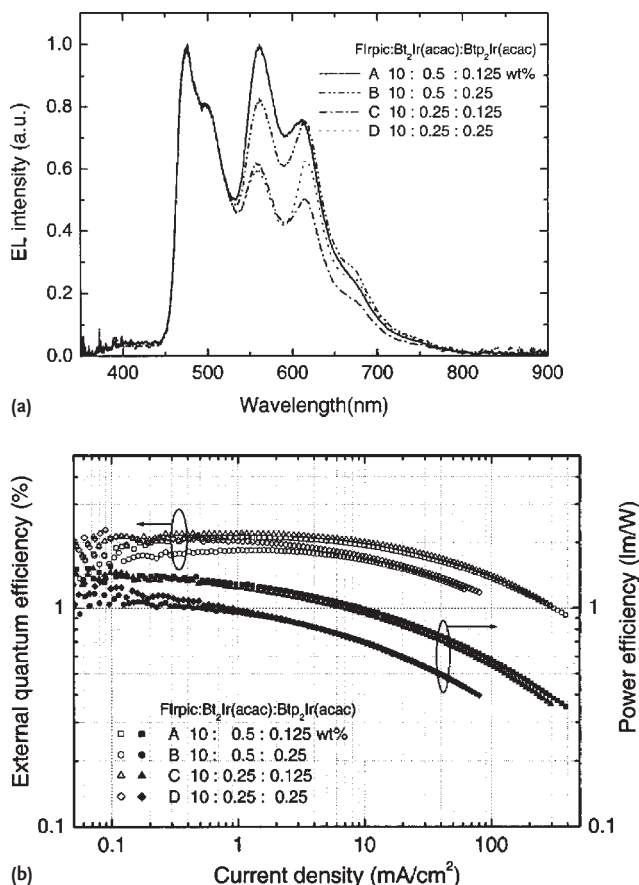
As expected, decreasing the injection barriers and adding electron-transporting molecules improves the efficiency of the device considerably. Today's best efficiencies have been reported for the structure ITO/PEDT:PSS/PVK:OXD-7:Firpic(12wt. %)/Ca/Al. As shown by the data in Fig. 11.19, the maximum EQE was 5.9 % (corresponding to 12 cd/A) and the peak PCE was 6.4 lm/W [84].

#### 11.4.4

##### White Electrophosphorescence from PVK-based Devices

Most attempts to obtain white phosphorescence use two or three different dyes doped into PVK [53,84,85]. For example, Fig. 11.20(a) shows the EL emission spectra of white-emitting diodes with different concentrations of Firpic, bis(2-(2'-phenylbenzothiazolato-N,C<sup>2'</sup>)(acetylacetonate)Ir(III) ( $\text{bt}_2\text{Ir}(\text{acac})$ ) and  $\text{btp}_2\text{Ir}(\text{acac})$ . As shown in Fig. 11.20(b), the devices had a maximum EQE of 2.2 % and a peak PCE of 1.4 lm/W[53]. Device B and D emitted white light with CIE coordinates of (0.33, 0.41). The color rendering index (CRI) of these devices was 77 (the CRI of a white light source is a measure of the color shift that an object undergoes when illuminated by the light source as compared with the color of the same object when illuminated by a reference source of comparable color temperature. The values of CRI range from 0 to 100, with 100 representing no shift in color).

The most efficient white device published to date uses Firpic and  $\text{Btp}_2\text{Ir}(\text{acac})$ , doped into a PVK:OXD-7 matrix at concentrations of 11.8 wt. % and 0.2 wt. %, respectively [84]. At 100 cd/m<sup>2</sup>, these devices exhibited an external quantum effi-

**Fig. 11.20**

(a) EL spectra of white emitting FIrpic:bt<sub>2</sub>Ir(acac):btp<sub>2</sub>Ir(acac) PHOLEDs at a current density of  $J = 10 \text{ mA/cm}^2$  (doping in wt % of device).

A: 10:0.5:0.125; device B: 10:0.5:0.25; device C: 10:0.25:0.125; device D: 10:0.25:0.25) [53].

(b) Dependence of  $\eta_{\text{ext}}$  and  $\eta_{\text{p}}$  on the current density for the white-emitting PHOLEDs in Figure 11.20(a) [53].

ciency of 4.9 %, a PCE of 2.6 lm/W and a CIE color coordinate of (0.33, 0.36), close to the white-point at (0.33, 0.33).

## 11.5

### Phosphorescent Devices with Other Host Polymers

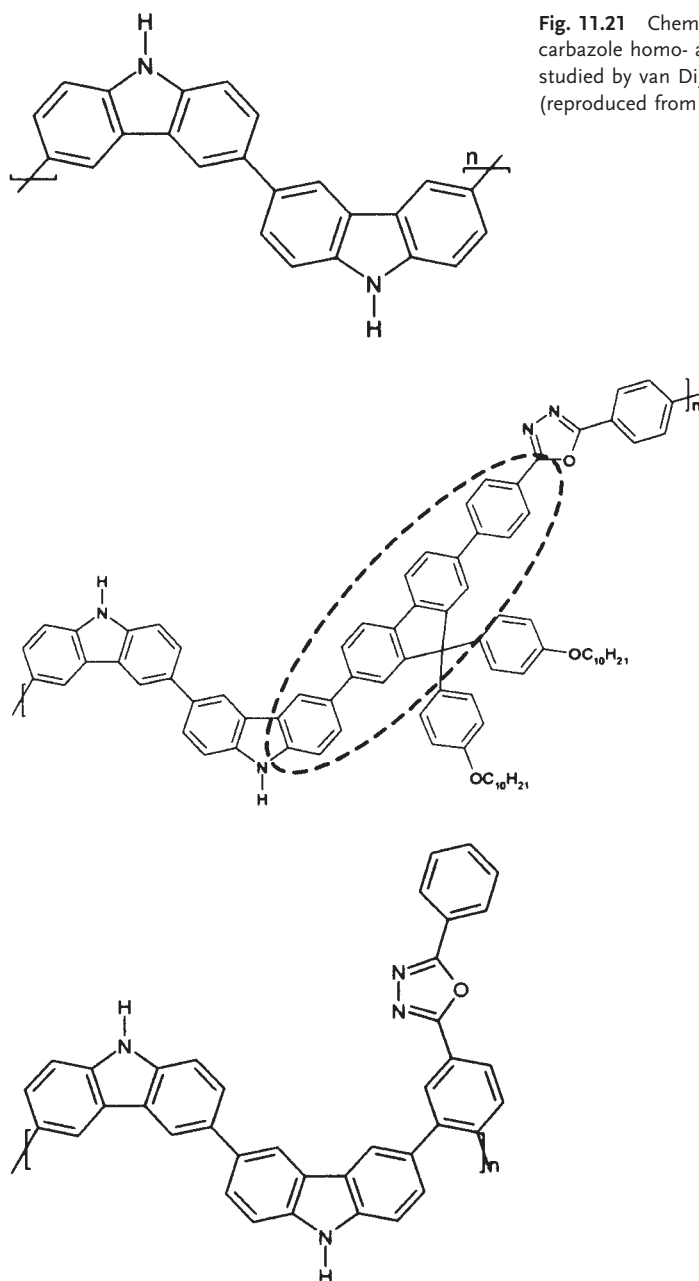
Up to now, PVK is the ideal host for green-emitting dyes. This is because its triplet energy is only slightly higher than that of the commonly used Ir(ppy)<sub>3</sub>. On the other hand, the rather deep HOMO position results in a large hole-injection barrier from ITO or ITO/PEDT:PSS. Also, because pure PVK exhibits a very small electron mobility, electron-transporting molecules such as PBD or OXD-7 have to be added to the PVK matrix to yield efficient devices with low driving voltages.

Despite the large number of available polymer hosts, only few of them have been successfully applied in conjunction with green phosphorescent dyes. One

example is poly(2-(6-cyano-6-methyl)-heptyloxy-1,4-phenylene) (CNPPP) [40]. The HOMO-level of alkoxy-substituted PPPs is at ca. 5.7 eV [86], slightly higher than (or at least comparable with) that of PVK. Devices with a butyl-substituted Ir(ppy)<sub>3</sub> doped at 2% into CNPPP exhibited a quantum efficiency of 4% at a brightness of 100 cd/m<sup>2</sup>. Unfortunately, polyfluorenes are not suitable for hosting Ir(ppy)<sub>3</sub>, because of its small triplet energy (2.1–2.3 eV) [30, 31]. In fact, efficient triplet back transfer between (ppy)<sub>2</sub>Ir(acac) and a PF oligomer has been demonstrated by Sudhakar et al. [52] as described above.

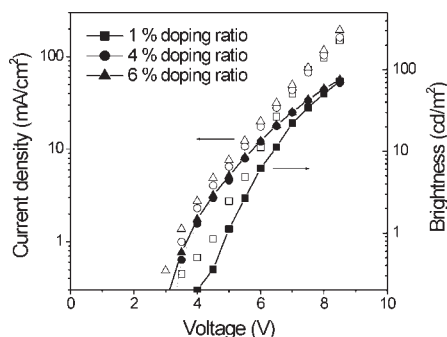
Recently, Brunner and coworkers [87] have presented a detailed study on carbazole-based homo- and copolymers as hosts for green-emitting phosphorescent dyes. A carefully study has been performed on the choice of comonomers and the chemical linkage between the units influence the HOMO position and the triplet energy. In particular the authors demonstrated that the longest oligo(p-phenylene) (OPP) segment in the chain largely determines the energy of the triplet exciton, in agreement with earlier studies on carbazole compounds by the same group [88]. In the homopolymer (see Fig. 11.21 for the chemical structure, the longest OPP segment is a biphenyl and the T<sub>1</sub> state of the polymer is at 2.6 eV, slightly lower than that of molecular biphenyl (2.85 eV [88]). This polymer should, therefore constitute a suitable host for most green-emitting Ir complexes. Surprisingly, single-layer devices containing a layer of fac-tris[2-(2-pyridinyl-kN)(5-3,4-bis(2-methylpropyloxy)phenyl)phenyl]-kC]iridium(III) (Ir-SC4) at a concentration of 8 wt. % in the homopolymer (anode: ITO/PEDT:PSS, cathode: BaAl) exhibited a rather low efficiency of only 0.4 cd/A. This can be partially understood considering the rather high HOMO level of this polymer at 5.25 eV, compared to 5.44 eV of the Ir-SC4 dye. In fact, including a TPBI hole-blocking layer considerably improved the device efficiency. On the other hand, the triplet energy of copolymers containing spirofluorene units was as low as 2.2 eV, due to the quarter-p-phenyl-segment, as indicated in Fig. 11.21. This resulted in low efficiencies due to quenching of the dye triplet state. The highest efficiencies were obtained for a copolymer containing an oxadiazole unit in the side chain (right structure in Fig. 11.21). This copolymer has a triplet energy of 2.56 eV and the HOMO at 5.45 eV. Single-layer devices with a dye concentration of 8 wt. % exhibited a luminance efficiency of 23 cd/A, independent of the current density. Even though the dye does not constitute a deep hole trap in the copolymer, incorporation of a TPBI hole-blocking layer did not affect the efficiency considerably. Most likely, the dye forms an electron trap in the copolymer matrix. Unfortunately, no driving conditions or PCE values were provided.

In contrast to green-emitting devices, choosing a host with a lower triplet state energy than that of PVK is rather meaningful for red-emitting dyes. In fact, PtOEP, PtOX and btp<sub>2</sub>Ir(acac) have been blended into various hosts such as polyfluorene [32, 35, 37, 80] or ladder-type MeLPPP [41, 42]. Unfortunately, only a few papers discuss a direct comparison between different hosts in combination with a specific dye (see, e.g., [35,54,80]). In general one expects that lowering the band-gap will also reduce the barriers for charge injection and, thus, the driving voltage. For example, Cao and coworkers [54] compared the performance of ITO/



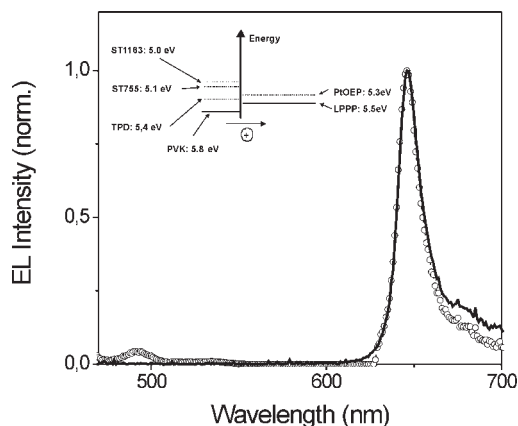
**Fig. 11.21** Chemical structures of carbazole homo- and copolymers studied by van Dijken et al. (reproduced from [87]).

**Fig. 11.22** Current–brightness–voltage characteristics of single-layer devices with different doping concentrations of PtOEP in MeLPPP. Solid and open symbols depict brightness–voltage and current–voltage curves, respectively [42].



PEDT:PSS/emission-layer/Ba/Al devices with the red dye  $\text{pic}_2\text{Ir}(\text{acac})$  blended into either a PVK:PBD(40 wt.%), a PFO:PBD (30 wt.%) or a PFTA:PBD (30 wt.%) host (where PFTA is a hyperbranched polyfluorene with a triphenylamine core). Even though the maximum efficiencies of all devices were quite comparable (10%), the voltage to drive the PFTA:PBD device at ca.  $1300 \text{ cd/m}^2$  was only 10.1 V, compared to 13.9 V for the PVK:PBD device.

Similarly to this, a single-layer device containing PtOEP in MeLPPP showed a brightness of  $70 \text{ cd/m}^2$  at 8.5 V, irrespective of the dye concentration (see Fig. 11.22) [42], while a similar device with PtOEP in PFO required more than 20 V to achieve the same brightness, with a strong dependence on dye concentration [37]. These results demonstrate that choosing the appropriate matrix for red dyes can be very beneficial with respect to the driving conditions. However, one disadvantage of using a host with the HOMO level close to that of the dye is that charges can be rapidly detrapped. In fact, the efficiency of a single-layer MeLPPP:PtOEP device was very poor (below  $0.1 \text{ cd/A}$ ). The efficiency improved considerably when adding a PMMA:Alq<sub>3</sub> electron-transporting layer and a PVK layer doped with hole-transporting molecules (HTMs). Apparently, the function of the PMMA:Alq<sub>3</sub> layer was to prevent holes exiting the devices through the cathode. Interestingly, the color and efficiency of the device depended strongly on the HOMO of the HTM blended into PVK. Figure 11.23 compares the EL spectra of



**Fig. 11.23** Comparison of the EL spectra of devices consisting of a MeLPPP:PtOEP emission layer and with (solid line) or without (open symbols) a PVK:ST1163 hole-injecting layer. The inset shows the relative positions of the HOMO levels of the doped hole injection layer and the MeLPPP:PtOEP emission layer [42].

devices with and without a PVK:ST1163 layer (ST1163 is N,N'-diphenyl-N,N'-bis-(4'-(N,N-bis(naphth-2-yl)-amino)-biphenyl-4-yl)-benzidine) at the same driving current. Most notable, the color purity is excellent for the device utilizing a PVK:ST1163 hole-transporting layer, while devices without a doped PVK layer exhibited significant host emission. In order to reveal the role of the hole-transporting dopant in PVK, we tested two other hole-transporting molecules with different ionization potentials. Only the devices utilizing ST1163 and ST755 (ionization potential 5.1 eV) emitted pure red light, without measurable MeLPPP emission, while a device with TPD (having a higher ionization potential of 5.4–5.5 eV) exhibited significant LPPP emission. This observation can be explained by the direct injection of holes from the HOMO of the hole-transporting molecule (either ST1163 or ST755) to the HOMO level of PtOEP, provided that transfer of holes from the HTM-HOMO to MeLPPP is slowed down by a considerable injection barrier.

Finally, white-emitting fluorescent/phosphorescent diodes using a polyfluorene host have been reported by Gong et al. Details about the composition and the performance of these devices are contained in Chapter 4.

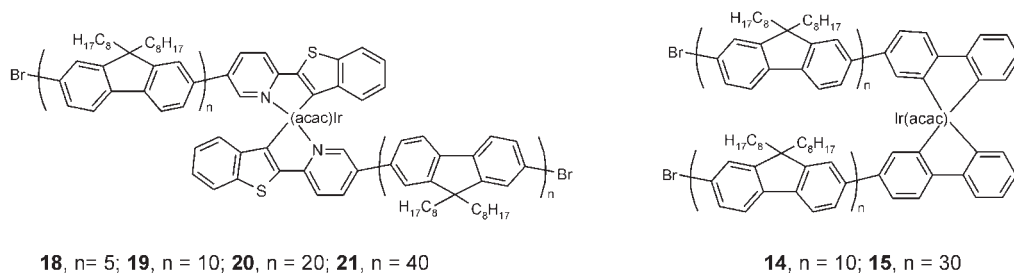
## 11.6

### Fully Functionalized Polymers

Finally, we would like to discuss some few examples for fully functionalized polymers. Chen et al. [89] presented a polyfluorene grafted with carbazole units and Btp<sub>2</sub>Ir(acac) dyes. For a copolymer with a dye concentration of 1.3 mol % (in the feed), the EL emission was purely red. Time-of-flight measurements indicated that the dye constitutes a hole trap. Also, the comparison of PL and EL spectra suggested that direct trapping of charges on the dye is the main excitation mechanism. Devices prepared with this copolymer exhibited good efficiencies (2.8 cd/A corresponding to 1.6 %) and high brightness at reasonable driving conditions (4321 cd/m<sup>2</sup> @ 15 V).

Tokito et al. [85] studied a series of copolymers based on a nonconjugated backbone, having carbazole and emissive Ir-complexes in the side chain. Even though the chemical structures of these polymers are quite simple, rather high quantum efficiencies (3 %, 9 % and 5 % for blue, green and red emission, respectively) were reported in a single-layer device structure.

Finally, Holmes and coworkers [90] reported a series of solution-processible polymers with iridium units covalently attached to oligofluorene segments (see Fig. 11.24 for the chemical structure). Most interestingly, even the polymers with an ppy<sub>2</sub>Ir(acac) emissive unit emitted almost pure green light. In contrast a blend of ppy<sub>2</sub>Ir(acac) in PFO with the same molar percentage showed significant emission from the host. It was concluded that the polymeric complex exhibits a mixed triplet state. This interpretation is supported by a considerable red-shift of the phosphorescence of the polymeric complexes when compared to the isolated chromophore. Unfortunately, the efficiency of devices made with



**Fig. 11.24** Chemical structure of solution-processible polymers with iridium units covalently attached to oligofluorene segments [90].

these polymers was very low. As expected, higher efficiencies were obtained with polymers containing the red-emitting  $\text{btp}_2\text{Ir}(\text{acac})$  dye, since exciton back transfer to the oligofluorene segments would be endothermic. In fact, devices with quantum efficiencies of up to 1.5 % could be realized.

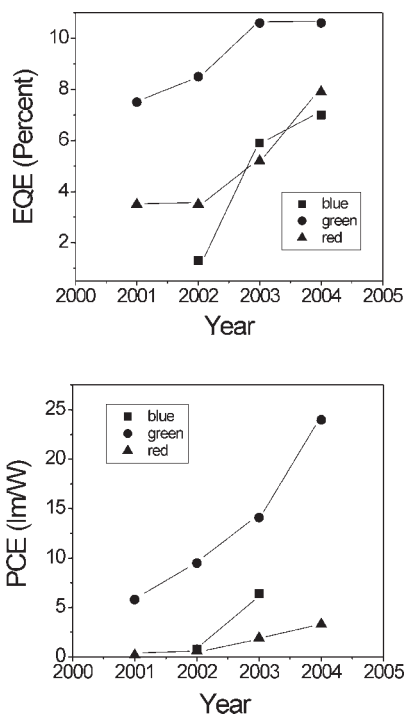
## 11.7

### Conclusion and Outlook

The results summarized above demonstrate that efficient electrophosphorescent diodes can be made using polymer hosts. In fact, the external quantum efficiencies and power conversion efficiencies of blue-, green- and red-emitting devices have increased considerably over the last 3 years (see Fig. 11.25). Moreover, many critical points relevant to the performance of polymer-based electrophosphorescent devices have now been identified, including insufficient trapping of excitons and charges on the dyes, injection barriers and concentration quenching.

Nevertheless, further efforts need to be made to increase the external quantum efficiency of these devices towards the quantum limit (which should be ca. 20 % for a phosphor with a phosphorescence efficiency of unity). In the case of the green-emitting  $\text{Ir}(\text{ppy})_3$  complex, small molecule multilayer devices indeed show quantum efficiencies close to this limit. Since polymer-based devices with  $\text{Ir}(\text{ppy})_3$  (or  $\text{Ir}(\text{mppy})_3$  or  $(\text{ppy})_2\text{Ir}(\text{acac})$ ) doped at an optimum concentration into a wide-bandgap polymer exhibit pure dye emission, all charge-carrier recombination events apparently lead to the excitation of the dye molecules. Thus, the lower EQE of polymer-based electrophosphorescent devices must be mainly related to the imbalanced injection and transport of charges. In small molecule multilayer stacks, balanced injection is achieved by using electron-transporting and hole-transporting layers with appropriate energy levels, including the usage of doped layers [75]. Also, optimizing the HOMO and LUMO energy offset between adjacent layers insures that charges recombine almost exclusively in the emission layer. One major task in the future must, therefore, be to insure efficient





**Fig. 11.25** Summary of best values of the external quantum efficiency and power conversion efficiency, reported for polymer-based electrophosphorescent devices over the past 3 years.

recombination of charges on the phosphor in the polymer matrix, e.g. by using direct injection of charges into the HOMO or LUMO of the phosphor.

### Acknowledgement

We would like to thank Prof. H. Yersin (University of Regensburg, Germany) for having a critical look through the manuscript. Part of our work presented in this Chapter was supported by the Bundesministerium für Bildung und Forschung (BMBF) through grant 13N8213.

### References

- 1 J. H. Burroughes, D. D. C. Bradley, A. R. Brown, R. N. Marks, K. Mackay, R. H. Friend, P. L. Burns, A. B. Holmes, *Nature* **1990**, 347, 539–541.
- 2 G. Gustafsson, Y. Cao, G. M. Treacy, F. Klavetter, N. Colaneri, A. J. Heeger, *Nature* **1992**, 357, 477–479.
- 3 N. C. Greenham, R. H. Friend, D. D. C. Bradley, *Adv. Mater.* **1994**, 6, 491–494.
- 4 A. R. Brown, K. Pichler, N. C. Greenham, D. D. C. Bradley, R. H. Friend, A. B. Holmes, *Chem. Phys. Lett.* **1993**, 210, 61–66.
- 5 Y. V. Romanovskii, A. Gerhard, B. Schweitzer, U. Scherf, R. I. Personov, H. Bassler, *Phys. Rev. Lett.* **2000**, 84, 1027–1030.

- 6 S. Sinha, C. Rothe, R. Güntner, U. Scherf, A. P. Monkman, *Phys. Rev. Lett.* **2003**, *90*, art. no.-127402.
- 7 J. M. Lupton, A. Pogantsch, T. Piok, E. J. W. List, S. Patil, U. Scherf, *Phys. Rev. Lett.* **2002**, *89*, art. no.-167401.
- 8 A. Köhler, J. S. Wilson, R. H. Friend, M. K. Al-Suti, M. S. Khan, A. Gerhard, H. Bassler, *J. Chem. Phys.* **2002**, *116*, 9457–9463.
- 9 Y. Cao, I. D. Parker, G. Yu, C. Zhang, A. J. Heeger, *Nature* **1999**, *397*, 414–417.
- 10 M. Wohlgenannt, K. Tandon, S. Mazumdar, S. Ramasesha, Z. V. Vardeny, *Nature* **2001**, *411*, 617–617.
- 11 J. S. Wilson, A. S. Dhoot, A. Seeley, M. S. Khan, A. Kohler, R. H. Friend, *Nature* **2001**, *413*, 828–831.
- 12 A. S. Dhoot, N. C. Greenham, *Adv. Mater.* **2002**, *14*, 1834–1837.
- 13 P. Herguch, X. Z. Jiang, M. S. Liu, A. K. Y. Jen, *Macromolecules* **2002**, *35*, 6094–6100.
- 14 Q. F. Xu, J. Y. Ouyang, Y. Yang, T. Ito, J. Kido, *Appl. Phys. Lett.* **2003**, *83*, 4695–4697.
- 15 M. A. Baldo, D. F. O'Brien, Y. You, A. Shoustikov, S. Sibley, M. E. Thompson, S. R. Forrest, *Nature* **1998**, *395*, 151–154.
- 16 R. J. Holmes, B. W. D'Andrade, S. R. Forrest, X. Ren, J. Li, M. E. Thompson, *Appl. Phys. Lett.* **2003**, *83*, 3818–3820.
- 17 M. Ikai, S. Tokito, Y. Sakamoto, T. Suzuki, Y. Taga, *Appl. Phys. Lett.* **2001**, *79*, 156–158.
- 18 C. Adachi, M. A. Baldo, M. E. Thompson, S. R. Forrest, *J. Appl. Phys.* **2001**, *90*, 5048–5051.
- 19 A. Tsuboyama, H. Iwawaki, M. Furugori, T. Mukaide, J. Kamatani, S. Igawa, T. Moriyama, S. Miura, T. Takiguchi, S. Okada, M. Hoshino, K. Ueno, *J. Am. Chem. Soc.* **2003**, *125*, 12971–12979.
- 20 C.-H. Yang, C.-C. Tai, I.-W. Sun, *J. Mater. Chem.* **2004**, *14*, 947–950.
- 21 J. Kido, K. Nagai, Y. Ohashi, *Chem. Lett.* **1990**, 657–660.
- 22 R. C. Kwong, S. Sibley, T. Dubovoy, M. Baldo, S. R. Forrest, M. E. Thompson, *Chem. Mater.* **1999**, *11*, 3709–3713.
- 23 M. A. Baldo, D. F. O'Brien, M. E. Thompson, S. R. Forrest, *Phys. Rev. B* **1999**, *60*, 14422–14428.
- 24 S. Lamansky, P. Djurovich, D. Murphy, F. Abdel-Razzaq, H. E. Lee, C. Adachi, P. E. Burrows, S. R. Forrest, M. E. Thompson, *J. Am. Chem. Soc.* **2001**, *123*, 4304–4312.
- 25 C. Adachi, R. C. Kwong, P. Djurovich, V. Adamovich, M. A. Baldo, M. E. Thompson, S. R. Forrest, *Appl. Phys. Lett.* **2001**, *79*, 2082–2084.
- 26 W. P. Finkenzeller, P. Stöckel, H. Yersin, *Chem. Phys. Lett.* **2004**, *397*, 289–295.
- 27 D. Kolosov, V. Adamovich, P. Djurovich, M. E. Thompson, C. Adachi, *J. Am. Chem. Soc.* **2002**, *124*, 9945–9954.
- 28 V. I. Adamovich, S. R. Cordero, P. I. Djurovich, A. Tamayo, M. E. Thompson, B. W. D'Andrade, S. R. Forrest, *Org. Electron.* **2003**, *4*, 77–87.
- 29 Y. Wang, N. Herron, V. V. Grushin, D. LeCloux, V. Petrov, *Appl. Phys. Lett.* **2001**, *79*, 449–451.
- 30 A. P. Monkman, H. D. Burrows, L. J. Hartwell, L. E. Horsburgh, I. Hamblett, S. Navaratnam, *Phys. Rev. Lett.* **2001**, *86*, 1358–1361.
- 31 D. Hertel, S. Setayesh, H. G. Nothofer, U. Scherf, K. Müllen, H. Bässler, *Adv. Mater.* **2001**, *13*, 65–70.
- 32 V. Cleave, G. Yahioglu, P. Le Barny, R. H. Friend, N. Tessler, *Adv. Mater.* **1999**, *11*, 285–288.
- 33 M. J. Yang, T. Tsutsui, *Jpn. J. Appl. Phys. Part 2 - Lett.* **2000**, *39*, L828–L829.
- 34 S. Lamansky, R. C. Kwong, M. Nugent, P. I. Djurovich, M. E. Thompson, *Org. Electron.* **2001**, *2*, 53–62.
- 35 V. Cleave, G. Yahioglu, P. Le Barny, D. H. Hwang, A. B. Holmes, R. H. Friend, N. Tessler, *Adv. Mater.* **2001**, *13*, 44–47.
- 36 D. F. O'Brien, C. Giebeler, R. B. Fletcher, A. J. Cadby, L. C. Palilis, D. G. Lidzey, P. A. Lane, D. D. C. Bradley, W. Blau, *Synth. Met.* **2001**, *116*, 379–383.
- 37 P. A. Lane, L. C. Palilis, D. F. O'Brien, C. Giebeler, A. J. Cadby, D. G. Lidzey, A. J. Campbell, W. Blau, D. D. C. Bradley, *Phys. Rev. B* **2001**, *63*, 235206.
- 38 T.-F. Guo, S.-C. Chang, Y. Yang, R. C. Kwong, M. E. Thompson, *Org. Electron.* **2000**, *1*, 15–20.
- 39 L. H. Campbell, D. L. Smith, S. Tretiak, R. L. Martin, C. J. Neef, J. R. Ferraris, *Phys. Rev. B* **2002**, *65*, 085210.

- 40 W. G. Zhu, Y. Q. Mo, M. Yuan, W. Yang, Y. Cao, *Appl. Phys. Lett.* **2002**, *80*, 2045–2047.
- 41 R. W. T. Higgins, A. P. Monkman, H. G. Nothofer, U. Scherf, *J. Appl. Phys.* **2002**, *91*, 99–105.
- 42 X. H. Yang, D. Neher, U. Scherf, S. A. Bagnich, H. Bässler, *J. Appl. Phys.* **2003**, *93*, 4413–4419.
- 43 A. W. Grice, D. D. C. Bradley, M. T. Bernius, M. Inbasekaran, W. W. Wu, E. P. Woo, *Appl. Phys. Lett.* **1998**, *73*, 629–631.
- 44 D. Sainova, T. Miteva, H. G. Nothofer, U. Scherf, I. Glowacki, J. Ulanski, H. Fujikawa, D. Neher, *Appl. Phys. Lett.* **2000**, *76*, 1810–1812.
- 45 D. Neher, *Macromol. Rapid Commun.* **2001**, *22*, 1366–1385.
- 46 U. Scherf, E. J. W. List, *Adv. Mater.* **2002**, *14*, 477–487.
- 47 Y. Y. Noh, C. L. Lee, J. J. Kim, K. Yase, *J. Chem. Phys.* **2003**, *118*, 2853–2864.
- 48 R. A. Negres, X. Gong, J. C. Ostrowski, G. C. Bazan, D. Moses, A. J. Heeger, *Phys. Rev. B* **2003**, *68*, 115209.
- 49 S. A. Bagnich, H. Bässler, D. Neher, *J. Chem. Phys.* **2004**.
- 50 C. Rothe, L. O. Palsson, A. P. Monkman, *Chem. Phys.* **2002**, *285*, 95–101.
- 51 A. A. Lamola, G. S. Hammond, *J. Chem. Phys.* **1965**, *43*, 2129.
- 52 M. Sudhakar, P. I. Djurovich, T. E. Hogen-Esch, M. E. Thompson, *J. Am. Chem. Soc.* **2003**, *125*, 7796–7797.
- 53 Y. Kawamura, S. Yanagida, S. R. Forrest, *J. Appl. Phys.* **2002**, *92*, 87–93.
- 54 C. Y. Jiang, W. Yang, J. B. Peng, S. Xiao, Y. Cao, *Adv. Mater.* **2004**, *16*, 537–541.
- 55 C. L. Lee, K. B. Lee, J. J. Kim, *Appl. Phys. Lett.* **2000**, *77*, 2280–2282.
- 56 W. D. Gill, K. K. Kanazawa, *J. Appl. Phys.* **1972**, *43*, 529.
- 57 S. Lamansky, P. I. Djurovich, F. Abdel-Razzaq, S. Garon, D. L. Murphy, M. E. Thompson, *J. Appl. Phys.* **2002**, *92*, 1570–1575.
- 58 K. M. Vaeth, C. W. Tang, *J. Appl. Phys.* **2002**, *92*, 3447–3453.
- 59 X. Gong, M. R. Robinson, J. C. Ostrowski, D. Moses, G. C. Bazan, A. J. Heeger, *Adv. Mater.* **2002**, *14*, 581–585.
- 60 X. Gong, J. C. Ostrowski, D. Moses, G. C. Bazan, A. J. Heeger, *Adv. Funct. Mater.* **2003**, *13*, 439–444.
- 61 X. H. Yang, D. Neher, D. Hertel, T. K. Daubler, *Adv. Mater.* **2004**, *16*, 161–166.
- 62 T. Q. Nguyen, R. C. Kwong, M. E. Thompson, B. J. Schwartz, *Appl. Phys. Lett.* **2000**, *76*, 2454–2456.
- 63 H. Hänsel, D. C. Müller, M. Gross, K. Meerholz, G. Krausch, *Macromolecules* **2003**, *36*, 4932–4936.
- 64 T. M. Brown, R. H. Friend, I. S. Millard, D. J. Lacey, J. H. Burroughes, F. Cacialli, *Appl. Phys. Lett.* **2001**, *79*, 174–176.
- 65 G. E. P. Box, W. G. Hunter, J. S. Hunter: *Statistics for Experimenters*, John Wiley, New York, **1978**.
- 66 G. E. Jabbour, J. F. Wang, B. Kippelen, N. Peyghambarian, *Jpn. J. Appl. Phys. Part 2 - Lett.* **1999**, *38*, L1553–L1555.
- 67 X. H. Yang, Y. Q. Mo, W. Yang, G. Yu, Y. Cao, *Appl. Phys. Lett.* **2001**, *79*, 563–565.
- 68 K. M. Vaeth, J. Dicillo, *J. Polym. Sci. Part B - Polym. Phys.* **2003**, *41*, 2715–2725.
- 69 X. H. Yang, D. Neher, *Appl. Phys. Lett.* **2004**, *84*, 2476–2478.
- 70 J. Kalinowski, W. Stampor, J. Mezyk, M. Cocchi, D. Virgili, V. Fattori, P. Di Marco, *Phys. Rev. B* **2002**, *66*, 235321.
- 71 D. M. Pai, J. F. Yanus, M. Stolka, *J. Phys. Chem.* **1984**, *88*, 4714–4717.
- 72 X. Jiang, R. A. Register, K. A. Killen, M. E. Thompson, F. Pschenitzka, T. R. Hebner, J. C. Sturm, *J. Appl. Phys.* **2002**, *91*, 6717–6724.
- 73 M. A. Baldo, S. Lamansky, P. E. Burrows, M. E. Thompson, S. R. Forrest, *Appl. Phys. Lett.* **1999**, *75*, 4–6.
- 74 T. Tsutsui, M. J. Yang, M. Yahiyo, K. Nakamura, T. Watanabe, T. Tsuji, Y. Fukuda, T. Wakimoto, S. Miyaguchi, *Jpn. J. Appl. Phys. Part 2 - Lett.* **1999**, *38*, L1502–L1504.
- 75 M. Pfeiffer, S. R. Forrest, K. Leo, M. E. Thompson, *Adv. Mater.* **2002**, *14*, 1633–1636.
- 76 M. D. McGehee, T. Bergstedt, C. Zhang, A. P. Saab, M. B. O'Regan, G. C. Bazan, V. I. Srdanov, A. J. Heeger, *Adv. Mater.* **1999**, *11*, 1349–1354.
- 77 J. B. Peng, N. Takada, N. Minami, *Thin Solid Films* **2002**, *405*, 224–227.

- 78 M. R. Robinson, J. C. Ostrowski, G. C. Bazan, M. D. McGehee, *Adv. Mater.* **2003**, *15*, 1547–1551.
- 79 H. Xia, C. B. Zhang, S. Qiu, P. Lu, J. Y. Zhang, Y. G. Ma, *Appl. Phys. Lett.* **2004**, *84*, 290–292.
- 80 F. C. Chen, Y. Yang, M. E. Thompson, J. Kido, *Appl. Phys. Lett.* **2002**, *80*, 2308–2310.
- 81 X. Gong, J. C. Ostrowski, G. C. Bazan, D. Moses, A. J. Heeger, *Appl. Phys. Lett.* **2002**, *81*, 3711–3713.
- 82 A. Nakamura, T. Tada, M. Mizukami, S. Yagyu, *Appl. Phys. Lett.* **2004**, *84*, 130–132.
- 83 Y. J. Su, H. L. Huang, C. L. Li, C. H. Chien, Y. T. Tao, P. T. Chou, S. Datta, R. S. Liu, *Adv. Mater.* **2003**, *15*, 884–888.
- 84 I. Tanaka, M. Suzuki, S. Tokito, *Jpn. J. Appl. Phys. Part 1 - Reg. Pap. Short Notes Rev. Pap.* **2003**, *42*, 2737–2740.
- 85 S. Tokito, M. Suzuki, F. Sato, M. Kamachi, K. Shirane, *Org. Electron.* **2003**, *4*, 105–111.
- 86 Y. Yang, Q. Pei, A. J. Heeger, *J. Appl. Phys.* **1996**, *79*, 934–939.
- 87 A. van Dijken, J. Bastiaansen, N. M. M. Kiggen, B. M. W. Langeveld, C. Rothe, A. Monkman, I. Bach, P. Stossel, K. Brunner, *J. Am. Chem. Soc.* **2004**, *126*, 7718–7727.
- 88 K. Brunner, A. van Dijken, H. Borner, J. Bastiaansen, N. M. M. Kiggen, B. M. W. Langeveld, *J. Am. Chem. Soc.* **2004**, *126*, 6035–6042.
- 89 X. W. Chen, J. L. Liao, Y. M. Liang, M. O. Ahmed, H. E. Tseng, S. A. Chen, *J. Am. Chem. Soc.* **2003**, *125*, 636–637.
- 90 A. J. Sandee, C. K. Williams, N. R. Evans, J. E. Davies, C. E. Boothby, A. Kohler, R. H. Friend, A. B. Holmes, *J. Am. Chem. Soc.* **2004**, *126*, 7041–7048.

## 12

### Low-threshold Organic Semiconductor Lasers

*Daniel Schneider, Uli Lemmer, Wolfgang Kowalsky, Thomas Riedl<sup>1)</sup>*

#### 12.1

##### Introduction

Almost 40 years ago the first organic lasers based on dye molecules in liquid solutions were demonstrated [1, 2]. Due to their broad gain spectra and wide tuning ranges throughout the visible and the adjacent ultraviolet and infrared parts of the spectrum they have been used in various applications (e.g. medicine, LIDAR, physics and chemistry). The inherent drawbacks of this technology are the use of predominantly toxic and flammable solvents together with an elaborate infrastructure (e.g. dye circulators) requiring regular maintenance. Thus, dye-doped solid-state matrices [3–5] and organic crystals [6] have been pursued as alternative gain materials with similar benefits.

In the 1980's the demonstration of efficient electroluminescence in organic thin-film heterostructures by Tang et al. [7–9] paved the way for a new era of organic (opto-)electronics. The remarkable progress in this field led to a variety of products that are already commercially available. Among them, flat-panel displays based on organic light-emitting diodes (OLEDs) are probably the most prominent representatives. These achievements seeded the prospect for future organic injection lasers that are expected to bring about several advantages compared to their established inorganic analogs. Wide tunability and low-cost fabrication are among their major strengths and render them very attractive, even for disposable devices. Therefore, it is of particular interest to study organic gain media that, in contrast to dye-doped solid-state matrices mentioned above, offer charge-transporting cap-

<sup>1)</sup> The results we present in this chapter are in part based on collaborations with several public and private research facilities and companies. We appreciate the cooperation with the group of Dr. Weimann from Physikalisch-Technische Bundesanstalt (PTB), Braunschweig (Germany), the group of Prof. Scherf from the University of Wuppertal (Germany), the group of Prof. Salbeck from

the University of Kassel (Germany). Special thanks also go to COVION and Ticona for supplying organic materials. The authors gratefully acknowledge financial support by the German Federal Ministry for Education and Research BMBF (FKZ 13N8166) within the OLAS collaboration and the Deutsche Forschungsgemeinschaft DFG through the Gottfried Wilhelm Leibniz award.

abilities. Optically pumped lasers based on thin films of conjugated polymers [10, 11] and small organic molecules [12, 13] were demonstrated in the second half of the 1990's. However, up to now no electrically driven organic semiconductor laser has been shown. One of the main obstacles thereby is connected to the prospective current densities, several orders of magnitude higher than in OLEDs, and the subsequently high carrier densities in the active medium leading to various optical-quenching processes [14]. Thus, key prerequisites for organic injection lasers are highly efficient amplifying materials that in connection with low-loss waveguides and resonator geometries allow for low-threshold operation.

The aim of this chapter is to shed light on recent achievements towards low-threshold organic semiconductor lasers without the claim to give an in-depth review of this exciting field of research in its completeness. For additional reading we refer the reader to the publications of Dodabalapur and Forrest regarding small-molecule organic lasers [15, 16] and the reviews of Lemmer, Tessler, Kratzelbinder, Frolov, McGehee, and Scherf regarding lasing in conjugated polymers [17–22].

In Section 12.2 we will introduce several organic materials that have recently received attention as candidates for organic semiconductor lasers. Furthermore, we discuss technological aspects like film formation and promising resonator geometries for these lasers. Section 12.3 will highlight some recent results in the field aimed at low-threshold operation. In Section 12.4, we will compare properties and threshold values of different organic materials. Prospects for electrical operation of organic semiconductor lasers will be discussed in Section 12.5.

## 12.2

### Fundamentals of Organic Semiconductor Lasers

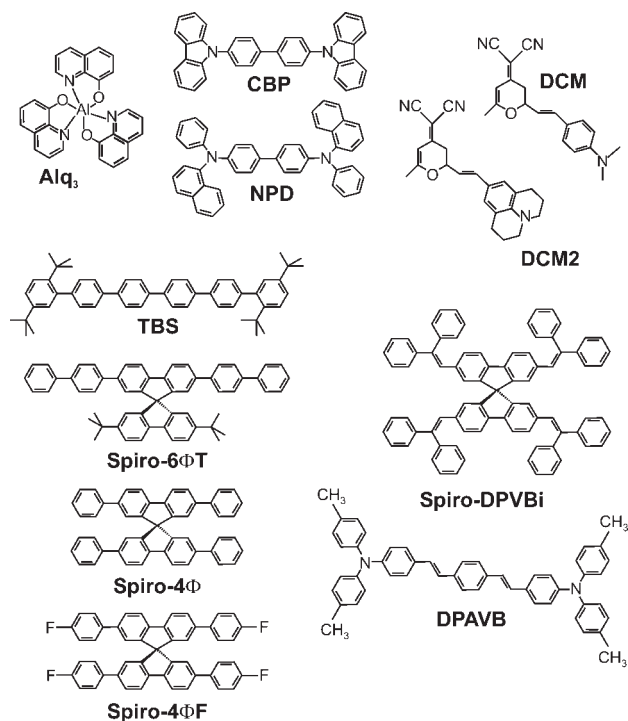
#### 12.2.1

##### Stimulated Emission in Organic Materials

When using solid-state films based on conventional laser dyes significant luminescence quenching resulting from a strong interaction of molecules normally prevents efficient stimulated emission processes [20, 21]. Therefore, organic solid-state lasers are often based on guest–host systems [23–25]. Here, the self-absorption of the matrix is efficiently circumvented by shifting the emission of the guest to a wavelength region where the host material is transparent, leading to very low laser thresholds.

In Fig. 12.1, the chemical structures of suitable low molecular weight materials for organic semiconductor lasers are shown. A very prominent system for solid-state organic lasers is the guest–host (G–H) system comprising the host material Tris-(8-hydroxyquinoline)aluminum ( $\text{Alq}_3$ ) and the guest molecules 4-(Dicyanomethylen)-2-methyl-6-(p-dimethylamino styryl)-4H-pyran (DCM) and 4-(Dicyanomethylene)-2-methyl-6-(julolidin-4-yl-vinyl)-4H-pyran (DCM2).  $\text{Alq}_3$  has been used as a green emitter and electron-transport layer in organic devices for two-

**Fig. 12.1** Various low molecular weight materials for use in organic lasers.



decades now [9, 26, 27]. DCM and DCM2 are well-known laser dyes for liquid-dye applications in the red spectral region [28, 29]. The G–H systems Alq<sub>3</sub>:DCM and Alq<sub>3</sub>:DCM2 are among the first low molecular weight material systems, in which stimulated emission in thin films was found [23, 30]. Lasing has been demonstrated in a variety of resonator designs including Fabry–Perot resonators, distributed Bragg reflection (DBR) and distributed feedback (DFB) structures [12, 31–34]. The wavelength of the photoluminescence maxima in DCM- and DCM2-doped systems can be tuned over a wide range by varying the doping concentration of the guest molecules. This is caused by the solid-state solvation effect (SSSE). By changing the concentration of guest molecules with a high polarity in a host material with a lower polarity, the polarity of the matrix can be varied, resulting in a wavelength shift of the emission. It has been shown that the photoluminescence maximum of Alq<sub>3</sub>:DCM2 thin films can be varied from 605 nm (0.5% DCM2) to 650 nm (10% DCM2) [35]. This effect was also reported for other host materials including *N,N*-di(1-naphthyl)-*N,N'*-diphenyl-1,1'-diphenyl-4,4'-diamine (NPD). Like NPD 4,4'-*N,N'*-dicarbazole-biphenyl (CBP) can also be used as host for DCM derivatives. CBP and NPD are normally used as hole-transport materials in OLEDs [36, 37]. NPD can also be used as a blue-emitting material [38] or as host material in the G–H system NPD:DCM2 resulting in white-emitting OLEDs [39].

Besides the guest–host systems, there are a number of low molecular weight materials where stimulated emission and lasing have been reported for neat films. They include stilbenes [40, 41], oligothiophenes [42–44], and oligophenylenes [45, 46]. Oligophenylenes are normally used as laser dyes in conventional liquid or vapor dye lasers [47–49]. Recently, stimulated emission and lasing could be observed in epitaxially grown nanofibers of *p*-sexiphenyl [45, 46]. When trying to deposit amorphous layers, *p*-sexiphenyl tends to form polycrystalline films with small domains, which induce optical losses at the grain boundaries that effectively prevent stimulated emission [50, 51].

One concept to enhance film quality and to hamper crystallization is the spiro-linkage of a chromophore to other molecular groups. These materials have been proven to be very stable materials for charge-transport and emitting layers in OLEDs [52, 53]. The spiro-linkage of two molecular groups by an additional carbon atom leads to a rigid structure and efficiently prevents crystallization. It has been demonstrated that the glass transition temperature  $T_G$  can be significantly increased utilizing this concept [54, 55]. Due to their improved morphological stability spiro-linked compounds are also known as promising active materials for organic solid-state lasers. Amplified spontaneous emission (ASE) or lasing has been observed in a variety of spiro-linked materials, including Spiro-quar-terphenyl (Spiro-4 $\Phi$ ) and Spiro-sexiphenyl (Spiro-6 $\Phi$ ) [56, 57]. The emission wavelength of spiro-linked oligophenylenes and their derivatives depends on the length of the phenyl chain and reaches from the UV region for Spiro-4 $\Phi$  and 2,2',7,7'-Tetrakis(4-fluorophenyl)-spiro-9,9'-bifluorene (Spiro-4 $\Phi$ F) to the blue region for sexiphenyl based compounds like Spiro-6 $\Phi$  and 2,7-bis(biphenyl-4-yl)-2',7'-di-*tert*-butyl-9,9'-spirobifluorene (Spiro-6 $\Phi$ T) [58, 59]. Another spiro-linked material that exhibits low-threshold lasing is 2,2',7,7'-tetrakis(2,2-diphenyl-vinyl)spiro-9,9'-bifluorene (Spiro-DPVBi) [25]. This material is based on the spiro-linkage of two DPVBi molecules, which belong to the group of highly emissive stilbenes. Aside from its emission in the green spectral region, Spiro-DPVBi also exhibits moderate electron and hole mobilities [60]. Furthermore, the stilbene compound 1,4-Bis[2-[4-[*N,N*-di(*p*-tolyl)amino]phenyl]vinyl]benzene (DPAVB) has been proven to be a low-threshold active laser material [41, 61].

Aside from the spiro-linkage one could also think of other sterical groups that prevent crystallization of the dye molecules. In the TBS (3,5,3''',5''''-Tetra-*tert*-butyl-*p*-sexiphenyl) molecule, *tert*-butyl groups are used at the benzene chain ends to hamper the mobility of the molecules in the film. Being a well-known laser dye for liquid-dye lasers [62] the molecule can also be used to form amorphous thin-films for laser applications [51].

The second group of organic materials that have enormous potential for laser applications are conjugated polymers. Similar to low molecular weight materials the electrical and optical properties are determined by the delocalized  $\pi$ -electron system along the polymer chain. Polymers that are suited for an application in solid-state thin-film organic lasers include derivatives of poly(*p*-phenylene vinylene) (PPV), poly(*p*-phenylene) (PPP) and polyfluorene (PF). They possess high luminescence efficiencies combined with a high chromophore density.



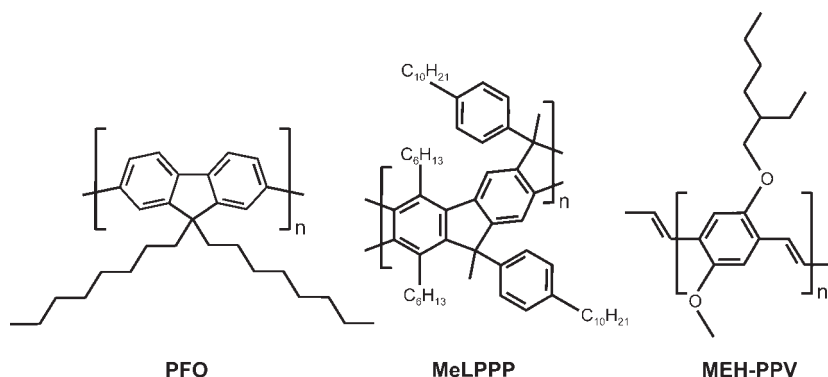


Fig. 12.2 Conjugated polymers for use in organic lasers.

Unsubstituted conjugated materials are known for their poor solubility, a property that is a considerable hindrance to the fabrication of thin-film solid-state lasers. A well-established strategy to increase solubility and therefore also processability is the introduction of solubilizing groups (alkyl-, alkoxy- or aryl substituents). One of the conjugated polymers with high optical gain is the methyl-substituted conjugated ladder-type poly(para-phenylene) (MeLPPP) [63]. The chemical structure is shown in Fig. 12.2. This polymer offers a large material gain beyond  $2000\text{ cm}^{-1}$ , excellent film-forming properties and high charge-carrier mobility together with low charge-trap densities [64–66]. Previous studies have shown that this polymer allows solid-state surface-emitting lasers based on second-order distributed feedback (DFB) structures to be built in linear and circular geometry as well as in two-dimensional DFB structures [67–71].

In the PPV system there is a large variety of substituted polymers suitable for use in organic lasers. Among the PPV derivatives with low laser thresholds, there is Poly(2-methoxy-5-(2'-ethylhexyloxy)-1,4-phenylenevinylene) (MEH-PPV). Asymmetric alkoxy side groups improve the solubility resulting in good morphological film properties [72]. The good optical properties make this polymer interesting for OLEDs [73] and also for laser applications. After demonstration of stimulated emission in solution [74] and solid-state matrices [11, 75, 76], ASE could be demonstrated also in neat films of MEH-PPV [77, 78]. Lasing using thin films of MEH-PPV has been shown for various resonator geometries [79–81].

The most widely used laser material from the PF system is poly(9,9-dioctylfluorene) (PFO). It exhibits superior blue photoluminescence and electroluminescence properties [82] and has excellent charge-transport properties [83]. The polymer shows strong, low-threshold stimulated emission in the blue spectral region and exhibits large net optical gain along with low losses in slab waveguide geometries [83–85].

## 12.2.2

**Resonators for Organic Lasers**

Aside from the active material a feedback mechanism is essential to complete a laser structure. In a simple case, a Fabry–Perot resonator may be utilized for this purpose by placing the organic material between two parallel mirrors. Here, standing electromagnetic waves are formed with wavelengths determined by the cavity length  $L$  and the effective refractive index  $n_{\text{eff}}$  of the waveguide,

$$m\lambda/2n_{\text{eff}} = L \quad (12.1)$$

with  $m$  being the order of the lasing mode. In this geometry, organic lasing has been demonstrated using G–H systems of low molecular weight materials [12, 24, 86]. Due to the easy handling and processing of the organic materials various resonator designs can be realized for lasing experiments. In Fig. 12.3, some of the already demonstrated resonator options for organic materials are shown. The first experiments were performed using microcavity lasers [10]. Here, the organic material is located between two planar metallic or dielectric mirrors with a spacing in the range of the lasing wavelength. The vertical design is similar to a conventional OLED. However, due to the limited gain length and rather lossy metal mirrors, these structures exhibit high threshold values [87]. The threshold values can be reduced by using dielectric mirrors on both sides of the microcavity [88–91]. The first experiments regarding tunable organic lasers incorporated an external cavity resonator in the *Littrow* configuration. Here, an optical grating is used on one side of the resonator that allows for the tuning of the laser wavelength [92, 93]. Other resonator geometries comprise microrings, microdiscs and microdroplets [94–99]. Organic laser structures exhibiting very low laser threshold va-

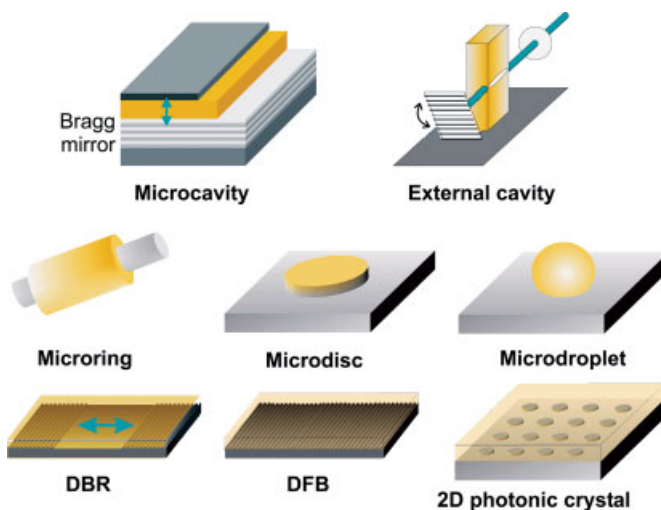


Fig. 12.3 Various resonator geometries for organic lasers.

lues have been demonstrated using resonators based on the distributed feedback principle [25, 58, 84, 85, 100–103]. Aside from distributed Bragg reflector (DBR) lasers and distributed feedback (DFB) lasers also two-dimensional (2D) structures belong to this class of resonators [68, 104–107].

Among the resonators described above, the concept of DFB is particularly promising as it allows for low laser thresholds and the possibility to easily tune the laser wavelength. For distributed feedback, a periodic modulation of the refractive index is incorporated in the waveguide, so that light is reflected by Bragg reflection. Laser emission occurs near the Bragg wavelength  $\lambda_{\text{Bragg}}$  that is related to the modulation period of the DFB resonator  $\Lambda$  by the effective refractive index  $n_{\text{eff}}$  of the gain material and the DFB order number  $m$  ( $m = 1, 2, \dots$ ):

$$\lambda_{\text{Bragg}} = 2n_{\text{eff}}\Lambda/m \quad (12.2)$$

The laser threshold  $g_{\text{th}}$  depends on the length of grating section  $L$  and the coupling between the electromagnetic wave and the grating, expressed by the DFB coupling coefficient  $\kappa$ : [108]

$$g_{\text{th}} \cong \frac{\pi^2}{\kappa^2 L^3} \quad (12.3)$$

For  $m = 1$ , first-order DFB operation is obtained. The laser radiation is observed from the sample edge in this case. For a second-order DFB resonator ( $m = 2$ ), laser radiation is also emitted perpendicular to the sample surface. This part of the emission does not participate in the feedback of the laser process and acts as radiation loss. Therefore lower coupling coefficients  $\kappa$  and higher threshold energy values are expected for second- and higher-order DFB lasers compared to first-order DFB structures.

## 12.3

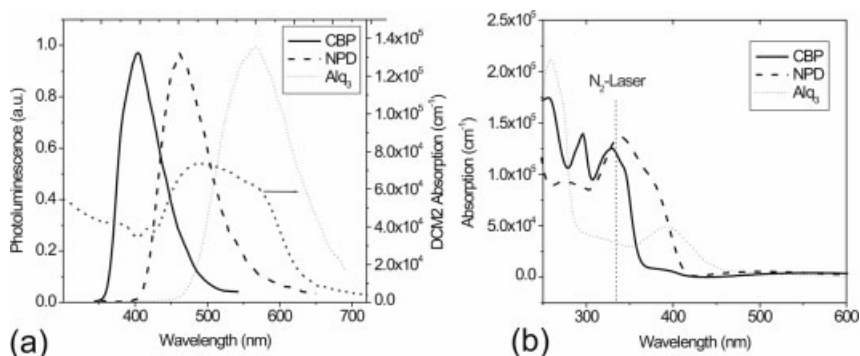
### Low-threshold Organic Lasing

This section presents some recent results for optically pumped organic DFB lasers with low-thresholds and large tuning ranges. Properties of first- and second-order DFB lasers using various organic materials are compared and discussed.

#### 12.3.1

##### Tunable Organic Lasers Based on G–H Systems Incorporating DCM and DCM2 Molecules

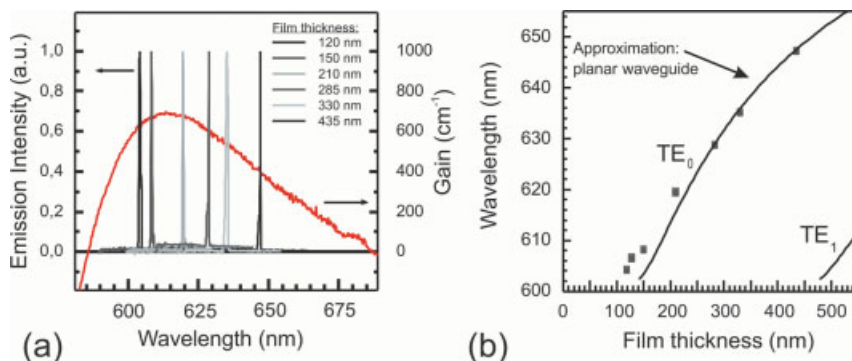
One possibility to realize low-threshold organic solid-state lasers is to utilize guest–host systems. In the following this is demonstrated for the example of DCM- and DCM2-doped organic semiconductors. As host materials the electron-transport material Alq<sub>3</sub> and the hole-conducting materials NPD and CBP are used.



**Fig. 12.4** Photoluminescence of host materials and absorption spectrum of DCM2 (a), and absorption coefficients of the host materials (b). The vertical line indicates the pump wavelength.

The energy transfer from the host to the dopant is based on the non radiative Förster transfer mechanism depending on the overlap integral of the host photoluminescence and the absorption spectrum of the dopant. In Fig. 12.4 (a), the photoluminescence spectra of the host materials together with the absorption spectrum of DCM2 are shown. The spectral overlap integral is maximum in the  $\text{Alq}_3\text{:DCM2}$  system, followed by  $\text{NPD:DCM2}$  and  $\text{CBP:DCM2}$ . The photoluminescence spectra of the doped systems are all red-shifted with respect to the host materials indicating an efficient energy transfer from the host to the DCM2. The same is valid for DCM molecules as guests. Here, the photoluminescence spectrum is slightly blue-shifted with respect to the DCM2 results presented above.

Gain measurements on these material systems have shown that optical gain can be found in a broad spectral range. Figure 12.5 (a) shows the spectral dependence of the gain coefficient in an  $\text{Alq}_3\text{:DCM}$  film with a DCM concentration of 2 wt % corresponding to a volume density  $N_{\text{DCM}} = 5 \times 10^{19} \text{ cm}^{-3}$  of DCM molecules in the film. After a time delay of  $\tau = 30 \text{ ps}$  a maximum gain coefficient of



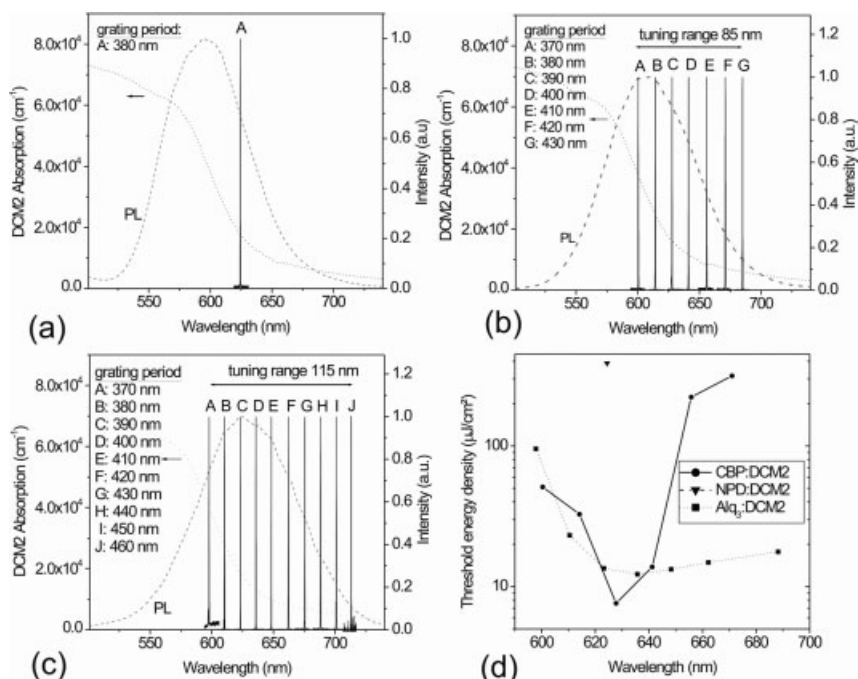
**Fig. 12.5** Optical gain of the G–H system  $\text{Alq}_3\text{:DCM}$  and laser intensity spectra for various layer thicknesses (a), and calculated and measured emission wavelengths (b).

$700\text{ cm}^{-1}$  was found at a wavelength of  $\lambda = 623\text{ nm}$ . The spectral range of optical gain spans over 100 nm from 585 nm to 685 nm. From  $N_{\text{DCM}}$  and the maximum gain coefficient a stimulated emission cross section of  $\sigma_{\text{SE}} \approx 1.3 \times 10^{-17}\text{ cm}^2$  is calculated. The gain spectrum more or less coincides with the photoluminescence spectrum on the long-wavelength side. On the short-wavelength side the gain spectrum is truncated by the tail of the residual absorption of the DCM molecules.

The broad extension of the gain spectrum and the high absolute values of gain open up the opportunity of widely tunable organic solid-state lasers. In the following, we present two possibilities to tune the laser wavelength of DCM- and DCM2-doped organic distributed feedback lasers. The Bragg equation (12.2) suggests that the tuning of the laser wavelength can be achieved by a variation of either the effective refractive index of the waveguide or the grating period  $\Lambda$ . Both ways are described in the following. It is well known that the effective refractive index of the waveguide strongly depends on the thickness of the active medium. Therefore the variation of the thickness of the organic layer can be used to tune the laser wavelength [109].

The various laser spectra shown in Fig. 12.5 (a) demonstrate that the laser wavelength can be tuned over a spectral range of  $\Delta\lambda_{\text{Las}} = 44\text{ nm}$  from 604 nm for a 120-nm thick film to 648 nm for a 435-nm thick film, respectively. The resulting peak positions of the laser emission are plotted versus the film thickness in Fig. 12.5 (b). Along with the measured laser wavelengths a curve based on the simulation of a planar waveguide structure is shown. The experimental data points correspond very well to the calculated curve for increased film thicknesses.

An alternative method to tune the emission wavelength is based on a grating structure comprising several segments with varied grating period [34]. In this context the material systems NPD:DCM2, CBP:DCM2 and Alq<sub>3</sub>:DCM2 have been studied. In Fig. 12.6 (a) the photoluminescence spectra of these three G–H systems based on DCM2 together with the observed laser wavelengths are shown. In NPD:DCM2, CBP:DCM2 and Alq<sub>3</sub>:DCM2 photoluminescence maxima at 595 nm, 607 and 625 nm are found, respectively. The data for NPD and Alq<sub>3</sub> agree with previous reports [110]. The red-shift in Alq<sub>3</sub> is caused by the higher polarity of the host (dipole moment  $p = 5.5\text{ D}$ ), compared to NPD (dipole moment  $p = 1.5\text{ D}$ ) as explained by the solid-state solvation effect (SSSE) [35, 111–113]. From our measurement it can be concluded that the dipole moment of CBP must be between the two other host materials. As the emission in the NPD:DCM2 system is considerably blue-shifted with respect to the other systems, there is an increased overlap with the absorption spectrum of DCM2 leading to an increased self-absorption. This self-absorption reduces the material gain of this G–H system resulting in a reduced net gain, which leads to only one supported laser line at  $\lambda = 624.4\text{ nm}$  at a grating period of 380 nm (see Fig. 12.6 (a)). The adjacent grating periods did not support laser activity. A segmented grating has been used with discrete grating periods ( $\Delta\Lambda = 10\text{ nm}$ ) corresponding to a wavelength shift of approximately 12–20 nm, depending on the effective refractive index of the waveguide mode. Therefore the tuning range in the NPD:DCM2 could be as large as almost



**Fig. 12.6** Spectra of second-order DFB lasers and tuning ranges together with the corresponding photoluminescence (dashed) spectra, for NPD:DCM2 (a), CBP:DCM2 (b), and Alq<sub>3</sub>:DCM2 (c). The absorption spectrum of DCM2 is given as the dotted curve. The lasing thresholds of the G–H systems are shown in (d).

twice the shift without observing laser emission at the adjacent grating segments. In the CBP host the PL maximum is red-shifted to 607 nm, located in a region with smaller self-absorption of the DCM2 guest. Therefore laser emission in the range between 600.4 and 684.9 nm is supported. The largest tuning range was achieved in the Alq<sub>3</sub> host. Here, laser activity could be established in the wavelength region between 597.8 and 713.1 nm, resulting in a tuning range of 115.3 nm [34]. It is worth noting that there is no inorganic semiconductor material known with a similarly broad tuning range in the wavelength region between orange and deep red. Typical values of the tuning range of GaInP–AlGaInP red DFB lasers are 12 nm [114] with a width of the gain spectra of up to 50 nm [115].

Figure 12.4 (b) shows the absorption spectra of the host materials. At the wavelength of the pump source  $\lambda_{N2} = 337$  nm, the absorption in Alq<sub>3</sub> is significantly smaller compared to CBP and NPD. Taking into account backreflections from the layer interfaces, a fraction of 74% of the pump light is absorbed in a 350-nm thick layer of Alq<sub>3</sub>. A similar layer of CBP absorbs 98% of the initial pump energy whereas a NPD layer absorbs 99%. In Fig. 12.6 (d), the laser thresholds for different host materials are shown. Here, only the calculated absorbed energy fractions of the pump pulses are considered. CBP:DCM2 exhibits a mini-

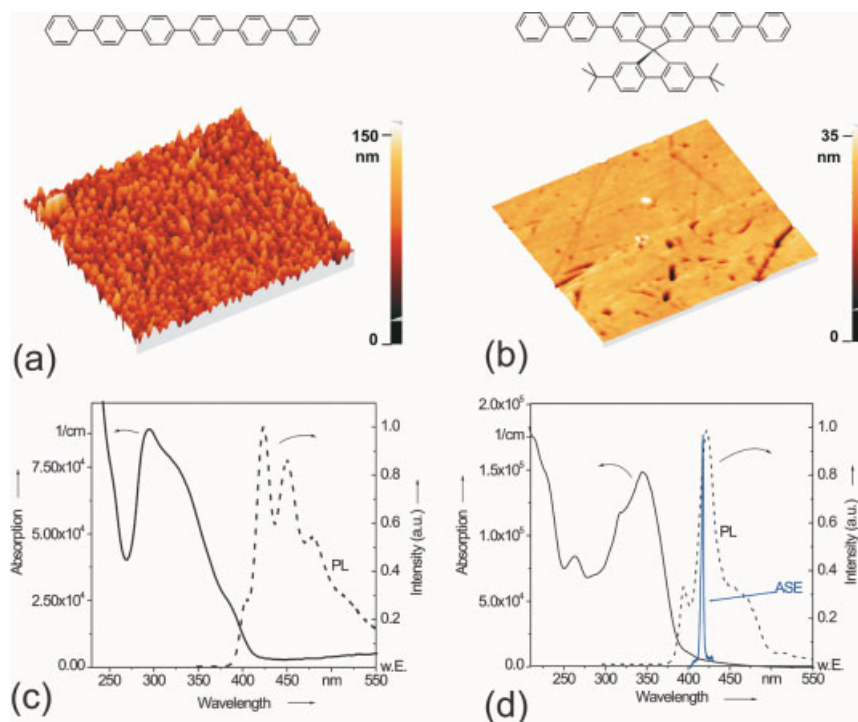
imum threshold of  $7.5 \mu\text{J}/\text{cm}^2$  at a wavelength of 628 nm. In  $\text{Alq}_3\text{:DCM2}$  the minimum threshold energy density was  $8.9 \mu\text{J}/\text{cm}^2$  at 636 nm. As expected from the location of the PL maximum, the threshold energy density in  $\text{NPD:DCM2}$  is much higher with  $383 \mu\text{J}/\text{cm}^2$  at 624.4 nm. When considering the pump pulse length of 500 ps the threshold power intensities can be calculated. The minimum values are  $15.0 \text{ kW}/\text{cm}^2$  in CBP,  $17.8 \text{ kW}/\text{cm}^2$  in  $\text{Alq}_3$ , and  $766 \text{ kW}/\text{cm}^2$  in NPD.

### 12.3.2

#### Spiro-linked Materials and Stilbenes

Because of their excellent optical properties, spiro-linked materials are a further option for low-threshold organic lasers. Among the large variety of possible spiro-linked systems particularly the blue-emitting oligophenyl-based spiro materials are of interest.

Due to their large sterical expansion, spiro-linked materials allow for the formation of thin films with improved morphological stability. This effect can be seen in Fig. 12.7 (a,b). Here, AFM images of the surface of 150-nm thick films of the oligophenyl *p*-sexiphenyl and the spiro-linked Spiro-6 $\Phi$ T on glass substrates are



**Fig. 12.7** AFM images of the surface morphology of evaporated thin films of *p*-sexiphenyl (a) and Spiro-6 $\Phi$ T (b) on glass substrates. The scan area was  $5 \times 5 \mu\text{m}^2$ . Photoluminescence, absorption and ASE spectra of the materials are shown in (c, d).



shown [51]. The inspected area is  $5 \times 5 \mu\text{m}^2$  in each case. As can be seen, the spiro-derivative shows a very planar surface with an RMS of 1.7 nm. In the case of the *p*-sexiphenyl, the surface roughness is considerably larger with an RMS value of 12.5 nm. Here, the entire surface is covered with large clusters sized between 140 and 200 nm. When calculating the sterical extension of the molecules, *p*-sexiphenyl is a slightly twisted chain of six benzene units with a length of 27.7 Å and a width of 4.9 Å. In the spiro-linked molecule the sexiphenyl chain undergoes some bending due to the spiro center. Therefore the length is slightly reduced to 25.8 Å. On the other hand, due to the spiro-linkage the biphenyl group is oriented perpendicularly to the sexiphenyl group resulting in a sterical width of 13.6 Å. It is apparent that the molecular structure strongly influences the surface morphology. Whereas the small *p*-sexiphenyl molecules tend to form large clusters, the layer surface of the spiro-derivative is very smooth. Here, the extended spiro molecules are effectively preventing recrystallization of the film that implies better optical properties [52].

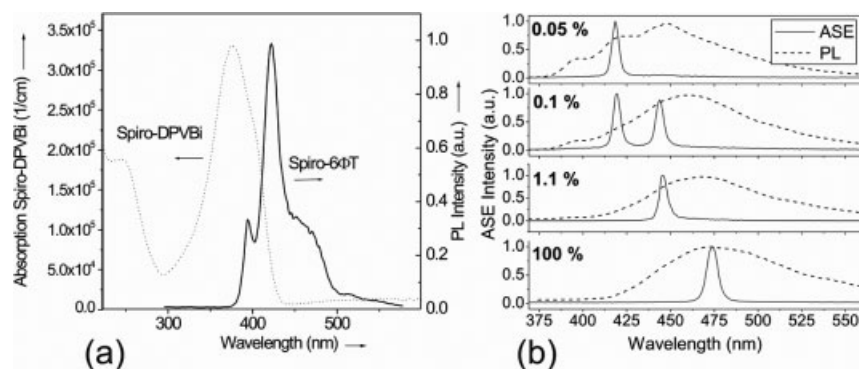
The absorption and photoluminescence spectra of both materials are shown in Fig. 12.7 (c,d). The luminescence of *p*-sexiphenyl is very similar to the spectrum of the spiro-derivative, only the vibronic sidebands are more pronounced. This shows that aside from the improved morphological stability, the spiro-linkage merely leaves the optical properties of the chromophore unaltered.

In Fig. 12.7 (d), an ASE spectrum is shown, which could be observed as significant spectral narrowing at higher excitation densities in the case of the spiro-derivative. In the *p*-sexiphenyl-film, no spectral narrowing due to stimulated emission could be observed, most probably due to the microcrystalline structure of the film comprising large clusters, which effectively deteriorate the waveguiding properties [50]. Absorption due to scattering losses on the cluster interfaces dominates over optical amplification in the material. The recently demonstrated *p*-sexiphenyl-lasers are based on epitaxially grown active layers with needle-like shape and sizes of  $1 \times 100 \mu\text{m}^2$ . The effective domain size was therefore many times larger than in our case [46].

When preparing solid-state thin films on second-order DFB substrates, Spiro-6ΦT can be used as a laser gain material in the deep blue wavelength range between 401 and 434 nm [58]. This tuning range can be extended by utilizing another spiro-linked material as a dopant in Spiro-6ΦT. Recently, we were able to demonstrate the applicability of the stilbene-based Spiro-DPVBi for this purpose [25].

The energy transfer from the host material to the dopant is based on the non-radiative Förster transfer mechanism and depends on the overlap integral of host photoluminescence and dopant absorption spectrum. In Fig. 12.8, the photoluminescence spectrum of the host material Spiro-6ΦT along with the absorption spectrum of the guest material Spiro-DPVBi is shown. Although the spectral overlap is limited, an energy transfer can be observed when investigating doped thin films. Starting with small doping concentrations of 0.05 %, the photoluminescence maximum shifts from 448 nm to 474 nm for a 100 % doping corresponding to the pure guest material similar to the solid-state solvation effect observed in



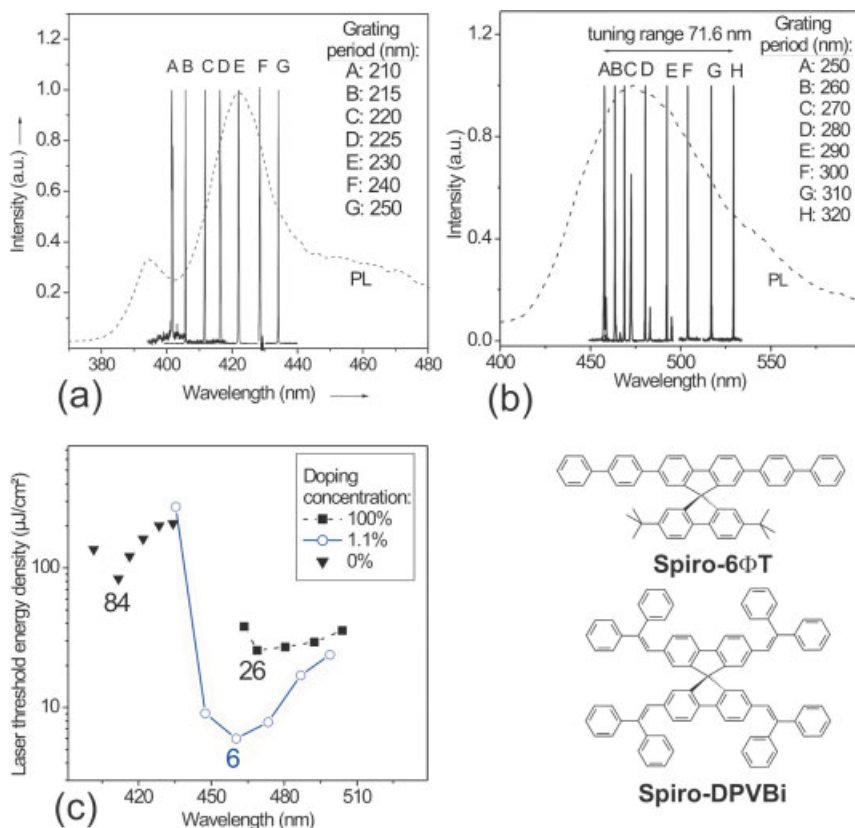


**Fig. 12.8** Guest–host system Spiro-6 $\Phi$ T: Spiro-DPVBi: absorption of guest and photoluminescence spectrum of host (a), spectral position of PL and ASE for different doping concentrations (b).

DCM2-doped organic semiconductors, described above. ASE can be observed throughout all investigated doping concentrations. In films with a small doping concentration of 0.05 % ASE is observed only due to the host material, indicating that the doping concentration is too small for an efficient energy transfer of excitons from the host to the guest. By increasing the doping concentration to 0.1 %, ASE due to both, host and guest, is observed. At a doping concentration of 1.1 %, most of the host excitons are transferred to the guest resulting in a vanishing ASE and PL of the host. Further increase of the doping concentration red-shifts the ASE maximum up to 473 nm for a neat Spiro-DPVBi film.

In contrast to previously reported solid-state G–H systems this material combination shows laser emission in neat films of both the pure host and the pure guest material. Figure 12.9(a,b) shows the normalized laser spectra for second-order DFB structures with different grating periods for pure Spiro-6 $\Phi$ T and pure Spiro-DPVBi films. In the latter material, the laser wavelength could be tuned over more than 70 nm from 457.8 to 529.3 nm by variation of the grating period. The minimum laser threshold energy density in Spiro-DPVBi (26  $\mu$ J/cm<sup>2</sup>) was smaller than that of the host material Spiro-6 $\Phi$ T (84  $\mu$ J/cm<sup>2</sup>). These values can be significantly reduced by using doped thin films of these two materials. Regarding the minimum threshold energy density an optimum doping concentration of 1.1 % was found. The observed threshold energy values of the second-order DFB lasers are displayed in Fig. 12.9 (c). The minimum threshold energy density in the doped system was found to be 6  $\mu$ J/cm<sup>2</sup> at 460 nm. This indicates a threshold reduction by a factor 4 compared to the pure guest film and a factor 14 in relation to the pure host material. This decrease is caused by an efficient energy transfer in the G–H system and a very low self-absorption due to the low concentration of guest molecules along with almost no host absorption in that wavelength region.

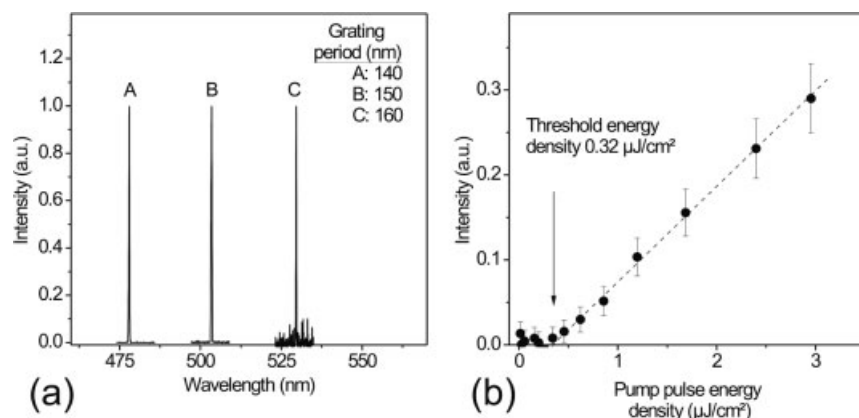
Further threshold reduction is expected for first-order DFB laser operation due to reduced waveguide losses compared to second-order DFB lasers. Therefore,



**Fig. 12.9** PL and second-order DFB laser spectra for different grating periods for neat thin films of Spiro-6ΦT (a) Spiro-DPVBi (b). The laser threshold energy densities of the neat guest, neat host and an optimized G-H system are compared (c).

DFB lasers in first-order geometry with the optimum doping concentration of 1.1% have been fabricated. In Fig. 12.10 (a) the normalized intensity spectra for first-order DFB lasers with varying grating periods are shown. Laser emission is observed between 478 and 530 nm. Shorter wavelengths were not supported because grating periods shorter than 140 nm were not available in this research. The minimum threshold energy density was measured to be 320 nJ/cm² at a wavelength of 478 nm. A further threshold reduction is expected for DFB gratings below 140 nm shifting the first-order DFB lasers to the wavelength where a minimum threshold was found in second-order DFB operation (Fig. 12.9 (c)).

Aside from Spiro-DPVBi other stilbene-based materials can be used as neat films or as guest in the host material Spiro-6ΦT resulting in low laser thresholds for blue-green emitting organic solid-state lasers. Among these stilbene materials, DPAVB and the similar DPAVBi can be used as green-emitting laser materials [116] or as dopant in G-H systems.

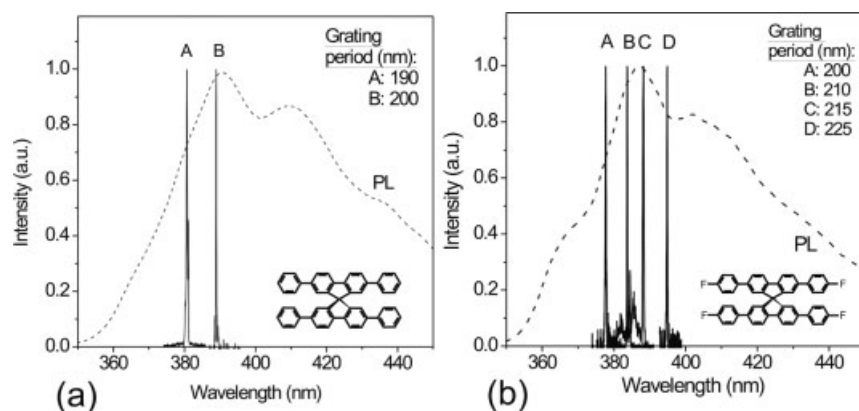


**Fig. 12.10** PL and first-order DFB laser spectra for different grating periods based on a Spiro-6PT thin-film doped with 1.1% of Spiro-DPVBi (a) and laser characteristics for a sample at a wavelength of 478 nm.

### UV-emitting Spiro Materials

The spectral position of the absorption and photoluminescence of oligophenyl-based chromophores is strongly dependent on the chain length. A reduced chain length in general implies a shorter emission wavelength. Therefore, when aiming at a laser emission below the visible spectral range one can utilize quarterphenyl-based chromophores as emitters. Among these materials the spiro-linked Spiro-4 $\Phi$  and Spiro-4 $\Phi$ F are possible gain materials for ultraviolet laser emission.

In Fig. 12.11, the photoluminescence spectra together with laser intensity spectra for second-order DFB lasers based on these quarterphenyl compounds are shown. The shape and spectral position of the photoluminescence are very simi-

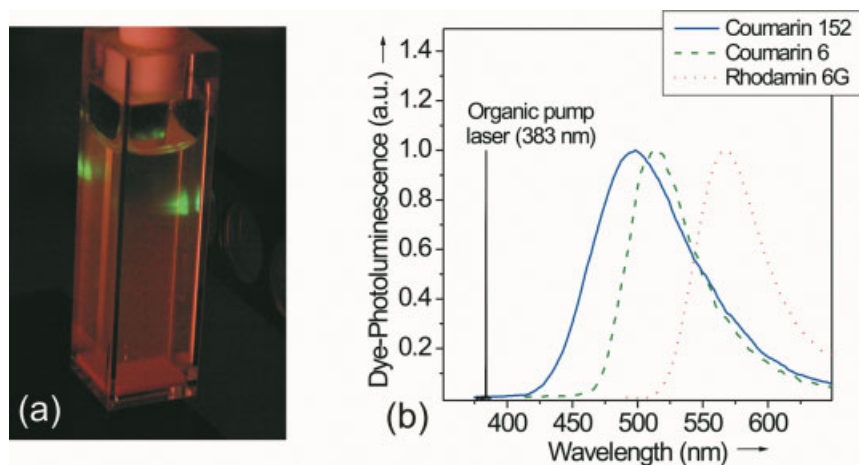


**Fig. 12.11** PL and second-order DFB laser spectra for different grating periods for neat thin films of the quarterphenyl based Spiro-4 $\Phi$  (a) and Spiro-4 $\Phi$ F (b).

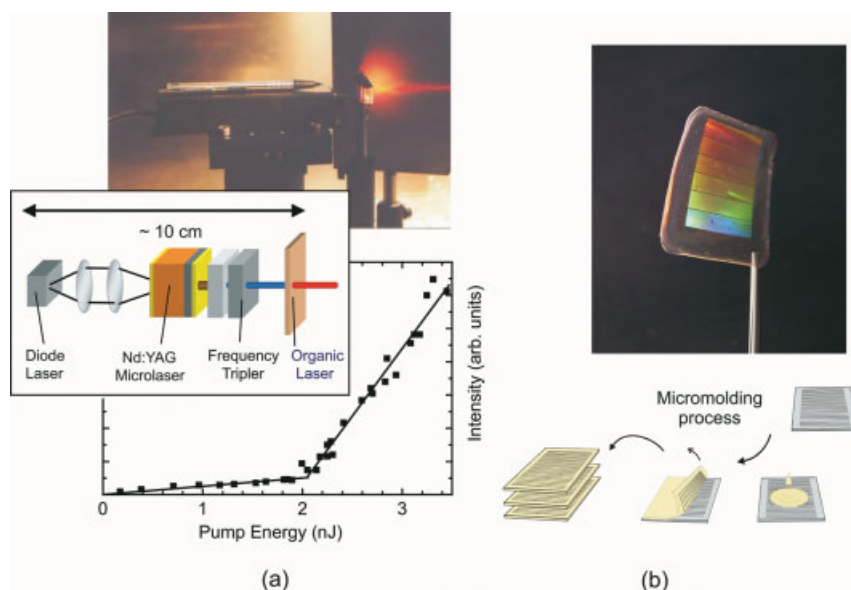
lar in both materials, indicating only weak influence of the a Fluorine substituents in the case of the Spiro-4 $\Phi$ F. The emission maximum is found at 391 nm in the Spiro-4 $\Phi$  and at 387 nm in the Spiro-4 $\Phi$ F. Depending on the grating period of the laser samples, the laser wavelength in the Spiro-4 $\Phi$ F could be tuned between 377.7 nm and 394.8 nm. The material exhibits a minimum pump energy threshold density of 62  $\mu\text{J}/\text{cm}^2$ . The tuning range in the Spiro-4 $\Phi$  is considerably smaller and spans from 381 nm to 389 nm. In addition, the minimum threshold energy density is much higher in this material (355  $\mu\text{J}/\text{cm}^2$ ).

### Applications for Optically Pumped Organic Lasers

At pump energy densities well above threshold the Spiro-4 $\Phi$ F laser output can be increased to a pulse power of 6.8 W. This is easily sufficient to utilize the organic UV laser as on excitation source in spectroscopic experiments. To demonstrate this possible field of application, solutions containing several fluorescent marker dyes have been prepared. Coumarin and Rhodamine dyes are commonly used as fluorescent dyes in biomarker spectroscopic applications. The organic laser was focused on a cuvette containing the dye solution. To ensure that no scattered pump laser light was included in the excitation beam, a 370-nm edge filter was placed between the organic laser and the dye cuvette. The above-described streak camera setup was used for measuring the photoluminescence spectra of the solutions. When placing the cuvette into the organic laser beam, the fluorescence of the dye in the solution is clearly visible. In Fig. 12.12 (a), a photograph of the pump experiment with Coumarin 6 is shown. Figure 12.12 (b) shows the measured photoluminescence spectra of the dye solutions pumped by an organic solid-state laser at 382 nm. Whereas for Rhodamine dyes visible excitation wavelengths could also be used, most of the Coumarin dyes need a UV excitation wa-



**Fig. 12.12** Photograph of a Coumarin 6 solution excited by the organic laser (a) and photoluminescence of the marker dyes Coumarin 152, Coumarin 6 and Rhodamine 6G measured with utilization of an organic solid-state laser as excitation source (b).



**Fig. 12.13** The inset of (a) shows the scheme of a very compact all solid-state laser using the organic semiconductor film as active medium. The pump source is a commercially available diode-pumped, Q-switched, frequency-tripled Nd:YAG-microchip laser (Uniphase NanoUV-355). The organic semiconductor laser can be placed directly in front of the pump laser. Thus the total length of this very compact solid-state “dye” laser is less than 10 cm. A photo of the setup is shown in the upper part of (a). The lower part of (a) shows the input–output characteristics at the laser wavelength when the beam is focused to a 125  $\mu\text{m}$  diameter spot. A micromolding process for the fabrication of low-cost DFB substrates is shown in (b).

velength. This experiments prove the feasibility of using an organic semiconductor laser as an excitation source.

For a future mass application in spectroscopy it is necessary to reduce the overall system costs. By using a compact pumping source like a diode-pumped frequency-tripled Nd:YAG microchip laser it is possible to simplify the optical system. A possible setup is shown in the inset of Fig. 12.13 (a). A diode-pumped passively Q-switched  $\text{Nd}^{3+}$ :YAG laser with an integrated frequency tripler is used as a pump source. The whole optical arrangement has a length of only 10 cm and a volume of 70  $\text{cm}^3$ . Fig. 12.13 (a) shows the input–output characteristics of a laser utilizing a 300-nm thick  $\text{Alq}_3$ :DCM film [109]. The observed laser threshold amounts to  $E_p = 2$  nJ when the pump laser is focused to an excitation spot with a diameter of 125  $\mu\text{m}$ . The threshold pump energy is lower by a factor of 50 than the maximum pulse energy provided by the compact pump laser. These results prove the feasibility of this setup for use with tunable organic lasers.

The second approach to reduce the system costs is directed towards the substrates. Mass application can be facilitated by microreplication of DFB gratings [101]. It has been shown that it is possible to fabricate all plastic sub-

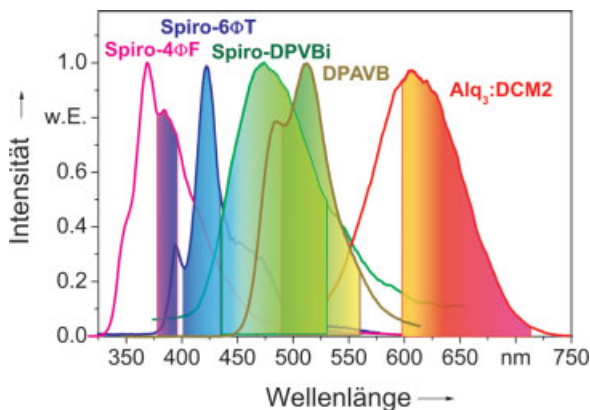
strates for organic DFB lasers by various micromolding techniques [32, 117]. For example, the cyclic olefin copolymer Topas 5013 has been used for fabrication of a flexible low-cost plastic substrate [59]. This material has a low water absorption and can act as a water barrier to protect the active organic layers [118]. Silicon substrates structured by e-beam lithography act as master gratings in the micromolding process. Topas is drop cast onto the master substrate from a toluene solution and may be easily separated from the master after drying [119]. In Fig. 12.13 (b), a photograph of the plastic substrate is shown. The different grating periods of the sections result in a varying diffracted color in the photograph.

Organic thin-film lasers with such a plastic substrate and the Spiro compound Spiro-4ΦF as active medium have been shown [59]. This demonstrates the feasibility of the fabrication of low-cost organic DFB lasers in the UV-wavelength region.

## 12.4

### Comparison of Organic Laser Properties

This section gives a comparative overview of the lasing properties of the materials shown in Section 12.3 and some of those omitted due to space limitations. The most important parameters like spectral position, tuning range and threshold energy density are summarized in Table 12.1. All samples are based on comparable substrates with film thickness in the range between 300 and 350 nm. Besides the already-described lasers based on low molecular weight materials conjugated polymers are also included in Table 12.1. As can be seen from the tuning ranges, it is possible to cover almost the entire visible spectrum from the UV to the deep red region with only a small number of active laser materials. For example, Fig. 12.14 shows the tuning ranges of the laser materials Spiro-4ΦF and the G–H systems Spiro-6ΦT: Spiro-DPVBi, Spiro-6ΦT: DPAVB and Alq<sub>3</sub>: DCM2. A further increase of the tuning range is also expected by using multiply doped systems.



**Fig. 12.14** DFB tuning ranges of the laser materials Spiro-4ΦF, and the G–H systems Spiro-6ΦT: Spiro-DPVBi, Spiro-6ΦT: DPAVB and Alq<sub>3</sub>: DCM2.

**Table 12.1** Comparison of laser properties of small-molecule organic materials and conjugated polymers.

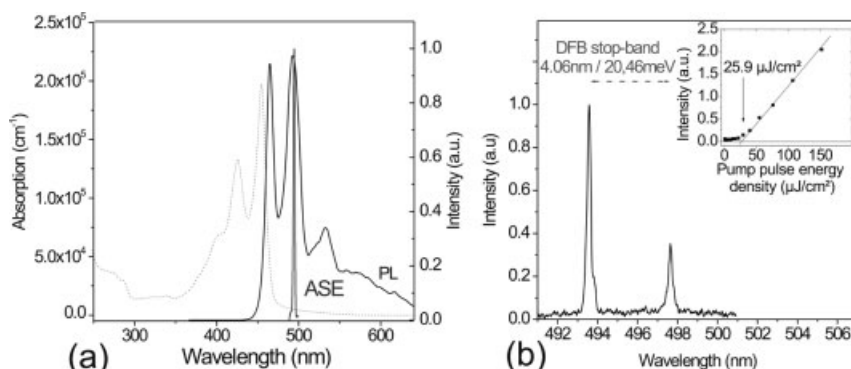
$m_G$	grating order
$\lambda_{PL}$	photoluminescence maximum
$\lambda_{ASE}$	ASE maximum
$\lambda_{Laser}$	tuning range
$\Delta\lambda_{tune}$	widths of tuning range
$I_{th_{min}}$	minimum threshold energy density
$I_{th_{min,a}}$	minimum absorbed threshold energy density

Organic material	$m_G$	$\lambda_{PL}$ [nm]	$\lambda_{ASE}$ [nm]	$\lambda_{Laser}$ [nm]	$\Delta\lambda_{tune}$ [nm]	$I_{th_{min}}$ [μJ/cm <sup>2</sup> ]	$I_{th_{min,a}}$ [μJ/cm <sup>2</sup> ]
Alq <sub>3</sub> :DCM2 (1.8 %)	2	640	624	598–713	115	12	8.9
– II –	1			605–703	98	2.2	1.6
CBP:DCM2 (1.8 %)	2	607	623	600–685	85	7.6	7.5
NPD:DCM2 (1.8 %)	2	595	619	624		387	384
Spiro-4ΦF	2	387	386	378–395	17	62	62
Spiro-4Φ	2	391	389	381–389	8	355	355
Spiro-6ΦT	2	422	418	402–434	33	83	82
TBS	2	412	406	390–435	45	45	45
Spiro-DPVBi	2	474	473	458–529	72	26	26
– in Spiro-4ΦF (1.69 %)	2	460	447	449–501	51	9.8	9.8
– in Spiro-6ΦT (1.1 %)	2	466	448	435–499	64	6.0	6.0
– II –	1			478 <sup>1)</sup> –530	52	0.32	0.32
DPAVB	2	516	517	507–554	47	11	10
– in Spiro-4ΦF (2 %)	2	460	508	487–553	66	2.0	2.0
– in Spiro-6ΦT (15 %)	2	512	508	490–559	69	4.0	4.0
– in TBS (5 %)	2	510	499	480–542	62	6.0	6.0
MeLPPP	2	493	494	488–496	8	232	102
– II –	1			494		26	11
PFO	2 <sup>2)</sup>	466	466	455		4	
MEH-PPV	2	589	625	615–643	28	64	26

1) The short end of the tuning range was limited by the available grating substrates.

2) A two-dimensional grating has been used in this case [85].

When comparing the laser threshold energy values it is apparent that the most promising candidates for low-threshold operation are guest–host systems. Here, the self-absorption of the material matrix is effectively separated from the spectral region of the emission. The doped systems containing DCM2 or the stilbene



**Fig. 12.15** Absorption, photoluminescence and ASE spectrum of MeLPPP (a) and spectrum of first-order DFB laser structure and laser characteristic (inset) (b).

Spiro-DPVBi and DPAVB as guest molecules therefore exhibit very low laser thresholds and rather large tuning ranges. Compared to these small molecular weight materials, most of the investigated conjugated polymers have larger threshold values. Among the low-threshold polymer materials are a few polyfluor- enes. With these polymers threshold energy densities below  $10 \mu\text{J}/\text{cm}^2$  have been demonstrated using 2D photonic-crystal resonators [85].

A technological approach to decrease the threshold of DFB lasers is the use of first-order grating structures instead of second-order DFB lasers. As can be seen in Table 12.1, this experiment was performed with three material systems, two low molecular weight based G–H systems and with the conjugated polymer MeLPPP. In all cases the laser threshold was reduced significantly – on average by a decade.

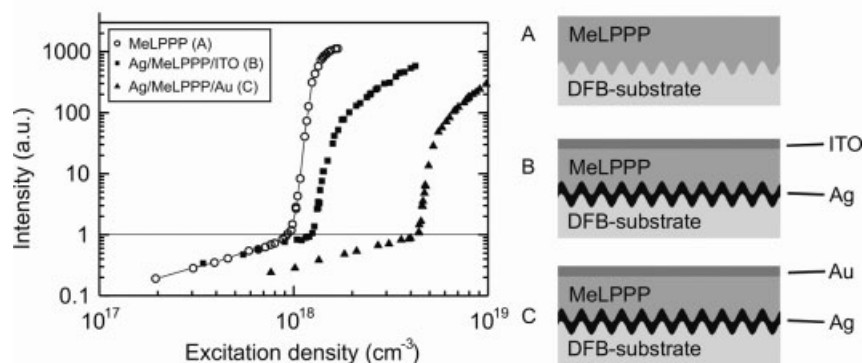
In Fig. 12.15 (a), the MeLPPP emission and absorption spectra together with the ASE position are shown. Figure 12.15 (b) displays the laser spectra of the first-order MeLPPP sample. Two competitive modes have been observed. Both of them have the same polarization, indicating the characteristic stop-band for an index-modulated distributed feedback laser without phase shift. In the stop-band region no lasing is possible due to the destructive interference of the left- and right-propagating waves [120]. Due to the increased coupling compared to second-order gratings, the stop-band width of the first-order samples was as large as 4.1 nm or 20.5 meV, respectively.

## 12.5

### Electrically Driven Organic Lasers

There are several prerequisites for the realization of an electrically driven organic laser diode. Aside from a low-threshold active organic material a suitable resonator structure incorporating electrical contacts has to be found.

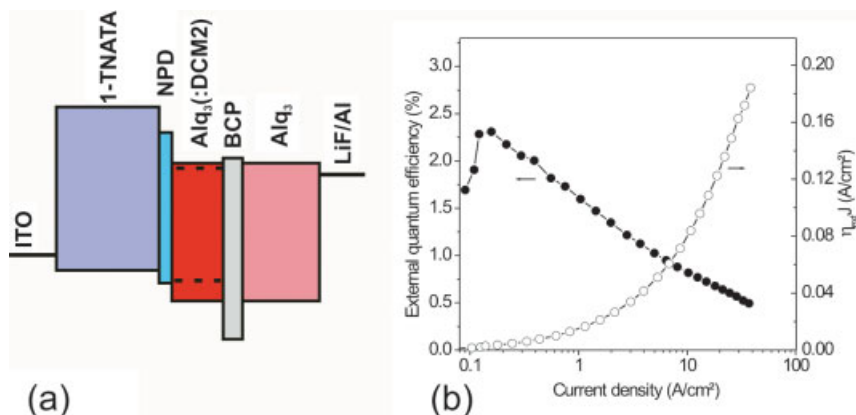




**Fig. 12.16** Second-order MeLPPP DFB lasers with electric contacts. Double-logarithmic plot of the emitted intensity at the laser wavelength against the excitation density in the active layer. All curves are normalized to the intensity at the laser threshold. On the right-hand side schematic cross a section of the samples is shown [122].

The problem for the optical design is to minimize losses arising from the contact layers, without deteriorating the electrical properties of the device. Thin organic films are compatible with either slab waveguide lasers or microcavities. Optical losses arise from the penetration of the electric field of the laser mode into the absorbing electrodes. Potential anode materials are either ITO or a high work-function metal film like Pt or Au. Cathodes typically consist of low work function metals or metal alloys, such as Al, Ag, Mg/Ag, or LiF/Al. A recent breakthrough in the development of OLEDs proved that ITO covered with a 5-nm thick transparent layer of bathocuproine can serve as efficient electron-injecting electrode [16]. Hence, both electrodes can be fabricated either from a metal or ITO. Increased charge conductivity due to doping of organic layers with either electron donors (for electron-transport materials) or electron acceptors (for hole-transport materials) [121] might offer the possibility of waveguide structures with increased thickness compared to conventional OLEDs and therefore a better mode confinement.

Organic lasing in the presence of metallic contacts has been investigated by several groups [16, 21, 97, 105, 123]. Recently, a second-order DFB structure based on the conjugated polymer MeLPPP has been presented, where the laser threshold was only slightly increased due to optical losses incorporated by electrical contacts [122]. Figure 12.16 shows a double-logarithmic plot of the input–output characteristics for three resonator structures: neat MeLPPP (A), Ag/MeLPPP/ITO (B) and Ag/MeLPPP/Au (C). Samples B and C are possible OLED structures. Laser emission was observed in all three samples. Deposition of a 20-nm layer of ITO on top of the polymer only slightly raises the laser threshold and does not modify the lasing characteristics. ITO introduces only small absorption losses and the thin layer does not significantly modify the confinement of the waveguide mode. In



**Fig. 12.17** Energy structure of an amorphous OLED utilizing a G–H emission layer (a) and external quantum efficiency  $\eta_{\text{ext}}$  against current density  $J$  together with product term  $\eta_{\text{ext}} \cdot J$  (b).

contrast, deposition of a thin (10 nm) semitransparent layer of gold as the top electrode raises the threshold by a factor of 4 due to strong absorption.

With regard to the realization of an organic diode laser two issues are worth mentioning: Organic semiconductor lasers work in the presence of electric contacts and, what is even more encouraging, the laser threshold is not substantially increased. Nevertheless, stimulated emission under electrical excitation has still to be demonstrated.

Optimistic estimates predict that the threshold current densities required for lasing action in organic semiconductor lasers might be of the order of 100 A/cm<sup>2</sup> [16, 21]. Although higher current densities have been demonstrated in a number of materials [124, 125], stimulated emission was not observed. In fact, values of up to 1 kA/cm<sup>2</sup> have been realized in organic thin films [126]. The current heating of the structures and contacts can be avoided by pulsed operation. The main problem today is the presence of additional nonradiative loss mechanisms like polaron absorption when operating OLEDs at high current densities [14].

In Figure 12.17(a), a typical amorphous multilayer OLED structure based on the G–H system Alq<sub>3</sub>:DCM2 as emitter is shown. Figure 12.17(b) shows the external quantum efficiency  $\eta_{\text{ext}}$  plotted against the current density  $J$  when operating in a pulsed mode. Although the efficiency is decreasing rapidly with the current density, the product term  $\eta_{\text{ext}} \cdot J$  is still increasing, indicating a growing overall light intensity.

The challenge on the way to the electrically driven organic laser diode is therefore to find a laser material with a low-threshold and a quantum efficiency that is relatively independent of current density and electric field [14].

## 12.6

### Summary and Outlook

In view of the previous sections one can say that organic semiconductor lasers have matured considerably over the past few years. More and more organic semiconducting gain media, polymers as well as small-molecules, have been developed and used in thin-film devices. With just a few of these materials it is possible to span the entire visible spectral region well into the ultraviolet part. Thus, concerning their spectral tunability organic semiconductor lasers by far outperform their inorganic counterparts. Aiming at low laser thresholds, particularly organic guest–host systems have become very attractive due to reduced optical quenching and low self-absorption. In combination with low-loss resonator geometries, e.g. first-order DFB, the laser threshold under optical excitation may be of the order of  $100 \text{ W/cm}^2$ . Diode-pumped, frequency-tripled Nd-YAG microchip lasers have been used as compact and cost-effective pump sources. The use of AlInGaIn-based laser diodes might enable even more attractive pump geometries for organic lasers in the near future.

There are a number of applications where it might be favorable to use optically driven organic semiconductor lasers without the need for additional processing steps. Easy to fabricate and thus cost-effective disposable devices are highly attractive, tunable laser sources for single-use spectroscopy applications, e.g. in medicine and biotechnology.

The main scientific challenge, however, is to establish electrically driven organic semiconductor lasers, which would be highly attractive for a wide range of applications. Considering the low-threshold values of organic lasers under optical excitation, this goal seems to be within reach. All the more as we know that organic materials are capable of transporting current densities several orders of magnitude higher than those applied in OLEDs. Due to waveguiding issues an organic semiconductor laser is expected to require an increased overall organic layer thickness. Therefore, highly efficient charge-transporting layers with excellent optical properties have to be incorporated into a low-loss waveguide geometry that provides an optimum overlap of the optical mode with the gain material. At elevated carrier densities many organic materials show considerable polaron-induced absorption. The key issue is to identify materials that require an overall low carrier density to provide optical gain and bring about diminished carrier-induced quenching phenomena. It is obvious that there are still some open questions on the way to the organic laser diode. The solution to each of them might also be of benefit for the optimization of OLEDs and other organic optoelectronic devices. In the case of inorganic semiconductors, the research on laser diodes has always been the driving force for advances – it might turn out the same way in the case of organics.

## References

- 1 P. P. Sorokin and J. R. Lankard. *IBM J. Res. Dev.*, **1966**. 10, 162.
- 2 F. P. Schäfer, W. Schmidt, and J. Volze. *Appl. Phys. Lett.*, **1966**. 9, 306–309.
- 3 H. Kogelnik and C. V. Shank. *Appl. Phys. Lett.*, **1971**. 4, 152.
- 4 H. P. Weber and R. Ulrich. *Appl. Phys. Lett.*, **1971**. 19, 38–40.
- 5 R. Reisfeld, D. Brusilovsky, M. Eyal, E. Miron, Z. Burstein, and J. Ivri. *Chem. Phys. Lett.*, **1998**. 160, 43–44.
- 6 N. Karl. *Phys. Stat. Sol. A*, **1972**. 13, 152.
- 7 C. W. Tang. *US patent 4,356,429*, **1980**.
- 8 S. A. VanSlyke and C. W. Tang. *US patent 4,539,507*, **1983**.
- 9 C. W. Tang and S. A. VanSlyke. *Appl. Phys. Lett.*, **1987**. 51, 913–915.
- 10 N. Tessler, G. J. Denton, and R. H. Friend. *Nature*, **1996**. 382, 695–697.
- 11 F. Hide, M. A. Díaz-García, B. J. Schwartz, M. R. Andersson, Q. Pei, and A. J. Heeger. *Science*, **1996**. 273, 1833–1836.
- 12 V. G. Kozlov, V. Bulović, P. E. Burrows, and S. R. Forrest. *Nature*, **1997**. 389, 362–364.
- 13 M. Berggren, A. Dodabalapur, R. E. Slusher, and Z. Bao. *Nature*, **1997**. 389, 466–469.
- 14 M. A. Baldo, R. J. Holmes, and S. R. Forrest. *Phys. Rev. B*, **2002**. 66, 035321.
- 15 A. Dodabalapur, M. Berggren, R. E. Slusher, Z. Bao, A. Timko, Schiortino, E. Laskowski, H. E. Katz, and O. Nalamasu. *IEEE J. Quantum Electron.*, **1998**. 4, 67–74.
- 16 V. G. Kozlov, G. Parthasarathy, P. E. B. V. B. Khalfin, J. Wang, S. Y. Chou, and S. R. Forrest. *IEEE J. Quantum Electron.*, **2000**. 36, 18–26.
- 17 U. Lemmer. *Polym. Adv. Technol.*, **1999**. 9, 476–487.
- 18 N. Tessler. *Adv. Mater.*, **1999**. 11, 363–369.
- 19 S. V. Frolov, M. Shkunov, A. Fujii, F. J. Yoshino, and Z. V. Vardeny. *IEEE J. Quantum Electron.*, **2000**. 36, 2–11.
- 20 G. Kranzelbinder and G. Leising. *Rep. Prog. Phys.*, **2000**. 63, 729–762.
- 21 M. D. McGehee and A. J. Heeger. *Adv. Mater.*, **2000**. 12, 1655–1668.
- 22 U. Scherf, S. Riechel, U. Lemmer, and R. F. Mahrt. *Curr. Opin. Solid State Mater. Sci.*, **2001**. 2, 143–154.
- 23 M. Berggren, A. Dodabalapur, and R. E. Slusher. *Appl. Phys. Lett.*, **1997**. 71, 2230–2232.
- 24 V. G. Kozlov, V. Bulović, P. E. Burrows, M. Baldo, V. B. Khalfin, G. Parthasarathy, S. R. Forrest, Y. You, and Thompson. *J. Appl. Phys.*, **1998**. 84, 4096–4108.
- 25 D. Schneider, T. Rabe, T. Riedl, T. Dobbertin, M. Kröger, E. Becker, H.-H. Johannes, W. Kowalsky, T. W. J. Wang, and P. Hinze. *Appl. Phys. Lett.*, **2004**. 85, 1659–1661.
- 26 C. W. Tang, S. A. VanSlyke, and C. H. Chen. *J. Appl. Phys.*, **1989**. 65, 3610–3616.
- 27 J. Littman and P. Martic. *J. Appl. Phys.*, **1992**. 72, 1957–1960.
- 28 P. R. Hammond. *Opt. Commun.*, **1979**. 29, 331–333.
- 29 F. P. Schäfer. *Dye Lasers*, volume 1 of *Topics in Applied Physics*. Springer, 3<sup>rd</sup> edition, **1989**.
- 30 V. Bulović, V. G. Kozlov, S. R. Khalfin, and S. R. Forrest. *Science*, **1998**. 279, 553–555.
- 31 V. G. Kozlov, V. Bulović, and S. R. Forrest. *Appl. Phys. Lett.*, **1997**. 71, 2575–2577.
- 32 M. Berggren, A. Dodabalapur, R. E. Slusher, A. Timko, and O. Nalamasu. *Appl. Phys. Lett.*, **1998**. 72, 410–411.
- 33 D. Schneider, S. Hartmann, T. Benstem, T. Dobbertin, D. Heithecker, D. Metzendorf, E. Becker, T. Riedl, H.-H. Johannes, W. Kowalsky, T. Weimann, J. Wang, and P. Hinze. *Appl. Phys.*, **2003**. B 77, 399–402.
- 34 D. Schneider, T. Rabe, T. Riedl, T. Dobbertin, M. Kröger, E. Becker, H.-H. Johannes, W. Kowalsky, T. W. J. Wang, and P. Hinze. *Appl. Phys. Lett.*, **2004**. 85, 1886–1888.
- 35 V. Bulović, R. Deshpande, M. E. Thompson, and S. R. Forrest. *Chem. Phys. Lett.*, **1999**. 308, 317–322.
- 36 S.-B. Lee, T. Yasuda, M.-J. Yang, K. Fujita, and T. Tsutsui. *Mol. Cryst. Liq. Cryst.*, **2003**. 405, 67–73.
- 37 J. Shinar and V. Savvateev. In J. Shinar, editor, *Organic Light-Emitting Devices*. Heidelberg: Springer 2004, pages 1–42.
- 38 Y. Kijima, N. Asai, and S. ichiro Tamura. *Jpn. J. Appl. Phys.*, **1999**. 38, 5274–5277.

- 39 R. S. Deshpande, V. Bulović, and S. R. Forrest. *Appl. Phys. Lett.*, **1999**. 75, 888–890.
- 40 Y. Okumura, M. Nagawa, C. Adachi, M. Satsuki, S. Suga, T. Koyama, and Y. Taniguchi. *Chem. Lett.*, **2000**. 29, 754–755.
- 41 M. Ichikawa, T. Tachi, M. Satsuki, S. Suga, T. Koyama, and Y. Taniguchi. *J. Photochem. Photobiol. A*, **2003**. 158, 219–221.
- 42 D. Fichou, S. Delysse, and J.-M. Nunzi. *Adv. Mater.*, **1997**. 9, 1178–1181.
- 43 G. Horowitz, P. Valat, F. Garnier, F. Kouki, and V. Wintgens. *Opt. Mater.*, **1998**. 9, 46–52.
- 44 M. Nagawa, R. Hibino, S. Hotta, H. Yanagi, M. Ichikawa, T. Koyama, and Y. Taniguchi. *Appl. Phys. Lett.*, **2002**. 80, 544–546.
- 45 H. Yanagi, T. Ohara, and T. Morikawa. *Adv. Mater.*, **2001**. 13, 1452–1455.
- 46 F. Quochi, F. Cordella, R. Orru, J. E. Communal, P. Verzeroli, A. Mura, and G. Bongiovanni. *Appl. Phys. Lett.*, **2004**. 84, 4454–4456.
- 47 V. S. Zuev, O. A. Logunov, Y. V. Savinov, A. V. Startsev, and Y. Y. Stoilov. *Appl. Phys.*, **1978**. 17, 321–323.
- 48 A. Corney, J. Manners, and C. E. Webb. *Opt. Commun.*, **1979**. 31, 354–358.
- 49 H. Telle, W. Hüffer, and D. Basting. *Opt. Commun.*, **1981**. 38, 402–403.
- 50 H.-J. Brouwer, V. V. Krasnikov, T.-A. Pham, R. E. Gill, and G. Hadzioannou. *Appl. Phys. Lett.*, **1998**. 73, 708–710.
- 51 D. Schneider, T. Rabe, T. Riedl, T. Dobbertin, M. Kröger, E. Becker, H.-H. Johannes, W. Kowalsky, T. W. J. Wang, and P. Hinze. *J. Appl. Phys.*, **2005**. 98, 043104.
- 52 J. Salbeck, F. Weissörtel, and J. Bauer. *Macromol. Symp.*, **1997**. 125, 121–122.
- 53 J. Salbeck, N. Yu, J. Bauer, F. Weissörtel, and H. Bestgen. *Synth. Met.*, **1997**. 91, 209–215.
- 54 H. Spreitzer, H. Schenk, J. Salbeck, F. Weissörtel, H. Riel, and W. Riess. *Proc. SPIE*, **1999**. 3797, 316–324.
- 55 T. Spehr, R. Pudzych, T. Fuhrmann, and J. Salbeck. *Org. Electron.*, **2003**. 4, 61–69.
- 56 N. Johansson, J. Salbeck, J. Bauer, F. Weissörtel, P. Bröms, A. Andersson, and W. R. Salaneck. *Adv. Mater.*, **1998**. 10, 1136–1141.
- 57 J. Salbeck, M. Schörner, and T. Fuhrmann. *Thin Solid Films*, **2002**. 417, 20–25.
- 58 D. Schneider, T. Rabe, T. Riedl, T. Dobbertin, O. Werner, M. Kröger, E. Becker, H.-H. Johannes, W. Kowalsky, T. Weimann, J. Wang, P. Hinze, A. Gerhard, P. Stössel, and H. Vestweber. *Appl. Phys. Lett.*, **2004**. 84, 4693–4695.
- 59 D. Schneider, T. Rabe, T. Riedl, T. Dobbertin, M. Kröger, E. Becker, H.-H. Johannes, W. Kowalsky, T. W. J. Wang, P. Hinze, A. Gerhard, P. Stössel, and H. Vestweber. *Adv. Mater.*, **2005**. 17, 31–34.
- 60 B. Ruhstaller, T. Beierlein, H. Riel, S. Karg, J. C. Scott, and W. Riess. *IEEE J. Sel. Top. Quantum Electron.*, **2003**. 9.
- 61 N. Tsutsumi, T. Kawahira, and W. Sakai. *Appl. Phys. Lett.*, **2003**. 83, 2533–2535.
- 62 C. C. Jensen and H. Schröder. *Appl. Opt.*, **1992**. 31, 7012–7021.
- 63 U. Scherf and K. Müllen. *Makromol. Chem. Rapid Commun.*, **1991**. 12, 489–497.
- 64 D. Hertel, U. Scherf, and H. Bässler. *Adv. Mater.*, **1998**. 10, 1119–1122.
- 65 G. Wegmann, B. Schweitzer, D. Hertel, H. Giessen, M. Oestreich, U. Scherf, K. Müllen, and R. F. Mahrt. *Chem. Phys. Lett.*, **1999**. 312, 376.
- 66 E. J. W. List, C. H. K. J. Shinar, A. Pogantsch, G. Leising, and W. Graupner. *Appl. Phys. Lett.*, **1999**. 76, 2083–2085.
- 67 A. Haugeneder, M. Hilmer, C. Kallinger, M. Perner, W. Spirk, U. Lemmer, J. Feldmann, and U. Scherf. *Appl. Phys.*, **1998**. B 66, 389–392.
- 68 S. Riechel, C. Kallinger, U. Lemmer, J. Feldmann, A. Gombert, V. Wittwer, and U. Scherf. *Appl. Phys. Lett.*, **2000**. 77, 2310–2312.
- 69 S. Riechel, U. Lemmer, T. Benstem, W. Kowalsky, U. Scherf, A. Gombert, and V. Wittwer. *Appl. Phys. B*, **2000**. 71, 897–900.
- 70 C. Bauer, H. Giessen, B. Schnabel, E. Kley, C. Schmitt, U. Scherf, and R. F. Mahrt. *Adv. Mater.*, **2001**. 13, 1161–1164.
- 71 N. Moll, C. Bauer, H. Giessen, B. Schnabel, E. B. Kley, U. Scherf, and R. F. Mahrt. *Appl. Phys. Lett.*, **2002**. 80, 734–736.
- 72 F. Wudl, P. M. Alleman, G. Srdanov, Z. Ni, and D. McBranch. In S. R. Marder, J. E. Sohn, and G. D. Stucky, editors, *Materials for Nonlinear Optics: Chemical Perspectives*. ACS Symp. Ser. 455, pages 683–686.

- 73 I. D. Parker. *J. Appl. Phys.*, **1994**. 75, 1656–1666.
- 74 D. Moses. *Appl. Phys. Lett.*, **1992**. 60, 3215–3216.
- 75 F. Hide, B. J. Schwartz, M. A. Díaz-García, and A. J. Heeger. *Chem. Phys. Lett.*, **1996**. 256, 424–430.
- 76 F. Hide, B. J. Schwartz, M. A. Díaz-García, and A. J. Heeger. *Synth. Met.*, **1997**. 91, 35–40.
- 77 J. Y. Park, V. I. Srdanaov, A. J. Heeger, C. H. Lee, and Y. W. Park. *Synth. Met.*, **1999**. 106, 35–38.
- 78 A. K. Sheridan, G. A. Turnbull, A. N. Safonov, and I. D. W. Samuel. *Phys. Rev. B*, **2000**. 62, R11929–R11932.
- 79 G. A. Turnbull, P. Andrew, M. J. Jory, W. L. Barnes, and I. D. W. Samuel. *Phys. Rev. B*, **2001**. 64, 125122.
- 80 G. Kranzelbinder, E. Toussaere, J. Zyss, A. Pogantsch, L. E. W. J., and H.-H. Tillmann, H. an Hörhold. *Appl. Phys. Lett.*, **2002**. 80, 716–718.
- 81 G. A. Turnbull, P. Andrew, W. L. Barnes, and I. D. W. Samuel. *Appl. Phys. Lett.*, **2003**. 82, 313–315.
- 82 A. W. Grice, D. D. C. Bradley, M. T. Bernius, M. Inbasekaran, W. W. Wu, and E. P. Woo. *Appl. Phys. Lett.*, **1998**. 73, 629–631.
- 83 R. Xia, G. Heliotis, and D. D. C. Bradley. *Appl. Phys. Lett.*, **2003**. 82, 3599–3601.
- 84 G. Heliotis, D. D. C. Bradley, G. A. Turnbull, and I. D. W. Samuel. *Appl. Phys. Lett.*, **2002**. 81, 415–417.
- 85 G. Heliotis, R. Xia, G. A. Turnbull, P. Andrew, W. L. Barnes, I. D. W. Samuel and D. D. C. Bradley. *Adv. Funct. Mater.*, **2004**. 14, 91–97.
- 86 V. G. Kozlov, G. Parthasarathy, P. E. Burrows, S. R. Forrest, Y. You, and M. E. Thompson. *Appl. Phys. Lett.*, **1998**. 72, 144–146.
- 87 M. A. Díaz-García, F. Hide, B. J. Schwartz, M. D. McGehee, M. R. Anderson, and A. J. Heeger. *Appl. Phys. Lett.*, **1997**. 70, 3191–3194.
- 88 T. Granlund, M. Theander, M. Berggren, M. Andersson, A. Ruzäckas, and V. Sundstrom. *Chem. Phys. Lett.*, **1998**. 288, 879–884.
- 89 S. E. Burns, G. Denton, N. Tessler, M. A. Stevens, F. Caicalli, and R. H. Friend. *Opt. Mater.*, **1998**. 9, 18–24.
- 90 A. Schülzgen, C. Spiegelberg, M. Morell, S. B. Mendes, B. Kippelen, and N. Peyghambarian. *Appl. Phys. Lett.*, **1998**. 72, 879–881.
- 91 T. Granlund, M. Theander, M. Berggren, M. Andersson, A. Ruzäckas, G. B. V. Sundström, M. Granstrom, and O. Inganäs. *Synth. Met.*, **1999**. 102, 1038–1041.
- 92 N. Deepak Kumar, J. D. Bhawalkar, P. N. Prasad, F. E. Karasz, and B. Hu. *Appl. Phys. Lett.*, **1999**. 71, 999–1001.
- 93 G. Wegmann, H. Giessen, A. Greiner, and R. F. Mahrt. *Phys. Rev. B*, **1998**. 57, R4218–4221.
- 94 S. V. Frolov, M. Shkunov, and Z. V. Vardeny. *Phys. Rev. B*, **1997**. 56, 4363–4365.
- 95 M. Berggren, A. Dodabalapur, Z. Bao, and R. E. Slusher. *Adv. Mater.*, **1997**. 9, 968–971.
- 96 Y. Kawabe, C. Spiegelberg, A. Schülzgen, M. F. Nabor, B. Kippelen, E. A. Mash, P. M. Allemand, M. Kuwata-Gonokami, K. Takeda, and N. Peyghambarian. *Appl. Phys. Lett.*, **1998**. 72, 141–143.
- 97 S. V. Frolov, Z. V. Vardeny, and K. Yoshino. *Appl. Phys. Lett.*, **1998**. 72, 1802–1804.
- 98 G. Ramos-Ortiz, C. Spiegelberg, N. Peyghambarian, and B. Kippelen. *Appl. Phys. Lett.*, **2000**. 77, 2783–2785.
- 99 R. C. Polson, G. Levina, and Z. V. Vardeny. *Appl. Phys. Lett.*, **2000**. 76, 3858–3860.
- 100 M. D. McGehee, M. A. Díaz-García, F. Hide, R. Gupta, E. K. Miller, D. Moses, and A. J. Heeger. *Appl. Phys. Lett.*, **1998**. 72, 1536–1538.
- 101 C. Kallinger, M. Hilmer, A. Haugeneder, M. Perner, W. Spirk, U. Lemmer, J. Feldmann, U. Scherf, K. Müllen, A. Gombert, and V. Wittwer. *Adv. Mater.*, **1998**. 10, 920–923.
- 102 M. Ichikawa, Y. Tanaka, N. Suganuma, T. Koyama, and Y. Taniguchi. *Jpn. J. Appl. Phys.*, **2001**. 40, L799–L801.
- 103 G. Heliotis, R. Xia, D. D. C. Bradley, G. A. Turnbull, I. D. W. Samuel, P. Andrew, and W. L. Barnes. *Appl. Phys. Lett.*, **2003**. 83, 2118–2120.
- 104 M. Meier, A. Mekis, A. Dodabalapur, A. Timko, R. E. Slusher, J. D. Joannopoulos, and O. Nalamasu. *Appl. Phys. Lett.*, **1999**. 74, 7–9.
- 105 J. Stehr, J. Crewett, F. Schindler, R. Sperling, G. v. Plessen, U. Lemmer, J. M. Lupton, T. A. Klar, J. Feldmann,

- A. W. Holleitner, M. Forster, and U. Scherf. *Adv. Mater.*, **2003**. 15, 1726–1729.
- 106** G. Langer, A. Pogantsch, K. F. I. T. Neger, and W. Kern. *Synth. Met.*, **2003**. 137, 997–998.
- 107** D. Wright, E. Brasselet, J. Zyss, G. Langer, A. Pogantsch, K. F. I. T. Neger, and W. Kern. *Opt. Expr.*, **2004**. 12, 325–330.
- 108** A. Yariv and M. Nakamura. *IEEE J. Quantum Electron.*, **1977**. QE-13, 233–253.
- 109** S. Riechel, U. Lemmer, J. Feldmann, S. Berleb, A. G. Mückl, W. Büttling, A. Gombert, and V. Wittwer. *Opt. Lett.*, **2001**. 26, 593–595.
- 110** R. Farchioni and G. Grosso. *Organic Electronic Materials*. Springer, Pisa, **2001**.
- 111** V. Bulović, V. B. Khalfin, G. Gu, P. E. Burrows, D. Z. Garbuzov, and S. R. Forrest. *Phys. Rev. B*, **1998**. 58, 3730–3740.
- 112** M. A. Baldo, Z. G. Soos, and S. R. Forrest. *Chem. Phys. Lett.*, **2001**. 347, 297–303.
- 113** C. F. Madigan and V. Bulović. *Phys. Rev. Lett.*, **2003**. 91, 247403.
- 114** H.-P. Gauggel, H. Artmann, C. Geng, F. Scholz, and H. Schweizer. *IEEE Photon. Technol. Lett.*, **1997**. 9, 14–18.
- 115** J. D. Thomson, H. D. Summers, P. J. Hulver, P. M. Smowton, and P. Blood. *Appl. Phys. Lett.*, **1999**. 75, 2527–2529.
- 116** M. Ichikawa, Y. Tanaka, N. Suganuma, T. Koyama, and Y. Taniguchi. *Jpn. J. Appl. Phys.*, **2003**. 42, 5590–5593.
- 117** M. Gaal, C. Gadermaier, H. Plank, E. Moderegger, A. Pogantsch, G. Leising, and E. J. W. List. *Adv. Mater.*, **2003**. 15, 1165–1167.
- 118** G. Khanarian and Hoechst Celanese. *Opt. Eng.*, **2001**. 40, 1024–1029.
- 119** T. Nielsen, D. Nilsson, F. Bundgaard, P. Shi, P. Szabo, O. Geschke, and A. Kristensen. *J. Vac. Sci. Technol. B*, **2004**. 22, 1770–1775.
- 120** H. Kogelnik and C. V. Shank. *J. Appl. Phys.*, **1972**. 43, 2327–2335.
- 121** J. Huang, M. Pfeiffer, A. Werner, J. Blochwitz, K. Leo, and S. Liu. *Appl. Phys. Lett.*, **2002**. 80, 139–141.
- 122** M. Reufer, S. Riechel, J. M. Lupton, J. Feldmann, U. Lemmer, D. Schneider, T. Benstem, T. Dobbertin, W. Kowalsky, A. Gombert, K. Forberich, V. Wittwer, and U. Scherf. *Appl. Phys. Lett.*, **2004**. 84, 3262–3264.
- 123** P. Andrew, G. A. Turnbull, I. D. W. Samuel, and W. L. Barnes. *Appl. Phys. Lett.*, **2002**. 81, 954–956.
- 124** N. Tessler, N. T. Harrison, and R. H. Friend. *Adv. Mater.*, **1998**. 10, 64–68.
- 125** I. H. Campbell and D. L. Smith. *Appl. Phys. Lett.*, **1999**. 74, 561–563.
- 126** W. Yokoyama, H. Sasabe, and C. Adachi. *Jpn. J. Appl. Phys.*, **2003**. 42, L1353–L1355.

## Index

### A

- absorption spectra 155
  - DCM2 376
  - luminescent conjugated polymers 95 f, 99
  - organic semiconductor lasers 370
  - phosphorescence devices 338 f
  - polyfluorenes 47, 174 f
  - polymer heterojunctions 35 ff
  - semiconducting polymers 154
  - sexiphenyl 381
- acceptors 40, 53
- acetylacetonates 335 f
- acrylates 300
- activation energies 58
- active layers 333 f
- active-matrix displays 151 ff, 167
- active sites 293
- aggregates
  - dendrimers 271 ff, 276 ff
  - luminescent conjugated polymers 102 ff
  - polymer heterojunctions 37
- AlAs/GaAs semiconductors 13
- AlGaInP semiconductors 1, 16
- alkoxy substituents
  - organic semiconductor lasers 373
  - phenylenevinylenes 97
  - phosphorescence devices 359
  - polymer synthesis 215, 223
- alkyl substituents
  - organic semiconductor lasers 373
  - phenylenevinylenes 97
  - polymer synthesis 215 f, 224
  - polythiophenes 235
- all-trans oligomers (DHep-OPVn) 97 ff
- aluminum cathodes 162, 389
- aluminum layers 63, 72
- aluminum/polymer interfaces 185 f, 196 f
- aluminum-tris-(8-hydroxyquinilone) (Alq<sub>3</sub>)
  - amorphous materials 249, 257
  - dendrimers 265
  - hybrid semiconductor nanocrystals 321
  - metal/polymer interfaces 181 ff, 208 ff
  - organic semiconductor lasers 370, 378, 388
  - phosphorescence devices 334
- aminonaphthalimides 298 f
- amorphous molecular materials 245–264
- amplified spontaneous emission (ASE) 307, 372, 388
- analytic molecular theory 95
- annealing 46, 50
- annihilation, triplet excitons 135
- anode materials 389
- anthracene core phenylacetylene 273
- antibonding orbitals 38
- antiside defects 7
- aqueous solution-processed nanocrystals 327 ff
- arenes 229
- aromatic units 304
- arrays 151–180
- Arrhenius plot 58, 65
- aryl substituents 215, 222–227, 373
- asymmetric dendronization 266, 272 f
- atomic transitions 13

### B

- band diagrams 1
- band edges 36 f, 71 ff, 88, 165
- bandgap 153
  - luminescent conjugated polymers 95
  - metal/polymer interfaces 183
  - phosphorescence devices 339
  - semiconductors 3
- barium cathode 160
- barrier-free capture 36 ff, 55 ff, 60 ff, 87 ff
- barrier height 162
- bathochromic shift 114
- bathocuproine (BCP) 258, 282, 334
- benzenes 131, 216–226, 379



- benzil 342
- benzphenone 143
- benzyl bromide 218
- bias 159
- bilayers 35, 62
- bimolecular recombination coefficient 2
- binary blend polymer films 45
- binding energy
  - calcium/F8BT interfaces 189
  - cesium/F8BT interfaces 194
  - luminescent conjugated polymers 95, 125
  - metal/polymer interfaces 184–214
  - polymer heterojunctions 42, 53
  - ytterbium/F8BT interfaces 198
- biomarking 385
- biphenyls
  - Bu-PBD 171, 255
  - dendrimers 272, 285
  - PBD 346 f
  - spiromaterials 379
  - triazole 325
- biphosphonates 220
- bis(methylphenyl)diphenyl(biphenyl)diamine (TPD) 325
  - amorphous materials 249 ff, 257 ff
  - crosslinking 305
  - phosphorescence devices 352
- bisbenzthiazole derivatives 305
- bit rate  $\times$  distance product 5
- blend thin films 35
- blocking interfaces 165
- blue emission 165
  - amorphous materials 260
  - crosslinking 306
  - edged exciplexes 62
  - luminescent conjugated polymers 104
  - P8BT 184 ff
  - polymer heterojunctions 58, 70, 81
  - polymer synthesis 223
  - PVK based phosphorescence devices 356 ff
  - spiromaterials 379
- blue-green-red (BGR) emission 335 ff
- Bohr exciton diameters 319
- Boltzmann constant 11, 85
- Boltzmann distribution 3
- bonding orbitals 38
- Born–Oppenheimer approximation 103
- boron containing compounds 256
- boronic acid dehydration 310
- Bragg reflector 13, 23, 375 ff
- branching 265, 268 f
- Brewster angle 23
- bridging 234 f
- brightness 161 ff, 178
  - hybrid semiconductor nanocrystals 322
  - metal/polymer interfaces 184 f
  - phosphorescence devices 347
- BuEh-PPV 154
- bulk exciton 71
- C**
  - calcium electrodes 72, 153, 160 f
  - calcium/polymer interfaces 185 f, 188 f, 196 f
  - capture-via-charge injection 36 ff, 60 ff, 87 ff
  - carbazole biphenyl (CBP)
    - dendrimers 282
    - organic semiconductor lasers 371, 375 f, 388
    - phosphorescence devices 334, 353, 360
  - carbonyl linkers 268
  - carriers *see*: charge carriers
  - cathode materials 160 ff, 321
    - metal/polymer interfaces 183
    - organic semiconductor lasers 389
  - cationic ring opening polymerization (CROP) 297, 303 ff
  - cavities 8 ff
  - CdSe/ZnS(CdS) nanocrystals 319
  - cesium/polymer interfaces 185 ff, 192 ff
  - C–H bonds 130
  - chains 215, 223
    - chromophore substitution 237
    - luminescent conjugated polymers 104
  - charge-blocking amorphous molecular materials 245–264
  - charge capture 54 ff
  - charge carriers 1 ff
    - drift mobilities 260
    - luminescent conjugated polymers 95, 125 ff
    - polymer heterojunctions 66
  - charge injection 151–177
    - amorphous materials 245 ff
    - crosslinking 293 ff
    - phosphorescence devices 333 ff, 351
    - polyenes 236
    - polymer heterojunctions 36, 60 ff, 70
    - polymer synthesis 215
    - substituent effects 226
  - charge transfer
    - amorphous molecular materials 245–264
    - dendrimers 266, 278 ff
    - hybrid semiconductor nanocrystals 320 ff
    - luminescent conjugated polymers 127

- organic semiconductor lasers 372
  - phosphorescence devices 338 ff
  - polymer heterojunctions 36, 40, 87
  - chemical properties, metal/polymer interfaces 188 ff, 198 ff, 205 ff
  - chemical structures
    - carbazole copolymers 360
    - crosslinkable semiconductors 299
    - dendrimers 282
    - F8BT 185
    - iridium dyes 336 f
    - luminescent conjugated polymers 98 ff
    - oligofluorenes 363
    - organic laser materials 370 ff
    - oxetane hole conductors 305, 308
    - PEDOT 2080
    - polyfluorenes 44
    - polynorbornenes 302
    - radical polymers 301 f
    - trichlorosilanes 310
  - chip shaping 2, 21
  - chloroform solutions 46, 67–78, 329
  - chromophores
    - dendrimers 266 ff, 271 ff
    - hybrid semiconductor nanocrystals 322
    - luminescent conjugated polymers 102 ff, 117
    - organic semiconductor lasers 372
    - polymer synthesis 237 f
  - cinnamate cycloaddition 298
  - cis–trans transformations 101
  - cladding layers 7
  - clustering 7, 165
  - color design 151 ff, 168
    - crosslinking 311
    - dendrimers 270–292
    - hybrid semiconductor nanocrystals 319
    - phosphorescence devices 333 ff, 348 f
    - polymer synthesis 215–244
    - semiconductors 4, 22
  - color rendering index (CRI) 176, 357
  - color temperature 155, 176
  - complexation 37 ff
  - composites 321
  - conducting polymers 181
  - conduction band 35, 159, 163 ff
  - conformational relaxation 56
  - conjugated polymers
    - aromatic units 304
    - crosslinking 293
    - dendrimers 268, 272 ff
    - heterojunctions 35
    - hybrid semiconductor nanocrystals 321 f
    - luminescent polymers 101, 134
    - phosphorescence 333
    - photophysics 95–150
    - synthesis 224
  - contacts 18, 389
  - co-oligomers 308
  - copolymers 153, 165, 235
  - copper cathode 162
  - copper phthalocyanine 250
  - core-shell nanocrystals 319 ff, 322 f
  - correlation time constants 81 f
  - Coulomb interactions
    - hybrid semiconductor nanocrystals 319
    - luminescent conjugated polymers 96
    - polymer heterojunctions 36, 42, 54, 71
  - coumarin 385
  - coupling 96, 105, 230, 375
  - covalent bonds 189, 199
  - crosslinkable organic semiconductors 293–318
  - CsF/Al/polymer interfaces 185 f, 196 f
  - curing 297
  - current crowding phenomena 2
  - current spreading layers 16
  - current transport 15
  - current–brightness–voltage characteristics 349 ff, 361
  - current density–voltage–luminance characteristics 187 ff, 196, 209
  - current–light–voltage curves 355
  - current–voltage curves 162, 279
  - cyano groups 224
  - cycloaddition 298, 313
  - cyclopolymerization 296
- D**
- Davidov splitting 153, 266
  - defects 174
    - polymer heterojunctions 35
    - polymer synthesis 219
    - semiconductors 7
  - deflection spectra, polyfluorenes 47 ff
  - degradation 168
  - dehydration 310
  - delayed emission 50
  - delayed fluorescence 127, 140, 286
  - delayed photoluminescence 81
  - demixed polymer blends 36 ff
  - dendrimer light emitting diodes 265–292
  - dendrimer oxidiazole 255
  - density matrix renormalization group theory 101
  - density of states (DOS) 140

- density–brightness voltage
    - characteristics 353
  - depletion depth 158
  - deposition techniques 294, 311
  - device parameters 155
  - Dexter transfer 47 ff, 338, 342 ff
  - diarylamine 247
  - dicyanomethylenemethyl(6-julolidin-vinyl)-4H-pyran (DCM2) 370–388
  - dicyanomethylenemethyl(p-dimethylamino-styryl)-4H-pyran (DCM) 98 ff, 119 f, 370–388
  - dielectric constant 36, 95
  - dienes 300
  - diffusion 111 f, 121 f, 141
  - dilute solutions 153
  - dimers 106, 296
  - dinaphthyl anthracene(DNA) 208
  - diodes 158
  - dipole layers 183 f
  - dipole–dipole coupling 266
  - dipoles 40, 106
  - direct band gap inorganic crystals 152
  - direct gap semiconductors 6
  - dislocations 7
  - dispersion 2 ff, 111
  - displays 151–180, 319
  - dissociation
    - excitons 71 ff, 88, 125
    - polymer heterojunctions 54 f
    - Yb/CsF/Au interface 202
  - distributed Bragg reflectors (DBRs) 23 ff, 375
  - distributed feedback (DFB) lasers 371–396
  - distributed heterojunction diodes 36
  - distyrylbenzene 274, 280
  - dodecyloxy-poly(p-phenylene) (DDO-PPV) 132
  - donor–acceptor heterojunctions 40, 44, 86
  - donor–acceptor/donor transfer 117
  - doping
    - amorphous materials 248, 260
    - conjugated fluorescent polymers 117
    - crosslinking 304
    - metal/F8BT interfaces 188 ff, 192 f
    - phosphorescence devices 338 ff, 342 ff
    - spiromaterials 381
  - double-layer device 181 ff
  - dyes
    - organic semiconductor lasers 369–396
    - phosphorescence devices 335 ff, 340 ff
    - semiconductors 20 f
- E**
- edge dislocations 7
  - effective medium approximation (EMA) 139 ff
  - efficiencies 162, 171
    - dendrimers 280
    - Yb/CsF cathodes 207 f
  - electric-field dependent photoluminescence spectra 35 ff
  - electrically-driven organic lasers 389
  - electrode materials 72, 153
  - electroluminescence 152
    - dendritic materials 265, 272 ff
    - hybrid NC/OLEDs 325
    - metal/polymer interfaces 181 ff
    - NPB/Alq<sub>3</sub> 210
    - polymer heterojunctions 56–94, 83
    - polymer synthesis 215–244
    - PtEoD/PFO 341
  - electron acceptors 165
  - electron affinity
    - amorphous materials 246 ff
    - hybrid semiconductor nanocrystals 319
    - metal/polymer interfaces 183
    - polymer synthesis 226
  - electron conductors 309
  - electron dispersion relation 2
  - electron-only devices 162
  - electron transport
    - amorphous materials 245 f, 254 ff
    - crosslinking 294, 304
    - dendrimers 266, 282
    - hybrid semiconductor nanocrystals 321 f, 324 f
    - polymer heterojunctions 35
  - electron transport layers (ETL) 178, 182, 294, 370
  - electron–electron interactions 95, 130
  - electron–hole capture 36 ff, 55 f, 87 ff
  - electron–hole pairs 117, 127
    - recombination 2, 20 f, 95 ff
  - electronic properties
    - dendrimers 267, 274 ff
    - metal/polymer interfaces 182, 188 ff, 198
    - semiconductor polymer heterojunctions 35–94
  - electronic transitions 97 ff, 130
  - electron–lattice interactions 95
  - electrophosphorescence devices 333–368
  - electroreflection 95
  - electrostatic discharge (ESD) 28
  - emission-color design
    - dendrimers 270–292

- hybrid semiconductor nanocrystals 319
- phosphorescence devices 333 ff
- polymer synthesis 215–244
- emission spectra 152
- luminescent conjugated polymers 96
- semiconductors 2 ff, 13, 154 ff, 370
- emissive layers (EMLs)
  - amorphous materials 246 ff
  - crosslinking 294, 308 ff
  - dendrimers 266
  - metal/polymer interfaces 182
  - organic semiconductor lasers 372
  - phosphorescence devices 333
- encapsulation 27, 63, 72
- end-capping 165 ff
- endothermic energy transfer 58, 61 ff, 70 ff
- energy back transfer 83, 344 f
- energy funneling 265 ff, 270 ff
- energy gap 95, 387
- energy transfer
  - hybrid semiconductor nanocrystals 322 ff
  - luminescent conjugated polymers 110, 131
  - PFO–fluorenone defect 174
  - polymer heterojunctions 61, 71 ff
- enhancement spectrum 10
- enthalpy / entropy 39
- epoxy resin encapsulant 27
- erbium-doped Si/SiO<sub>2</sub> resonant cavity 13
- evaporation rate 46
- excimers
  - crosslinking 301
  - dendrimers 277
  - luminescent conjugated polymers 106
  - polymer heterojunctions 37 f
- exciplexes 36 ff, 61, 86
- excitations
  - luminescent conjugated polymers 108
  - PFO–fluorenone defect 174
  - PVK matrix 347
- excitons 153 f
  - binding energies 95
  - crosslinking 293
  - delayed photoluminescence 81
  - dendrimers 266 ff, 275 ff
  - density of states (EDOS) 111 ff, 115 ff, 121 ff
  - dissociation 54 f, 71 ff, 88, 135
  - hybrid semiconductor nanocrystals 326
  - luminescent conjugated polymers 110
  - metal/polymer interfaces 182
  - polymer heterojunctions 35 ff
  - regeneration 71
  - retrapping 78 ff, 83 ff
  - extinction spectra 45
  - extraction efficiency 2, 15, 19 ff

**F**

  - F8 (poly(9,9'-dioctylfluorene) 43–94
  - F8:PFB/TFB exciplex 51 f
  - F8BT (poly(9,9'-dioctylfluorene-co-benzothiadiazole) 43–94
  - F8BT/metal interfaces 185 ff
  - Fabry–Perot resonators 8, 371, 374
  - fan cooling 28
  - Fermi levels 158 ff, 183, 190
  - ferrocene 254
  - field-effect transistors 35
  - films 182, 297
  - FIrpic (iridium) dyes 336 ff, 344 ff, 356 ff
  - flat-band condition 159 ff
  - flip-chip GaInN LED 18
  - fluorenes
    - crosslinking 308 ff
    - dendrimers 272
    - metal/polymer interfaces 184 ff
    - polymer synthesis 229
    - thiophene substituent effects 236
  - fluorenonones 173 f
  - fluorescence 1
    - amorphous materials 245
    - doped conjugated polymers 117 ff
    - luminescent conjugated polymers 95–150
    - phosphorescence devices 333
    - polymer heterojunctions 59
    - PPV 114
  - Förster mechanism 175 f
    - hybrid semiconductor nanocrystals 322 ff
    - luminescent conjugated polymers 112 ff
    - organic semiconductor lasers 381
    - phosphorescence devices 338 f, 348 ff
  - forward bias 159
  - Fowler–Norheim mechanism 151 ff, 158 ff, 163 ff
  - fractals 265
  - Franck–Condon principle
    - luminescent conjugated polymers 96, 103, 126 ff, 144
    - polymer heterojunctions 39
  - Fréchet type poly(aryl ether) 272
  - frustrated energy relaxation 142
  - full-color emission 169 ff, 174
    - crosslinking 294 ff
    - hybrid semiconductor nanocrystals 319
  - full width at half maximum (FWHM)
    - cesium/F8BT interfaces 194

- luminescent conjugated polymers 142
- semiconductors 6
- gold 186
- functional groups 327, 362
- functional inks 168

## G

- GaAsP semiconductors 1
- gain spectrum, DCM2 377
- GaIn/AlGaInP resonant cavity 15
- gap states 35
- gas phase 40
- gate detection techniques 131
- Gaussian density distribution 114, 141
- Gaussian optical spectra 6, 11, 106
- gel-permeation chromatography (GPC) 270
- geminate pairs 71–88, 117, 127
- Gilch polymerization 218
- glass substrate 152
- glass transition 247, 254, 372
- gold electrodes 162, 389
- gold polymer interfaces 201
- grating periods 388
- grazing incidence X-ray diffraction (GIXD) 102
- green emission
  - F8BT 185
  - Ir(ppy)<sub>3</sub> 344
  - iridium dyes 336
  - polymer synthesis 224
  - PVK based phosphorescence devices 346 ff
- Grignard metathesis (GRIM) 232
- ground state complex 37
- group II–VI/III–V nanocrystals 319
- guest–host systems 338 ff, 370–396

## H

- Hagihara–Sonogashira coupling 227
- haloarenes 221, 227
- head-to-tail coupling 227
- heatsink slug 27
- Heck coupling 221, 237
- heterocyclic polysynthesis 233
- heterojunction 1, 35–94
- hexane dithiol 321
- high-efficiency polymers 219 ff
- high-voltage limit 66
- highest occupied molecular orbital (HOMO) 166, 176
  - amorphous materials 257
  - crosslinking 306
  - hybrid semiconductor nanocrystals 324

- luminescent conjugated polymers 96, 106, 129
- metal/polymer interfaces 183 f, 190
- phosphorescence devices 336, 352
- polymer heterojunctions 38 f, 43 ff, 53, 66
- highly reflective mirrors 2
- hole acceptors 165
- hole blocking layers 165 ff
  - amorphous materials 246 ff, 257
  - phosphorescence devices 346 f
- hole conductors 305
- hole dispersion relation 2
- hole drift mobilities 261
- hole-induced triplet decay 137
- hole injection 35, 159, 293
- hole-only devices 162 f
- hole transport layers (HTL) 178
  - amorphous materials 245 ff
  - crosslinking 294
  - dendrimers 266, 282
  - hybrid semiconductor nanocrystals 321 f, 324 f
  - metal/polymer interfaces 182
  - phosphorescence devices 361
- homopolymers 153, 235
- hopping
  - crosslinking 293
  - dendrimers 266 ff, 276 ff
  - hybrid semiconductor nanocrystals 323
  - luminescent conjugated polymers 139
  - metal/polymer interfaces 182
- Hörhold polymerization 218, 222
- Horner polycondensation 220, 237
- host–guest systems 338 ff, 358 ff
- Huang–Rhys factor 103 ff, 115 f, 96 ff
- hybrid OLEDs 319–332
- hydrolysis 310

## I

- illuminance 155
- impurities 7, 165, 174
- InAs/ZnS 329
- indirect gap semiconductors 6
- indium cathode 162
- indium tin oxide (ITO) 152, 160
  - amorphous materials 249
  - crosslinking 293
  - dendrimers 279
  - hybrid semiconductor nanocrystals 321
  - metal/polymer interfaces 182 ff, 185 ff
  - organic semiconductor lasers 389
  - polymer heterojunctions 63, 71
- injection barrier 182

- injection geometry 16
  - ink-jet printing 168
    - crosslinking 294
    - dendrimers 265 f
    - polymer heterojunctions 60
  - inorganic semiconductors 1–34
  - insulating substrates 17
  - intensity 155
  - interchain interactions 153
  - interchromophoric coupling 102, 276
  - interdigitated structures 18
  - interfaces
    - metal/polymer 181–214
    - polymer heterojunctions 37, 78 f, 88
  - intermediates 216
  - intermolecular dendrimer interactions 267, 274 ff
  - intermolecular distance 42
  - internal reflection 2, 307
  - interstitials 7
  - intersystem crossing (ISC) 130, 135, 342
  - intrinsic photogeneration 125 f
  - iodonium 303
  - ionization potential 183, 246 ff
  - iridium-based dendritic materials 272 ff, 283 f
  - iridium dyes 336 ff
    - HFP complexes 173 ff
    - Ir(DPF)<sub>3</sub> 347
    - Ir(ppy)<sub>3</sub> 336 f, 344 ff
  - isolated chains 104
- J**
- J-aggregates 102
  - joint dispersion relation 4
  - Joule heating 70
- K**
- Knoevenagel polycondensation 220, 237
  - Kohlrausch–Williams–Watt (KKW) function 118
- L**
- ladder type poly(phenylene)s (LPPPs)
    - luminescent conjugated polymers 144
    - phosphorescence devices 333 ff, 343 ff
    - photophysics 101 ff
    - polymer synthesis 228
  - see also*: methyl substituted–
  - Lambertian intensity profile 155 f
  - Langevin electron hole recombination 95 ff
  - Langmuir–Blodgett technique 298
  - large-band gap blue emitting polymers 165
  - laser-induced thermal imaging (LITI) 294, 311 f
  - lasers, organic semiconductor 369–396
  - lattice atoms 6
  - layers 7, 16, 153
    - amorphous materials 246
    - crosslinking 293, 298 ff
    - dendrimers 266 f
    - hole-blocking 165 f
    - luminescent conjugated polymers 102
    - metal/polymer interfaces 181 ff, 196
    - phosphorescence 333 ff
  - leakage currents 67
  - lifetimes 1
    - excitation states 109
    - luminescent conjugated polymers 126
    - polymer heterojunctions 85
    - semiconductors 9
    - triplet excitons 137
  - ligand shells 319
  - light-emitting diodes (LEDs) 1–34 ff
  - light-to-heat conversion (LTHC) 311
  - linewidth 4
  - linkers
    - dendrimers 268 ff
    - hybrid semiconductor nanocrystals 321
    - organic semiconductor lasers 372
  - liquid-crystal technology 167, 293
  - lithium fluoride calcium cathode 351, 389
  - lithium/polymer interfaces 185 ff, 196 f
  - Littrow configuration 374
  - localization effect, dendrimers 276
  - Lorentzian enhancement spectrum 11
  - losses 389
  - low-temperature barrier-free capture 62
  - lower band gap substrates 2
  - lowest unoccupied molecular orbital (LUMO) 166, 176
    - amorphous materials 257
    - hybrid semiconductor nanocrystals 323
    - luminescent conjugated polymers 96, 106, 129
    - metal/polymer interfaces 183 f, 190
    - phosphorescence devices 336, 352
    - polymer heterojunctions 38 f, 43 ff, 53, 66
  - low-threshold organic semiconductor lasers 369–396
  - luminescence 13, 95–150, 155, 161 ff, 177
  - luminescence efficiency 156
    - crosslinking 304
    - metal/polymer interfaces 182
    - phosphorescence devices 336
    - semiconductors 22

luminescent polymers 166 f  
lumophores 276, 319

## M

magnesium electrode 160, 321  
magnesium-silver electrode 321, 389  
main chains 237, 296  
matrix-assisted laser desorption/ionization  
time-of-flight (MALDI-TOF) 270  
McCulloch crosscoupling 231 f  
McMurry polycondensation 222  
mechanical stress 297  
meta-conjugations, dendrimers 268, 272  
metal-to-ligand charge transfer  
(MLCT) 336 ff  
metal/polymer interfaces 181–214  
metaphenylenes 224  
meta-substitution 285  
metathesis polymerization 216, 222 ff  
methacrylates 298 ff  
methoxylation 216, 225  
methyl substituted ladder ladder type  
poly(phenylene) (MeLPPP)  
– organic semiconductor lasers 373  
– phosphorescence devices 359  
– luminescent conjugated polymers 99 ff,  
126  
methyltetrahydrofuran (MTHF) 97 ff, 107 ff  
microinjection molding in capillaries  
(MIMIC) 314, 386  
Miller–Abrahams equation 139  
mirror symmetry 97  
mobilities 111, 260  
moieties 295  
molecular complexes/excimeres 37 ff, 40 f  
molecular materials, amorphous 245–264  
momentum 3  
monochromatic spectrum 5  
monochrome displays 167  
monodispersivity 270, 286  
monomer crosslinking 297  
Monte Carlo simulation 139 ff  
morphology dependent exciton  
retrapping 78 ff  
multilayer deposition 294 ff, 311  
multilayer heterojunction structures 36 f  
multilayer white PLEDs 178  
multiple quantum well (MQW) 26

## N

n-type contacts 18  
nanocrystal semiconductors 319–3332  
nanometer scale morphologies 86

naphthalenes 219  
 $\alpha$ -naphthylphenylbiphenyl diamine  
(NPD) 249, 257 ff  
– dendrimers 273  
– hybrid semiconductor nanocrystals 329  
– metal interfaces 208 ff  
– organic semiconductor lasers 371, 375 f,  
388  
near infrared (NIR)-LEDs 328  
network formation 301 ff

## O

octaethyl-porphine platinum (pPtEOP) 335  
ohmic contacts 16 f  
olefin copolymers 386  
oligo(p-phenylene)s (OPPs) 359  
oligoarylenes 237  
oligofluorenes 344 f, 362  
oligomers  
– crosslinking 293  
– luminescent conjugated polymers 97 ff  
– phosphorescence devices 333 f  
oligophenylenes  
– organic semiconductor lasers 372  
– polymer synthesis 226  
– spiromaterials 379  
oligothiopenes 372  
omnidirectional reflectors (ODRs) 23 ff  
onium compounds 303  
Onsager's theory 128  
operating voltage 162  
optical fibers 5, 14  
optical gain 376  
optical processes 9, 37 ff  
optical properties 155, 297  
optical spectra 1 ff, 106  
  *see also*: luminescence, phosphorescence  
  etc.  
optical transfer matrix method 25  
optical triplet generation 145  
optically detected magnetic resonance  
(ODMR) 131  
optically-induced charge carrier  
generation 125 ff  
orbitals 38  
  *see also*: HOMO, LUMO  
organic semiconductor lasers 369–396  
organic solvents processing 321 ff  
orthogonal solvents processing 295  
orthophenylenes 221, 225  
ortho-substituents 224  
oscillator strength 117 ff, 143, 170  
oxetanes 303

- oxidation potentials 254
- oxidative coupling 229
- oxiadazole derivatives 255, 321
- oxiadazolelphenylene (OXD) 346 f
- oxygen plasma treated indium tin oxide 63, 71
- P**
- p-type contacts 18
- packaging 27 ff
- paraphenylenes 225
- parasitic perturbations 266
- parasitic voltage drops 2
- para-substitution 285
- parity forbidden states 105
- passivation 319
- patterning 311
- pedestal shaped chips 21
- permeability 168
- permittivity, dielectric 95
- PET substrate 152
- PFB (poly(9,9'-dioctylfluorene-co-bis-N,N-(4-butylphenyl)-bis-N,N'-phenyl-1,4-phenylenediamine) 43
- PFB:F8BT exciplexes 46 ff
- phase separation 165
  - dendrimers 267
  - polymer heterojunctions 42
- phenyl groups 97, 133, 198
- phenyl substituted poly(phenylene vinylene) (PhPPV)
  - doped conjugated polymers 117
  - luminescent conjugated polymers 98 ff, 109 ff
  - triplet states 135, 137 ff
- phenylacetylene 272, 276
- phenylenes 221
- phonons 108, 111
- phosphorescence
  - amorphous materials 245
  - luminescent conjugated polymers 95–150
- phosphorescence devices 333–368
- photocurrents 71
- photoelectron spectra, metal/polymer interfaces 185 ff
- photoemission 36, 54, 125 f, 129
- photoexcitation 342
- photoinduced electron transfer (PET) 304
- photoinduced triplet–triplet absorption (PIA) 131
- photoluminescence 153, 171, 220, 319
- photoluminescence spectra
  - CdSe/ZnS 320
  - DCM2 376
  - F8BT 185 f
  - InAs/ZnS NCs 329
  - PhPPV 110
  - polyfluorenes 46–94
  - polymer heterojunctions 35–94
  - semiconductors 14
  - sexiphenyl 381
- photoluminescence upconversion (PLUC) 72 f
- photometry 155
- photonic crystal structures 7
- photons 2 f, 293
- photophysics
  - luminescent conjugated polymers 95–150
  - polymer heterojunctions 35–94
- photopic luminosity 155
- photoresists 312
- photothermal deflection spectra, polyfluorenes 47 ff
- photovoltaic behavior, heterojunctions 36
- photovoltaic cells 35
- photovoltaic diodes 44, 71
- $\pi$  bands 159 ff, 163 ff
- $\pi$  conjugated polymers
  - luminescent 97 ff, 105 ff, 143
  - phosphorescent 333
  - heterojunctions 35
- pixilated displays 151, 167 ff
- Planck's constant 2, 162
- plastic optical fibers 14
- platinum anodes 389
- platinum-porphyrin 273, 283
- platinum tetraethyl-tetramethylporphyrin (PtOX) 354
- p-n junctions 1 f, 17
- point defects 7
- Poisson formula 122
- polarity change 295
- polarons 160
  - calcium/F8BT interfaces 190
  - dendrimers 286
  - luminescent conjugated polymers 95
  - polymer heterojunctions 83
- polyacetylenes 95
- polyaddition 296
- poly(allylamine hydrochloride) (PAH) 327
- polyamidoamine 272
- polyaniline 152, 160
- poly(arylene ethylene) (PAE) 227
- poly(arylene vinylene) (PAV) 215 ff
- polyarylenes 227 ff, 233
- poly(2,7-9,9-bis(2-ethyl)fluorene) (PF2/6) 98 ff, 112, 132– 144



- poly(9,9-bis(2-ethylhexyl)fluorene-2,7-diyl) (PF2/6) 342
- polycarbonate 119
- polychinoxalin 128
- polycondensation 216, 220 ff, 296
- poly(2-(6-cyanomethylheptyloxy)-phenylene) (CN-PPP) 328
- poly(9,9-(dihexylfluorenyl-diyl)co-benzothiadiazole) (F6BT) 328
- poly(diallyldimethylammonium chloride) (PDDA) 328
- poly(9,9'-dioctylfluorene) (F8) 43–94
- poly(9,9'-dioctylfluorene-co-benzothiadiazole) (F8BT) 43–94, 184 ff
- poly(9,9'-dioctylfluorene-co-bis-N,N-(4-butylphenyl)-bis-N,N'-phenyl-1,4-phenylene-diamine) (PFB) 43
  - see also*: PFB
- poly(9,9'-dioctylfluorene-co-N-(4-butylphenyl)-diphenylamine) (TFB) 43–94, 71 ff, 76
  - see also*: TFB
- polyenes 95
- poly(3,4-ethylene dioxathiophene) (PEDOT) 160
  - crosslinking 295, 306
  - interfaces 196, 208
  - PEDOT:PSS 63, 176, 250, 324
- poly(fluorene phenylene) copolymers 308
- polyfluorenes (PFOs) 173 ff
  - crosslinking 301, 308
  - dendrimers 286
  - exciplex-to-exciton energy transfer 61
  - heterojunctions 35–94
  - luminescent conjugated polymers 112 ff
  - metal/polymer interfaces 182 f, 184 ff
  - organic semiconductor lasers 372 ff, 388
  - phosphorescence devices 333 ff
  - polymer heterojunctions 86
  - white electrophosphorescent 176
  - ytterbium/F8BT interfaces 199
- polyimides 295
- poly(2,8-indenofluorene (PIF) 132
- polymer backbone 133
- polymer blends 42 ff, 55 f, 71
- polymer electrophosphorescence devices 333–368
- polymer heterojunctions 35–94
- polymer hosts/guests 340 ff
- polymer light emitting electrodes (PLEDs) 151–185
- polymerization routes 216 ff, 295
- polymers, conjugated luminescent 95–150
- polymethacrylic acid (PMA) 323
- poly(2-methoxy-5-(2-ethylhexyloxy)-1,4-phenylenevinylene) (MEH-PPV) 153 ff, 161 f, 170
  - dendrimers 266
  - hybrid semiconductor nanocrystals 328 f
  - luminescent conjugated polymers 102 ff
  - organic semiconductor lasers 373, 388
  - phosphorescence devices 348
  - polymer synthesis 215 ff
  - ytterbium/F8BT interfaces 199
- poly(methyl methacrylate) (PMMA) encapsulants 29
- polynorbornenes 302
- poly(phenyl phenylene-vinylene) (PPP) 98 ff, 119
- poly(phenylene oxadiazole)s 233
- poly(phenylene)s, photophysics 101 ff
- poly(p-phenylene) (PPP)
  - organic semiconductor lasers 372 ff
  - phosphorescence devices 333 ff
  - polymer synthesis 232 f
  - ytterbium/F8BT interfaces 199
- poly(p-phenylene vinylene) (PPV) 158, 170
  - crosslinking 295
  - dendrimers 266 f
  - hybrid semiconductor nanocrystals 321 ff, 327 f
  - luminescent conjugated polymers 98 ff, 114
  - metal/polymer interfaces 184 ff
  - organic semiconductor lasers 372 ff
  - phosphorescence devices 333 ff
  - polymer heterojunctions 35
  - synthesis 215 f, 228
- polypyrrole 160
- polyquinolines 233
- polystyrene 305, 324
- polythiophenes 229, 235 f
- poly(vinylcarbazole) (PVK) based phosphorescence devices 345 ff, 354 ff
- poly(vinylcarbazole)sulfonic lithium (PVK-SO<sub>3</sub>Li) 178
- porphyrins 274, 340
- power packaging 27
- precursors
  - crosslinking 295
  - dendrimers 266
  - polymer synthesis 215 ff, 232 ff
- printed-circuit board (PCB) 29
- proton generation 304
- pulse radiolysis-induced energy transfer 131
- pyrene derivatives 308

**Q**

- Q band 336
- quantum confinement 319
- quantum efficiency 1, 153
  - amorphous materials 245
  - crosslinking 298 f
  - dendrimers 279
  - hybrid semiconductor nanocrystals 322
  - phosphorescence devices 333 ff, 346 f
  - polymer heterojunctions 71
  - semiconductors 19
- quantum-well structures 153
- quartz crystal microbalance 187
- quaterphenyl-based spiromaterials 384 f
- quenching 153, 171
  - dendrimers 275, 278
  - luminescent conjugated polymers 129, 136
  - phosphorescence devices 344
  - polymer heterojunctions 72, 75
- quinodimethane polymerization 216 ff

**R**

- radiance 155
- radiative recombination processes 1
- radical polymerization 95, 300 ff, 313
- radiometry 155
- random-walk theory 126
- rare-earth central metals 335
- reabsorption 113
- reactive groups 297
- recombination 1
  - amorphous materials 248
  - electron–hole 95 ff
  - geminate pairs 71 ff
  - hybrid semiconductor nanocrystals 324
  - luminescent conjugated polymers 128
  - nonradiative 6
  - phosphorescence devices 333, 342 ff
  - polymer heterojunctions 44
- red emission
  - excitons 72
  - iridium dyes 336
  - luminescent conjugated polymers 102
  - polymer heterojunctions 46, 58, 61
  - polymer synthesis 223
  - PtOEP 335 ff, 339 ff
  - PVK based phosphorescence devices 354 ff
  - semiconductors 4
- red-green-blue emission (RGB) 294, 308, 312
- red-tail aggregate 277
- reductive coupling 229

## reflection

- crosslinking 307
  - luminescent conjugated polymers 95
  - semiconductors 2, 13, 19, 24 ff
- refractive index
- organic semiconductor lasers 374
  - phosphorescence devices 333
  - semiconductors 9, 24
- regeneration, heterojunctions 71 ff, 77 ff
- regioregularity 221, 228, 231 f
- relaxation
- crosslinking 293
  - luminescent conjugated polymers 97, 112
  - phosphorescence devices 334
  - polymer heterojunctions 40, 54 ff
- renormalization group theory 101
- residual gas analyzer (RSG) 186
- resistance, thermal 28
- resonant cavity LEDs (RC-LEDs) 2, 7 ff, 20
- resonators 370, 374 ff
- retrapping 78 ff, 83 ff
- reverse photoinduced charge transfer 87
- rhodamine 385
- Rieke crosscoupling 231 f
- ring-opening metathesis polymerization (ROMP) 222 f
- roll-to-roll manufacturing 169, 179

**S**

- Scheibe-aggregates 102
- Schottky–Mott limit 183
- screw dislocations 7
- self-absorption 370
- semiconductors 152
  - crosslinkable 293–318
  - direct band gap 6
  - inorganic 1–34
  - lasers 369–396
  - nanocrystals 319–332
  - polymer heterojunctions 35–94
- sensitized photogeneration 129
- sexiphenyl 372 ff, 379 f
- shielding dendrimers 275
- Shockley–Read recombination 7
- shrinkage 297, 303
- side chains 153
  - metal/polymer interfaces 185, 199
  - polymer synthesis 223, 238
  - reaction doping 304
- silicone encapsulants 28
- silole derivatives 256
- silver cathodes 162, 321, 389
- silver layers 193, 196

- silyl chains 215, 224
  - single-layer devices 162 f, 324, 359
  - singlets 171
    - crosslinking 294
    - luminescent conjugated polymers 95 ff, 110, 126–137
    - phosphorescence devices 338
  - site hopping 139
  - site-selectively excited defect emission 105
  - sodium/polymer interfaces 185 ff
  - solid-state solvation effect (SSSE) 371, 377
  - solutions 37–53, 167, 266
  - Soret band 335
  - spacers 237, 286, 297
  - spectral broadening 97 ff, 107
  - spectral diffusion 111 f, 121 f
  - spectral linewidth 4
  - spectral position 387
  - spectroradiometry 155
  - spin coating 153, 167, 215
    - amorphous materials 247
    - crosslinking 294, 297 f
    - heterojunctions 46, 63, 67, 71
    - hybrid semiconductor nanocrystals 325
    - luminescent conjugated polymers 102
    - metal/polymer interfaces 182 f
  - spin multiplicity 60, 77, 294
  - spin orbit coupling 130, 335 ff
  - spirobifluorenes 308
  - spirocompounds 247, 372–388
  - splitting 102 ff, 145, 153, 266
  - spontaneous emission 1, 9
  - stability, electroluminescent polymers 239
  - stabilization energy, heterojunctions 38 ff
  - stacking 311
  - starbursts 266, 270
  - Stark shifts 72
  - steric effects 104, 223, 379
  - Stern–Volmer plots 344
  - stilbenes
    - dendrimers 272
    - DPVB/Bi compounds 372 ff, 384 ff
    - organic semiconductor lasers 371 ff, 379 ff, 388
  - stimulated emission 370
  - Stokes shift 97, 106 f, 113, 144
  - structure–property relationship 223 ff, 234 ff, 267
  - substituents 217 ff
    - dendrimers 285
    - emission color tuning 223 ff
  - substrate-independent cathodes 207 ff
  - substrates 152
  - sulfinyl precursors 217
  - sulfonium precursors 295, 303
  - surface analysis 1, 155
    - dendrimers 269 ff
    - metal/polymer interfaces 185
    - semiconductors 20
    - sexiphenyl 380
  - Suzuki polycondensation 230 f, 237
  - symmetry 97
  - synthetic routes
    - electroluminescent polymers 215–244, 295
    - hybrid semiconductor nanocrystals 319
- T**
- temperature-dependent fluorescence 114
  - temperature-dependent luminescence 35 ff, 57
  - temperature-dependent capture 62
  - terbium complexes 335 ff
  - termed dendrons 268
  - tetraarylmethane 247
  - tetracene 97
  - TFB (9,9'-dioctylfluorene-co-N-(4-butylphenyl)diphenylamine) 43–94  
*see also:* (poly(9,9'-dioctylfluorene-co-N-(4-butylphenyl)diphenylamine)
  - TFB:F8BT 49, 71 ff, 76
  - thermal activation 59
  - thermal phonons 111
  - thermal resistance 28
  - thermalization distances 78
  - thickness dependence, electroluminescence 170
  - thienyl pyridine platinum (Pt(thpy)<sub>3</sub>) 354
  - thin film transistors (TFTs) 167
  - thin films 153, 171
    - crosslinking 297
    - organic semiconductor lasers 379
    - polymer heterojunctions 35
  - thin-layer chromatography (TLC) 270
  - thioacids 327
  - thioamines 327
  - thiophenes 226
  - time-correlated single photon counting (TCSPC) 55, 72
  - time-dependent spectral diffusion 111 f, 121 f
  - time-resolved emission spectra (TRES) 48 ff
  - time-resolved phosphorescence spectra 343
  - time-resolved photoluminescence spectra 35 ff

- Topas olefines 386  
 total internal reflection 19  
 transient absorption spectra 35 ff  
 transition dipole moments 106  
 transition metal complexes  
   – crosslinking 303  
   – dendrimers 267 ff, 272 ff, 283  
   – polycoupling 216, 221 ff, 230 f  
 transition rate 8, 95 ff  
 transmission line model (TLM) 18  
 transmittance 10, 55  
 transparent anode 293  
 transport properties 215  
 transporting layers 266  
   *see also:* electron/hole transport layers  
 trapping  
   – hybrid semiconductor nanocrystals 323  
   – phosphorescence devices 339 ff  
   – polymer heterojunctions 79  
   – semiconductors 19  
 triarylamine 247, 305  
 triarylbenzenes (TBB) 258  
 triarylboranes (TPhB) 259  
 triazine 269  
 triazole (TAZ) 256  
 trichlorosilanes 310  
 trifluorovinylethers 296  
 trilayer hybrid semiconductor  
   nanocrystals 325  
 trimers 280  
 trinitrofluorene (TNF) 98 ff, 117 ff  
 trioctylphosphin (TOPO) 320  
 triphenylamine monomers 48  
 triphenylene derivatives 300 ff  
 triple layers 24, 183  
 triplet excitons 171  
   – crosslinking 294  
   – dendrimers 281 ff  
   – hybrid semiconductor nanocrystals 326  
   – luminescent conjugated polymers 95, 110, 128–138 ff  
   – phosphorescence devices 333, 338 f  
   – polymer heterojunctions 60  
 tris(2-N-phenylbenzimidazolyl) (TPBI) 282, 346 f, 256  
 tris-(8-hydroxyquinoline)aluminum (Alq<sub>3</sub>) *see:* aluminum-tris-(8-hydroxyquinoline)  
 tris(diphenylamino)benzene (TDAB) 247 ff  
 tris(diphenylamino)phenylbenzene (TDPB) 247 ff  
 tris(diphenylamino)triphenylamine (TDATA) 247 ff  
 tris(n-carbozoyl)triphenylamine (TCTA) 282, 334  
 tris(oligoarylenyl)amine 247, 253  
 tris(phenylquinoxaline) (TQP) 256  
 tris(methylphenyl(phenyl)aminotriphenylamine) (MTDATA) 249  
 tritolylamine (TTA) 309  
 truncated inverted pyramid (TIP) chip 21  
 truxene 272  
 tunable organic lasers 375, 387  
 tunneling, Fowler–Northheim 158 ff  
 type II heterojunctions 35 ff, 44 ff, 71, 86 f
- U**
- uncertainty principle 108  
 UV emission, spiromaterials 384 f  
 UV photoelectron spectroscopy (UPS) 185 ff  
 UV/VIS spectra 97 ff, 270
- V**
- vacancies 7  
 vacuum deposition 293  
 vacuum level 36, 183  
 valence band 35, 159 ff, 163 ff  
 Vanderzane polymerization 217 f  
 vibrational energy 6  
 vibronic coupling 105  
 vibronic relaxation 334  
 vibronic structure 61, 96  
 vinyl 269  
 vinylbromobenzenes 221  
 vinylene 218  
 visible spectrum 152 f  
 voltage drops 2
- W**
- wave number 108  
 Wessling–Zimmermann polymerization 216 ff  
 wet chemical deposition 293  
 white electrophosphorescence 176 f, 357 f  
 white-line emission 151, 173 ff  
 Williamson condensation 238  
 window layers 16  
 Wittig polycondensation 220, 237
- X**
- X-ray photoelectron spectra (XPS) 185–200  
 xylene solutions 63  
 xylenyl sulfonium salts 216

**Y**

Yamamoto coupling 229, 237  
yellow emission 223, 296  
ytterbium/cesium fluoride cathodes 207 ff  
ytterbium/polymer interfaces 187 ff, 197 ff

**Z**

zero bias 159  
zero phonon lines 107